UNIVERSITÉ PARIS-SUD 11 - ORSAY

ÉCOLE DOCTORALE PHENIICS

Habilitation à Diriger des Recherches

Defended by

Dr. Grégory Moreau

On December 3rd, 2015

A walk on the Higgs side : from data-analysis to theories beyond the Standard Model

---

Prepared at the *Laboratoire de Physique Théorique*

– Jury –

Reviewers :	M. Karim Benakli	-	LPTHE Paris
	M. Aldo Deandrea	-	IPN Lyon
	M. Jean-Marie Frère	-	ULB Brussels
Examinators :	M. Abdelhak Djouadi	-	CERN Geneva
	M. François Richard	-	LAL Orsay
	Mrs. Verónica Sanz	-	US Brighton

Abstract

In the first chapter of the report, we present a synthesis of all the projects carried out during the academic career, starting with the PhD Thesis. The following chapters focus on the main results obtained in the sector of the Brout-Englert-Higgs boson, which has been discovered in 2012 at the Large Hadron Collider. Various theories underlying the Standard Model of elementary particle physics are considered. The results presented cover statistical analyses of the experimental data, phenomenological studies and more formal aspects of the theories.

Contents

To Félix.

Chapter 1

Overview of the studies

As an introduction to this report, we present a summary of the research activity covering the whole career since the PhD Thesis at the "Institut de Physique Théorique" of the C.E.A. in Saclay/France.

1.1 Supersymmetry

1.1.1 Colliders

The PhD Thesis as well as the following years of research were dedicated to phenomenological studies at high-energy colliders, aimed at developing tests for supersymmetric extensions of the Standard Model (SM) of elementary particles. Probably one of the strongest motivations for supersymmetry is to render possible the existence of a new physics energy scale much higher than the ElectroWeak (EW) symmetry breaking scale, by stabilizing the quantum corrections to the Higgs boson mass (gauge hierarchy problem). Nowadays, the quest for supersymmetric signatures at colliders has been extensively developed, from both the points of view of theory (model building, higher-order calculations) and phenomenology (*Monte Carlo* generators,...). Our studies have focused on the supersymmetric interactions violating the so-called R-parity symmetry [1] on which we have written a review [1].

Tevatron.- In the search for supersymmetry at colliders, the possibility of producing supersymmetric partners through s-channel resonances benefits from a lower phase space suppression compared to their pair production. During the Tevatron Run II, we have studied [2], in collaboration with experimentalists, the single chargino production in association with a lepton, $p\bar{p} \to \tilde{\nu}_i \to \tilde{\chi}_1^{\pm}\ell_i^{\mp}$, as induced by the resonant sneutrino production via a coupling of type, $\lambda'_{i11}L_iQ_1D_1^c \in W$, in the superpotential. Such a coupling breaks the R-parity symmetry. Within a supergravity model, we have studied the three-leptons final state induced by the cascade decay, through the lightest neutralino

[1] The symmetry, called R-parity (R_p), is defined as $R_p = (-1)^{3B+L+2S}$, where B, L and S denote the baryon number, the lepton number and the spin, such that $R_p = -1$ ($R_p = +1$) for any supersymmetric (SM) particle.

(Lightest Supersymmetric Particle here) and a W-boson decaying both leptonically, $\tilde{\chi}_1^{\pm} \to \tilde{\chi}_1^0 W^{\pm(\star)}$, $\tilde{\chi}_1^0 \to \ell_i^+ \bar{u} d$, $W^{\pm(\star)} \to \ell_j^{\pm} \nu_k$. The comparison with the simulated SM background – from running a PYTHIA version interfaced with the SHW detector simulation package – has demonstrated that this signature was able to extend the sensitivity on the superpartner mass spectrum beyond the LEP limits and to probe the relevant R-parity violating couplings down to values one order of magnitude smaller than their most stringent low-energy indirect bounds. Besides, the trilepton signal offered the opportunity to reconstruct the neutralino mass in a model-independent way with good accuracy. Indeed, the experimental data of the Tevatron Run II have finally allowed both the CDF and D0 Collaborations to constrain minimal supersymmetry breaking scenarios with R-parity breaking, exactly via such reaction investigations (last experimental analyses in 2006-2007).
In a more complete study [3], we have considered as well the charged slepton resonant production and the superpartner decays into charginos and neutralinos. The non-resonant single superpartner productions, like $\bar{d}_j d_k \to W^+ \tilde{\ell}_{iL}$, were also included in the analysis. The scattering amplitudes for the s, t, u channels of all these reactions have been calculated analytically and numerically computed using the COMPHEP routine. We have suggested there to scrutinize the like sign dilepton signature as well. This study has allowed to extend the potential sensitivity on several λ'_{ijk} couplings and to propose promising kinematical reconstructions of superpartners, namely the lightest chargino, lightest neutralino, sneutrino and charged slepton.

LHC.- As a complementary analysis, the resonant production of sneutrinos via the R-parity violating couplings of the superpotential, $\lambda'_{ijk} L_i Q_j D^c_k$, was studied through its three-leptons signature at the Large Hadron Collider (LHC) [4]. A detailed particle level study of signal and background was performed using a fast simulation of the ATLAS detector. Through the full reconstruction of the cascade decay, a model-independent and precise measurement of the masses of the involved sparticles was be performed. This signature can be detected for a broad class of supersymmetric models, and for a wide range of values of several λ'_{ijk} coupling constants. An illustrative quantitative result is that within the Minimal Supersymmetric Standard Model (MSSM), the production of a 900 GeV sneutrino with $\lambda'_{211} > 0.05$, and of a 350 GeV sneutrino for $\lambda'_{211} > 0.01$, could be observed at the 14 TeV LHC running up to an integrated luminosity of 30 fb^{-1}.

Leptonic Colliders.- In an optimistic scenario of supersymmetry discovery at the LHC, the future leptonic colliders with clean environment (low background) would constitute ideal frames for precision measurements of the superpartner characteristics. The first works of my thesis were focused on the attractive possibility to produce superpartners through resonances at leptonic colliders with center of mass energies up to 500 GeV – 1 TeV [5]. Such resonant productions can be induced by lepton number violating interactions breaking the R-parity symmetry (of type λ_{ijk}) and create a single fermion (charginos, neutralinos) or scalar field (sleptons, sneutrinos) through $2 \to 2$ body processes.
We have first calculated analytically and systematically the resonant probability amplitudes, as well as the decay branching ratios for the superpartners, and explored the parameter space (m_0,

$m_{1/2}$, A, $sign(\mu)$, $\tan\beta$) of a minimal supergravity model assuming grand unification of gauge interactions and universal (flavor independent) soft supersymmetry breaking parameters at the unification scale. The predictions obtained for the total and partial rates showed that the single production reactions have a good potential of observability at the next linear collider energies, for values of R-parity violating coupling constants close to their indirect bounds and slepton/gaugino masses below the TeV scale. Then we have implemented the amplitude rates, obtained analytically, in the `SUSYGEN` event generator. Based on this code, a *Monte Carlo* simulation for the single gaugino productions was performed to point out some characteristic final state dynamical distributions (transverse momentum, missing energy,...) allowing to discriminate the signal from backgrounds and superpartner pair productions (R-parity conserving).
In Ref. [6], it was shown quantitatively that the background for the single superpartner production can be reduced using the initial beam polarization of future linear colliders (selecting helicities of the initial electrons-positrons). It was then illustrated how the single chargino production – in association with a charged lepton – would allow to reconstruct the charginos, $\tilde{\chi}^{\pm}_{1,2}$, and sneutrino masses, using the clear two-body final state kinematics and including the Initial State Radiation effect (important in the regime where the s-channel sneutrino would be produced on-shell).

As a possible indirect test of supersymmetry, we have also examined [7] the effects of the R-parity odd interactions [$\lambda_{ijk}, \lambda'_{ijk}$ with CP odd complex phases] on flavour changing rates and CP violation asymmetries in the production of fermion-antifermion pairs (leptons, up/down-quarks) at e^+e^- colliders, for center of mass energies from the Z-boson pole up to 1 TeV. Off the Z-boson pole, the flavor changing rates are controlled by tree level amplitudes and the CP asymmetries by interference terms between tree and loop (photon and Z-boson vertex corrections involving $\lambda^{(\prime)}_{ijk}$ couplings) amplitudes. In contrast, at the Z-boson pole, both observables involve loop amplitudes, that we have calculated using the Passarino-Veltman formalism.
In particular, the contribution from the R-parity violating interactions to the associated production of a top quark with a charm antiquark ($t\bar{c}$) has been examined for high-energy leptonic colliders [8]. We have been concentrating on the reactions associated with the semileptonic top decay ($t \to b\bar{\ell}\nu$). A set of characteristic dynamical distributions for the signal events was evaluated and the results contrasted against those from the SM background (W-boson pair production). Then, we turned to a study of a CP odd observable, associated with the top spin, which leads to an asymmetry in the energy distribution of the emitted charged leptons for the pair of CP-conjugate final states, $b\bar{\ell}\nu\bar{c}$ and $\bar{b}\ell\bar{\nu}c$. A non-vanishing asymmetry arises once more from a CP odd phase, embedded in the R-parity violating coupling constants, through interference terms between the R-parity violating amplitudes at the tree and loop levels.
In the spirit of pinning down R-parity odd interactions, flavour non-diagonal rates and CP violation asymmetries in the production of slepton pairs at future e^+e^- colliders – induced by such interactions – were also calculated [9]. The flavour changing rates are controlled by tree level amplitudes (and quadratic products of different R-parity violating couplings), while the CP asymmetry observables come from interference terms between tree and loop level amplitudes (involving quartic

coupling products).

1.1.2 Fermion mass models

One of the mysteries of the SM is the neutrino mass scale being about 12 orders of magnitude smaller than the EW breaking scale, and than the top quark mass. We have proposed a mechanism [10] to generate such neutrino mass values within the Next-to-Minimal Supersymmetric Standard Model (NMSSM). The primary motivation for the NMSSM is to address the so-called μ-problem in supersymmetry [2] thanks to the introduction of a new superfield being singlet under the SM gauge symmetries and acquiring a Vacuum Expectation Value (VEV) constituting the μ parameter. Our mechanism uses a compensation between the gaugino and singlino (singlet superpartner) tree-level contributions to the neutrino masses. Such an explanation of the neutrino mass question is thus connected to the μ-problem, through the singlet superfield. Indeed, we considered an R-parity violating NMSSM version where the neutrinos mix with higgsinos via the R-parity violating bilinear terms $\mu_i L_i H_u$ of the superpotential. Then the neutrinos acquire Majorana masses since the higgsinos in turn mix with the massive gauginos or singlino.
Based on this mechanism, we have generated realistic neutrino mass values without requiring any strong hierarchy amongst the fundamental parameters, in contrast with alternative models. In particular, the ratio $|\mu_i/\mu|$ can reach $\sim 10^{-1}$, unlike in the MSSM where it has to be much smaller than unity. We have checked that the obtained parameters also satisfy the collider constraints and internal consistencies of the NMSSM. The price to pay for this new cancellation-type mechanism of neutrino mass reduction is a certain fine tuning, which gets significantly improved in some regions of parameter space. Besides, we have discussed the feasibility of our scenario when the R-parity violating bilinear terms have a common origin with the μ-term, that is when those are generated via a VEV of the singlet scalar component from the couplings, $\lambda_i S L_i H_u$.

Besides, in the MSSM with bilinear R-parity violation, only one neutrino eigenstate acquires a mass at tree level. Consequently experimental data on neutrinos cannot be accommodated at tree level. We have shown [11] that in its NMSSM extension, it is possible to generate two massive neutrino states at tree level. Hence, the global three-flavour neutrino data can be reproduced at tree level, without appealing to loop dynamics which is vulnerable to model-dependent uncertainties. We have given analytical expressions for the neutrino mass eigenvalues and presented examples of realistic parameter choices.

1.1.3 Astrophysics

The supersymmetry and supergravity were also considered within an astrophysical context [12,13]. We have calculated the lifetime of the gravitino in scenarios where a gravitino, relic from the hot

[2] Generate an acceptable energy scale for the dimension-one coupling constant (μ) of the mixing term for Higgs superfields, $\mu H_u H_d$.

big-bang, constitutes the Lightest Supersymmetric Particle (LSP) and hence a candidate of type WIMP (Weakly Interacting Massive Particle) for the dark matter of the universe. The decay of the gravitino may occur there through one or several of the bilinear/trilinear R-parity violating interactions and possesses either two-body ($\tilde{G} \to \gamma\ \nu$, $\tilde{G} \to Z^0\nu, W^+\ell^-$, $\tilde{G} \to h\ \nu, h^+\ell^-, a\ \nu$) or three-body final states (involving three quarks and/or leptons). The results are that a decay previous to the big-bang nucleosynthesis is difficult to realise in the MSSM (for scalar superpartner masses not exceeding $\mathcal{O}(10)$ TeV), while the gravitino lifetime is typically larger than the age of the universe by two orders of magnitude within the NMSSM (decay channels suppressed by the weak gravitational strength). Therefore, the considered minimal scenarios would either upset the standard big-bang nucleosynthesis or predict gravitinos decaying after the present epoch, so that those do not seem to constitute natural solutions to the cosmological gravitino problem. Other aspects were considered quantitatively in those works: WIMP candidates of type sneutrino LSP or neutralino LSP, as well as gauge-mediated supersymmetry breaking scenarios and the additional constraints on gravitino decays coming from the flux data of indirect dark matter detection experiments. Both the one-flavor simplification hypothesis and the realistic scenario of three neutrino flavors were analyzed. Technically, we have modified the `NMHDECAY` program in order to extend the neutralino mass matrix to the present framework.

In the other astrophysical context of solar neutrinos, we have presented a general study [14] of a three-neutrino flavour transition model based on the supersymmetric interactions which violate R-parity. These interactions induce flavour violating scattering reactions between solar matter and neutrinos. The model does not contain any vacuum mass or mixing angle for the first generation neutrino. Instead, the effective mixing in the first generation is induced via the new interactions. The model provides a natural interpretation of the atmospheric neutrino anomaly, and is consistent with reactor experiments. We have determined all R-parity violating couplings which can contribute to the effective neutrino oscillations, and summarized the laboratory bounds. Independent of the specific nature of the (supersymmetric) flavour violating model, the experimental data on the solar neutrino rates and the recoil electron energy spectrum were found to be inconsistent with the theoretical predictions. The confidence level of the χ^2-analysis ranges between $\sim 10^{-4}$ and $\sim 10^{-3}$. The incompatibility, is due to the SNO results, and excludes the proposed model. It must thus be concluded that a non-vanishing vacuum mixing angle for the first generation neutrino is necessary. It can be expect that this statement also applies to the solutions based on other flavour violating interactions having constraints of the same order of magnitude.

1.2 Extra dimensions

During the post-doctorate position at the Bruxelles University [2002-2004], we have started to study the extensions of the SM with Extra spatial Dimensions (ED). Such extensions, first introduced in high-energy physics by string theorists, have attracted a particular attention since the years 1999-

2000. The reason was mainly the appearance of two classes of scenarios, denoted by ADD and RS (from the initial letters of their respective author names), which brought new kinds of solution to the gauge hierarchy problem. Those scenarios constitute thus alternatives to supersymmetry. The RS model (RS2 version), containing warped extra dimensions, even allows to almost have a unique order of magnitude for the fundamental energy scales of nature (SM and gravity scales). The RS framework constitutes a new paradigm in the sense that it has a dual description, through the *AdS*-CFT correspondence, in terms of a composite Higgs scenario. For instance, the gauge-Higgs unification [3] corresponds to composite Higgs models with a pseudo-Goldstone Higgs boson. Such models have the additional advantage to address the little hierarchy problem. Finally, both the ADD (with thick branes) and RS (version with matter propagating in the bulk) scenarios further provide original geometric solutions to the flavour puzzle and fermion mass hierarchy question.

1.2.1 Colliders

Indirect effects.- As in the context of supersymmetry, we have studied possible signatures of the scenarios with ED at colliders. First, we have interpreted [15] the long-standing anomaly (discrepancies in experimental data with respect to their SM predictions) observed at LEP in the forward-backward asymmetry of the bottom quark pair production channel ($A_{\rm FB}^b$), both at the Z-boson pôle and off the pôle. More recently, we have explained [16] similar significant anomalies for the forward-backward asymmetry in the top quark pair production ($A_{\rm FB}^t$) at Tevatron Run II [detected both by the CDF and D0 Collaborations]. Our interpretations rely on the couplings or mixings between the SM fields (top, bottom quarks, EW gauge bosons, gluons) and their Kaluza-Klein (KK) excitations, in scenarios of type RS with matter propagating in the bulk. As will be discussed in next subsection, within such a framework, the heavy SM fermions (especially the top and bottom quarks) are localized towards the ED boundary where the Higgs boson is stuck. Since the KK excitations are also localized towards the Higgs brane, one expects the new physics effects (from the KK modes) arising with the strongest intensity in the top and bottom sector (largest wave function overlaps between heavy quarks and KK states). It is interesting to note that the only robust experimental SM anomalies reported so far at colliders concern the bottom ($A_{\rm FB}^b$ at LEP) and top ($A_{\rm FB}^t$ at Tevatron) quark sector. A careful study [17] of the EW precision observables measured at LEP (oblique parameters S,T,U...) was performed to establish what are the precise lower limits (~ 3 TeV) on the first KK mass scale, in models achieving the $A_{\rm FB}^b$ puzzle explanation. At this level it must be mentioned that it is generally difficult to explain the $A_{\rm FB}^b$, $A_{\rm FB}^t$ anomalies in supersymmetric extensions of the SM which are limited there to loop-level effects.
Let us bring some important precisions here. In the considered RS framework, the SM gauge symmetry was extended in the bulk to the custodial symmetry, $\mathrm{SU(2)_L \times SU(2)_R \times U(1)_X}$, which enlarges the field content to additional gauge bosons (Z', W') together with their KK towers. The

[3] In this interesting model, the Higgs scalar boson comes from the new spatial component of a gauge field embedded in a higher-dimensional background.

motivation is twofold, protecting the EW precision observables measured at LEP against too large corrections (from KK sates) and possibly contributing to address the $A_{\rm FB}^b$ anomaly. The models contain enough degrees of freedom to solve the $A_{\rm FB}^b$ anomaly without affecting dangerously the other crucial observable of the bottom sector, namely R_b, which is already in good agreement with its theoretical (SM) prediction. Those kinds of model addressing simultaneously $A_{\rm FB}^b$ and $A_{\rm FB}^t$ predict in particular new s-channel effects, induced by a KK gluon excitation exchange, in the top quark pair production at LHC [18]. This brings a logical transition with the next paragraph.

Direct effects.- The direct effects of ED at colliders, from the on-shell productions of KK modes, have also been investigated – sometimes in collaboration with experimentalists. First, in the custodially protected RS models, some specific KK states (without zero-modes), being the extra-components of the fermion multiplets promoted to $\mathrm{SU(2)_R}$ representations, can constitute the lightest KK states. It is thus relevant to scrutinize the productions of these co-called custodians at colliders, that could come out in the future as the first evidence for physics beyond the SM. The custodians, as any KK fermionic mode in this context, are vector-like fermions (identical quantum numbers for the two chiralities, L, R). It must be noticed that present Higgs boson data put bounds on the KK scale (reference KK photon mass) in the RS scenarios around 10 TeV. Nevertheless, such bounds hold within the minimal RS versions and it is important to keep a bottom-up approach at this time where the LHC is exploring the TeV scale area.
We have studied in Ref. [19] the LHC signatures of TeV scale vector-like quarks b', t' and some with an exotic electromagnetic charge 5/3 that may appear in custodially protected RS models. In addition to the usually studied pair-production channels which depend on the strong coupling (custodians are usually embedded into triplet representations under $\mathrm{SU(3)_c}$ as the SM quarks), we have put equal emphasis on single production channels that depend on EW couplings and EW symmetry breaking induced mixing effects between the heavy vector-like quarks and SM quarks. We have then identified new promising gg-initiated pair as well as single production channels (like $gg \to bb'Z^0$) and find the luminosity required for discovering the associated final states at the LHC. For these channels, we have further proposed a cut that allows one to extract the relevant electroweak couplings of the vector-like quarks (bringing information on the underlying ED model). Different fermionic representations under the $\mathrm{SU(2)_L \times SU(2)_R \times U(1)_X}$ gauge group were considered.
Although the primary motivation was from warped extra dimension models, we have presented many of the results model-independently using vector-like terminology and effective parameters. Indeed, the vector-like fermions could be realised generically as KK excitations in ED models or as excited bound states of their dual composite Higgs scenarios.

The phenomenology of KK excitations of gauge bosons is also attractive to look at as those can be produced resonantly. Among them, the KK gluon has the additional advantage to benefit from strong interactions. Within the RS model addressing flavour, the KK gluon would mainly decay into top and bottom quark pairs, given the favoured wave function overlap between the top quark

and the KK modes (inducing large effective 4D couplings).
In Ref. [20], we have studied the manifestations of both the strongly-interacting and electroweak gauge boson KK excitations at the LHC, with masses of the order of a few TeV. We have first analyzed the two-body tree-level production processes $pp \to t\bar{t}$ and $b\bar{b}$ in which the KK excitations of gauge bosons are exchanged. We found that the additional channels can lead to a significant excess of events with respect to the SM prediction; characteristic top quark polarization and angular asymmetries were quantitatively studied and turned out to potentially probe the chiral structure of couplings to excited states. We then analyzed higher-order production processes for the gauge boson excitations which have too weak or no couplings to light quarks and, in particular, the loop induced process $gg \to g^{\rm KK} \to t\bar{t}$ and $b\bar{b}$ in which the anomalous $ggg^{\rm KK}$ four-dimensional vertex has to be regulated. The RS effects in this process, as well as in the four-body reactions $pp \to t\bar{t}b\bar{b}$, $t\bar{t}t\bar{t}$, $b\bar{b}b\bar{b}$ and the related three-body reactions $gb \to \bar{b}t\bar{t}$, $bb\bar{b}$, in which the $g^{\rm KK}$ excitations are mainly radiated off the heavy quarks, are shown to be difficult to test at LHC – due to small phase space and low parton density above $M_{g^{\rm KK}} \sim 3$ TeV.

In the specific case of the custodial O(3) symmetry implemented in the RS background, as suggested primarily to protect the $Z^0 b\bar{b}$ vertex, the left-handed lepton locations (along the ED) can be moved closer to the Higgs brane (TeV-brane). This would enhance lepton couplings to KK gauge boson modes while keeping an acceptable compatibility with EW precision data and allowing to reproduce the measured lepton masses (thanks to right-handed leptons moved closer the Planck-brane). In Ref. [21], we have considered such a possibility that a resonant KK gauge boson decays into leptons, at the LHC, namely the contribution from the exchange of KK excitations of gauge bosons to the clear Drell-Yan reaction. We have shown that this contribution is detectable (even with the low luminosities of the LHC regime) for KK masses around the TeV scale and for sufficiently large lepton couplings to KK gauge bosons. This LHC phenomenological analysis was realistic in the sense that it was based on fermion localizations which reproduce all the correct quark/lepton masses plus mixing angles and respect Flavour Changing Neutral Current (FCNC) constraints in both the hadron and lepton sectors. This leads us naturally to the next subsection.

1.2.2 Fermion mass models

Within the RS version with gauge bosons and fermions propagating in the bulk, while the Higgs boson remains stuck on the TeV boundary (as necessary to solve the gauge hierarchy problem), a simple geometrical mechanism was proposed to address the SM flavour question. Indeed, the observed quark/lepton mixing angles [CKM and PMNS matrix textures] as well as the SM fermion mass hierarchy can be generated (meaning: generated from same order fundamental parameters) by controlling the amplitude of the effective 4-Dimensional (4D) Yukawa coupling constants, responsible for the fermion masses in the EW symmetry breaking mechanism. Those effective couplings are controlled by the overlaps between the Higgs boson and different fermion wave functions along the ED(s).

A similar geometrical mechanism arises in the context of flat extra dimensions (ADD), from controlling the overlaps between the two chiralities of each fermion generation. In such models, the fermions may spread along a thick brane. A field theory method to localize the chiral fermions at different points along this domain wall is to couple them to a solitonic background.

We have elaborated concrete realizations of these two types of mechanism, applied to the RS [22, 23] and ADD [24] frameworks, in order to reproduce the quark/lepton masses and their structure in flavour space. It is remarkable that such flavour models can accommodate the neutrino sector as well and generate their tiny masses (just by introducing a right-handed neutrino), thus representing alternatives to the usual See-saw mechanism. The models provided predictions for neutrino observables to be tested in future neutrino experiments ($\sin\theta_{13}$, the m_{ν_1} eigenstate mass and neutrino mass combinations), both in the cases of flat [24] and warped [23] extra dimensions.

In the ED context, specific mechanisms were proposed to suppress the neutrino mass scale with respect to the EW energy scale (not full flavour models). The idea was to extend the SM with an additional right-handed neutrino propagating along a flat extra dimension, while the SM fields would remain confined on a 3-brane. The wave function overlap between the left-handed and right-handed neutrinos would then be responsible for a volume suppression factor. We have also constructed such models able to reproduce the neutrino data, both within the ADD framework [25] and in the RS multi-brane extensions [26]. In particular, in the ADD context, we have found that the strong phenomenological constraints on mixing angles between active and sterile neutrinos (especially those derived from the SNO experiment data) do not conflict with the possibility of generating a realistic neutrino mass spectrum.

1.2.3 Astrophysics

In the context of the ED paradigm, and more specifically within the ADD scenario with a new right-handed neutrino propagating along the fifth dimension (compactified over a S^1/Z_2 orbifold), we have also discussed astrophysical aspects, simultaneously to the generation of a realistic neutrino mass scale. Our discussions concerned the possibility of a successful leptogenesis through the (tree and loop level) decays of massive KK excitations of right-handed neutrinos into a charged lepton and a charged Higgs boson [25]. The leptogenesis, affecting the baryon sector via sphaleron induced processes, would allow to explain the baryon asymmetry of the observable universe (excess of matter with respect to anti-matter).

1.3 Higgs boson

The Higgs boson discovery at the LHC in 2012, beyond bringing the missing cornerstone of the SM and its EW symmetry breaking mechanism, marked the beginning of a new era of rate measurements constituting new windows on the physics underlying the SM. Today, grouping the ATLAS and CMS

Collaboration public results, there are no less than ~ 80 measurements of Higgs production and decay rates that are deduced from the data collected at the center of mass energies of 7 and 8 TeV.

1.3.1 Data analysis

Our effort concerning the treatment of the Higgs rate measurements was to clarify the statistical methods that experimentalists and theorists should apply regarding the theoretical uncertainties, in order to fit the data in any effective/theoretical framework. For that purpose, we have recently produced a guide [27] of the various statistical methods (marginalisation / biais, frequentist / Bayesian approaches...) allowing to fit the Higgs data, focusing on the theoretical errors (QCD, EFT, PDF...) which are crucial and open up different questions like the choice of the 'prior' distributions (flat / Gaussian...). We have reviewed the individual sources of theoretical error and combined them, one-by-one, taking into account the intricate correlation effects among Higgs production reactions, decay modes and detection channels.

Besides, methods to constrain the invisible width of the Higgs [decays into hypothetical stable particles] were elaborated [28]. The determination of the Higgs parity [its CP composition] was also worked out from the LHC data on Higgs rates. In the same paper, it was suggested to the community to measure/use some specific *ratios* of cross sections (times Higgs branching ratios) in order to cancel the main theoretical errors between each other and even some experimental ones – like the uncertainty from the luminosity determination – within the Higgs rate fits.

1.3.2 Phenomenology

The second part of our contributions, to the global effort of understanding the EW symmetry breaking sector, included the calculations of various new physics effects on the Higgs interactions [29] and its VEV [30]. The goal here is clearly to learn on the Ultra-Violet completion of the SM from Higgs data.

The impact of several fermionic/bosonic KK excitations on the Higgs production/decay modes was estimated. This impact may be caused either by the new contributions of KK modes exchanged in the loops generating the Higgs-gluon-gluon or Higgs-photon-photon vertex, or by the quantum mixing effects between SM fermions/bosons and their KK excitations. Those mixings further produce corrections to the EW precision observables (M_W, M_Z masses, Γ_Z width...) that required some control [30]. Some of our studies are based on specific ED models and others [31, 32] follow a more effective approach by considering extra vector-like fermions that could arise as KK modes (in several ED models) or excited bound states (dual composite Higgs framework).

In a different context, the potential modifications of the Higgs couplings, induced by its mixings with the extended Higgs sector of supersymmetric extensions of the SM, were estimated [33]. Fits of the LHC Higgs data have been realised in 2D and 3D parameter spaces – depending on the theoretical regimes considered – in order to constrain minimal supersymmetric models.

Besides, we have shown that there exist new promising Higgs production reactions at LHC, induced by possible new physics scenarios [34]. Indeed, for instance the (QCD) pair production of t' vector-like quarks, followed by their decays into a Higgs scalar field, $t' \to tH$, can reach significant rates.

1.3.3 Theory

The third part of the investigations on the Higgs sector concerns some formal aspects. We have first pointed out a non-commutativity in the calculation ordering for the mass spectrum of bulk fermions coupled to a Higgs boson localised on a 3-brane [4] [35], as occurs in the scenarios à la RS addressing both the fermion mass and gauge hierarchies. This order is between the two limits $N \to \infty$ ($N \equiv$ number of modes in the KK tower) and $\epsilon \to 0$ ($\epsilon \equiv$ Higgs Dirac peak regularisation parameter) and affects the analytical expressions of the fermion masses. The question arising is thus: which one of the two is the correct calculation order? Helped by the exact matching between the 4D and 5D calculations, we were able to address this apparent paradox: the two orderings should be numerically equivalent since they constitute two physical regularisations.

With my first PhD student, we have constructed a supersymmetric extension of the RS model [36]. Such models could constitute effective low-energy models whose Ultra-Violet completion would be a superstring theory (candidate for a quantum description of gravity). In order to write the 4D effective Lagrangian, useful for any phenomenological study, we had first to set up technics of regularisation – based on the completeness relation for wave functions along the fifth dimension. Indeed, divergences (of $\delta(0)$ type) appear in the couplings of sfermions to the Higgs boson, if the latter is localised on the TeV-brane as motivated by the gauge hierarchy. Those singularities turn out to be precisely cancelled out by contributions to the couplings coming from the tree-level exchanges of infinite towers of KK scalar fields – with boundary conditions of type Dirichlet-Dirichlet (arising in higher-dimensional supersymmetric models).
This first regularisation of the Higgs couplings has then allowed a clear approach the other subtle regularisation, called the KK regularisation, leading to the cancellation of the quadratic 'divergences' in the quantum corrections to the Higgs mass. Note that this quadratic divergence cancellation is induced by the 5D supersymmetry structure and the 5D anomaly cancellation.
Those theoretical developments have lead us to answer a more phenomenological question: in the case where a superpartner would be produced and observed at the LHC, how one could distinguish experimentally between a pure 4D supersymmetric scenario and its higher-dimensional version, like for example the supersymmetric RS model? Several phenomenological discriminating tests were proposed, using for instance differences arising at the level of the Higgs coupling to sleptons.

[4] ED fixed point.

Bibliography

[1] R. Barbier, C. Berat, M. Besancon, M. Chemtob, A. Deandrea, E. Dudas, P. Fayet, S. Lavignac, G. Moreau, E. Perez and Y. Sirois, Phys. Rept. 420 (2005) 1.

[2] G. Moreau, M. Chemtob, F. Déliot, C. Royon, E. Perez, Phys. Lett. B475 (2000) 184.

[3] F. Déliot, G. Moreau and C. Royon, Eur. Phys. J. C19 (2001) 155.

[4] G. Moreau, E. Perez and G. Polesello, Nucl. Phys. B604 (2001) 3.

[5] M. Chemtob and G. Moreau, Phys. Rev. D59 (1999) 055003.

[6] G. Moreau, Linear Collider note LC-TH-2000-040, arXiv:hep-ph/0009140.

[7] M. Chemtob and G. Moreau, Phys. Rev. D59 (1999) 116012.

[8] M. Chemtob and G. Moreau, Phys. Rev. D61 (2000) 116004.

[9] M. Chemtob and G. Moreau, Phys. Lett. B448 (1999) 57.

[10] A. Abada and G. Moreau, JHEP 0608 (2006) 044.

[11] A. Abada, G. Bhattacharyya and G. Moreau, Phys. Lett. B642 (2006) 503.

[12] G. Moreau and M. Chemtob, Phys. Rev. D65 (2002) 024033.

[13] C.-C. Jean-Louis and G. Moreau, J. Phys. G37 (2010) 105015.

[14] H. K. Dreiner and G. Moreau, Phys. Rev. D67 (2003) 055005.

[15] A. Djouadi, G. Moreau and F. Richard, Nucl. Phys. B773 (2007) 43.

[16] A. Djouadi, G. Moreau, F. Richard and R. K. Singh, Phys. Rev. D82 (2010) 071702.

[17] C. Bouchart and G. Moreau, Nucl. Phys. B810 (2009) 66.

[18] A. Djouadi, G. Moreau and F. Richard, Phys. Lett. B701 (2011) 458.

[19] S. Gopalakrishna, T. Mandal, S. Mitra and G. Moreau, JHEP 1408 (2014) 079.

[20] A. Djouadi, G. Moreau and R. K. Singh, Nucl. Phys. B797 (2008) 1.

[21] F. Ledroit, G. Moreau and J. Morel, JHEP 0709 (2007) 071.

[22] G. Moreau and J. I. Silva-Marcos, JHEP 0603 (2006) 090.

[23] G. Moreau and J. I. Silva-Marcos, JHEP 0601 (2006) 048.

[24] J.-M. Frère, G. Moreau and E. Nezri, Phys. Rev. D69 (2004) 033003.

[25] A. Abada, P. Dey and G. Moreau, JHEP 0709 (2007) 006.

[26] G. Moreau, Eur. Phys. J. C40 (2005) 539.

[27] S. Fichet and G. Moreau, to appear in Nucl. Phys. B, arXiv:1509.00472 [hep-ph].

[28] A. Djouadi and G. Moreau, Eur. Phys. J. C73 (2013) 9, 2512.

[29] A. Djouadi and G. Moreau, Phys. Lett. B660 (2008) 67.

[30] C. Bouchart and G. Moreau, Phys. Rev. D80 (2009) 095022.

[31] G. Moreau, Phys. Rev. D87 (2013) 015027.

[32] N. Bonne and G. Moreau, Phys. Lett. B717 (2012) 409.

[33] A. Djouadi, L. Maiani, G. Moreau, A. Polosa, J. Quevillon and V. Riquer, Eur. Phys. J. C73 (2013) 2650.

[34] A. Azatov, O. Bondu, A. Falkowski, M. Felcini, S. Gascon-Shotkin, D. K. Ghosh, G. Moreau, A. Y. Rodriguez-Marrero and S. Sekmen, Phys. Rev. D85 (2012) 115022.

[35] R. Barceló, S. Mitra and G. Moreau, Eur. Phys. J. C75 (2015) 11, 527.

[36] C. Bouchart, A. Knochel and G. Moreau, Phys. Rev. D84 (2011) 015016.

Chapter 2

A first guide to statistical treatments of the theoretical uncertainties in Higgs fits

Adapted from: *S. Fichet and G. Moreau*, `arXiv:1509.00472 [hep-ph]`.

2.1 Introduction and summary

Besides the historical discovery of a resonance around 125 GeV [1,2] that is most probably the Brout-Englert-Higgs boson responsible for the ElectroWeak (EW) symmetry breaking [3], the ATLAS and CMS Collaborations have provided a set of 88 rate measurements – based on the full dataset collected so far with luminosities of ~ 5 fb^{-1} at the center of mass energy $\sqrt{s} = 7$ TeV and ~ 20 fb^{-1} at $\sqrt{s} = 8$ TeV [4, 5] (see also Ref. [6, 7]) – that constitutes a new and precious source of indirect information on physics beyond the Standard Model (SM). Indeed, observing deviations of the Higgs boson rates with respect to their SM predictions would reveal the presence of an underlying theory while the absence of such deviations allows one to strongly constrain new models (see for example Ref. [8] for higher-dimensional models, Ref. [9] for composite Higgs theories and Ref. [10] for supersymmetric scenarios). So far, no signs from an unknown world have came out from the data, but this is only the beginning of a long exploration, given the expected LHC upgrades [11].

The fits of the Higgs rates (*c.f.* Ref. [12] for the first set of analyses, Ref. [13–16] for the results after the Moriond 2013 winter conference and Ref. [4, 5] for the latest official ATLAS and CMS analyses) are thus obviously important. Now certain aspects of these analyses remain to be worked out in order to obtain the final fits for testing new physics. First, the precise likelihood functions associated to the experimental rates (in particular their specific shapes and the complete correlations between channels) are not provided in the present public papers, although they might

be expected at some point. Second, a major part of the theoretical uncertainties is due to QCD calculations of the Higgs production rates [17–20] and their treatments in the fits raise questions in the Higgs physics community (see Ref. [21,22] for recent discussions). Taking carefully into account these theoretical uncertainties is crucial for the Higgs fits due to the following reasons.

First, theoretical uncertainties can be sizeable with respect to the experimental ones. The QCD uncertainty on the gluon-gluon fusion mechanism dominantly involved in most of the Higgs discovery channels induces typically an error of $\sim 10\%$ on signal strengths (see Section 2.6), that is already comparable to the experimental error bars in several Higgs channels which reach values down to $\sim 20\%$ [4–7]. Besides, considering for instance the CMS prospectives at $\sqrt{s} = 14$ TeV with a luminosity of 300 fb^{-1}, the experimental error bars are around $\sim 5\%$ (with same systematic errors as today) for the diphoton final state and less than $\sim 10\%$ for the τ-lepton, Z and W boson channels [11] so that the theoretical error might even become the dominant one in some channels. Second, theoretical uncertainties might be of the same magnitude as the main potential deviations due to new physics. For instance the maximal corrections to Higgs couplings estimated in Ref. [23] for characteristic composite Higgs and supersymmetric models [1] lead typically to deviations of the signal strengths between $\sim 2\%$ and tens of percent compared to SM. This is of the same order as the theoretical error mentioned above, so that one is precisely in the situation where the theoretical error deserves a careful treatment to test new physics scenarios. [2]

Therefore, in this work, our primarily goal is to answer precisely the question : *what is the correct treatment of the theoretical uncertainties in the fits of the Higgs boson rates?* [3] This seemingly simple question has lead us to several new developments, summarized in the three lines of work described in the paragraphs below.
First, we present a systematic survey of the various statistical treatments of the theoretical error and their applications to the Higgs fits within a unified formalism. We confront the frequentist and Bayesian frameworks, [4] [5] that prove to exhibit a certain degree of convergence at the level of accuracy of the present LHC data. [6] We also compare the marginalisation and bias treatments. In the former, we consider the representative cases of Gaussian and flat combined priors because of the lack of knowledge inherent to the distribution of theoretical uncertainties. [7] We find the Gaussian

[1] In the case of no new states, related to the EW symmetry breaking, directly observed at the LHC.
[2] This intermediate situation is to be contrasted with the two extreme cases of expected signal strength deviations much higher than the theoretical error (which can then be neglected) or deviations well smaller (no hope to detect them). In both of these cases, a detailed treatment of the theoretical error would not be really needed to test new physic scenarios.
[3] Throughout this work, we use generically the expression "theoretical error" to denote any error on the SM prediction for the Higgs rates. This is a slight wording abuse, because certain of these errors like the ones from the PDF determination have a partial experimental origin.
[4] Sometimes in the literature, there are inconsistencies in the sense that errors are combined in a frequentist way (combination depending on the prior shape) while the priors are convoluted in a Bayesian way (convolution via integrations).
[5] A pure Bayesian fit of the Higgs rates has been carried out in Ref. [16].
[6] To be contrasted with the preliminary study of Ref. [24] based on simulated Higgs data.
[7] To the best of our knowledge, a flat prior for the theoretical uncertainty is for the first time applied to the Higgs

prior to be well motivated by the full combination of each individual theoretical uncertainty. It turns out that the choice of one among all these statistical approaches may affect significantly the determination of the Higgs properties. It is thus important to understand precisely the conceptual differences between these approaches. Finally, this survey is the opportunity to provide useful analytical expressions for the marginalised likelihood functions, including the theoretical correlations among the Higgs channels.

Second, we explain precisely the principle of bias [8] and its fundamental differences with the marginalisation principle. The bias principle is more conservative than the marginalisation principle by construction and does not depend on the shape of the priors of the nuisance parameters. This thorough examination of the bias principle leads naturally to introduce a statistical framework for biasing. We propose two realisations of the bias, referred to as the extremal bias and the envelope method, that apply in both frequentist and Bayesian contexts. Regarding the error combinations, important differences arise between the marginalisation and bias frameworks. [9]

Third, we discuss and implement several improvements in the treatment of the theoretical uncertainties. *(i)* For the cross sections, the combinations of all the individual uncertainties are discussed exhaustively, including in particular the several errors constituting the parton PDF uncertainty. The so-called leading moment approximation is developed to facilitate the combination of such a high number of errors. *(ii)* The error contamination by various production modes and the errors on the Higgs branching ratios are taken into account. *(iii)* The correlations between the theoretical errors on the various Higgs detection channels are included. [10] We show that these theoretical correlations induce significant shifts of the best-fit regions in the Higgs coupling parameter space. *(iv)* A Higgs fit with more conservative theoretical errors is shown to illustrate the potential impact from the imperfect knowledge of the magnitude of these errors.

For each of the statistical approaches developed along these three lines of work, we provide the up-to-date Higgs fit results based on the latest available data from the 7 and 8 TeV LHC, that can be readily used for new physics tests. From the theory side, we have updated the major gluon-gluon Fusion mechanism by using its reduced perturbative QCD error, issued from the recent calculation up to N^3LO [25]. We have also included the theoretical uncertainty on this production mode due to the use of an Effective Field Theory in the amplitude calculation [25–27], so that the whole error on the cross section remains at $\sim 10\%$.

fits. Notice also that the combination in quadrature of the theoretical and experimental errors, sometimes made in the literature, is equivalent to a marginalisation assuming Gaussian distributions for both sources of errors and neglecting the correlations. This is true in both frequentist and Bayesian cases.

[8] A bias has been applied once in Ref. [14]. The analysis developed here improves the bias performed in Ref. [14] by including more effects like the production contamination, the individual scale/EFT/PDF errors, the branching fraction uncertainties, the correlations between Higgs channels and the Bayesian/frequentist cases.

[9] For example, the PDF and amplitude uncertainties for the ggF mechanism are summed in quadrature in the Bayesian marginalisation, whereas they are linearly summed in the bias approach.

[10] We notice that such correlations were included *e.g.* in Ref. [15] for the specific assumption of errors with Gaussian priors and neglecting the correlations among different Higgs production modes.

2.2 Statistical preliminaries

This section condenses the basic elements of frequentist and Bayesian statistics that will be used along the work. In addition to statistical basics, the principle of bias is also presented.

2.2.1 Need-to-know frequentist and Bayesian statistics

In order to extract some information about a new physics model from a set of data, the central quantity to study is the likelihood function [28]. [11] The likelihood function is equal to the conditional probability density for obtaining the observed data, taken as a function of the hypothesis. In the case of predictions made in a given hypothesis H with n parameters $\{\theta_n\} \equiv \theta$, the likelihood function reads

$$L(\theta) \equiv p(d|H,\theta)\,, \tag{2.1}$$

where d represents the set of data. Note that the likelihood is defined up to an overall factor. In the present work, the data we will consider are the set of signal strength measurements from LHC and Tevatron, described in Section 2.4.1.

In particle physics, the likelihood function encloses a *statistical* uncertainty associated with the data. This is the uncertainty coming from the fluctuations inherent to the observation of a quantum process. This statistical uncertainty tends to zero in the limit of a large amount of data. However, other sources of uncertainty can be present, both on the experimental or the theoretical side. For example, uncertainties arise from the finite resolution of a detector, or from the finite accuracy of a computation. These *systematic* uncertainties do not depend on the amount of data, and need to be taken into carefully. In this work, we are going to have a close look at the *theoretical* systematic uncertainties.

The starting point for modeling a systematic uncertainty is to explicitly parametrize it. Namely, one introduces a set of new parameters, $\delta \equiv \{\delta_i\}$, which explicitly modifies the likelihood,

$$L(\theta,\delta)\,. \tag{2.2}$$

These new parameters are named *nuisance* parameters, as opposite to the θ's which are considered as the parameters of interest. This step of parametrisation is common to the frequentist and Bayesian frameworks, and is fairly universal. Discrepancies will appear in the way the δ's are treated, and will be at the center of our attention in the rest of the work. Two fundamentally different points of view on how to treat the nuisance parameters, denoted as *marginalisation* and *bias*, will be further identified (in both the frequentist and Bayesian contexts).

In Bayesian statistics, model parameters are genuine random variables. They are associated

[11] Note this is an abuse of language, the likelihood function is actually a distribution.

with a so-called prior distribution, noted $\pi(\theta)$. In order to carry out a process of inference (for example, setting exclusion bounds), the relevant object to study is the posterior distribution,

$$p(H,\theta|d) \propto L(\theta)\,\pi(\theta)\,. \tag{2.3}$$

In this framework, a so-called $1-\alpha$ Bayesian credible region is defined by the domain $\Omega_\alpha = \{\theta\,|\,p(H,\theta|d) > p_\alpha\}$, where p_α is determined by the fraction of integrated posterior

$$\frac{\int_{\Omega_\alpha} d\theta\, p(H,\theta|d)}{\int_{\Omega} d\theta\, p(H,\theta|d)} = 1-\alpha\,, \tag{2.4}$$

Ω being the whole parameter space. The $1-\alpha$ Bayesian Credible (BC) contour is the boundary of Ω_α and it corresponds to the contour level defined as $\{\theta\,|\,p(H,\theta|d) = p_\alpha\}$. In what follows we will use the BC contours at

$$1-\alpha = \{68.27\%\,,\,95.45\%\,,\,99.73\%\}\,. \tag{2.5}$$

In frequentist statistics, the likelihood function is employed to build a statistical test, like the likelihood ratio [12]

$$q(\theta) = -2\log\left[\frac{L(\theta)\pi(\theta)}{\max\limits_{\theta\in\Omega} L(\theta)\pi(\theta)}\right]\,. \tag{2.6}$$

The probability density function (*pdf*) of this test is then computed by simulation (typically, using Monte-Carlo pseudo-data). The *pdf* of $q(\theta)$, noted f_q, can then be used to evaluate a **p**-value, typically of the form

$$\mathbf{p}(\theta) = \int_{q_d}^{\infty} f_q(q'|\theta)\,dq'\,, \tag{2.7}$$

where q_d is the value given by the actual data. The $1-\alpha$ confidence regions are then obtained by solving $\mathbf{p}(\theta) = \alpha$, *i.e.* the confidence regions are given by $\Omega_\alpha = \{\theta|\mathbf{p}(\theta) > \alpha\}$.

Whenever the likelihood is Gaussian, q follows a χ^2 distribution. One has then $1-\alpha = F^{(n)}_{\chi^2}(q_\alpha)$, where $F^{(n)}_{\chi^2}$ is the χ^2 cumulative function with n degrees of freedoms. Confidence regions can thus be obtained by plotting $q(\theta) = q_\alpha$. This simpler procedure is commonly used in the literature, even when the likelihood is not Gaussian. We adopt this procedure throughout this work. In the case where the likelihoods are bivariate (which will be the case of our example of Higgs fit), we adopt the threshold values

$$q = \{2.30,\,6.18,\,11.83\}\,. \tag{2.8}$$

[12] In classical frequentist statistics, hypotheses and parameters are not associated with probabilities. In this work, for the frequentist side, we adopt the more general framework of hybrid Bayesian-frequentist statistics, in which a distribution can be attributed to a nuisance parameter. Conceptually, such distribution cannot be seen as a prior *pdf*, but corresponds to the likelihood for a real or imaginary measurement constraining the nuisance parameter (see Ref. [29], p. 4). However, by abuse of language, we will sometimes use the term "prior" in frequentist statistics as well. Classical frequentist statistics are recovered by giving a flat shape to these frequentist "prior" distributions.

In the Gaussian limit, these values match exactly the confidence levels $1-\alpha = \{68.27\%,\ 95.45\%,\ 99.73\%\}$.

2.2.2 Treatment of nuisance parameters

Marginalisation principle

Having introduced the nuisance parameters δ [13] in the likelihood $L(\theta, \delta)$, the next step is to eliminate them. This will effectively deform the likelihood, enlarging the preferred regions, and possibly shift their central values. In the Bayesian framework, this is naturally done by integrating over δ, so that

$$L_{\rm B}(\theta) = \int_{\mathcal{D}} d\delta\, L(\theta, \delta)\pi(\delta)\,, \tag{2.9}$$

where $\pi(\delta)$ is the prior distribution for the δ parameters. This operation is named *marginalisation*. In the frequentist framework, the likelihood is instead maximized,

$$L_{\rm F}(\theta) = \max_{\delta\in\mathcal{D}} \left[L(\theta, \delta)\pi(\delta)\right]\,. \tag{2.10}$$

This operation is usually named *profiling*. Here however, in order to emphasize the parallel between Bayesian and frequentist cases, we also refer to it as "marginalisation". The outcome of Bayesian and frequentist marginalisation gives respectively the marginal likelihoods $L_{\rm B}$ and $L_{\rm F}$. The best-fit regions are then obtained by using $L_{\rm B}$ and $L_{\rm F}$ in Eqs. (2.4) and (2.6), respectively. Finally, let us notice that in the frequentist case, it is clear that the marginalisation operation has the effect of selecting the values of δ preferred by the data.

Bias principle

The common feature of Bayesian and frequentist marginalisations is that nuisance parameters contribute to goodness-of-fit. This implies that the nuisance parameters can relax a tension among various measurements, which in turn induces a shift of the best-fit regions. In the context of the search for new physics, such a shift could also be characteristic of the presence of a new physics signal. It is thus of highest importance to correctly understand the effects of nuisance parameters, in order not to confuse systematic uncertainties with the presence of new physics!

In order to explicitly expose the shifts induced by nuisance parameters, and ultimately obtain more conservative results, a useful approach is to define a new operation, alternative to marginalising, with the requirement that the nuisance parameters *do not* contribute to goodness-of-fit. We will refer to this principle as *bias*, as opposite to the marginalisation principle. We will see that

[13] Recall that we have defined δ as a set of nuisance parameters, $\delta \equiv \{\delta_i\}$. The subsequent integrations and maximisations will thus be multidimensional.

the bias principle provides results that are independent of the shape of the prior of the nuisance parameters.

The bias principle can be intuitively grasped as follows. Consider the likelihood $L(\theta, \delta)$ with a single nuisance parameter on the interval $\delta \in [\delta_a, \delta_b]$. Instead of marginalising over δ, one can look at the contours of the likelihood for various *discrete* values of δ, say $\delta = \delta_a, \delta_b$. For each value of δ, the contours are given by Eq. (2.4) (Bayesian) or Eq. (2.6) (frequentist). To obtain the contours, we can see that the likelihood is separately normalised for δ_a and δ_b. This normalisation is in general not the same for δ_a and δ_b. Because of this normalisation factor, no particular value of δ is preferred by the fit. It is this normalisation factor that concretely realises the bias principle.

In Bayesian statistics, the bias principle finds a general realisation as follows. The requirement one wants to implement is that the nuisance parameters δ do not contribute to goodness-of-fit. This is equivalent to ask that the δ do not have a preferred region once data are taken into account. To translate formally this condition, the relevant quantity to involve is the marginal posterior of δ, $p(\delta|d)$. To implement the bias principle, one should thus require $p(\delta|d)$ to be constant, which translates into the condition

$$\frac{\partial}{\partial \delta} p(\delta|d) = 0\,, \tag{2.11}$$

with

$$p(\delta|d) = \int_\Omega d\theta\, L(\theta, \delta)\, \pi(\delta)\, \pi(\theta)\,. \tag{2.12}$$

We see that the condition (2.11) fixes the $\pi(\delta)$ prior to be

$$\pi(\delta) = \frac{1}{\int_\Omega d\theta\, L(\theta, \delta)\, \pi(\theta)}\,. \tag{2.13}$$

This peculiar prior is not independent on data, and is thus not orthodox with respect to the usual Bayesian philosophy. This is an expected consequence of biasing and all quantities are nevertheless well defined. It follows that the posterior for θ and δ has the form $L(\theta, \delta)\pi(\theta)/\int d\theta\, [L(\theta, \delta)\pi(\theta)]$. The Bayesian bias likelihood is then given by marginalising this particular posterior with respect to the nuisance parameters,

$$\bar{L}_{\rm B}(\theta) = \int_{\mathcal{D}} d\delta \left[\frac{L(\theta, \delta)}{\int_\Omega d\theta L(\theta, \delta)\pi(\theta)}\right]\,. \tag{2.14}$$

In frequentist statistics, the bias principle is realized in a very similar way to the Bayesian case. The quantity telling how δ is constrained by the data is the marginal likelihood for δ (with its associated "prior"), $\max_{\theta\in\Omega} [L(\theta, \delta)\pi(\theta)\pi(\delta)]$, which selects the preferred θ for a given δ. One requires this marginal likelihood to be constant,

$$\frac{\partial}{\partial \delta} \max_{\theta\in\Omega} [L(\theta, \delta)\pi(\theta)\pi(\delta)] = 0\,. \tag{2.15}$$

This implies that the $\pi(\delta)$ "prior" satisfies

$$\pi(\delta) = \frac{1}{\max\limits_{\theta\in\Omega} L(\theta,\delta)\pi(\theta)} \,. \tag{2.16}$$

The marginal likelihood of θ is then given by

$$\bar{L}_{\rm F}(\theta) = \max_{\delta\in\mathcal{D}} \left[\frac{L(\theta,\delta)}{\max\limits_{\theta\in\Omega}[L(\theta,\delta)\pi(\theta)]} \right] \,. \tag{2.17}$$

This operation is sometimes referred to as the envelope method. This is because, for a continuous domain $\mathcal{D}$, it draws continuous regions which are wider than the ones obtained by marginalising. [14]

Comparing the Bayesian and frequentist realisations of the bias principle, Eq. (2.14) and Eq. (2.17), it appears that the resulting bias operations are fully similar: the expressions Eq. (2.14) and Eq. (2.17) are identical up to interchanging maximisation and integration.

Let us finally comment about the best-fit regions for the bias likelihoods. The Bayesian bias is a particular case of Bayesian marginalisation with a well-chosen prior. The contours are thus obtained by integration, using $\bar{L}_{\rm B}$ in Eq. (2.4). For the frequentist bias, the bias likelihood $\bar{L}_{\rm F}$ can be treated using the usual likelihood ratio test and computing the associated p-value, as described in Eq. (2.6). We conclude that the best-fit regions for both the Bayesian and frequentist bias are well-defined.

Let us make an important comment which will turn useful for the frequentist treatments in Section 2.8. For a single δ in the discrete domain $\mathcal{D} = \{\delta_a, \delta_b\}$, the best-fit regions obtained by inserting the likelihood (2.17) in Eq. (2.6) reproduce exactly the ones in the discrete version of the bias described earlier in this subsection. Indeed, the normalized likelihood (2.17) will lead to a denominator equal to one in Eq. (2.6) and the role of this denominator in the contour definition will be played instead by the denominator of Eq. (2.17).

In this work, we will refer to the general realisations of the bias principle given by Eq. (2.14), (2.17) as the *envelope method*, for both the Bayesian and frequentist versions. In contrast, the discrete version of the bias previously introduced can be seen as a minimal realisation of this principle. In this work, we will refer to it as the *extremal bias*, for both the Bayesian and frequentist versions.

[14] Using $L = e^{-\chi^2/2}$, one has the equivalent formulation of the envelope method in terms of χ^2,

$$\bar{\chi}^2(\theta) = \min_{\delta} \Big[\chi^2(\theta,\delta) - 2\log\pi(\theta) - \min_{\theta}[\chi^2(\theta,\delta) - 2\log\pi(\theta)] \Big] \,. \tag{2.18}$$

In case of classical frequentist statistics, $\pi(\theta)$ is a constant, so that the two $\log\pi(\theta)$ terms cancel.

2.3 Combinations of theoretical uncertainties

This section applies to any systematic uncertainties. Nevertheless, since in this work our main focus is on theoretical uncertainties, we will readily use this term. In the previous section, we have seen that the correct procedure to incorporate theoretical uncertainties into the likelihood is to model these uncertainties using nuisance parameters and treat them using either the marginalisation or the bias approach. From the practical point of view, this step of marginalisation can be computationally heavy to carry out, both in the Bayesian and frequentist cases. Indeed, for each point in the space of parameters of interest, for n nuisance parameters, either a n-dimensional integration or a n-dimensional maximisation has to be done, whose complexity typically grows exponentially with n.

Because of the cost of exact marginalisation, it is a common practice in the high-energy physics community to combine certain uncertainties in a preliminary step, before carrying out the operation of marginalising. This approach of "preliminary combinations" should be followed with some care, because it can be approximative and may contain implicit assumptions. In this section, we revisit and develop the various operations of preliminary combination on a firm statistical ground.

2.3.1 Error modelisation

Let Q be an arbitrary quantity entering into a base likelihood $L[Q]$. The uncertainty about Q can be modelled via a dependence of the form

$$Q \mapsto Q \times (1 + \delta\,\Delta)\,, \tag{2.19}$$

where δ is the nuisance parameter, associated with a distribution $\pi(\delta)$, defined over the domain $\mathcal{D}$. Here and throughout this work, without loss of generality, we let all the δ follow a "standard distribution", such that all the information about the magnitude of the uncertainty will be contained in the coefficient Δ. With this parametrisation, Δ represents the *relative* uncertainty associated with Q. This linear model (2.19) is valid for any π distribution, provided that the magnitude of the relative error is small, $\Delta \ll 1$. The actual definition of π depends on the statistical approach adopted. In the Bayesian case, δ is a random variable, so that one chooses $\mathrm{E}[\delta] = 0$, $\mathrm{V}[\delta] = 1$. [15] Note that the domain of δ can be either finite or infinite. In the hybrid frequentist case, one can follow the same conventions as for the Bayesian case. The classical frequentist case is equivalent to have a flat π, and one sets the domain to be $\mathcal{D} \equiv [-1, 1]$ in that case. For the errors we will consider, π will always be centred on zero.

[15] E and V respectively denote the expected value and variance operators, $\mathrm{E}[\delta] = \int_{\mathcal{D}} d\delta\,\delta\,\pi(\delta)$ and $\mathrm{V}[\delta] = \int_{\mathcal{D}} d\delta\,\delta^2\,\pi(\delta) - (\mathrm{E}[\delta])^2$.

2.3.2 Bayesian combination of theoretical uncertainties

In the Bayesian framework, a nuisance parameter δ is rigorously taken as a random variable with prior distribution π. In presence of various nuisance parameters, one may wish to combine various sources of error, say δ_A and δ_B. A combination of these sources can be done if they appear systematically into a single combination inside the likelihood, $L[\delta_A\Delta_A + \delta_B\Delta_B]$. One can then define the combined error $\delta_C\Delta_C = \delta_A\Delta_A + \delta_B\Delta_B$, so that

$$L[\delta_C\Delta_C]\,\pi_C(\delta_C) \propto \int d\delta_A\; d\delta_B\; \delta[\delta_A\Delta_A + \delta_B\Delta_B - \delta_C\Delta_C]\, L[\delta_A\Delta_A + \delta_B\Delta_B]\; \pi_{A,B}(\delta_A, \delta_B)\,, \quad (2.20)$$

where $\delta[x]$ is the Dirac distribution. Here $\pi_{A,B}$ is the common prior of δ_A, δ_B. If these are independent, one has $\pi_{A,B}(\delta_A, \delta_B) = \pi_A(\delta_A)\pi_B(\delta_B)$. Note that the integration over δ_C of the left-hand side of this equation recovers Eq. (2.9).

When δ_A and δ_B are independent, Eq. (2.9) implies that the distribution of δ_C is exactly given by a convolution product,

$$\pi_C\left(\frac{x_C}{\Delta_C}\right) = \int dx\; \pi_A\left(\frac{x}{\Delta_A}\right)\, \pi_B\left(\frac{x_C - x}{\Delta_B}\right)\,. \quad (2.21)$$

The variable x can be seen as $\delta\Delta$. It is convenient to define $\bar{\pi}_C(x) = \pi_C\left(\frac{x}{\Delta_C}\right)$, so that the width of $\bar{\pi}_C$ is given by Δ_C. In contrast, recall that the width of π_C is always normalized to one by convention. Using the $\bar{\pi}$ definition, the convolution (2.21) can simply be written as

$$\bar{\pi}_C\left(x_C\right) = \int dx\; \bar{\pi}_A\left(x\right)\, \bar{\pi}_B\left(x_C - x\right)\,, \quad (2.22)$$

or more shortly

$$\bar{\pi}_C = \bar{\pi}_A \star \bar{\pi}_B\,. \quad (2.23)$$

The resulting distribution π_C has in general a non trivial shape, except for example when both $\pi_A$and π_B are Gaussian, in which case π_C is Gaussian as well. In contrast, Eq. (2.21) implies that the magnitudes of the errors Δ_A, Δ_B are combined following

$$\Delta_C^2 = \Delta_A^2 + \Delta_B^2\,, \quad (2.24)$$

irrespective of the shape of the distributions. That is, the errors are always combined in quadrature, *i.e.* the variances always add-up. Note the Δ^2's correspond to the variance of the $\bar{\pi}$ distributions.

In case of two independent sets of several correlated variables $\delta_{A,i}$, $\delta_{B,i}$ with respective covariance

matrices $\mathcal{C}_A$, $\mathcal{C}_B$, combined as $\delta_{C,i} = \delta_{A,i} + \delta_{B,i}$, [16] the combination is naturally generalized to

$$\mathcal{C}_C = \mathcal{C}_A + \mathcal{C}_B \,. \tag{2.25}$$

Again, this is independent of the prior shapes. The distribution of $\delta_{C,i}$ is again obtained using Eq. (2.20).

Finally, one may wish to combine nuisance parameters that are themselves correlated. In the case of two nuisance parameters δ_A, δ_B with a correlation coefficient ρ, one gets

$$\Delta_C^2 = \Delta_A^2 + \Delta_B^2 + 2\rho\Delta_A\Delta_B \,, \tag{2.26}$$

giving rise to a linear combination in the fully (anti-)correlated case $\rho = \pm 1$, and to Eq. (2.24) in the de-correlated case $\rho = 0$. The combination (2.26) is still independent of the prior shapes. Note that in this case π_C is still obtained from Eq. (2.20), but is not given anymore by a convolution product because π_A and π_B are not factorised anymore.

Finally, in the case of two sets of nuisance parameters $\delta_{A,i}$, $\delta_{B,i}$ with a relative correlation matrix $\mathcal{C}_{AB}$, one gets

$$\mathcal{C}_C = \mathcal{C}_A + \mathcal{C}_B + 2\mathcal{C}_{AB} \,. \tag{2.27}$$

All the results of this subsection are straightforward to derive using characteristic functions (more details are given in the Appendix of Ref. [30]).

In the limit $\Delta_A \gg \Delta_B$, it appears that $\pi_C \sim \pi_A$, *i.e.* the combined prior has mainly the shape of the leading uncertainty. In Section 2.3.4, we demonstrate that it is well justified to use Eq. (2.24), which is exact, together with the approximation $\pi_C \approx \pi_A$. Beyond the $\Delta_A \gg \Delta_B$ limit, if one wishes to care about the shape of π_C, a conservative approach is to consider both extreme cases $\pi_C = \pi_A$ and $\pi_C = \pi_B$. This is because the actual shape of π_C is always an intermediate distribution between π_A and π_B, as dictated by the convolution product.

2.3.3 Frequentist combination of theoretical uncertainties

Let us start again with the nuisance parameters δ_A, δ_B and their associated "prior" distribution $\pi_{A,B}$. If the nuisance parameters enter as a single combination in the likelihood, $L[\delta_A\Delta_A + \delta_B\Delta_B]$, one can define the nuisance parameter δ_C as above, and write

$$L[\delta_C\Delta_C]\ \pi_C(\delta_C) \ \propto \max_{\delta_A,\delta_B} \Big[\delta[\delta_A\Delta_A + \delta_B\Delta_B - \delta_C\Delta_C]\, L[\delta_A\Delta_A + \delta_B\Delta_B]\ \pi_{A,B}(\delta_A,\delta_B)\Big] \,, \tag{2.28}$$

[16] Note that in this case, for simplicity, we used a different convention from the one-variable case: we do not factor out the magnitude of the uncertainties (Δ_i) in front of the δ_i.

where again $\delta[x]$ is the Dirac distribution. [17] We emphasis that this formula is exactly similar to the Bayesian one, Eq. (2.20), with integration replaced by marginalisation. When $\pi_{A,B}(\delta_A, \delta_B) = \pi_A(\delta_A)\pi_B(\delta_B)$, it appears then that the distribution of δ_C is given by

$$\pi_C\left(\frac{x_C}{\Delta_C}\right) \propto \max_x \left[\pi_A\left(\frac{x}{\Delta_A}\right)\pi_B\left(\frac{x_C - x}{\Delta_B}\right)\right]. \tag{2.29}$$

This formula has a convolution product structure, where the integration has been replaced by a maximisation. From that point, it is then possible to compute the frequentist correlation matrix, $\mathcal{C}_{ij}^{-1} = -\partial^2 \log L/\partial\theta_i\partial\theta_j$. The general formula for the combination of $\mathcal{C}_A$, $\mathcal{C}_B$ is straightforward but tedious to compute. In sharp contrast with the Bayesian case, it appears in the frequentist case that the combination of the correlation matrices $\mathcal{C}_A$, $\mathcal{C}_B$ accordingly to Eq. (2.29) depends on the shape of the π_A, π_B distributions.

In the particular case where both π_A, π_B are Gaussian, the combination appears to be in quadrature, as in the Bayesian case. The combination formulas then match exactly the Bayesian ones, Eqs. (2.24) and (2.25). Moreover π_C is also Gaussian. Another important particular case is the one of flat priors. In that case, π_C appears to be flat, and the combination is *linear*,

$$\Delta_C = \Delta_A + \Delta_B\,. \tag{2.30}$$

Note that no correlation matrix can be defined in the flat case. [18]

In the case where δ_A and δ_B are correlated, they should be treated with a common "prior" as in the Bayesian case.

2.3.4 The leading moment approximation

Consider again the Bayesian case of a combination of two nuisance parameters, $\delta_C\Delta_C \equiv \delta_A\Delta_A + \delta_B\Delta_B$. Recall that the δ parameters have zero mean and have a standard distribution so that $\mathrm{E}[\delta] = 0$, $\mathrm{V}[\delta] = 1$. Assume further that the magnitude of the uncertainty B is small with respect to the uncertainty A,

$$\Delta_A \gg \Delta_B\,. \tag{2.31}$$

When this condition is satisfied, the source of uncertainty B can be treated as a perturbation to the source of uncertainty A. Starting from this observation, one can obtain π_C up to Δ_B/Δ_A corrections. This is demonstrated in the Appendix of Ref. [30] using characteristic functions. In particular, for independent variables, at the first non-trivial order in the expansion, one obtains

[17] Here $\delta[x]$ can be taken as the regularised Dirac peak.

[18] In the multivariate case, $\delta_{A,i}$ and $\delta_{B,i}$ have in general a non-trivial domain $\mathcal{D}_A$, $\mathcal{D}_B$. The combined domain $\mathcal{D}_C$ is given by the distance $||\delta_{C,i}||$ for which the centers of $\mathcal{D}_A$ and $\mathcal{D}_B$ are aligned with $\delta_{C,i}$ and the domain $\mathcal{D}_A$ and $\mathcal{D}_B$ share a single point. For example if $\mathcal{D}_A$, $\mathcal{D}_B$ are "hyper-rectangles" with size $\Delta_{A,i}$, $\Delta_{B,i}$, the sizes simply add up just like in the one-dimensional case, $\Delta_{C,i} = \Delta_{A,i} + \Delta_{B,i}$.

that

$$\pi_C \approx \pi_A \tag{2.32}$$

$$\Delta_C^2 = \Delta_A^2 + \Delta_B^2 \,. \tag{2.33}$$

Recall that π_C is determined by the convolution product $\bar{\pi}_C = \bar{\pi}_A \star \bar{\pi}_B$. Hence for $\Delta_A \gg \Delta_B$, one can intuitively expect that the shape of $\bar{\pi}_A$ and $\bar{\pi}_C$ are similar (see Eq. (2.32)), even though their widths are different (according to Eq. (2.33)). In case δ_A and δ_B are correlated, Eq. (2.33) has to be replaced be Eq. (2.26).

This "leading moment" approximation is useful in presence of a hierarchy between the magnitude of the various uncertainties. It dictates how to consistently capture the main effects of the uncertainties into the likelihood. This in turn allows one to obtain an approximate form for the combined priors, which opens up the possibility of obtaining analytical expressions for the marginal likelihoods.

The leading moment approximation also applies when δ_A and δ_B appear in various linear combinations within the likelihood. This situation typically happens when various observables are affected by the same source of uncertainty. The case of two nuisance parameters and two combinations is discussed in the Appendix of Ref. [30]. One considers two combinations $\delta_{C_1}\Delta_{C_1} = \delta_A\Delta_{A_1} + \delta_B\Delta_{B_1}$, $\delta_{C_2}\Delta_{C_2} = \delta_A\Delta_{A_2} + \delta_B\Delta_{B_2}$. It is found that the $\Delta_{C_{1,2}}$ are obtained as in the one-combination case discussed above. The correlation coefficient between δ_{C_1} and δ_{C_2} requires more attention. If $\Delta_{A_1} \gg \Delta_{B_1}$, $\Delta_{A_2} \gg \Delta_{B_2}$, it is found to be approximately equal to one. This implies that the shapes of the distributions of δ_{C_1}, δ_{C_2} and δ_A are the same up to $\Delta_{B_{1,2}}/\Delta_{A_{1,2}}$ corrections (see Appendix of Ref. [30]), that is

$$\pi_{C_1C_2}(\delta_{C_1}, \delta_{C_2}) \approx \pi_A(\delta_{C_1})\, \delta[\delta_{C_1} - \delta_{C_2}] \,. \tag{2.34}$$

From Eq. (2.34), it appears that the leading moment approximation reduces the number of nuisance parameters in the likelihood. In the case where $\Delta_{A_1} \gg \Delta_{B_1}$, $\Delta_{A_2} \ll \Delta_{B_2}$, it appears that the correlation coefficient between δ_{C_1} and δ_{C_2} is approximately equal to the correlation coefficient between δ_A and δ_B (see Appendix of Ref. [30]), so that

$$\pi_{C_1C_2} \approx \pi_{AB} \,. \tag{2.35}$$

In the particular case where δ_A and δ_B are independent, one has

$$\pi_{C_1C_2} \approx \pi_{C_1}\pi_{C_2} \,, \quad \pi_{C_1} \approx \pi_A \,, \quad \pi_{C_2} \approx \pi_B \,. \tag{2.36}$$

In the other particular case where δ_A and δ_B are 100% correlated or anti-correlated, one has

$$\pi_{C_1C_2}(\delta_{C_1}, \delta_{C_2}) \approx \pi_A(\delta_{C_1})\, \delta[\delta_{C_1} \pm \delta_{C_2}] \,. \tag{2.37}$$

All the cases with more variables or more combinations can be deduced recursively from the case with two parameters and two combinations studied here. [19]

2.3.5 Combining uncertainties in the bias approach

We now analyse how the combination of uncertainties arises in the case of the method of bias. We still consider a combination of nuisance parameters $\delta_{A,B}$ entering in the likelihood as $L[\delta_A\Delta_A + \delta_B\Delta_B]$. Recall that in our conventions, δ is a random variable with a fixed domain, while Δ is a number representing the magnitude of the uncertainty. In the bias approach, by definition, the shape of the distribution of δ is set so that δ does not participate to the fit. The information about the uncertainty is thus encoded only in the *domain* of the variable $\delta\Delta$. The choice of this domain has some degree of arbitrariness. This choice depends on how conservative one wants the results to be. In the following we choose to let δ vary in the interval $[-1, 1]$ and we identify Δ as a 1σ error, *i.e.* the same way it is defined for the marginalisation.

The operation of Bayesian bias can be seen as a special case of marginalisation, where the prior is set by Eq. (2.13). As the likelihood we consider in this section depends only on the combination $\delta_A\Delta_A+\delta_B\Delta_B$, this peculiar prior depends only on the combination $\delta_A\Delta_A+\delta_B\Delta_B$ by construction. Let us denote it as $\pi^B_{\text{bias}}(\delta_A\Delta_A + \delta_B\Delta_B)$. In order to get the combination $\delta_C\Delta_C = \delta_A\Delta_A + \delta_B\Delta_B$, one applies the definition of Eq. (2.20) using the π^B_{bias} prior. It turns out that $\pi_C(\delta_C) = \pi^B_{\text{bias}}(\delta_C\Delta_C)$. This means that the domain of $\delta_C\Delta_C$ is given by the domain of $\delta_A\Delta_A + \delta_B\Delta_B$,

$$\mathcal{D}_{\delta_C\Delta_C} = \mathcal{D}_{\delta_A\Delta_A+\delta_B\Delta_B}\,. \tag{2.38}$$

When δ_A and δ_B are independent, one has simply

$$\Delta_C = \Delta_A + \Delta_B\,. \tag{2.39}$$

When δ_A and δ_B are 100% correlated positively (*i.e.* $\delta_A = \delta_B$), it turns out that one has again the combination

$$\Delta_C = \Delta_A + \Delta_B\,. \tag{2.40}$$

When δ_A and δ_B are 100% correlated negatively (*i.e.* $\delta_A = -\delta_B$), the combination reads

$$\Delta_C = |\Delta_A - \Delta_B|\,. \tag{2.41}$$

Let us stress that the correlation between δ_A and δ_B is determined by their common domain $\mathcal{D}_{\delta_A\Delta_A,\delta_B\Delta_B}$. The above extreme cases are easily determined. The case of an intermediate correlation is trickier as it requires a precise definition of the domain. The case of an arbitrary correlation

[19] This leading moment approximation will be applied to the theoretical uncertainties on the Higgs rates in Sections 2.6.4 and 2.6.5.

will not be needed throughout this work. We see that the uncertainties are automatically combined *linearly* in the Bayesian bias method.

These results above can be applied recursively to more complex combinations. For example if $\delta_D\Delta_D = \delta_A\Delta_A + \delta_B\Delta_B + \delta_C\Delta_C$, with δ_A and δ_B 100% anti-correlated and δ_c independent from the two others, the bias combination gives

$$\Delta_D = |\Delta_A - \Delta_B| + \Delta_C \,. \tag{2.42}$$

Also, the bias combination applies in presence of various linear combinations (labelled by i) of the same nuisance parameters. In that case, the result of the combination is a common nuisance parameter δ, coming with different magnitudes Δ_i for each combination.

The frequentist bias has the same structure as the Bayesian bias. The starting point to determine the error combination is to use the frequentist version of the bias prior of Eq.(2.16) in Eq. (2.28). It follows that the frequentist combinations are the same as in the Bayesian case. We can thus conclude that in the bias approach, the preliminary combinations of uncertainties are done linearly, in both the frequentist and Bayesian cases. One should remark that such a combination is systematically more conservative than the combinations from both the Bayesian and frequentist marginalisations, as can be seen comparing Eqs. (2.39), (2.40), (2.41) with for example Eq. (2.26). Note that the combination in the frequentist marginalisation with flat prior (see *e.g.* Eq. (2.30)) is the same as the bias combination. Therefore the bias method is also more conservative than the standard marginalisation at the level of error combinations.

2.4 The Higgs boson rates

The couplings of the Higgs boson h are all predicted in the Standard Model, so that any deviation from the SM predictions would constitute a sign of the existence of physics beyond the SM. The Higgs couplings can be probed by collider experiments, which can produce the Higgs on-shell and observe its decays. This process of Higgs production followed by its decay is parametrised as

$$pp\,(p\bar{p}) \xrightarrow{X} h \to Y \,. \tag{2.43}$$

The SM Higgs production mechanisms accessible at the LHC (and Tevatron) are *i)* gluon-gluon fusion (ggF), *ii)* vector boson fusion (VBF), *iii)* associated production with an electroweak gauge boson $V = W, Z$ (VH), and *iv)* associated production with a $t\bar{t}$ pair (ttH). The main SM Higgs decays observed at the colliders are decays into gauge bosons, $h \to \gamma\gamma$, ZZ, W^+W^-, and into heavy fermions, $h \to b\bar{b}$, $\tau\bar{\tau}$. The production modes X and final states Y will be therefore taken in the following list,

$$X = \{\text{ggF, VBF, VH, ttH}\}\,, \tag{2.44}$$

$$Y = \{\gamma\gamma, ZZ, WW, b\bar{b}, \tau\bar{\tau}\}\,. \tag{2.45}$$

2.4.1 The data

The Higgs searches at ATLAS, CMS and the Tevatron are focussed on a specific final state Y. For each final state, various channels are defined using mutually exclusive cuts. Throughout this work, these experimental channels will be labelled by lower case latin indices $(i, j \dots)$. We will consider all the 88 channels. A given i contains the information on the final state and the specific channel. In the following, it will be sometimes useful to refer to the final state Y corresponding to a given channel i. We will use the short notation Y_i, meaning that Y is taken as a function of the variable i, *i.e.* $Y_i \equiv Y(i)$.

The results from Higgs searches at the LHC and the Tevatron are reported in terms of signal strengths $\mu_i^{\rm ex}$. A signal strength is defined as the ratio of the observed event number with the expected SM event number,

$$\mu_i^{\rm ex} = \frac{N_i^{\rm ex}}{N_i^{\rm SM}}\,. \tag{2.46}$$

The predicted SM event rate of a process $pp\,(p\bar{p}) \xrightarrow{X} h \to Y$ is given, in the narrow width approximation, by $\mathscr{L}\sigma_X^{\rm SM}B_Y^{\rm SM}$. Here $\sigma_X^{\rm SM}$ is the production rate, $B_Y^{\rm SM}$ is the branching ratio $B_Y^{\rm SM} = \Gamma_Y^{\rm SM}/\sum_{Y'}\Gamma_{Y'}^{\rm SM}$ and $\mathscr{L}$ is the integrated luminosity. However, from the experimental viewpoint, all the production processes contribute to a given final state. Hence the Higgs production cross sections have to be weighted by a selection efficiency $\epsilon_{X,i}^{\rm SM}$ encoding the effects of kinematical cuts. The actual expected event rates are thus given by

$$N_i^{\rm SM} = \mathscr{L}\sum_X \epsilon_{X,i}^{\rm SM}\sigma_X^{\rm SM}B_i^{\rm SM}\,, \tag{2.47}$$

where the notation $B_i^{\rm SM}$ is a shortcut for $B_{Y(i)}^{\rm SM}$, *i.e.* the index i selects the final state Y. The experimental Higgs signal strengths have thus the form

$$\mu_i^{\rm ex} \;=\; \frac{N_i^{\rm ex}}{\mathscr{L}\,\sum_X \epsilon_{X,i}^{\rm SM}\sigma_X^{\rm SM}\,B_i^{\rm SM}}\,. \tag{2.48}$$

Note that the kinematical cuts have been to some extent designed to disentangle the production modes, so that often one of the efficiencies will dominate over the others.

The experimental central values of the $\mu_i^{\rm ex}$, the associated statistical errors, the experimental systematic errors, and the selection efficiencies $\epsilon_{X,i}^{\rm SM}$ that we will exploit in our analysis are taken from the following references. The statistical and experimental systematic errors are often combined within these references and will be denoted here as $\Delta\mu_i^{\rm ex}$.
Regarding the ATLAS data, the diphoton final state results are taken from Ref. [31], the ZZ channel is from Ref. [32], the WW channel from Ref. [33], the $b\bar{b}$ from Ref. [34] and the $\tau\bar{\tau}$ from

Ref. [35]. Results are presented as well in Ref. [6] and the combined channels are studied in Ref. [4]. As for the CMS results, the diphoton final state has been presented in Ref. [36], the ZZ channel measurements are provided in Ref. [37], the WW ones in Ref. [38], the $b\bar{b}$ in Ref. [39] and the $\tau\bar{\tau}$ in Ref. [40] (see also Ref. [7] and the combined channel analyses [5]).
Finally, the latest results from the Tevatron (D0 and CDF Collaborations) can be found in Ref. [41, 42].

Apart from statistical and experimental systematic errors, certain theoretical errors on $\mu_i^{\rm ex}$ are included in the public results. To the best of our knowledge, the combination between these experimental and theoretical uncertainties is often made in quadrature. We thus subtract in quadrature these theoretical errors from the provided total uncertainties. How to properly (re)introduce the theoretical errors constitutes the main topic of this work, and will be discussed at length in the upcoming sections.

Finally, we mention that we do not include in our fits more challenging observables related to the Higgs pair production [43], off-shell effects, loop-induced $Z\gamma$ final state, electron/muon pair final states, final states induced by flavour-changing Higgs couplings, nor exotic or invisible final states. Some of those would require to introduce new parameters in the Lagrangian that we will consider in Eq. (2.49). The motivation is to keep a simple physical framework in order to discuss easily the statistical aspects. In any case, the present experimental limits on such Higgs observables are still not stringent enough to affect drastically the Higgs fits. Moreover, all the statistical concepts discussed throughout the work can be simply extended to new Higgs observables.

2.4.2 New physics parametrisation

The new physics possibly lying beyond the SM may induce a distortion of the SM Higgs couplings. The correct way of dealing with the low-energy manifestation of heavy new physics is through the use of an effective Lagrangian (see *e.g.* Ref. [16] for global fits of the Higgs effective Lagrangian). The leading effects on the Higgs sector appear through dimension-6 operators. The effective Lagrangian then induces anomalous couplings between the Higgs and the SM particles. The anomalous couplings to weak bosons and to heavy fermions can be parametrised as

$$\begin{aligned}\mathcal{L}_H \;=\;& c_W\; g_{hWW}\; h\; W^+_\mu W^{-\mu} + \; c_Z\; g_{hZZ}\; h\; Z^0_\mu Z^{0\mu} \\ & - \; c_t\; y_t\; h\; \bar{t}_L t_R \; - c_b\; y_b\; h\; \bar{b}_L b_R \; - c_c\; y_c\; h\; \bar{c}_L c_R \; - c_\tau\; y_\tau\; h\; \bar{\tau}_L \tau_R + \; \text{h.c.}\end{aligned} \tag{2.49}$$

where $y_{t,b,c,\tau}$ are the SM Yukawa coupling constants (in mass eigenbasis), the subscript L/R indicates the fermion chirality, v is the Higgs vacuum expectation value, $g_{hWW} = 2M_W^2/v$ and $g_{hZZ} = M_Z^2/v$ are the EW gauge boson couplings. The $c_{W,Z,t,b,c,\tau}$ parameters are defined such that the limiting case $c_{W,Z,t,b,c,\tau} \to 1$ corresponds to the SM. New tensor structures are also generated by the effective Lagrangian but are not taken into account here.

Our focus being on theoretical uncertainties, we adopt a fairly simple parametrisation of the new physics effects. We assume universal deviations for fermion couplings, $c_f \equiv c_t = c_b = c_c = c_\tau$, and for weak bosons, $c_V \equiv c_W = c_Z$. The c_f are assumed to be real. Clearly, this simplified description of the new physics effects represents only a piece (operators with no extra derivatives) of the full dimension-6 effective Lagrangian. Having $c_W \approx c_Z$ and c_f universality is however approximately compatible with certain new physics scenarios, like for a warped extra-dimension with bulk custodial symmetry vanishing IR brane kinetic terms for EW gauge bosons [44, 45]. [20] Having only two parameters in this simplified framework, the results of our fits will systematically be presented in the $c_V - c_f$ plane.

In the hypothesis of the existence of a physics Beyond the SM (BSM) parametrised by $c_V - c_f$, the expected signal strength is given by

$$\mu_i^{\rm th}[c_V, c_f] \;= \frac{N_i^{\rm BSM}[c_V, c_f]}{N_i^{\rm SM}} = \frac{\sum_X \epsilon_{X,i}^{\rm BSM} \sigma_X^{\rm BSM}\, B_i^{\rm BSM}}{\sum_X \epsilon_{X,i}^{\rm SM} \sigma_X^{\rm SM}\, B_i^{\rm SM}}\,, \tag{2.50}$$

$N_i^{\rm SM}$ being defined in Eq. (2.47). This is the theoretical prediction of the experimental signal strength defined in Eq. (2.48). Both BSM cross sections and branching ratios $\sigma_X^{\rm BSM}$, $B_i^{\rm BSM}$ can be expressed in terms of the SM amplitudes and of c_V, c_f. The expressions can for example be found in Ref. [46], whose procedure is closely followed here. In all generality, the BSM efficiencies are not the same as the ones of the SM either. However, this happens when couplings with new tensors structures are generated by new physics. In our simplified framework, this does not happen, such that one can safely take $\epsilon_{X,i}^{\rm BSM} = \epsilon_{X,i}^{\rm SM} \equiv \epsilon_X^i$.

The SM production cross sections and partial decay widths for the Higgs boson are taken, respectively, from the LHC Higgs cross section Working Group (LHCHWG) Ref. [17] (see also Ref. [18–20] as well as the recent N^{3}LO ggF computation [25]) and Ref. [17, 20]. These numerical results correspond to the rates calculated at the highest orders of EW and QCD corrections known so far (mixed EW-QCD at NNLO for the ggF mechanism [27] and at NLO for other Higgs production modes).

2.5 The Higgs likelihood

2.5.1 The base likelihood

Having introduced the statistical framework and the Higgs data in Sections 2.2 to 2.4, we can proceed with building the Higgs likelihood function. We define the *base* likelihood L_0 as the likelihood containing the central values of Higgs signal strengths, and the experimental uncertainties. The theoretical uncertainties are kept apart from now. Their inclusion into the base likelihood will be

[20] Note that contrary to a widespread belief, $c_W = c_Z$ is not entirely justified by custodial symmetry [44].

discussed at length in the next sections and is the central topic of this work.

In absence of any experimental systematic errors, a signal strength variable follows a Poisson statistics, and the associated likelihood is thus a Poisson distribution. Whenever the event number is large enough, about $O(10)$ in practice, the likelihood can be approximated by a Gaussian. In contrast, in presence of systematic uncertainties, this approximation generally does not hold. In practice however, the complete likelihood resulting from the combination of statistical and experimental systematic errors is not provided in the experimental public results. We will therefore model the base likelihood using Gaussian distributions, just as if the shape came out only from the statistical error. Such an approximation is expected to be good as long as the systematic error is small with respect to the statistical error, as shown in Section 2.3.4.

The observed rates in the current 88 channels (labelled by i, j) are potentially correlated, for example because of the experimental error on the luminosity. The base likelihood follows therefore a multivariate normal distribution,

$$L_\mu(\mu_i^{\rm th};\mu_i^{\rm ex}) = \exp\left[-\frac{1}{2}\sum_{i,j}(\mu_i^{\rm th}-\mu_i^{\rm ex})\,\mathcal{C}_{ij}^{\rm ex\,-1}\,(\mu_j^{\rm th}-\mu_j^{\rm ex})\right], \tag{2.51}$$

where $\mathcal{C}_{ij}^{\rm ex}$ is the correlation matrix among all channels.

Ideally, each individual observed channel i must be considered in order to take into account all the experimental information available on the signal strengths. In practice, few elements of this correlation matrix have been provided by the Collaborations up to now. Therefore in the following, we will include only the diagonal elements of $\mathcal{C}_{ij}^{\rm ex}$, given by $\mathcal{C}_{ii}^{\rm ex} = (\Delta\mu_i^{\rm ex})^2$, where $\Delta\mu_i^{\rm ex}$ is the experimental uncertainty extracted from the public experimental results. For future releases, we encourage the experimental Collaborations to provide as many elements as possible for the correlation matrix of the individual signal strengths. [21]

Alternatively, to perform the Higgs fits one could think of using the correlations between the combined observed rates, that are currently provided by the LHC Collaborations. Although instructive, these combined rates do not keep track of all information since they are grouping together different Higgs production modes (which were originally measured independently), like $\mu^{\rm ex}_{\rm VBF,VH}$ and $\mu^{\rm ex}_{\rm ggF,ttH}$ for each Higgs decay channel [6, 7]. Notice that such combined signal strengths also hide some information in the sense that they can result from summations over various exclusive selection cut categories.

[21] Also, we suggest that both the magnitudes of the uncertainties $\Delta\mu_i^{\rm ex}$ and the correlations should be presented without ambiguities, so that the people exterior to the Collaborations be able to properly reconstruct the likelihood function.

2.5.2 The uncertainty on the signal strengths

The Higgs theoretical uncertainties we will refer to are the theoretical uncertainties associated with the *expected* event rates $N_i^{\rm SM}$ defined in Eq. (2.47), that are obtained through analytical and numerical computations in quantum field theory. These uncertainties will propagate both into the experimental signal strengths $\mu_i^{\rm ex}$ and into the theoretical strengths $\mu_i^{\rm th}$, defined in Eqs. (2.48), (2.50). Following our conventions (see Section 2.3, Eq. (2.19)), the theoretical uncertainty on the Standard Model expected rate in a channel i is written under the form

$$N_i^{\rm SM}(1+\delta_i^N\Delta_i^N)\,, \tag{2.52}$$

where δ_i^N is the nuisance parameter with $\mathrm{E}[\delta_i^N]=0$, $\mathrm{V}[\delta_i^N]=1$, and Δ_i^N represents the relative magnitude of the uncertainty.

The theoretical uncertainty on $N_i^{\rm SM}$ propagates to the experimental signal strength as

$$\mu_i^{\rm ex}(1+\delta_i^\mu\Delta_i^\mu)=\mu_i^{\rm ex}(1-\delta_i^N\Delta_i^N)\,. \tag{2.53}$$

The case of the theoretical signal strength $\mu_i^{\rm th}=N_i^{\rm BSM}/N_i^{\rm SM}$ is slightly trickier. Here we focus on the most realistic case where the deviations induced by new physics are small, so that the anomalous couplings c_a (with $a=(W,Z,t,b,c,\tau)$) are close to one, *i.e.* $|c_a-1|\ll 1$. The contributions from new physics can be linearised with respect to the small parameters c_a-1, so that the BSM event rate in the channel i can be written as

$$N_i^{\rm BSM}=N_i^{\rm SM}+\sum_a (c_a-1)N_{a,i}^{\rm BSM}+O((c_a-1)^2)\,. \tag{2.54}$$

In this expression, it appears that the leading source of uncertainty comes from the SM event rate uncertainty Δ_i^N. In the expression of $\mu_i^{\rm th}$, it turns out that this uncertainty cancels out at first order between the numerator ($N_i^{\rm BSM}$) and the denominator ($N_i^{\rm SM}$). The subleading uncertainties would then come from a term quadratic in Δ_i^N and from the relative uncertainty $(c_a-1)\frac{\Delta N_{a,i}^{\rm BSM}}{N_{a,i}^{\rm BSM}}$ on the components $N_{a,i}^{\rm BSM}$. Notice that one can reasonably expect similar QCD errors in the SM and BSM predictions so that $\frac{\Delta N_{a,i}^{\rm BSM}}{N_{a,i}^{\rm BSM}}\sim\Delta_i^N$. These higher-order contributions are subleading compared to the error on the experimental signal strength, given in Eq. (2.53), which is of order Δ_i^N. In the following, we will thus focus only on the uncertainty of the experimental signal strength $\mu_i^{\rm ex}(1+\delta_i^\mu\Delta_i^\mu)$.

2.5.3 The structure of the Higgs theoretical uncertainties

The theoretical uncertainty on $N_i^{\rm SM}$ comes from the errors on the Higgs cross sections $\sigma_X^{\rm SM}$ and partial decay widths $\Gamma_Y^{\rm SM}$. Still following our conventions, these relative uncertainties are written

as

$$\sigma_X^{\rm SM}(1+\delta_X^\sigma\Delta_X^\sigma)\,, \tag{2.55}$$

$$\Gamma_Y^{\rm SM}(1+\delta_Y^\Gamma\Delta_Y^\Gamma)\,. \tag{2.56}$$

The exact content of these errors will be discussed in details in the next section.

The uncertainty on the partial decay width propagates to the branching ratios. Defining the relative error on the branching ratios as $B_Y^{\rm SM}(1+\delta_Y^B\Delta_Y^B)$, one has [22]

$$\delta_Y^B\Delta_Y^B = \sum_{Y'}\delta_{Y'}^\Gamma\Delta_{Y'}^\Gamma\left(B_{Y'}^{\rm SM}-\delta_{YY'}\right). \tag{2.57}$$

The uncertainty from the cross sections and branching ratios then propagates to the signal strength (2.48) and is thus encoded in a factor $\mu_i^{\rm ex}(1+\delta_i^\mu\Delta_i^\mu)$ where

$$\delta_i^\mu\Delta_i^\mu = -\delta_i^N\Delta_i^N = -\frac{\sum_X \epsilon_X^i\sigma_X^{\rm SM}\,\delta_X^\sigma\Delta_X^\sigma}{\sum_{X'}\epsilon_{X'}^i\sigma_{X'}^{\rm SM}} - \delta_{Y_i}^B\Delta_{Y_i}^B\,, \tag{2.58}$$

$Y_i = Y(i)$ being the Y decay mode of the Higgs channel detection i. Note that the sign after the first equal symbol is just a convention if the errors are symmetric.

Finally, the errors on cross sections and partial widths come from several sources. One can write those generically as

$$\delta_X^\sigma\Delta_X^\sigma = \sum_n \delta_X^n\Delta_X^n\,, \tag{2.59}$$

$$\delta_Y^\Gamma\Delta_Y^\Gamma = \sum_{n'}\delta_Y^{n'}\Delta_Y^{n'} \tag{2.60}$$

with the relative errors Δ_X^n, $\Delta_Y^{n'}$ to be detailed in the following. [23]

Knowing the base likelihood of Eq. (2.51), and knowing where exactly the theoretical uncertainties enter, we have the complete Higgs likelihood as a function of all the quantities that will have to be treated statistically, namely the nuisance parameters and the effective BSM parameters, [24]

$$L_\mu\left(\mu_i^{\rm th}[c_V,c_f];\,\mu_i^{\rm ex}(1+\delta_i^\mu\Delta_i^\mu)\right) = L_0\left(c_V,c_f;\delta_X^n,\delta_Y^{n'}\right). \tag{2.61}$$

Rigorously, the next step is to eliminate the nuisance parameters, δ_X^n, $\delta_Y^{n'}$, applying either the marginalisation or the bias method. In general these steps should be performed numerically, and are computationally heavy. Here however, we will use the methods of preliminary combinations

[22] $\delta_{YY'}$ represents the Kronecker symbol.

[23] Throughout the work, we will systematically denote the values of Δ_X^n, $\Delta_Y^{n'}$ taken from the literature by $\Delta\,|_0$ or $\Delta\,^0$. The possible ambiguities in the interpretation of these numbers will be discussed case by case.

[24] In the following, to adopt compact notation, we will omit the c_V, c_f arguments of the likelihood function when no ambiguity is possible.

advocated in Section 2.3. Then it will appear that the subsequent Higgs likelihoods are much lighter to treat.

2.6 Combining the Higgs rate uncertainties

In this section we shall combine the Higgs rate uncertainties that will be used in the marginal likelihood studied in Section 2.7. The most clear and rigorous statistical context for the marginalisation procedure is arguably the one of Bayesian statistics. In particular, the nuisance parameters are treated on the same ground as the variables of interest and are thus automatically given a probability distribution (see for instance Ref. [47]). For that reason we focus in this section on the error combinations within the *Bayesian* context. The resulting likelihood involving the combined errors will be formally treated within both the Bayesian and frequentist marginalisations in Section 2.7.

As we have described in Section 2.2.2, the Bayesian marginalisation procedure eliminates the dependence of the likelihood on the nuisance parameters through an integration. For the Higgs likelihood Eq. (2.61), this integration reads

$$L(c_V, c_f) \;=\; \int \left(\prod_{n,n',X,Y} d\delta_X^n \; d\delta_Y^{n'} \right) \pi_0(\delta_X^n, \delta_Y^{n'}) \;\; L_0(c_V, c_f; \delta_X^n, \delta_Y^{n'}) \,, \tag{2.62}$$

where π_0 is the joint prior of all the nuisance parameters. Recall that this prior factorises when parameters are independent. More explicitly, this marginal likelihood reads

$$\begin{aligned} L(c_V, c_f) \;=\; & \int \left(\prod_{n,n',X,Y} d\delta_X^n \; d\delta_Y^{n'} \right) \pi_0(\delta_X^n, \delta_Y^{n'}) \;\times \\ & \exp\left[-\frac{1}{2} \sum_{i,j} (\mu_i^{\rm th}[c_V, c_f] - \mu_i^{\rm ex}(1 + \delta_i^\mu \Delta_i^\mu)) \, \mathcal{C}_{ij}^{\rm ex\,-1} \, (\mu_j^{\rm th}[c_V, c_f] - \mu_j^{\rm ex}(1 + \delta_j^\mu \Delta_j^\mu)) \right] . \end{aligned} \tag{2.63}$$

The theoretical uncertainties $\delta_i^\mu \Delta_i^\mu$ on each signal strength μ_i are expressed in terms of the uncertainties on cross section $\delta_X^n \Delta_X^n$ and partial decay width $\delta_Y^{n'} \Delta_Y^{n'}$ through Eqs. (2.57) to (2.60).

In the following subsections, starting from Eq. (2.63), we will combine all the sources of uncertainty step-by-step, following the combination formalism established in Section 2.3. The aim of this section is to provide a clear and exhaustive treatment of all the Higgs theoretical uncertainties.

2.6.1 Combining the PDF and α_s uncertainties

Let us first discuss the errors on QCD predictions for the Higgs production cross sections at the proton level. Those are induced by the uncertainties on the parton Probability Density Functions (PDF) inside the proton. First, one may distinguish between two distinct origins to the PDF un-

certainties: an experimental source – as the PDF are reconstructed from collider data – and the choice of a specific PDF set (MSTW, CT/CTEQ, NNPDF...).
Second, we consider simultaneously the parametric uncertainty coming from the strong coupling constant, α_s. We consider both PDF and α_s uncertainties simultaneously because they contribute in an intricate way to the cross section, as α_s enters both in the hard process matrix element and the PDF themselves.

• Modeling the uncertainties:
The uncertainties from α_s and the collider data are modeled by the nuisance parameters δ^{α_s}, $\delta^{\rm data}$ and constitute independent sources of uncertainty (hence with factorisable priors). The relative uncertainties on α_s and the PDF data can be parametrised as

$$\alpha_s(1+\delta^{\alpha_s}\Delta^{\alpha_s})\,, \quad {\rm data}(1+\delta^{\rm data}\Delta^{\rm data})\,. \tag{2.64}$$

The α_s error enters in the cross section in two different ways. On one hand, α_s is used in the fit of the data aimed at determining the PDF themselves. On the other hand, α_s is also involved in the hard subprocess that is convoluted with the PDF to obtain the final cross section. These two contributions to the cross section uncertainty, named here as $\Delta^{\alpha_s,{\rm fit}}$ and $\Delta^{\alpha_s,{\rm hard}}$, are not available in the literature. However, we will show that the knowledge of these two separate contributions is not necessary either. Rather, provided that the relative errors $\Delta^{\alpha_s,{\rm fit}}$ and $\Delta^{\rm data}$ are small enough to be linearised, only the sum $\Delta^{\alpha_s,{\rm hard}}+\Delta^{\alpha_s,{\rm fit}}$ is needed. This sum can typically be inferred from the literature.

In order to understand the interplay among the α_s and the data uncertainties, it is instructive to write explicitly how they enter into the cross section. One should start with the form

$$\sigma_X^{\rm SM}[f_{\rm PDF}[\alpha_s,{\rm data}],\alpha_s]\,, \tag{2.65}$$

where the first argument corresponds to the PDF input, while the second argument represents the α_s-dependence coming from the partonic process. From this general form, one then introduces the δ^{α_s} and $\delta^{\rm data}$ nuisance parameters, and expand the expression at first order, [25]

$$\begin{aligned}\sigma_X^{\rm SM}\big[f_{\rm PDF}[\alpha_s(1+\delta^{\alpha_s}\Delta^{\alpha_s}),{\rm data}(1+\delta^{\rm data}\Delta^{\rm data})],\alpha_s(1+\delta^{\alpha_s}\Delta^{\alpha_s})\big] = \\ \sigma_X^{\rm SM}\big[f_{\rm PDF}\,[\alpha_s,{\rm data}],\alpha_s\big]\Big(1+\delta^{\alpha_s}(\partial_1 f_{\rm PDF}\,\partial_1\sigma_X^{\rm SM}\,\Delta^{\alpha_s})+\delta^{\rm data}(\partial_2 f_{\rm PDF}\,\partial_1\sigma_X^{\rm SM}\,\Delta^{\rm data}) \\ +\delta^{\alpha_s}(\partial_1 f_{\rm PDF}\,\partial_2\sigma_X^{\rm SM}\,\Delta^{\alpha_s})+O(\Delta^2)\Big)\,.\end{aligned} \tag{2.66}$$

The terms in the last two lines represent the errors propagated to the cross section at first order in Δ, expressed as partial derivatives of $\sigma_X^{\rm SM}$, and correspond precisely to the relative errors on the

[25] The $\partial_{1,2}$ represents derivative with respect to the first and second argument of the function respectively, $\partial_1 f = \partial f(x,y)/\partial x$, $\partial_2 f = \partial f(x,y)/\partial y$.

cross section, [26]

$$\delta^{\alpha_s}\Delta_X^{\alpha_s,\text{fit}} + \delta_X^{\text{data}}\Delta_X^{\text{data}} + \delta^{\alpha_s}\Delta_X^{\alpha_s,\text{hard}} \,. \tag{2.67}$$

It appears clearly that only the sum $\Delta_X^{\alpha_s,\text{hard}}+\Delta_X^{\alpha_s,\text{fit}}$ is needed. Fortunately, this is what is provided in the literature. This sum $\Delta_X^{\alpha_s} \equiv \Delta_X^{\alpha_s,\text{hard}} + \Delta_X^{\alpha_s,\text{fit}}$ can be read for example from Ref. [20]. Note also that the nuisance parameter δ^{α_s} is common to any production mode, *i.e.* it does not carry the index X. In contrast, the nuisance parameter δ_X^{data} carries an index X because each production mode potentially involves different initial states. These initial states correspond to different PDF, which are fitted from different data sets.

Finally, one should check the validity of the error propagation at linear order in the cross sections (*i.e.* that the $O(\Delta^2)$ in Eq. (2.66) is well negligible). From Eq. (2.66)-(2.67), one can see that at linear order, for any fixed value of α_s (*i.e.* fixed value of δ^{α_s}), the error bar on σ_X^{SM} induced by the data uncertainty (obtained from varying δ^{data}, e.g. in [-1,1]) should have the same size. A change with α_s of this bar size could thus come only from higher order terms such like

$$\delta^{\alpha_s}\delta^{\text{data}}\,(\partial_1\partial_2 f_{\text{PDF}}\;\partial_1^2\sigma_X^{\text{SM}}\,\Delta^{\alpha_s}\,\Delta^{\text{data}}).$$

On the Fig. (57)-(58)-(59) of Ref. [20] for the various Higgs production reactions at the 8 TeV LHC, we see that the change of this bar size (vertical bar there) is small with respect to the shift (*i.e.* $\Delta_X^{\alpha_s}$) of the bar central values. We conclude that one can restrict the expansion Eq. (2.66) to linear order in a good approximation.

Notice that a customary way to write these uncertainties is by splitting between the overall PDF error and the hard subprocess error, $\delta_X^{\text{PDF}}\Delta_X^{\text{PDF}} + \delta^{\alpha_s}\Delta_X^{\alpha_s,\text{hard}}$, with $\delta_X^{\text{PDF}}\Delta_X^{\text{PDF}} = \delta^{\alpha_s}\Delta_X^{\alpha_s,\text{fit}} + \delta_X^{\text{data}}\Delta_X^{\text{data}}$. The trouble when using this form is that the δ_X^{PDF} and $\delta^{\alpha_s,\text{hard}}$ contributions are correlated via α_s. Combining these uncertainties then requires to know such a correlation coefficient, which is fixed by $\Delta^{\alpha_s,\text{fit}}$, as well as $\Delta^{\alpha_s,\text{hard}}$. We emphasize that the use of this intermediate parametrisation brings unnecessary complications, and we recommend thus to avoid it.

Hence according to Eq. (2.67), the parametric uncertainties from α_s are cast into a single error $\Delta_X^{\alpha_s}$, and add up with the statistical error from the data as

$$\delta_X^{\text{data}}\Delta_X^{\text{data}} + \delta^{\alpha_s}\Delta_X^{\alpha_s} \,. \tag{2.68}$$

Using this approach, one deals directly with the elementary sources of uncertainty. These two sources of error have no intrinsic relation and are thus independent, meaning that δ^{data} and δ^{α_s} have factorisable priors.

Similarly, the uncertainty from the choice of a specific PDF set, modeled by δ^{set}, can be added

[26] Note that the Δ's in Eq. (2.67) can be negative as they are identified from the partial derivatives in Eq. (2.66). In the rest of the work however, the Δ's are taken positive by convention. Different signs for the Δ's would correspond to a negative correlation, that is instead included at the level of the δ's in the rest of the work.

up linearly to the errors of Eq. (2.68) in a good approximation. The linear approximation can be justified from Fig. (57) in Ref. [20]. There one can see that the size of the data error bars as well as the shifts induced by α_s depend only weakly on the PDF set choice. The $\delta^{\rm set}$ error is also independent from the $\delta_X^{\rm data}$, δ_s^{α} errors and in turn possesses its own prior distribution. All those errors induce three terms in the sum of theoretical errors entering Eq. (2.59). These terms can be cast into a global PDF uncertainty,

$$\delta_X^{\rm PDF+\alpha_s}\Delta_X^{\rm PDF+\alpha_s} \,\hat{=}\, \delta^{\rm set}\Delta_X^{\rm set} + \delta_X^{\rm data}\Delta_X^{\rm data} + \delta^{\alpha_s}\Delta_X^{\alpha_s} \ . \tag{2.69}$$

We recall that $X = \{{\rm ggF}, {\rm VBF}, {\rm VH}, {\rm ttH}\}$ and that the Δ's are relative errors, which are chosen by convention to correspond to one standard deviation. Those are related to the 1σ absolute errors on the SM Higgs cross section through *e.g.*

$$\Delta_X^{\rm data} \,\hat{=}\, \frac{\Delta\sigma_X^{\rm data}}{\sigma_X^{\rm SM}} \ .$$

• Combining the three uncertainties:
Here we combine the three sources of theoretical uncertainty described in Eq. (2.69). We will add up more and more errors progressively in the following subsections. These three independent sources of error are associated with three priors π^{α_s}, $\pi_X^{\rm data}$, $\pi^{\rm set}$. These nuisance parameters appear in Eq. (2.63), where they are integrated over. We now proceed to combine these errors following the analysis of Section 2.3, starting from Eq. (2.20). In practice, for the discussion, it will be convenient to combine only two errors at a time. One then finds a likelihood of the type (2.63) depending only on the nuisance parameter $\delta_X^{\rm PDF+\alpha_s}$. The distribution of this nuisance parameter comes with a 1σ width $\Delta_X^{\rm PDF+\alpha_s}$ given by

$$(\Delta_X^{\rm PDF+\alpha_s})^2 = (\Delta_X^{\rm set})^2 + (\Delta_X^{\rm data})^2 + (\Delta_X^{\alpha_s})^2 \ . \tag{2.70}$$

The nuisance parameter $\delta_X^{\rm PDF+\alpha_s}$ obeys a new prior $\pi_X^{\rm PDF+\alpha_s}$, obtained via two successive convolutions of the initial priors (as in Eq. (2.21)-(2.22)-(2.23)),

$$\bar\pi_X^{\rm PDF+\alpha_s} \;=\; \bar\pi_X^{\rm set} \star \bar\pi_X^{\rm data} \star \bar\pi_X^{\alpha_s} \ , \tag{2.71}$$

where $\bar\pi_X^{\rm PDF+\alpha_s}(x) = \pi_X^{\rm PDF+\alpha_s}(x/\Delta_X^{\rm PDF+\alpha_s})$ and the variable x corresponds to the relative error $\delta_X^{\rm PDF+\alpha_s}\Delta_X^{\rm PDF+\alpha_s}$. For the initial priors one has for example $\bar\pi_X^{\alpha_s}(x) = \pi^{\alpha_s}(x/\Delta_X^{\alpha_s})$. The Eq. (2.70) and then (2.71) are justified in details in the rest of this subsection.

• Details on the data and α_s error combinations:
We emphasize that the Bayesian combination of the 1σ widths, as here in Eq. (2.70), is *independent* of the shapes of the prior distributions. This combination only depends on the possible correlations

among individual errors [*c.f.* Section 2.3.2]. In the present case, there is no correlation between the $\delta_X^{\rm data}$ and $\delta_X^{\alpha_s}$ parameters, as explained right below Eq. (2.68). This leads to the sum in quadrature of the 1σ errors $(\Delta_X^{\rm data})^2 + (\Delta_X^{\alpha_s})^2$ in Eq. (2.70).

Let us comment about those uncertainties. First, the error associated to $\pi_X^{\rm data}$ originates mainly from measurements: it is mainly induced by the limited accuracy of data points used to perform the fit for reconstructing PDF. Hence this error is mostly of statistical nature. There exists of course systematic errors as well, but it has been checked by several groups that the final $\pi_X^{\rm data}$ distribution can be reasonably taken as Gaussian [18].

Second, the uncertainty on α_s originates mainly from lattice calculation errors (mainly theoretical) and especially from perturbative truncation errors [48] [27]. Indeed the α_s determination from lattice methods (most accurate one in Ref. [48]) represents today the most precise determination and hence essentially dictates the final world average error [49]. The FLAG Working Group on lattice calculations has estimated a more conservative uncertainty on α_s, which is increased by a new QCD perturbative error estimation [50], thus still leading to a dominant theoretical uncertainty.

At this level, a comment is needed on the link between the 1σ errors and the uncertainty magnitudes provided in literature. To remain conservative we use $\Delta_X^{\alpha_s} = \Delta_X^{\alpha_s}|_0$ for the 1σ error, where $\Delta_X^{\alpha_s}|_0$ is the error provided by Ref. [17, 20]. There is indeed a somewhat arbitrary choice for the relation between $\Delta_X^{\alpha_s}$ and $\Delta_X^{\alpha_s}|_0$, due to the theoretical (QCD) nature of the uncertainty. The origin of this arbitrariness is the fact that the QCD errors are just estimated by varying the renormalisation and factorisation scales on arbitrary intervals. We present a similar discussion in the beginning of next Section (2.6.2) for $\Delta_X^{\rm scale}$. Concerning the 1σ error from data, one can adopt $\Delta_X^{\rm data} = \Delta_X^{\rm data}|_0$ ($\Delta_X^{\rm data}|_0$ being read from Ref. [17, 20]). Indeed, the probability distribution for the uncertainty induced by the experimental data can be safely described by a Gaussian, as described above, so that the errors provided by Ref. [17, 20] can reasonably be interpreted as 1σ errors.

Let us now discuss the convolution between $\bar{\pi}_X^{\rm data}$ and $\bar{\pi}_X^{\alpha_s}$ that appears in Eq. (2.71). For that purpose, we first need to discuss the form of the π^{α_s} distribution. The shape of π^{α_s} can be taken as flat since the uncertainty on α_s originates mainly from theoretical uncertainty, as mentioned above. However, the choice of the prior for a theoretical uncertainty is often controversial, so that we will also consider the case of a non-flat π^{α_s} distribution. [28]

Finally, the convolution of the Gaussian prior, $\bar{\pi}_X^{\rm data}$, with a flat prior, $\bar{\pi}_X^{\alpha_s}$, gives rise to a Gaussian distribution, $\bar{\pi}_X^{\rm data} \star \bar{\pi}_X^{\alpha_s}$, in a good approximation for the various Higgs production modes. The justification is that the $\bar{\pi}_X^{\alpha_s}$ width, $\Delta_X^{\alpha_s}$, is systematically smaller or of the same order as $\Delta_X^{\rm data}$, [29]

[27] The only source of experimental error is, m_{η_c},m_{η_b}, and is minor – as can be read from the Table IV of Ref. [48].

[28] To be consistent throughout the work, concerning the initial priors, we will assume a flat shape for the distributions whose shape is unknown (uncertainties from QCD, parametrisation...).

[29] For the ggF example, our conservative treatment of the errors provided in Fig. (59) of Ref. [20] gives an half absolute width, $W/2 \hat{=} \sqrt{3}\Delta\sigma_X^{\alpha_s} = \sqrt{3}\Delta\sigma_X^{\alpha_s}|_0 \simeq 0.5$ pb, which is indeed comparable to, $\Delta\sigma_X^{\rm data} = \Delta\sigma_X^{\rm data}|_0 \simeq 0.5$ pb. In the alternative case (see the analogous discussion at the start of Section 2.6.2), one has instead, $W/2 \hat{=} \sqrt{3}\Delta\sigma_X^{\alpha_s} = \Delta\sigma_X^{\alpha_s}|_0 \simeq 0.3$ pb, which is clearly smaller than, $\Delta\sigma_X^{\rm data} \simeq 0.5$ pb, so that the Gaussian approximation for the final convolution would be even better because this case would tend to a situation where the non-Gaussian error becomes negligible.

in which case the convolution leads to an almost pure Gaussian prior. This will be demonstrated explicitly in Fig. (2.2) for other priors.

• Details on the combination with the PDF set error:
The various PDF estimations provided by the different fitting groups reflect several sources of error [51–53]. Indeed, these groups make different choices/hypotheses about the numbers of free parameters used to model the PDF [30], the statistical methods adopted to fit the data [31], the number of independently parameterized PDF (in particular regarding (anti-) strangeness), the collider results exploited, the matching methods applied to include heavy-quark mass effects in the flavour number scheme and the variable- or fixed-flavour number scheme. All these sources of uncertainty are synthesized in the 1σ error on the Higgs production rates noted $\Delta_X^{\rm set}$. To remain conservative, we assume $\Delta_X^{\rm set} = \Delta_X^{\rm set}|_0$, where $\Delta_X^{\rm set}|_0$ is the error read from Fig. (57)-(59) of Ref. [20]. $\Delta_X^{\rm set}|_0$ can be estimated by taking half the interval obtained by using the various PDF sets which lead to a finite number of predictions for the Higgs rate central values. Of course, this determination of $\Delta_X^{\rm set}|_0$ is probably underestimated as *(i)* the hypotheses made by the groups provide illustrative examples which do not necessarily indicate the extremal values of the PDF, and, *(ii)* the effects of the various sources of error listed above can potentially compensate each other. We comment on this point in the following paragraph.
In Eq. (2.70), the sum in quadrature between the $\Delta_X^{\rm set}$ error and the data and α_s errors is justified because these are independent uncertainties. Nevertheless, in practice, for our numerical applications, we use the so-called envelope method [32] to determine $\Delta_X^{\rm PDF+\alpha_s}$ as done in Ref. [20, 54] [33] and calculated by the LHCHWG [17]. Note that the envelope method overestimates the combined errors, compensating somehow for the underestimation of the PDF set error. For the ggF mechanism, the $\Delta\sigma_{\rm ggF}^{\rm PDF+\alpha_s}$ error derived in this way has to be reduced by $\sim 40\%$ to recover the quadrature summation of Eq. (2.70), and the decrease is smaller for the other Higgs production reactions. Hence, we conclude that the use of the envelope method to determine the global PDF uncertainties gives rise to a substantial overestimation of these errors.

We finally discuss the shape of the prior of the final combination $\pi_X^{\rm PDF+\alpha_s}$. Most of the sources of error taken into account in $\Delta_X^{\rm set}$ are of theoretical nature and all the errors have unknown distributions. The shape of $\pi_X^{\rm set}$ is therefore assumed to be flat. The convolution of $\bar{\pi}_X^{\rm set}$ (see Eq. (2.71)) with the nearly Gaussian distribution $\bar{\pi}_X^{\rm data} \star \bar{\pi}_X^{\alpha_s}$ leads in a good approximation to a

[30] The infinite-dimensional problem of representing a space of functions is reduced to a finite-dimensional form, in order to be manageable, by introducing a parametrisation of the PDF.

[31] There exist mainly two classes of methodology currently used to determine a confidence interval represented in the space of functions: some variations of the Hessian approach (multi-Gaussian probability distributions) and the Monte Carlo approach. Both types of methods have their own limitations.

[32] This "envelope method" corresponds precisely to the uncertainty combinations in the bias approach, see Section 2.3.5. What we call envelope method in the present work is rather described in Section 2.2.2.

[33] In the envelope method used in this reference, the whole uncertainty interval is found by searching at the minimum and maximum rates (considering the various PDF sets, α_s values and including the possibility to move along the data-error bars). Then dividing by two this interval gives an estimation of the combined error as well as a central value for the rate.

final Gaussian prior, $\pi_X^{\text{PDF}+\alpha_s}$ [34]. Once more, this is guaranteed by the fact that for any Higgs production mode at the LHC, Δ_X^{set} is smaller or comparable to the combination of Δ_X^{data} and $\Delta_X^{\alpha_s}$ (see for instance Ref. [20]).

2.6.2 Scale and EFT errors: the amplitude uncertainties

• Scale error:

There exists another major type of error, this time at the parton level, on the QCD prediction for Higgs production cross sections. It originates from the lack of knowledge on the higher order contributions to the amplitude in the perturbative expansion, and can be recast into the dependence on the QCD renormalisation and factorisation scales. We note δ_X^{scale} the nuisance parameter representing this "scale uncertainty".

There are no strong arguments to choose the shape for π_X^{scale}. As for many other theoretical uncertainties, the choice of the prior is typically a subject of controversy. Here we choose π_X^{scale} to be flat. Concerning the magnitude of the scale uncertainty Δ_X^{scale}, it is also not clear to which width exactly corresponds the provided value, noted Δ_X^0 here, that is found in Ref. [17,18,25]. It is reasonable to expect Δ_X^{scale} to be of order Δ_X^0. To be more precise, we could make the two different assumptions, $\Delta_X^0 \hat{=} \Delta_X^{\text{scale}}$ or $\Delta_X^0 \hat{=} \mathcal{W}/2$ where $\mathcal{W}$ is defined as the support of the distribution, [35] with *e.g.* in the case of a flat distribution on an interval with size $\mathcal{W}$: $2\Delta_X^{\text{scale}} \hat{=} \mathcal{W}/\sqrt{3} = 2\Delta_X^0/\sqrt{3}$. In order to be conservative in the choice of Δ_X^{scale}, we choose the former hypothesis throughout this work: $\Delta_X^{\text{scale}} = \Delta_X^0$.

It is remarkable that recently [25], the calculation for the ggF mechanism has been pushed up to the complete N^{3}LO order in perturbative QCD. This has allowed a reduction of the symmetrized [36] scale error from $\Delta_{\text{ggF}}^0 \simeq 7.51\%$ (with the renormalisation/factorisation scale $\mu_0 = m_H/2$ to absorb some of the soft-gluon resummation corrections [55]) [17, 18], down to $\Delta_{\text{ggF}}^0 \simeq 4.16\%$ (with $\mu_0 = m_H$ [37]) [25]. The error was obtained in both cases by spanning the interval $[\mu_0/2, 2\mu_0]$, for the renormalisation/factorisation scale $\mu = \mu_{\text{R}} = \mu_{\text{F}}$, at an energy $\sqrt{s} = 8$ TeV and for $m_H \simeq 125.2$ GeV.

• EFT error:

In the specific case of the ggF mechanism, another source of error arises in the amplitude of the Higgs production [56], that we describe now. The evaluation of this amplitude beyond the NLO

[34] Given that there are several sources of errors contained in the PDF set uncertainty, one may expect the π_X^{set} prior to be somehow peaked. This feature improves even more the Gaussian approximation of $\pi_X^{\text{PDF}+\alpha_s}$.

[35] Recall that the support of a distribution is the domain where this distribution is not zero-valued.

[36] Symmetrized over the positive and negative errors as, $\Delta = [(\Delta_+^2 + \Delta_-^2)/2]^{1/2}$.

[37] Choosing instead, $\mu_0 = m_H/2$, could be motivated by a faster convergence of the perturbative series [25]. However, since it would lead to a significantly smaller uncertainty, $\Delta_{\text{ggF}}^0 \simeq 2.13\%$, we stick to the central choice, $\mu_0 = m_H$, in order to remain conservative.

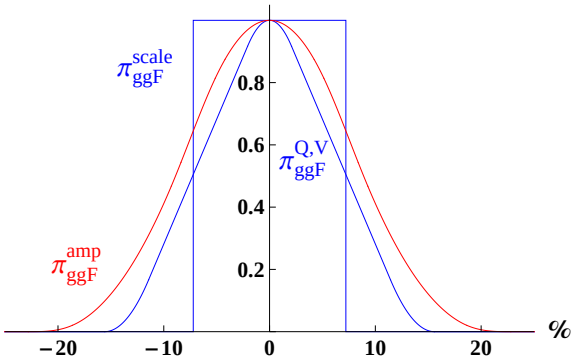

Figure 2.1: Probability density distribution, $\pi^{\rm amp}_{\rm ggF}(x/\Delta^{\rm amp}_{\rm ggF})$ (in red), involving the relative error x (in %) of the ggF cross section, as derived through the convolution of the $\pi^{\rm Q,V}_{\rm ggF}$ and $\pi^{\rm scale}_{\rm ggF}$ priors (both in blue). The quantity $\Delta^{\rm amp}_{\rm ggF}$ represents the relative 1σ error on the Higgs production rate (see text). For better comparison, the normalisation is chosen such that all the functions possess the same maximum, equal to unity at the origin.

level is possible within the Effective Field Theory (EFT) approach, where the particles running in the triangle loop are assumed to be much heavier than the produced Higgs boson to integrate out the heavy particles.

For the top quark exchange, the infinite mass assumption, $m_t \gg m_H$, induces a negligible error on the ggF amplitude [27, 57]. In contrast, the EFT approach is clearly not valid for the other significant ggF contribution: the bottom quark exchange [25]. This inappropriate use of the EFT limit introduces some non-negligible error mainly through the interference between the bottom and dominant top quark loops (this error being smaller at the Tevatron than at the LHC) [58].

A similar uncertainty originates from the mixed QCD-EW corrections to the ggF process [27]. Those have been calculated at NNLO via the EFT approach based on the simplifying but unrealistic assumption, $M_{W,Z} \gg m_H$. For all the EFT errors, some approximative estimations can be computed at NNLO (using K-factors obtained at NLO and NNLO for the top loop) [26, 57].

A related uncertainty comes from the freedom in the choice of a renormalisation scheme for the bottom quark mass, involved in the ggF amplitude (on-shell scheme, $\overline{\rm MS}$ scheme...). The error from the renormalisation scheme dependence can be approximately estimated at NLO [57].

These three sources of theoretical uncertainty, namely the two kinds of EFT assumptions (on the heavy quark masses, m_Q ($Q = b, t$), and vector boson masses, M_V ($V = W, Z$)) and the m_b scheme dependence, are independent and their respective priors are unknown. We assume these priors to be flat. To be conservative, we take the three 1σ errors to be equal to the numbers estimated in Ref. [26, 57], for the 8 TeV LHC. Summing those in quadrature gives rise to the relative rate error, $\Delta^{\rm Q,V}_{\rm ggF} \hat{=} \Delta\sigma^{\rm Q,V}_{\rm ggF}/\sigma^{\rm SM}_{\rm ggF} \simeq 5.6\%$. The convolution of the three flat priors (accordingly to Eq. (2.23)) leads to the blue distribution, $\pi^{\rm Q,V}_{\rm ggF}$, shown in Fig. (2.1), which already resembles a Gaussian shape as predicted by the central limit theorem.

• COMBINING THE $\Delta_{\rm ggF}^{\rm scale}$ AND $\Delta_{\rm ggF}^{\rm Q,V}$ ERRORS:
The theoretical scale and EFT uncertainties on the ggF mechanism are of different nature and are thus independent. The combined ggF 1σ error is in turn given by

$$(\Delta_{\rm ggF}^{\rm amp})^2 \;=\; (\Delta_{\rm ggF}^{\rm scale})^2 + (\Delta_{\rm ggF}^{\rm Q,V})^2 \;. \tag{2.72}$$

This error constitutes the characteristic width of the $\pi_{\rm ggF}^{\rm amp}$ distribution obtained by convoluting the $\bar{\pi}_{\rm ggF}^{\rm scale}$ and $\bar{\pi}_{\rm ggF}^{\rm Q,V}$ priors, as performed in Fig. (2.1) (see the final red curve). Remarkably, this distribution,

$$\bar{\pi}_{\rm ggF}^{\rm amp} \;\equiv\; \bar{\pi}_{\rm ggF}^{\rm scale} \star \bar{\pi}_{\rm ggF}^{\rm Q,V} \;, \tag{2.73}$$

derived from four purely flat priors, is Gaussian in a good approximation. This can be also seen in Fig. (2.3) where $\pi_{\rm ggF}^{\rm amp}$ is plotted together with a pure Gaussian distribution (blue curves). Recall that $\bar{\pi}_{\rm ggF}^{\rm amp}(x) = \pi_{\rm ggF}^{\rm amp}(x/\Delta_{\rm ggF}^{\rm amp})$ and the variable x corresponds to $\delta_{\rm ggF}^{\rm amp}\Delta_{\rm ggF}^{\rm amp}$.

2.6.3 Combination of the PDF and amplitude errors

For the various Higgs production modes – except the ggF process that will be discussed separately below, one has to combine the PDF and scale errors to determine the final uncertainty on the whole cross section. The scale error adds up to the PDF error of Eq. (2.69), according to Eq. (2.59), defining the total uncertainty on the cross section,

$$\delta_X^\sigma \Delta_X^\sigma = \delta_X^{\rm PDF+\alpha_s}\Delta_X^{\rm PDF+\alpha_s} + \delta_X^{\rm scale}\Delta_X^{\rm scale} \;. \tag{2.74}$$

These errors being independent, the 1σ widths add-up in quadrature,

$$(\Delta_X^\sigma)^2 = (\Delta_X^{\rm PDF+\alpha_s})^2 + (\Delta_X^{\rm scale})^2 \;, \tag{2.75}$$

as dictated by Section 2.3.2, *i.e.* irrespective of the $\pi_X^{\rm PDF+\alpha_s}$ and $\pi_X^{\rm scale}$ shapes. Recall that Δ_X^σ is the 1σ width of the resulting $\bar{\pi}_X^\sigma$ distribution. The prior π_X^σ of this total uncertainty is then given by (see Eq. (2.23))

$$\bar{\pi}_X^\sigma \;\equiv\; \bar{\pi}_X^{\rm PDF+\alpha_s} \star \bar{\pi}_X^{\rm scale} \;, \tag{2.76}$$

with $\bar{\pi}_X^\sigma(x) = \pi_X^\sigma(x/\Delta_X^\sigma)$ and x corresponding to $\delta_X^\sigma\Delta_X^\sigma$.

Let us discuss the form of the π_X^σ function, as generated through Eq. (2.76). The shape of $\pi_X^{\rm scale}$ being unknown, we assume a flat $\pi_X^{\rm scale}$ distribution. Remind that this error is simply obtained by varying the QCD scale, so that no favoured value is predicted for the cross section. It is therefore a sensible choice to assign equal probabilities to all the values of $\delta_X^{\rm scale}$ (or equivalently of the Higgs cross section) inside a certain range. On the other hand, we have seen in Section 2.6.1 that $\pi_X^{\rm PDF+\alpha_s}$

is approximatively Gaussian. Given the relative values of $\Delta_X^{\rm PDF+\alpha_s}$ and $\Delta_X^{\rm scale}$ for each process X – which are systematically such that either $\Delta_X^{\rm PDF+\alpha_s} > \Delta_X^{\rm scale}$ or $\Delta_X^{\rm PDF+\alpha_s} \approx \Delta_X^{\rm scale}$ [38] – a Gaussian $\pi_X^{\rm PDF+\alpha_s}$ and a flat $\pi_X^{\rm scale}$ lead in a good approximation to a final Gaussian π_X^σ. This combination is shown in Fig. (2.2) for ZH production, for which $\Delta_{ZH}^{\rm PDF+\alpha_s} \simeq 2.5\%$ and $\Delta_{ZH}^{\rm scale} = \Delta_{ZH}^0 \simeq 3.1\%$ (at $\sqrt{s} = 8$ TeV with $m_H \simeq 125.2$ GeV) [17].

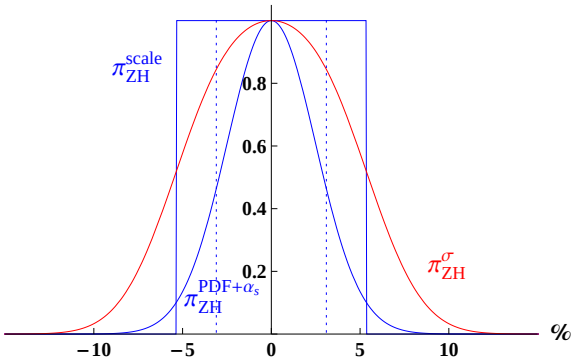

Figure 2.2: Probability density distribution, $\pi_{ZH}^\sigma(x/\Delta_{ZH}^\sigma)$ (in red), involving the relative error x (in %) of the ZH production cross section, as derived through the convolution of a Gaussian $\pi_{ZH}^{\rm PDF+\alpha_s}$ and a flat $\pi_{ZH}^{\rm scale}$ priors (both in blue). The quantity, Δ_{ZH}^σ, represents the relative 1σ error on the Higgs production rate. The normalisation is chosen such that all the functions possess the same maximum, equal to unity at the origin. The 1σ band for the $\pi_{ZH}^{\rm scale}$ distribution is indicated by the vertical dotted lines.

• The ggF reaction:

In the case of Higgs production via the ggF mechanism, the PDF error has to be combined with the whole amplitude error studied previously in Section 2.6.2. The resulting total error on the cross section is

$$\delta_{\rm ggF}^\sigma \Delta_{\rm ggF}^\sigma = \delta_{\rm ggF}^{\rm PDF+\alpha_s} \Delta_{\rm ggF}^{\rm PDF+\alpha_s} + \delta_{\rm ggF}^{\rm amp} \Delta_{\rm ggF}^{\rm amp} . \tag{2.77}$$

These two errors being independent, their widths add-up in quadrature,

$$(\Delta_{\rm ggF}^\sigma)^2 = (\Delta_{\rm ggF}^{\rm PDF+\alpha_s})^2 + (\Delta_{\rm ggF}^{\rm amp})^2 \ , \tag{2.78}$$

and their priors are convoluted following

$$\bar\pi_{\rm ggF}^\sigma \ \equiv \ \bar\pi_{\rm ggF}^{\rm PDF+\alpha_s} \star \bar\pi_{\rm ggF}^{\rm amp} . \tag{2.79}$$

This convolution (2.79) is performed in Fig. (2.3), using the $\pi_{\rm ggF}^{\rm amp}$ distribution obtained in Fig. (2.1) and the value $\Delta_{\rm ggF}^{\rm PDF+\alpha_s} \simeq 7.20\%$ (at $\sqrt{s} = 8$ TeV with $m_H \simeq 125.2$ GeV) [17]. Both priors $\pi_{\rm ggF}^{\rm amp}$, $\bar\pi_{\rm ggF}^{\rm PDF+\alpha_s}$ being nearly Gaussian, the final distribution is almost Gaussian. [39]

[38] whatever is the prescription: $\Delta_X^{\rm scale} = \Delta_X^0$ or $\Delta_X^{\rm scale} = \Delta_X^0/\sqrt{3}$.

[39] Recall the convolution of two Gaussian distributions gives rise to a Gaussian distribution.

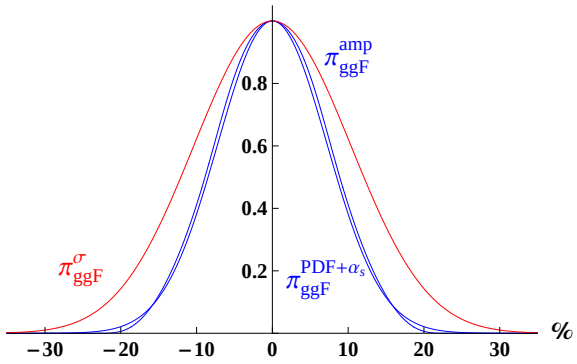

Figure 2.3: Probability density distribution, $\pi^{\sigma}_{\rm ggF}(x/\Delta^{\sigma}_{\rm ggF})$ (in red), involving the relative error x (in %) of the ggF cross section, as derived through the convolution of a Gaussian $\pi^{\rm PDF+\alpha_s}_{\rm ggF}$ prior and the $\pi^{\rm amp}_{\rm ggF}$ distribution obtained in Fig. (2.1) (both in blue). The quantity, $\Delta^{\sigma}_{\rm ggF}$, represents the relative 1σ error for the ggF rate.

2.6.4 The production contamination

There are several production mechanisms for the Higgs boson (recall that $X = \{$ggF, VBF, WH, ZH, ttH$\}$). The cross section for each of these production modes is associated with a theoretical uncertainty, that has been obtained through subsections 2.6.1 to 2.6.3. In fact, one may note that the uncertainties of these various cross sections are potentially correlated, as they partly arise from common sources like the α_s parametric error. Therefore the δ^{σ}_X follow a common distribution π^{σ}, which does not necessarily factorise into $\pi^{\sigma}_{\rm ggF}\pi^{\sigma}_{\rm VBF}\times\ \ldots$ The aspect of correlations among the cross section errors will be further discussed in Section 2.7.1. Here we shall proceed using the most general prior π^{σ}, and we denote the resulting correlation matrix as $\rho^{\sigma}_{XX'}$. [40]

The contribution from the cross sections errors in a given detection channel can be read from Eq. (2.58). Let us first adopt a more compact notation,

$$\frac{\sum_X \epsilon^i_X \sigma^{\rm SM}_X\, \delta^{\sigma}_X \Delta^{\sigma}_X}{\sum_{X'} \epsilon^i_{X'} \sigma^{\rm SM}_{X'}} \;\hat{=}\; \sum_X \delta^{\sigma}_X \Delta_{X,i}\,, \tag{2.80}$$

where the $\delta^{\sigma}_X\Delta^{\sigma}_X$ are defined in Eqs. (2.74), (2.77). The Higgs detection channels have been designed to select predominantly a certain mode of production. That is, for a given channel i, the experimental cuts are profiled so that typically the efficiency ϵ^i_X for one of the production modes X (see Eq. (2.48)) is much larger than for the others, implying a hierarchy among the $\Delta_{X,i}$. We can therefore use the leading moment approximation, developed in Section 2.3, to proceed to the combination of the errors. Applying the leading moment approximation amounts to treat the contaminations as a small perturbation of the uncertainty from the leading production mode. The

[40] In Section 2.7.1, the assumptions adopted for $\rho^{\sigma}_{XX'}$ will allow us to express π^{σ} in terms of the π^{σ}_X.

cross section uncertainties propagate in a given detection channel as (P stands for production)

$$\delta^P_{X_i}\Delta^P_i \;=\; \delta^\sigma_{\rm ggF}\Delta_{{\rm ggF},i} + \delta^\sigma_{\rm VBF}\Delta_{{\rm VBF},i} + \delta^\sigma_{\rm ZH}\Delta_{{\rm ZH},i} + \delta^\sigma_{\rm WH}\Delta_{{\rm WH},i} + \delta^\sigma_{\rm ttH}\Delta_{{\rm ttH},i}\,. \tag{2.81}$$

Here the label of the combined nuisance parameter $\delta^P_{X_i}$ is chosen to be the label of the dominant production mode in the i channel. Note that X_i should be understood as $X(i)$. This naming refers to the fact that the shape of the combined nuisance parameter prior corresponds approximatively to the shape for the dominant uncertainty, see Eq. (2.32). For example, if the production mode ggF dominates in the channel i, one has

$$\delta^P_{X_i} = \delta^P_{\rm ggF}\,. \tag{2.82}$$

The various nuisance parameters δ^P_X are potentially correlated. They should thus follow a joint prior distribution, π^P, generating a correlation matrix $\rho^P_{XX'}$.

Assuming generic correlations $\rho^\sigma_{XX'}$ among the various cross section errors, the magnitude of the combined production uncertainty in a channel i is given exactly by

$$(\Delta^P_i)^2 = \sum_{XX'}\rho^\sigma_{XX'}\Delta_{X,i}\Delta_{X',i}\,. \tag{2.83}$$

The leading moment approximation then dictates (see Eqs. (2.34)–(2.37)) that

$$\pi^P \approx \pi^\sigma\,. \tag{2.84}$$

Equation (2.84) implies that the correlations among the δ^P_X are approximatively the same as the ones between the δ^σ_X, *i.e.*

$$\rho^P_{XX'} \approx \rho^\sigma_{XX'}\,. \tag{2.85}$$

This fact can be understood as follows. Consider only two detection channels, i and j. If the same production mode $X \mathrel{\hat{=}} X_i = X_j$ dominates in both channels, they are nearly 100% correlated, so that they are described by a single nuisance parameter δ^P_X, which is equivalent to say that $\rho^P_{XX} \approx 1$. Note that one has $\rho^\sigma_{XX} = 1$ by definition, so that $\rho^P_{XX} \approx \rho^\sigma_{XX}$. Besides, if two different production modes $X_i \neq X_j$ dominate respectively in the i and j channels, the uncertainties in both channels are respectively described by $\delta^P_{X_i}$ and $\delta^P_{X_j}$. These two nuisance parameters inherit the correlation from the leading production modes X_i and X_j, which is given by $\rho^\sigma_{X_iX_j}$. Therefore one recovers Eq. (2.85).

Finally, notice that for certain kinematical cuts selecting the ttH mode in the diphoton decay channel [31], even additional production modes can slightly contribute, like the bbH, tHW and $tHbq$ productions. These production modes participate in the contamination and have thus been included in the combination of production modes in Eq. (2.81).

2.6.5 The uncertainties on branching ratios

Two sources of error affect the Higgs signal strengths: the production and the decay rate uncertainties (see Eq. (2.48)). The latter is often not considered in the Higgs fits. Still following our approach of step-by-step combinations, one should start with the signal strength error Eq. (2.58), where all uncertainties on production modes have been already combined (Eq. (2.81)). The uncertainties on production and decay rates combine thus as, up to an irrelevant global sign,

$$\delta^{\mu}_{X_i}\Delta^{\mu}_i = \delta^{P}_{X_i}\Delta^{P}_i + \delta^{B}_{Y_i}\Delta^{B}_{Y_i} \quad \text{with} \quad \Delta^{B}_{Y_i} = \frac{\Delta B_i^{\rm SM}}{B_i^{\rm SM}} \ , \ B_i^{\rm SM} = \frac{\Gamma_{Y_i}^{\rm SM}}{\Gamma_{\rm tot}} \tag{2.86}$$

where $\Gamma_{Y_i}^{\rm SM}$ is the SM partial decay width for the detection channel i. In this equation, we apply the leading moment approximation to treat the branching ratios errors as perturbations of the leading error from production modes. This is why the $\delta^{\mu}_{X_i}$ parameters carry the index X_i, which is the index of the dominant production mode in the channel i, as in the previous subsection. For example, if the production mode ggF dominates in the channel i, one has

$$\delta^{\mu}_{X_i} = \delta^{\mu}_{\rm ggF} \, . \tag{2.87}$$

The relative error $\delta^{B}_{Y_i}\Delta^{B}_{Y_i}$ on the SM branching ratio is expressed as in Eq. (2.57), where the decay width uncertainty (2.60) can now be specified in terms of the various sources of error (*c.f.* Section 3 of Ref. [57] for a recent overview, and references therein),

$$\delta^{\Gamma}_{Y}\Delta^{\Gamma}_{Y} \ = \ \sum_a \delta^{{\rm pu}_a}_{Y}\Delta^{{\rm pu}_a}_{Y} + \delta^{\rm thu}_{Y}\Delta^{\rm thu}_{Y} \quad \text{where } e.g. \quad \Delta^{\rm thu}_{Y} = \frac{\Delta\Gamma^{\rm thu}_{Y}}{\Gamma^{\rm SM}_{Y}} \ . \tag{2.88}$$

The partial decay width errors $\Delta\Gamma_Y^{\rm thu/pu_a}$ are taken from the LHCHWG [17, 18, 20]. The $\Delta\Gamma^{\rm thu}_Y$ denote the theoretical uncertainties due to the limitations of QCD perturbative calculations. The $\Delta\Gamma^{{\rm pu}_a}_Y$ represent the parametric uncertainties induced by the experimental errors on the input parameters, labelled by $a \equiv \alpha_s, m_c, m_b, m_t$ (charm, bottom and top quark masses). Typically, one has $\Delta^{\rm thu/pu_a}_{b\bar{b}} \gg \Delta^{\rm thu/pu_a}_{VV^*}, \Delta^{\rm thu/pu_a}_{\tau\bar{\tau}}$ since the QCD corrections to the $h \to VV^*$, $\tau\bar{\tau}$ decay channels arise only at orders higher or equal to $O(\alpha_s^2)$.

The $\Delta\Gamma^{{\rm pu}_a}_Y$ errors are associated to Gaussian distributions, and are thus identified without ambiguity with the errors defined in Ref. [20]. The $\Delta\Gamma^{\rm thu}_Y$ errors are purely theoretical, so that one associates them with flat priors. To adopt a conservative prescription, as in Section 2.6.3, we interpret the numbers given in [17] as 1σ-widths. These numbers are thus directly identified with the $\Delta\Gamma^{\rm thu}_Y$.

Now inserting Eq. (2.88) into Eq. (2.57) provides the contributions of the theoretical and para-

metric uncertainties to the branching ratios,

$$\begin{aligned}\delta^B_{Y_i}\Delta^B_{Y_i} &= \sum_{Y,a}\delta_Y^{\mathrm{pu}_a}\Delta_Y^{\mathrm{pu}_a}\left(B_Y^{\mathrm{SM}}-\delta_{Y_iY}\right)+\sum_Y\delta_Y^{\mathrm{thu}}\Delta_Y^{\mathrm{thu}}\left(B_Y^{\mathrm{SM}}-\delta_{Y_iY}\right)\\ &\hat{=} \sum_{Y,a}\delta_Y^{\mathrm{pu}_a}\Delta^a_{Y,i}+\sum_Y\delta_Y^{\mathrm{thu}}\Delta_{Y,i}\ ,\end{aligned} \tag{2.89}$$

where in the last line one introduces a compact notation for the error magnitudes. The sum over Y here must include all the individual Higgs decay channels (not only the ones effectively detected at colliders), namely $Y \equiv b\bar{b}, c\bar{c}$, WW, ZZ, $\tau\bar{\tau}$, $\gamma\gamma$, gg ...

We stress that the parametric error $\delta_Y^{\mathrm{pu}_a}\Delta_Y^{\mathrm{pu}_a}$ on various decay rates Y arises from the same source (namely, varying the fundamental parameter a). The parametric errors on the various decays are thus fully correlated. Therefore, one could in principle drop the Y index on $\delta_Y^{\mathrm{pu}_a}$. There is however a subtlety, because these errors can be either 100% correlated or 100% anti-correlated. The use of parameters δ^{pu_a} would render the full correlation manifest, but minus signs would have to be included in certain $\Delta_Y^{\mathrm{pu}_a}$. Here instead, we chose positive Δ's by convention. We have thus to keep the Y index on $\delta_Y^{\mathrm{pu}_a}$, bearing in mind that this Y labels only 100% correlation or anti-correlation. A second subtlety is that these signs are actually not clearly given in the literature. Rather, only the absolute values of the $\Delta_Y^{\mathrm{pu}_a}|_0$ are provided. We adopt a conservative choice by assuming that all these errors are 100% correlated.

We can now apply the leading moment approximation on the combination of Eqs. (2.86)-(2.89), where the leading uncertainty is $\delta^P_{X_i}\Delta^P_i$ and the perturbation is $\delta^B_{Y_i}\Delta^B_{Y_i}$, *i.e.* $\Delta^P_i \gg \Delta_{Y,i}, \Delta^a_{Y,i}$. The 1σ-width of the global theoretical uncertainty in a channel i is given by

$$(\Delta_i^\mu)^2 = (\Delta_i^P)^2 + \sum_a\left[\sum_Y\Delta^a_{Y,i}\right]^2+\sum_Y(\Delta_{Y,i})^2\ , \tag{2.90}$$

with Δ_i^P given by Eq. (2.83). Regarding the prior distribution of the δ_X^μ, the discussion is exactly the same as the one in Section 2.6.4. That is, following the leading moment approximation, the joint distribution of the δ_X^μ corresponds to the one of the leading uncertainties δ_X^P, so that

$$\pi^\mu \approx \pi^P\ . \tag{2.91}$$

This implies in particular that the δ_X^μ inherit the correlations from the δ_X^P, that is $\rho^\mu_{XX'} \approx \rho^P_{XX'}$.

Let us discuss the correlations used to derive Eq. (2.90), which are drawn from Ref. [17,18,20]. First, a given parametric uncertainty associated to $\delta_Y^{\mathrm{pu}_a}$ introduces 100% correlated errors among the various decay modes Y, so that the sum over Y of the $\Delta^a_{Y,i}$ is linear. Recall the parametric correlations are taken to be all positive. There is also a slight correlation between $\delta^P_{X_i}\Delta^P_i$ and $\delta_Y^{\mathrm{pu}_{\alpha_s}}\Delta^{\alpha_s}_{Y,i}$, because δ^P_X also contains a contribution from the α_s error. The α_s contribution being subleading in δ^P_X, its correlation with $\delta_Y^{\mathrm{pu}_{\alpha_s}}$ is expected to be small, so that we can neglect it. All

the other sources of uncertainties are independent due to their different origins, so that summations in quadrature appear everywhere else in Eq. (2.90).
Using the definitions of the reduced Δ's in Eq. (2.89), we finally write explicitly the total theoretical uncertainty on the signal strength of a Higgs detection channel i,

$$(\Delta_i^\mu)^2 = (\Delta_i^P)^2 + \sum_a \left[\sum_Y \Delta_Y^{\mathrm{pu}_a} \left(B_Y^{\mathrm{SM}} - \delta_{Y_i Y} \right) \right]^2 + \sum_Y \left[\Delta_Y^{\mathrm{thu}} \left(B_Y^{\mathrm{SM}} - \delta_{Y_i Y} \right) \right]^2 . \tag{2.92}$$

2.6.6 Summary

In this section we have assembled step by step all the theoretical uncertainties on the Higgs signal strengths, starting from the Higgs likelihood Eq. (2.63). This combination is made possible by the statistical analysis of Section 2.3, whose results have been extensively used here. The final Higgs likelihood involving the combined errors reads

$$\begin{aligned} L(c_V, c_f) \quad &= \int \left(\prod_X d\delta_X^\mu \right) \pi^\mu(\delta_X^\mu) \times \\ \exp \quad &\left[-\frac{1}{2} \sum_{i,j} \left(\mu_i^{\mathrm{th}}[c_V, c_f] - \mu_i^{\mathrm{ex}}(1 + \delta_{X_i}^\mu \Delta_i^\mu) \right) \mathcal{C}_{ij}^{\mathrm{ex}\,-1} \left(\mu_j^{\mathrm{th}}[c_V, c_f] - \mu_j^{\mathrm{ex}}(1 + \delta_{X_j}^\mu \Delta_j^\mu) \right) \right] . \end{aligned} \tag{2.93}$$

The only label for the combined nuisance parameters $\delta_{X_i}^\mu$ is X_i, the dominant production mode for a given channel i (see for instance Eq. (2.87)). The prior π^μ is approximately equal to the prior of the production mode uncertainties π^σ, through Eq. (2.84) and Eq. (2.91). In Section 2.7.1, the assumptions on the correlations among the production modes will allow us to express π^σ in terms of the priors of individual production mode uncertainties π_X^σ (see Eqs. (2.34)–(2.37)).

One of the outcome of the combination procedure followed throughout this section is that the shape of the combined priors π_X^σ appears to be almost Gaussian. This comes partly because some of the priors for the individual sources of uncertainty are Gaussian. However, the main reason is actually that a substantial number of the individual sources of uncertainty are independent and of same order of magnitude. These conditions resemble to the ones of the *central limit theorem*, which predicts that the combination would converge towards a Gaussian distribution. Besides, the small errors from contamination and partial decay widths do not affect either the final prior shape under the leading moment approximation. It follows that the π^μ distribution is close to a multivariate Gaussian distribution.

Finally, we stress again that the famous question of the linear versus quadratic summation of individual errors (as the ones used in this section to derive Δ_i^μ in Eq. (2.92)) relies uniquely on the correlations among the errors, and is therefore independent of the shapes of the priors. This general feature holds when uncertainties are combined using Bayesian statistics.

2.7 Marginalising the Higgs likelihood

2.7.1 Correlations of the detection channels

In this subsection we focus on the correlations among Higgs detection channels induced by the theoretical uncertainties. These correlations appear whenever a source of uncertainty contributes simultaneously to various channels.

As a preliminary observation, let us recall that these correlations are sometimes not taken into account in the literature. What is typically done in such case is that some amount of error, typically from Refs. [17–20], is added independently to the statistical error of each detection channel. Such combination typically reads $(\Delta\mu_i^{\rm ex})^2 + (\Delta\mu_i^{\rm th})^2$ if done in quadrature. From the point of view of nuisance parameters, this combination would correspond to associating one independent $\delta_i^\mu \Delta_i^\mu$ to each detection channel, and thus performing one integration per channel in the marginal likelihood.

The issue with such approach is that the correlations among channels induced by the theoretical uncertainties are lost. As stated in Section 2.2.2, these correlations are crucial because they potentially change the tension among the various channel measurements, which in turn can modify the best-fit regions. As slight modifications of the best-fit regions are expected in presence of new physics, treating correctly the theoretical uncertainties is fundamental.

Taking into account the correlations among channels amounts to consistently propagate the theoretical errors into the different detection channels. This is precisely what is done through the combination procedure of Section 2.6. Combining the errors together and using the leading moment approximation to treat subdominant errors, only five nuisance parameters $\delta^\mu_{\rm ggF}$, $\delta^\mu_{\rm VBF}$, $\delta^\mu_{\rm ZH}$, $\delta^\mu_{\rm WH}$ and $\delta^\mu_{\rm ttH}$ arise (see Eqs. (2.92)–(2.93)). The uncertainty on each channel is described by only one of these δ^μ_X, where the X corresponds to the dominant production mode in this channel. That is, all channels dominated by the same production mode X have the same nuisance parameter δ^μ_X. This implies that these channels are 100% correlated.

In principle, the combination procedure of Section 2.6 describes the complete distribution for the δ^μ_X, π^μ, including the correlations $\rho^\mu_{XX'}$ *among* the different δ^μ_X. In practice, a complete knowledge of the correlations among the individual sources of uncertainties is needed to obtain $\rho^\mu_{XX'}$. Here we consider the determination of $\rho^\mu_{XX'}$ as beyond the scope of this work, since for example one would have to work out clearly the correlations among the Higgs production modes induced by the PDF data uncertainties ($\delta_X^{\rm data}$). Using the information available in the literature we will rather consider some characteristic cases for $\rho^\mu_{XX'}$.

Let us first discuss the typical correlations induced by the PDF uncertainties (originating from the PDF data fit) and the scale uncertainties (*c.f.* Section 2.6.2) on the production cross sections.

From now on, the δ_X^μ are denoted as δ_X for simplicity,

$$\delta_X^\mu \hat{=} \delta_X \, . \tag{2.94}$$

First, we will set $\delta_{\rm ggF} = -\delta_{\rm ttH}$ since an anti-correlation between the corresponding PDF errors is reported in Ref. [29] [41]. Note that in reality, this anti-correlation is not total (its value is -0.6 in Ref. [29]) and furthermore the other source of error, the scale uncertainty, does not correlate the ggF and ttH cross sections as these come from independent QCD calculations.
The correlation coefficients of the PDF errors – between ~ 0.63 and 0.93 [29] – for the three other production modes motivate us to take $\delta_{\rm VBF} = \delta_{\rm ZH} = \delta_{\rm WH}$. This assumption is further justified by the fact that the PDF error is larger than the scale error (particularly for VBF) and that the scale error most probably correlates the ZH and WH modes.
The correlation coefficients of the PDF errors between ggF and WH (-0.23), ZH (-0.14) or VBF (-0.57) suggest to consider the two extreme cases of vanishing correlation and 100% anti-correlation. The scale uncertainties tend to decorrelate these modes. It is thus coherent to consider the cases of vanishing correlation and 100% anti-correlation as the two extreme cases to study. All these assumptions are summarized as the two following configurations on the nuisance parameters, [42]

$$\delta_{\rm ggF} = -\delta_{\rm ttH} \ , \ \delta_{\rm VBF} = \delta_{\rm ZH} = \delta_{\rm WH} \ , \tag{2.95}$$

$$-\delta_{\rm ggF} = \delta_{\rm ttH} = \delta_{\rm VBF} = \delta_{\rm ZH} = \delta_{\rm WH} \ , \tag{2.96}$$

keeping in mind that the realistic situation lies in between these extreme cases.

Regarding the PDF set error, the individual uncertainties giving rise to this error are not available in the literature. Rather, only the global PDF set error is estimated by changing various assumptions at a time. One can at least notice that the PDF set errors can be potentially correlated either negatively or positively, respectively, for the ggF and VBF reactions or the VBF and VH processes, as observed from the relative signs of rate variations in Fig. (57) of Ref. [20] when changing the PDF set. [43] These correlations are roughly consistent with the ones in Eq. (2.96).

Let us describe how the correlation configurations of Eq. (2.95)-(2.96) are related to the π^μ appearing in the marginal likelihood (2.93). The prior π^μ is approximately equal to the prior of the production mode uncertainties π^σ (Eq. (2.84) and Eq. (2.91)) which can itself be expressed (according to (2.36)–(2.37)) in terms of the π_X^σ under the assumptions (2.95)-(2.96). One ends up with the two final priors, associated respectively to the correlation configurations of Eqs. (2.95)-

[41] It is not clear from this reference whether the correlations include as well the whole error from α_s which is 100% correlated between the production modes. Nevertheless this source of error is minor compared to the other ones.
[42] For consistency, these two configurations are used as well to determine the $\rho^\sigma_{XX'}$ correlation matrix of Eq. (2.83).
[43] Recall that the Fig. (57) of Ref. [20] is for the 8 TeV LHC.

(2.96),

$$\pi^{\mu}(\delta_X) = \pi^{\sigma}_{\rm ggF}(\delta_{\rm ggF})\ \delta(\delta_{\rm ggF}+\delta_{\rm ttH})\ \pi^{\sigma}_{\rm VBF}(\delta_{\rm VBF})\ \delta(\delta_{\rm VBF}-\delta_{\rm ZH})\ \delta(\delta_{\rm VBF}-\delta_{\rm WH})\ , \tag{2.97}$$

$$\pi^{\mu}(\delta_X) = \pi^{\sigma}_{\rm ggF}(\delta_{\rm ggF})\ \delta(\delta_{\rm ggF}+\delta_{\rm ttH})\ \delta(\delta_{\rm ggF}+\delta_{\rm VBF})\ \delta(\delta_{\rm ggF}+\delta_{\rm ZH})\ \delta(\delta_{\rm ggF}+\delta_{\rm WH})\ , \tag{2.98}$$

where $\delta()$ denotes the Dirac distribution.

2.7.2 The Bayesian analytical likelihood

The π^{σ}_X priors deduced from the combination of all the cross section errors, in Section 2.6.3, have been found to be nearly Gaussian distributions. These Gaussian shapes are obtained by choosing flat shapes for all the unknown priors for theoretical uncertainties. As mentioned in Section 2.6.6, one expects this result to hold approximatively for other choices of initial priors. Nevertheless, in order to take into account in our numerical results the possibility of non-flat initial shapes, we also consider a totally different form of the final prior: we take it as a flat distribution. The choice of these two shapes (Gaussian and flat) provides an estimate of the impact of the prior shape on the final results. The distributions π^{σ}_X appearing in Eqs. (2.97)-(2.98) are hence defined as

$$\pi^{\sigma}_X(\delta^{\sigma}_X) = \frac{1}{\sqrt{2\pi}} e^{-(\delta^{\sigma}_X)^2/2}\,, \tag{2.99}$$

$$\pi^{\sigma}_X(\delta^{\sigma}_X) = \begin{cases} 1/2\sqrt{3} & \text{if}\ \ \delta^{\sigma}_X \in [-\sqrt{3},\sqrt{3}]\,, \\ 0 & \text{otherwise} \end{cases} \tag{2.100}$$

for the Gaussian and flat cases respectively. Recall that the variance of all the δ's, including δ^{σ}_X, are chosen to be equal to one for any prior shape. This appears clearly in Eq. (2.99) and implies the $[-\sqrt{3},\sqrt{3}]$ interval in Eq. (2.100).

For analytical integrations of the final likelihood (2.93), it is convenient to denote by $\mathcal{X}$ a subset of fully correlated production modes, $\{X, X', \ldots\}$. We then denote by $\Omega_{\mathcal{X}}$ the subset of channels (labelled by i) dominated by the production modes contained in $\mathcal{X}$. In presence of anti-correlations, one further divides $\Omega_{\mathcal{X}}$ into two anti-correlated subsets $\Omega^{+}_{\mathcal{X}}$, $\Omega^{-}_{\mathcal{X}}$. Finally, the set of all channels is written Ω. Assuming the correlations among production modes follow Eq. (2.95), the set of detection channels is splitted into $\Omega_{\{\rm ggF,ttH\}}$ and $\Omega_{\{\rm VBF,WH,ZH\}}$. $\Omega_{\{\rm ggF,ttH\}}$ is then splitted into the anti-correlated subsets $\Omega^{+}_{\{\rm ggF,ttH\}} = \Omega_{\rm ggF}$, $\Omega^{-}_{\{\rm ggF,ttH\}} = \Omega_{\rm ttH}$. Assuming the correlations of Eq. (2.96), there is instead a unique set $\Omega = \Omega_{\{\rm ggF,ttH,VBF,WH,ZH\}}$. It is splitted into the anti-correlated subsets $\Omega^{+}_{\{\rm ggF,ttH,VBF,WH,ZH\}} = \Omega_{\rm ggF}$, $\Omega^{-}_{\{\rm ggF,ttH,VBF,WH,ZH\}} = \Omega_{\{\rm ttH,VBF,WH,ZH\}}$.

At that point it is also convenient to introduce the following quantities $\zeta_{\mathcal{X}}$ and $\eta_{\mathcal{X}\mathcal{X}'}$ defined as

$$\begin{aligned}\zeta_{\mathcal{X}} &= \sum_{i\in\Omega_{\mathcal{X}},\, j\in\Omega} \kappa_i\, \Delta_i^{\mu}\, (\mu_i^{\rm th} - \mu_i^{\rm ex})\, \mathcal{C}_{ij}^{{\rm ex}\,-1}\, \mu_j^{\rm ex}\,, \quad \kappa_i = \begin{cases} 1 \text{ if } i \in \Omega_{\mathcal{X}}^{+} \\ -1 \text{ if } i \in \Omega_{\mathcal{X}}^{-} \end{cases} \\ \eta_{\mathcal{X}\mathcal{X}'} &= \sum_{i\in\Omega_{\mathcal{X}},\, j\in\Omega_{\mathcal{X}'}} \kappa_i\, \Delta_i^{\mu}\, \mu_i^{\rm ex}\, \mathcal{C}_{ij}^{{\rm ex}\,-1}\, \kappa_j\, \Delta_j^{\mu}\, \mu_j^{\rm ex}\,. \end{aligned} \tag{2.101}$$

The overall sign of $\zeta_{\mathcal{X}}$ is irrelevant. Note also that if $\mathcal{X} \neq \mathcal{X}'$ (as may occur in the $\eta_{\mathcal{X}\mathcal{X}'}$ function), there are no theoretical correlations at all between the channels belonging to $\Omega_{\mathcal{X}}$ and $\Omega_{\mathcal{X}'}$.

In the case of a Gaussian prior (Eq. (2.99)), it is noticeable that the most general likelihood (2.93) can be integrated analytically and results in the simple analytical expression [44]

$$\boxed{L_{\rm B}^{\rm Gauss} = L_{\mu}\, \exp\left[\frac{1}{2}\sum_{\mathcal{X}\mathcal{X}'} \zeta_{\mathcal{X}} (\delta_{\mathcal{X}\mathcal{X}'} + \eta_{\mathcal{X}\mathcal{X}'})^{-1} \zeta_{\mathcal{X}'}\right]}\,. \tag{2.102}$$

Here $\delta_{\mathcal{X}\mathcal{X}'}$ is the Kronecker symbol. L_{μ} is the base likelihood defined in Eq. (2.51), *i.e.* the likelihood before introducing nuisance parameters. One observes that the marginal likelihood takes the form of a product of the base likelihood with a term generated by the theoretical uncertainties. This term, which depends on c_V, c_f through $\zeta_{\mathcal{X}}$, as well as on all theoretical and experimental uncertainties, implements all the deformations and correlations induced by the theoretical uncertainties.

For the case of no experimental correlations between different group of channels of dominant production modes, including the case considered without experimental correlations at all (see Section 2.5.1), one has $\eta_{\mathcal{X}\mathcal{X}'} = 0$ for $\mathcal{X} \neq \mathcal{X}'$ and

$$\eta_{\mathcal{X}\mathcal{X}} \equiv \eta_{\mathcal{X}} = \sum_{i,j\in\Omega_{\mathcal{X}}} \kappa_i \Delta_i^{\mu} \mu_i^{\rm ex} \mathcal{C}_{ij}^{{\rm ex}\,-1} \kappa_j \Delta_j^{\mu} \mu_j^{\rm ex}\,. \tag{2.103}$$

The marginal likelihood (2.102) then reduces to,

$$L_{\rm B}^{\rm Gauss} = L_{\mu} \prod_{\mathcal{X}} e^{\zeta_{\mathcal{X}}^2/2(\eta_{\mathcal{X}}+1)}\,. \tag{2.104}$$

Note that this product is over different $\mathcal{X}$ subsets *i.e.* there are no theoretical correlations among the channels belonging to the different $\Omega_{\mathcal{X}}$ groups.

Note that if one assumes a single independent nuisance parameter per channel, there is no sum in Eqs. (2.101), meaning that no correlation among channels is induced. [45] One can directly verify that in the purely de-correlated case (neither experimental nor theoretical correlations), Eq.(2.104)

[44] A similar expression can also be obtained for an arbitrary correlation matrix $\rho_{\mathcal{X}\mathcal{X}'}^{\mu}$. Note one dropped an overall factor, as the likelihood is defined up to a normalisation constant.

[45] We recall that such a combination should be avoided as it is not realistic.

gives back the primary likelihood (2.51) with a summation in quadrature between the absolute experimental and theoretical errors, $\Delta\mu_i^{\rm ex}$ and $\mu_i^{\rm ex}\Delta_i^\mu$.

In the case of the flat prior of Eq. (2.100), there is no simple general form such as Eq. (2.102). However, assuming no experimental correlations among various $\Omega_{\mathcal{X}}$ subsets, the marginal likelihood takes a simple form,

$$L_{\rm B}^{\rm flat} = L_\mu \prod_{\mathcal{X}} e^{\zeta_{\mathcal{X}}^2/2\eta_{\mathcal{X}}} \left[{\rm Erf}\left(\frac{\sqrt{3}\sqrt{\eta_{\mathcal{X}}}}{\sqrt{2}} + \frac{\zeta_{\mathcal{X}}}{\sqrt{2\eta_{\mathcal{X}}}} \right) - {\rm Erf}\left(\frac{\sqrt{3}\sqrt{\eta_{\mathcal{X}}}}{\sqrt{2}} - \frac{\zeta_{\mathcal{X}}}{\sqrt{2\eta_{\mathcal{X}}}} \right) \right] , \tag{2.105}$$

where Erf is the standard error function.

2.7.3 The frequentist treatment

The marginal likelihood

In classical frequentist statistics, hypotheses are not associated with probabilities, so that there is no such thing as a prior distribution for a nuisance parameter. In the hybrid frequentist framework however, one can associate a parameter with a "prior" distribution that can be seen as an extra likelihood constraining the nuisance parameter. Pushing forward the analogy with the Bayesian case, we worked out the way to combine uncertainties within frequentist statistics in Section 2.3.3. One may find however that the Bayesian combination of uncertainties are better defined than the frequentist one.

More pragmatically, frequentist combinations are also more complicated, as the combination of the magnitude of the errors (the Δ's) depends on the shape of the frequentist "priors", contrary to the Bayesian case. These drawbacks can constitute motivations to rather follow the Bayesian approach developed in previous sections. Nevertheless, for completeness we describe here the final part of the frequentist method for the Higgs fit. For that purpose we consider in the following, a generic prior, $\pi^\mu(\delta_X^\mu)$, of width Δ_i^μ, obtained after a first phase of frequentist combination.

Recall that the frequentist marginalisation procedure, also called profiling, consists in maximizing over δ_X^μ, instead of integrating as done in Eq. (2.93). Hence the frequentist marginal Higgs likelihood reads

$$\begin{aligned} L(c_V, c_f) \quad &= \quad \max_{\delta_X^\mu} \left[\pi^\mu(\delta_X^\mu) \times \right. \\ &\exp \quad \left. \left[-\frac{1}{2} \sum_{i,j} (\mu_i^{\rm th}[c_V, c_f] - \mu_i^{\rm ex}(1 + \delta_{X_i}^\mu \Delta_i^\mu))\, \mathcal{C}_{ij}^{\rm ex\,-1}\, (\mu_j^{\rm th}[c_V, c_f] - \mu_j^{\rm ex}(1 + \delta_{X_j}^\mu \Delta_j^\mu)) \right] \right]. \end{aligned} \tag{2.106}$$

As often done in practice for the frequentist treatment, one can equivalently minimize the χ^2

distribution, $\chi^2 = -2\log L$, instead of the maximisation in Eq. (2.106),

$$\chi^2(c_V, c_f) = \min_{\delta_X^\mu} \Bigg[-2\log \pi^\mu(\delta_X^\mu) + \sum_{i,j} \left(\mu_i^{\rm th}[c_V, c_f] - \mu_i^{\rm ex}(1+\delta_{X_i}^\mu \Delta_i^\mu)\right) \mathcal{C}_{ij}^{\rm ex\,-1} \left(\mu_j^{\rm th}[c_V, c_f] - \mu_j^{\rm ex}(1+\delta_{X_j}^\mu \Delta_j^\mu)\right) \Bigg]. \tag{2.107}$$

The best-fit point given by the χ^2 minimum in the (c_f, c_V) parameter space is noted $(\hat{c}_f, \hat{c}_V)$ and the best-fit regions are obtained by drawing contour levels of the difference (*c.f.* Section 2.2.1)

$$\Delta\chi^2(c_f, c_V) = \chi^2(c_f, c_V) - \chi^2(\hat{c}_f, \hat{c}_V) \tag{2.108}$$

at the values given by Eq. (2.8).

The frequentist analytical likelihood

Assuming that the Bayesian and frequentist combinations of the errors lead to analogous shapes for the final priors, we consider both a Gaussian and a flat shape for each π_X^σ prior, as in Eqs. (2.99)–(2.100). In the Gaussian case, the marginal likelihood (2.106) can be computed analytically,

$$\boxed{L_{\rm F}^{\rm Gauss} = L_\mu \exp\left[\frac{1}{2}\sum_{\mathcal{X}\mathcal{X}'} \zeta_{\mathcal{X}} (\delta_{\mathcal{X}\mathcal{X}'} + \eta_{\mathcal{X}\mathcal{X}'})^{-1} \zeta_{\mathcal{X}'}\right]}, \tag{2.109}$$

where the $\zeta_{\mathcal{X}}$, $\eta_{\mathcal{X}\mathcal{X}'}$ are defined as in Section 2.7.2. This is precisely the same result as for the Bayesian likelihood of Eq. (2.102), $L_{\rm B}^{\rm Gauss}$.

For the case of no experimental correlations between the $\Omega_{\mathcal{X}}$'s, the marginal likelihood with Gaussian prior thus simplifies just like in Eq. (2.104). [46] In this case, the marginal likelihood with a flat prior also gets an analytical expression,

$$L_{\rm F}^{\rm flat} = \prod_{\mathcal{X}} \exp\left[-\frac{1}{2}\sum_{i,j} \left(\mu_i^{\rm th}[c_V, c_f] - \mu_i^{\rm ex}(1+\xi_{\mathcal{X}}\kappa_i \Delta_i^\mu)\right) \mathcal{C}_{ij}^{\rm ex\,-1} \left(\mu_j^{\rm th}[c_V, c_f] - \mu_j^{\rm ex}(1+\xi_{\mathcal{X}}\kappa_j \Delta_j^\mu)\right)\right] \tag{2.110}$$

[46] Hence the same likelihood (with a sum in quadrature) as in the Bayesian framework arises, in the case of neither experimental nor theoretical correlations.

with

$$\xi_{\mathcal{X}} = \begin{cases} \zeta_{\mathcal{X}}/\eta_{\mathcal{X}} & \text{if } \zeta_{\mathcal{X}}/\eta_{\mathcal{X}} \in [-\sqrt{3}, \sqrt{3}] \\ \sqrt{3} & \text{if } \zeta_{\mathcal{X}}/\eta_{\mathcal{X}} > \sqrt{3} \\ -\sqrt{3} & \text{if } \zeta_{\mathcal{X}}/\eta_{\mathcal{X}} < -\sqrt{3} \end{cases} , \tag{2.111}$$

where $\zeta_{\mathcal{X}}$, $\eta_{\mathcal{X}}$ are defined as in Eq. (2.101), (2.103).

2.7.4 Numerical results

The frequentist marginalisation (likelihood (2.109) for the Gaussian prior or (2.110) for the flat one) is not illustrated here because the frequentist framework may seem slightly less consistent than the Bayesian one and the error combinations are more delicate. For these reasons, we rather recommend to use the Bayesian marginalisation technics for the Higgs fits. In any case, the Bayesian and frequentist approaches are expected to converge as the experimental uncertainties become small relatively to the theoretical ones. This situation will gradually occur in the next LHC Runs due to the decrease of the statistical uncertainties and the expected improvement in the knowledge of the experimental systematic errors. We have described this feature in Ref. [59].

Now as a general remark allowing a better comprehension of the following subsections, let us try to explain in simple words the reason why the presence of nuisance parameters can indeed modify the size and the location of the best-fit domains in $c_V - c_f$.
For the sake of understanding the impact on the size, it is easier to focus on frequentist marginalisation. Frequentist marginalisation can be seen as an approximation of Bayesian marginalisation, so that the same explanation holds for both. The frequentist marginalisation consists of a maximisation of the nuisance parameter (say δ_X^μ) at any point in the space of the parameters of interest. This means that the value of δ_X^μ at a given point is chosen in order to maximise goodness-of-fit. Now, this improvement of goodness-of-fit is typically larger for the points far away from the best-fit point than for those close by the best-fit point. When this fact is true (which is usually the case), the operation of marginalising tends to enlarge the best-fit regions.
The effect of the nuisance parameters on the location of the best-fit regions in $c_V - c_f$ can be understood as follows. Recall that the nuisance parameters enter in the likelihood as $\mu_i^{\text{ex}}(1 + \delta_{X_i}^\mu \Delta_i^\mu)$ (see Eq. (2.93)), so that they shift the central experimental value of the signal strength. This in turn can induce a change in the location of the best-fit point in $c_V - c_f$. Such a shift actually occurs if a non-zero value of δ_X^μ is preferred. This happens when a non-zero value for δ_X^μ helps relaxing the tensions (*i.e.* different preferred values of c_V, c_f) among various signal strengths μ_i^{ex}. Notice that this means that the likelihood itself favours a non-zero value for δ_X^μ, even though the prior of δ_X^μ is centered on zero.

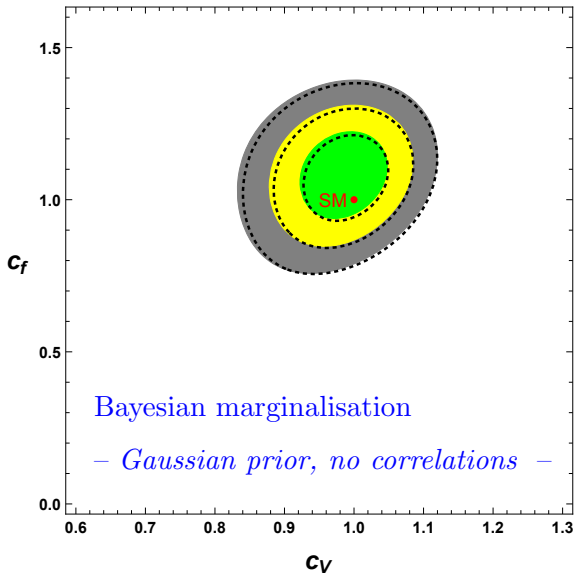

Figure 2.4: The best-fit regions in the $c_V - c_f$ plane obtained from Bayesian marginalisation and Gaussian priors for the theoretical uncertainties. The 68%, 95% and 99% credible regions are represented respectively by the green, yellow and grey domains. No theoretical error correlations between the Higgs detection channels are taken into account in this figure. The dashed contours illustrate the case without theoretical uncertainties. The SM prediction is shown by the red point.

The forbidden case: no correlations

Following our overview approach, let us start with the simplest case: the Bayesian marginalisation in the absence of correlations between the theoretical errors of the different Higgs channels. Let us take for instance a Gaussian prior (taking a flat one would not change our conclusions). This case was described in more details in the beginning of Section 2.7.1 as well as in Section 2.7.2. In this "de-correlated" case, the likelihood is simply the primary likelihood (2.51) with a summation in quadrature of the absolute experimental and theoretical errors, $(\Delta\mu_i^{\rm ex})^2 + (\mu_i^{\rm ex}\Delta_i^{\mu})^2$. The best-fit domains in the $c_V - c_f$ plane are derived following the standard procedure described in Section 2.2, and are shown in Fig. (2.4). Here and throughout Section 2.7.4, the priors for c_V, c_f are taken flat, $\pi(c_{V,f}) \propto 1$.

We see on this figure that the theoretical SM prediction ($c_V = c_f = 1$) lies well within the 68% C.L. [47] region. Physically, this implies that, with such a fit, no physics beyond the SM is required to interpret the 8 TeV LHC measurements of the Higgs rates. The increase of the best-fit domain sizes induced by the existence of theoretical errors is relatively weak, due to the sum in quadrature, as observed when comparing to the best-fit regions obtained with vanishing theoretical errors. The latter regions are superimposed on Fig. (2.4) for illustration purpose (as the dashed contours) and to ease the comparison with next plots.

However let us recall that the likelihood used here (and leading to the colored regions of Fig. (2.4)) is not realistic as the correlations among the Higgs channels should not be neglected. We thus do

[47] The acronym C.L. will stand for Credible Level within the Bayesian framework and for Confidence Level in the frequentist framework.

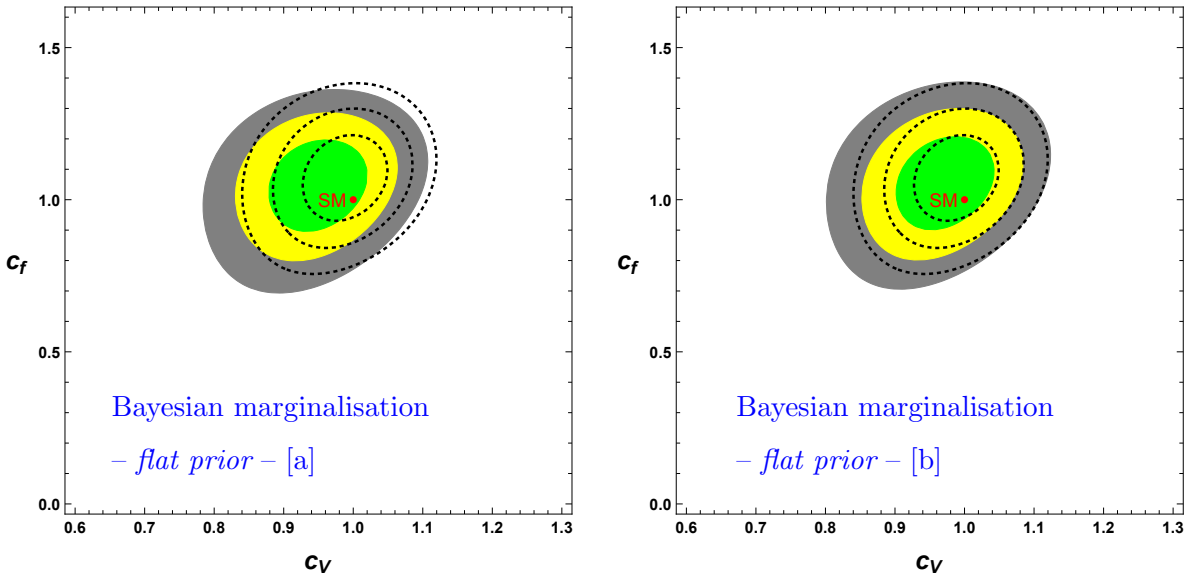

Figure 2.5: The best-fit regions in the $c_V - c_f$ plane obtained from Bayesian marginalisation and flat priors for the theoretical uncertainties. The 68%, 95% and 99% credible regions are represented respectively by the green, yellow and grey domains. The [a] and [b] plots correspond, respectively, to the two characteristic correlation configurations described in Eq. (2.97) and Eq. (2.98). The dashed contours illustrate the case without theoretical uncertainties. The SM prediction is shown by the red point.

not recommend the use of this likelihood.

Flat prior

From now on we consider the more realistic likelihoods obtained in Section 2.7.2. These likelihoods contain all the correlations between Higgs channels induced by the theoretical uncertainties. First, we consider the configuration with two independent nuisance parameters (see Eq. (2.95) and Eq. (2.97)). The Bayesian marginalisation over these two nuisance parameters leads to the analytical likelihood (2.105) for flat final priors. Applying the standard Bayesian procedure, described in Section 2.2, we find the best-fit regions of Fig. (2.5)[left].

By comparing the colored plots in Fig. (2.4) and Fig. (2.5)[left], one observes clearly a shift of the best-fit regions. This shift originates from the theoretical correlations that are taken into account in Fig. (2.5)[left]. This shift occurs because the relaxation of the tensions between the individual signal strength measurements (see discussion in the introduction of Section 2.7.4) is different in the correlated case and in the "de-correlated" one. We emphasize that this shift is a consequence of taking into account the theoretical correlations. Indeed we will see in next subsection that the same effect occurs for a different prior shape. Concerning the region size, a slight increase occurs relatively to Fig. (2.4). This comparison can be done by looking at the reference case (dashed contours) without theoretical errors at all, which is once more superimposed on Fig. (2.5)[left].

The plot on the right hand side of Fig. (2.5) is the same as the left plot but for the second corre-

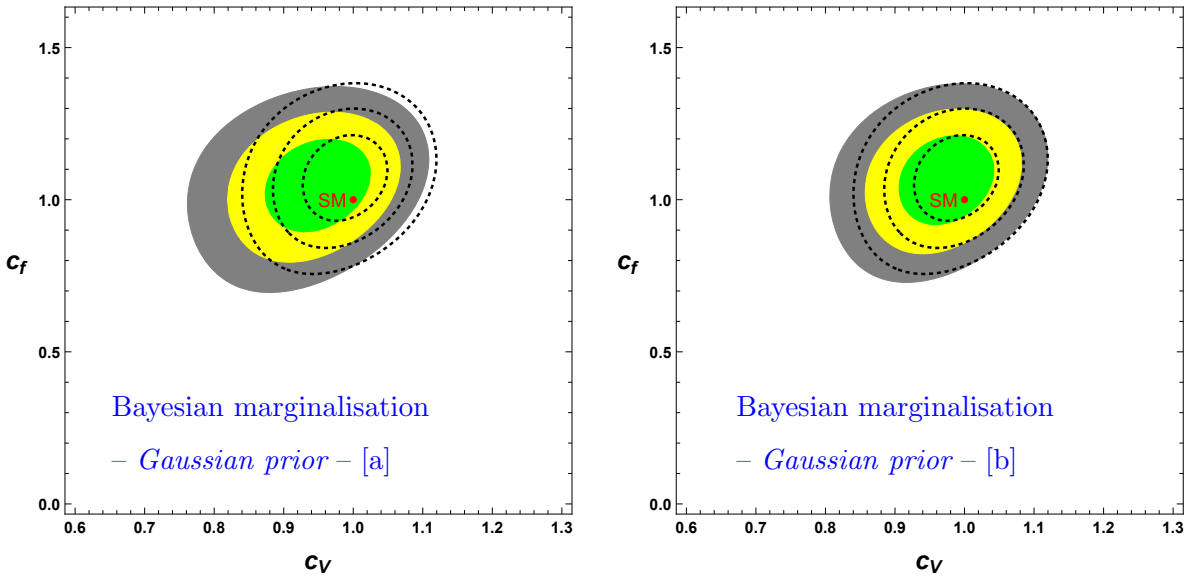

Figure 2.6: The best-fit regions in the $c_V - c_f$ plane obtained from Bayesian marginalisation and Gaussian priors for the theoretical uncertainties. The 68%, 95% and 99% credible regions are represented respectively by the green, yellow and grey domains. The [a] and [b] plots correspond, respectively, to the two characteristic correlation configurations described in Eq. (2.97) and Eq. (2.98). The dashed contours illustrate the case without theoretical uncertainties. The SM prediction is shown by the red point.

lation configuration, involving a single nuisance parameter (discussed in Eq. (2.96) and Eq. (2.98)). The effect of the theoretical correlations (relatively to Fig. (2.4)) appears to be softer than for the left plot: the shift is smaller. This difference between the two colored regions of Fig. (2.5) makes clear that the theoretical correlations have an important impact on the fits, and should thus be carefully taken into account.

As described below Eq. (2.96), the most realistic correlation configuration is most probably an intermediate configuration between those adopted in the two plots of Fig. (2.5). We thus conclude that, with the statistical treatment adopted here, the SM prediction remains in a good agreement (1σ level) with the 8 TeV LHC Higgs data, even once realistic theoretical correlations are taken into account.

Gaussian prior

Fig. (2.6) illustrates the same case as in Fig. (2.5) except that the final priors are now Gaussian, [48] which leads to the marginalised Bayesian likelihood of Eq. (2.102) and Eq.(2.104). It appears that there is no substantial difference (neither in location, size nor shape of the best-fit regions) between these two figures. This illustrates the mild impact of the choice of the shape for the prior of the theoretical uncertainties. We conclude that, with the present statistical uncertainties on Higgs

[48] At this stage, we recall that the Gaussian priors are obtained from a combination of all the individual priors, while the flat priors have just been chosen 'by hand' to illustrate what happens for completely different distributions.

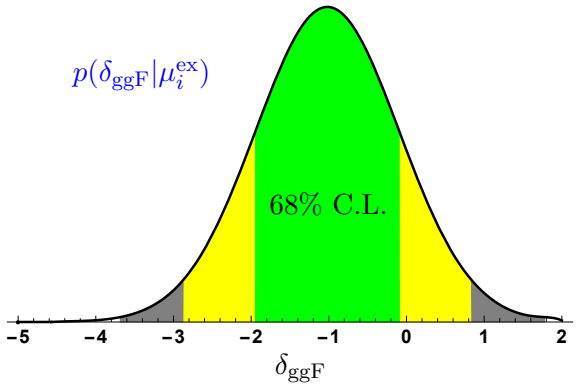

Figure 2.7: The data-dominated posterior $p(\delta_{\rm ggF}|\mu_i^{\rm ex})$ (Eq. (2.112)). The 68%, 95% and 99% credible domains are indicated respectively by the green, yellow and grey areas.

data, the recurring question of the exact shape of the prior, [49] in particular for the errors due to truncated perturbative expansions in QCD, is nearly irrelevant.

However we should stress that this insensitivity to the prior shape occurs because the experimental uncertainties of the current data are typically larger or of the same order as the theoretical ones. This situation is expected to change with the upcoming LHC runs, as the statistical uncertainties will decrease with the integrated luminosity.

The nuisance parameters favoured by the data

Let us now consider the posterior distribution for the theoretical uncertainties themselves, instead of the posterior for the parameters of interest. Here we shall take the priors associated with the theoretical uncertainties (π_X^σ) as flat and with an *infinite* range. For such choice of prior, the information of the posterior is fully contained in the likelihood (second line in Eq. (2.112)). The interest of this data-dominated posterior is that it allows us to study exclusively the information that the sole Higgs data provide about the theoretical uncertainties, Δ_i^μ.

We first consider the case with a single nuisance parameter $\delta_{\rm ggF}$ (*i.e.* the fully correlated case), given in Eq. (2.96), and we present in Fig. (2.7) the data-dominated posterior for $\delta_{\rm ggF}$,

$$p(\delta_{\rm ggF}|\mu_i^{\rm ex}) = \int dc_V\, dc_f\; \pi(c_V,c_f)\; \pi^\sigma_{\rm ggF}(\delta_{\rm ggF}) \;\times \tag{2.112}$$
$$\exp\left[-\frac{1}{2}\sum_{i,j}\left(\mu_i^{\rm th}[c_V,c_f]-\mu_i^{\rm ex}(1\pm\delta_{\rm ggF}\Delta_i^\mu)\right)\mathcal{C}_{ij}^{\rm ex\,-1}\left(\mu_j^{\rm th}[c_V,c_f]-\mu_j^{\rm ex}(1\pm\delta_{\rm ggF}\Delta_j^\mu)\right)\right].$$

[49] Including the details of the form at the boundaries in case *e.g.* of a flat distribution.

This posterior is obtained by integrating the likelihood of Eq. (2.93) (with π^μ given by Eq. (2.97)) over all δ's but one, chosen to be $\delta_{\rm ggF}$, and marginalising with respect to the c_V, c_f parameters with $\pi(c_V, c_f) \propto 1$.

It appears in Fig. (2.7) that the posterior for $\delta_{\rm ggF}$ is centred on $\delta_{\rm ggF} \simeq -1$. [50] This means that for each signal strength, the data typically favour a value falling at $\pm 1\sigma$ (*i.e.* at $\pm\Delta_i^\mu$) from the nominal value $\mu_i^{\rm ex}$. In other words, for the correlation configuration of Eq. (2.96) the Higgs data provide a non-trivial indication that the magnitudes of the theoretical errors are reasonably well estimated. Indeed, the theoretical estimations predict the $\mu_i^{\rm ex}$ to lie typically within the 1σ interval $\pm\Delta_i^\mu$.

This compatibility suggests that the Δ_i^μ uncertainties, whose estimations rely on quite ad hoc QCD scale variations and on the arbitrariness in the choice of PDF sets, are nevertheless quite robust. On the other hand, one also notices in Fig. (2.7) that the credible intervals for $p(\delta_{\rm ggF}|\mu_i^{\rm ex})$ go beyond -1. This could be taken as an argument for slightly increasing the overall magnitude of the theoretical uncertainties (see next subsection).

The correlation configuration with two nuisance parameters, given by Eq. (2.95), leads to larger preferred values for the nuisance parameters $\delta_{\rm ggF} \simeq -2$, $\delta_{\rm VBF} \simeq -5$. We interpret these very large values as the fact that neglecting totally the correlation between the two nuisance parameters is an unrealistic hypothesis (as already described in Section 2.7.1). As a matter of fact, if one restored the usual prior for the δ's (*i.e.* a prior with unit variance, $V[\delta] = 1$), a hypothesis testing would show that the data favour the correlation configuration of Eq. (2.96) with respect to the configuration of Eq. (2.95).

More conservative theoretical errors

Throughout this work, we have been observing that, among the various origins of theoretical uncertainty involved in the Higgs fit, some are of a nature (see Section 2.6.1 - 2.6.5) which renders difficult the *exact determination* of the associated 1σ interval. These are the truncation of the perturbative expansion for the QCD calculation of Higgs rates translated into an arbitrary error range for the renormalisation/factorisation scale $\mu = \mu_{\rm R} = \mu_{\rm F}$ (affecting the production and decay amplitudes as well as the α_s coupling constant), the choices made (on the statistical method, the number of free parameters...) in the different PDF sets, and finally the m_b renormalisation scheme and EFT assumptions for the ggF mechanism. These considerations can be taken as a motivation to adopt more conservative theoretical errors.

Moreover, we have seen in the previous subsection (see Fig. (2.7)) that the data tend to prefer theoretical uncertainties that are somewhat larger than the combined 1σ width Δ_i^μ obtained in Section 2.6, see *e.g.* the 68% C.L. interval in Fig. (2.7). Taking seriously this fact, it makes sense

[50] For comparison, the maximum of $p(\delta_{\rm ggF}, c_V = c_f = 1|\mu_i^{\rm ex})$ is reached for $\delta_{\rm ggF} \simeq -0.7$.

to perform the fits with a slight overall increase of the uncertainties. We suggest a rescaling

$$\Delta_i^\mu \to 1.5\,\Delta_i^\mu \tag{2.113}$$

as a reasonable estimation for a most conservative choice of theoretical uncertainties. Notice that the rescaling of Eq. (2.113) is equivalent (*c.f.* Eq. (2.93)) to rescale by 1.5 the axis on Fig. (2.7). For example, the point $\delta_{\rm ggF} = -1$ becomes $\delta_{\rm ggF} = -1.5$.

The best-fit regions with $\Delta_i^\mu \times 1.5$ are shown in Fig. (2.8) for the two correlation configurations and considering the flat prior case (Eq. (2.105)), keeping in mind that with the current Higgs data, the final prior shape does not affect significantly those best-fit domains. The impact of the increase of the theoretical uncertainties (Eq. (2.113)) on the fit of the current Higgs data can be seen by comparing Fig. (2.5) and Fig. (2.8). It turns out that the shift of the preferred regions with respect to the case without theoretical errors gets slightly accentuated. In the correlation configuration of Eq. (2.97), *i.e.* with two independent δ_X, it even appears (see Fig. (2.8)[left]) that the SM point moves just outside the 68% C.L. region.

The increase of this shift can be understood by recalling that rescaling the Δ_i^μ is equivalent to increase the width of the δ_X prior. It is then clear that more possibilities are opened for the preferred values of δ_X. It turns out that these preferred values move further away from zero, which induces a more pronounced shift of the best-fit regions.

Even though these effects are not statistically significant for the current Higgs data, we stress that the impact of the theoretical errors will increase while more data will be accumulated at the LHC. The ambiguity existing in the theoretical errors estimation deserves thus to be taken into account. For future LHC phenomenological studies, we suggest to take into account, in the same way as proposed in this subsection, the impact on the fits from the lack of knowledge in theoretical errors.

2.8 Biasing the Higgs likelihood

The principle of bias has been presented in Section 2.2.2. To have a self-consistent section, we recall here the basics of a "biasing" procedure. We distinguish two realisations of the bias principle: the *extremal bias* and the *envelope method*.

The method of extremal biasing consists in drawing the best-fit regions for the parameters of interest for extreme fixed values of the theoretical errors. By the word 'extreme', we mean that we set the nuisance parameters δ at ± 1 (corresponding to one-standard deviations with our conventions) in order to obtain a strong impact on the fit. In our Higgs fit, the theoretical uncertainties affect the signal strengths $\mu_i^{\rm ex}$, which in turn modify the preferred value of $\mu_i^{\rm th}(c_f, c_V)$ and thus the best-fit regions of c_V, c_f. Note that the choice of extreme values $\delta \pm 1$ can be seen as natural, and

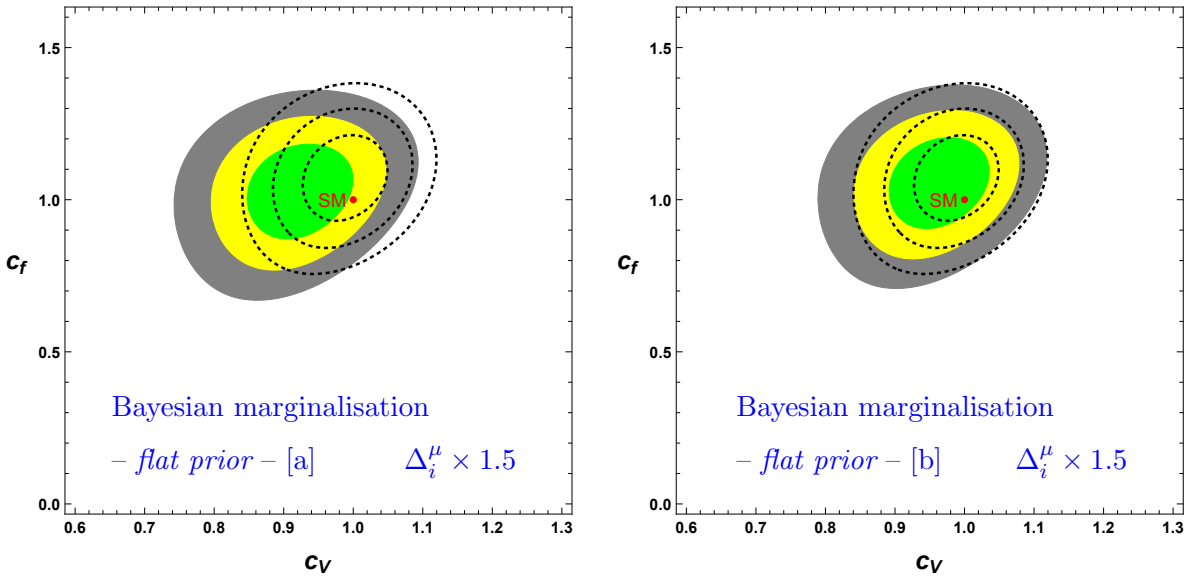

Figure 2.8: The best-fit regions in the $c_V - c_f$ plane obtained from Bayesian marginalisation and flat priors for the theoretical uncertainties. The 68%, 95% and 99% credible regions are represented respectively by the green, yellow and grey domains. The [a] and [b] plots correspond, respectively, to the characteristic correlation configurations described in Eq. (2.97) and Eq. (2.98). The dashed contours illustrate the case without theoretical uncertainties. The SM prediction is shown by the red point. The difference with Fig. (2.5) is the enhancement of the uncertainties, accordingly to $\Delta_i^\mu \to \Delta_i^\mu \times 1.5$.

for that reason will be used in our numerical results, but strictly speaking remains only a choice with a certain degree of arbitrariness.

The envelope method corresponds formally to the continuous version of this extremal biasing. Loosely speaking, this is what one obtains if one does the fit for each fixed value of the nuisance parameters between the extreme values $\delta = \pm 1$. One expects typically a deformed contour somehow interpolating between the regions of extremal biasing. For a more formal and unified description of these biasing methods, see Section 2.2.2.

What are the motivations for choosing the marginalisation or the bias approaches (extremal bias or envelope method) in the Higgs fits? The lack of knowledge on the shape of the prior associated to the main QCD uncertainties discussed in Section 2.6.3 encourages one to apply a bias method, which does not rely on the prior shape – in contrast with the marginalisation.
Besides, the bias is more conservative. Indeed, while in the marginalisation the best-fit domain corresponds roughly to nuisance parameters centered around a preferred δ_X value, in the bias methods δ_X rather spans by construction its $[-1, 1]$ interval without favouring any value. Hence, generally speaking (and this is the case for the Higgs fit), the best-fit regions in the space of the parameters of interest obtained through the bias methods are wider than the ones from marginalising.
In addition, the envelope method allows one to see at a glance the whole best-fit domain in the $c_V - c_f$ plane spanned by varying the nuisance parameters inside their entire $[-1, 1]$ intervals. The price to pay here is maybe a heavier technical approach than in the marginalisation procedure: compare the marginalisation definitions in Eqs. (2.9),(2.10) with the biasing definitions in

Eqs. (2.14),(2.17) (see for example Eq. (2.93) and Eq. (2.118) for the application to the Higgs likelihood). It is clear that more operations (either integrations or maximisations) are needed for the envelope method.

2.8.1 Combining the uncertainties

The starting point is the likelihood (2.51), and then (2.61). Applying the Eqs. (2.39)-(2.40)-(2.41)-(2.42) together with the definition of Eq. (2.89) and,

$$\Delta^{\rm P}_{X,i} \hat{=} \frac{\epsilon^i_X \sigma^{\rm SM}_X}{\sum_{X'} \epsilon^i_{X'} \sigma^{\rm SM}_{X'}} \left(\Delta^{\rm amp}_X + \Delta^{\rm PDF+\alpha_s}_X \right) , \tag{2.114}$$

which is a new compact notation comparable to Eq. (2.80), we obtain the likelihood depending on a unique nuisance parameter, δ_b,

$$L_{\rm bias}(\delta_b) = \exp\left[-\frac{1}{2} \sum_{i,j} \left(\mu^{\rm th}_i[c_V, c_f] - \mu^{\rm ex}_i (1+\delta_b \Delta^b_i) \right) \mathcal{C}^{\rm ex\,-1}_{ij} \left(\mu^{\rm th}_j[c_V, c_f] - \mu^{\rm ex}_j (1+\delta_b \Delta^b_j) \right) \right] \tag{2.115}$$

relying on the combined error,

$$\Delta^b_i = \left| \Delta^{\rm P}_{\rm ggF,i} - \Delta^{\rm P}_{\rm ttH,i} \right| + \Delta^{\rm P}_{\rm VBF,i} + \Delta^{\rm P}_{\rm WH,i} + \Delta^{\rm P}_{\rm ZH,i} + \sum_{Y,a} (\Delta^a_{Y,i} + \Delta_{Y,i}) , \tag{2.116}$$

or,

$$\Delta^b_i = \left| \Delta^{\rm P}_{\rm ggF,i} - (\Delta^{\rm P}_{\rm ttH,i} + \Delta^{\rm P}_{\rm VBF,i} + \Delta^{\rm P}_{\rm WH,i} + \Delta^{\rm P}_{\rm ZH,i}) \right| + \sum_{Y,a} (\Delta^a_{Y,i} + \Delta_{Y,i}) , \tag{2.117}$$

for the two configurations of correlations defined in Eq. (2.95)-(2.96), respectively.

The combinations of the errors on the partial decay widths are dictated by the fact that their nuisance parameters are either independent (among them and from the nuisance parameters at the production level) or taken 100% correlated to each other, as discussed in Section 2.6.5.
In Eq. (2.114), $\Delta^{\rm amp}_X$ is either equal to $\Delta^{\rm scale}_X$ (see Section 2.6.2) or taken as $\Delta^{\rm amp}_{\rm ggF} = \Delta^{\rm scale}_{\rm ggF} + \Delta^{\rm Q,V}_{\rm ggF}$, for the ggF channel (instead of Eq. (2.72)) with now, $\Delta^{\rm Q,V}_{\rm ggF} \simeq 9\%$, from the linear sum of the three errors originating from EFT assumptions and m_b scheme dependence [26]. These linear summations are all motivated by the fact that these errors are independent.
The $\Delta^{\rm PDF+\alpha_s}_X$ uncertainty entering Eq. (2.114) is obtained from Ref. [20, 54] using an "envelope method", which corresponds exactly to the combinations in the bias approach presented in Section 2.3.5. Indeed, this combination is equivalent to a linear sum of the individual errors $\Delta^{\rm set}_X$, $\Delta^{\rm data}_X$ and $\Delta^{\alpha_s}_X$, which are independent (*c.f.* Section 2.6.1). Finally, the linear sum in Eq. (2.114) is justified by the independence of the errors $\Delta^{\rm amp}_X$ and $\Delta^{\rm PDF+\alpha_s}_X$.

The 1σ-errors (Δ's) are taken to be exactly the symmetrized errors provided by the LHCHWG [17, 18, 20] in order to be conservative (similar discussion as in Sections 2.6.3 and 2.6.5). These errors are consistent with the previous marginalisation framework, so that the results from bias and marginalisation can readily be compared.

2.8.2 The Bayesian approach

Extremal bias

According to Section 2.2.2, the extremal bias within the Bayesian framework consists in deriving the best-fit regions in the $c_V - c_f$ plane for two fixed values of the nuisance parameters, $\delta_b = \pm 1$, using the likelihood $L_{\rm bias}(\delta_b)$ of Eq. (2.115). Recall that in the Bayesian case, the best-fit regions are computed by integrating the posterior density probability, according to Eqs. (2.3)-(2.4)-(2.5). The priors ($\pi(\theta)$) for the parameters of interest (here $\theta \equiv c_V, c_f$) entering Eq. (2.3) are taken flat, *i.e.* $\pi(c_{V,f}) \propto 1$.

Note that, if the two extreme regions have an overlap, one cannot display them together consistently. Instead, one has to follow the rigorous definition of Eq. (2.14), using a discrete domain $\mathcal{D} = \{-1, 1\}$. This equation dictates to use the sum of the posteriors at $\delta_b = -1$ and $\delta_b = 1$, with each posterior separately normalised by its integral over the $c_V - c_f$ plane.

Envelope method

The envelope method corresponds to letting vary continuously δ_b within $[-1, 1]$, *i.e.* this is the continuous version of the extremal bias, as discussed in Section 2.2.2. The corresponding likelihood is

$$\bar{L}_{\rm B}(c_f, c_V) = \int_{-1}^{1} d\delta_b \left[\frac{L_{\rm bias}(c_f, c_V, \delta_b)}{\int dc_f \int dc_V \; L_{\rm bias}(c_f, c_V, \delta_b)} \right] . \tag{2.118}$$

This likelihood is derived by applying Eq. (2.14) with the likelihood $L_{\rm bias}(c_V, c_f, \delta_b)$ from Eq. (2.115). The best-fit regions are obtained through the standard procedure of Eqs. (2.3)-(2.4)-(2.5). Again, we take the priors for the parameter of interest to be flat, $\pi(c_{V,f}) \propto 1$.

2.8.3 The frequentist approach

Extremal bias

For the extremal bias in the frequentist framework (see Section 2.2.2), one uses again the likelihood $L_{\rm bias}(\delta_b)$ (Eq. (2.115)), with δ_b fixed at the two extreme values $\delta_b = \pm 1$. In practice, in order to

draw the best-fit regions in $c_V - c_f$, one can define a χ-squared function difference

$$\Delta\chi^2(c_f, c_V, \delta_b) = \chi^2(c_f, c_V, \delta_b) - \chi^2(\hat{c}_f, \hat{c}_V, \delta_b) \ , \quad \chi^2(c_f, c_V, \delta_b) = -2\log[L_{\rm bias}(\delta_b)] \, , \tag{2.119}$$

as follows from Eq. (2.6). Remind that $\chi^2(\hat{c}_f, \hat{c}_V, \delta_b)$ stands for the minimum of χ^2 with respect to c_f, c_V for a given δ_b. The best-fit regions are obtained by drawing the contour levels of $\Delta\chi^2$ set at the values given in Eq. (2.8). Once more, the prior for the parameters of interest entering in Eq. (2.6) are taken flat, $\pi(c_{V,f}) \propto 1$.

If the two extreme regions overlap, the same remark as in the Bayesian case holds. To display consistently the two regions together, one has to follow the rigorous definition of Eq. (2.17), using a discrete domain $\mathcal{D} = \{-1, 1\}$. This equation dictates to use the minimum of the two $\Delta\chi^2$, *i.e.* $\min_{\delta_b \in \{-1,1\}}[\Delta\chi^2(c_f, c_V, \delta_b)]$.

Envelope method

For the envelope method in the frequentist case, one can proceed with the χ^2 introduced in Eq. (2.119) and define

$$\bar{\chi}^2(c_f, c_V) = \min_{\delta_b \in [-1,1]} \left[\chi^2(c_f, c_V, \delta_b) - \chi^2(\hat{c}_f, \hat{c}_V, \delta_b) \right] \, , \tag{2.120}$$

according to the general definition of Eq. (2.17). This equation is the frequentist analog of Eq. (2.118). In order to draw the best-fit regions in the $c_V - c_f$ plane, one should then define

$$\Delta\bar{\chi}^2(c_f, c_V) = \bar{\chi}^2(c_f, c_V) - \bar{\chi}^2(\hat{c}_f, \hat{c}_V) \ . \tag{2.121}$$

The best-fit regions are obtained by drawing the contour levels of $\Delta\bar{\chi}^2$ set at the values given in Eq. (2.8). Again, the prior for the c_V, c_f parameters entering in Eq. (2.6) are taken flat, $\pi(c_{V,f}) \propto 1$.

Let us finally recall the parallel between Eq. (2.118) and Eq. (2.120). As first explained in Section 2.2.2, the subtracted term in Eq. (2.120) is the frequentist analogy of the ratio over $\int dc_f dc_V \, L_{\rm bias}(c_f, c_V, \delta_b)$ in Eq. (2.118). In both cases, the effect of this term is to remove the contribution of δ_b to goodness-of-fit (which avoids favouring specific values of δ_b). Both formulas are analog up to exchanging integration over δ_b with minimisation over δ_b. The fact that the integration/minimisation over δ_b is performed on the whole range $[-1, 1]$, rather than on the discrete domain $\{-1, 1\}$, leads to an envelope in the $c_f - c_V$ plane, instead of two distinct domains as in the extremal bias.

2.8.4 Numerical results

In this section, we apply both the frequentist and Bayesian versions of the bias method to the Higgs likelihood. We stress that the Higgs likelihood $L_{\rm bias}(\delta_b)$ is exactly the same in the two statistical frameworks, so that the discrepancies observed among the plots originate solely from the different statistical treatments. These two treatments differ in their definition of the best-fit regions (see Section 2.2.1) and their realisation of the bias principle (see Eqs. (2.14), (2.17)).

Extremal bias

In Fig. (2.9), we present the best-fit regions obtained through the Bayesian and frequentist bias methods, respectively described in Sections 2.8.2 and 2.8.3. The likelihood, $L_{\rm bias}(\delta_b)$ of Eq. (2.115), is used together with one of the two combined errors (2.116)-(2.117) depending on which correlation configuration is considered (Eq. (2.95) or Eq.(2.96) respectively).
The left and right pannels of Fig. (2.9) correspond to the two correlation configurations surrounding the case with realistic correlations. It turns out that the best-fit regions obtained in these two extreme correlation configurations have only mild differences.
Now, compare the two upper plots and lower plots of Fig. (2.9), corresponding respectively to the frequentist and Bayesian treatments. A small difference appears at the junction of the two set of regions, coming from the different realisation of the bias principle in the two statistical frameworks. Besides, the frequentist best-fit regions are slightly larger than the Bayesian ones, due to the non-equivalent definitions of the Bayesian and frequentist contours. Overall, there is a strong resemblance between the Bayesian and frequentist results. This reflects the weak impact of choosing the Bayesian or frequentist procedure for the extremal bias.

Let us now compare the lower plots of Fig. (2.9) with the previous Bayesian marginalisation plots obtained in Fig. (2.5) – considering of course respectively the two correlation configurations used in the left and right plots. One can clearly see that the best-fit regions [51] obtained from the extremal bias are larger than the ones obtained through marginalisation. This is because the regions in Fig. (2.5), derived by marginalising, correspond somehow to fix the nuisance parameters to their values favoured by the fit. For the present Higgs fits, it turns out that these preferred values are close to $\delta \approx -1$. Hence, the regions from the extremal bias (Fig. (2.9)) being obtained for $\delta_b = \pm 1$ (lower left set is for $\delta_b = -1$ [52]), they clearly cover more space in the $c_V - c_f$ plane than the domains in Fig. (2.5).

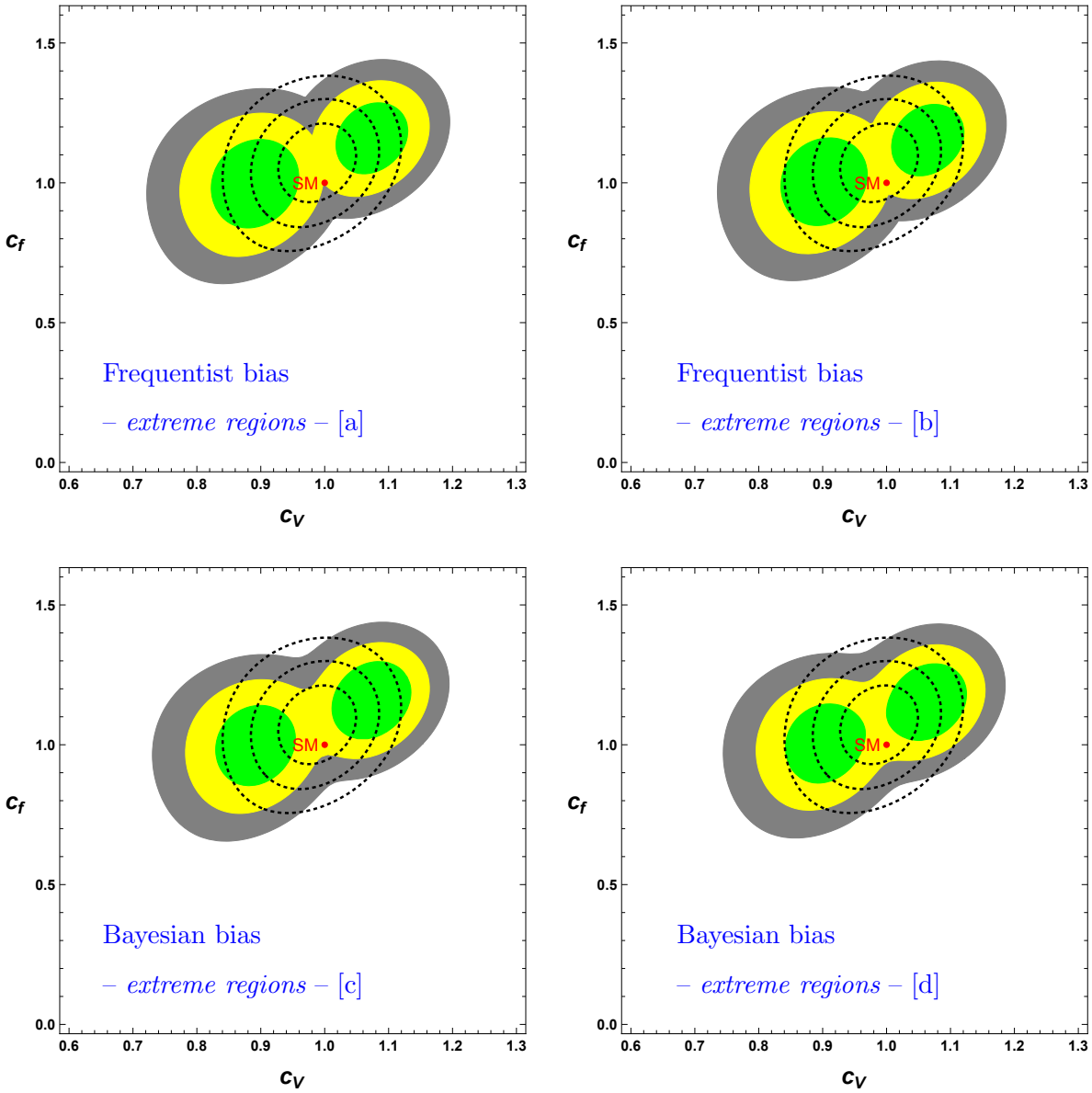

Figure 2.9: The best-fit regions in the $c_V - c_f$ plane obtained through an extremal bias. The 68%, 95% and 99% confidence regions are represented respectively by the green, yellow and grey domains. The upper plots illustrate the frequentist approach whereas the two lower ones show the Bayesian approach. The [a], [c] and [b], [d] plots correspond, respectively, to the characteristic correlation configurations described in Eq. (2.116) and Eq. (2.117). The dashed contours illustrate the case without theoretical uncertainties. The SM prediction is shown by the red point.

Envelope method

The four plots of Fig. (2.10) illustrate the Bayesian and frequentist envelope methods performed accordingly to Sections 2.8.2 and 2.8.3. Again, both correlation configurations, giving rise to the

[51] Notice that these best-fit regions include essentially the two extreme sub-domains corresponding to $\delta_b = \pm 1$.

[52] The dependence of the best-fit region location on the nuisance parameter is induced by the dependence of the likelihood (2.115) on, $\mu_i^{\rm ex}[1 + \delta_b \Delta_i^b]$.

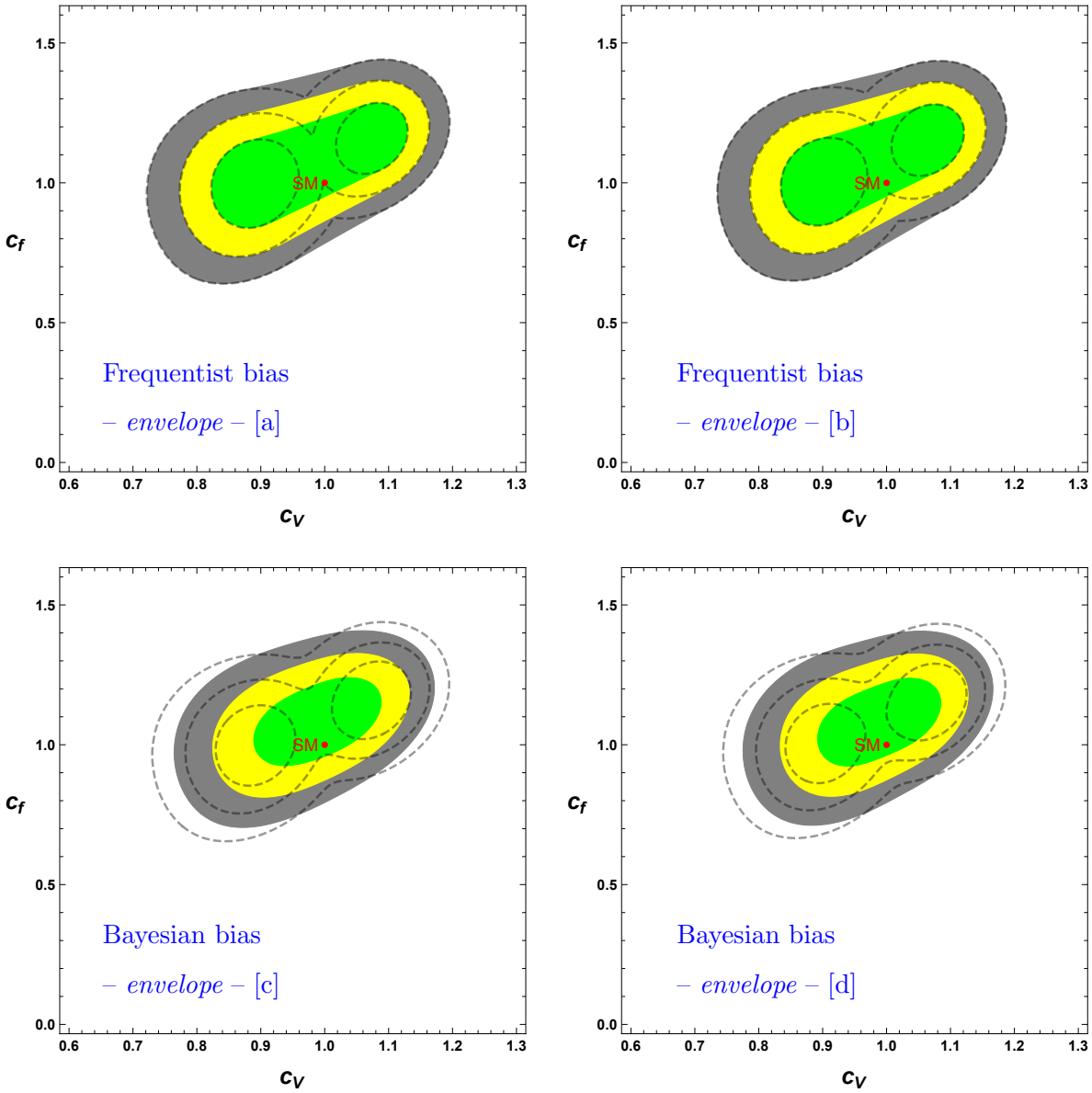

Figure 2.10: The best-fit regions in the $c_V - c_f$ plane obtained through the envelope method. The 68%, 95% and 99% confidence regions are represented respectively by the green, yellow and grey domains. The upper plots illustrate the frequentist approach whereas the two lower ones show the Bayesian approach. The [a], [c] and [b], [d] plots correspond, respectively, to the characteristic correlation configurations described in Eq. (2.116) and Eq. (2.117). The dashed grey contours illustrate the best-fit regions at 68% C.L., 95% C.L. and 99% C.L., obtained in Fig. (2.9). The SM prediction is shown by the red point.

combined errors of Eq. (2.116)-(2.117), are studied numerically. The two upper and lower plots of Fig. (2.10) differ due to the direct envelope method being not equivalent within the Bayesian and frequentist cases.

The sets of frequentist envelopes represent the best-fit areas that would be obtained by superimposing the best-fit regions of the extremal bias, but for δ_b spanning continuously the interval $[-1, 1]$.

This correspondence between the envelope method and extremal bias appears clearly when one realises (*c.f.* end of Section 2.2.2) that the former is based on the Eqs. (2.120)-(2.121) while the latter can be obtained through the same equations just with a minimisation over the discrete domain $\delta_b \in \mathcal{D} = \{-1, 1\}$ in Eq. (2.120), instead of the continuous range $[-1, 1]$. The correspondence is visible when comparing the envelopes with the extreme sets of best-fit domains at $\delta_b = \pm 1$, obtained previously from the frequentist bias method and also superimposed on upper plots of Fig. (2.10), as dashed contours: these contours draw exactly the extreme limits of the envelopes. The two sets of Bayesian envelopes obtained in the two lower plots of Fig. (2.10) represent less conservative regions with respect to the frequentist envelope. Besides, the envelopes of these plots cover smaller regions than the best-fit domains that would be obtained by superimposing the best-fit regions of the extremal bias, but for δ_b spanning continuously the interval $[-1, 1]$. This appears clearly when comparing those envelopes to the extreme sets of best-fit regions at, $\delta_b = \pm 1$, obtained previously from the Bayesian bias method (once more superimposed on the lower plots of Fig. (2.10), as dashed contours).

Finally, we mention that the SM point belongs to all the 68% C.L. regions of Fig. (2.10). At this level, we can illustrate one of the interests of the bias. Let us consider an hypothetical but plausible situation. For example, suppose that with future LHC data, the SM point would fall outside the 3σ region obtained by marginalising. Such a discrepancy could be interpreted either as an indirect effect of physics underlying the SM on the Higgs sector, or as a shift of the best-fit regions induced by values of the nuisance parameters favoured statistically by the fit. This shift induced by the nuisance parameters would come from the fact that the nuisance parameters and the parameters of interest are determined simultaneously. In contrast, in the envelope method, a SM prediction falling beyond the 3σ region would indicate the presence of new physics without any alternative explanation relying on the statistical treatment (the entire interval of the nuisance parameters being covered). This example provides a motivation to apply both bias and marginalisation methods, which are somehow complementary.

2.9 Conclusions

The main goal of this analysis was to work out a consistent statistical treatment of the theoretical uncertainties in the fits of the Higgs boson rates. We have analysed in a unified formalism both the Bayesian and frequentist approaches to theoretical uncertainties. We systematically analysed how to perform error combinations in a given statistical context and we have introduced a framework to use the bias principle on firm ground.

This analysis has been the opportunity to update the Higgs rate fit based on the latest LHC data at 7 and 8 TeV. In the case of Bayesian marginalisation, we have found that the SM prediction for the Higgs couplings still falls into the 68% C.L. region of the $c_V - c_f$ plane. Bayesian marginalisation benefits from well-defined distributions for the nuisance parameters and from an easier convolution

of these error distributions compared to frequentist marginalisation.

We have reviewed all the fundamental sources of the individual theoretical errors involved in the SM Higgs cross sections and branching ratios. Then those errors have been combined in a careful 'step-by-step' approach following the Bayesian rules. In this task of combining a significant number of uncertainties (various Higgs production modes, decay channels...), we were helped by the leading moment approximation – which has been deduced from considerations on the moment-generating function.

This has allowed us to show that the prior of the total uncertainty resulting from the combination of all the theoretical errors (using flat priors for the unknown ones) converges to a nearly Gaussian shape. Besides, it also came out from the numerical results that the precise form of this final theoretical prior is not crucial with respect to the determination of the best-fit regions. This conclusion holds only for the present data, which still have large experimental errors with respect to the theoretical ones.

In contrast, our analysis has shown that the correlations of the theoretical uncertainties among the Higgs detection channels induce a significant shift of the best-fit domains in the space of the parameters of interest. These correlations appear thus to be an unavoidable ingredient of the fits. The Higgs fits were performed in two extreme configurations of theoretical correlations between the various detection channels. The most realistic correlation setup is an intermediate configuration between those two. Such an approach is thus conservative. Besides, considering characteristic configurations has allowed us to derive simple analytic expressions for the marginal likelihood functions.

For future Higgs fits, given the ambiguities inherent to the estimation of the theoretical error magnitudes, we recommend to present an additional analysis with 1σ errors enhanced by a typical factor of 1.5 as a conservative benchmark. Such a factor is consistent with the 1σ theoretical errors preferred by the data. Of course the present degree of arbitrariness in the theoretical error magnitudes could be improved for instance with future higher order QCD calculations or new methods to determine the PDFs.

Finally, we have provided a rigorous statistical framework for the bias principle, which constitutes an alternative to marginalisation. This framework has lead us to define two complementary bias treatments: the extremal bias and the envelope method. The bias principle is more conservative than marginalisation by construction, and does not depend on the shape of the priors of the nuisance parameters, which are not always known. Therefore, a reasonable advice is to apply both the marginalisation and bias methods to the Higgs data. Using the envelope method, we find that the SM prediction belongs to the 68% C.L. region of the $c_V - c_f$ plane.

Bibliography

[1] The ATLAS Collaboration, Phys. Lett. B716 (2012) 1.

[2] The CMS Collaboration, Phys. Lett. B716 (2012) 30.

[3] P. Higgs, Phys. Lett. 12 (1964) 132; Phys. Rev. Lett. 13 (1964) 506; F. Englert and R. Brout, Phys. Rev. Lett. 13 (1964) 321; G. Guralnik, C. Hagen and T. Kibble, Phys. Rev. Lett. 13 (1964) 585; S. Weinberg, Phys. Rev. Lett. 19 (1967) 1264.

[4] The ATLAS Collaboration, CONF-2013-014; CONF-2013-034; CONF-2015-007; arXiv:1507.04548 [hep-ex].

[5] The CMS Collaboration, PAS-HIG-12-036; PAS-HIG-12-045; PAS-HIG-14-009; arXiv:1412.8662 [hep-ex].

[6] ATLAS web page, `http://atlas.web.cern.ch/Atlas/Collaboration/` .

[7] CMS web page, `https://twiki.cern.ch/twiki/bin/view/CMSPublic/PhysicsResults` .

[8] A. Djouadi and G. Moreau, Phys. Lett. B660 (2008) 67; C. Bouchart and G. Moreau, Phys. Rev. D80 (2009) 095022.

[9] A. Azatov and J. Galloway, Int. J. Mod. Phys. A Volume 28 (2013) 1330004.

[10] A. Arbey, M. Battaglia, A. Djouadi and F. Mahmoudi, JHEP 1209 (2012) 107; Phys. Lett. B720 (2013) 153; A. Djouadi, L. Maiani, G. Moreau, A. Polosa, J. Quevillon and V. Riquer, Eur. Phys. J. C73 (2013) 2650.

[11] Physics Briefing Book, Input for the Strategy Group to draft the update of the European Strategy for Particle Physics, **CERN-ESG-005**.

[12] D. Carmi, A. Falkowski, E. Kuflik, T. Volansky and J. Zupan, JHEP 1210 (2012) 196; J. Espinosa, C. Grojean, M. Muhlleitner and M. Trott, JHEP 1212 (2012) 045; P. Giardino, K. Kannike, M. Raidal, and A. Strumia, Phys. Lett. B718 (2012) 469; J. Ellis and T. You, JHEP 1209 (2012) 123; T. Corbett, O. J. P. Eboli, J. Gonzalez-Fraile and M. C. Gonzalez-Garcia, Phys. Rev. D86 (2012) 075013; F. Bonnet, T. Ota, M. Rauch and W. Winter, Phys. Rev. D86 (2012)

093014; A. Alves *et al.*, Eur. Phys. J. C73 (2013) 2, 2288; J. Cao, Z. Heng, J. M. Yang and J. Zhu, JHEP 1210, 079 (2012); S. Banerjee, S. Mukhopadhyay and B. Mukhopadhyaya, JHEP 1210 (2012) 062; I. Low, J. Lykken and G. Shaughnessy, Phys. Rev. D86 (2012) 093012; M. Klute, R. Lafaye, T. Plehn, M. Rauch and D. Zerwas, Phys. Rev. Lett. 109 (2012) 101801; T. Plehn and M. Rauch, Europhys. Lett. 100 (2012) 11002; G. Cacciapaglia, A. Deandrea, G. Drieu La Rochelle and J.-B. Flament, JHEP 1303 (2013) 029; N. Bonne and G. Moreau, Phys. Lett. B717 (2012) 409; G. Bélanger, B. Dumont, U. Ellwanger, J. F. Gunion and S. Kraml, JHEP 1302 (2013) 053; C. Cheung, S. D. McDermott and K. M. Zurek, JHEP 1304 (2013) 074; K. Cheung, J. S. Lee and P. -Y. Tseng, JHEP 1305 (2013) 134; G. Moreau, Phys. Rev. D87 (2013) 015027.

[13] J. Ellis and T. You, JHEP 1306 (2013) 103; T. Alanne, S. Di Chiara and K. Tuominen, JHEP 1401 (2014) 041; A. Falkowski, F. Riva and A. Urbano, JHEP 1311 (2013) 111; T. Corbett *et al.*, arXiv:1505.05516 [hep-ph]; S. Banerjee, T. Mandal, B. Mellado and B. Mukhopadhyaya, arXiv:1505.00226 [hep-ph].

[14] A. Djouadi and G. Moreau, Eur. Phys. J. C73 (2013) 9, 2512.

[15] P. P. Giardino, K. Kannike, I. Masina, M. Raidal and A. Strumia, JHEP 1405 (2014) 046.

[16] B. Dumont, S. Fichet and G. von Gersdorff, JHEP 1307 (2013) 065.

[17] LHC Higgs Cross Section Working Group web page, `https://twiki.cern.ch/twiki/bin/view/LHCPhysics/LHCHXSWG` .

[18] "Handbook of LHC Higgs Cross Sections: 1. Inclusive Observables", arXiv:1101.0593 [hep-ph], **CERN-2011-002**.

[19] "Handbook of LHC Higgs Cross Sections: 2. Differential Distributions", arXiv:1201.3084 [hep-ph], **CERN-2012-002**.

[20] "Handbook of LHC Higgs Cross Sections: 3. Higgs Properties", arXiv:1307.1347 [hep-ph], **CERN-2013-004**.

[21] K. Cranmer, S. Kreiss, D. Lopez-Val and T. Plehn, Phys. Rev. D91 (2015) 054032.

[22] M. Cacciari and N. Houdeau, JHEP 1109 (2011) 039; E. Bagnaschi, M. Cacciari, A. Guffanti and L. Jenniches, JHEP 1502 (2015) 133.

[23] R. S. Gupta, H. Rzehak and J. D. Wells, Phys. Rev. D86 (2012) 095001.

[24] R. Lafaye, T. Plehn, M. Rauch, D. Zerwas and M. Duehrssen, JHEP 0908 (2009) 009.

[25] C. Anastasiou, C. Duhr, F. Dulat, F. Herzog and B. Mistlberger, Phys. Rev. Lett. 114 (2015) 212001.

[26] J. Baglio, A. Djouadi and R. M. Godbole, Phys. Lett. B716 (2012) 203.

[27] C. Anastasiou, R. Boughezal and F. Petriello, JHEP 0904 (2009) 003.

[28] J. O. Berger and R. L. Wolpert, *The likelihood principle*, Institute of Mathematical Statistics Lecture Notes - Monograph Series 6 (1988).

[29] The ATLAS and CMS Collaborations and The LHC Higgs Combination Group, "Procedure for the LHC Higgs boson search combination in Summer 2011", CMS-NOTE-2011-005, ATL-PHYS-PUB-2011-11.

[30] S. Fichet and G. Moreau, submitted to Nucl. Phys. B, arXiv:1509.00472 [hep-ph].

[31] The ATLAS Collaboration, CONF-2013-012; Phys. Rev. D90 (2014) 112015; Phys. Lett. B740 (2015) 222.

[32] The ATLAS Collaboration, CONF-2013-013; Phys. Lett. B726 (2013) 88; Phys. Lett. B738 (2014) 234; Phys. Rev. D91 (2015) 012006.

[33] The ATLAS Collaboration, CONF-2013-030; CONF-2014-060; CONF-2015-006; CONF-2015-005; arXiv:1412.2641 [hep-ex].

[34] The ATLAS Collaboration, CONF-2012-170; CONF-2014-043; JHEP 1501 (2015) 069; arXiv:1503.05066 [hep-ex].

[35] The ATLAS Collaboration, CONF-2012-160; CONF-2014-061; JHEP 1504 (2015) 117.

[36] The CMS Collaboration, PAS-HIG-13-001; PAS-HIG-13-029; JHEP 1409 (2014) 087.

[37] The CMS Collaboration, PAS-HIG-13-002.

[38] The CMS Collaboration, PAS-HIG-13-003; PAS-HIG-13-023.

[39] The CMS Collaboration, PAS-HIG-12-020; PAS-HIG-12-035; PAS-HIG-13-012; PAS-HIG-14-004; PAS-HIG-14-010.

[40] The CMS Collaboration, PAS-HIG-13-004; PAS-HIG-13-033.

[41] CDF web page, `http://www-cdf.fnal.gov` ; D0 web page, `http://www-d0.fnal.gov` .

[42] The CDF and D0 Collaborations, CDF Note 10884, D0 Note 6348, arXiv:1207.0449 [hep-ex].

[43] A. Djouadi, Phys. Rept. 457 (2008) 1.

[44] S. Fichet and G. von Gersdorff, JHEP 1403 (2014) 102.

[45] P. R. Archer, M. Carena, A. Carmona and M. Neubert, JHEP 1501 (2015) 060.

[46] G. Moreau, Phys. Rev. D87 (2013) 015027.

[47] R. Trotta, Contemp. Phys. 49 (2008) 71.

[48] C. Mc Neile, C. T. H. Davies, E. Follana, K. Hornbostel and G. P. Lepage, Phys. Rev. D82 (2010) 034512.

[49] J. Beringer *et al.* (Particle Data Group), Phys. Rev. D86 (2012) 010001; K. A. Olive *et al.* (Particle Data Group), Chin. Phys. C38 (2014) 090001.

[50] "Review of lattice results concerning low energy particle physics", Eur. Phys. J. C74 (2014) 2890.

[51] "The PDF4LHC Working Group Interim Recommendations", arXiv:1101.0538 [hep-ph].

[52] PDF4LHC Working Group web page, `http://www.hep.ucl.ac.uk/pdf4lhc` .

[53] S. Forte and G. Watt, Annu. Rev. Nucl. Part. Sci. 63 (2013) 291.

[54] A. D. Martin, W. J. Stirling, R. S. Thorne and G. Watt, Eur. Phys. J. C64 (2009) 653.

[55] C. Anastasiou, S. Buehler, F. Herzog and A. Lazopoulos, JHEP 1204 (2012) 004.

[56] J. Baglio, A. Djouadi, S. Ferrag and R. M. Godbole, Phys. Lett. B699 (2011) 368 [Erratum-ibid. B702 (2011) 105]; J. Baglio, A. Djouadi and R. M. Godbole, arXiv:1107.0281 [hep-ph] (Extended version of talks given at several winter conferences).

[57] J. Baglio and A. Djouadi, JHEP 1103 (2011) 55.

[58] J. Baglio and A. Djouadi, JHEP 1010 (2010) 64.

[59] Proceedings of the *New Physics Working Group* of the 2013 Les Houches Workshop, "Physics at TeV Colliders", Les Houches 3-21 June 2013, 201 pages, arXiv:1405.1617 [hep-ph].

[60] S. Fichet, Int. J. Mod. Phys. A30 (2015) 09, 1550039.

Chapter 3

The couplings and CP properties of the Higgs boson from fits of its rates and their ratios

Adapted from: *A. Djouadi and G. Moreau*, Eur. Phys. J. **C73** (2013) 9, 2512.

3.1 Introduction

The ATLAS and CMS collaborations have released their analyses of the mass and the production times decay rates of the 126 GeV Higgs–like particle using the full set of data collected so far, ≈ 5 fb^{-1} at $\sqrt{s} = 7$ TeV and ≈ 20 fb^{-1} at $\sqrt{s} = 8$ TeV [1–4]. This closes a very successful first run at the LHC, which culminated with the historical discovery of the state in July 2012 [5, 6]. To be convinced that the observed particle is indeed the Higgs boson that is responsible of the spontaneous breaking of the electroweak symmetry [7, 8], one needs to prove that the particle: *i*) has spin–zero, *ii*) is a CP–even state, *iii*) couples to fermions and gauge bosons proportionally to their masses and, ultimately, *iv*) has a self–coupling that is also proportional to its mass. While there is little doubt on the spin–zero nature of the observed state [1], and the probing of the self–coupling has to await for a high–luminosity LHC [11] or a future lepton collider, a first determination of the couplings [12–14] and the CP–properties [15, 16] can be performed with the current results. The ATLAS and CMS collaborations themselves have given a first "portrait" of the observed particle which indicates that indeed it has the properties of a Higgs boson and even more, the properties of the unique Higgs boson that is predicted in the Standard Model (SM) [1–4, 17].

However, in the case of the particle coupling determination, the ATLAS and CMS analyses

[1] The observation of the $H \to \gamma\gamma$ decay rules out the spin–1 case [9] and the graviton–like spin–2 possibility is extremely unlikely and, from the particle rates, is ruled out in large classes of models [10].

suffer from two serious drawbacks [18, 19]. The first one is that the signal strength modifiers μ_{XX}, that are identified with the Higgs cross section times decay branching ratio normalized to the SM expectation in a given $H \to XX$ search channel, are affected by large theoretical uncertainties that are now becoming a dominant source of error. Indeed, the combined theoretical uncertainty in the rate of the by far dominant Higgs production process at the LHC, gluon fusion $gg \to H$, is estimated to be of order $\pm$15–20% [20, 21] even before it is broken into jet categories which significantly increases the uncertainty [22, 23]. The uncertainty is similar in the vector boson fusion channel when the large contamination from the $gg \to Hjj$ process is taken into account [23]. Another drawback of the analyses [18, 19] is that they involve strong theoretical assumptions on the total Higgs width since some contributing decay channels not accessible at the LHC are assumed to be SM–like and possible invisible Higgs decays in scenarios beyond the SM are supposed not to occur.

In this letter, we consider ratios of Higgs production cross sections times decay branching fractions in which these two sources of uncertainties and, eventually, also some systematical and parametrical uncertainties such as the error on the luminosity measurement and the one on the Higgs branching ratios [2] [21, 24], should be absent [18, 19]. Using the Higgs signal strengths in which the theoretical uncertainty is taken to be a bias and not a nuisance (as is done generally), as well as the ratios $\mu_{\gamma\gamma}/\mu_{ZZ}$ and $\mu_{\tau\tau}/\mu_{WW}$ which are free from the ambiguities above, we perform a fit of the latest ATLAS and CMS data and conclude that, already at the 68% confidence level (CL), there is no deviation of the Higgs couplings to fermions and gauge bosons from the SM expectation.

On an other front, the attempts made so far for the determination of the CP nature of the particle mainly exploit the kinematical features of the $H \to VV$ decays with $V = W, Z$ [15] or the production in the vector boson fusion $V^*V^* \to H$ and Higgs–strahlung $V^* \to VH$ processes [16]. Since a CP–odd particle has not have tree level couplings to VV states [3], all these processes project out only the CP–even component of the HVV coupling [30] and the considered distributions can be thus only those of a 0^{++} state.

We will show that a much better way to measure the CP composition of the observed Higgs state is to consider the measured signal strength in the $H \to VV$ decays; see also Ref. [31]. Using μ_{ZZ}, we demonstrate that, if the magnitude of the Higgs couplings to fermions is as in the SM, the pure CP–odd possibility is excluded at the 4σ level, irrespective of the (mixed CP) Higgs couplings to light fermions.

Finally, assuming that the Higgs couplings to fermions and gauge bosons are SM–like and using mainly the signal strength μ_{ZZ}, one obtains a limit on the rate for invisible Higgs decays,

[2] There are parametric uncertainties that affect the hadronic Higgs decay widths. For a $\approx$ 126 GeV SM Higgs boson, this translates into an uncertainty on the total Higgs width which is found to be of order $\approx$ 4% in Ref. [24] and slightly higher in Ref. [21].

[3] The effective VV coupling of a pseudoscalar A boson, $\propto M_V^2 V^{\mu\nu}\widetilde{V}_{\mu\nu}$ with $\widetilde{V}_{\mu\nu} = \epsilon^{\mu\nu\rho\sigma}V_{\rho\sigma}$, should be generated through tiny loop corrections. To make this coupling as large as the SM tree–level HVV coupling, one needs a very low new physics scale that would spoil the precision electroweak data.

$\Gamma_H^{\rm inv}/\Gamma_H^{\rm SM} \leq 0.52$ at the 68%CL (see also Ref. [14, 25] for an indirect limit), that is stronger than the one obtained from direct invisible Higgs searches [26, 27].

3.2 The signal strengths and their ratios

Let us first summarize the LHC Higgs data collected in the 2011 and 2012 runs for the various SM Higgs decay channels that have been searched for by the ATLAS and CMS collaborations: $H \to ZZ^* \to 4\ell^\pm$, $H \to WW^* \to 2\ell 2\nu$, $H \to \gamma\gamma$, $H \to \tau^+\tau^-$ and $H \to b\bar{b}$; we will ignore the additional search channels $H \to \mu^+\mu^-$ and $H \to Z\gamma$ (see e.g. Ref. [28]) for which the sensitivity is still too low. In most cases, the various Higgs production channels have been used: the by far dominant gluon–gluon fusion mechanism $gg \to H$ (ggF) that has the large production rates but also the subleading channels, vector boson fusion (VBF) $qq \to Hqq$ and Higgs–strahlung (HV) $q\bar{q} \to HV$ with $V = W, Z$; the top quark associated $p\bar{p} \to t\bar{t}H$ mechanism (ttH) has too low a cross section to be relevant. At least the ggF and VBF channels have been considered in the $H \to ZZ, WW, \gamma\gamma$ and $H \to \tau^+\tau^-$ channels, while in the case $H \to \tau^+\tau^-$ and $H \to WW^* \to 2\ell 2\nu$ decays, also the HV production mode in which the $H \to b\bar{b}$ decay has been searched for, has been considered.

ATLAS and CMS have provided the signal strengths for the various final states with a luminosity of, respectively, ≈ 5 fb^{-1} for the 2011 run at $\sqrt{s} = 7$ TeV and ≈ 20 fb^{-1} the 2012 run at $\sqrt{s} = 8$ TeV. We will identify these μ values with the Higgs cross section times decay branching fractions normalized to the SM expectation and, for the $H \to XX$ decay, one would have indeed in the narrow width approximation,

$$\mu_{XX}|_{\rm th} \simeq \frac{\sigma(pp \to H \to XX)}{\sigma(pp \to H \to XX)|_{\rm SM}} \simeq \frac{\sigma(pp \to H) \times {\rm BR}(H \to XX)}{\sigma(pp \to H)|_{\rm SM} \times {\rm BR}(H \to XX)|_{\rm SM}}. \tag{3.1}$$

From the experimental point of view (and in our fits), this would correspond to

$$\mu_{XX}|_{\rm exp} \simeq \frac{N_{XX}^{\rm evts}}{\epsilon \times \sigma(pp \to H)|_{\rm SM} \times {\rm BR}(H \to XX)|_{\rm SM} \times \mathcal{L}}, \tag{3.2}$$

where $N_{XX}^{\rm evts}$ stands for the measured number of events in the $H \to XX$ search channel, ϵ denotes the selection efficiency and $\mathcal{L}$ is the luminosity.

In this work, we consider the decay ratios D_{XX} discussed in Ref. [18] and defined as

$$D_{XX}^{\rm p} = \frac{\sigma^{\rm p}(pp \to H \to XX)}{\sigma^{\rm p}(pp \to H \to VV)} = \frac{\sigma^{\rm p}(pp \to H) \times {\rm BR}(H \to XX)}{\sigma^{\rm p}(pp \to H) \times {\rm BR}(H \to VV)} = \frac{\Gamma(H \to XX)}{\Gamma(H \to VV)} \tag{3.3}$$

for a specific production process p = ggF, VBF, VH or all (for inclusive production) and for a given decay channel $H \to XX$ when the reference channel $H \to VV$ with $V = W$ or/and Z is used. In these ratios, the cross sections $\sigma(pp \to H)$ and hence, their significant theoretical uncertainties will

cancel out as discussed previously, leaving out only the ratio of decay branching fractions and hence of partial decay widths. Thus, the total decay width which includes contributions from channels not under control such as possible invisible Higgs decays, do not appear in the decay ratios $D^{\rm p}_{XX}$. Some common experimental systematical uncertainties such as the one from the luminosity measurement as well as the uncertainties in the Higgs decay branching ratios also cancel out. We are thus, in principle, left with mostly the statistical uncertainty and some systematical errors [4].

The ratios D_{XX} involve, up to kinematical factors, only the ratios $|c_X|^2/|c_V|^2$ of the reduced couplings of the Higgs boson to the particles X and V compared to the SM expectation, $c_X \equiv g_{HXX}/g^{\rm SM}_{HXX}$. For the SM Higgs boson with a mass of $M_H = 125$ GeV, the kinematical factors can be straightforwardly obtained using the program HDECAY [34] for the evaluation of the Higgs branching ratios when the SM inputs recommended by the LHC Higgs working group [20] are adopted; they are given in Ref. [18] for the various normalisations (and, for simplicity, are then set to unity in that work).

In practice, to take into account the fact that there are four different Higgs production channels with different topologies, the cross section part is more involved and the ratio D_{XX} can be more precisely written as

$$D_{XX} \propto \frac{\epsilon_X^{gg}\sigma(gg\to H)+\epsilon_X^{\rm VBF}\sigma(Hqq)+\epsilon_X^{HV}\sigma(HV)+\epsilon_X^{t\bar{t}H}\sigma(t\bar{t}H)}{\epsilon_V^{gg}\sigma(gg\to H)+\epsilon_V^{\rm VBF}\sigma(Hqq)+\epsilon_V^{HV}\sigma(HV)+\epsilon_V^{t\bar{t}H}\sigma(t\bar{t}H)} \times \frac{\frac{\Gamma(H\to XX)}{\Gamma(H\to XX)|_{\rm SM}}}{\frac{\Gamma(H\to VV)}{\Gamma(H\to VV)|_{\rm SM}}} \tag{3.4}$$

where the ϵ_X^p, provided by the ATLAS and CMS collaborations, denote the experimental efficiencies to select the Higgs events in the gg, VBF, HV, $t\bar{t}H$ production and $H \to XX$ decay channels (exclusive cut categories are also considered). D_{XX} is only proportional to the above expression due to the presence of another identical ratio of cross sections but within the SM [5]. Nevertheless for almost the same selection efficiencies, and even for $\epsilon_X^p = k\epsilon_V^p$ with k a constant, the expression eq. (3.4) simplifies to that in eq. (3.5).

In fact, the decay ratios D_{XX} can be simply written in terms of the signal strengths

$$D_{XX} \hat{=} \frac{\mu_{XX}}{\mu_{VV}} \simeq \frac{\frac{\sigma(pp\to H)\times{\rm BR}(H\to XX)}{\sigma(pp\to H)|_{\rm SM}\times{\rm BR}(H\to XX)|_{\rm SM}}}{\frac{\sigma(pp\to H)\times{\rm BR}(H\to VV)}{\sigma(pp\to H)|_{\rm SM}\times{\rm BR}(H\to VV)|_{\rm SM}}} = \frac{\frac{{\rm BR}(H\to XX)}{{\rm BR}(H\to XX)|_{\rm SM}}}{\frac{{\rm BR}(H\to VV)}{{\rm BR}(H\to VV)|_{\rm SM}}} = \frac{\frac{\Gamma(H\to XX)}{\Gamma(H\to XX)|_{\rm SM}}}{\frac{\Gamma(H\to VV)}{\Gamma(H\to VV)|_{\rm SM}}} = \frac{|c_X|^2}{|c_V|^2} \tag{3.5}$$

where have used as normalisations in the ratios the channels [6] $H \to VV$ with $V = Z$ or W.

[4] The theoretical and common systematical uncertainties will completely cancel out only when the same selection cuts are applied for the different final state topologies in a given production process (the selection efficiencies should be $\epsilon^{\rm p}_X = k\,\epsilon^{\rm p}_V$, k being a constant). This is obviously not the case in all the channels that we are considering here. We will assume, nevertheless, that this will be the case and we consider that the remaining uncertainty in the ratio is, to a good approximation, only of statistical nature. We hope that in the future, with the much larger data sample that is expected, the ATLAS and CMS collaborations will analyze the various search channels under the same experimental conditions.

[5] Without derivative Higgs couplings, the kinematics and selection efficiencies are as in the SM.

[6] In fact, one can assume custodial symmetry and use the combined $H \to WW$ and $H \to ZZ$ channels as a

Nevertheless, performing the ratios of signal strengths leads to a loss of information and, in some case, we will need at least one signal strength to set the normalisation. Rather than using the global $\mu_{\rm tot}$ value obtained by combining all search channels, we will consider the cleaner $H \to ZZ$ channel alone as it is fully inclusive and thus does not involve the additional large scale uncertainties that occur when breaking the $gg \to H$ cross section into jet categories [7]. The combination of the ATLAS and CMS data in the ZZ channel gives

$$\mu_{ZZ} = 1.10 \pm 0.22^{\,\rm exp} \pm 0.2^{\,\rm th} \tag{3.6}$$

where the first uncertainty is experimental and the second one theoretical and that we assume to be, conservatively, $\Delta^{\rm th} = \pm 0.2$. It has been advocated in Ref. [18, 21] that, since the main effect of the theoretical uncertainty (which has no statistical ground) is to modify the normalisation of the SM cross section, it should be considered as a bias (rather than a nuisance as in the case of the experimental error) and, hence, one needs to perform two separate fits: one with $\mu_{ZZ} + \Delta^{\rm th}$ and another with $\mu_{ZZ} - \Delta^{\rm th}$.

3.3 A combined fit of the Higgs couplings

In order to study the Higgs at the LHC we define the (now usual) effective Lagrangian,

$$\begin{aligned} \mathcal{L}_h \;&=\; c_W\; g_{HWW}\; H\; W^+_\mu W^{-\mu} + \; c_Z\; g_{HZZ}\; H\; Z^0_\mu Z^{0\mu} \\ &-\; c_t\; y_t\; H\bar{t}_L t_R - c_c\; y_c\; H\bar{c}_L c_R - c_b\; y_b\; H\bar{b}_L b_R - c_\tau\; y_\tau\; H\bar{\tau}_L \tau_R \;+\; \text{h.c.} \end{aligned} \tag{3.7}$$

where $y_{t,c,b,\tau} = m_{t,c,b,\tau}/v$ are the SM Yukawa coupling constants in the mass eigenbasis (L/R indicates the fermion chirality and we consider only the heavy fermions that have substantial couplings to the Higgs boson), $g_{HWW} = 2M_W^2/v$ and $g_{HZZ} = M_Z^2/v$ are the electroweak gauge boson couplings and v is the Higgs vacuum expectation value. The c parameters are all defined such that the limit $c \to 1$ corresponds to the SM case. For the present task, we assume no or negligible new contributions to the Higgs couplings to photons or gluons, e.g. as induced by new particles.

We will present the results for the fits of the Higgs signal strengths, μ_i (i labels each channel and cut category investigated), in the plane c_f versus c_V. We have chosen universal coupling corrections, $c_f = c_t = c_c = c_b = c_\tau$ and $c_V = c_W = c_Z$, for an illustrative purpose. All the Higgs production/decay channels are considered here and the data used are the latest ones and are

reference to increase the statistical accuracy of the normalization factor. The ratio $D_{ZZ} = \mu_{ZZ}/\mu_{WW}$ has been measured for instance by the ATLAS collaboration to be $D_{ZZ} \simeq |c_Z|^2/|c_W|^2 = 1.6^{+0.8}_{-0.5}$ [2] (with the error expected to be only statistical), hence, supporting this approach.

[7] In addition, contrary to the global signal strength $\mu_{\rm tot}$, it does not involve the channel $\Gamma(H \to \gamma\gamma)$ which, at least in the ATLAS case, deviates from the SM prediction and might indicate the presence of new physics in the $H\gamma\gamma$ loop which is not reflected in the other couplings.

borrowed from Ref. [35] for the Tevatron, from Refs. [36–40] and the combined results of Refs. [1,2] for the ATLAS collaboration as well as Refs. [3, 4, 41–45] and the combined analysis of Ref. [3] for the CMS collaboration and finally the LHC results presented at the Moriond conference this month [29, 33].

We will closely follow the procedure of Ref. [13] (to which we refer for the relevant details) for the fit of these data, with one major difference though, the treatment of the theoretical uncertainty. The errors used in the present fit are those given by the collaborations as quoted above and, thus, contain the experimental and theoretical uncertainties added in quadrature, $\delta\mu_i = \sqrt{\delta\mu_i|^2_{\rm exp} + \delta\mu_i|^2_{\rm th}}$, which completely dilutes the effect of $\delta\mu_i|_{\rm th}$. In the present analysis, we treat the theoretical uncertainty as a bias (and not as if it were associated with a statistical distribution) and perform the fit for the two extremal values of the signal strength : $\mu_i|_{\rm exp}[1 \pm \delta\mu_i/\mu_i|_{\rm th}]$ with the theoretical uncertainty $\delta\mu_i/\mu_i|_{\rm th}$ conservatively assumed to be 20% for both the gluon and vector boson fusion mechanisms.

The results of the fit of the data is presented in Fig. 3.1 and relies on established values [46] of $\Delta\chi^2 = \chi^2 - \chi^2_{\rm min}$ with the following χ^2 function

$$\chi^2 \;=\; \sum_i \frac{[\mu_i(c_f, c_V) - \mu_i|_{\rm exp}]^2}{(\delta\mu_i)^2} \;. \tag{3.8}$$

In addition to the fit that is usually performed, leading to the colored regions on the left plot of Fig. 3.1 for the best fits at the $1\sigma, 2\sigma$ and 3σ levels in the c_f versus c_V plane [8], we also present the results of the fit for a treatment of the theoretical uncertainty as a bias. The value, $\mu_i|_{\rm exp} + (\delta\mu_i/\mu_i|_{\rm th})\big|\mu_i|_{\rm exp}\big|$, corresponds to the plain contours on Fig. 3.1 while the dashed contours are for the lower $\mu_i|_{\rm exp}$ expectations (negative sign in front of the error). The distances between the two contours represent the theoretical uncertainty induced on the fitted parameters. The treatment of the theoretical uncertainty as a bias is also illustrated on the right plot of Fig. 3.1 using colored domains.

A first conclusion that can be drawn from this figure is that, with the latest LHC data, in particular the new CMS di-photon rate which has no excess compared to (and is even slightly below) the SM expectation, the SM point is now included inside the 1σ domain. Before the CMS update, there was a large deviation in the di–photon channel which triggered discussions about the possibility that $c_f < 0$ (as shown in the figure for the 2σ and 3σ regions) which leads to a constructive interference between the top quark and W-boson loop contributions to increase the di-photon rate. This possibility has been elaborated within several effective scenarios in the recent literature to generate such a di–photon enhancement (see examples in Ref. [12]).

The statement that the fit result is compatible with the SM expectation is true regardless of the method chosen to implement the theoretical uncertainty. Nevertheless, it appears clearly on the figure that treating this uncertainty as a bias enhances significantly its effects in the c-parameter

[8] Because of the exact reflection symmetry under, $c \to -c$, leaving the squared amplitudes of the Higgs rates unaffected, only the part, $c_V > 0$, is presented in Fig. 3.1.

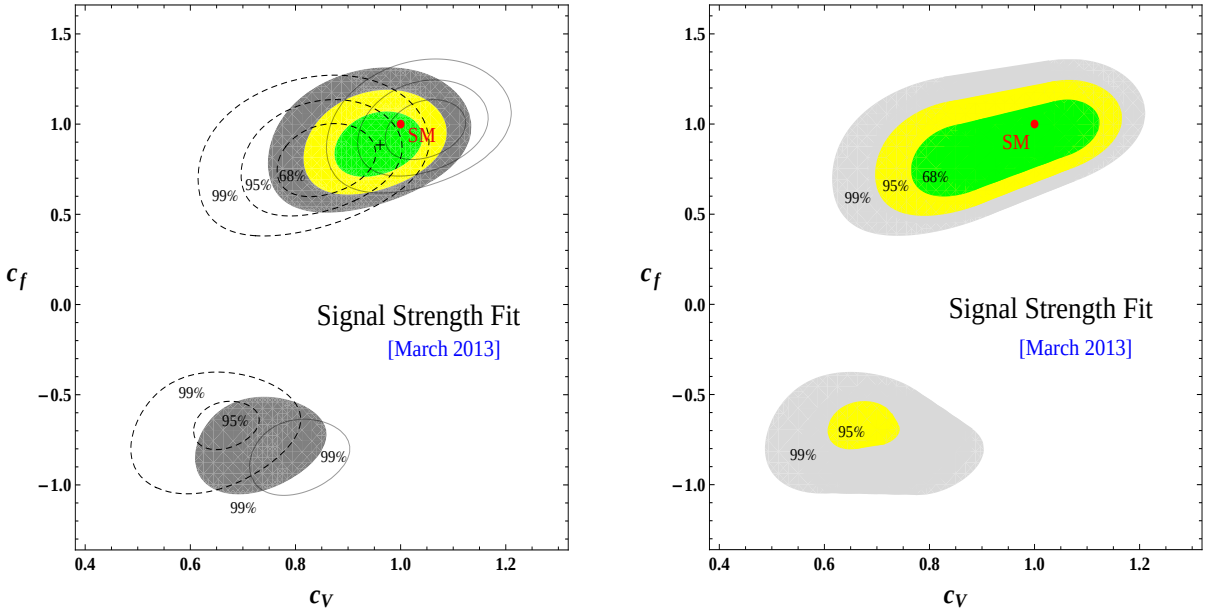

Figure 3.1: Left plot Best-fit regions at 68.27%CL (green), 95.45%CL (yellow) and 99.73%CL (grey) in the plane c_f versus c_V, based on the χ^2 function of eq. (3.8); the best-fit location is indicated by a (black) cross. The 'concentric' best-fit domains at the same CLs obtained also from χ^2 but for the two extreme theoretical predictions – upper (plain contours) and lower (dashed contours) – of the Higgs signal strengths, are presented. The SM (red) point at $c_f = c_V = 1$ is also shown. Right plot Best-fit domains at the 68.27%CL (green), 95.45%CL (yellow) and 99.73%CL (light grey) based on the χ^2 function; these domains were obtained by varying continuously the Higgs signal strengths from their lowest to highest theoretical predictions.

determination. For instance, the entire 1σ domain on the plot is larger when taking into account the possible shifts due to the theoretical uncertainty.

As this theoretical uncertainty cancels out in the ratios D_{XX} of signal strengths of eqs. (3.4,3.5), we have performed a fit based on the χ^2_R function [9]:

$$\chi^2_R = \frac{[D^{gg}_{\gamma\gamma}(c_f,c_V) - \frac{\mu_{\gamma\gamma}}{\mu_{ZZ}}|^{gg}_{\rm exp}]^2}{\left[\delta(\frac{\mu_{\gamma\gamma}}{\mu_{ZZ}})_{gg}\right]^2} + \frac{[D^{gg}_{\tau\tau}(c_f,c_V) - \frac{\mu_{\tau\tau}}{\mu_{WW}}|^{gg}_{\rm exp}]^2}{\left[\delta(\frac{\mu_{\tau\tau}}{\mu_{WW}})_{gg}\right]^2} + \frac{[D^{\rm VBF}_{\tau\tau}(c_f,c_V) - \frac{\mu_{\tau\tau}}{\mu_{WW}}|^{\rm VBF}_{\rm exp}]^2}{\left[\delta(\frac{\mu_{\tau\tau}}{\mu_{WW}})_{\rm VBF}\right]^2}. \quad (3.9)$$

We have considered the inclusive di-photon channels of CMS [4,33] and ATLAS [36] that are largely dominated the ggF mechanism. Regarding the ZZ final state in ATLAS [37] and CMS [42], we have also used inclusive production [10]. Finally, for the WW and $\tau\tau$ searches in ATLAS [38, 40] and in CMS [43, 45], we have selected Higgs production in ggF with an associated 0/1 jet or the VBF production mechanism. Hence for both ATLAS and CMS, the situation is equivalent in a

[9] The fact that the distribution of μ ratios is not gaussian is not expected to modify our results. Also, we refrain from including the $H \to b\bar{b}$ channel as the ATLAS and CMS sensitivities are still too low [3, 39].

[10] In fact, for $\mu_{\gamma\gamma}/\mu_{ZZ}|_{\rm exp}$, we will use the more accurate $\rho_{\gamma\gamma/ZZ}$ value provided by the ATLAS collaboration [2]; this quantity corresponds exactly to the branching fraction ratio and it is deduced from a combination of the ggF and VBF channels.

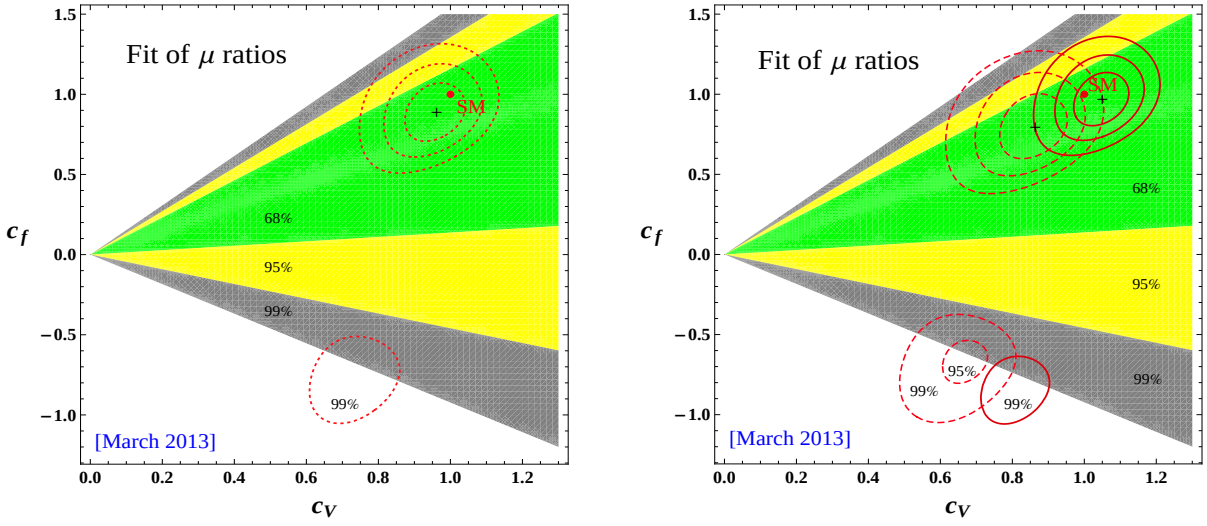

Figure 3.2: Left: Best-fit regions at 68.27%CL (green), 95.45%CL (yellow) and 99.73%CL (grey) in the plane c_f versus c_V, based on the χ^2_R function. The best-fit (dotted) contours obtained from the χ^2 function in case of a theoretical error added in quadrature (as in Fig. 3.1) are superimposed (in red). The associated best-fit point (cross) and SM (red) point are also shown. Right: Same plot as the left one but the best-fit domains from the χ^2 analysis are now derived for the two extreme theoretical predictions of the signal strengths (as in Fig. 3.1).

good approximation to have vanishing selection efficiencies except, $\epsilon^Z_{gg} \simeq \epsilon^\gamma_{gg} \simeq 1$ and $\epsilon^\tau_{gg} \simeq \epsilon^W_{gg} \simeq 1$ or $\epsilon^\tau_{\rm VBF} \simeq \epsilon^W_{\rm VBF} \simeq 1$, so that the theoretical predictions for the ratios simply read as in eq. (3.5).

The combined ratio values measured by the ATLAS and CMS collaborations are

$$\left.\frac{\mu_{\gamma\gamma}}{\mu_{ZZ}}\right|_{\rm exp} = 1.1^{+0.4}_{-0.3} \ , \quad \left.\frac{\mu_{\tau\tau}}{\mu_{WW}}\right|^{\rm VBF}_{\rm exp} = -0.24 \pm 0.83 \ \ \text{and} \ \ \left.\frac{\mu_{\tau\tau}}{\mu_{WW}}\right|^{gg}_{\rm exp} = 1.2 \pm 0.75 \tag{3.10}$$

The errors $\delta(\mu_{\gamma\gamma}/\mu_{ZZ})$ and $\delta(\mu_{\tau\tau}/\mu_{WW})$ are computed assuming no correlations between the different final state searches. These uncertainties on the ratios are derived from the individual errors, $\delta\mu_i$ – provided in the experimental papers – and are thus also dominated by the experimental uncertainties, e.g. $\delta(\mu_{\gamma\gamma}/\mu_{ZZ}) \approx \delta(\mu_{\gamma\gamma}/\mu_{ZZ})|_{\rm exp}$, as expected from the fact that the theoretical uncertainty largely cancels in ratios $D_{\gamma\gamma}$ and $D_{\tau\tau}$. These ratios are given by

$$\begin{aligned} D_{\gamma\gamma} &\simeq \frac{1}{|c_Z|^2}\left\{\frac{\left|\frac{1}{4}c_W A_1[m_W] + (\frac{2}{3})^2 c_t A[m_t] + (-\frac{1}{3})^2 c_b A[m_b] + (\frac{2}{3})^2 c_c A[m_c] + \frac{1}{3}c_\tau A[m_\tau]\right|^2}{\left|\frac{1}{4}A_1[m_W] + (\frac{2}{3})^2 A[m_t] + (-\frac{1}{3})^2 A[m_b] + (\frac{2}{3})^2 A[m_c] + \frac{1}{3}A[m_\tau]\right|^2}\right\} \\ D_{\tau\tau} &\simeq \frac{|c_\tau|^2}{|c_W|^2} \ , \end{aligned} \tag{3.11}$$

where $A[m] \equiv A_{1/2}[\tau(m)]$ and $A_1[\tau(m)]$ are respectively the form factors for spin 1/2 and spin 1 particles [8] normalized such that $A[\tau(m) \ll 1] \to 1$ and $A_1[\tau(m) \ll 1] \to -7$ with $\tau(m) = M_H^2/4m^2$ and, for $m_H \simeq 125$ GeV, one has $A_1[\tau(m_W)] \simeq -8.3$ and $A_{1/2}[\tau(m_t)] \approx 1$.

In Figure 3.2, we show the results from fitting the Higgs decay ratios through the function χ^2_R.

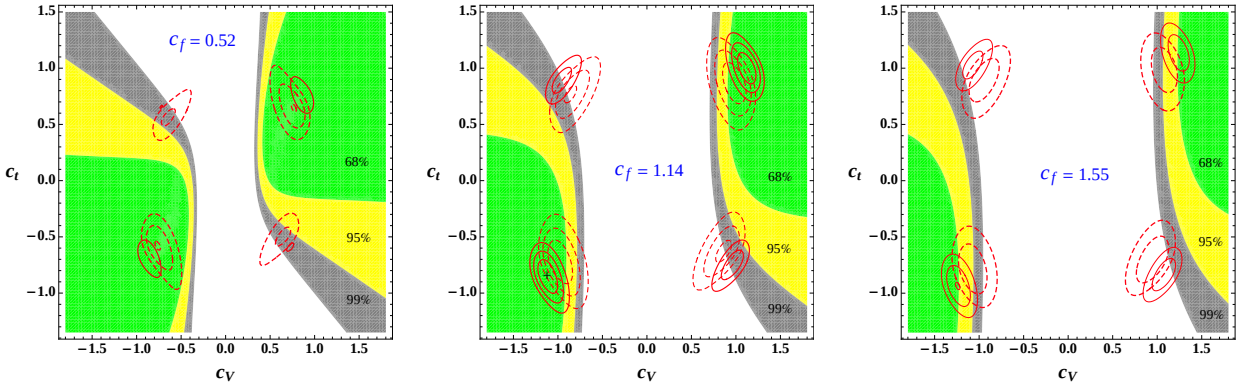

Figure 3.3: Best-fit regions at 68.27%CL (green), 95.45%CL (yellow) and 99.73%CL (grey) in the plane c_t versus c_V as obtained from a three-dimensional fit (whose best-fit point is the black cross on the central plot) of the 3 free parameters, c_f, c_t, c_V, based on the χ^2_R function. The three two-dimensional plots correspond to the slices of these three-dimensional domains at $c_f = 0.52$, 1.14 and 1.55. Superimposed are the best-fit domains at 68.27%CL, 95.45%CL, 99.73%CL obtained from χ^2 for the two theoretical signal strength predictions – upper (red plain) and lower (red dashed contours).

In the left panel, the best-fit domains obtained e.g. at 1σ do not exclude parts of the 1σ regions obtained from χ^2; such a compatibility was expected since the main theoretical uncertainty cancels out in the D_{XX} ratios and is negligible for the signal strengths since it is added in quadrature to the experimental error as already described. The domains from χ^2 are even more restricted as (i) this function exploits the full experimental information on the Higgs rates and not only on the ratios and (ii) the experimental error on a ratio of rates is obviously higher than on the rates alone.

In the case where the theoretical error for each Higgs channel is taken into account as a bias, the best-fit contours span wider regions of the parameter space. This could be seen in Fig. 3.1 and the same contours appear in the left–hand side of Fig. 3.2 as well as in its right–hand side part where the theoretical uncertainty enters as a bias for χ^2. In the latter case, the large 1σ domain from χ^2_R excludes a small part of the 1σ region (near the SM point) obtained from χ^2. Besides, the lower 95.45%CL region from the χ^2 fit is completely excluded by the χ^2_R domain (in yellow) at the same CL. In conclusion, within the more realistic case of treating the theoretical uncertainty as a bias, the χ^2_R domains can thus play an important role by excluding parts of the χ^2-fit regions; this is due to the increased contribution of the theoretical error, in χ^2, which does not affect χ^2_R.

In Fig. 3.3, we present the three-dimensional χ^2-fit results in the case where the parameters c_f, c_t and c_V are free. It shows how precisely are presently known the top quark Yukawa and the gauge boson interactions with the Higgs scalar (in the case of a preserved custodial symmetry). For either lower (left plot) or higher (right plot) bottom quark Yukawa couplings as compared to the SM, the size of the characteristic 1σ regions decrease significantly, which also gives an idea of the present knowledge of the coupling c_b. This more realistic three-dimensional fit illustrates as well the potential interest of the χ^2_R-fit : for instance, one observes on the central plot, that it excludes at 1σ the lower-right (i.e. the dysfermiophilia solution $c_t < 0$) and upper-left (i.e. its

almost symmetric domain) 1σ regions resulting from the χ^2-fit.

Since χ^2_R is only affected by the experimental uncertainty, it is interesting to quantify the evolution of the fit when the experimental systematic and statistical errors are reduced [47]. For this purpose, we combine the present measurements with the expected results from the 14 TeV LHC in each channel investigated by ATLAS and CMS. We assume the central values at 14 TeV to be identical to those from the combination of the 7 and 8 TeV data, and that the future experimental errors, $\delta\mu_i|_{\rm exp}$, will reduce essentially like the inverse of the square roots of number of events, $\sqrt{\sigma_i \mathcal{L}}$ with $\mathcal{L}$ the integrated luminosity [11].

The estimated χ^2 fit results at 14 TeV are presented in Fig. 3.4 assuming luminosities of $\mathcal{L} \equiv 300$ and 3000 fb^{-1} [47]. The behavior of the best-fit χ^2_R regions appearing in the figure originates from the compensation between the enhancement of $\Gamma(H \to \gamma\gamma)$ and that of $\Gamma(H \to ZZ)$ as c_V increases, leading to relatively stable $D_{\gamma\gamma}$ values; the increase of $\Gamma(H \to \tau\tau)$ and $\Gamma(H \to WW)$ with increasing c_τ or c_W also compensate each other in $D_{\tau\tau}$. Best-fit values of c_f and c_V in Fig. 3.4 would be illustrative only since the precise central values are of course not yet known, neither the exact experimental uncertainties. However, the above estimation of the statistical error provides an indication of the typical relative sizes of the best-fit χ^2 and χ^2_R domains in the future.

The main features that the plots of Fig. 3.4 exhibit are that when increasing the luminosity and hence, reducing the experimental error as shown by the smaller ellipses on the right plot, the χ^2-fit reaches the level where the theoretical error is dominating and fixes the typical uncertainty scale (stable red band length on the two plots), whereas for the χ^2_R-fit in which the theoretical uncertainty is absent, the precision obtained on the couplings c_f and c_V improves as long as the experimental error decreases (decrease of the colored region widths on the right plot). Thus, for high LHC luminosities, the fit of the decay ratios will play a crucial role and will have to be combined with the common Higgs rate fit, as illustrated on the right plot of Fig. 3.4: there for instance the 1σ region from χ^2 (typically the red band) is wider than when restricted to its intersection with the χ^2_R domain at 1σ (green band). This corresponds, to an improvement of the whole accuracy from $\sim 10\%$ down to $\sim 5\%$ on both c_f and c_V; with such accuracies one starts to be really sensitive to deviations in the Higgs couplings arising in supersymmetric theories or composite Higgs models as, for instance, discussed in Ref. [48].

For illustration, we present in Fig. 3.5 the expected results of the χ^2 fit, at 14 TeV with $\mathcal{L} \equiv 3000$ fb^{-1}, when adding the theoretical error to the experimental one in quadrature; the associated best-fit regions are obviously different from the pairs of ellipse-like best-fit domains obtained for a theoretical uncertainty treated as a bias [Fig. 3.4]. Furthermore, in Fig. 3.5, there exist best-fit regions at negative c_f values. This comparison between Fig. 3.4 and Fig. 3.5 clearly allows to convince oneself that the choice of the treatment of theoretical errors will be crucial for

[11] This is justified for the statistical error and corresponds to an optimistic situation for the systematic error, which is difficult to predict for each channel but depends partially on the background rate uncertainties which have a statistical behavior as well.

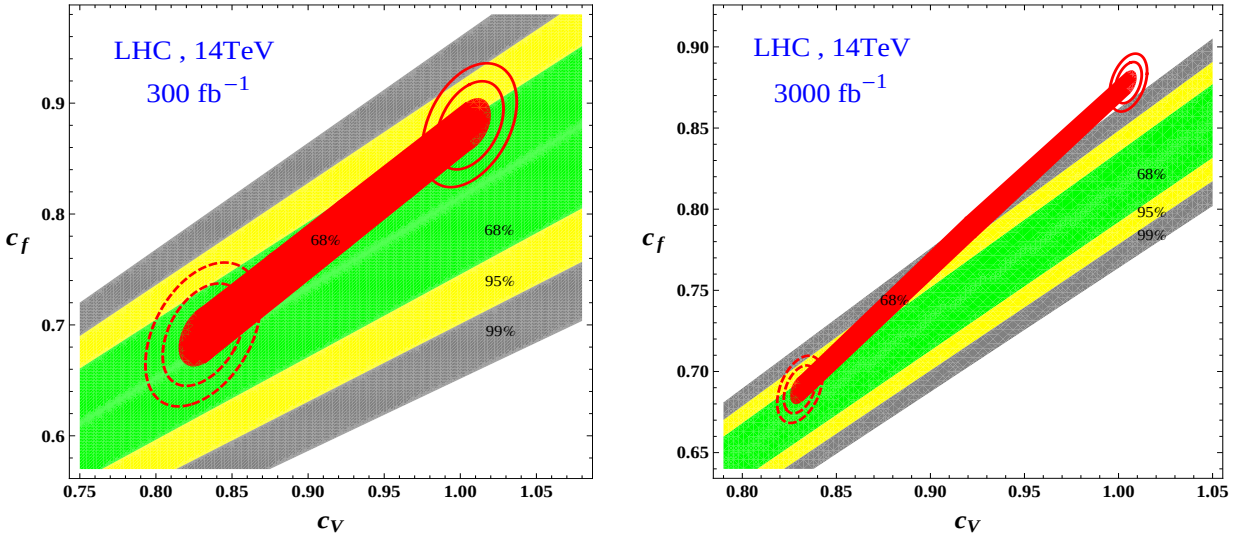

Figure 3.4: Best-fit regions at 68.27%CL (green), 95.45%CL (yellow) and 99.73%CL (grey) in the plane c_f versus c_V, based on the χ^2_R function and including hypothetical data from the 14 TeV LHC with $\mathcal{L} = 300$ fb^{-1} [left plot] or 3000 fb^{-1} [right plot]. The best-fit $\Delta\chi^2$ contours at 95.45%CL and 99.73%CL obtained in the same conditions, for the two extreme theoretical predictions of signal strengths (red plain and dashed ellipses), are superimposed; the 68.27%CL domain presented (in red) was obtained by varying continuously the signal strengths from their lowest to highest theoretical predictions. So typically the length of this domain indicates the theoretical uncertainty and its width the experimental error. The exactly symmetric domains, obtained via $c_f \to -c_f$, $c_V \to -c_V$, are not shown.

the determination of the Higgs couplings. Nevertheless, even in the case of a theoretical uncertainty combined in quadrature, the fit of rate ratios (independent of the theoretical error and presented again in Fig. 3.5) allows to select a sub-part of the 1σ, 2σ, 3σ ellipses derived from the signal strength fit.

3.4 The parity or CP–composition of the Higgs boson

As mentioned in the introduction, the observables such as correlations in Higgs decays into vector boson pairs [15] or in Higgs production with or through these states [16] that are usually used to probe the Higgs parity project out only the CP–even component of the HVV coupling even if the state has both CP–even and CP–odd components. Thus, in these CP studies, one is simply verifying, a posteriori, that a CP–even Higgs state has been indeed produced. The HVV coupling takes the general form (here, we assume $c_V > 0$)

$$g^{\mu\nu}_{HVV} = -i\, c_V (M_V^2/v)\, g^{\mu\nu} \tag{3.12}$$

where c_V measures the departure from the SM: $c_V = 1$ for a pure CP–even state with SM–like couplings and $c_V = 0$ for a pure CP–odd state. Indeed, the coupling of a pseudoscalar A state to

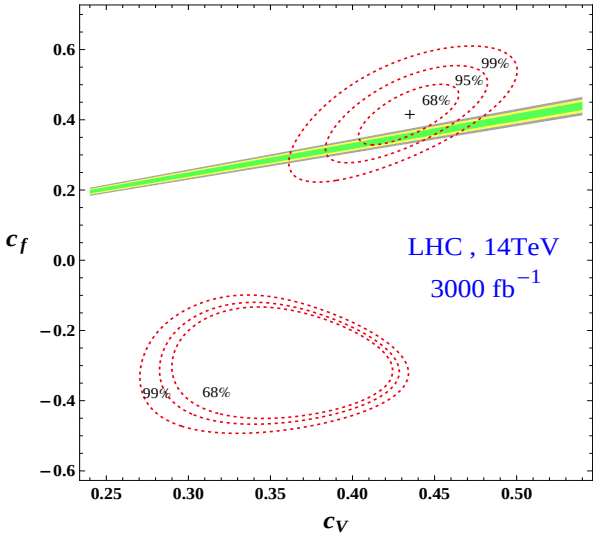

Figure 3.5: Best-fit regions at 68.27%CL (green), 95.45%CL (yellow) and 99.73%CL (grey) in the plane c_f versus c_V, based on the χ^2_R function and including hypothetical data from the 14 TeV LHC with $\mathcal{L} = 3000$ fb^{-1} [as in Fig. 3.4]. The best-fit $\Delta\chi^2$ contours at 68.27%CL, 95.45%CL, 99.73%CL obtained in the same conditions, and with the theoretical error added in quadrature, are superimposed as dotted (red) contours; the best central point is indicated as a (black) cross.

W/Z bosons is zero at tree-level and is generated only through loop corrections which are expected to tiny. The measurement of c_V should allow to determine the CP composition of a Higgs boson if it is indeed a mixture of CP–even and CP–odd states.

However, having $c_V \neq 1$ does not automatically imply that the observed state has a pseudoscalar component. As a matter of fact, the Higgs sector could be enlarged to contain other neutral Higgs particles H_i that have not been detected so far because they are too heavy or too weakly coupled. In this case, the sum of the squared couplings of each state H_i to gauge bosons, $c^2_{Vi}\, g^2_{HVV}$, should reduce to the SM Higgs coupling, g^2_{HVV}. Hence, $c^2_V < 1$, could mean that there are other CP–even states which share the SM Higgs coupling to VV with the observed Higgs boson. Nevertheless, in all cases, the quantity $\kappa_{\rm CP} = 1 - c^2_V$ gives an *upper bound* on the CP–odd contribution to the HVV coupling [12].

In contrast to the couplings to massive gauge boson, the CP–even and CP–odd components of the state can couple to fermions with the same magnitude and one can write

$$g_{Hff} = -i\frac{m_f}{v}\left[\mathrm{Re}\,(c_f) + i\ \mathrm{Im}\,(c_f)\,\gamma_5\right] \tag{3.13}$$

[12]The best example of an extended Higgs sector with CP–violation is the minimal supersymmetric extensions of the Standard Model (MSSM) with complex soft–SUSY breaking parameters [32]. One has then three neutral Higgs states H_1, H_2 and H_3 with indefinite parity and their CP–even components will share the SM HVV coupling, $c^2_{V1} + c^2_{V2} + c^2_{V3} = 1$. There are no antisymmetric CP–odd couplings $H_i V_{\mu\nu}\widetilde{V}^{\mu\nu}$ at tree-level and those generated at the one–loop level are extremely tiny [32].

where in the SM one has $\mathrm{Re}(c_f)=1$ and $\mathrm{Im}(c_f)=0$ but in general, the normalisation of the coupling, $\mathrm{Re}(c_f)^2+\mathrm{Im}(c_f)^2=|c_f|^2$, should be taken arbitrary as in the previous section.

Hence, one can consider the same effective Lagrangian as in eq. (3.7) where $c_V = c_Z = c_W$ represents exclusively the CP–even component of the observed boson assumed to be one eigenstate of an enlarged Higgs sector. In contrast, the $c_f=c_b=c_c=c_\tau$ and c_t parameters for light fermions and the top quark contain the CP compositions of eq. (3.13) with the possibility of a deviation of the normalisation $|c_f|^2$ compared to the SM Yukawa interaction.

In the case of the light fermions, one has $M_H \gg m_f$ so that chiral symmetry holds and the partial decay widths (the only place where they enter if one neglects their tiny contribution to the loop induced vertices) can be simply written as $\Gamma(H\to f\bar{f}) \propto \mathrm{Re}(c_f)^2+\mathrm{Im}(c_f)^2 \propto |c_f|^2$ and the discussion in the previous section should entirely hold.

In the case of the top quark, the situation is different as $m_t > M_H$. The top quark enters the Hgg and $H\gamma\gamma$ vertices and the loop form factors for the CP–even $A^H_{1/2}$ and CP–odd $A^A_{1/2}$ parts are in principle different [8]. Fortunately, in these vertices the approximation $m_t \gg M_H$ is extremely good and in this limit, the form factors take simple forms: $A^H_{1/2}=\frac{4}{3}$ and $A^A_{1/2}=2$. Ignoring the small contributions of the light fermions for simplicity, the Higgs rates normalized to the SM expectations can be written as,

$$\begin{aligned}
\frac{\Gamma(H\to\gamma\gamma)}{\Gamma(H\to\gamma\gamma)|_{\rm SM}} &\simeq \frac{\left|\frac{1}{4}c_W A_1[m_W]+(\frac{2}{3})^2\mathrm{Re}(c_t)\right|^2+|(\frac{2}{3})^2\frac{3}{2}\mathrm{Im}(c_t)|^2}{\left|\frac{1}{4}A_1[m_W]+(\frac{2}{3})^2\right|^2} \\
\frac{\sigma(gg\to H)}{\sigma(gg\to H)|_{\rm SM}} &= \frac{\Gamma(H\to gg)}{\Gamma(H\to gg)|_{\rm SM}} \simeq \left|\mathrm{Re}(c_t)\right|^2+|\frac{3}{2}\mathrm{Im}(c_t)\right|^2
\end{aligned} \tag{3.14}$$

with $A_1[m_W]\simeq -8.3$ for $M_H\approx 125$ GeV. For a pure pseudoscalar state, $\mathrm{Re}(c_t)=0$, there is no W contribution to the $H\to\gamma\gamma$ rate; there are also no $H\to ZZ$ and WW decays, a possibility that is clearly excluded by the present data as the 4ℓ and $2\ell 2\nu$ signals have been observed. To quantify the degree of exclusion of this possibility, one needs to measure $\kappa_{\rm CP}=1-c_V^2$ (and ideally, independently of the fermion couplings c_f).

Based on these rates, one can perform a fit using the same χ^2 function as in eq. (3.8) but with the dependence, $\chi^2=\chi^2[\mathrm{Re}(c_t),\mathrm{Im}(c_t),c_f,c_V]$. The numerical results are displayed in Fig. 3.6 for the χ^2-fit and the χ^2_R-fit which reveals itself to be useful as well for measuring the CP-odd component of the Higgs boson. In this case, we have made the simplifying assumption (besides $c_V\geq 0$) that the absolute normalisation of the fermion couplings is the same as in the SM, $|c_t|^2=|c_f|^2=1$, but in the case of the top quark, $\mathrm{Im}(c_t)$ is assumed to be free. We assume $\mathrm{Re}(c_t)\geq 0$ and the obtained plot is symmetric under $\mathrm{Im}(c_t)\to -\mathrm{Im}(c_t)$.

The conclusion is that, at the 99.73%CL or at the 3σ level, the CP–odd component of the observed Higgs boson obeys the upper bound $\kappa_{\rm CP}=1-c_V^2<0.68$. A pure CP–odd Higgs state, i.e. the case $\kappa_{\rm CP}\approx 1$, is excluded with more than 4σ. This is much more severe than the constraint from the correlations in $H\to ZZ$ decays, which (with its inherent limitation discussed above)

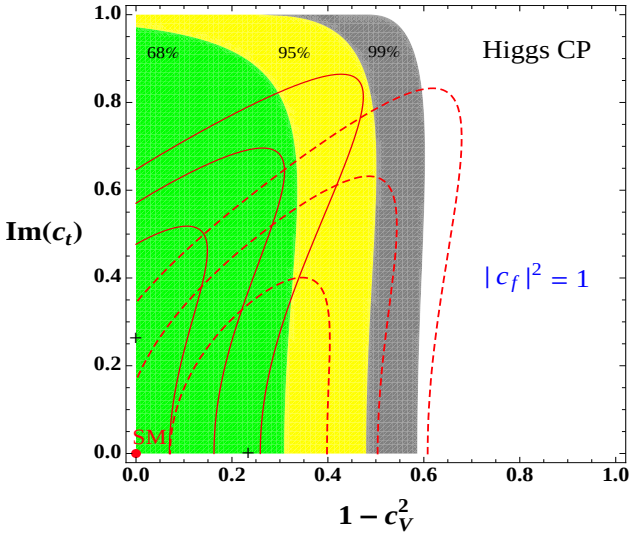

Figure 3.6: Best-fit regions at 68.27%CL (green), 95.45%CL (yellow) and 99.73%CL (grey) in the plane $1 - c_V^2$ versus $\mathrm{Im}(c_t)$ for $|c_t|^2 = |c_f|^2 = 1$; these regions are obtained from a two-dimensional fit based on the χ^2_R function. Superimposed are the best-fit regions at 68.27%CL, 95.45%CL, 99.73%CL obtained from χ^2 for the two theoretical signal strength predictions (plain and dashed contours in red). The SM (red) point is represented at the origin together with the best-fit points (the two black crosses) for the χ^2 fits.

allows only a $\lesssim 3\sigma$ discrimination between the CP–even and CP–odd cases [2, 3].

3.5 The invisible Higgs decay width

In the previous discussion, the signal strength μ_{ZZ} in the channel $H \to ZZ \to 4\ell^{\pm}$ played a prominent role because the theoretical ambiguities are minimised: the measurement is inclusive and does not involve the additional theoretical uncertainties that are introduced when breaking the cross section into jet categories and there is no loop induced new physics effect as in the $H \to \gamma\gamma$ case; besides that, it is the most accurate single signal strength measurement. One can also use μ_{ZZ} for the determination of the invisible Higgs decay width which enters in the signal strength through the total decay width $\Gamma_H^{\rm tot}$, $\mu_{ZZ} \propto \Gamma(H \to ZZ)/\Gamma_H^{\rm tot}$ with

$$\Gamma_H^{\rm tot} = \Gamma_H^{\rm inv} + \Gamma_H^{\rm SM}(c_f, c_V) \tag{3.15}$$

$\Gamma_H^{\rm SM}(c_f, c_V)$ is the SM total width which is calculated with free coefficients c_f and c_V and including the state-of-the art radiative corrections [21,24]. One can write the ZZ signal strength as a function of $\Gamma_H^{\rm inv}$ and the Higgs couplings, $\mu_{ZZ}|_{\rm th} = \mu_{ZZ}(\Gamma_H^{\rm inv}, c_V, c_t, c_f = c_c = c_b = c_\tau)$, and impose that it lies within its 1σ or 2σ ranges. This restricts the parameter space to specific regions as is shown in Fig. 3.7 where in the left-hand hand side c_f is SM–like and c_V is varied and in the right–hand side, it is the opposite c_f is varied while $c_V = 1$.

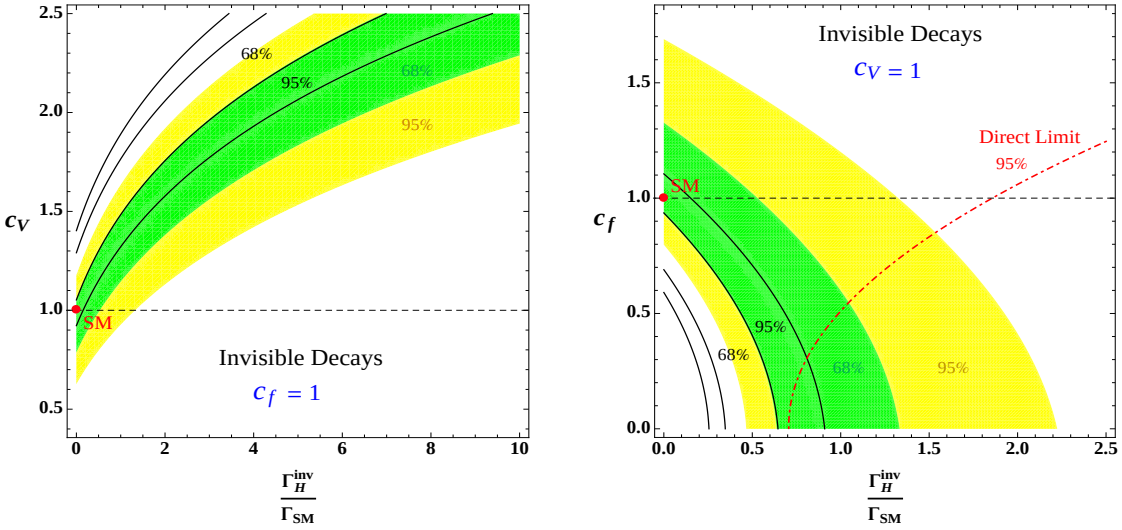

Figure 3.7: Domains at 1σ (green), 2σ (yellow) from the central value of μ_{ZZ}, in the plane c_V (left plot) or c_f (right plot) versus $\Gamma_H^{\rm inv}/\Gamma_H^{\rm SM}$ [$\Gamma_H^{\rm SM}$ being the total SM Higgs width] for $c_t = 1$ and $c_f = 1$ (left plot) or $c_V = 1$ (right plot). The dependence of these constraints on the theoretical uncertainties is illustrated by the (black) curves which indicate the other possible extreme domains. The direct upper limit on $\Gamma_H^{\rm inv}$ from invisible searches at LHC (derived for $c_V = 1$) [27, 29] is shown on the right plot.

On the figure, we also display for comparison the recent direct limit [27, 29] on the invisible Higgs width obtained from combining the 7+8 TeV LHC data in the $q\bar{q} \to ZH \to Z+\not{E}_T$ direct search channel. This gives $B_H^{\rm inv} < 65\%$ at the 95.45%CL if the assumption $c_V = 1$ is made. With the simplifying $c_f = c_V = 1$ assumption, the indirect limit on the invisible width that one obtains from the signal strengths is better, as can be seen from the figure; at 1σ, it reads as

$$\mu_{\rm inv} = \Gamma_H^{\rm inv}/\Gamma_H^{\rm SM} \leq 0.52 \ @68\%{\rm CL} \tag{3.16}$$

This limit is at least a factor of two worse than those obtained in the similar fits of Refs. [14] using the latest LHC data, the reason being that, here, we assume a 20% theoretical uncertainty on the Higgs production cross sections that we treat as a bias and do not combine quadratically with the experimental uncertainty.

3.6 Conclusion

We have analyzed the Higgs production cross sections at the LHC for the different Higgs decay channels that have been searched for, $H \to WW, ZZ, \tau\tau, b\bar{b}$ and $H \to \gamma\gamma$. Using the latest results given by the ATLAS and CMS collaborations with the ≈ 25 fb^{-1} data collected in the runs at $\sqrt{s} = 7$ and 8 TeV, we have first performed a fit of the Higgs couplings to fermions and massive gauge bosons and shown that they are now compatible with the SM expectation at the 1σ level.

The accuracy of the various experimental measurements is now almost saturated by the theoretical uncertainties stemming from QCD.

We have argued that ratio of cross sections times branching ratios in different Higgs search channels are essentially free from these uncertainties and do not require further theoretical assumptions, on the total Higgs decay width for instance. These ratios, in particular in the $H \to \gamma\gamma$ v.s. $H \to ZZ$ and $H \to \tau\tau$ v.s. $H \to WW$ channels, are being measured quite accurately already with the present data and provide tests of the SM predictions in a less model–dependent way. We show that at the 14 TeV LHC with a high luminosity, 300 fb^{-1} and even 3000 fb^{-1}, they could allow the measurement of ratios of Higgs couplings with an accuracy at the level of a few percent which should allow to test the small deviations expected in realistic new physics models.

In a second part of this work, we have considered together with the ratios of cross sections times branching ratios in the most important search channels, the signal strength in the extremely clean $H \to ZZ$ channel in which the theoretical uncertainty is taken to be a bias. We have then shown that first, the particle observed at the LHC is at most 68% CP–odd at the 99%CL and the possibility that it is a pure pseudoscalar state (and hence does not couple to ZZ states at tree–level) is excluded at the 4σ level when including both the experimental and theoretical uncertainties. The signal strengths in the $H \to ZZ$ channel also measure the invisible Higgs decay width which is shown to be $\Gamma_H^{\rm inv}/\Gamma_H^{\rm SM} \leq 0.52$ at the 68%CL if the Higgs couplings to fermions and gauge bosons are assumed to be SM–like.

All these results give us great confidence that the state observed at the LHC in July 2012 is indeed a Higgs particle and, more than that, it resembles very closely to the Higgs particle predicted in the Standard Model.

Bibliography

[1] The ATLAS collaboration, ATLAS-CONF-2013-014.

[2] The ATLAS collaboration, ATLAS-CONF-2013-034.

[3] The CMS collaboration, CMS PAS-HIG-12-045.

[4] The CMS collaboration, CMS PAS-HIG-13-001.

[5] The ATLAS collaboration, arXiv:1207.7214 [hep-ex].

[6] The CMS collaboration, arXiv:1207.7235 [hep-ex].

[7] P. Higgs, Phys. Lett. 12 (1964) 132; Phys. Rev. Lett. 13 (1964) 506; F. Englert and R. Brout, Phys. Rev. Lett. 13 (1964) 321; G. Guralnik, C. Hagen and T. Kibble, Phys. Rev. Lett. 13 (1964) 585; S. Weinberg, Phys. Rev. Lett. 19 (1967) 1264.

[8] For a review of the SM Higgs boson, see: A. Djouadi, Phys. Rept. 457 (2008) 1.

[9] L. Landau, Dokl. Akad. Nauk Ser. Fiz. 60 (1948) 207; C. Yang, Phys. Rev. 77 (1950) 242.

[10] See e.g. J. Ellis, V. Sanz and T. You, arXiv:1211.3068 [hep-ph]; arXiv:1303.0208 [hep-ph].

[11] For a recent account, see: J. Baglio et al., arXiv:1212.5581 [hep-ph].

[12] D. Carmi, A. Falkowski, E. Kuflik, T. Volansky and J. Zupan, arXiv:1207.1718 [hep-ph]; J. Espinosa, C. Grojean, M. Muhlleitner and M. Trott, arXiv:1207.1717 [hep-ph]; P. Giardino, K. Kannike, M. Raidal, and A. Strumia, arXiv:1207.1347 [hep-ph]; J. Ellis and T. You, arXiv:1207.1693 [hep-ph]; T. Corbett et al., arXiv:1207.1344 [hep-ph]; F. Bonnet, T. Ota, M. Rauch and W. Winter, arXiv:1207.4599 [hep-ph]; A. Alves et al., arXiv:1207.3699 [hep-ph]; S. Banerjee, S. Mukhopadhyay and B. Mukhopadhyaya, arXiv:1207.3588 [hep-ph]; A. Arbey et al., arXiv:1207.1348 [hep-ph]; arXiv:1211.4004 [hep-ph]; I. Low, J. Lykken and G. Shaughnessy, arXiv:1207.1093 [hep-ph]; M. Klute et al., arXiv:1205.2699 [hep-ph]; M. Peskin, arXiv:1207.2516v1 [hep-ph]; J. Baglio, A. Djouadi and R. Godbole, arXiv:1207.1451 [hep-ph]; T. Plehn and M. Rauch, arXiv:1207.6108 [hep-ph]; G. Cacciapaglia et al., arXiv:1210.8120 [hep-ph]; N. Bonne and G. Moreau, Phys. Lett. B717 (2012) 409; G. Belanger et al., JHEP 1302

(2013) 053; C. Cheung et al., arXiv:1302.0314 [hep-ph]; K. Cheung, J. S. Lee and P. -Y. Tseng, arXiv:1302.3794 [hep-ph]; A. Azatov and J. Galloway, Int. J. Mod. Phys. A Volume 28 (2013) 1330004.

[13] G. Moreau, Phys. Rev. D87, 015027 (2013).

[14] J. Ellis and You, arXiv:1303.3879 [hep-ph]; T. Alanne, S. Di Chiara and K. Tuominen, arXiv:1303.3615 [hep-ph]; Pier Paolo Giardino et al., arXiv:1303.3570 [hep-ph]; A. Falkowski, F. Riva and A. Urbano, arXiv:1303.1812 [hep-ph].

[15] J. Dell'Aquila and C. Nelson, Phys. Rev. D33, 80 (1986) and Phys. Rev. D33, 93 (1986); V. Barger et al., Phys. Rev. D49, 79 (1994); C. Buszello, I. Fleck, P. Marquard and J. van der Bij, Eur. Phys. J. C32, 209 (2004); D. Miller et al., Phys. Lett. B505, 149 (2001); S. Choi, D. Miller, M. Muhlleitner and P. Zerwas, Phys. Lett. B553, 61 (2003); R. Godbole, D. Miller and M. Mühlleitner, JHEP 0712, 031 (2007); A. de Rujula et al, Phys. Rev. D82, 013003 (2010); N. Desai, D. Ghosh and B. Mukhopadhyaya, Phys. Rev. D83, 113004 (2011); N. Christensen, T. Han and Y. Li, Phys. Lett.B693, 28 (2010); Y. Gao et al., Phys. Rev. D81 (2010) 075022; F. Campanario, M. Kubocz and D. Zeppenfeld, Phys. Rev. D84, 095025 (2011); C. Englert, M. Spannowsky and M. Takeuchi, JHEP 1206, 108 (2012); S. Bolognesi et al, arXiv:1208.4018 [hep-ph]; I. Low, J. Lykken and G. Shaughnessy, arXiv:1207.1093 [hep-ph]; J. Ellis et al. arXiv:1210.5229; E. Masso and V. Sanz, arXiv:1211.1320 [hep-ph].

[16] T. Plehn, D. L. Rainwater and D. Zeppenfeld, Phys. Rev. Lett. 88, 051801 (2002); B. Zhang et al., Phys. Rev. D67, 114024 (2003); C. P. Buszello and P. Marquard, arXiv:hep-ph/0603209; V. Del Duca et al., JHEP 0610, 016 (2006); K. Odagiri, JHEP 0303, 009 (2003); V. Hankele, G. Klamke, D. Zeppenfeld and T. Figy, Phys. Rev. D74 (2006) 095001; J.R. Andersen, K. Arnold and D. Zeppenfeld, JHEP 1006, 091 (2010); C. Englert, D. Gonsalves-Netto, K. Mawatari and T. Plehn, arXiv1212.0843 [hep-ph]; A. Djouadi, R. M. Godbole, B. Mellado and K. Mohan, arXiv:1301.4965 [hep-ph].

[17] The CMS collaboration, Phys. Rev. Lett. 110 (2013) 081803.

[18] A. Djouadi, arXiv:1208.3436 [hep-ph].

[19] D. Zeppenfeld, R. Kinnunen, A. Nikitenko and E. Richter-Was, Phys. Rev. D62 (2000) 013009; A. Djouadi et al., hep-ph/0002258; M. Dührssen et al., Phys. Rev. D70 (2004) 113009; K. Assamagan et al., hep-ph/0406152.

[20] S. Dittmaier et al., "Handbook of LHC Higgs cross sections", arXiv:1101.0593 [hep-ph].

[21] J. Baglio and A. Djouadi, JHEP 1103 (2011) 055.

[22] C.F. Berger et al., JHEP 1104 (2011) 092; I.W. Stewart and F.J. Tackmann, Phys. Rev. D85 (2012) 034011; A. Banfi, G.P. Salam and G. Zanderighi, JHEP 1206 (2012) 159.

[23] S. Dittmaier et al. (LHC Higgs cross section working group), arXiv:1201.3084 [hep-ph].

[24] A. Denner, S. Heinemeyer, I. Puljak, D. Rebuzzi and M. Spira, Eur. Phys. J. C71 (2011) 1753.

[25] G. Belanger et al., arXiv:1302.5694 [hep-ph].

[26] A. Djouadi, A. Falkowski, Y. Mambrini and J. Quévillon, arXiv:1205.3169 [hep-ph]; based on the ATLAS and CMS monojet searches, ATLAS-COM-CONF-2011-119 and CMS-PAS-EXO-11-059.

[27] The ATLAS collaboration, ATLAS-CONF-2013-011.

[28] D. Stolarski and R. Vega-Morales, arXiv:1208.4840 [hep-ph].

[29] V. Martin, (ATLAS collaboration), "Rencontres de Moriond", 2-16 March 2013, La Thuile.

[30] B. Grzadkowski, J. Gunion and X. He, Phys. Rev. Lett. 77 (1996) 5172; J. Gunion and J. Pliszka, Phys. Lett. B444 (1998) 136; P. Bhupal Dev et al., Phys. Rev. Lett. 100 (2008) 051801.

[31] A. Freitas and P. Schwaller, Phys. Rev. D 87 (2013) 055014.

[32] A. Djouadi, Phys. Rept. 459 (2008) 1; E. Accomando et al., hep-ph/0608079; M. Carena and H. Haber, Prog. Part. Nucl. Phys. 50 (2003) 63.

[33] Christophe Ochando,"Study of Higgs Production in Bosonic Decay Channels in CMS", Talk [on behalf of the CMS collaboration] at the XLVIIIth "Rencontres de Moriond", 2-16 March 2013, La Thuile, Italy.

[34] A. Djouadi, J. Kalinowski and M. Spira, Comput. Phys. Commun. 108 (1998) 56.

[35] The CDF and D0 collaborations, CDF Note 10884, D0 Note 6348, arXiv:1207.0449 [hep-ex].

[36] The ATLAS collaboration, ATLAS-CONF-2013-012.

[37] The ATLAS collaboration, ATLAS-CONF-2013-013.

[38] The ATLAS collaboration, ATLAS-CONF-2013-030.

[39] The ATLAS collaboration, ATLAS-CONF-2012-170.

[40] The ATLAS collaboration, ATLAS-CONF-2012-160.

[41] The CMS collaboration, CMS PAS-HIG-12-053.

[42] The CMS collaboration, CMS PAS-HIG-13-002.

[43] The CMS collaboration, CMS PAS-HIG-13-003.

[44] The CMS collaboration, CMS PAS-HIG-12-020.

[45] The CMS collaboration, CMS PAS-HIG-13-004.

[46] J. Beringer et al. (Particle Data Group), Phys. Rev. D86 (2012) 010001.

[47] Physics Briefing Book, Input for the Strategy Group to draft the update of the European Strategy for Particle Physics, CERN-ESG-005.

[48] R. S. Gupta, H. Rzehak and J. D. Wells, Phys. Rev. D86, 095001 (2012).

Chapter 4

Constraints on extra-fermions from the Higgs boson rates

Adapted [1] from: *G. Moreau*, Phys. Rev. **D87** (2013) 015027.

4.1 Introduction

Based on the combined LHC data collected at the center-of-mass energies of $\sqrt{s} = 7$ TeV and 8 TeV, the ATLAS [1] and CMS [2] Collaborations have independently announced the discovery at the $\sim 5\sigma$ level of a new resonance – with a mass close to 125 GeV – which can be identified as the missing Standard Model (SM) cornerstone : the Higgs boson [3–6]. The long list of measurements of the various Higgs boson rates provided by the two LHC Collaborations [7, 8] constitutes a new precious source of experimental results which can be exploited to test and constrain indirectly theories beyond the SM.

Most of the theories, underlying the SM and addressing the gauge hierarchy problem, predict the existence of new fermions, like charginos/neutralinos in supersymmetry, fermionic Kaluza-Klein (KK) excitations in higher-dimensional scenarios (*e.g.* Gauge-Higgs unification frameworks as in Ref. [9] or the warped extra-dimension setup [10, 11] with matter in the bulk [12–31]), excited resonances of bounded states in the dual composite Higgs [32–39] or composite top [40, 41] models and top quark multiplet components in the little Higgs context [42–44]. Additional fermions could also arise as fourth generations [45] or as components embedded *e.g.* in simple SU(5) representations of gauge unification theories [46].

In the first part of this work, we will combine all the Higgs rate measurements to constrain any model with extra-fermions [i.e. of any baryon/lepton number, Yukawa/gauge coupling] that are

[1] Updated figures in Appendix A.

able to induce corrections to the Higgs couplings [2]. We will assume that the presence of Extra-Fermion(s) [EF] constitutes the only origin of significant deviations to the Higgs interactions. Note that our results also apply to any model with extra scalar field(s) or vector boson(s) leading to significant Higgs interaction deviations, but not through their mixing(s) respectively with the Higgs boson or SM gauge bosons (*c.f.* end of Section 4.2.2). By using a generic parametrization, we will determine the corrections to the Higgs couplings – coming from fermion mixing or new loop-level exchanges – which are favored by the fits of the Higgs boson rates. We will show that the best Higgs rate fits obtained could be seen as first indirect indications of the presence of EF since those fits can be better than the SM fit; another way of seeing this indication will be to observe that the best-fit regions for the EF-induced corrections to the Higgs couplings do not contain the vanishing-correction point (SM point).
In the second part of the work, the Higgs fit constraints will be applied to characteristic and well-motivated classes of single EF scenarios (extra-quark/lepton) and will reveal themselves to be already quite predictive. We will focus on single EF in same color representations as the SM quarks or leptons; various [including extreme] electric charges will be considered for the extra-quark whereas the extra-lepton will be assumed to have the same charge as the SM charged leptons.

Let us close the introduction by comparing our analysis to the related literature. The constraints from Higgs rate fits on corrections to the Higgs couplings, induced exclusively by EF, have been partly studied in analyses aimed at studying all the possible types of corrections [47–61] (see Ref. [62] for a statistical analysis by the ATLAS Collaboration). A first extension of the present work is to describe qualitatively and quantitatively the effect of varying the correction to the bottom-quark Yukawa coupling [parametrized here by c_b, the ratio of the bottom Yukawa coupling over its SM prediction] on constraints for other Higgs couplings; similarly, we study the dependence of the rate fit on c_τ, namely the ratio of the tau-lepton Yukawa coupling over its SM value (without the simplifying assumption $c_\tau = c_b$). Another extension is the inclusion of the data on the Higgs production in association with a top-quark pair (relying on the top ratio c_t) and on the Higgs decay channel $h \to \bar{\tau}\tau$ (involving c_τ) which can play a role in constraining fermion-mixings. Because of the inclusion of the former data, we do not integrate out the top quark which allows us to explicitly study the c_t parameter (and we do not take *e.g.* $c_t = c_b$) : we point out in particular that the c_t variation leads to simple translations of the best-fit domains obtained.
Let us note that our fits are performed over the three free parameters c_b, c_{gg} and $c_{\gamma\gamma}$ (related to the hgg and $h\gamma\gamma$ coupling corrections defined later) for characteristic fixed values of c_τ and c_t [3]. In a second step, we fix c_b for studying examples of EF scenarios.

In Section 4.2, we discuss the theoretical context and the formalism used. Then the measurements of the Higgs boson rates are summarized in Section 4.3 and confronted to the parameter

[2] The extra-fermions are assumed to be heavier than the Higgs field to avoid new Higgs decay openings (in particular invisible decays into stable particles) that would require special treatments.

[3] In order to explain clearly the influences of these five relevant parameters on the Higgs rate fit, we do not marginalize any of those parameters.

space of EF scenarios in Section 4.4. In the part 4.4.1 we describe the fit procedure and in the part 4.4.2 we present the numerical results while in the part 4.4.3 we study the simplified case of a unique EF. We conclude in Section 4.5.

4.2 Theoretical framework

4.2.1 The physical context

We consider the general framework with any EF able to modify the Higgs couplings. In our context, no other source of physics beyond the SM is responsible for deviations of the Higgs couplings; this choice allows to concentrate one's efforts on the class of models with EF and in turn to have a deeper analysis of the parameter space. In particular, we assume the Higgs scalar field to receive no coupling modifications due to significant mixings with other scalars as it can occur *e.g.* in extended Higgs sectors.

For example, such a framework could be realized concretely in warped extra-dimension scenarios where some so-called custodians (fermionic KK modes) [63–74] would be below the TeV scale inducing *e.g.* large top mixings, while the decoupling KK gauge boson excitations would be much above ~ 3 TeV (the order of the lower bound from Electro-Weak (EW) precision tests [63, 75, 76]) forbidding in particular significant corrections to the Higgs couplings with gauge bosons.

From a more basic point of view, in a bottom-up approach without prejudice, this hypothesis that mainly EF affect the Higgs observables is one simple possibility, among others, to be considered. This possibility has been considered for instance in Ref. [77–84] where the sole effects from some EF species – namely the vector-like fermions (which can arise in many SM extensions) – on the Higgs production cross sections and branching ratios were considered.

In a different context from here, other sources of large Higgs coupling deviations could exist as well – like extra-bosons below ~ 10 TeV as could be needed *e.g.* in a UV completion theory allowing a vacuum stability in the presence of new fermions at the EW energy scale with large Yukawa couplings [85]; then the present results might be used to understand specifically the impact of EF on the Higgs rate fits.

Since we adopt a generic approach, we will not make assumptions in particular regarding the EF representations under the $\mathrm{SU(2)_L}$ gauge group. Hence it will not be possible to study EW precision tests on EF as those tests depend on the $\mathrm{SU(2)_L}$ isospins of EF. Such tests can be performed once a given EF model is chosen, like for instance in Ref. [79–81, 86] where it was shown that some EF models can pass the EW constraints.

4.2.2 The effective Lagrangian

In our framework, all the Higgs couplings receiving corrections can be written in the following effective Lagrangian, which allows to work out the current Higgs phenomenology at the LHC and Tevatron colliders :

$$\begin{aligned}\mathcal{L}_h \;=\; & -\, c_t Y_t\; h\; \bar{t}_L\; t_R \;-\, c_b Y_b\; h\; \bar{b}_L\; b_R \;-\, c_\tau Y_\tau\; h\; \bar{\tau}_L\; \tau_R \\ & +\, C_{h\gamma\gamma}\frac{\alpha}{\pi v}\; h\; F^{\mu\nu}F_{\mu\nu} \;+\; C_{hgg}\frac{\alpha_s}{12\pi v}\; h\; G^{a\mu\nu}G^a_{\mu\nu} \;+\; \text{h.c.}\end{aligned} \tag{4.1}$$

where $Y_{t,b,\tau}$ are the SM Yukawa coupling constants of the associated fermions in the mass eigenbasis, v is the Higgs vacuum expectation value, the subscript L/R indicates the fermion chirality and the tensor fields in the $h\gamma\gamma$ and hgg coupling terms (following *e.g.* the normalization adopted in Ref. [59]) are respectively the electromagnetic and gluon field strengths. The $c_{t,b,\tau}$ parameters – taken real for simplicity – are defined such that the limiting case $c_{t,b,\tau} \to 1$ corresponds to the SM; deviations from unity of those parameters can be caused by mixings of EF (like t' states,...) with the SM fermions. Only the Yukawa couplings of the third generation are supposed to receive potentially important corrections from EF mixing effects since EF are closer in mass to the third generation and this heavy generation is in general more intimately connected to the ultraviolet physics, like the top quark in warped/composite frameworks.

A few remarks are in order regarding terms absent from the Lagrangian (4.1). First, we only consider tree-level (loop-level) corrections to couplings induced at the tree-level (loop-level) in the SM, i.e. we calculate exclusively the dominant corrections; in the absence of tree-level correction from EF origins for a certain SM tree-level induced coupling, we do not go to the next order so that the global analysis coherence is preserved. Secondly, we have not included in the Lagrangian the $hZ\gamma$ coupling [87] as it is not constrained by a dedicated experimental analysis *e.g.* in the $Z\gamma$ channel, and, the EF-induced corrections to the relatively small $\Gamma(h \to Z\gamma)$ width are expected to be too weak to change significantly the total Higgs width (involved in all branching fractions). For similar reasons, we have not considered flavor-changing Yukawa couplings (those are not excluded in some EF scenarios and could induce new partial Higgs decay widths).

Let us make another comment about the Lagrangian (4.1). Neglecting the mixings with the first two SM flavors, one gets, $-Y_{t,b,\tau} = m_{t,b,\tau}/v$ [the minus sign is due to the sign taken in front of the Yukawa couplings in Eq. (4.1)], where $m_{t,b,\tau}$ are the final masses generated after EW symmetry breaking. The EF mixing effect on the Yukawa couplings enters via the $c_{t,b,\tau}$ parameters. These parameter values also contain the 3×3 SM flavor mixing effect in case it is not neglected. This 3×3 mixing is considerable in the lepton sector (while CKM mixing angles [88] are typically small) but there a possibility is that the strongest mixing angles originate from the neutrino mass matrix. Now even if a Higgs decay channel into neutrinos is open, like in the simple case of added right-handed neutrino singlets leading to neutrino Yukawa couplings, the partial width into neutrinos would typically be so tiny compared to others – even for huge neutrino Yukawa coupling enhancements

by say two orders of magnitude – that it would not affect the Higgs fit analysis.

Summing over the dominant loop contributions, the coefficients of the dimension-five operators in Eq. (4.1) can be written as,

$$C_{hgg} = 2C(t)\ A[\tau(m_t)]\ (c_t + c_{gg}) + 2C(b)\ A[\tau(m_b)]\ c_b + 2C(c)\ A[\tau(m_c)], \tag{4.2}$$

$$C_{h\gamma\gamma} = \frac{N_c^t}{6}Q_t^2 A[\tau(m_t)]\ (c_t + c_{\gamma\gamma}) + \frac{N_c^b}{6}Q_b^2 A[\tau(m_b)]\ c_b + \frac{N_c^c}{6}Q_c^2 A[\tau(m_c)] + \frac{N_c^\tau}{6}Q_\tau^2 A[\tau(m_\tau)]\ c_\tau + \frac{1}{8}A_1[\tau(m_W)], \tag{4.3}$$

where m_c (m_W) is the charm quark ($W^\pm$-boson) mass, $C(\mathrm{r})$ is defined for the color representation, r, by $\mathrm{Tr}(T_\mathrm{r}^a T_\mathrm{r}^b) = C(\mathrm{r})\delta^{ab}$ [T^a denoting the eight generators of $\mathrm{SU(3)_c}$], N_c^f is the number of colors for the fermion f, Q_f is the electromagnetic charge for f, $A[\tau(m)]$ and $A_1[\tau(m)]$ are respectively the form factors for spin 1/2 and spin 1 particles [87, 89] normalized such that $A[\tau(m) \ll 1] \to 1$ and $A_1[\tau(m) \ll 1] \to -7$ with $\tau(m) = m_h^2/4m^2$ (for $m_h \simeq 125$ GeV one has $A_1[\tau(m_W)] \simeq -8.3$ whereas $A[\tau(m > 600\mathrm{GeV})] \simeq 1.0$). The terms proportional to c_t, c_b and c_τ account for the contributions from the fermionic triangular loops involving respectively the top, bottom quark and tau lepton Yukawa coupling. The $A[\tau(m_c)]$ and $A_1[\tau(m_W)]$ terms are for the SM loop-exchanges of the charm quark and $W^\pm$-boson. The dimensionless c_{gg} and $c_{\gamma\gamma}$ quantities – vanishing in the SM – parametrize the EF loop-exchange contributions to the hgg and $h\gamma\gamma$ couplings. This choice of parametrization in Eq. (4.2) with a common factor in front of c_t and c_{gg} [as well as for c_t and $c_{\gamma\gamma}$ in Eq. (4.3)] makes easier the understanding of the c_t influence on the best-fit c_{gg} [or $c_{\gamma\gamma}$] ranges, that will be discussed in Section 4.4.2.
Note also that extra scalar field(s), unmixed with the Higgs boson h (like a squark in supersymmetry), or extra vector boson(s), unmixed with the SM gauge bosons, could affect the Higgs couplings only through new loop-contributions to the c_{gg} and $c_{\gamma\gamma}$ quantities studied here.

4.2.3 Higgs rate modifications

Within the present context, let us write explicitly certain Higgs rates, normalized to their SM prediction, which will prove to be useful in the following. The expression for the cross section of the gluon-gluon fusion mechanism of single Higgs production, over its SM prediction, reads as (for the LHC or Tevatron),

$$\frac{\sigma_{\mathrm{gg\to h}}}{\sigma_{\mathrm{gg\to h}}^{\mathrm{SM}}} \simeq \frac{\left|(c_t + c_{gg})A[\tau(m_t)] + c_b A[\tau(m_b)] + A[\tau(m_c)]\right|^2}{\left|A[\tau(m_t)] + A[\tau(m_b)] + A[\tau(m_c)]\right|^2}\ . \tag{4.4}$$

The expression for the ratio of the diphoton partial decay width over the SM expectation is,

$$\frac{\Gamma_{h\to\gamma\gamma}}{\Gamma^{SM}_{h\to\gamma\gamma}} \simeq \frac{\left|\frac{1}{4}A_1[\tau(m_W)] + (\frac{2}{3})^2(c_t + c_{\gamma\gamma})A[\tau(m_t)] + (-\frac{1}{3})^2 c_b A[\tau(m_b)] + (\frac{2}{3})^2 A[\tau(m_c)] + \frac{1}{3}c_\tau A[\tau(m_\tau)]\right|^2}{\left|\frac{1}{4}A_1[\tau(m_W)] + (\frac{2}{3})^2 A[\tau(m_t)] + (-\frac{1}{3})^2 A[\tau(m_b)] + (\frac{2}{3})^2 A[\tau(m_c)] + \frac{1}{3}A[\tau(m_\tau)]\right|^2}. \tag{4.5}$$

The ratios for the partial decay widths into the bottom quark and tau lepton pairs as well as for the cross section of Higgs production in association with a top pair (LHC or Tevatron) are given by,

$$\frac{\Gamma_{h\to\bar{b}b}}{\Gamma^{SM}_{h\to\bar{b}b}} \simeq |c_b|^2 \ , \quad \frac{\Gamma_{h\to\bar{\tau}\tau}}{\Gamma^{SM}_{h\to\bar{\tau}\tau}} \simeq |c_\tau|^2 \ , \quad \frac{\sigma_{h\bar{t}t}}{\sigma^{SM}_{h\bar{t}t}} \simeq |c_t|^2 \ . \tag{4.6}$$

Let us make a comment related to the mass insertion in the triangular loops of fermions inducing the $h\gamma\gamma$ and hgg couplings. Strictly speaking, a factor ϵ_t, equal to the ratio of the sign of m_t in the SM over sign(m_t) in the EF scenario, should multiply c_t in Eq. (4.2)-(4.3) or Eq. (4.4)-(4.5) [similarly for $\epsilon_b c_b$ and $\epsilon_\tau c_\tau$]; in other words, if for instance $\epsilon_t = -1$ the values for c_t obtained below would have to be interpreted instead as values for $-c_t$ (the observables of Eq. (4.6) being insensitive to the $c_{t,b,\tau}$ signs).

4.2.4 Ratio of $c_{\gamma\gamma}$ and c_{gg}

For a better understanding of the above parametrization, we finally provide the examples of expressions for the c_{gg} and $c_{\gamma\gamma}$ quantities, in the case of the existence of a t' quark [same color number and electromagnetic charge as the top] (possibly vector-like as *e.g.* in Ref. [90, 91]), an exotic $q_{5/3}$ quark with electromagnetic charge 5/3 and an additional ℓ' lepton (colorless), in terms of their physical Yukawa couplings and mass eigenvalues :

$$c_{gg} = \frac{1}{C(t)A[\tau(m_t)]/v}\left[- C(t')\frac{Y_{t'}}{m_{t'}}A[\tau(m_{t'})] - C(q_{5/3})\frac{Y_{q_{5/3}}}{m_{q_{5/3}}}A[\tau(m_{q_{5/3}})] + \dots \right], \tag{4.7}$$

$$c_{\gamma\gamma} = \frac{1}{N_c^t Q_t^2 A[\tau(m_t)]/v}\left[- 3\left(\frac{2}{3}\right)^2 \frac{Y_{t'}}{m_{t'}}A[\tau(m_{t'})] - N_c^{q_{5/3}}\left(\frac{5}{3}\right)^2 \frac{Y_{q_{5/3}}}{m_{q_{5/3}}}A[\tau(m_{q_{5/3}})] \right.$$
$$\left. - Q_{\ell'}^2 \frac{Y_{\ell'}}{m_{\ell'}}A[\tau(m_{\ell'})] + \dots \right]. \tag{4.8}$$

The dots stand for any other EF loop-contributions. The mass assumption made in the first Footnote leads to real $A[\tau(m_{f'})]$ functions and thus real c_{gg}, $c_{\gamma\gamma}$ values, for real masses and Yukawa coupling constants, as appears clearly in the two above expressions.

It will turn out to be instructive to express the ratio of these parameters in the simplified

scenario where a new single q' quark is affecting the Higgs couplings; denoting its electromagnetic charge as $Q_{q'}$ and assuming the q' to have the same color representation as the top quark, this ratio reads as :

$$\left.\frac{c_{\gamma\gamma}}{c_{gg}}\right|_{q'} = \frac{Q_{q'}^2}{(2/3)^2} \ . \tag{4.9}$$

This ratio takes indeed a simple form that will be exploited in Section 4.4.3. In particular, notice that $c_{\gamma\gamma}|_{t'} = c_{gg}|_{t'}$. Clearly, q' should have non-vanishing Yukawa couplings to satisfy Eq. (4.9), otherwise $c_{\gamma\gamma}|_{q'} = c_{gg}|_{q'} = 0$. In the specific case of a vector-like $q'_{L/R}$, this one could for example constitute a singlet under the $\mathrm{SU(2)_L}$ gauge group and have a Yukawa coupling with another $q''_{R/L}$ state of same $Q_{q'}$ charge but embedded in a $\mathrm{SU(2)_L}$ doublet; then the heaviest $q^{(2)}_{L/R}$ mass eigenstate, composed of $q'_{L/R}$ and $q''_{L/R}$, could decouple from the Higgs sector so that the orthogonal $q^{(1)}_{L/R}$ composition would represent the considered unique new quark influencing significantly the Higgs couplings.

4.3 The Higgs boson data

All the Higgs rates which have been measured at the Tevatron and LHC [for $\sqrt{s} = 7$ and 8 TeV] are defined in this section. The references with their experimental values are also given below (these values have been summarized in Ref. [58]).
Generically, the measured observables are the signal strengths whose theoretical predictions read as (in the narrow width approximation as used in Ref. [62]),

$$\mu^p_{s,c,i} \simeq \frac{\sigma_{\mathrm{gg\to h}}|_s + \frac{\epsilon_{\mathrm{hqq}}}{\epsilon_{\mathrm{gg\to h}}}|^p_{s,c,i}\ \sigma^{\mathrm{SM}}_{\mathrm{hqq}}|_s + \frac{\epsilon_{\mathrm{hV}}}{\epsilon_{\mathrm{gg\to h}}}|^p_{s,c,i}\ \sigma^{\mathrm{SM}}_{\mathrm{hV}}|_s + \frac{\epsilon_{\mathrm{h\bar{t}t}}}{\epsilon_{\mathrm{gg\to h}}}|^p_{s,c,i}\ \sigma_{\mathrm{h\bar{t}t}}|_s}{\sigma^{\mathrm{SM}}_{\mathrm{gg\to h}}|_s + \frac{\epsilon_{\mathrm{hqq}}}{\epsilon_{\mathrm{gg\to h}}}|^p_{s,c,i}\ \sigma^{\mathrm{SM}}_{\mathrm{hqq}}|_s + \frac{\epsilon_{\mathrm{hV}}}{\epsilon_{\mathrm{gg\to h}}}|^p_{s,c,i}\ \sigma^{\mathrm{SM}}_{\mathrm{hV}}|_s + \frac{\epsilon_{\mathrm{h\bar{t}t}}}{\epsilon_{\mathrm{gg\to h}}}|^p_{s,c,i}\ \sigma^{\mathrm{SM}}_{\mathrm{h\bar{t}t}}|_s} \frac{B_{\mathrm{h\to XX}}}{B^{\mathrm{SM}}_{\mathrm{h\to XX}}} \ ,$$

$$\text{with,} \qquad \sigma_{\mathrm{gg\to h}}|_s = \frac{\sigma_{\mathrm{gg\to h}}}{\sigma^{\mathrm{SM}}_{\mathrm{gg\to h}}}\sigma^{\mathrm{SM}}_{\mathrm{gg\to h}}|_s \ , \quad \sigma_{\mathrm{h\bar{t}t}}|_s = \frac{\sigma_{\mathrm{h\bar{t}t}}}{\sigma^{\mathrm{SM}}_{\mathrm{h\bar{t}t}}}\sigma^{\mathrm{SM}}_{\mathrm{h\bar{t}t}}|_s \ ,$$

$$\Gamma_{\mathrm{h}\to\gamma\gamma} = \frac{\Gamma_{\mathrm{h}\to\gamma\gamma}}{\Gamma^{\mathrm{SM}}_{\mathrm{h}\to\gamma\gamma}}\Gamma^{\mathrm{SM}}_{\mathrm{h}\to\gamma\gamma} \ , \quad \Gamma_{\mathrm{h}\to\bar{\mathrm{b}}\mathrm{b}} = \frac{\Gamma_{\mathrm{h}\to\bar{\mathrm{b}}\mathrm{b}}}{\Gamma^{\mathrm{SM}}_{\mathrm{h}\to\bar{\mathrm{b}}\mathrm{b}}}\Gamma^{\mathrm{SM}}_{\mathrm{h}\to\bar{\mathrm{b}}\mathrm{b}} \ , \quad \Gamma_{\mathrm{h}\to\bar{\tau}\tau} = \frac{\Gamma_{\mathrm{h}\to\bar{\tau}\tau}}{\Gamma^{\mathrm{SM}}_{\mathrm{h}\to\bar{\tau}\tau}}\Gamma^{\mathrm{SM}}_{\mathrm{h}\to\bar{\tau}\tau} \ , \tag{4.10}$$

where the p-exponent labels the Higgs channel defined by its production and decay processes, the s-subscript represents the squared of the energy [we will note $\sqrt{s} = 1.96, 7, 8$ in TeV] of the realized measurement, the c-subscript stands for the experimental collaboration (CDF and D0 at the Tevatron, ATLAS or CMS at LHC) having performed the measurement and i is an integer indicating the event cut category considered. σ_{hqq} is the predicted cross section for the Higgs production in association with a pair of light SM quarks and σ_{hV} is for the production in association with a gauge boson [$V \equiv Z^0, W^\pm$ bosons]; their s-subscript indicates the energy and in turn which collider is

considered. The $B_{\rm h\to XX}$ (X stands for any possible final state particle) are the branching ratios defined from all the opened Higgs decay widths which are modified according to the second line of Eq. (4.10) and taken as in the SM for the others. The SM rates at LHC for a given energy, like $\sigma^{\rm SM}_{\rm gg\to h}|_s$, and the SM partial widths, $\Gamma^{\rm SM}_{\rm h\to XX}$, are taken from Ref. [92] (including the cross section corrections at next-to-next-to leading order in QCD and next-to leading order in the EW sector, except for $\sigma^{\rm SM}_{\rm htt}$ at next-to leading order in QCD), while the SM rates at Tevatron are from Ref. [93] (QCD corrections at next-to-next-to leading order). The cross section and partial width ratios in the second line of Eq. (4.10) are those in the considered effective theory with EF expressed in Eq. (4.4)-(4.5)-(4.6). The EW/QCD corrections are expected typically to be compensated in these ratios (especially for heavy EF in the same gauge group representation as the SM fermions). Finally, $\epsilon_{\rm gg\to h}$, for the gg $\to$ h reaction example, is the experimental efficiency [detector acceptance, particle identification, isolation,...] including the (kinematical) selection cut effects; the efficiency ratios entering Eq. (4.10) are obtained by multiplying the SM cross section ratios by the ratios of expected Higgs reaction compositions (in %) – derived via simulations and provided in the relevant experimental papers [see just below]. These selection efficiencies, relying on the Higgs mass, are identical in the SM and in EF frameworks (i.e. in the denominator and numerator of $\mu^p_{s,c,i}$).

Here is the list of Higgs channels that have been experimentally investigated (corresponding, once summed, to 55 measured signal strengths) :

• For the process I, pp $\to$ h, h $\to \gamma\gamma$, the Higgs field is mainly produced by the gluon-gluon fusion; the signal strengths $\mu^I_{7/8,\rm ATLAS/CMS,i}$ are proportional to $B_{\rm h\to\gamma\gamma}$ and depend on the efficiency ratios like *e.g.* $\epsilon_{\rm hqq}/\epsilon_{\rm gg\to h}|^I_{7/8,\rm ATLAS/CMS,i}$ which can be derived from the reaction compositions provided in Ref. [94] (ATLAS) and Ref. [95] updated by Ref. [96] (CMS). While for ATLAS nine cut categories ($i = 1,\ldots,9$) have been applied on the data collected at $\sqrt{s} = 7$ TeV in 2011 (4.8 fb^{-1}) and 8 TeV in 2012 (5.8 fb^{-1}) – leading to a measured mass $m_h \simeq 126.0$ GeV after combination with other channels [97] – CMS has chosen four cut classes ($j = 0,\ldots,3$) to treat the 2011 (5.1 fb^{-1}) and 2012 (5.3 fb^{-1}) data – pointing out a mass $m_h \simeq 125.3$ GeV from combination with the ZZ channel. Note that in Eq. (4.10), the terms,

$$\frac{\epsilon_{\rm hZ}}{\epsilon_{\rm gg\to h}}|^I_{7/8,\rm ATLAS,i}\ \sigma^{\rm SM}_{\rm hZ}|_{7/8} + \frac{\epsilon_{\rm hW}}{\epsilon_{\rm gg\to h}}|^I_{7/8,\rm ATLAS,i}\ \sigma^{\rm SM}_{\rm hW}|_{7/8}\ ,$$

for the ATLAS data must be replaced by, $(\epsilon_{\rm hZ+hW}/\epsilon_{\rm gg\to h}|^I_{7/8,\rm CMS,j})(\sigma^{\rm SM}_{\rm hZ} + \sigma^{\rm SM}_{\rm hW})|_{7/8}$, for CMS (a common efficiency is set).

• In the diphoton channel, other series of cuts have been employed to increase the vector boson fusion contribution, pp $\to$ hqq, h $\to \gamma\gamma$, defining the process noted II. The signal strengths $\mu^{II}_{7/8,\rm ATLAS/CMS,i}$ rely on the efficiency ratios obtained from the reaction compositions in Ref. [94] and Ref. [95,96]. A unique cut category is selected by ATLAS, to tag the dijet final state, whereas

two of them ($i \equiv$tight,loose) are used with the CMS data at $\sqrt{s} = 8$ TeV.

- The last diphoton channel analyzed, process III, is the inclusive Higgs production at the Tevatron, $p\bar{p} \to h,\ h \to \gamma\gamma$. The $\mu^{III}_{1.96,\mathrm{CDF+D0}}$ strength is simply fixed by $\epsilon/\epsilon_{gg\to h}|^{III}_{1.96,\mathrm{CDF+D0}} \simeq 1$ [93] for each Higgs production cross section in Eq. (4.10).

- For the process IV, $pp \to hV$ [$V \to$ leptons], $h \to \bar{b}b$, all selection efficiencies vanish except, $\epsilon_{hV}|^{IV}_{7/8,\mathrm{ATLAS/CMS}} \simeq 1$ [97–99] (of course in such a case, one should not divide by $\epsilon_{gg\to h}$ in Eq. (4.10)), so that, $\mu^{IV}_{7/8,\mathrm{ATLAS/CMS}} \simeq B_{h\to\bar{b}b}/B^{\mathrm{SM}}_{h\to\bar{b}b}$, since $\sigma^{\mathrm{SM}}_{hV}$ does not receive corrections in the EF framework.

- Similarly, for the process V, $p\bar{p} \to hV$ [$V \to$ leptons], $h \to \bar{b}b$, one has $\mu^{V}_{1.96,\mathrm{CDF+D0}} = \mu^{IV}_{7/8,\mathrm{ATLAS/CMS}}$ [93].

- The process VI, $pp \to h\bar{t}t,\ h \to \bar{b}b$, is characterized by vanishing efficiencies except, $\epsilon_{h\bar{t}t}|^{VI}_{7,\mathrm{CMS}} \simeq 1$, leading to,

$$\mu^{VI}_{7,\mathrm{CMS}} \simeq \frac{\sigma_{h\bar{t}t}}{\sigma^{\mathrm{SM}}_{h\bar{t}t}} \frac{B_{h\to\bar{b}b}}{B^{\mathrm{SM}}_{h\to\bar{b}b}} . \tag{4.11}$$

The experimental value, which will be mentioned in next section, is $\mu^{VI}_{7,\mathrm{CMS}}|_{\mathrm{exp}} = -0.75^{+2}_{-1.8}$ [99].

- The reaction VII, $pp \to h,\ h \to ZZ$, has a strength $\mu^{VII}_{7/8,\mathrm{ATLAS/CMS}}$ calculated according to selection efficiencies all equal to unity (for CMS see Ref. [99] and for ATLAS Ref. [100] at $\sqrt{s} = 7$ TeV or Ref. [97] at 8 TeV).

- In the same way, for the reaction $VIII$, $pp \to h,\ h \to WW$, the strength $\mu^{VIII}_{7/8,\mathrm{ATLAS}}$ is computed with efficiencies at unity (see Ref. [98] for 7 TeV and Ref. [101] for 8 TeV, both updated by Ref. [97]), whereas $\mu^{VIII}_{7/8,\mathrm{CMS}}$ is based on vanishing efficiencies except $\epsilon_{gg\to h}|^{VIII}_{7/8,\mathrm{CMS}} \simeq 1$ [99].

- From analog considerations as in the channel IV, one predicts, $\mu^{IX}_{7/8,\mathrm{CMS}} \simeq \mu^{X}_{7,\mathrm{CMS}} \simeq B_{h\to WW}/B^{\mathrm{SM}}_{h\to WW}$, for the processes IX, $pp \to hqq,\ h \to WW$, and X, $pp \to hV,\ h \to WW$ [99].

- The channel XI, $p\bar{p} \to h,\ h \to WW$, has a strength $\mu^{XI}_{1.96,\mathrm{CDF+D0}}$ containing exclusively efficiencies at unity [93].

- As in channel IV, one has the theoretical predictions, $\mu^{XII}_{7/8,\mathrm{CMS}} \simeq \mu^{XIII}_{7,\mathrm{CMS}} \simeq B_{h\to\bar{\tau}\tau}/B^{\mathrm{SM}}_{h\to\bar{\tau}\tau}$, for the processes XII, $pp \to hqq,\ h \to \bar{\tau}\tau$, and $XIII$, $pp \to hV,\ h \to \bar{\tau}\tau$ [99].

- Finally, for the process XIV, $pp \to h,\ h \to \bar{\tau}\tau$, the strength $\mu^{XIV}_{7,\mathrm{ATLAS}}$ has the efficiencies equal

to one [97, 98] and $\mu^{XIV}_{7/8,\text{CMS}}$ has all efficiencies equal to zero but $\epsilon_{gg\to h}|^{XIV}_{7/8,\text{CMS}} \simeq 1$ [99].

4.4 The Higgs rate fits

4.4.1 The fit procedure

In order to analyze the fit of the Higgs boson data from colliders within the effective theory described above, we assume gaussian error statistics and we use the χ^2 function,

$$\chi^2 \;=\; \sum_{p,s,c,i} \frac{(\mu^p_{s,c,i} - \mu^p_{s,c,i}|_{\text{exp}})^2}{(\delta\mu^p_{s,c,i})^2} \;, \tag{4.12}$$

where the sum is taken over all the different channel observables defined in Section 4.3 and $\mu^p_{s,c,i}|_{\text{exp}}$ are the measured central values for the corresponding signal strengths. $\delta\mu^p_{s,c,i}$ are the uncertainties on these values and are obtained by symmetrizing the provided errors below and above the central values : $(\delta\mu^p_{s,c,i})^2 = [(\delta\mu^p_{s,c,i}|^+)^2 + (\delta\mu^p_{s,c,i}|^-)^2]/2$. $\mu^p_{s,c,i}|_{\text{exp}}$ and $\delta\mu^p_{s,c,i}|^\pm$ are given in the experimental papers listed in Section 4.3 which contain the QCD error estimations.

The summation over all the signal strengths in Eq. (4.12) allows to compare the maximum of available experimental information with the theoretical predictions, in order to optimize the test of the effective EF theory. Note that the i-subscript in this summation corresponds to exclusive cut categories into which the event samples are split.

The global fit is performed without including the correlation coefficient effects which are currently not supplied in the experimental papers. Nevertheless, this does not affect the statistical and uncorrelated systematic errors.

4.4.2 Fits in the $\{c_{gg}, c_{\gamma\gamma}, c_b\}$ space

In Eq. (4.12), $\chi^2 = \chi^2(c_t, c_b, c_\tau, c_{gg}, c_{\gamma\gamma})$ depends on the five effective parameters $c_t, c_b, c_\tau, c_{gg}, c_{\gamma\gamma}$ through Eq. (4.10) and Eq. (4.4)-(4.5)-(4.6). A priori, the fit analysis should be performed over these five free parameters but to still be able to draw plots of the whole parameter space (and in turn study it graphically) one has to restrict it to a three-dimensional space. In this section, we will indeed choose three freely varying parameters, $c_{gg}, c_{\gamma\gamma}, c_b$, and search for the best-fit regions in this three-dimensional space. Then we will show slices of these regions at several chosen values of c_b (i.e. in the plane $c_{\gamma\gamma}$ versus c_{gg}). This will be repeated for different fixed values of c_t and c_τ.
The motivation for fixing c_t and c_τ, among the five effective parameters, is the following one. First, the $|c_\tau|$ range compatible at 1σ with the Higgs data is known and turns out to be roughly $[0; \sim 1.8]$ (for $c_t \approx 1$ and reasonable c_b values described later on) because the measured values for $\mu^{XII}_{7/8,\text{CMS}}$ are negative – even with the errors – so that $B_{h\to\bar\tau\tau}$, and in turn $\Gamma_{h\to\bar\tau\tau}$ and $|c_\tau|$, cannot be too

large. Hence, there is no need to apply the numerical global fit analysis on c_τ, then treated as a free parameter, to find its relevant range. Secondly, for the purpose of demonstrating the c_t peculiarity (correlation with c_{gg}, $c_{\gamma\gamma}$) discussed in Section 4.4.2, it is easier to choose ourselves its fixed values than to have those values dictated by the numerical best-fit search method.

So now, having the three free parameters, $c_{gg}, c_{\gamma\gamma}, c_b$, we are going to show the best-fit domains in this three-dimensional space at 68.27%C.L. (1σ), 95.45%C.L. (2σ) and 99.73%C.L. (3σ) which correspond to established values of $\Delta\chi^2 = \chi^2 - \chi^2_{\rm min}$ ($\chi^2_{\rm min}$ being the minimum χ^2 value reached in the $\{c_{gg}, c_{\gamma\gamma}, c_b\}$ space) [see for instance Ref. [88]].
In Fig.(4.1), we present four slices of these three-dimensional best-fit regions at four c_b values ($c_b = 0.75$ [a]; 1 [b]; 2.08 [c]; 10 [d]) in the plane $c_{\gamma\gamma}$ versus c_{gg}. These regions are shown for three different fixed values of c_t but for the unique choice $c_\tau = 1$. The c_τ parameter is varied in the several plots of Fig.(4.2) (again for three c_t values) where the behavior of the domain-slice at $c_b = 2.08$ is still shown in the $\{c_{\gamma\gamma}, c_{gg}\}$ plane; note that Fig.(4.1)[c] has also been included in Fig.(4.2) [see plot [b]] for an easier comparison with Fig.(4.2)[a,c]. All these plots of Fig.(4.1)-(4.2) are discussed in the following subsections.

The c-ranges

A few comments are in order with respect to the reasonable choice of parameter ranges in Fig.(4.1)-(4.2). The naive perturbativity condition $|c_t Y_t| \lesssim 4\pi$ leads to $|c_t| \lesssim 18$ since $|Y_t| \simeq |m_t/v|$. The similar theoretical constraints for $|c_b|$ and $|c_\tau|$ are even less stringent due to the smaller $m_{b,\tau}$ values. The perturbativity considerations on $c_{\gamma\gamma}$ and c_{gg} are model-dependent; for example, in the case of a t' state with $m_{t'}$ of the order of m_t, Eq. (4.7)-(4.8) show that $c_{\gamma\gamma}$ and c_{gg} would typically set the t' Yukawa coupling (relatively to Y_t) and would thus have to satisfy roughly the same condition as c_t : $|c_{\gamma\gamma}| \lesssim 18$, $|c_{gg}| \lesssim 18$. For the sake of generality, we consider the whole ranges of $c_{\gamma\gamma}$, c_{gg} values pointed out by the Higgs rate fits.
The $c_{t,b,\tau}$ choice is also related to the generation of fermion masses through Yukawa couplings. In the SM, the top quark mass determines Y_t up to CKM mixing angles. For large deviations with respect to the SM Yukawa coupling, i.e. for c_t values very different from unity, the physical top mass may be recovered by new strong mixing effects like in $t - t'$ mixings. $|c_t|$ values different from unity by a factor ~ 5 would certainly already require strong $t - t'$ mixings, to be predicted by specific scenarios. Similar comments hold for c_b and c_τ. From this point of view, the value of $c_b = 10$ in Fig.(4.1)[d], and $c_\tau = 0.05$ in Fig.(4.2)[a], are respectively large and tiny; those have been chosen for the purpose of explaining the behavior of the best-fit domains in the large c_b and low c_τ regimes.

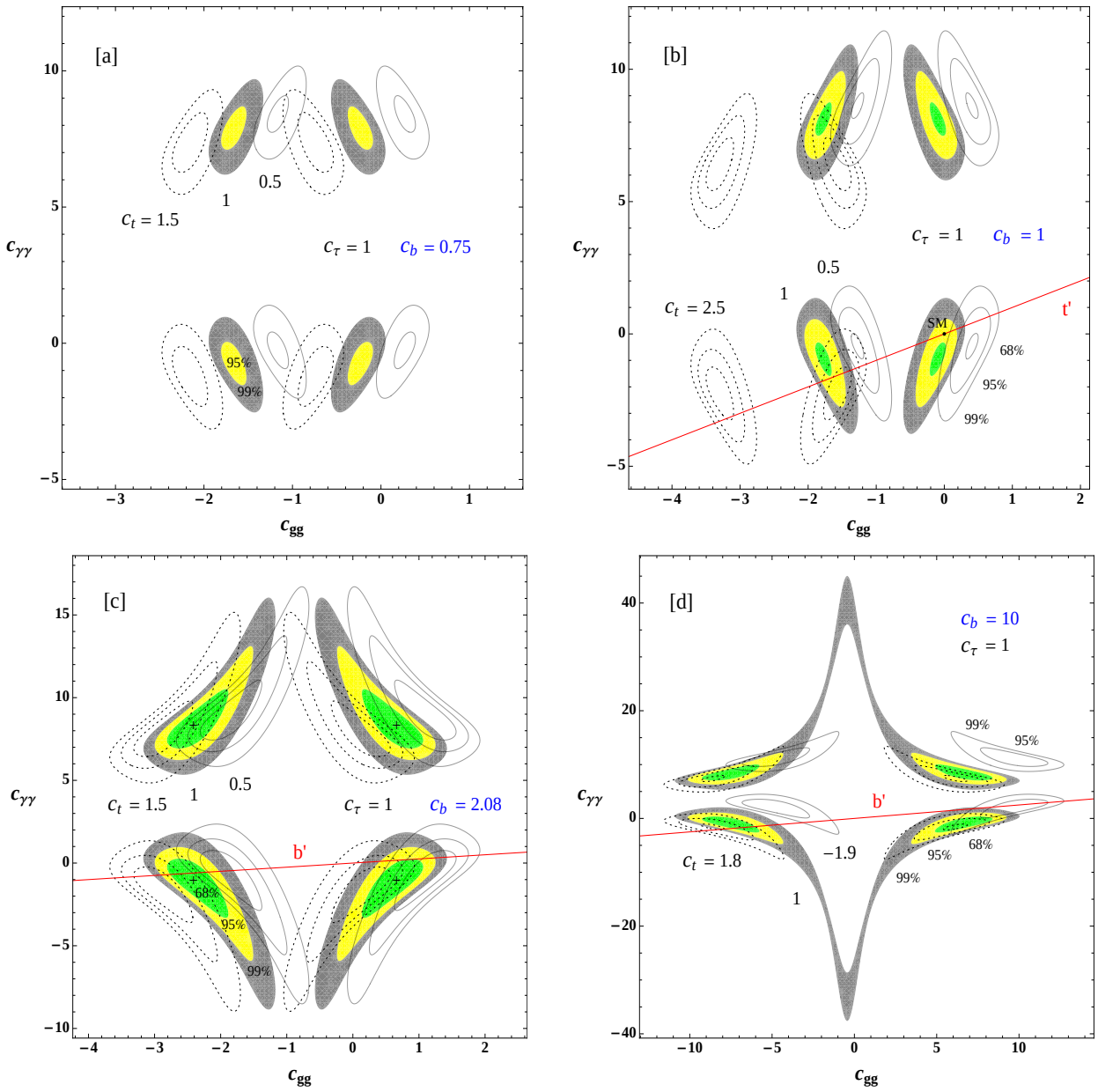

Figure 4.1: Best-fit regions at 68.27%C.L. (in green), 95.45%C.L. (yellow) and 99.73%C.L. (grey) in the plane $c_{\gamma\gamma}$ versus c_{gg}, for $c_\tau = 1$. Each one of the four figures [a,b,c,d] is associated to a certain c_b value written (in blue) on the figure itself. In each figure, the regions are drawn for three c_t values, the corresponding value being indicated nearby the relevant region; the regions for the lowest, intermediate, highest c_t values are respectively shown by the plain contours, colored filled domains, dotted contours. The SM (black) point, at $c_t = c_b = c_\tau = 1$, $c_{\gamma\gamma} = c_{gg} = 0$, is shown on the plot [b]. Finally, the four best-fit point locations are indicated by crosses in the plot [c]. The theoretically predicted lines for extra-quarks of type b' (plot [c,d]) and t' (plot [b]) are also represented (in red).

Best-fit points

The best-fit points reachable, when varying the three free parameters, $c_b, c_{gg}, c_{\gamma\gamma}$, for fixed values $c_t = 1$ and $c_\tau = 1$, are at $c_b = 2.08$ and the c_{gg}, $c_{\gamma\gamma}$ values corresponding to the four crosses drawn

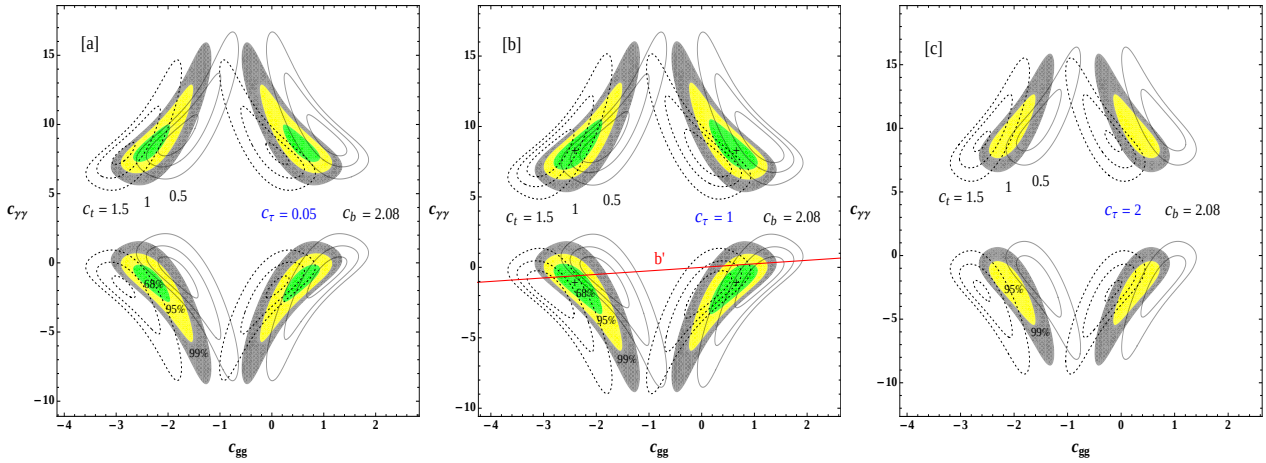

Figure 4.2: Best-fit regions at 68.27%C.L. (green), 95.45%C.L. (yellow) and 99.73%C.L. (grey) in the plane $c_{\gamma\gamma}$ versus c_{gg}, for $c_b = 2.08$. Each one of the three figures is obtained for a c_τ value which is indicated (in blue). In each figure, the regions are drawn for three c_t values [same conventions as in Fig.(4.1)]. The predicted (red) line for an extra-quark of type b' is also represented in the plot [b].

in Fig.(4.1)[c]. Since there are exact symmetries along the c_{gg} and $c_{\gamma\gamma}$ axes (see discussion below), those four cross-points are all associated to the same $\chi^2_{\rm min} = 52.36$.
For comparison, the best-fit point reachable, when varying the five effective parameters, c_t, c_b, c_τ, c_{gg}, $c_{\gamma\gamma}$, is $\{c_t = 0.0; c_b = 1.13; c_\tau = 0.0; c_{gg} = -0.79; c_{\gamma\gamma} = -0.11\}$ leading to $\chi^2 = 50.26$. A vanishing c_t (a top-phobic Higgs boson) imposes $\mu^{VI}_{7,\rm CMS} = 0$ [via Eq. (4.6)] which lies inside the 1σ experimental interval and is even the possible value the closest to the measured negative central value [given just after Eq. (4.11)]. Similarly, $c_\tau = 0$ (tau-phobic) induces $\mu^{XII}_{7/8,\rm CMS} = 0$ which is the closest value to the negative experimental central values. In view of the generation of fermion masses through the Yukawa couplings, one could require say $|c_\tau| > 0.3$ and $|c_t| > 0.3$ which leads instead to the best-fit point $\{c_t = 0.3; c_b = 1.18; c_\tau = -0.3; c_{gg} = 0.67; c_{\gamma\gamma} = -0.42\}$ having $\chi^2 = 50.44$.
All these minimal χ^2 values are smaller than the SM one, $\chi^2_{\rm SM} = 57.10$ [from taking all the strength predictions at unity in Eq. (4.12)]. The regions at 68.27%C.L. in Fig.(4.1)[b] do not even contain the SM point ($\{c_t = 1; c_b = 1; c_\tau = 1; c_{gg} = 0; c_{\gamma\gamma} = 0\}$).

Let us interpret the c-values of the best-fit points obtained in Fig.(4.1)[c] (or equivalently Fig.(4.2)[b]). For example the best-fit point at, $c_b = 2.08$, $c_{gg} = 0.66$ and $c_{\gamma\gamma} = -1.09$, shown on Fig.(4.1)[c] (for fixed $c_t = c_\tau = 1$) indicates in particular that an increase of the diphoton partial width is favored by the data. Indeed, a negative $c_{\gamma\gamma}$ implies a constructive interference between EF loops and the main SM $W^\pm$-boson exchange, as shows Eq. (4.5). Interestingly, the preferred $c_{\gamma\gamma}$ value approximatively cancel the top-loop contribution. The obtained indication for a $\Gamma_{h\to\gamma\gamma}$ enhancement is not surprising as most of the measured strengths in the diphoton channel – described in Section 4.3 – are above their SM expectations (even significantly for some of those).

The best-fit value, $c_{gg} = 0.66$, also outlines the preference for a $\sigma_{gg\to h}$ increase [see Eq. (4.4)] related to the excesses with respect to the SM rates of the experimental values for some of the diphoton rates.
Finally, a $\Gamma_{h\to\bar{b}b}$ increase is favored (see Eq. (4.6) with $c_b = 2.08$) which tends to enhance the $\mu^{V}_{1.96,\mathrm{CDF+D0}}$ strength and suppress $\mu^{XII}_{7/8,\mathrm{CMS}}$ relatively to the SM, as indicated by the experimental results (all at more than 1σ from the SM).
The three other best-fit points of Fig.(4.1)[c] can be obtained through the symmetries described in the next subsection and are thus interpretable with the same physical arguments about the Higgs rates.

The symmetries

Some exact reflection symmetries with respect to vertical and horizontal axes appear clearly on Fig.(4.1) and Fig.(4.2). Indeed, for a $c_{\gamma\gamma}$ value giving rise to a certain $\Delta\chi^2$, there always exists a $c_{\gamma\gamma}$ partner value leading to the opposite-sign $h \to \gamma\gamma$ amplitude [squared in Eq. (4.5)] and in turn to the same $\Delta\chi^2$. The same kind of symmetry occurs for c_{gg} entering the $h \to gg$ (or $gg \to h$) amplitude.
Another type of symmetry is constituted by the transformation, $c_b \to -c_b$, leaving invariant the $\bar{b}b$ partial width [*c.f.* Eq. (4.6)]. This symmetry is approximative due to the dependence of $\sigma_{gg\to h}$ and $\Gamma_{h\to\gamma\gamma}$ on c_b; for c_b values such that the bottom-exchange contributions to $\sigma_{gg\to h}$ and $\Gamma_{h\to\gamma\gamma}$ remain sub-leading (as in the SM), the transformation, $c_b \to -c_b$, keeps unchanged, at the percent level, the $c_{\gamma\gamma}$, c_{gg} values associated to a given $\Delta\chi^2$. The similar symmetry arises for, $c_\tau \to -c_\tau$.

Dependence of the best-fit regions on c_{gg} and $c_{\gamma\gamma}$

At this level, one is able to interpret the typical shapes of the obtained best-fit regions. The typical oblique direction (diagonal positioning) of the best-fit domains, for example for the fixed value, $c_t = 1$, around the best-fit point, at $c_{gg} = 0.66$ and $c_{\gamma\gamma} = -1.09$ in Fig.(4.1)[c], can be understood as follows – the orientations of the three other best-fit region groups are then deduced through the reflection symmetries along c_{gg} and $c_{\gamma\gamma}$. Starting from this best-fit point and decreasing c_{gg} tends to decrease $\sigma_{gg\to h}$ and hence to degrade the fits for diphoton rates, a degradation which must be compensated by the $c_{\gamma\gamma}$ decrease ($|c_{\gamma\gamma}|$ increase enhancing $\Gamma_{h\to\gamma\gamma}$) to remain below 68.27%C.L.

Dependence of the best-fit regions on c_t

We discuss now the modifications of the best-fit domains as the effective parameter, c_t, is varying. We observe separately on Fig.(4.1)[a,b,c] and Fig.(4.2) that a c_t variation of amount, δc_t, leads in a good approximation to a translation (no domain shape modification) of $-\delta c_t$ along both the $c_{\gamma\gamma}$ and c_{gg} axes, for each one of the three best-fit regions. It is particularly clear in Fig.(4.1)[b] where

a large δc_t is exhibited.
Indeed, considering a given Confidence Level, the $\Delta\chi^2 = \chi^2 - \chi^2_{\rm min}$ value is fixed which determines [*c.f.* Eq. (4.12)] in particular the c_t correction factor for the major top loop-exchanges and the parameters for EF loop-contributions, c_{gg}, $c_{\gamma\gamma}$, entering the predicted strengths [*c.f.* Eq. (4.10)] through the sums $(c_t + c_{gg})$ and $(c_t + c_{\gamma\gamma})$ [*c.f.* Eq. (4.4)-(4.5)]. Hence for a δc_t parameter variation, since the $\chi^2_{\rm min}$ value is unchanged (for similar compensation reasons to the following one), the induced χ^2 modification should be exactly compensated by variations, $\delta c_{gg} = \delta c_{\gamma\gamma} = -\delta c_t$.
Note that for different c_t, c_{gg} and $c_{\gamma\gamma}$ definitions from here (then distinguished by a prime), say generalizing to effective parameters entering Eq. (4.4)-(4.5) via $(\alpha_g c'_t + \beta_g c'_{gg})$ and $(\alpha_\gamma c'_t + \beta_\gamma c'_{\gamma\gamma})$ with new constants $\alpha_{g,\gamma}, \beta_{g,\gamma}$, the translations would be instead of

$$\delta c'_{gg} = -\frac{\alpha_g}{\beta_g}\,\delta c'_t \ , \ \text{and,} \ \ \delta c'_{\gamma\gamma} = -\frac{\alpha_\gamma}{\beta_\gamma}\,\delta c'_t \ .$$

The measured signal strength of Eq. (4.11) is also sensitive to c_t [4] and there is no possible δc_t compensation in it, as shows Eq. (4.6), which invalidates the above argumentation strictness. Nevertheless, since the error bar on this measured rate is quite large, the above translation estimations remain a good approximation up to relatively large $|c_t|$ values where the three reference best-fit domain sizes start to decrease – before disappearing. This is visible for instance in Fig.(4.1)[d]; in fact these more central, i.e. more fit-favored, domains in the $\{c_{\gamma\gamma}, c_{gg}\}$ plane mainly allow to balance the degradation of the $\mu^{VI}_{7,\rm CMS}$ fit due to larger $|c_t|$ values (tending to increase too much the $\rm h\bar{t}t$ production cross section). This effect of decreasing domain widths appears in Fig.(4.1)[d] for smaller $|c_t|$ values than in all the other figures because, for this extremely large $c_b = 10$ enhancing $B_{\rm h\to\bar{b}b}$, $\mu^{VI}_{7,\rm CMS}$ is getting above its 1σ range faster as $|c_t|$ increases.

To conclude on this part, this strong parameter interdependence implies that in order to determine experimentally the $c_{\gamma\gamma}$ and c_{gg} quantities, it is crucial to determine as well the c_t Yukawa correction whose measurement is essentially relying on the μ^{VI} analysis; now this analysis requires in particular good efficiencies for the challenging simultaneous reconstruction of the top and bottom quark pairs in the final state.

Dependence of the best-fit regions on c_b

Concerning the c_b variation (for fixed $c_t = c_\tau = 1$), we first explain the impact of the c_b increase on the typically allowed $c_{\gamma\gamma}$, c_{gg} values – starting from the best-fit domains around the best-fit point, $\{c_b = 2.08; c_{gg} = 0.66; c_{\gamma\gamma} = -1.09\}$, in Fig.(4.1)[c] – and the reasons why huge values up to $c_b \simeq 50$ could still agree with present Higgs rate fits. For such a c_b increase, the strengths $\mu^{VII,VIII}_{7/8,\rm ATLAS/CMS}$, $\mu^{XI}_{1.96,\rm CDF+D0}$ and $\mu^{XIV}_{7/8,\rm CMS}$ are reduced via $\Gamma_{\rm h\to\bar{b}b}$, a reduction which has to be

[4] Other signal strengths, like in the diphoton channel, are also sensitive to c_t [*c.f.* Eq. (4.10)] but less, due to the experimental selection efficiencies and the smallness of $\sigma_{\rm h\bar{t}t}$ relatively to the dominant Higgs production reactions.

compensated by a $\sigma_{gg\to h}$ increase through a c_{gg} enhancement to conserve a satisfactory χ^2 (or equivalently here, $\Delta\chi^2$). This explains the shift of the considered best-fit domains, around $\{c_b = 2.08; c_{gg} = 0.66; c_{\gamma\gamma} = -1.09\}$ in Fig.(4.1)[c], to higher c_{gg} values in the plot [d] where $c_b = 10$ (still with $c_t = 1$). This necessary compensation between the $\Gamma_{h\to\bar{b}b}$ and $\sigma_{gg\to h}$ increases also guarantees the stability of diphoton rates (there is also a significant gluon-gluon fusion contribution in the three dijet-tagged final states) letting the χ^2 at the same level, without $c_{\gamma\gamma}$ modifications – explaining nearly identical $c_{\gamma\gamma}$ values for the studied regions in Fig.(4.1)[c] and [d]. The $\Gamma_{h\to\bar{b}b}$ increase leads to enhancements of the strengths $\mu^{IV}_{7/8,\text{ATLAS/CMS}}$, $\mu^{V}_{1.96,\text{CDF+D0}}$ and $\mu^{VI}_{7,\text{CMS}}$ without major consequences on the fit; a c_b increase up to ~ 50 [leading to $\Gamma_{h\to\bar{b}b} \lesssim 5$ GeV] would still leave existing domains at 68.27%C.L. since in the theoretical limit, $c_b \to \infty$, $B_{h\to\bar{b}b}$ tends obviously to a finite value compatible with data : $B_{h\to\bar{b}b} \to 1$. Similarly, the $\Gamma_{h\to\bar{b}b}$ induced decrease of $\mu^{IX,X,XII,XIII}_{7/8,\text{CMS}}$ does not affect significantly the global fit; in the limit, $c_b \to \infty$, all these signal strengths tend to zero (via the involved branching ratios) which is clearly in agreement at 1σ with their experimental central value [and $\mu^{XII}_{7/8,\text{CMS}}|_{\text{exp}}$ is negative].
There is another effect induced by the c_b enhancement; as c_b is increasing, its contribution to $\sigma_{gg\to h}$ renders softer the $\sigma_{gg\to h}$ evolution with c_{gg} so that the c_{gg} interval, spanning the $\sigma_{gg\to h}$ range allowed by the fit, gets larger; this can be seen by comparing the considered best-fit domain widths along the c_{gg} axis in Fig.(4.1)[c] and [d].
Now in the other direction, when c_b decreases from its value in Fig.(4.1)[c] down to its values in the plots [b] and finally [a], the dominant effect of surface area diminution (and disappearance) for the best-fit regions is related to $\mu^{V}_{1.96,\text{CDF+D0}}$ which is reduced and thus moved away from its best-fit value.

What is the experimental impact of the above c_b variation analysis ? The present experimental results do not prevent c_b from taking extremely large values – due in particular to Higgs rate compensations. In order to put a more stringent experimental upper limit on it, one could of course if possible improve the accuracies on the signal strengths involving $\sigma_{gg\to h}$ and $\Gamma_{h\to\bar{b}b}$. A new possibility to measure c_b (or equivalently the bottom Yukawa coupling constant) would be to investigate the processes, $\bar{q}q \to h\bar{b}b$ and $gg \to h\bar{b}b$ (or $\bar{b}b \to h$ and $bg \to hb$), followed by the decay, $h \to \bar{b}b$. Indeed, here both the production and decay rates should increase with c_b ($\Gamma_{h\to\bar{b}b}$ being the dominant partial width) so that compensations should not occur; then too large c_b values would be experimentally ruled out. This Higgs production in association with bottom quarks could have significant cross sections for high LHC luminosities and enhanced c_b values compared to the SM [102] as the present fit points out. The sensitivity to such a reaction relies deeply on the b-tagging capability [87]. This reaction suffers from large QCD backgrounds but new search strategies have been developed for such a bottom final state topology, as in Ref. [103].

Dependence of the best-fit regions on c_τ

Finally, to complete our discussion on the parameter variations, we describe the c_τ influence on the best-fit domains.
If the fixed c_τ parameter is chosen at a larger value, like in Fig.(4.2)[c] compared to the plot [b], the induced best-fit c_b value, obtained by χ^2 minimization, is modified. The best-fit $\mu^{XII}_{7/8,\rm CMS}$ value, minimizing χ^2, can involve (via $B_{\rm h\to\bar\tau\tau}$) a larger best-fit c_b value in the case of [c] than in case [b], to compensate the higher c_τ (also entering $B_{\rm h\to\bar\tau\tau}$). In consequence, along the c_b axis, the distance of the regions in the plot [c] (at $c_b = 2.08$) to the best-fit point at $c_b > 2.08$ is larger than the distance of the domain-slices in [b] (also at $c_b = 2.08$) to the best-fit point at $c_b = 2.08$ [indicated by the cross(es) on the figure]. Along the $c_{\gamma\gamma}$ and c_{gg} axes, the typical distances of contours at a given Confidence Level to the respective central best-fit points are shorter in [c] than in [b]. In other terms, best-fit regions in [c] are smaller than in [b].
The c_τ decrease from Fig.(4.2)[b] to [a] leads to a softer region size reduction [in the limit $c_\tau \to 0$, $\mu^{XII}_{7/8,\rm CMS} \to 0$ which is the preferred strength].

4.4.3 The case of single EF scenarios

In this Section 4.4.3, we apply the constraints from the Higgs rate fit to examples of simple scenarios where a unique EF state significantly affects the Higgs interactions.

An EF mixed with SM fermions

For instance, a single b' state [same color representation and electromagnetic charge as the bottom quark], that could be a light custodian top-partner in warped/composite frameworks, would lead to a ratio in Eq. (4.9), $(c_{\gamma\gamma}/c_{gg})|_{b'} = 1/4$, corresponding to the straight line drawn on Fig.(4.1)[c,d]. Generically, a b' would be mixed with the SM bottom quark so that possibly, $c_b \neq 1$, whereas one would have, $c_t = c_\tau = 1$ – like in Fig.(4.1)[c,d]. These figures show that there exist $c_{\gamma\gamma}$, c_{gg} and c_b values for which the predicted b' line crosses the 68.27%C.L. region. The simultaneous knowledge of the exact position on the b' line and the c_b value fixing the C.L. regions, necessary to determine the goodness of fit, requires the specification of the bottom mass matrix and hence of the considered model.

The other example of EF candidate able to be mixed with SM quarks is the t' state, possibly constituted *e.g.* by a light top-partner in little Higgs models. For a dominant t' state, the ratio of Eq. (4.9) tends to one which corresponds to the straight line on Fig.(4.1)[b]. Since a t' field can mix with the top quark, $c_t \neq 1$, but in the context of a single t' one should have, $c_b = c_\tau = 1$, as in Fig.(4.1)[b]. The predicted t' line crosses two 95.45%C.L. regions *e.g.* for, $c_t = 0.5$, as well as two 68.27%C.L. regions exclusively in the range, $c_t \sim 1.1 \leftrightarrow 2.6$ (above ~ 2.6 the region sizes decrease as explained in Section 4.4.2).

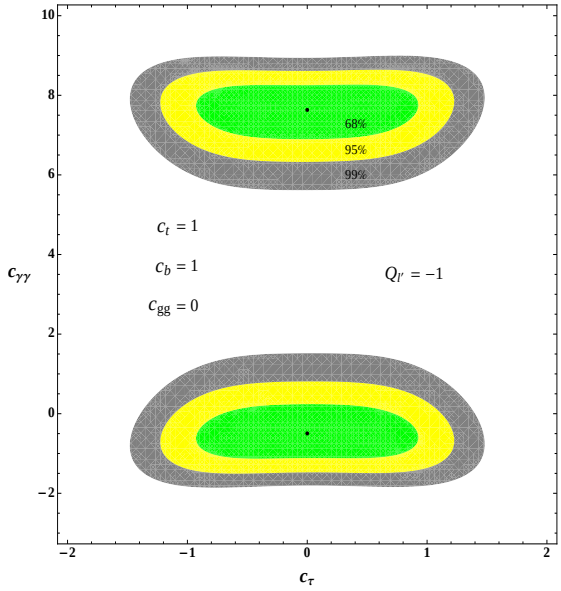

Figure 4.3: Best-fit regions at 68.27%C.L., 95.45%C.L. and 99.73%C.L. in the plane $c_{\gamma\gamma}$ versus c_τ, for the case of an extra-lepton with electric charge, $Q_{\ell'} = -1$, corresponding to $c_t = c_b = 1$, $c_{gg} = 0$. The two best-fit points are indicated (in black).

These discussions on the b' and t' states illustrate the fact that it is useful to study the best-fit domains in the $\{c_{\gamma\gamma}, c_{gg}\}$ plane as, in simplified models, the theoretical prediction for the $c_{\gamma\gamma}/c_{gg}$ ratio takes a simple form independent of the extra-quark masses and Yukawa couplings.

For a single extra-lepton (colorless) with charge, $Q_{\ell'} = -1$, potentially mixed with the SM τ-lepton, the parameters, $c_b = c_t = 1$, $c_{gg} = 0$ [see Eq. (4.7)], are fixed and there remain two free effective parameters, namely $c_{\gamma\gamma}$ and c_τ. The best-fit regions for such a two-dimensional fit are presented in Fig.(4.3). The two best-fit points shown in this figure correspond to, $\chi^2_{\rm min} = 52.54$.

An EF unmixed with SM fermions

It is also possible theoretically that the new single t' (or b') particle does not mix with the SM top (bottom) quark. This would be the case as well for additional q' quarks with exotic electric charges. For illustration, let us first concentrate on the components of possible extensions of the SM quark multiplets under $\mathrm{SU(2)_L}$, as in warped/composite frameworks where SM multiplets are promoted to representations of the custodial symmetry [63–74]. The charges for such q' components obey the relation, $\mathcal{Y}_{q'} = Q_{q'} - I^{q'}_{3L}$ ($\mathcal{Y} \equiv$ hypercharge, $I_{3L} \equiv \mathrm{SU(2)_L}$ isospin). We will consider the electric charges of smallest absolute values, $Q_{q'} = -1/3,\ 2/3,\ -4/3,\ 5/3,\ -7/3$ and $8/3$, keeping in mind that the naive perturbative limit on the electric charge reads as, $|Q_{q'}| \lesssim \sqrt{4\pi/\alpha} \simeq 40$ ($\alpha \equiv$ fine-structure constant [88]). The q' states are in the same color representation as the SM quarks.

In the case of the presence of such a q' quark, unmixed with SM quarks, while $c_t = c_b = c_\tau = 1$, one has $c_{\gamma\gamma} \neq 0$ and $c_{gg} \neq 0$ if the q' state possesses non-zero Yukawa couplings; the best-fit domains for a two-dimensional fit keeping the fixed parameters, $c_t = c_b = c_\tau = 1$, are shown in Fig.(4.4) together with the four best-fit points associated to, $\chi^2_{\rm min} = 55.04$. On this plot, we also represent the theoretically predicted regions in the cases of a single q' quark with electric charge $Q_{q'}$: these regions are the straight lines defined by Eq. (4.9). All the predicted lines – whatever is the $Q_{q'}$ charge – cross the SM point which is reached in the decoupling limit, $c_{\gamma\gamma} \to 0$, $c_{gg} \to 0$. The first result is that the upper-left best-fit regions, around $c_{\gamma\gamma} \sim 8$, $c_{gg} \sim -1.8$, cannot be explored in single q' models [no line can reach it]. We also observe on Fig.(4.4) that the predicted line being the closest to a best-fit point is for, $Q_{q'} = -7/3$. This result means that, among any possible SM multiplet extension component, the fit prefers the $q_{-7/3}$ state compared for example to a t' or $q_{5/3}$ state. For instance, this latter $q_{5/3}$ state leads to a smaller $|c_{\gamma\gamma}/c_{gg}|_{q'}$ ratio ($\propto Q^2_{q'}$) which is less favored by the data due in particular to the observed diphoton rate enhancements.
A possibility in the future is that, as the measurements of the Higgs signal strengths will improve their accuracies – leading typically to smaller best-fit regions in plots such as Fig.(4.4) – some absolute charges like for example, $|Q_{q'}| = 2/3$, could get excluded at 68.27%C.L. (the overlaps of the associated line with any 1σ region could disappear). This kind of exclusion would be quite powerful in the sense that it would be independent of the $Y_{q'}$ Yukawa coupling constants, the q' mass values ($m_{q'}$) and the q' representations under $\mathrm{SU(2)_L}$. This is due to the simplifications occurring in the ratio of Eq. (4.9) or in other terms to the correlations between $c_{\gamma\gamma}$ and c_{gg} [see Eq. (4.7)-(4.8)].

• **Best-fit domains in the plane of the Yukawa coupling versus the EF mass:** Now we determine the physical parameters corresponding typically to an overlap between a given line in Fig.(4.4) and the best-fit regions; we consider the characteristic examples of the charges, $Q_{q'} = -1/3$, $5/3$ and $8/3$. More precisely, we plot in Fig.(4.5) the regions in the plane $|m_{q'}|$ versus $\tilde{Y}_{q'} = -Y_{q'}/\mathrm{sign}(m_{q'})$ which correspond [see Eq. (4.7)-(4.8)] to $c_{\gamma\gamma}$, c_{gg} quantities giving rise to the best $\Delta\chi^2$ values in the case of one free effective parameter, say c_{gg} (related to $c_{\gamma\gamma}$ through the fixed ratio $c_{\gamma\gamma}/c_{gg}|_{q'} \propto Q^2_{q'}$).
In Fig.(4.5), we also illustrate the case of a single additional ℓ' lepton (colorless) without significant mixing to SM leptons [$c_\tau = 1$], as may be justified by exotic $Q_{\ell'}$ charges or the large mass difference between the SM and extra-leptons. Here we choose, $Q_{\ell'} = -1$, being quite common for extra-lepton scenarios (as for instance recently in Ref. [81]). There is, again, a unique free effective parameter, $c_{\gamma\gamma}$, since $c_{gg} = 0$.

Let us discuss the results shown in Fig.(4.5). For a given Confidence Level, the linear dependence of $\tilde{Y}_{b'}$ on $|m_{b'}|$ appearing clearly on the upper left plot is explained by the expressions (4.7)-(4.8) and the constant limit, $A[\tau(m_{b'} \gg m_h)] \to 1$ [described after Eq. (4.3)]. This linear behavior also holds for the three other cases illustrated in this figure, even if for those it is hidden by the chosen

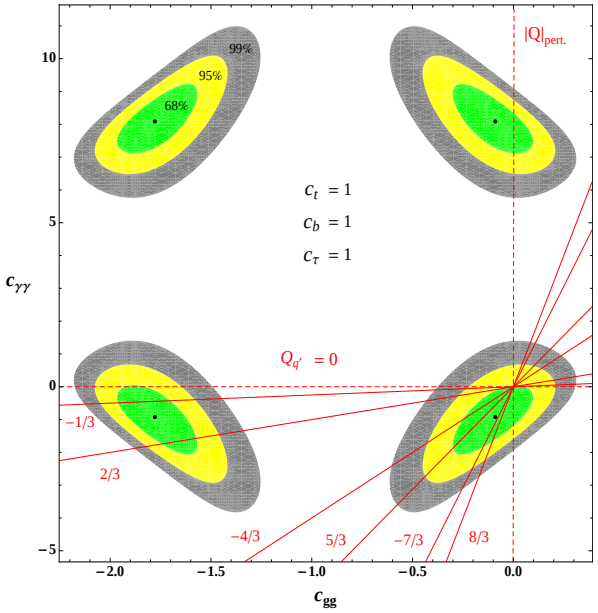

Figure 4.4: Best-fit regions at 68.27%C.L., 95.45%C.L. and 99.73%C.L. in the plane $c_{\gamma\gamma}$ versus c_{gg}, for $c_t = c_b = c_\tau = 1$. Also represented are the predicted (red plain) lines for extra-quarks with the several electric charges, $Q_{q'} = -1/3,\ 2/3,\ -4/3,\ 5/3,\ -7/3$ and $8/3$. The extreme (red dashed) lines for, $Q_{q'} = 0$, and, $|Q_{q'}| = |Q_{q'}|_{\rm pert.} = \sqrt{4\pi/\alpha}$, are shown as well. The four best-fit points are indicated (in black).

logarithmic scale (allowing for a better view of the couplings in the small mass ranges). Eq. (4.7)-(4.8) show that increasing $Q_{q'}$ leads to a slower evolution of $|\tilde{Y}_{q'}|$ with $|m_{q'}|$ (perturbative limit, -4π, reached for higher $|m_{q'}|$) and a smaller allowed $\tilde{Y}_{q'}$ range at fixed $|m_{q'}|$ as can be observed by comparing $Q_{q'} = 5/3$ and $8/3$ in Fig.(4.5). Comparing a ℓ' extra-lepton with the b' extra-quark, it appears in Eq. (4.8) that the smaller $N_c^{\ell'} = 1$ color number tends to compensate the larger $Q_{\ell'}^2 = 1$ squared charge (the favored $c_{\gamma\gamma}|_{f'}$ interval size also affects the $\tilde{Y}_{f'}$ range width). The two unconnected 95.45%C.L. regions in the $\{|m_{b'}|, \tilde{Y}_{b'}\}$ plane correspond basically to the two overlaps between the 95.45%C.L. domains and the b' line in Fig.(4.4).

We now describe the direct experimental constraints indicated on the various plots of Fig.(4.5). The LHC bound, $m_{b'} > 611$ GeV, illustrated on the upper left plot is the strongest direct experimental constraint on a b' state; this bound is based on the QCD b' pair production and it is less stringent for a branching ratio, $B_{\rm b'\to tW^-} < 1$ [104]. The bound for, $B_{\rm b'\to tW^-} = 1$, combined with the 68.27%C.L. region push the Yukawa couplings towards large absolute values, as Fig.(4.5) is demonstrating. The experimental bounds from investigations of other decay channels, like $\rm b' \to bZ$ or $\rm b' \to bh$, are not relevant in the context of a b' field unmixed with SM quarks.
The bound, $m_{q_{5/3}} > 611$ GeV, from the LHC shown in Fig.(4.5) is imposed by the search for the same decay final state, $\rm q_{5/3} \to tW^+$, following the $q_{5/3}$ pair production; this bound is obtained for, $B_{\rm q_{5/3}\to tW^+} = 1$ [104], and it leaves a possible region at 68.27%C.L. in Fig.(4.5). Concerning the $q_{8/3}$ particle which could decay as, $\rm q_{8/3} \to tW^+W^+$, there have been no experimental searches so

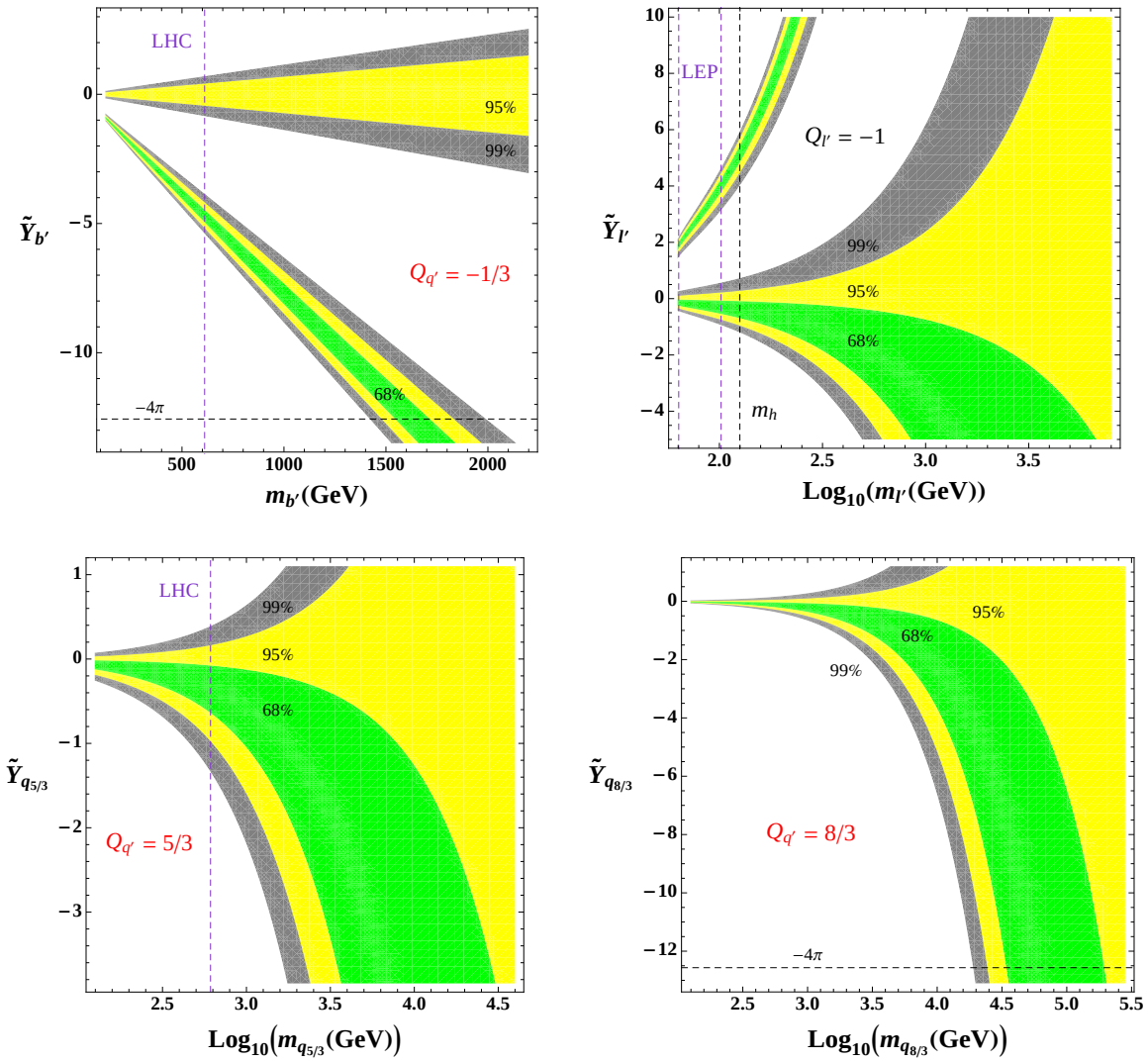

Figure 4.5: Best-fit regions at 68.27%C.L., 95.45%C.L. and 99.73%C.L. in the plane of the $|m_{f'}|$ absolute mass (in GeV) versus the $\tilde{Y}_{f'}$ coupling, with $c_t = c_b = c_\tau = 1$, for the cases $Q_{q'} = -1/3$, $5/3$, $8/3$ and $Q_{\ell'} = -1$. Also represented as dashed lines are the lower perturbative limit on Yukawa couplings, -4π [black horizontal lines], and the direct LHC bounds, $m_{b'} > 611$ GeV, $m_{q_{5/3}} > 611$ GeV, or LEP constraint, $m_{\ell'} > 63.5$ GeV (> 101.9 GeV) for $m_{\ell'} - m_{\nu'} > 7$ GeV (> 15 GeV) [purple vertical lines]. The mass ranges start at the Higgs mass, m_h (see the first Footnote, except for the ℓ'-lepton case (see text) where the m_h value is indicated by a [black dashed vertical] line.

far.

There exist bounds on extra-leptons from the LEP collider; those read as, $m_{\ell'} > 63.5$ GeV ($m_{\ell'} > 101.9$ GeV) for $m_{\ell'} - m_{\nu'} > 7$ GeV (> 15 GeV) [81, 88], in the case of the existence of an additional ν' neutrino (which would have no effects on the Higgs couplings to charged fermions or gauge bosons). These constraints have been obtained from investigating the channel, $\ell' \to \mathrm{W}^{(\star)}\nu' \to \ell + \not{E}$, where ℓ denotes a SM charged lepton and $\not{E}$ stands for missing energy, assuming a stable ν' on collider time-scales. The results for the domain, $m_h > m_{\ell'}$, shown in Fig.(4.5)

are valid in the absence of new significant partial Higgs decay widths (see the first Footnote).

To conclude on all these aspects of Fig.(4.5), one can say that the collider constraints from Higgs rate measurements on representative single EF models are already significant, especially in the low-mass regime where the allowed range for Yukawa coupling constants can be quite predictive. The constraints are sensitive to larger masses in cases of higher electric charges, as expected, and this indirect sensitivity on EF candidates can reach large mass scales up to ~ 200 TeV.

• **Constraints on the signs of fundamental parameters:** Concerning the constraints on the signs, as shown in Fig.(4.5) based on the present Higgs data, the sign, $\tilde{Y}_{q'} < 0$ [leading to $c_{\gamma\gamma} < 0$], is preferred at 68.27%C.L. [except with absolute charges, $|Q_{q'}| \gtrsim 7$, i.e. in a range close to the $|Q_{q'}|_{\rm pert.}$ limit as illustrated in Fig.(4.4)] for any single extra-quark as it creates a constructive interference with the $W^{\pm}$-boson exchange increasing the diphoton rates. The specific sign configuration, $\tilde{Y}_{q'} < 0$, is selected by the two relevant best-fit points which pin down, $c_{\gamma\gamma} < 0$, as obtained for extra-quarks in Fig.(4.4). This predicted condition means that the Yukawa coupling constant [$-Y_{q'}$ in our conventions] must have a sign opposite to $m_{q'}$ which could be written,

$$\text{sign}\left(\frac{-Y_{q'}}{m_{q'}}\right) \; < \; 0 \; . \tag{4.13}$$

Related to this condition, there are comments on the configuration denoted as *dysfermiophilia* in the literature. As described at the end of Section 4.2.3, strictly speaking the $c_{t,b,\tau}$ parameters entering Eq. (4.4)-(4.5) – whose values are generally given in best-fit plots such as the present ones in Fig.(4.1) – should in fact be understood as being,

$$\epsilon_t c_t \; = \; \frac{\text{sign}(m_t)}{\text{sign}(m_t^{\rm EF})}\, c_t \; = \; \frac{\text{sign}(m_t)}{\text{sign}(m_t^{\rm EF})}\,\frac{\text{sign}(-Y_t^{\rm EF})}{\text{sign}(-Y_t)}\,|c_t| \; = \; \frac{\text{sign}(-Y_t^{\rm EF})}{\text{sign}(m_t^{\rm EF})}\,|c_t| \; = \; \text{sign}\left(\frac{-Y_t^{\rm EF}}{m_t^{\rm EF}}\right)\left|\frac{Y_t^{\rm EF}}{Y_t}\right| ,$$

in our conventions of Lagrangian (4.1), and similarly for $\epsilon_{b,\tau} c_{b,\tau}$; here the EF-exponent indicates that the parameter is considered within the context of an EF model (and remind that m_t, Y_t are in the SM). Therefore, the *dysfermiophilia* property of increasing, $\Gamma_{\rm h\to\gamma\gamma}/\Gamma^{\rm SM}_{\rm h\to\gamma\gamma}$, via changing the top Yukawa sign is in fact relying on the possibility to have, $\epsilon_t c_t < 0$, or equivalently, $\text{sign}(-Y_t^{\rm EF}/m_t^{\rm EF}) < 0$. This makes sense as it is the sign of, $-Y_t^{\rm EF}/m_t^{\rm EF}$, which has a physical meaning and appears in $\Gamma_{\rm h\to\gamma\gamma}$ [see Eq. (4.8) for an analogy with the t'-loop].
The other comment is that the *dysfermiophilia* possibility of having, $\epsilon_t c_t < 0$, can indeed gives rise to an acceptable agreement with the Higgs data (see *e.g.* Fig.(4.1)[d]) but it is not necessary to achieve a good agreement (*c.f.* Fig.(4.4) where $\epsilon_t c_t = 1$) since the constructive interference with the $W^{\pm}$-loop increasing the diphoton rates can be realized with an EF-loop inducing, $c_{\gamma\gamma} < 0$.
Hence the above condition (4.13) can be called an *extra-dysfermiophilia* as it is exactly the same as for the top quark transposed to an EF. Besides, this condition (4.13) leads to a decrease of, $\sigma_{\rm gg\to h}/\sigma^{\rm SM}_{\rm gg\to h}$, for a single EF [see Eq. (4.7)] through negative c_{gg} values [*c.f.* Fig.(4.4)]. Generally

speaking, an *extra-dysfermiophilia* is probably easier to realize than a *dysfermiophilia* due to the potentially higher degree of freedom (allowing to de-correlate EF masses and Yukawa couplings) which can come *e.g.* from additional mass terms not induced by EW symmetry breaking, like KK masses.

4.5 Conclusions

We have learnt from varying the effective parameters of the Higgs rate fit that shifts of the correction factor affecting the top quark Yukawa coupling, c_t, lead to translations of the best-fit domains in the $\{c_{\gamma\gamma}, c_{gg}\}$ plane ($c_{\gamma\gamma}$ and c_{gg} parametrize respectively new loop-contributions to the $h\gamma\gamma$ and hgg vertex) proportional to δc_t. This means that to constrain precisely the new loop-contributions to the hgg and $h\gamma\gamma$ couplings, one has to determine simultaneously the top Yukawa coupling which might be an experimental challenge.
The c_{gg} determination relies as well significantly on the correction factor affecting the bottom quark Yukawa coupling, namely c_b, for which extremely large values are not ruled out by the combination of present Higgs data; for that purpose, new Higgs reactions, like $gg \to h\bar{b}b$, $h \to \bar{b}b$, would be interesting to investigate experimentally.

We have then considered the effective case of a single EF affecting the Higgs rates. It could for example be the lightest KK mode of some higher-dimensional theory and have dominant effects on collider physics; the lightest KK state effects are generically at least the strongest ones so assuming this state to be the sole one is quantitatively a good (starting) approximation. In contrast, within theories containing several crucial EF, one could of course combine the (different) single EF effects described here and there could be compensations.
In this basic single EF framework, significant constraints have been placed on extra-leptons. We have also found that the Higgs rate measurements put non-trivial constraints on $c_{\gamma\gamma}$ and c_{gg} for b', t' states able to mix with the SM b, t quarks. Regarding unmixed EF candidates [still with same color number as SM quarks], it is remarkable that, due to the $c_{\gamma\gamma} - c_{gg}$ correlations, the Higgs fit can potentially constrain intervals of absolute electric charges independently of the $SU(2)_L$ representations, Yukawa couplings and masses for the EF. Another related result is that, among any possible components of SM quark multiplet extensions, the $q_{-7/3}$ field is the one preferred by the fit. The Higgs rate fit also allows to constrain significantly the EF Yukawa couplings for $m_{q'}$ values up to ~ 200 TeV, and, points out at 68.27%C.L. an *extra-dysfermiophilia* [condition (4.13)] for any single q' quark (independently of $Q_{q'}$ as long as it does not approach non-perturbative couplings).

Finally, let us note that any model with EF predicts certain values for the parameters, c_t, c_b, c_τ (c_τ : correction factor for the τ-lepton Yukawa coupling) and $c_{\gamma\gamma}$, c_{gg} [easily calculable through Eq. (4.7)-(4.8)], which can then be located on the best-fit plots obtained in this study in order to determine the degree of compatibility with the Higgs data. Anyone could also use the synthesized fit

informations contained in Fig.(4.4) to constrain one's extra-quark electric charge, and, in Fig.(4.5) to study the $\{|m_{f'}|, \tilde{Y}_{f'}\}$ plane of one's single f' model.

In the Appendix A, we present updated numerical results for the Higgs fits.

Bibliography

[1] F. Gianotti, CERN Seminar, *Update on the Standard Model Higgs searches in ATLAS*, July, 4, 2012, `http://indico.cern.ch/conferenceDisplay.py?confId=197461`.

[2] J. Incandela, CERN Seminar, *Update on the Standard Model Higgs searches in CMS*, July, 4 2012, `http://indico.cern.ch/conferenceDisplay.py?confId=197461`.

[3] F. Englert and R. Brout, Phys.Rev.Lett. **13**, 321 (1964).

[4] P. W. Higgs, Phys.Lett. **12**, 132 (1964a).

[5] P. W. Higgs, Phys.Rev.Lett. **13**, 508 (1964b).

[6] G. Guralnik, C. Hagen, and T. Kibble, Phys.Rev.Lett. **13**, 585 (1964).

[7] ATLAS web page, `https://twiki.cern.ch/twiki/bin/view/AtlasPublic`.

[8] CMS web page, `https://twiki.cern.ch/twiki/bin/view/CMSPublic/PhysicsResults`.

[9] M. S. Carena, E. Ponton, J. Santiago, and C. E. M. Wagner, Nucl.Phys. **B759**, 202 (2006), arXiv:hep-ph/0607106.

[10] M. Gogberashvili, Int.J.Mod.Phys. **D11**, 1635 (2002), arXiv:hep-ph/9812296.

[11] L. Randall and R. Sundrum, Phys.Rev.Lett. **83**, 3370 (1999), arXiv:hep-ph/9905221.

[12] T. Gherghetta and A. Pomarol, Nucl.Phys. **B586**, 141 (2000), arXiv:hep-ph/0003129.

[13] S. J. Huber and Q. Shafi, Phys.Lett. **B498**, 256 (2001a), arXiv:hep-ph/0010195.

[14] S. J. Huber and Q. Shafi, Phys.Lett. **B512**, 365 (2001b), arXiv:hep-ph/0104293.

[15] S. J. Huber and Q. Shafi, Phys.Lett. **B544**, 295 (2002), arXiv:hep-ph/0205327.

[16] S. J. Huber and Q. Shafi, Phys.Lett. **B583**, 293 (2004), arXiv:hep-ph/0309252.

[17] S. Chang, C. Kim, and M. Yamaguchi, Phys.Rev. **D73**, 033002 (2006), arXiv:hep-ph/0511099.

[18] G. Moreau and J. Silva-Marcos, JHEP **0603**, 090 (2006a), arXiv:hep-ph/0602155.

[19] G. Moreau and J. Silva-Marcos, JHEP **0601**, 048 (2006b), arXiv:hep-ph/0507145.

[20] K. Agashe, G. Perez, and A. Soni, Phys.Rev. **D71**, 016002 (2005a), arXiv:hep-ph/0408134.

[21] K. Agashe, G. Perez, and A. Soni, Phys.Rev.Lett. **93**, 201804 (2004), arXiv:hep-ph/0406101.

[22] K. Agashe, G. Perez, and A. Soni, Phys.Rev. **D75**, 015002 (2007), arXiv:hep-ph/0606293.

[23] K. Agashe, A. E. Blechman, and F. Petriello, Phys.Rev. **D74**, 053011 (2006a), arXiv:hep-ph/0606021.

[24] F. del Aguila, J. Aguilar-Saavedra, B. Allanach, J. Alwall, Y. Andreev, et al., Eur.Phys.J. **C57**, 183 (2008), arXiv:0801.1800[hep-ph].

[25] M. Raidal, A. van der Schaaf, I. Bigi, M. Mangano, Y. K. Semertzidis, et al., Eur.Phys.J. **C57**, 13 (2008), arXiv:0801.1826[hep-ph].

[26] Y. Grossman and M. Neubert, Phys.Lett. **B474**, 361 (2000), arXiv:hep-ph/9912408.

[27] T. Appelquist, B. A. Dobrescu, E. Ponton, and H.-U. Yee, Phys.Rev. **D65**, 105019 (2002), arXiv:hep-ph/0201131.

[28] T. Gherghetta, Phys.Rev.Lett. **92**, 161601 (2004), arXiv:hep-ph/0312392.

[29] G. Moreau, Eur.Phys.J. **C40**, 539 (2005), arXiv:hep-ph/0407177.

[30] C. Bouchart, A. Knochel, and G. Moreau, Phys.Rev. **D84**, 015016 (2011), arXiv:1101.0634[hep-ph].

[31] F. Goertz, U. Haisch, and M. Neubert, Phys.Lett. **B713**, 23 (2012), arXiv:1112.5099[hep-ph].

[32] D. B. Kaplan and H. Georgi, Phys.Lett. **B136**, 183 (1984).

[33] D. B. Kaplan, H. Georgi, and S. Dimopoulos, Phys.Lett. **B136**, 187 (1984).

[34] R. Contino, Y. Nomura, and A. Pomarol, Nucl.Phys. **B671**, 148 (2003), arXiv:hep-ph/0306259.

[35] K. Agashe, R. Contino, and A. Pomarol, Nucl.Phys. **B719**, 165 (2005b), arXiv:hep-ph/0412089.

[36] R. Contino, L. Da Rold, and A. Pomarol, Phys.Rev. **D75**, 055014 (2007), arXiv:hep-ph/0612048.

[37] G. Burdman and L. Da Rold, JHEP **0712**, 086 (2007), arXiv:0710.0623[hep-ph].

[38] L. Da Rold, JHEP **1102**, 034 (2011), arXiv:1009.2392[hep-ph].

[39] A. Azatov and J. Galloway, Phys.Rev. **D85**, 055013 (2012), arXiv:1110.5646[hep-ph].

[40] C. T. Hill, Phys.Lett. **B266**, 419 (1991).

[41] A. Pomarol and J. Serra, Phys.Rev. **D78**, 074026 (2008), arXiv:0806.3247[hep-ph].

[42] N. Arkani-Hamed, A. G. Cohen, and H. Georgi, Phys. Lett. **B513**, 232 (2001), arXiv:hep-ph/0105239.

[43] N. Arkani-Hamed et al., JHEP **08**, 021 (2002a), arXiv:hep-ph/0206020.

[44] N. Arkani-Hamed, A. Cohen, E. Katz, and A. Nelson, JHEP **0207**, 034 (2002b), arXiv:hep-ph/0206021.

[45] K. Ishiwata and M. B. Wise, Phys.Rev. **D84**, 055025 (2011), arXiv:1107.1490[hep-ph].

[46] C. Kilic, K. Kopp, and T. Okui, Phys.Rev. **D83**, 015006 (2011), arXiv:1008.2763[hep-ph].

[47] V. Barger, M. Ishida, and W.-Y. Keung (2012), arXiv:1203.3456[hep-ph].

[48] I. Low, J. Lykken, and G. Shaughnessy (2012), arXiv:1207.1093[hep-ph].

[49] T. Corbett, O. Eboli, J. Gonzalez-Fraile, and M. Gonzalez-Garcia (2012), arXiv:1207.1344[hep-ph].

[50] P. P. Giardino, K. Kannike, M. Raidal, and A. Strumia (2012a), arXiv:1203.4254[hep-ph].

[51] P. P. Giardino, K. Kannike, M. Raidal, and A. Strumia (2012b), arXiv:1207.1347[hep-ph].

[52] J. Ellis and T. You (2012a), arXiv:1204.0464[hep-ph].

[53] J. Ellis and T. You (2012b), arXiv:1207.1693[hep-ph].

[54] A. Azatov, R. Contino, and J. Galloway, JHEP **1204**, 127 (2012a), arXiv:1202.3415[hep-ph].

[55] A. Azatov, R. Contino, D. Del Re, J. Galloway, M. Grassi, et al. (2012b), arXiv:1204.4817[hep-ph].

[56] M. Montull and F. Riva (2012), arXiv:1207.1716[hep-ph].

[57] J. Espinosa, C. Grojean, M. Muhlleitner, and M. Trott, JHEP **1205**, 097 (2012a), arXiv:1202.3697[hep-ph].

[58] J. Espinosa, C. Grojean, M. Muhlleitner, and M. Trott (2012b), arXiv:1207.1717[hep-ph].

[59] D. Carmi, A. Falkowski, E. Kuflik, T. Volansky, and J. Zupan (2012), arXiv:1207.1718[hep-ph].

[60] S. Banerjee, S. Mukhopadhyay, and B. Mukhopadhyaya, JHEP **1210**, 062 (2012), arXiv:1207.3588[hep-ph].

[61] T. Plehn and M. Rauch (2012), arXiv:1207.6108[hep-ph].

[62] ATLAS Collaboration (2012a), NoteCONF-2012-127.

[63] K. Agashe, A. Delgado, M. J. May, and R. Sundrum, JHEP **0308**, 050 (2003), arXiv:hep-ph/0308036.

[64] K. Agashe, R. Contino, L. Da Rold, and A. Pomarol, Phys.Lett. **B641**, 62 (2006b), arXiv:hep-ph/0605341.

[65] A. Djouadi, G. Moreau, and F. Richard, Nucl.Phys. **B773**, 43 (2007), arXiv:hep-ph/0610173.

[66] M. S. Carena, E. Ponton, J. Santiago, and C. E. M. Wagner, Phys.Rev. **D76**, 035006 (2007), arXiv:hep-ph/0701055.

[67] A. Djouadi, G. Moreau, and R. K. Singh, Nucl.Phys. **B797**, 1 (2008), arXiv:0706.4191[hep-ph].

[68] A. Djouadi and G. Moreau, Phys.Lett. **B660**, 67 (2008), arXiv:0707.3800[hep-ph].

[69] F. Ledroit, G. Moreau, and J. Morel, JHEP **0709**, 071 (2007), arXiv:hep-ph/0703262.

[70] C. Bouchart and G. Moreau, Nucl.Phys. **B810**, 66 (2009a), arXiv:0807.4461[hep-ph].

[71] C. Bouchart and G. Moreau, Phys.Rev. **D80**, 095022 (2009b), arXiv:0909.4812[hep-ph].

[72] A. Djouadi, G. Moreau, F. Richard, and R. K. Singh, Phys.Rev. **D82**, 071702 (2010), arXiv:0906.0604[hep-ph].

[73] S. Casagrande, F. Goertz, U. Haisch, M. Neubert, and T. Pfoh, JHEP **1009**, 014 (2010), arXiv:1005.4315[hep-ph].

[74] A. Djouadi, G. Moreau, and F. Richard, Phys.Lett. **B701**, 458 (2011), arXiv:1105.3158[hep-ph].

[75] F. del Aguila, M. Perez-Victoria, and J. Santiago, JHEP **0302**, 051 (2003), arXiv:hep-th/0302023.

[76] J. A. Cabrer, G. von Gersdorff, and M. Quiros, JHEP **1201**, 033 (2012), arXiv:1110.3324[hep-ph].

[77] S. Dawson and E. Furlan, Phys.Rev. **D86**, 015021 (2012), arXiv:1205.4733[hep-ph].

[78] M. Carena, I. Low, and C. E. Wagner, JHEP **1208**, 060 (2012a), arXiv:1206.1082[hep-ph].

[79] A. Azatov, O. Bondu, A. Falkowski, M. Felcini, S. Gascon-Shotkin, et al., Phys.Rev. **D85**, 115022 (2012c), arXiv:1204.0455[hep-ph].

[80] N. Bonne and G. Moreau, Phys.Lett. **B717**, 409 (2012), arXiv:1206.3360[hep-ph].

[81] A. Joglekar, P. Schwaller, and C. E. Wagner (2012), arXiv:1207.4235[hep-ph].

[82] J. Kearney, A. Pierce, and N. Weiner (2012), arXiv:1207.7062[hep-ph].

[83] M. Voloshin (2012), arXiv:1208.4303[hep-ph].

[84] B. Batell, S. Gori, and L.-T. Wang (2012), arXiv:1209.6382[hep-ph].

[85] N. Arkani-Hamed, K. Blum, R. T. D'Agnolo, and J. Fan (2012), arXiv:1207.4482[hep-ph].

[86] L. G. Almeida, E. Bertuzzo, P. A. Machado, and R. Z. Funchal (2012), arXiv:1207.5254[hep-ph].

[87] A. Djouadi, Phys.Rept. **457**, 1 (2008), arXiv:hep-ph/0503172.

[88] K. Nakamura et al. (Particle Data Group), J.Phys. **G37**, 075021 (2010).

[89] G. Cacciapaglia, A. Deandrea, and J. Llodra-Perez, JHEP **0906**, 054 (2009), arXiv:0901.0927[hep-ph].

[90] G. Cacciapaglia, A. Deandrea, D. Harada, and Y. Okada, JHEP **1011**, 159 (2010), arXiv:1007.2933[hep-ph].

[91] G. Cacciapaglia, A. Deandrea, L. Panizzi, N. Gaur, D. Harada, et al., JHEP **1203**, 070 (2012), arXiv:1108.6329[hep-ph].

[92] LHC Higgs Cross Section Working Group, webpage `https://twiki.cern.ch/twiki/bin/view/LHCPhysics/CrossSections`.

[93] C. Group, D. Collaborations, the Tevatron New Physics, and H. Working (Tevatron New Physics Higgs Working Group, CDF Collaboration, D0 Collaboration) (2012), arXiv:1207.0449[hep-ex].

[94] ATLAS Collaboration (2012b), NoteCONF-2012-091.

[95] CMS Collaboration (2012a), NotePASHIG-12-015.

[96] S. Chatrchyan et al. (CMS Collaboration), Phys.Lett. **B716**, 30 (2012a), arXiv:1207.7235[hep-ex].

[97] G. Aad et al. (ATLAS Collaboration), Phys.Lett. **B716**, 1 (2012), arXiv:1207.7214[hep-ex].

[98] ATLAS Collaboration (2012c), NoteCONF-2012-093.

[99] CMS Collaboration (2012b), NotePASHIG-12-020.

[100] ATLAS Collaboration (2012d), NoteCONF-2012-019.

[101] ATLAS Collaboration (2012e), NoteCONF-2012-098.

[102] S. Dawson and P. Jaiswal, Phys.Rev. **D81**, 073008 (2010), arXiv:1002.2672[hep-ph].

[103] M. Carena, S. Gori, A. Juste, A. Menon, C. E. Wagner, et al., JHEP **1207**, 091 (2012b), arXiv:1203.1041[hep-ph].

[104] S. Chatrchyan et al. (CMS Collaboration), JHEP **1205**, 123 (2012b), arXiv:1204.1088[hep-ex].

[105] XLVIIIth "Rencontres de Moriond", Session devoted to ELECTROWEAK INTERACTIONS AND UNIFIED THEORIES, March 2nd - 16th, 2013, La Thuile, Italy.

[106] ATLAS Collaboration (2013a), NoteCONF-2013-012.

[107] ATLAS Collaboration (2013b), NoteCONF-2013-013.

[108] ATLAS Collaboration (2013c), NoteCONF-2013-030.

[109] ATLAS Collaboration (2012f), NoteCONF-2012-170.

[110] ATLAS Collaboration (2012g), NoteCONF-2012-160.

[111] ATLAS Collaboration (2013d), NoteCONF-2013-014.

[112] ATLAS Collaboration (2013e), NoteCONF-2013-034.

[113] C. Ochando, Talk [on behalf of the CMS Collaboration] at the Moriond Conference [105] (2013).

[114] CMS Collaboration (2013a), NotePASHIG-13-002.

[115] CMS Collaboration (2013b), NotePASHIG-13-003.

[116] CMS Collaboration (2012c), NotePASHIG-12-045.

[117] CMS Collaboration (2013c), NotePASHIG-13-004.

Chapter 5

Producing the Higgs boson via vector-like top-partner decays

Adapted from: *A. Azatov, O. Bondu, A. Falkowski, M. Felcini, S. Gascon-Shotkin, D. K. Ghosh, G. Moreau, A. Y. Rodriguez-Marrero and S. Sekmen*, Phys. Rev. **D85** (2012) 115022.

5.1 Introduction

One of the primary goals of the Large Hadron Collider (LHC) was the direct search for the cornerstone of the Standard Model (SM), namely the Higgs boson, or for any signal from alternative Electro-Weak Symmetry Breaking (EWSB) mechanisms. The SM is probably not the ultimate model of nature. It is clear that new channels for Higgs production, that can arise in extensions of the SM, would have profound impact on the physics of the Higgs boson sector, while providing insight in the physics beyond the SM. An attractive possibility is the Higgs production in decays of additional heavy colored particles that can be copiously pair produced at the LHC via strong interactions.

Within well-motivated theories beyond the SM, there are some candidates for such new heavy colored states, extra quarks with vector-like couplings, whose existence is predicted by most of the alternatives to supersymmetry. In this context, to maintain a naturally light Higgs boson, divergent quantum corrections from loops of the top quark are often canceled by top-partner contributions [1–3]. Let us describe important examples here. In the so-called little Higgs scenarios, the vector-like quarks arise as partners of the SM fields being promoted to larger multiplets. In the composite Higgs [4–8] and composite top [4–9] models, the vector-like quarks are excited resonances of the bounded states constituting the SM particles. In the extra-dimensional models with (SM) quarks in the bulk, the vector-like quarks are prevalent as Kaluza-Klein (KK) excitations of those bulk fields [10] like in the Gauge-Higgs unification mechanism (see e.g. Ref. [11, 12]) or in the Randall-

Sundrum (RS) scenario [13–15] – where some of those KK excitations, the so-called custodians, can be as light as a few hundred's of GeV [16–21]. Another example is a gauge coupling unification theory where vector-like quarks are embedded into the simplest SU(5) representations [22].

Vector-like quarks with same electric charge as the up-type quarks are often called top-partners (noted t') as these new heavy states mix in general predominantly with the top quark – due to the large top mass and to the related feature that the top quark is in general more intimately connected to ultraviolet physics, like e.g. in composite Higgs models. A t' can also be called a top-partner in the sense that it is contained in the same group representation as the top quark with respect to symmetries, like the approximate global symmetry of the little Higgs models [1–3], the gauge unification symmetry [22] or the custodial symmetry of RS versions with bulk matter [16–21] (explaining the SM fermion mass hierarchies [23–39]).

At this level, one must mention that the phenomenology of the search for direct production of vector-like quarks at the LHC has been studied from a model-independent point of view in Ref. [40–45] but also in specific frameworks such as the little Higgs models (versions sufficiently safe from EW precision constraints) [46–50] or the composite Higgs hypothesis [51, 52] and the dual RS context [11, 53–58]. These past searches focus generally on the discovery of the vector-like quarks, rather than using these extra quarks to enhance the discovery and identification potential for other unknown particles such as Higgs scalars.

In relation to Higgs detection, there exist studies utilizing the possible Higgs production through vector-like quark decays, as described in the following. Indeed, it is well known since some time [59, 60] that vector-like quark production could be a copious source of Higgs bosons (a possible Higgs factory).
Relatively light Higgs bosons produced from the decay of top-partners can be highly boosted and good candidates for analyses based on jet substructure. This method has been applied [61] for a ∼130 GeV Higgs decaying to $b\bar{b}$ at the 14 TeV LHC to improve the Higgs identification capability and reduce the background. In the simple model considered there, the t' is a singlet under the $SU(2)_L$ gauge group, which determines the t' couplings and its tree level decays into the Higgs boson and the two EW gauge bosons $t' \to th$, $t' \to tZ$, $t' \to bW$.
The top-partner can also be singly produced which leads to different final states as compared to the pair production; because of the phase space suppression, the single production becomes competitive with the pair production at a high t' mass, depending upon the considered model (since the involved t' couplings to $h, Z^0, W^\pm$ are fixed by the t' quantum numbers) [1]. The reconstruction of the Higgs boson produced in the t' decay, itself singly produced at the 14 TeV LHC, was studied in Ref. [62] assuming the Higgs mass known (to be 120 GeV) and focusing on the channel $h \to b\bar{b}$ – with the combinatorial background only. This was performed for a singlet t' in the "Littlest Higgs" model with the asymptotic branching ratio values of the high $m_{t'}$ regime: $B_{t' \to th} = 25\%$, $B_{t' \to tZ} = 25\%$,

[1] The single production becomes dominant typically around $m_{t'} \sim 700$ GeV as in the scenario with a singlet t' [43] or in little Higgs models [62].

$B_{t' \to bW} = 50\%$ (from the EW equivalence theorem).
Similarly, a vector-like colored b' state produced at the 14 TeV LHC can act as a Higgs factory thanks to its decay $b' \to bh$. It was shown [22] that a Higgs mass reconstruction can be obtained with a limited accuracy, concentrating on the decay $h \to WW$ ($W \to l\nu$) for $m_h = 200$ GeV and assuming the $m_{b'}$ value to be deduced from a preliminary analysis based on the more appropriate channel $b' \to bZ$. Theoretically, the b' was originating from the upper component of a $\mathrm{SU(2)_L}$ doublet so there was no significant channel $b' \to tW$.
Higgs mass reconstructions via t' and b' decays were also studied for the 14 TeV LHC, based on a light Higgs decaying to $b\bar{b}$ in the basic models with a unique extra t' and/or a unique extra b' [44].

In the present study, we use the pair production and decay of a vector-like top to develop new search strategies for Higgs boson discovery and mass measurements in the $h \to \gamma\gamma$ (diphoton) and $h \to ZZ$ channels. We consider t' masses up to ~ 800 GeV, so that the t' single productions (involving a model-dependent coupling) are generally subleading compared to the t' pair production not yet significantly suppressed by phase space factors [2]. The original theoretical and illustrative model considered here, including two top-partners, is constructed to allow interesting interpretations correlating the indirect (via vector-like top decay) and direct Higgs production searches at the LHC, as described in the following. A few characteristic parameter sets – with vector-like top mass in the range between ~ 400 and 800 GeV – are chosen as benchmark points avoiding too large t' contributions to the Higgs rates (constrained by present LHC data) and simultaneously allowing for significant branching fraction values ($\gtrsim 10\%$) of the vector-like top decay to the Higgs boson.
Assuming the presence at low-energy scales only of extra vector-like quark multiplets containing some t', we have elaborated a minimal model allowing to strongly suppress the Higgs production via gluon fusion, as compared to the SM. In this simple but non-trivial model, the $gg \to h$ cross section suppression factor possibly reaches values below 10^{-1} at hadron colliders; this is to be put in contrast with the t' representations taken usually in the RS scenario [21,63–66] [3] and with minimal supersymmetric theories for which such a suppression is not possible to obtain (see respectively Ref. [21, 63] and Ref. [67]). The chiral case of a fourth quark generation can even only increase considerably the gluon fusion rate.
The illustrative minimal t' model suggested here is interesting in the sense that it can easily lead to the following interpretations: for example, a 255 GeV Higgs is excluded in the SM by the present LHC results [68,69] but can still exist in the above minimal SM extension with t' where the reduced Higgs production cross section can be below the LHC upper limits. In other words, the Higgs boson would really be light but not detectable with the present luminosity/energy, via conventional channels. A channel that could then allow the Higgs discovery would be through the t' pair production and decays, as illustrated in this study. Another possibility is that the slight excess of events observed in data for a Higgs mass hypothesis of ∼125 GeV [70, 71] is confirmed by the 2012

[2] Note that adding the contribution of the t' single production would increase the Higgs production rate.
[3] t' representations (to which SM fields are promoted) with analog rate suppression effects can arise with the O(3) subgroup [20] implementable in the composite Higgs model [93, 94] and RS scenario [95, 96] which can reach strong suppressions, respectively of $\sigma_{\mathrm{gg}\to\mathrm{h}}/\sigma^{\mathrm{SM}}_{\mathrm{gg}\to\mathrm{h}} \sim 35\%$ and $\sim 10\%$.

searches at the LHC. Then the measured Higgs production cross section times branching ratios could certainly be reproduced by the present t' model, given the parameter freedom in this model and its capability of inducing large Higgs rate corrections of both signs. Then investigating this additional Higgs production channel as the t' decay, as discussed here, would of course be relevant in particular to confirm the Higgs existence. Finally, in the case of a signal from a heavy Higgs, say above 500 GeV [4] as we will consider here, the same fit of Higgs data would be instructive as a test of the present t' model and similarly the t' decay should be considered as a complementary channel of Higgs production.

5.2 The theoretical model

At low scale, let us assume the presence of a unique additional vector-like quark multiplet including a t' component. Then, irrespective of the representation of this multiplet under the $\mathrm{SU(2)_L}$ gauge group (i.e. the t' belongs to a singlet, doublet,...), the interferences between the next heavier top mass eigenstate t_2 [composed of t, t', t''] and the t_1 [$\equiv$ the physical top quark whose mass is measured] contributions [5] to the triangular loop of the gluon-gluon fusion mechanism will be systematically constructive. This is due to the fact that the physical signs of the Yukawa coupling and mass insertion involved in this loop – two chirality flips are necessary – will be systematically identical giving rise to a positive product (for t_1 as well as for t_2). Hence, the cross section of the gluon fusion mechanism may be increased or slightly decreased (because of a possible t Yukawa coupling reduction) relatively to the SM case.
To get the minimal scenario with only additional vector-like quark multiplets including t' components able to strongly suppress the gluon fusion, one needs to introduce a first top-partner t' in a $\mathrm{SU(2)_L}$ doublet as well as a second top-partner t'' in a gauge singlet. For simplification, we do not consider the doublet including a b' [6] that would also be exchanged in the triangular loop. So we end up with the doublet $(q_{5/3}, t')$, $q_{5/3}$ being an exotic quark with electric charge 5/3 and without self-Yukawa coupling (in turn no possible loop exchange). Indeed, with this field content, all the possible generic mass terms and Yukawa couplings appearing in the Lagrangian are,

$$\begin{aligned}\mathcal{L}_{\text{Yuk.}} = {} & Y\overline{\begin{pmatrix} t \\ b \end{pmatrix}}_L H^\dagger t^c_R + Y'\overline{\begin{pmatrix} q_{5/3} \\ t' \end{pmatrix}}_L H t^c_R + Y''\overline{\begin{pmatrix} q_{5/3} \\ t' \end{pmatrix}}_{L/R} H t''_{R/L} + \tilde{Y}\overline{\begin{pmatrix} t \\ b \end{pmatrix}}_L H^\dagger t''_R \\ & + Y_b\overline{\begin{pmatrix} t \\ b \end{pmatrix}}_L H b^c_R + m\ \bar{t}''_L t^c_R + m'\overline{\begin{pmatrix} q_{5/3} \\ t' \end{pmatrix}}_L \begin{pmatrix} q_{5/3} \\ t' \end{pmatrix}_R + m''\ \bar{t}''_L t''_R + \text{H.c.} \end{aligned} \tag{5.1}$$

[4] Such a heavy Higgs would be neither SM-like, as disfavored by the EW precision tests, nor belonging to a supersymmetric extension, as forbidden by the Higgs sector structure. However, it could perfectly be e.g. in a RS scenario where its contributions to the oblique T parameter can be compensated by new KK-induced contributions.
[5] The top quark exchange in the loop is the dominant contribution in the SM.
[6] Similar results are expected in such a situation.

where H represents the SM Higgs doublet and L/R the fermion chiralities. By construction, the vector-like quarks possess same quantum numbers and gauge group representations for the left-handed and right-handed states. We have not written the Yukawa couplings for the first two quark generations as their mixings with the top-partners t', t'' are negligible compared to the t-t'-t'' mixing and the CKM mixing angles are typically small, so that the first two quark generations are decoupled from b, t, t', t''. Note that a field redefinition rotating t^c_R and t''_R can allow to eliminate the m term without loss of generality. A last remark is that the Y'' term could be split in two terms with different chiralities and coupling constants. The Lagrangian (5.1) gives rise, after EWSB, to this top mass matrix:

$$\mathcal{L}_{\text{mass}} = \overline{\begin{pmatrix} t \\ t' \\ t'' \end{pmatrix}}_L \begin{pmatrix} Yv & 0 & \tilde{Y}v \\ Y'v & m' & Y''v \\ m & Y''v & m'' \end{pmatrix} \begin{pmatrix} t^c \\ t' \\ t'' \end{pmatrix}_R + \text{H.c.} \tag{5.2}$$

with $v \simeq 174$ GeV the SM vacuum expectation value of the Higgs boson. In our notations of Eq.(5.2), the parameters Y, Y', Y'' and $\tilde{Y}$ contain the whole sign (i.e. the combination of the SU(2)_L contraction signs and Yukawa coupling constant signs). Note that vector-like fermions do not require EWSB to acquire mass. The non-trivial consequence of the present t', t'' charge assignment choice is the presence of Yukawa terms in the block diagonal matrix of Eq.(5.2) associated to the top-partners [7] (such Yukawa matrix elements would be absent in the first case of a unique top-partner). This feature of the mass structure allows strong suppressions of the gluon fusion mechanism. In particular, the own top-partner (t', t'') Yukawa coupling (Y'') sign can be chosen independently of the top (t) Yukawa coupling (Y) sign in order to generate destructive interferences between the top and top-partner loops.

5.3 t_2 rates and direct constraints

We consider here the model described in the previous section, where t', t'' denote the states in the interaction basis while t_1, t_2 and t_3 stand for the mass eigenstates, with $m_{t_3} > m_{t_2} > m_{t_1}$, t_1 being the standard top quark and m_{t_1} its physical mass. We concentrate on the phenomenology of the next-to-lightest top mass eigenstate t_2; the t_3 eigenstate production is sub-dominant given its larger mass. In a second stage, one could add the contributions to the Higgs production from the t_3 decays like $t_3 \to t_1 h$ or $t_3 \to t_2 Z$.

In Table 5.1, we define our benchmark points by the values of the fundamental parameters – including the Higgs mass m_h – and the corresponding m_{t_2}, m_{t_3} values. These sets of parameters are selected in particular to have a large branching fraction $B_{t_2 \to t_1 h}$ enhancing the studied Higgs signal. Note that in the minimal model with a unique doublet $(q_{5/3}, t')$, $B_{t_2 \to bW}$ is negligible compared to

[7] Namely the last two lines and columns of this mass matrix.

$B_{t_2\to t_1 h}$ and $B_{t_2\to t_1 Z}$ [44]. For none of the considered benchmark points, the channel $t_2 \to q_{5/3}W$ is open. Table 5.1 also provides the theoretical t_2 widths and the $\sigma_{\bar{t}_2 t_2}$ cross sections for the t_2 pair production at LHC computed with the HATHOR program [72] at NNLO. As a comparison, we give also in Table 5.1 the expected SM cross sections [73] for Higgs production via gluon fusion, $\sigma^{\rm SM}_{\rm gg\to h}$. It is physically important to note that the branching ratios $B_{t_2\to t_1 h}$ and $B_{t_2\to t_1 Z}$ are not vanishing in contrast with the case of a fourth generation t' quark so that the observation of such decays (discussed in Section 5.6) would even prove the vector-like nature of a heavy top-like quark.

Table 5.1 presents finally the CMS constraints on the observables $\sigma_{\bar{t}_2 t_2} B^2_{t_2}$ derived from the search for pair production of a heavy top-like quark [68, 74, 75] (present bounds from ATLAS are less stringent [69,76]). It appears that the corresponding theoretical values, predicted in the models considered here, respect those experimental limits for m_{t_2} as low as $\sim$ 400 GeV [8]. Increasing theoretically $B_{t_2\to t_1 h}$, and consequently lowering $B_{t_2\to t_1 Z}$ and $B_{t_2\to bW}$, is allowed within these constraints.

Due to these lower limits on m_{t_2} typically around 400 GeV, the t_2 pair production suffers from a significant phase space suppression so that the whole rate for a single Higgs production through the t_2 decay is smaller than for the standard gluon fusion mechanism; there is e.g. a factor of ~ 10 for point A1 at 14 TeV, as shown the Table 5.1. However, the number of Higgs events issued from the t_2 decay can be significant at 14 TeV with suitable luminosities. This Higgs production channel can thus be an interesting Higgs boson (and t_2) discovery channel, among others, and especially in cases where the gluon fusion mechanism is suppressed by the presence of t', t'' states, as it occurs for instance with point B (see Table 5.1).

5.4 Constraints from the direct Higgs boson search

Sets **A1/A2** - At $m_h = 125$ GeV, all the sensitive channels for searching the Higgs boson at hadron colliders are the decays $h \to \gamma\gamma$, $h \to WW$ (with $W \to \ell\nu$), $h \to ZZ$ (with $Z \to \ell\bar{\ell}$), $h \to \tau\bar{\tau}$ and $h \to b\bar{b}$. At the time of this study, the bounds on the Higgs boson rates obtained at the LHC were, $\sigma_{\rm gg\to h} B_{\rm h\to\gamma\gamma}/\sigma^{\rm SM}_{\rm gg\to h} B^{\rm SM}_{\rm h\to\gamma\gamma} \lesssim 2$, $\sigma_{\rm gg\to h} B_{\rm h\to WW}/\sigma^{\rm SM}_{\rm gg\to h} B^{\rm SM}_{\rm h\to WW} \lesssim 1.30$, $\sigma_{\rm gg\to h} B_{\rm h\to ZZ}/\sigma^{\rm SM}_{\rm gg\to h} B^{\rm SM}_{\rm h\to ZZ} \lesssim 2.2$, $\sigma_{\rm gg\to h} B_{\rm h\to\tau\tau}/\ \sigma^{\rm SM}_{\rm gg\to h} B^{\rm SM}_{\rm h\to\tau\tau} \lesssim 3.2$ and $\sigma_{\rm gg\to h} B_{\rm h\to bb}/\sigma^{\rm SM}_{\rm gg\to h} B^{\rm SM}_{\rm h\to bb} \lesssim 3.2$ [68–71, 77, 78]. These bounds are compatible with the rates calculated taking into account the $t - t' - t''$ mixing effect on the top quark Yukawa coupling as well as the t_2 and t_3 eigenstate contributions in the triangular loop of the gluon fusion mechanism, for our parameter sets A1/A2. This parameter set yields indeed:

$$\sigma^{\rm t'}_{\rm gg\to h} B^{\rm t'}_{\rm h\to\gamma\gamma}/\sigma^{\rm SM}_{\rm gg\to h} B^{\rm SM}_{\rm h\to\gamma\gamma} = 1.16\ (1.19)\ \ ;\ \ \sigma^{\rm t'}_{\rm gg\to h} B^{\rm t'}_{\rm h\to WW}/\sigma^{\rm SM}_{\rm gg\to h} B^{\rm SM}_{\rm h\to WW} = 1.25\ (1.28) \qquad (5.3)$$

$$\sigma^{\rm t'}_{\rm gg\to h} B^{\rm t'}_{\rm h\to ZZ}/\sigma^{\rm SM}_{\rm gg\to h} B^{\rm SM}_{\rm h\to ZZ} = 1.25\ (1.28)\ \ ;\ \ \sigma^{\rm t'}_{\rm gg\to h} B^{\rm t'}_{\rm h\to\tau\tau}/\sigma^{\rm SM}_{\rm gg\to h} B^{\rm SM}_{\rm h\to\tau\tau} = 1.25\ (1.28) \qquad (5.4)$$

[8] We have also checked that the Tevatron constraints are satisfied.

Parameter Set	A1	A2	B	C	D
Y / $\tilde{Y}$	-1.43 / 2	1.02 / -0.1	1.15 / 0.4	1.12 / -0.5	1.05 / -0.3
Y' / Y''	1.85 / -1	1 / 0.55	-1.5 / 1.6	1.1 / 1.65	1.7 / 1.9
m / m' (GeV)	0 / 370	0 / 675	0 / 770	0 / 810	80 / 1100
m'' (GeV)	510	645	980	850	1100
m_{t_3} (GeV)	722	804	1181	1125	1454
m_{t_2} (GeV)	403	599	626	572	788
m_h (GeV)	125	125	255	320	540
$\sigma^{\rm SM}_{\rm gg\to h}$ (pb) @ 7 TeV	15.31	15.31	3.18	2.25	0.58
$\sigma^{\rm SM}_{\rm gg\to h}$ (pb) @ 14 TeV	49.85	49.85	13.50	10.59	3.85
$\sigma^{\rm t'}_{\rm gg\to h}/\sigma^{\rm SM}_{\rm gg\to h}$	1.27	1.31	0.45	0.40	0.65
$\sigma^{t'}_{\bar{t}_1 t_1 h}$ (pb) @ 7 TeV	0.0194	0.0760	0.0037	0.0016	$7\ 10^{-4}$
$\sigma^{t'}_{\bar{t}_1 t_1 h}$ (pb) @ 14 TeV	0.138	0.539	0.036	0.021	0.015
$\sigma_{\bar{t}_2 t_2}$ (pb) @ 7 TeV	1.361	0.0936	0.0709	0.1360	0.0115
$\sigma_{\bar{t}_2 t_2}$ (pb) @ 14 TeV	13.53	1.465	1.164	1.975	0.284
$B_{t_2\to t_1 h}$ (%)	62.6	82.1	60.8	13.5	43.0
$B_{t_2\to t_1 Z}$ (%)	28.6	14.7	25.0	46.1	40.3
$B_{t_2\to bW}$ (%)	8.8	3.2	14.2	40.4	16.6
Γ_{t_2} (GeV)	4.4	3.5	19.8	6.5	8.8
$\sigma_{\bar{t}_2 t_2} B^2_{t_2\to bW}$ (pb)	0.01	$9\ 10^{-5}$	0.001	0.022	0.000(3)
LHC bound [74]	< 0.26	< 0.14	< 0.14	< 0.16	$\times$
$\sigma_{\bar{t}_2 t_2} B^2_{t_2\to t_1 Z}$ (pb)	0.11	0.002	0.004	0.029	0.002
LHC bound [75]	< 0.5	< 0.4	< 0.4	< 0.4	$\times$
S / T	0.05 / 0.05	0.03 / 0.03	-0.01 / 0.23	-0.01 / 0.30	-0.01 / 0.28

Table 5.1: Benchmark scenarios in the present t', t'' model, defined by the values of the fundamental parameters, including the Higgs mass, m_h, and the resulting m_{t_2} and m_{t_3} physical masses of the heavy top-like quarks. The cross sections at NNLO, $\sigma_{\bar{t}_2 t_2}$, for the $pp \to \bar{t}_2 t_2$ process, are shown at $\sqrt{s} = 7$ TeV or 14 TeV, together with the t_2 widths Γ_{t_2} and the t_2 branching fraction values. For comparison, the SM Higgs production cross section values via gluon fusion are also given, together with the ratio $\sigma^{\rm t'}_{\rm gg\to h}/\sigma^{\rm SM}_{\rm gg\to h}$, between the gluon fusion cross section in the present model and in the SM. Furthermore, the NLO cross sections for Higgs production in association with a $\bar{t}t$ pair, $\sigma^{t'}_{\bar{t}_1 t_1 h}$, in the present model, are shown for comparison with the $\sigma_{\bar{t}_2 t_2}$ cross sections [the $\sigma^{t'}_{\bar{t}_1 t_1 h}$ values are too small to contribute to the signal, analyzed in this study, from $\bar{t}_2 t_2$ production, with $t_2 \to th$ decay]. Finally, the LHC upper limits and theoretical predictions for the observables $\sigma_{\bar{t}_2 t_2} B^2_{t_2\to bW}$, $\sigma_{\bar{t}_2 t_2} B^2_{t_2\to t_1 Z}$ are shown just above the last line (the crosses indicate the absence of experimental limit at the associated m_{t_2} values). In the last line the values of the oblique parameters S and T are given [after subtraction of the SM contributions to include only new physics effects]. For the point A1 (A2), we have used the indicated Y'' value for the t'_R coupling and $Y'' = -0.3$ (-1.75) for the t'_L vertex.

$$\sigma^{\rm t'}_{\rm gg\to h} B^{\rm t'}_{\rm h\to bb}/\sigma^{\rm SM}_{\rm gg\to h} B^{\rm SM}_{\rm h\to bb} = 1.25\ (1.28) \quad [A1]\ ([A2]) \tag{5.5}$$

The cross section for the Higgs production is enhanced,

$$\sigma^{\rm t'}_{\rm gg\to h}/\sigma^{\rm SM}_{\rm gg\to h} = 1.27\ [A1]\ (1.31\ [A2]),$$

due to the combination of two possible effects: the increase of the t_1 Yukawa coupling and the constructive interferences between the t_1 contribution and the t_2, t_3 ones. In contrast, the branching fraction for the decay channel into diphoton is slightly decreased,

$$B^{\rm t'}_{\rm h\to\gamma\gamma}/B^{\rm SM}_{\rm h\to\gamma\gamma} = 0.91\ [A1]\ (0.90\ [A2]).$$

But the resulting product $\sigma^{\rm t'}_{\rm gg\to h}B^{\rm t'}_{\rm h\to\gamma\gamma}$ is increased relatively to the SM case as shown in Eq.(5.3). Such an increased value of the observable $\sigma_{\rm gg\to h}B_{\rm h\to\gamma\gamma}$, induced here by the presence of t' quarks (*c.f.* Eq.(5.3)), could induce a slight excess in the ATLAS [69, 70, 77, 78] and CMS [68, 71, 77] data corresponding to a possible ∼125 GeV Higgs signal in the diphoton channel. All the values of the quantities, $\sigma^{\rm t'}_{\rm gg\to h}B^{\rm t'}_{\rm h\to\gamma\gamma}/\sigma^{\rm SM}_{\rm gg\to h}B^{\rm SM}_{\rm h\to\gamma\gamma}$, $\sigma^{\rm t'}_{\rm gg\to h}B^{\rm t'}_{\rm h\to WW}/\sigma^{\rm SM}_{\rm gg\to h}B^{\rm SM}_{\rm h\to WW}$, $\sigma^{\rm t'}_{\rm gg\to h}B^{\rm t'}_{\rm h\to ZZ}/\sigma^{\rm SM}_{\rm gg\to h}B^{\rm SM}_{\rm h\to ZZ}$, $\sigma^{\rm t'}_{\rm gg\to h}B^{\rm t'}_{\rm h\to\tau\tau}/\sigma^{\rm SM}_{\rm gg\to h}B^{\rm SM}_{\rm h\to\tau\tau}$ and $\sigma^{\rm t'}_{\rm gg\to h}B^{\rm t'}_{\rm h\to bb}/\sigma^{\rm SM}_{\rm gg\to h}B^{\rm SM}_{\rm h\to bb}$, in Eq.(5.3)-(5.5), are also compatible with the CMS and ATLAS best-fit values whose central value, from the combination of all search channels, is of $1.22^{+0.31}_{-0.39}$ [71] (for a Higgs mass hypothesis of 124 GeV) [9] and $0.90^{+0.40}_{-0.37}$ [78] (for a Higgs mass hypothesis of 126 GeV), respectively [10].
It is also interesting to note that the present theoretical model allows for either an increase of $\sigma^{\rm t'}_{\rm gg\to h}$ compared to the SM, as here for A1/A2, or a decrease as with the parameter sets in the following.

Sets **B,C** - For these sets of parameters where $m_h = 255$ GeV or 320 GeV, all the Higgs decays have negligible widths relatively to the dominant channels $h \to ZZ$ and $h \to WW$, as in the SM case. Hence the branching fractions $B_{\rm h\to ZZ}$ and $B_{\rm h\to WW}$ remain unchanged in the present model with vector-like top quarks where only the decay widths for $h \to t\bar{t}$, $h \to gg$, $h \to \gamma\gamma$ and $h \to \gamma Z$ are modified. In consequence, the experimental limits on $\sigma_{\rm gg\to h}/\sigma^{\rm SM}_{\rm gg\to h} \lesssim 0.45\ (0.40)$ [for $m_h \simeq 255\ (320)$ GeV] issued from the LHC combined investigations using the $h \to ZZ, WW$ channels exclusively [68–71, 77, 78] can be applied directly to our framework where one gets

$$\sigma^{\rm t'}_{\rm gg\to h}/\sigma^{\rm SM}_{\rm gg\to h} = 0.45\ \ [B]\ \ ;\ \ 0.40\ \ [C] \tag{5.6}$$

which does not conflict with the above LHC limits.
Note that for the point C, $\sigma^{\rm t'}_{\rm gg\to h}$ is strongly reduced compared to SM. A factor 1/10 could even be achieved in the present theoretical model but variants of the multiplet choice (non-minimal in term of field content), allowing coupling correction cancellations, should then be used instead to pass the indirect constraints discussed in Section 5.5.

Set **D** - For $m_h = 540$ GeV, the Higgs boson is searched only through its decays into ZZ and WW. The strongest bounds on the Higgs rates from the LHC read as $\sigma_{\rm gg\to h}B_{\rm h\to ZZ}/\sigma^{\rm SM}_{\rm gg\to h}B^{\rm SM}_{\rm h\to ZZ} \lesssim 0.90$ and $\sigma_{\rm gg\to h}B_{\rm h\to WW}/\sigma^{\rm SM}_{\rm gg\to h}B^{\rm SM}_{\rm h\to WW} \lesssim 1.45$ [68–71, 77, 78]. These upper limits are clearly in good agreement with the rates calculated in the presence of the t' and t'' states (that modifies $B_{\rm h\to t\bar{t}}$)

[9] This number has just been updated to $0.94^{+0.26}_{-0.34}$ for a 125 GeV Higgs [97].
[10] The present parameters lead to a Higgs rate, for the WW channel, standing slightly outside the 1σ range but the experimental error bars obtained by both the ATLAS and CMS Collaborations are significant.

for the set D, namely,

$$\sigma^{t'}_{gg\to h} B^{t'}_{h\to ZZ}/\sigma^{SM}_{gg\to h} B^{SM}_{h\to ZZ} = 0.69 \qquad \sigma^{t'}_{gg\to h} B^{t'}_{h\to WW}/\sigma^{SM}_{gg\to h} B^{SM}_{h\to WW} = 0.69 \tag{5.7}$$

where

$$B^{t'}_{h\to ZZ}/B^{SM}_{h\to ZZ} = 1.06 \qquad B^{t'}_{h\to WW}/B^{SM}_{h\to WW} = 1.06 \quad [D].$$

5.5 The indirect constraints and oblique parameters

Given the absence of precise measurement for the $Zt\bar{t}$ vertex (coupling directly modified by the $t-t'-t''$ mixing), the main indirect constraints to the present model come from the corrections to the gauge boson vacuum polarizations induced by the loops of $q_{5/3}$,t',t'' states. The values of the oblique parameters S, T that we obtain, according to the preliminary calculations of Ref. [79, 80], are given in Table 5.1. They appear to belong to the 1σ regions induced by the long list of EW precision observables measured mainly at the LEP collider [81].
Remark that the input parameters of Table 5.1 (i.e. the theoretical values in the first four lines) have been chosen to fix a panel of characteristic benchmark points for m_{t_2} that pass the indirect constraints as well as the bounds from direct Higgs search described in previous section; however those two types of constraints allow large domains of the parameter space (varying also m_h). The precise setting of the Y coupling reflects mainly the experimental precision on the top quark mass measurement (and not any fine-tuning).

The t', t'' states could contribute to Flavor Changing Neutral Current (FCNC) reactions which are experimentally well constrained; from the theoretical point of view, these FCNC contributions rely precisely on the whole set of Yukawa coupling constants for the entire quark sector. The treatment of such an high degree of freedom in the parameter space is beyond the scope of the present study.

Finally, given the relative heavyness of the t_2 quark, we have checked that the predicted value for the V_{tb} CKM matrix element is in agreement with the experimental measurement close to unity obtained (without assuming 3×3 unitarity) through the single top quark production cross section at Tevatron [81].

5.6 Higgs signal reconstruction in $\bar{t}_2 t_2 \to th + X$ events

We have studied the sensitivity at the LHC with $\sqrt{s} = 14$ TeV of a search for $pp \to t_2\bar{t}_2$ production, with one of the t_2 decaying to th, and the other decaying to bW or tZ or th, resulting into $thbW$, $thtZ$ and $thth$ final states, respectively. For a best sensitivity and in order to measure the Higgs mass precisely, we have exploited the Higgs decay channel into ZZ to four charged leptons for the

signals with Higgs mass above 200 GeV (points B, C, D) while the Higgs decay into two photons is considered for the signals with a Higgs mass of 125 GeV (sets A1 and A2).

For the signal event generation, we have implemented [11] the couplings of our t_2 model in `FeynRules` [82] interfaced with `MadGRAPH` [83] for the *Monte Carlo* generation, `PYTHIA` [84] for the hadronization part and `DELPHES` [85] for the fast simulation of a typical LHC detector response. Signal events are generated for the t_2 and h masses corresponding to the parameter sets described in Table 5.1, for the three final states $thbW$, $thtZ$ and $thth$. Events corresponding to points A1 and A2 are generated with the Higgs decaying through $h \to \gamma\gamma$, while for points B, C and D the $h \to ZZ$ decay is retained for the sensitivity studies described in this Section. The main backgrounds were generated with `ALPGEN` [86] interfaced to `PYTHIA` and `DELPHES`, as for the signal events. Physics objects used for the analysis (photons, leptons and jets) were defined emulating the requirements used in real CMS Higgs searches in the 2011 data. In particular, we followed closely the physics object definition as for the real data 7 TeV Higgs analysis in the diphoton channel [87] and in the four lepton channel [88].

In the following the quoted number of events and distributions are normalized to an integrated luminosity of 20 fb^{-1} multiplied by, for the different signal final states, their expected $\sigma_{\bar{t}_2 t_2}$ cross section times branching fractions (hereafter referred to as signal event yield per unit of integrated luminosity), while, for background processes, their `ALPGEN` cross sections are used. The signal event yield in the different final states depends upon the parameter set under consideration. In Table 5.2, we summarize, for each parameter set described in Table 5.1, the physical signal m_{t_2} and m_h masses, the $\sigma_{\bar{t}_2 t_2}$ cross sections, the t_2 branching fractions into bW ($B_{t_2 \to bW}$), tZ ($B_{t_2 \to tZ}$), th ($B_{t_2 \to th}$) final states, as well as the h branching fractions into $\gamma\gamma$ (for sets A1 and A2) and into ZZ (for sets B, C and D), reporting the expected SM branching fraction values and the factor $f^{t'/SM}_{h \to VV}$ (see Section 5.4) by which it is modified in the present model. The last three columns of Table 5.2 show the expected signal event yield, for $thbW$, $thtZ$ and $thth$ final states, with one Higgs boson decaying via to diphoton or ZZ final state. They are calculated as follows:

$$
\begin{aligned}
&thbW \text{ final state}, && Y_S(h \to VV) = \; 2\; B_{t_2 \to th} B_{t_2 \to bW}\; B^{SM}_{h \to VV} f^{t'/SM}_{h \to VV}\; \sigma_{\bar{t}_2 t_2} \\
&thtZ \text{ final state}, && Y_S(h \to VV) = \; 2\; B_{t_2 \to th} B_{t_2 \to tZ}\; B^{SM}_{h \to VV} f^{t'/SM}_{h \to VV}\; \sigma_{\bar{t}_2 t_2} \\
&thth \text{ final state}, && Y_S(h \to VV) = \; 2\; B^2_{t_2 \to th}\; B^{SM}_{h \to VV} f^{t'/SM}_{h \to VV}\; \sigma_{\bar{t}_2 t_2}
\end{aligned}
$$

For $thth$ events, the event yield is given for events where one h decays to vector bosons, while the second h decays inclusively. The signal event yield (in fb) multiplied by the integrated luminosity (in fb^{-1}) results into the numbers of produced signal events for that luminosity. We note that, for a chosen Higgs decay, the signal yield depends on both $\sigma_{\bar{t}_2 t_2}$ and $B_{t_2 \to th}$. Then, for example, in spite of the fact that $\sigma_{\bar{t}_2 t_2}$ is larger for point C than B, the signal event yield is higher for point B than C, because of the larger $B_{t_2 \to th}$ value in point B. The background cross sections are listed in Tablel 5.3, for the four lepton search channel, and in Table 5.4 for the diphoton search channel.

[11] We thank Claude Duhr and Benjamin Fuks for their precious help in this implementation.

Parameter set	m_{t_2}	m_h	$\sigma_{\bar{t}_2 t_2}$(fb)	$B_{t_2 \to th}$	$B_{t_2 \to tZ}$	$B_{t_2 \to bW}$	$B^{SM}_{h \to VV}$	$f^{t'/SM}_{h \to VV}$	$Y_S(h \to VV)$(fb)		
									$thbW$	$thtZ$	$thth$
Point A1	403	125	$1.353\ 10^4$	0.626	0.286	0.088	$2.29\ 10^{-3}$	0.91	3.11	10.1	22.1
Point A2	599	125	$1.465\ 10^3$	0.821	0.147	0.032	$2.29\ 10^{-3}$	0.90	0.159	0.729	4.07
Point B	626	255	$1.164\ 10^3$	0.608	0.250	0.142	0.298	1.00	59.9	105	256
Point C	572	320	$1.975\ 10^3$	0.135	0.461	0.404	0.309	1.00	66.6	76.0	22.2
Point D	788	540	$0.284\ 10^3$	0.430	0.403	0.166	0.265	1.06	11.4	27.6	29.5

Table 5.2: Information entering the signal event yield Y_S calculation. The t_2 pair production cross section at 14 TeV and t_2 branching fraction values are from Table 5.1. The ratio $f^{t'/SM}_{h \to VV} = B^{t'}_{h \to VV}/B^{SM}_{h \to VV}$ values are calculated in Section 5.4. The event yield Y_S, per unit of integrated luminosity, is given for the different final states $\bar{t}_2 t_2 \to thbW,\ thtZ,\ thth$ and $h \to \gamma\gamma$, for points A1 and A2, or $h \to ZZ$, for points B, C, D. For $thth$ events, the event yield is calculated for the case where one h decays to vector bosons, while the second h decays inclusively. This synoptic table summarizes at once, for convenience, all the relevant numbers useful for the experimental search. The m_{t_2} and m_h masses are given in GeV.

5.6.1 Search for $\bar{t}_2 t_2 \to th + X$ signal in the four leptons plus multijets channel

In order to estimate the sensitivity of a search for $thbW,\ thtZ$ and $thth$ final states, when the Higgs boson is relatively heavy, as expected for the points B, C and D, with $m_h = 255, 320, 540$ GeV, respectively, we exploit the decay channel into four charged leptons $h \to ZZ \to 4l$. Signals from $thbW,\ thtZ,\ thth$, $h \to ZZ \to 4l$, final states are characterized by four high transverse momentum leptons, from the Higgs decay, and a large number of energetic jets, from accompanying top and heavy vector boson decays.

The event selection, exploiting the large number of high transverse momentum (p_T) leptons and jets, as well as the b-jet content of the event, consists of the following criteria:

- Four leptons (muons or electrons) are required with transverse momentum $p_T > 20$ GeV and pseudo-rapidity $|\eta| < 2.4$ or 2.5 for muons or electrons, respectively, and two lepton pairs, each pair with same flavor but opposite charge leptons. The lepton pair of highest p_T is required to have a dilepton invariant mass consistent with the Z mass, $M_{2l} = M_Z \pm 15$ GeV, while the lepton pair with second highest dilepton p_T must have a dilepton invariant mass $M_{2l} > 12$ GeV;
- $H_T > 1000$ GeV and $N_j > 5$, with H_T being defined as the scalar sum of the transverse momenta of identified leptons, photons, jets, and the missing energy, and N_j being the number of hadronic jets with $p_T > 30$ GeV and $|\eta| < 2.4$;
- At least two b-tagged jets in the event.

The motivation for the H_T and N_j cuts is evident from Figure 5.1, showing the H_T and N_j distributions after the four lepton requirements. The event numbers are shown for an integrated luminosity $L = 20$ fb^{-1}, with the signal event numbers multiplied by a factor of fifty, for shape comparison. Expectations for the signals, by final state, and the backgrounds processes, after the

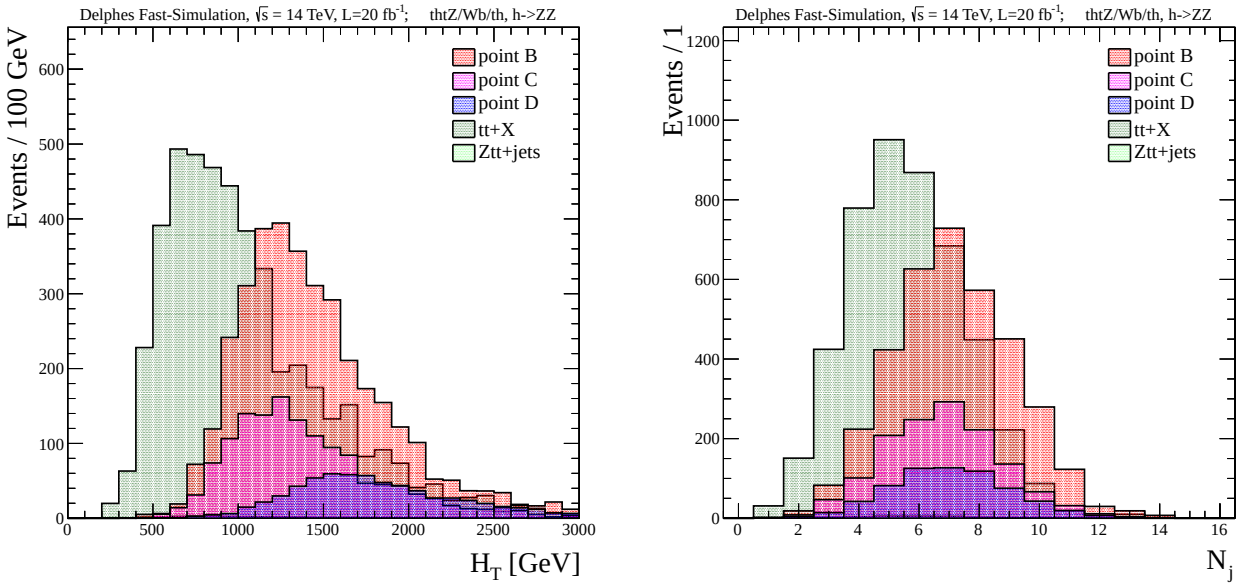

Figure 5.1: Distributions of the H_T variable and the jet multiplicity N_j after four lepton requirements. Background and signal distributions are shown overlaid, to compare the different distribution shapes, with the background normalized to the expected events for 20 fb^{-1} and the corresponding signal expectation multiplied by a factor of fifty.

selection cuts, for an integrated luminosity of $L = 20$ fb^{-1}, are shown in Table 5.3, where the following quantities are reported:

- Y_S, the signal event number produced, per unit of integrated luminosity, given for each signal parameter set and final state under study, as reported in Table 5.2;
- σ, the cross sections, as calculated by the ALPGEN generator, for the background processes included in the present study;
- N_{4l}, the number of events after four lepton requirements;
- N_{N_j,H_T}, the number of events after the additional requirements $H_T > 1000$ GeV and $N_j > 5$;
- N_{2b}, the number of events after the additional requirements of two b-tagged jets in the event;
- S and B, the total number of signal (summed over all signal final states) and background (summed over all background processes), after a cut on the reconstructed four lepton invariant mass, M_{4l}, with ΔB being the expected uncertainty on the total number of background events. Here we only consider the statistical uncertainty $\Delta B = \sqrt{B}$, but a more realistic estimation should also include systematic uncertainties on the number of background events. Some of the dominant systematic uncertainties are depending on detector effects (for instance jet energy resolution) and can be best evaluated with real data. In the following, an estimation of the

signal sensitivity is given as the ratio $S/\Delta B$, measuring the signal in terms of background standard deviations.

	Signal: $thbW/thtZ/thth$, $h \to ZZ$				Total signal S, M_{4l}(GeV) cut			
Param. set	Y_S (fb)	N_{4l}	N_{N_j,H_T}	N_{2b}	no M_{4l} cut	$M_{4l} > 200$	> 300	> 500
Point B	59.9 /105 /256	8.1 /23.7 /37.8	5.5 /18.0 /28.9	3.52 /11.5 /18.5	33.4	30.4	17.0	4.9
Point C	66.6 /76.0 /22.2	7.7 /15.8 /3.1	4.8 /11.3 /2.2	3.07 /7.23 /1.41	11.7	10.7	7.4	2.0
Point D	11.4 /27.6 /29.5	1.5 /6.6 /4.7	1.1 /5.3 /3.9	0.70 /3.40 /2.50	6.6	6.2	5.1	2.7
	Background				Total background B, M_{4l}(GeV) cut			
Process	σ(fb)	N_{4l}	N_{N_j,H_T}	N_{2b}	no M_{4l} cut	$M_{4l} > 200$	> 300	> 500
$t\bar{t}$ + jets	9.19 10^5	4680	1480	27.5	35.5	23.5	13.2	6.8
$t\bar{t}b\bar{b}$ + jets	2.50 10^3	5.60	3.10	2.0	Statistical ΔB, M_{4l}(GeV) cut			
$t\bar{t}W$ + jets	1.99 10^2	1.20	0.40	0.036	no M_{4l} cut	$M_{4l} > 200$	> 300	> 500
$t\bar{t}Z$ + jets	97.3	25.0	9.5	6.0	6.0	4.9	3.6	2.6

Table 5.3: Cross section and number of expected events after different selection cuts (see text), for an integrated luminosity of 20 fb^{-1} at $\sqrt{s} = 14$ TeV, in the search for $thbW$, $thtZ$ and $thth$ final states, with $h \to ZZ$, in the four leptons plus multijets channel. The number of events is given separately for each signal final state ($thbW/thtZ/thth$) and for each background process. In the four rightmost columns, S, the total number of signal events (summed over all signal final states), and B, the total number of background events (summed over all background processes), are given after all selection cuts but the M_{4l} cut, in column "no M_{4l} cut", and after three different M_{4l} cut values. The S values for points B, C and D are given on the same lines as indicated in column "Parameter set". The B values in the column "no M_{4l} cut" are the sum of the individual background contributions as reported in the background column under "N_{2b}". The quantity $\Delta B = \sqrt{B}$ is the expected statistical uncertainty on the total number of background events. In the text, the signal sensitivity is given as the ratio $S/\Delta B$.

The need for additional cuts, after the leptons, jets and H_T requirements, is seen in Table 5.3, where the N_{N_j,H_T} column shows that after these cuts, a large background, predominantly from $t\bar{t}$ + jets production, is still present. Further background rejection can be obtained with requirements on the number of b-tagged jets. The motivation is the following: in $t\bar{t}$ events the requirement of four high p_T leptons strongly reduces the number of b-taggable jets. Indeed, in $t\bar{t}$+jets events, while two high p_T leptons are provided by the two leptonic W decay, the additional two leptons are preferentially resulting from the two b decays. Thus, applying a b-tagging requirement can reduce significantly the $t\bar{t}$ contribution. In the signal case, the four leptons come mainly from the $h \to ZZ \to 4l$ decay so that there are in average at least two b-taggable jets in the event, for which a b-tagging requirement can have high efficiency. Since no detailed b-tagging information is presently available in `DELPHES`, we make use of known b-tagging and mis-tagging efficiency values as measured by LHC experiments (see *e.g.* Ref. [89]), to estimate the effect on background and signal of requiring two b-tagged jets in the event. The probability for a b-jet to be b-tagged is taken to be $\epsilon_{b-tag} = 0.8$ and for a mis-tagging the probability is $\epsilon_{mis-tag} = 0.05$. An event-by-event weight, that is an estimation of the probability that two b-jets be identified in the event, is applied to both background and signal events. The number of expected events, for signals and backgrounds, resulting from leptons, jets and b-tagging requirement are shown in the column N_{2b} of Table 5.3.

The corresponding distributions of the invariant mass of the four leptons, M_{4l}, for signals and backgrounds are shown in Figure 5.2. The mass peak corresponding to the generated Higgs mass is reconstructed at the correct mass value with good resolution ($\Delta M_{4l}/M_{4l} \lesssim 10\%$). Signal events,

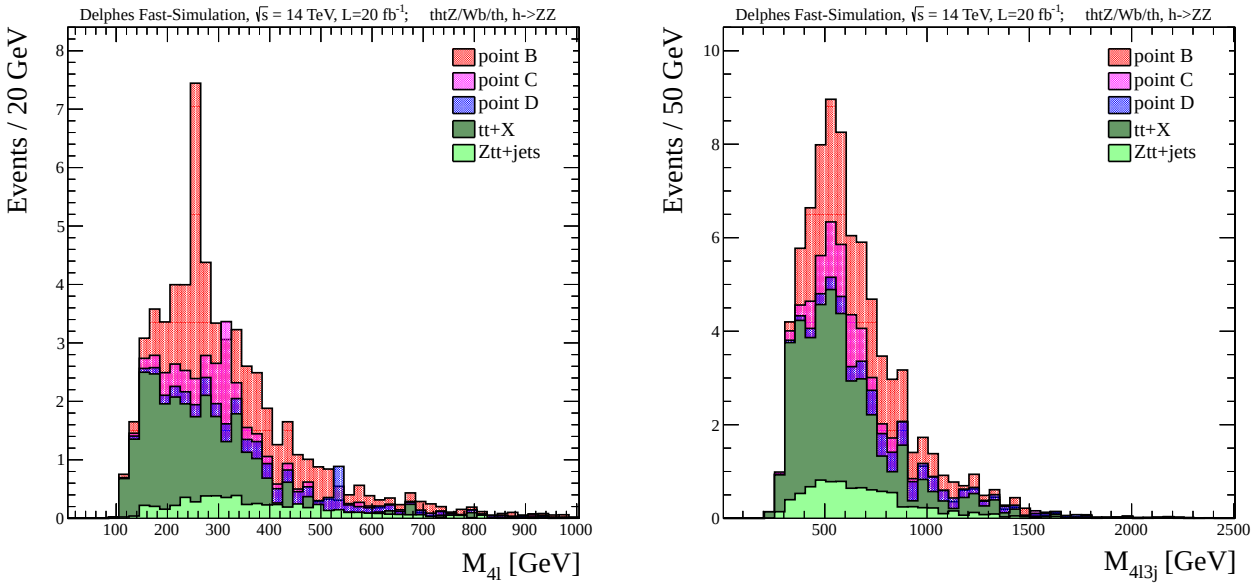

Figure 5.2: Distributions of the four lepton invariant mass, M_{4l}, and of the reconstructed heavy top-partner mass, M_{4l3j} (see text), after all selection cuts. Signal and background distributions, normalized to the expected events for 20 fb^{-1}, are shown stacked to indicate their relative contributions. Signal distributions for points B, C and D correspond to Higgs mass m_h = 255, 320 and 540 GeV, respectively.

with reconstructed mass significantly lower, or higher, than the generated Higgs mass value, are in general events where one lepton from the $h \to ZZ \to 4l$ decay does not pass the lepton selection criteria, while another lepton from an accompanying W or Z decays is selected to reconstruct the four lepton invariant mass. The background, mainly from the $t\bar{t}$ + jets process, is mostly concentrated in the M_{4l} region below 200 GeV. Applying a lower cut on M_{4l} removes a large fraction of the background and improves the signal significance, as shown in Table 5.3.

An additional distribution of the variable, M_{4l3j}, is shown after all but the M_{4l} cuts. This variable can help estimating directly the mass of the heavy top-like quark. It is defined as the invariant mass of the system obtained by associating to the four lepton momentum direction the three closest jets (expected to come from the decay of the accompanying top-quark, $t \to bW$, $W \to 2\ jets$), choosing among all the jets in the event those with the smallest $\Delta R \equiv \sqrt{\Delta\eta^2 + \Delta\phi^2}$ with respect to the four lepton momentum direction. The distributions of M_{4l3j} for signals and backgrounds are shown in Figure 5.2. A broad peak, whose width is dominated by the jet energy resolution and jet combinatorics, is observed centered at about the generated t_2 mass value (the t_2 physical width is given in Table 5.1) for the points B and C having larger t_2 pair production rates than for the set D. Therefore, this mass reconstruction method, together with the four lepton mass reconstruction, will give an early indication that a heavy particle has been produced in the collision and decayed into a Higgs boson (identified by the four lepton mass peak) plus three jets. Another mass reconstruction method, described in the next section, that exploits the property of

the two heavy particles having equal mass, will give another characterization of the origin of the observed signal. Ultimately, a kinematic fit technique (utilized, for instance, in top quark mass measurements, see e.g. [90]), to test on an event-by-event basis the hypothesis that the event results from the production of two heavy particles of equal mass (see e.g. [91]) – one of which decays into two particles with known decays and masses (three jets, with invariant mass around the top mass, and four leptons, with invariant mass around the value measured from the four lepton mass peak, see Figure 5.2) – can be properly applied in real data events, when the detailed parameterizations of the experimental resolutions of the physics objects entering the fit can be obtained from data.

The numbers of signal and background events expected after all cuts, and for M_{4l} >200, 300 and 500 GeV, are shown in the three rightmost columns of Table 5.3 together with the expected statistical background standard deviation ΔB for the three signal points investigated in this search channel. We estimate that, for an integrated luminosity of 20 fb^{-1}, a signal corresponding to point B is detectable with a significance $S/\Delta B \sim 6$ (after M_{4l} >200 GeV cut). For this benchmark point the $B_{t_2\to th}$ branching fraction is ~ 0.6. Then, for similar t_2 cross section, t_2 mass and h mass values, a signal could be discovered, with $S/\Delta B \gtrsim 5$, for $B_{t_2\to th} \gtrsim 0.5$. For point C, with $B_{t_2\to th} \sim 0.1$ we obtain a signal significance $S/\Delta B \sim 2$. A signal significance of five and above is then obtained for $B_{t_2\to th} \gtrsim 0.25$. For smaller $B_{t_2\to th}$ values, a larger integrated luminosity, or a more optimal analysis, would be needed for a signal significance of five or above. For point D, with $B_{t_2\to th} \sim 0.4$, we obtain a signal significance $S/\Delta B \sim 1.4$ thus even for maximal $B_{t_2\to th} \sim 1$ a signal significance of ~ 3.5 is attainable. Higher integrated luminosity, or higher background rejection, depending on the $B_{t_2\to th}$ value (for $B_{t_2\to th} \sim 0.4$, about a factor of ten larger luminosity or background rejection) is needed for a five sigma signal significance corresponding to the D scenario, with a t_2 mass of about 800 GeV and a pair production cross section of about 0.3 pb.

5.6.2 Search for $\bar{t}_2 t_2 \to th + X$ signal in the diphoton plus multijets channel

To study the sensitivity of a search for $thtZ$, $thbW$ and $thth$ final states, when the Higgs boson is relatively light, as for points A1 and A2, with $m_h = 125$ GeV, we exploit the $h \to \gamma\gamma$ decay channel. As for a light Higgs boson in the SM, in spite of the relatively small expected B($h \to \gamma\gamma$) value, this is expected to be a channel with good signal sensitivity, due to the good diphoton mass resolution, allowing to identify the Higgs mass signal over a background that can be well measured in the side-bands.

The background processes considered in this study are listed in Table 5.4. To reduce generation time for the background events, we have applied cuts on `ALPGEN` generated parton quantities, that are looser than the cuts applied on the reconstructed physics objects. The generator level cuts are: photon $p_T > 20$ GeV and $|\eta|$ <3.0, jet $p_T > 20$ GeV and $|\eta| < 2.5$, $\Delta R_{\gamma j} < 0.4$, $\Delta R_{\gamma l} < 0.4$, , $\Delta R_{jj} < 0.4$ and $\Delta R_{t\bar{t}} < 0.4$. Background cross sections for these generator level cuts as calculated by `ALPGEN` are listed in Table 5.4. An additional background is the $\gamma\gamma$+jets process. A relatively

large inclusive diphoton cross section is expected [92] and is going to be measured at the LHC, together with the contribution from fake diphoton pairs. The inclusive diphoton cross section in the diphoton mass region of interest can be large (order of pb), but we expect that the large jet multiplicity requirement scales down this contribution by at least three orders of magnitude, thus reducing its cross section to few fb. An additional handle to minimize this background will be the b-tagging, that can reduce the contribution from light flavored multi-jets events by two or three order of magnitudes (as discussed in the previous section), while retaining a large fraction of the signal events containing at least two b-jets. However, b-tagging will not effectively reduce backgrounds with t-quark pairs in the final state, as in the case of $t\bar{t}\gamma\gamma+$ jets process. Thus, conservatively we have not exploited b-tagging for this analysis of the $h \to \gamma\gamma$ channel.

Signals from $thbW$, $thtZ$, $thth$, $h \to \gamma\gamma$, final states are characterized by a large number of energetic jets, from top and heavy vector boson decays, in addition to the two high transverse momentum photons from the Higgs decay. The event selection consists of the following criteria:

- Photons are required to be within $|\eta| < 2.5$ and isolated. The isolation requirements imply that, within a cone $\Delta R = 0.4$ around the photon direction, the charged particle energy measured in the tracker is < 2.0 GeV, the electromagnetic calorimeter (ecal) energy in the cone is < 4.2 GeV, the hadronic calorimeter (hcal) energy in the cone is < 2.2 GeV and the ratio between the ecal and hcal energy in the cone is < 0.05. Two isolated photons are required, with the leading photon $p_T > 45$ GeV and the second photon $p_T > 30$ GeV. The invariant mass of the two photon is required to be $M_{2\gamma} > 90$ GeV.
- Hadronic jets are counted if they have $p_T >$30 GeV and $|\eta| < 2.4$. Events are required to have a number of jets $N_j > 6$, at preselection, or $N_j > 8$, for the final selection, after which the signal sensitivity is evaluated in a sliding window in the diphoton invariant mass $M_{2\gamma}$.

Figure 5.3 shows the H_T and N_j distributions after the after diphoton requirements, including a diphoton invariant mass cut $M_{2\gamma} > 90$ GeV. The distributions are shown for an integrated luminosity $L = 20$ fb^{-1}, with the signal expectation for point A2 multiplied by a factor of ten, for shape comparison. Because of the relatively light t_2 mass in point A1, an $H_T > 1000$ GeV cut, as applied for points B, C and D, would reject a significant fraction of this signal. A lower H_T cut would not improve significantly the signal-over-background ratio after the N_j requirement, thus no H_T cut is applied in this channel. Expectations for the signals, by final state, and the backgrounds processes, after the selection cuts, for an integrated luminosity of $L = 20$ fb^{-1}, are shown in Table 5.4, where the following quantities are reported:

- Y_S, the signal event number produced, per unit of integrated luminosity, given for each signal parameter set and final state under study, as reported in Table 5.2;
- σ, the background cross sections, as calculated from the ALPGEN generator, for the background processes included in the present study;

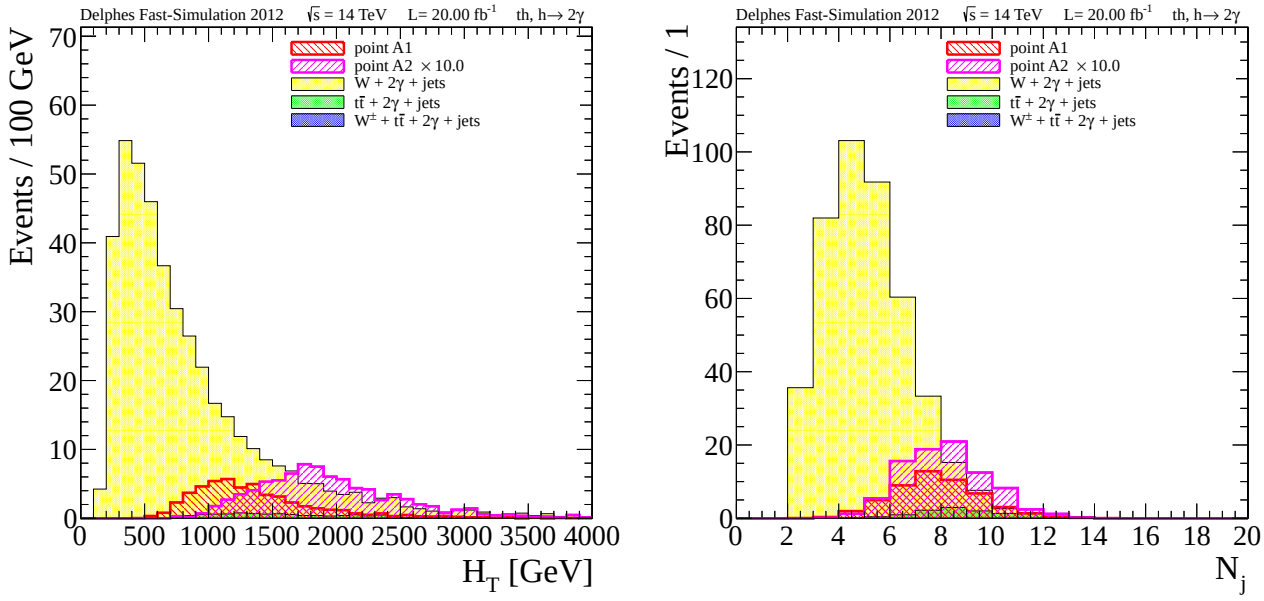

Figure 5.3: Distributions of the H_T variable and the jet multiplicity N_j after diphoton requirements, including a diphoton invariant mass cut $M_{2\gamma} > 90$ GeV.

- $N_{2\gamma}$, the number of events after diphoton and $M_{2\gamma} > 90$ GeV requirements;
- $N_{N_j>6}$ and $N_{N_j>8}$ the number of events after the additional jet multiplicity cuts;
- S and B, the total number of signal (summed over all signal final states) and background (summed over all background processes), after a cut $M_{2\gamma}$, with ΔB being the expected statistical uncertainty (standard deviation) on the total number of background events. An estimation of the expected signal sensitivity can then be evaluated as the ratio $S/\Delta B$, measuring the signal in terms of background standard deviations.

In virtue of the good diphoton mass resolution (∼1% to 5% for a 110 to 130 GeV Higgs boson, depending on photon selection criteria) of the detector, a highly discriminating quantity after selection is the reconstructed diphoton mass. The diphoton invariant mass distribution for signals and backgrounds events, after the $N_j > 8$ requirement, is shown in Figure 5.4. Also shown is the distribution of an additional variable, $M_{re\ nj}$, that could help estimating the mass of the heavy top-like quark. This is defined as the invariant mass of the system of n jets recoiling against the diphoton+m jets system, where the m jets are the closest in ΔR to the diphoton direction. The recoiling n jets, with $n = N_j - m$, are counted to minimize, among all m and n choices in the event, the difference between the mass of the diphoton+m jets system and the mass of the recoiling n jets. The goal of this procedure is to separate the event into two hemispheres, one identified by the diphoton+m jets system and the other by the recoiling n jets, with m and n chosen in such a way that the invariant masses of the physics objects in the two hemispheres are about the same (within

	Signal: $thbW/thtZ/thth$, $h \to \gamma\gamma$				Total signal S, $M_{2\gamma}$(GeV) cut	
Param. set	Y_S (fb)	$N_{2\gamma}$	$N_{N_j>6}$	$N_{N_j>8}$	$M_{2\gamma} > 90$	$M_{2\gamma} \in$[115,135]
Point A1	3.1 / 10.1 / 22.1	5.4 / 15.4 / 30.4	4.1 / 12.7 / 27.1	1.4 / 6.2 / 14.5	22.1	17.7
Point A2	0.16 / 0.73 / 4.1	0.34 / 1.35 / 6.98	0.27 / 1.17 / 6.6	0.10 / 0.62 / 3.8	4.5	3.2
	Background				Total background B, $M_{2\gamma}$(GeV) cut	
Process	σ(fb)	$N_{M_{2\gamma}>90}$	$N_{N_j>6}$	$N_{N_j>8}$	$M_{2\gamma} > 90$	$M_{2\gamma} \in$ [115,135]
$W\gamma\gamma$ + jets	450	422	110	19.6	27.8	4.38
$t\bar{t}\gamma\gamma$ + jets	15.5	11.8	11.3	8.18	Statistical ΔB, $M_{2\gamma}$(GeV) cut	
$t\bar{t}W\gamma\gamma$ + jets	0.0678	0.0577	0.0515	0.0272	$M_{2\gamma} > 90$	$M_{2\gamma} \in$[115,135]
					5.3	2.1

Table 5.4: Cross section and number of expected events after different selection cuts (see text), for an integrated luminosity of 20 fb^{-1} at $\sqrt{s} = 14$ TeV, in the search for $thbW$, $thtZ$ and $thth$ final states, with $h \to \gamma\gamma$, in the diphoton plus multijets channel. The number of events is given separately for each signal final state ($thbW/thtZ/thth$) and for each background process. In the two rightmost columns, S, the total number of signal events (summed over all signal final states), and B, the total number of background events (summed over all background processes), are given after all selection cuts in column "$M_{2\gamma} > 90$" and within a mass window $M_{2\gamma} \in$[115,135] GeV in the next column. The S values for points A1 and A2 are given in the same lines as indicated in column "Parameter set". The B values in the column "$M_{2\gamma} > 90$" are the sum of the individual background contributions as reported in the background column under "$N_{N_j>8}$". The quantity $\Delta B = \sqrt{B}$ is the expected statistical uncertainty on the total number of background events. In the text, the signal sensitivity is given as the ratio $S/\Delta B$.

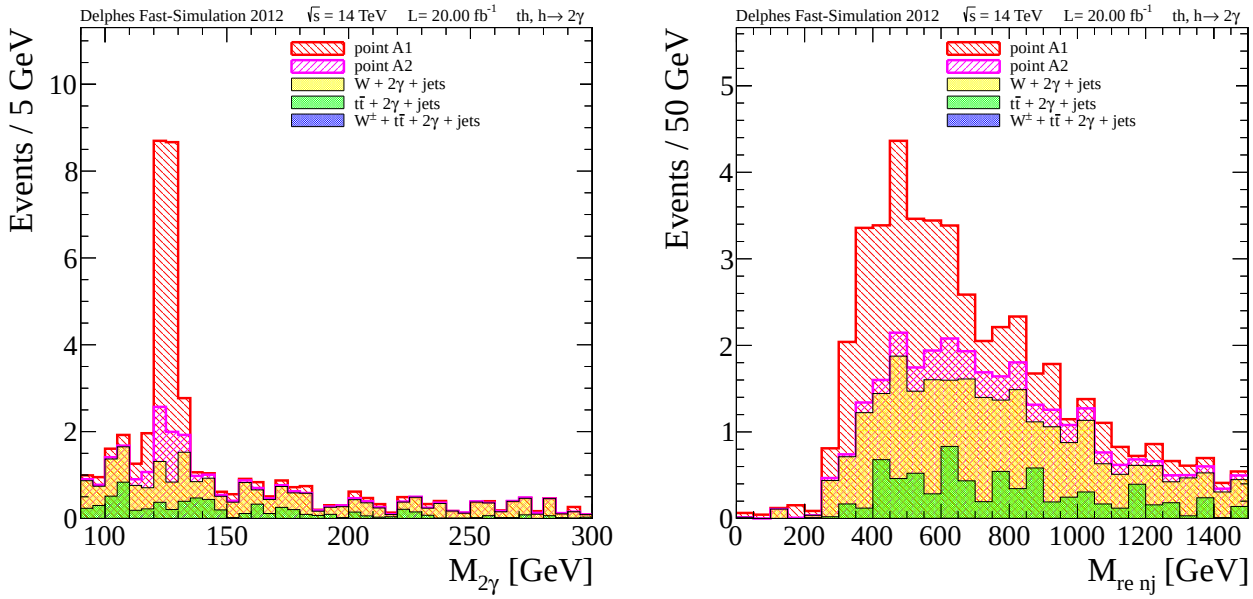

Figure 5.4: Distributions of the diphoton mass, $M_{2\gamma}$, and of the reconstructed heavy recoil mass, $M_{re\ nj}$ (see text), after all selection cuts. Signal and background distributions, normalized to the expected events for 20 fb^{-1}, are shown stacked to indicate their relative contributions. Signal distributions for points A1 and A2 correspond to a Higgs mass $m_h = 125$ GeV.

resolution), as in the case of two heavy particles decaying in diphoton plus jets, in one hemisphere, and into jets, in the other hemisphere.

On the distributions of $M_{re\ nj}$ for signals and backgrounds, after all but the $M_{2\gamma}$ window cut, shown in Figure 5.4, a broad peak, whose width is dominated by the jet energy resolution, is

observed centered at about the generated t_2 masses. Hence, this mass reconstruction method will provide an early indication that two heavy particles of equal mass have been produced in the event and a first estimation of the t_2 mass. In real data, where the detailed measurements of the experimental resolutions are available, kinematic fits can be applied to test the pair production and decay hypothesis and possibly to reduce the uncertainty on the t_2 mass estimation.

The total number of signal and background events, after diphoton and jet multiplicity requirements, with a diphoton mass in the window between 115 GeV and 135 GeV, is also given in Table 5.4. We estimate that for an integrated luminosity of 20 fb^{-1}, a signal, corresponding to the benchmark point A1, is detectable with a significance $S/\Delta B \sim 9$. For this benchmark point the $B_{t_2 \to th} \sim 0.6$. Then, for a similar t_2 cross section and t_2, h mass values, a signal could still be discovered, with a signal significance of about or above five, if $B_{t_2 \to th} \gtrsim 0.3$. For point A2, where the $\sigma_{\bar{t}_2 t_2}$ is about an order of magnitude lower than in point A1, while $B_{t_2 \to th} \sim 0.8$, the expected signal significance is ~ 1.5. Then, to reach a signal significance of five, at least a factor of ten larger luminosity, or a better background rejection, is needed to observe this signal.

5.7 Conclusions

In this work, we have shown that there exist regions of the parameter space in beyond SM scenarios, allowed by present phenomenological and experimental constraints, in particular by the direct Higgs searches, where heavy vector-like top partner production at the LHC may give rise to new Higgs production channels, over a large Higgs mass range, extending from $\sim$ 120 GeV to more than 500 GeV. Indeed the SM Higgs mass exclusion, in the range between $\sim$ 130 and 600 GeV, does not hold in these beyond SM scenarios. In this context, we have also illustrated how the observation of a 125 GeV Higgs signal in the diphoton channel at LHC, with a cross section larger than expected in the SM, could be compatible with the presence of vector-like heavy quarks.

We have shown that for a variety of characteristic top-partner and Higgs mass values, the expected heavy top pair production cross sections and decay branching fractions lead to a signal of Higgs production (from the decay of the heavy top quark) which could be detectable at the 14 TeV LHC, with an integrated luminosity between $\sim$20 fb^{-1} and $\sim$200 fb^{-1}, over a large Higgs mass range ($\sim$120 GeV to $\sim$550 GeV). The good diphoton and four lepton invariant mass resolution ($\lesssim$ 10%), in spite of the large number of jets present in the signal events, makes the discovery possible with moderate luminosity. Finally, we have proposed new mass variables from which the heavy top mass could be estimated.

Bibliography

[1] N. Arkani-Hamed, A. G. Cohen, and H. Georgi, Phys. Lett. **B513**, 232 (2001), arXiv:hep-ph/0105239.

[2] N. Arkani-Hamed et al., JHEP **08**, 021 (2002a), arXiv:hep-ph/0206020.

[3] N. Arkani-Hamed, A. Cohen, E. Katz, and A. Nelson, JHEP **0207**, 034 (2002b), arXiv:hep-ph/0206021.

[4] R. Contino, Y. Nomura, and A. Pomarol, Nucl.Phys. **B671**, 148 (2003), arXiv:hep-ph/0306259.

[5] K. Agashe, R. Contino, and A. Pomarol, Nucl.Phys. **B719**, 165 (2005a), arXiv:hep-ph/0412089.

[6] K. Agashe and R. Contino, Nucl.Phys. **B742**, 59 (2006), arXiv:hep-ph/0510164.

[7] R. Contino, L. Da Rold, and A. Pomarol, Phys.Rev. **D75**, 055014 (2007), arXiv:hep-ph/0612048.

[8] G. Burdman and L. Da Rold, JHEP **0712**, 086 (2007), arXiv:0710.0623[hep-ph].

[9] C. T. Hill, Phys.Lett. **B266**, 419 (1991).

[10] H.-C. Cheng, B. A. Dobrescu, and C. T. Hill, Nucl.Phys. **B589**, 249 (2000), arXiv:hep-ph/9912343.

[11] M. S. Carena, E. Ponton, J. Santiago, and C. E. M. Wagner, Nucl.Phys. **B759**, 202 (2006), arXiv:hep-ph/0607106.

[12] M. S. Carena, E. Ponton, J. Santiago, and C. E. M. Wagner, Phys.Rev. **D76**, 035006 (2007), arXiv:hep-ph/0701055.

[13] L. Randall and R. Sundrum, Phys.Rev.Lett. **83**, 3370 (1999), arXiv:hep-ph/9905221.

[14] M. Gogberashvili, Int.J.Mod.Phys. **D11**, 1635 (2002), arXiv:hep-ph/9812296.

[15] T. Gherghetta and A. Pomarol, Nucl.Phys. **B586**, 141 (2000), arXiv:hep-ph/0003129.

[16] K. Agashe, A. Delgado, M. J. May, and R. Sundrum, JHEP **0308**, 050 (2003), arXiv:hep-ph/0308036.

[17] C. Bouchart and G. Moreau, Nucl.Phys. **B810**, 66 (2009a), arXiv:0807.4461[hep-ph].

[18] A. Djouadi, G. Moreau, and F. Richard, Nucl.Phys. **B773**, 43 (2007), arXiv:hep-ph/0610173.

[19] A. Djouadi, G. Moreau, and R. K. Singh, Nucl.Phys. **B797**, 1 (2008), arXiv:0706.4191[hep-ph].

[20] K. Agashe, R. Contino, L. Da Rold, and A. Pomarol, Phys.Lett. **B641**, 62 (2006a), arXiv:hep-ph/0605341.

[21] C. Bouchart and G. Moreau, Phys.Rev. **D80**, 095022 (2009b), arXiv:0909.4812[hep-ph].

[22] C. Kilic, K. Kopp, and T. Okui, Phys.Rev. **D83**, 015006 (2011), arXiv:1008.2763[hep-ph].

[23] S. J. Huber and Q. Shafi, Phys.Lett. **B498**, 256 (2001a), arXiv:hep-ph/0010195.

[24] S. J. Huber and Q. Shafi, Phys.Lett. **B512**, 365 (2001b), arXiv:hep-ph/0104293.

[25] S. J. Huber and Q. Shafi, Phys.Lett. **B544**, 295 (2002), arXiv:hep-ph/0205327.

[26] S. J. Huber and Q. Shafi, Phys.Lett. **B583**, 293 (2004), arXiv:hep-ph/0309252.

[27] S. Chang, C. Kim, and M. Yamaguchi, Phys.Rev. **D73**, 033002 (2006), arXiv:hep-ph/0511099.

[28] G. Moreau and J. Silva-Marcos, JHEP **0603**, 090 (2006a), arXiv:hep-ph/0602155.

[29] G. Moreau and J. Silva-Marcos, JHEP **0601**, 048 (2006b), arXiv:hep-ph/0507145.

[30] K. Agashe, G. Perez, and A. Soni, Phys.Rev. **D71**, 016002 (2005b), arXiv:hep-ph/0408134.

[31] K. Agashe, G. Perez, and A. Soni, Phys.Rev.Lett. **93**, 201804 (2004), arXiv:hep-ph/0406101.

[32] K. Agashe, G. Perez, and A. Soni, Phys.Rev. **D75**, 015002 (2007), arXiv:hep-ph/0606293.

[33] K. Agashe, A. E. Blechman, and F. Petriello, Phys.Rev. **D74**, 053011 (2006b), arXiv:hep-ph/0606021.

[34] Y. Grossman and M. Neubert, Phys.Lett. **B474**, 361 (2000), arXiv:hep-ph/9912408.

[35] T. Appelquist, B. A. Dobrescu, E. Ponton, and H.-U. Yee, Phys.Rev. **D65**, 105019 (2002), arXiv:hep-ph/0201131.

[36] T. Gherghetta, Phys.Rev.Lett. **92**, 161601 (2004), arXiv:hep-ph/0312392.

[37] G. Moreau, Eur.Phys.J. **C40**, 539 (2005), arXiv:hep-ph/0407177.

[38] F. del Aguila, J. Aguilar-Saavedra, B. Allanach, J. Alwall, Y. Andreev, et al., Eur.Phys.J. **C57**, 183 (2008), arXiv:0801.1800[hep-ph].

[39] M. Raidal, A. van der Schaaf, I. Bigi, M. Mangano, Y. K. Semertzidis, et al., Eur.Phys.J. **C57**, 13 (2008), arXiv:0801.1826[hep-ph].

[40] G. Cacciapaglia, A. Deandrea, D. Harada, and Y. Okada, JHEP **1011**, 159 (2010a), arXiv:1007.2933[hep-ph].

[41] G. Cacciapaglia, A. Deandrea, L. Panizzi, N. Gaur, D. Harada, et al. (2011), arXiv:1108.632[hep-ph]9.

[42] S. Gopalakrishna, T. Mandal, S. Mitra, and R. Tibrewala, Phys.Rev. **D84**, 055001 (2011), arXiv:1107.4306[hep-ph].

[43] J. Aguilar-Saavedra, Phys.Lett. **B625**, 234 (2005), arXiv:hep-ph/0506187.

[44] J. Aguilar-Saavedra, JHEP **0911**, 030 (2009), arXiv:0907.3155[hep-ph].

[45] A. Ivanov (CDF and D0 Collaboration) (2011), 14 pages, 6 figures, FPCP 2011 Conference Proceedings, arXiv:1109.1025[hep-ph].

[46] G. Burdman, M. Perelstein, and A. Pierce, Phys.Rev.Lett. **90**, 241802 (2003), arXiv:hep-ph/0212228.

[47] T. Han, H. E. Logan, B. McElrath, and L.-T. Wang, Phys.Rev. **D67**, 095004 (2003), arXiv:hep-ph/0301040.

[48] M. Perelstein, M. E. Peskin, and A. Pierce, Phys.Rev. **D69**, 075002 (2004), arXiv:hep-ph/0310039.

[49] H.-C. Cheng, I. Low, and L.-T. Wang, Phys.Rev. **D74**, 055001 (2006), arXiv:hep-ph/0510225.

[50] G. Cacciapaglia, S. Choudhury, A. Deandrea, N. Gaur, and M. Klasen, JHEP **1003**, 059 (2010b), arXiv:0911.4630[hep-ph].

[51] N. Vignaroli (2011), arXiv:1107.4558[hep-ph].

[52] R. Contino and G. Servant, JHEP **0806**, 026 (2008), arXiv:0801.1679[hep-ph].

[53] C. Dennis, M. Karagoz, G. Servant, and J. Tseng (2007), arXiv:hep-ph/0701158.

[54] K. Agashe and G. Servant, JCAP **0502**, 002 (2005), arXiv:hep-ph/0411254.

[55] G. Brooijmans et al. (New Physics Working Group), pp. 191–380 (2010), arXiv:1005.1229[hep-ph].

[56] C. Bini, R. Contino, and N. Vignaroli, JHEP **1201**, 157 (2012), arXiv:1110.6058[hep-ph].

[57] R. Barceló, A. Carmona, M. Masip, and J. Santiago, Phys.Lett. **B707**, 88 (2012a), arXiv:1106.4054[hep-ph].

[58] R. Barceló, A. Carmona, M. Chala, M. Masip, and J. Santiago, Nucl.Phys. **B857**, 172 (2012b), arXiv:1110.5914[hep-ph].

[59] F. del Aguila, L. Ametller, G. L. Kane, and J. Vidal, Nucl. Phys. **B334**, 1 (1990).

[60] F. del Aguila, G. L. Kane, and M. Quiros, Phys.Rev.Lett. **63**, 942 (1989).

[61] G. D. Kribs, A. Martin, and T. S. Roy (2010), arXiv:1012.2866[hep-ph].

[62] G. Azuelos, K. Benslama, D. Costanzo, G. Couture, J. Garcia, et al., Eur.Phys.J. **C39S2**, 13 (2005), arXiv:hep-ph/0402037.

[63] A. Djouadi and G. Moreau, Phys.Lett. **B660**, 67 (2008), arXiv:0707.3800[hep-ph].

[64] A. Djouadi, G. Moreau, F. Richard, and R. K. Singh, Phys.Rev. **D82**, 071702 (2010), arXiv:0906.0604[hep-ph].

[65] A. Djouadi, G. Moreau, and F. Richard, Phys.Lett. **B701**, 458 (2011), arXiv:1105.3158[hep-ph].

[66] A. Azatov, M. Toharia, and L. Zhu, Phys.Rev. **D82**, 056004 (2010), arXiv:1006.5939[hep-ph].

[67] A. Djouadi, Phys.Lett. **B435**, 101 (1998), arXiv:hep-ph/9806315.

[68] CMS web page, `https://twiki.cern.ch/twiki/bin/view/CMSPublic/PhysicsResults` (2012).

[69] ATLAS web page, `https://twiki.cern.ch/twiki/bin/view/AtlasPublic` (2012).

[70] ATLAS Collaboration (2012a), arXiv:1202.1408[hep-ex].

[71] S. Chatrchyan et al. (CMS Collaboration) (2012a), arXiv:1202.1488[hep-ex].

[72] M. Aliev, H. Lacker, U. Langenfeld, S. Moch, P. Uwer, et al., Comput.Phys.Commun. **182**, 1034 (2011), arXiv:1007.1327[hep-ph].

[73] S. Dittmaier et al. (LHC Higgs Cross Section Working Group) (2011), arXiv:1101.0593[hep-ph].

[74] S. Chatrchyan et al. (CMS Collaboration) (2012b), submitted to Physics Letters B, arXiv:1203.5410[hep-ex].

[75] S. Chatrchyan et al. (CMS Collaboration), Phys.Rev.Lett. **107**, 271802 (2011a), arXiv:1109.4985[hep-ex].

[76] G. Aad et al. (ATLAS Collaboration) (2012), arXiv:1202.3076[hep-ex].

[77] CERN Council Presentation, December 2011: http://indico.cern.ch/conferenceDisplay.py?confId=164890 (2011).

[78] ATLAS Collaboration (2012b), ATLAS-CONF-2012-019.

[79] R. Barbieri, L. J. Hall, Y. Nomura, and V. S. Rychkov, Phys.Rev. **D75**, 035007 (2007), arXiv:hep-ph/0607332.

[80] L. Lavoura and J. P. Silva, Phys.Rev. **D47**, 2046 (1993).

[81] K. Nakamura et al. (Particle Data Group), J.Phys. **G37**, 075021 (2010).

[82] N. D. Christensen and C. Duhr, Comput.Phys.Commun. **180**, 1614 (2009), arXiv:0806.4194[hep-ph].

[83] M. Herquet and F. Maltoni, Nucl.Phys.Proc.Suppl. **179-180**, 211 (2008).

[84] T. Sjostrand, S. Mrenna, and P. Z. Skands, JHEP **05**, 026 (2006), arXiv:hep-ph/0603175.

[85] S. Ovyn, X. Rouby, and V. Lemaitre (2009), arXiv:0903.2225[hep-ph].

[86] M. L. Mangano, M. Moretti, F. Piccinini, R. Pittau, and A. D. Polosa, JHEP **07**, 001 (2003), arXiv:hep-ph/0206293.

[87] S. Chatrchyan et al. (CMS Collaboration) (2012c), arXiv:1202.1487[hep-ex].

[88] S. Chatrchyan et al. (CMS Collaboration) (2012d), arXiv:1202.1997[hep-ex].

[89] S. Chatrchyan et al. (CMS Collaboration) (2011b), CMS-PAS-BTV-11-002.

[90] A. Abulencia et al. (CDF Collaboration), Phys.Rev. **D73**, 032003 (2006), arXiv:hep-ex/0510048.

[91] S. Chatrchyan et al. (CMS Collaboration) (2011c), CMS-PAS-EXO-11-051.

[92] S. Catani, L. Cieri, D. de Florian, G. Ferrera, and M. Grazzini, Phys. Rev. Lett. **108**, 072001 (2012).

[93] A. Falkowski, Phys.Rev. **D77**, 055018 (2008), arXiv:0711.0828[hep-ph].

[94] J. Espinosa, C. Grojean, and M. Muhlleitner, JHEP **1005**, 065 (2010), arXiv:1003.3251[hep-ph].

[95] F. Ledroit, G. Moreau, and J. Morel, JHEP **0709**, 071 (2007), arXiv:hep-ph/0703262.

[96] S. Casagrande, F. Goertz, U. Haisch, M. Neubert, and T. Pfoh, JHEP **1009**, 014 (2010), arXiv:1005.4315[hep-ph].

[97] M. Pieri (CMS Collaboration), "Searches for the SM Scalar Boson at CMS", Moriond EW, La Thuile, 3-10 March 2012.

Chapter 6

Corrections to the Higgs couplings and VEV shift within warped extra dimension models

Adapted from: *C. Bouchart and G. Moreau*, Phys. Rev. **D80** (2009) 095022.

6.1 Introduction

The Standard Model (SM) represents a successful description of the ElectroWeak (EW) interactions. Nevertheless, the instability of the EW scale under radiative corrections is a strong indication for a new physics underlying the SM. The attractive scenario proposed by Randall and Sundrum (RS) [1] to stabilize the EW scale is based on a 5–dimensional (5D) theory where the extra dimension is warped and compactified. The non–factorisable metric there is of type Anti–de Sitter and the space-time, which is thus a slice of AdS_5, has two 4–dimensional boundaries: the ultra–violet (UV) boundary at the Planck scale and the infra–red (IR) brane with an exponentially suppressed scale in the vicinity of the TeV scale. The Higgs boson has to be localized at this so–called TeV–brane if the EW scale is to be stabilized by such a geometrical structure.
In contrast, letting propagate the other SM fields in the bulk [2] allows to suppress higher dimensional operators, potentially troublesome with respect to Flavor–Changing Neutral Current effects, by energy scales larger than the TeV scale. This feature has also the advantage to possibly generate the fermion mass hierarchy and flavor structure by a simple geometrical mechanism [2–4] (even including the small neutrino mass scale [5]). In addition, this RS version with bulk matter allows for the unification of gauge couplings at high–energies [6]. More generically speaking, this RS version often turns out to constitute a suitable framework for model building issues.

From a general point of view, those RS models with a fundamental Higgs boson, the alternative

models of gauge–Higgs unification [7] and the Higgsless models [8] can be thought of as warped extra dimension models constituting dual descriptions, through the AdS/CFT correspondence [9], of 4D strongly coupled gauge theories (in the limit of a large number of colors) predicting the effective Higgs field as a composite state (see e.g. [10]).

Within this new paradigm about the Higgs field sector, one has to take care of the realization of the ElectroWeak Symmetry Breaking (EWSB). In particular, additional contributions to the SM observables arise e.g. for the EW gauge boson masses $m_{W,Z}$ and, in turn, for the Fermi coupling constant G_F. More precisely, within the RS scenario, these tree–level $m_{W,Z}$ corrections, with respect to the pure Higgs boson Vacuum Expectation Value (VEV) contribution, originate from the mixing between zero–mode gauge bosons and their Kaluza–Klein (KK) excitations. Even for relatively heavy KK states, this gauge boson mixing, induced by mass mixing terms also driven by the Higgs VEV, could be quite large since the KK boson wave functions are generally peaked at the TeV–brane where is confined the Higgs boson. Therefore significant corrections to the SM Higgs VEV can be expected, with various important phenomenological implications.

In the present work, we first compute the Higgs VEV in the RS context from EW data, including SM loop corrections, and find that significant deviations w.r.t. the SM Higgs VEV can be reached in large regions of the allowed parameter space. This computation allows us to treat precisely the oblique parameters S,T,U [11] which depend on the Higgs VEV, and hence to analyze the constraints from precision EW observables. A new aspect that matters for these EW Precision Tests (EWPT) is that the correlation between S and T through the RS parameters is modified by the new VEV dependence on these parameters. These EWPT, based on updated experimental data, are studied under the theoretical assumption of a bulk gauge custodial symmetry $\mathrm{SU(2)_L \times SU(2)_R \times U(1)_X}$ which allows to reduce the final bound on the mass of the first KK gauge boson excitation M_{KK} (strictly, the KK photon mass) from ~ 10 TeV [12] down to roughly a few TeV [13], avoiding then the little hierarchy problem. However, an important result here is that this EWPT analysis leads to more severe bounds on M_{KK} when the obtained VEV deviations are taken into account: the increase of this limit, at $95\% C.L.$, can reach $\sim +1$ TeV in some extreme situations.

Such increases of the limit on M_{KK} are crucial for the next–coming LHC search of resonances due to the direct production of KK excitations of gluons or EW gauge bosons [14] in RS–like models. Another possibility for discovering signatures of RS models at next colliders is to observe deviations of the Higgs boson couplings from their values predicted by the SM. Such deviations may also of course play a primordial role in the experimental observation of the Higgs boson.

Hence, we compute the Higgs boson couplings, based on the VEV determination mentioned above. We find that the deviations of the Higgs couplings from the SM values can be large and also that major parts of those are due to the VEV corrections in RS. The Higgs couplings to pairs of fermions and EW gauge bosons as well as the effective couplings at loop level to two gluons or two photons are calculated, taking into account the studied EW precision constraints on

M_{KK}. In particular, we make the connection between the possible RS solution [15] of the anomaly on the forward–backward b–quark asymmetry A_{FB}^b observed in e^+e^- collisions [16] and the cross section $\sigma(gg \to h)$ for the main Higgs production process at the LHC: the gluon–gluon fusion mechanism which proceeds through heavy (KK) quark triangular loops. Those past and present collider observables A_{FB}^b and $\sigma(gg \to h)$ are indeed connected through the choice of localization in the bulk, for the bottom and top quarks, that fixes their couplings and own masses.

At this stage, one has to mention related works about the Higgs boson couplings within the AdS/CFT paradigm. First, the gluon–gluon–Higgs amplitude has been computed in the context of a 5D gauge–Higgs unification as a dual realization of 4D composite Higgs scenarios [18]. $\sigma(gg \to h)$ has also been evaluated in warped extra dimension models [19] (based on a bulk custodial symmetry [20,21]) without a precise consideration of EWPT. The effective Higgs coupling to two photons has been compared among various extra dimensional models for some fixed sets of parameters [19,21]. Besides, the rate deviations from SM predictions, for various Higgs detection channels at LHC, have been computed within the strongly–interacting light Higgs models [22]: the LHC will be able to explore values of the cut–off scale $4\pi f$ (where the model becomes strongly coupled) up to $5-7$ TeV. Finally, the deviations of the Higgs couplings to EW gauge bosons have been computed in the framework of the so–called gaugephobic Higgs boson scenarios [23]. There, the Higgs couplings can be very suppressed (in case of a bulk Higgs) [24].

The organization of the study is as follows. In Section 6.2, the corrections to the Higgs VEV arising in the RS framework are computed. The connections with EWPT and the Higgs boson phenomenology are studied in the next sections. In Section 6.3, an analysis of the oblique parameters is performed in order to derive the induced bounds on the KK scale. Then in Section 6.4, the Higgs couplings are discussed. Finally, variations on the main scenario studied are briefly discussed in Section 6.5.

6.2 Higgs boson VEV

6.2.1 Theoretical framework

Energy scales: Within the RS model, the gravity scale on the Planck–brane is $M_{\rm Planck} = 2.44 \times 10^{18}$ GeV, whereas the effective scale on the TeV–brane $M_\star = e^{-\pi k R_c} M_{\rm Planck}$ is suppressed by the warp factor which depends on the curvature radius of the AdS space $1/k$ and on the compactification radius R_c. For a product $kR_c \simeq 11$, $M_\star = \mathcal{O}(1)$ TeV allowing to address the gauge hierarchy problem. We will take $kR_c \simeq 10.11$ so that the maximum value of $M_{KK} \simeq 2.45 k e^{-\pi k R_c}$, fixed by the theoretical consistency bound $k < 0.105 M_{\rm Planck}$, is ~ 10 TeV in agreement with the the typical EWPT limits at a few TeV and the range of M_{KK} values considered here.
The parameters noted c_f fix the 5D masses $\pm c_f k$, affected to each fermion f, and thus control the fermion localizations in the bulk. Those satisfy $|c_f| = \mathcal{O}(1)$ to avoid the introduction of new

fundamental scales.

Gauge symmetry breaking: The SM gauge group is recovered after the breaking of the $SU(2)_R$ group into $U(1)_R$, by boundary conditions and possibly also by a small breaking of $SU(2)_R$ in the bulk effectively parametrized by the $\widetilde{W}^{\pm}$ mass $\tilde{M}$ (the $\widetilde{W}^{\pm}_{\mu}$ boson associated to $SU(2)_R$ without zero–mode). Then the breaking $U(1)_R \times U(1)_X \to U(1)_Y$ occurs via a VEV on the UV brane: the state $\widetilde{W}^3$, associated to $U(1)_R$, mixes with $\widetilde{B}$, associated to $U(1)_X$, to give the SM hypercharge B boson, the orthogonal linear combination being the extra Z' boson. The Z' has no zero–mode and its first KK mass is close to M_{KK}: $M'_{KK} \simeq 2.40ke^{-\pi kR_c}$.

6.2.2 VEV modification

As in the SM, the Higgs VEV value is determined by the Fermi constant G_F. Nevertheless, the corrections to G_F due to the mixing of the SM boson $W^{\pm}$ with its KK excitations introduce a dependence on the bare EW gauge coupling constants g and g' [1]. So within the RS context two other observables must be used to fix the values of the Higgs VEV noted $\tilde{v}$ and the two bare parameters g, g'. The natural choice is to use the EW gauge boson masses m_W and m_Z. The divergent parts of the one–loop EW loop corrections to respectively G_F and $m_{Z,W}$ will affect the hVV coupling ($V = Z^0, W^{\pm}$), via $\tilde{v}$, g, g', but will be canceled out by the SM quantum corrections to the coupling itself: respectively the Higgs boson self–energy and the vertex irreducible correction [25]. The inputs G_F and m_Z are among the most accurately measured quantities and serve as excellent reference points for EWPT as will be described later. The tiny experimental error on m_W (see updated value in [26]) turns out to not affect significantly the $\tilde{v}$ value obtained that way.

The Z boson mass defined as the pole of its propagator reads as [2],

$$m_Z^2 = (g^2 + g'^2)\frac{\tilde{v}^2}{4} + (g^2 + g'^2)\ \Pi_{33}(m_Z^2) + \delta^{\rm SM} m_Z^2, \tag{6.1}$$

where $\Pi_{33}(q^2)$ is the vacuum polarization amplitude taking into account the RS–type corrections, more precisely the KK gauge mixing effect [13]:

$$\Pi_{33}(q^2) = \pi R_c \left(\frac{\tilde{v}^2}{4}\right)^2 \left[(g^2 + g'^2)\ (G^{5D}_{q(++)} - G^{(0)}_{q(++)}) + g^2_{Z'}\ \cos^4\theta'\ G^{5D}_{q(-+)}\right]. \tag{6.2}$$

$G^{5D}_{q(++)}$ ($G^{5D}_{q(-+)}$) is the 5D propagator for the W^3,B (Z') KK excitations. $(++)$ $((-+))$ indicates Neumann (Dirichlet) and Neumann boundary conditions on the Planck–brane and TeV–brane, respectively. The massless pole is subtracted from the W^3 and B towers. The new mixing angle is given by $\sin\theta' \equiv \tilde{g}'/g_{Z'}$ with $g^2_{Z'} = \tilde{g}^2 + \tilde{g}'^2$, where $\tilde{g}$ and $\tilde{g}'$ are respectively the $SU(2)_R$ and

[1] We have checked numerically that the main RS corrections to G_F are oblique, the direct corrections to the leptonic vertex $Wl\nu$ being negligible in comparison.

[2] There is no Π_{3Q} neither Π_{QQ} terms in the m_Z^2 expression as there is no KK mixing involving the photon.

$\mathrm{U(1)_X}$ couplings; the coupling g' of the SM $\mathrm{U(1)_Y}$ group reads as $g' = \tilde{g}\tilde{g}'/g_{Z'}$. One deduces $2\sin^2\theta' = 1 \pm \sqrt{1-(2g'/g_{Z'})^2}$.
$\delta^{\rm SM} m_Z^2$ is the SM one–loop correction [25]:

$$\delta^{\rm SM} m_Z^2 = \frac{3g_Z^2}{16\pi^2}\sum_{f=t,b} m_f^2\left(\frac{\mu}{m_f}\right)^{2\epsilon}\left[\frac{1}{2\epsilon}+\frac{\pi^2\epsilon}{24}+\mathcal{O}(\epsilon^2)\right], \tag{6.3}$$

$D = 4-2\epsilon$ being the space-time dimension in dimensional regularization and μ the 't Hooft renormalization scale. For the SM corrections, we restrict to top–quark loops as those constitute the dominant EW corrections to productions and decays of a light Higgs boson ($m_h \ll 2m_t$). Indeed, we will consider Higgs masses below 150 GeV leading to the lowest EWPT limits on M_{KK} as preferred by little hierarchy arguments.
Similarly, one has,

$$m_W^2 = g^2\frac{\tilde{v}^2}{4} + g^2\ \Pi_{11}(m_W^2) + \delta^{\rm SM} m_W^2, \tag{6.4}$$

with,

$$\Pi_{11}(q^2) = \pi R_c\left(\frac{\tilde{v}^2}{4}\right)^2\left[g^2\ (G^{5D}_{q(++)} - G^{(0)}_{q(++)}) + \tilde{g}^2\ G^{5D}_{q(-+)}\right], \tag{6.5}$$

$$\delta^{\rm SM} m_W^2 = \frac{3g^2}{16\pi^2}\left(\frac{\mu}{m_t}\right)^{2\epsilon}\left[\frac{m_b^2+m_t^2}{2\epsilon}+\frac{m_b^2+m_t^2}{4}+\frac{m_b^4\ ln(m_b^2/m_t^2)}{2(m_t^2-m_b^2)}+\mathcal{O}(\epsilon)\right]. \tag{6.6}$$

Taking the limit $q^2 \to 0$, one obtains

$$\frac{1}{4\sqrt{2}G_F} = \frac{\tilde{v}^2}{4} + \Pi_{11}(0) + \delta^{\rm SM} G_F^{-1}, \tag{6.7}$$

with at first order in $1/k\pi R_c$

$$\Pi_{11}(0) = -k\pi R_c\frac{g^2}{32}\left(\frac{\tilde{v}^2}{ke^{-\pi k R_c}}\right)^2\left[1-\frac{1}{k\pi R_c}\right] - k\pi R_c\frac{\tilde{g}^2}{32}\left(\frac{\tilde{v}^2}{ke^{-\pi k R_c}}\right)^2\left[1-\frac{\tilde{M}^2}{4k^2}\right], \tag{6.8}$$

and,

$$\delta^{\rm SM} G_F^{-1} = \frac{6}{(8\pi)^2}\left[\frac{m_b^2+m_t^2}{2}+\frac{m_b^2\ ln(m_b^2/m_t^2)}{(1-m_b^2/m_t^2)}\right]. \tag{6.9}$$

Numerically, the SM loop corrections are small compared to the RS tree–level ones, as we are going to see. We do not consider higher order corrections involving both loops and KK excitations. Hence, the quantities $\tilde{v}$, g and g' can be determined within given RS scenarios by solving the system formed by the three equations: Eq.(6.1), Eq.(6.4) and Eq.(6.7). We have checked that the computation of the gauge boson masses through Eq.(6.1)-(6.4) is equivalent to their calculation within the perturbation approach in the limit of the inclusion of a large number of KK excitations [see the description of the KK gauge boson mass matrix in Section 6.4]. The obtained value for the coupling constant g is $g = 0.653$ in both the SM and RS models, which means with and without

the corrections due to KK mixing. g' takes similar values in the SM and RS models: $g' = 0.356$ and $g' = 0.357$ respectively. The numerical results for $\tilde{v}$ with characteristic values of the parameters M_{KK} and $g_{Z'}$ are shown in Table 6.1. The motivation for the chosen values of M_{KK} will become clear in Section 6.3. The allowed range for the $g_{Z'}$ value is defined as follows. The minimum $g_{Z'}$ value is equal to $2g' \simeq 0.72$ for consistency reasons about the θ' mixing angle. On the other side, the perturbativity condition for the Z' boson coupling is that $2k\pi R_c g_{Z'}^2 Q_{Z'}^2/16\pi^2$ must be smaller than unity according to the naive dimensional argument [10,14]. The reason being that the effective 4D coupling of Z' is increased by a factor as large as $\sqrt{2\pi kR_c}$ for fields at the TeV–brane. In general even for reproducing the correct top mass, the top quark field is not exactly located on the TeV–brane but has only a peaked profile there, so that the real overlap factor should be significantly smaller than $\sqrt{2k\pi R_c}$. We will consider the coupling constant constraint $g_{Z'} < 2\sqrt{2\pi/kR_c} \simeq 1.57$, keeping in mind that the new charge $Q_{Z'}$ is an additional source for suppressing the Z' coupling given e.g. the $\mathrm{SU(2)_R}$ fermionic representations addressing the A_{FB}^b anomaly [28].
The first observation from Table 6.1 is that the RS induced deviations to the Higgs VEV are large compared to the pure SM quantum corrections: the Higgs VEV is at the reference value of $v = 246$ GeV in the SM at tree–level and at $v_{SM} = 245$ GeV after including the one–loop EW corrections in Eq.(6.7) for $m_t = 173.1$ GeV [27]. Because of the negative sign of $\Pi_{11}(0)$, the variation of the Higgs VEV induced in RS is positive as show the $\tilde{v}$ values in Table 6.1 which are significantly larger than v_{SM}. This increase of the VEV is higher with the reduction of M_{KK} (e.g. at fixed $g_{Z'} = 1.57$) or with the enhancement of $g_{Z'}$ is explained by a larger KK gauge mixing effect in Eq.(6.1)-(6.4)-(6.7). The increase of the KK mixing with $g_{Z'}$ will be clear from the texture of the KK gauge boson mass matrix (see Appendix B.1).

6.3 EW precision tests

The mixings with KK gauge boson excitations induce modifications of the EW gauge boson propagators, the oblique corrections, that can be parametrized by the three $S_{\rm RS}$,$T_{\rm RS}$,$U_{\rm RS}$ quantities [11] (we define those such that they vanish in the absence of KK mixing). Here, we are interested in variations of the constraints from considerations on S,T due to the corrections on the Higgs VEV. There exist also constraints on the W, Y parameters [29] [3]. Compared to S,T, these parameters are proportional to higher derivatives of the vacuum polarization amplitudes, involved in higher order terms of the $\Pi_V(q^2)$ expansion, that are not considered within the present RS models. W and Y allow to take into account the relevant LEP2 observables, namely, the differential cross sections for $e^+e^- \to f\bar{f}$ which we already partially include in this analysis: the process $e^+e^- \to b\bar{b}$ is included in the A_{FB}^b solution above the Z pole studied in Section 6.4. The corrections to EW observables in the third quark generation sector [b and t] are treated separately through a fit independent from the oblique parameters. In contrast, for the light SM fermions, the associated parameters

[3] The present model does not belong to the category of universal theories considered in [29].

A] $m_h = 120$ GeV, $g_{Z'} = 1.57$	**B]** $m_h = 120$ GeV, $g_{Z'} = 0.72$	**C]** $m_h = 150$ GeV, $g_{Z'} = 1.57$
$M_{KK} = 4025$ GeV	$M_{KK} = 3370$ GeV	$M_{KK} = 4095$ GeV
$\tilde{v} = 322$ GeV	$\tilde{v} = 257$ GeV	$\tilde{v} = 311$ GeV
$g^{RS}_{hZZ}/g^{SM}_{hZZ} = 57.3\%$	$g^{RS}_{hZZ}/g^{SM}_{hZZ} = 87.2\%$	$g^{RS}_{hZZ}/g^{SM}_{hZZ} = 60.1\%$
$g^{RS}_{hWW}/g^{SM}_{hWW} = 57.5\%$	$g^{RS}_{hWW}/g^{SM}_{hWW} = 87.4\%$	$g^{RS}_{hWW}/g^{SM}_{hWW} = 60.3\%$
$\lambda^{RS}_{\tau}/\lambda^{SM}_{\tau} = 76.2\%$	$\lambda^{RS}_{\tau}/\lambda^{SM}_{\tau} = 95.5\%$	$\lambda^{RS}_{\tau}/\lambda^{SM}_{\tau} = 79.1\%$
$\lambda^{RS}_{b}/\lambda^{SM}_{b} = [71, 75]\%$	$\lambda^{RS}_{b}/\lambda^{SM}_{b} = [90, 93]\%$	$\lambda^{RS}_{b}/\lambda^{SM}_{b} = [74, 78]\%$
$g^{RS}_{hgg}/g^{SM}_{hgg} = [77.6, 80.8]\%$	$g^{RS}_{hgg}/g^{SM}_{hgg} = [96.2, 99.1]\%$	$g^{RS}_{hgg}/g^{SM}_{hgg} = [80.1, 83.3]\%$
$g^{RS}_{h\gamma\gamma}/g^{SM}_{h\gamma\gamma} = [74.9, 75.1]\%$	$g^{RS}_{h\gamma\gamma}/g^{SM}_{h\gamma\gamma} = [100.6, 100.8]\%$	$g^{RS}_{h\gamma\gamma}/g^{SM}_{h\gamma\gamma} = [77.1, 77.3]\%$

Table 6.1: Numerical results for the lower limit at 95.45%$C.L.$ on M_{KK} (from EWPT) and for the Higgs boson VEV within the RS scenario, with three characteristic sets of parameters [called A, B and C]. $\tilde{M}/k = 0.11$, 0.41 and 0.12 respectively (optimized values leading to the minimum M_{KK} limits) for the points A, B and C. Note that $\tilde{v}$ is obtained for the indicated allowed M_{KK} value, and reciprocally, the M_{KK} limit corresponds to the given Higgs VEV. For these 3 points, the values for the ratios (RS over SM) of the effective Higgs couplings to EW gauge bosons (Z, W, γ), gluons (g) and fermions (τ, b) are also given. The Yukawa coupling ratios for the other light fermions are identical to the τ lepton one given here.

$c_{\rm light}$ are taken larger than 0.5 to generate small masses [3] and to minimize their couplings to KK gauge boson excitations (and thus corrections to EW observables). Then the fermion–Higgs higher–dimensional operators, obtained after having integrated out heavy KK modes, get a special form which allows one to redefine their effects into purely oblique corrections [13]. The effects from the effective 4–fermion operators are negligible [13] for $c_{\rm light} > 0.5$ and $M_{KK} \geq 3$ TeV.

For $c_{\rm light} \geq 0.5$, the oblique parameter $S_{\rm RS}$ reads as (not writing terms suppressed e.g. by $1/k\pi R_c$ factors [13, 30] which are however included numerically),

$$S_{\rm RS} \simeq 2\pi \left(\frac{2.45\ \tilde{v}}{M_{KK}}\right)^2 - \pi^2 k R_c\ \frac{g^2 + g'^2 + g^2_{Z'}\cos^4\theta'}{16} \left(\frac{2.45\ \tilde{v}}{M_{KK}}\right)^4 , \tag{6.10}$$

where the first term is the contribution from fermion–Higgs higher–dimensional operators. The

other term comes from the gauge–Higgs sector and is at order $(\tilde{v}/M_{KK})^4$ thus smaller than the first one. Here, we insist on the fact that g and g' are the bare coupling constants, that are computed as described in Section 6.2.2. It was shown recently that the KK mixing induces one–loop contributions (considering only the Higgs sector [31]) to the S parameter which are not finite and are cut–off dependent (or depend on an energy scale). The physical m_h dependence in S should be approached with care in such a 5D theory as it can be affected by a renormalization procedure. Therefore here, given our goal of studying the Higgs VEV correction effect, we do not consider higher order corrections to S involving both loops and KK excitations.
the oblique parameter $T_{\rm RS}$ is given by,

$$\alpha_0 T_{\rm RS} \equiv \frac{g^2+g'^2}{m_Z^2}(\Pi_{11}(0)-\Pi_{33}(0)) \simeq k\pi R_c \, \frac{g^2+g'^2}{m_Z^2} \, \frac{\tilde{g}^2}{32} \, \frac{\tilde{M}^2}{4k^2} \left(\frac{2.45\ \tilde{v}^2}{M_{KK}}\right)^2 , \tag{6.11}$$

where $\alpha_0 = \alpha(q^2=0)$ is the QED fine structure constant given e.g. in [32] and $\tilde{M}$ is the $\widetilde{W}^{\pm}$ mass originating from the small bulk breaking of $\mathrm{SU(2)_R}$. This expression has the interest of illustrating the custodial protection of $T_{\rm RS}$. Other scenarios, including in particular the case where $\mathrm{SU(2)_R}$ remains unbroken in the bulk, are discussed later.
The parameter $U_{\rm RS}$ is non–vanishing only at the order $(\tilde{v}/M_{KK})^4$ in the KK expansion, in contrast with $S_{\rm RS}$ and $T_{\rm RS}$. Hence, for the relevant values of RS parameters, the $U_{\rm RS}$ values obtained are totally negligible compared to $S_{\rm RS}$, $T_{\rm RS}$. We thus fix $U_{\rm RS}$ at zero in an extremely good approximation.

The corrections to EW observables measured up to the m_Z scale can be expressed in function of the three variables $S_{\rm RS}$,$T_{\rm RS}$,$U_{\rm RS}$ (we keep $U_{\rm RS}$ at this stage for the completeness of given formulas). We concentrate on the experimental measurements of m_W, $\sin^2\theta_{\rm eff}^{\rm lept}$ [4] and the partial Z width into charged leptons $\Gamma_{\ell\ell}$ as those are the most precise and crucial in constraining the plan $\{T,S\}$ [32]. The theoretical expression for the observable $m_{W^\pm}$ reads as

$$m_W^2 = m_W^2|_{ref} + \frac{\alpha_0\ c^2}{c^2-s^2} m_Z^2 \left(-\frac{1}{2}\ S_{\rm RS} + c^2\ T_{\rm RS} + \frac{c^2-s^2}{4s^2}\ U_{\rm RS}\right) \tag{6.12}$$

where $m_{W^\pm}|_{ref}$ represents the value calculated as accurately as possible within the pure SM and s (c) stands for $\sin\theta_W$ ($\cos\theta_W$), θ_W being the EW mixing angle. Here we emphasize that the strict expression for m_W involves the bare value of the EW mixing angle θ_W. The expression for $\sin^2\theta_{\rm eff}^{\rm lept}$ is

$$\sin^2\theta_{\rm eff}^{\rm lept} = \sin^2\theta|_{ref} + \frac{\alpha_0}{c^2-s^2}\left(\frac{1}{4}\ S_{\rm RS} - s^2c^2\ T_{\rm RS}\right). \tag{6.13}$$

[4] $\theta_{\rm eff}^{\rm lept}$ denotes the *Weinberg angle* modified by radiative corrections and the exponent "lept" means that it is the value which can be obtained directly from lepton asymmetry measurements.

The partial Z width reads as,

$$\Gamma_{\ell\ell} = \Gamma_{\ell\ell}|_{ref} + \alpha_0\ \Gamma^0_{\ell\ell}\Bigg(-\frac{2(1-4\sin^2\theta_0)}{(1+(1-4\sin^2\theta_0)^2)}\frac{S_{\rm RS}}{c^2-s^2} + \Bigg\{1+\frac{8(1-4\sin^2\theta_0)}{(1+(1-4\sin^2\theta_0)^2)}\frac{s^2c^2}{c^2-s^2}\Bigg\}T_{\rm RS}\Bigg), \tag{6.14}$$

with,

$$\Gamma^0_{\ell\ell} = \frac{m_Z^3\ G_F}{3\sqrt{2}\pi}(2\sin^4\theta_0 - \sin^2\theta_0 + \frac{1}{4}).$$

$\sin\theta_0$ involves the electroweak mixing angle obtained in the improved Born approximation, namely by taking into account only the well–known QED running of α up to m_Z:

$$\sin^2\theta_0 = \frac{1}{2}\left[1-\sqrt{1-4\frac{\pi\alpha}{\sqrt{2}G_F m_Z^2}}\right] = 0.2310$$

where $\alpha = \alpha(q^2=m_Z^2) = \alpha_0/(1-\Delta\alpha)$ [33] with $\Delta\alpha = \Delta\alpha_{lept}+\Delta\alpha_{had}+\Delta\alpha_{top}$, $\Delta\alpha_{lept} = 0.0315$ [34] and $\Delta\alpha_{top} = -0.00007$ [34]. By virtue of the theorem obtained in Ref. [35], only SM fermions contribute to the α running and hence to the leptonic contribution $\Delta\alpha_{lept}$, the hadronic contribution $\Delta\alpha_{had}$ and the top quark one $\Delta\alpha_{top}$.
At the moment, there is a small controversy on the precise experimental value of $\Delta\alpha_{had}(m_Z^2)$. This value enters in our EWPT analysis through $\sin^2\theta_0$ as well as through the SM loop calculations of the fitted observables (see later). Recent measurements of $\Delta\alpha_{had}$ [32] via the e^+e^- annihilation cross sections give the results 0.02758 ± 0.00035 [36]; 0.027594 ± 0.000219 [37]; 0.02768 ± 0.00022 [38], whereas the measurement gives $\Delta\alpha_{had} = 0.02782 \pm 0.00016$ using the hadronic τ decays [39]. The consensus is still to use the e^+e^- data, which are close to each other. We thus use $\Delta\alpha_{had} = 0.02768 \pm 0.00022$, keeping in mind that the result from τ data is higher. If τ data are used in the calculation of a_μ^{SM}, the muon magnetic anomaly discrepancy decreases (from 3.1σ for e^+e^--based results [40]) down to 1.8σ (see recent updates in [39, 41]). While almost solving Δa_μ, the τ data, which raise the value of $\Delta\alpha_{had}$, lead to an EWPT upper bound on m_h of 133 GeV [39] leaving a narrow window for the SM Higgs mass, given the direct LEP2 lower bound of 114.4 GeV [42]. It is interesting to note that such a tension does not appear, within the RS framework, where both the EWPT limit can be higher (there is possibly a positive contribution to T) and the LEP2 limit smaller [see later]. For example, with $M_{KK} = 4.1$ TeV, $g_{Z'} = 1.51$ and $\tilde{M}/k = 0.14$, the EWPT limit at $95\% C.L.$ on m_h is 150 GeV for $\Delta\alpha_{had} = 0.02782$.

As shows e.g. Eq.(6.13), the accurate measurements of EW observables translate into limits in the plan $T_{\rm RS}$ versus $S_{\rm RS}$. These limits depend on the SM expectation e.g. noted $\sin^2\theta|_{ref}$ for $\sin^2\theta^{\rm lept}_{\rm eff}$. In general, the precise predictions of EW observable values calculated within the SM from QCD/EW corrections [43–45] depend in turn on the top and Higgs masses as well as on the strong coupling constant and the photon vacuum polarization $\Delta\alpha$.
In Fig.(6.1) are presented the limits in the plan $\{T_{\rm RS}, S_{\rm RS}\}$ [for $m_h = 120$ GeV] corresponding to values of $m_W = 80.399 \pm 0.025$ GeV (combined LEP2 and Tevatron Run II data) [26], $\Gamma_{\ell\ell} =$

83.985 ± 0.086 MeV (single lepton channel) [34, 46] and $\sin^2\theta^{\rm lept}_{\rm eff}$ within 1σ deviation from their experimental central value. The experimental value used here for $\sin^2\theta^{\rm lept}_{\rm eff}$ is a combination of the 5 values resulting from the 5 asymmetry measurements: $A^{\ell}_{FB}(m_Z)$, $\mathcal{A}_\ell(P_\tau)$, $\mathcal{A}_\ell(SLD)$, $A^{c}_{FB}(m_Z)$ and Q^{had}_{FB} [34, 46].

In Fig.(6.1) are also shown the contour levels in $\{T_{\rm RS}, S_{\rm RS}\}$ [$m_h = 120$; 150 GeV] associated to the confidence levels at $68.27\% C.L.$ and $95.45\% C.L.$. Those result from a χ^2–analysis of the fit between the RS theoretical predictions for the considered observables and their respective experimental value. In particular, the 95.45% level corresponds to $\chi^2/d.o.f. = 12.85/6$.

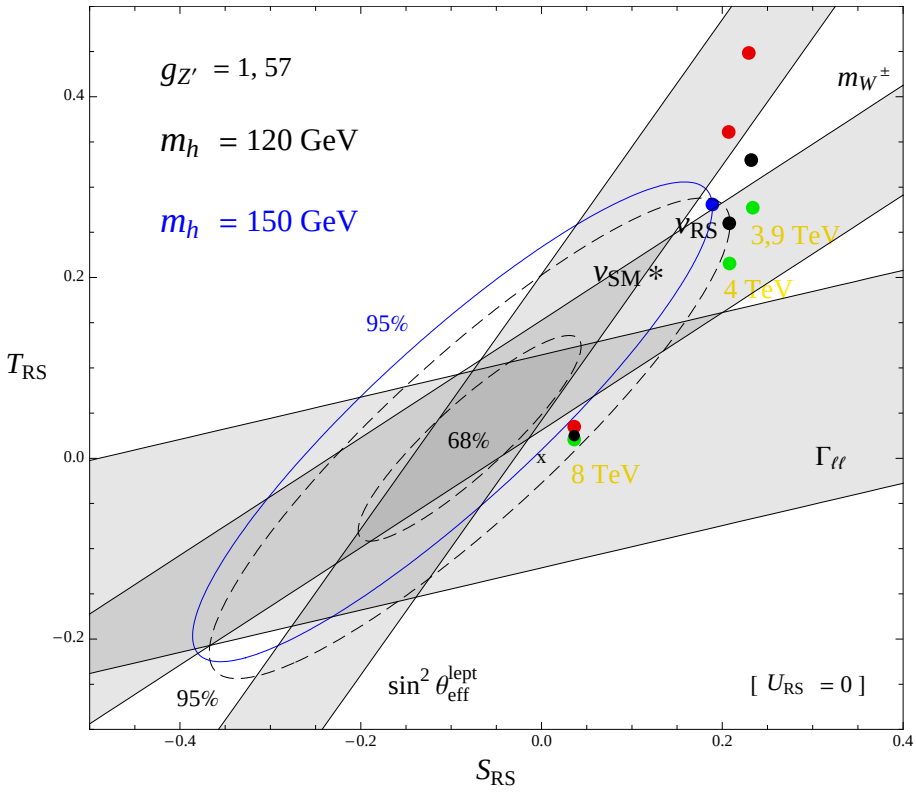

Figure 6.1: Contour levels in the plan $\{T_{\rm RS}, S_{\rm RS}\}$ at $68.27\% C.L.$ and $95.45\% C.L.$ for the fit of m_W, $\Gamma_{\ell\ell}$ and $\sin^2\theta^{\rm lept}_{\rm eff}$: the two ellipses in dashed–line are for $m_h = 120$ GeV, whereas the blue one in plain–line is for $m_h = 150$ GeV. Also shown, for $m_h = 120$ GeV, are the 1σ bands for the experimental values of the considered EW observables. We use the exact results from the two–loop calculations for $m_W|_{ref}$ (valid for 100 GeV $\lesssim m_h <$ 1 TeV) [43], $\Gamma_{\ell\ell}|_{ref}$ (75 GeV $< m_h <$ 350 GeV) [44] and $\sin^2\theta|_{ref}$ (10 GeV $< m_h <$ 1 TeV) [45]. The other quantities, on which these SM predictions depend, are fixed at $m_t = 173.1 \pm 1.3$ GeV (in agreement with the recent Tevatron data [27]), $\alpha_s = 0.1204 \pm 0.0009$ [34, 46, 47]. The plot is obtained for $g_{Z'} = 1.57$ and $U_{\rm RS} \simeq 0$. The three red, black, green points are associated to the theoretical predictions for the coordinates $S_{\rm RS}$,$T_{\rm RS}$ with $\tilde{M}/k = 0.13$; 0.11; 0.10 respectively. Those correspond to $m_h = 120$ GeV and $M_{KK} = 3980$, 4025, 8000 GeV from right to left – as indicated. While the blue point is for $m_h = 150$ GeV, $M_{KK} = 4095$ GeV and $\tilde{M}/k = 0.12$, the star corresponds to $m_h = 120$ GeV, $M_{KK} = 4025$ GeV and $\tilde{M}/k = 0.11$ but using $v_{SM} = 245$ GeV (rather than $v_{RS} = \tilde{v} = 322$ GeV). The cross is located at the origin.

The correlation between $S_{\rm RS}$ and $T_{\rm RS}$ through M_{KK}, $g_{Z'}$ is modified by the new dependence of

the Higgs VEV ($\tilde{v}$ entering Eq.(6.10)-(6.11)) on these parameters and on $\tilde{M}/k$ (via Eq.(6.1)-(6.8)). In particular, the lower limit at 95.45%$C.L.$, from the global EW fit, on M_{KK} as a function of $\tilde{M}/k$ possesses a minimum depending on $g_{Z'}$ and m_h. This feature is illustrated by the fact that, if e.g. $g_{Z'} = 1.57$ and $m_h = 120$ GeV, the lower limit is $M_{KK} = 4025$ GeV for $\tilde{M}/k = 0.11$ [5] (theoretical point in black exactly on the 95.45%$C.L.$ contour in the plan $\{T_{\rm RS}, S_{\rm RS}\}$ of Fig.(6.1)) whereas it is higher than 4025 GeV for $\tilde{M}/k = 0.10$ (green point on the 95.45%$C.L.$ contour for $8000 > M_{KK} > 4025$ GeV) as well as $\tilde{M}/k = 0.13$ (red points). The lower limit on M_{KK} at 95.45%$C.L.$ (for an optimized $\tilde{M}/k$ value corresponding to the minimum of that limit) increases with $\tilde{v}$ (making $S_{\rm RS}$ and $T_{\rm RS}$ larger) and hence with $g_{Z'}$, as shows Table 6.1 for $m_h = 120$ GeV. Finally, the effect of the increase of m_h on the M_{KK} limit is an enhancement (as shows Table 6.1) as it shifts the 95.45%$C.L.$ ellipsoidal contour according to Fig.(6.1), so that a larger M_{KK} is required to decrease $\tilde{v}$ and directly the $S_{\rm RS}$ coordinate of the theoretical point. Fig.(6.1) also illustrates that the behavior of the theoretical predictions for $S_{\rm RS}$ and $T_{\rm RS}$ in the limit of high M_{KK} is a convergence to zero. By consequence, for too large M_{KK}'s in the case e.g. $m_h = 150$ GeV, the theoretical points go out of the 95.45%$C.L.$ ellipse as this one does not contain the origin. There exist thus an upper limit at 95.45%$C.L.$ on M_{KK} due to EWPT which is $M_{KK} < 4490$ GeV for $g_{Z'} = 1.57$, $\tilde{M}/k = 0.12$ (even at this upper limit $\tilde{v} = 286$ GeV i.e. there is still a significant RS contribution).

An important result is the impact of the Higgs VEV corrections on the EWPT constraint on M_{KK}. Let us consider for instance the point A of parameter space given in Table 6.1 and represented in Fig.(6.1) as the black point sitting on the 95.45%$C.L.$ limit: replacing now the 'should–be' Higgs VEV $\tilde{v} = 322$ GeV by the SM value $v_{SM} = 245$ GeV, both the $S_{\rm RS}$ and $T_{\rm RS}$ values are reduced and the black point becomes the black star on the plot. To shift this star back to the 95.45%$C.L.$ ellipsoidal contour, one can decrease M_{KK} (at fixed $g_{Z'}$ and m_h) which would increase $S_{\rm RS}$ and $T_{\rm RS}$. Indeed, for $g_{Z'} = 1.57$, $m_h = 120$ GeV and the optimized $\tilde{M}/k = 0.14$, we find numerically that the 95.45%$C.L.$ lower limit is reduced from $M_{KK} = 4025$ GeV down to $M_{KK} = 3055$ GeV if one assumes instead a lower VEV fixed at $v_{SM} = 245$ GeV. In other words, the increase of the VEV due to included RS corrections has to be compensated by an increase of M_{KK}. In conclusion, the obtained significant increase of the Higgs VEV in RS [see the effect by comparing the black point and star in Fig.(6.1)] can lead to a large enhancement of the M_{KK} lower limit from EWPT, for given sets of RS parameters (it never translates into a reduction of the limit).

[5] The $\tilde{M}$ values considered are at worst an order of magnitude close to k, so that no new energy scale is introduced in the RS scenario, but remain smaller than k so that a small bulk breaking of the custodial–isospin is guaranteed.

6.4 Higgs boson couplings

6.4.1 Couplings to EW gauge bosons

After EWSB, the neutral gauge bosons (Z^0 and Z') and their KK excitations get masses through their couplings to the Higgs boson which has a bidoublet structure under the custodial symmetry group $\mathrm{SU}(2)_\mathrm{L}\times\mathrm{SU}(2)_\mathrm{R}$. These mass terms can be written, in the 4D Lagrangian including the first three KK excitations, as

$$\mathcal{L}^\mathrm{n}_\mathrm{mass}=\frac{1}{2}(Z^0_\mu \;\; Z^{(1)}_\mu \;\; Z'_\mu \;\; \dots \;\; Z^{(3)}_\mu \;\; Z'^{(3)}_\mu)\,\mathcal{M}_0^2\,(Z^{0\mu} \;\; Z^{(1)\mu} \;\; Z'^{\mu} \;\; \dots \;\; Z^{(3)\mu} \;\; Z'^{(3)\mu})^T$$

where the squared mass matrix $\mathcal{M}_0^2$ is given in Eq.(B.1). Numerically, we indeed include the KK tower up to the third excitations $Z^{(3)}$ and $Z'^{(3)}$ (included). This effective truncation of the tower induces an error of less than the percent on the hVV couplings computed in this section. Similarly, the charged gauge bosons ($W^\pm$ and $\widetilde{W}^\pm$) get KK–type and VEV–induced masses (*c.f.* Eq.(B.2)):

$$\mathcal{L}^\mathrm{c}_\mathrm{mass}=(W^+_\mu \;\; W^{+(1)}_\mu \;\; \widetilde{W}^+_\mu \;\; \dots \;\; W^{+(3)}_\mu \;\; \widetilde{W}^{+(3)}_\mu)\,\mathcal{M}_\pm^2\,(W^{-\mu} \;\; W^{-(1)\mu} \;\; \widetilde{W}^{-\mu} \;\; \dots \;\; W^{-(3)\mu} \;\; \widetilde{W}^{-(3)\mu})^T.$$

The mass matrix $\mathcal{M}_0^2$ is diagonalized by a 7×7 unitary matrix U, via the basis transformation $(Z_\mu \;\; Z^1_\mu \;\; Z^2_\mu \;\; \dots)^T = U\,(Z^0_\mu \;\; Z^{(1)}_\mu \;\; Z'_\mu \;\; \dots)^T$:

$$\mathcal{M}'^2_0 \equiv U\;\mathcal{M}_0^2\;U^\dagger \;=\; \mathrm{diag}\;(m_Z^2, m_{Z^1}^2, \dots, m_{Z^6}^2), \tag{6.15}$$

m_Z having to be associated with the experimental value for the Z boson mass (the unitary matrix is chosen such that $m_Z < m_{Z_1} < m_{Z_2} < \dots$). The Z_μ and Z^i_μ $[i=1,2,\dots]$ components are the mass eigenstates. The mass matrix $\mathcal{M}_\pm^2$ is diagonalized by a 7×7 unitary matrix V through,

$$\mathcal{M}'^2_\pm \equiv V\;\mathcal{M}_\pm^2\;V^\dagger \;=\; \mathrm{diag}\;(m_W^2, m_{W^1}^2, \dots, m_{W^6}^2). \tag{6.16}$$

The values of $\tilde{v}$, g and g' are obtained by solving the system formed by Eq.(6.7) and Eq(6.15)-(6.16) [first eigenvalue]. The $\tilde{v}$ values obtained that way do not differ significantly from the ones derived using the method developed in Section 6.2.2. From the obtained values of $\tilde{v}$, g, g', one can now deduce the rotation matrices U and V needed to compute the couplings.

In the weak basis, the 4D Higgs couplings to neutral gauge bosons are then

$$\mathcal{L}^\mathrm{n}_\mathrm{coupling}=\;\frac{h}{\tilde{v}}\;(Z^0_\mu \;\; Z^{(1)}_\mu \;\; Z'_\mu \;\; \dots \;\; Z^{(3)}_\mu \;\; Z'^{(3)}_\mu)\,\mathcal{C}_0\,(Z^{0\mu} \;\; Z^{(1)\mu} \;\; Z'^{\mu} \;\; \dots \;\; Z^{(3)\mu} \;\; Z'^{(3)\mu})^T$$

the matrix $\mathcal{C}_0$ being given in Eq.(B.3). For the charged gauge bosons [*c.f.* Eq.(B.5)],

$$\mathcal{L}^\mathrm{c}_\mathrm{coupling}=\;2\,\frac{h}{\tilde{v}}\,(W^+_\mu \;\; W^{+(1)}_\mu \;\; \widetilde{W}^+_\mu \;\; \dots \;\; W^{+(3)}_\mu \;\; \widetilde{W}^{+(3)}_\mu)\,\mathcal{C}_\pm\,(W^{-\mu} \;\; W^{-(1)\mu} \;\; \widetilde{W}^{-\mu} \;\; \dots \;\; W^{-(3)\mu} \;\; \widetilde{W}^{-(3)\mu})^T.$$

Moving to the mass basis, the neutral gauge boson interactions are described by the Lagrangian:

$$\mathcal{L}'^{\rm n}_{\rm coupling} \;=\; \frac{h}{\tilde{v}}\,(Z_\mu \;\; Z^1_\mu \;\; Z^2_\mu \;\; \dots)\,\mathcal{C}'_0\,(Z^\mu \;\; Z^{1\mu} \;\; Z^{2\mu} \;\; \dots)^T,\ \text{where, } \mathcal{C}'_0 \;=\; U\,\mathcal{C}_0\,U^\dagger. \quad (6.17)$$

Similarly,

$$\mathcal{L}'^{\rm c}_{\rm coupling} \;=\; 2\,\frac{h}{\tilde{v}}\,(W_\mu \;\; W^1_\mu \;\; W^2_\mu \;\; \dots)\,\mathcal{C}'_\pm\,(W^\mu \;\; W^{1\mu} \;\; W^{2\mu} \;\; \dots)^T,\ \text{with, } \mathcal{C}'_\pm \;=\; V\,\mathcal{C}_\pm\,V^\dagger. \quad (6.18)$$

Therefore, the hZZ and hWW effective dimensionful coupling constants calculated within the RS framework are respectively the $(1,1)$–matrix elements: $g^{\rm RS}_{hZZ} = (\mathcal{C}'_0|_{11})/\tilde{v}$ and $g^{\rm RS}_{hWW} = 2\,(\mathcal{C}'_\pm|_{11})/\tilde{v}$. In contrast, within the pure SM case, the Higgs coupling constants are $g^{\rm SM}_{hZZ} = (\{g^2+g'^2\}v^2_{SM}/4 + \delta^{\rm SM}g_{hZZ})/v_{SM}$ and $g^{\rm SM}_{hWW} = 2\,(g^2v^2_{SM}/4+\delta^{\rm SM}g_{hWW})/v_{SM}$ where g,g' are calculated from Eq.(6.1)-(6.4), of course without the RS corrections, and the δ's parts represent the SM loop corrections [given in Eq.(B.4)-(B.6)].

The obtained values of the ratios $g^{\rm RS}_{hVV}/g^{\rm SM}_{hVV}$ are given in Table 6.1 for three characteristic points of the parameter space. These parameter sets respect the EWPT constraints. In particular, the Higgs boson VEV's $\tilde{v}$ corresponding to these sets, and involved in $g^{\rm RS}_{hVV}$, lead to $S_{\rm RS}$ and $T_{\rm RS}$ values within the $95.45\%C.L.$ contour levels. The obtained Z and W coupling strengths are nearly identical because of the approximate custodial symmetry. The first conclusion about these numerical results is that the RS corrections of the Higgs boson couplings to EW gauge bosons can be quite strong. Secondly, the given $\tilde{v}$ values in the same table show that the role of the Higgs VEV modification in the RS corrections to g_{hVV} is major. For the example of point A, the total relative correction on the Higgs coupling to Z is of $\delta g_{hZZ}/g_{hZZ} = (g^{\rm RS}_{hZZ} - g^{\rm SM}_{hZZ})/g^{\rm SM}_{hZZ} = -42.7\%$ and an included correction of -23.9% is explained by the VEV: assuming *only* a variation in the denominator through the VEV (both RS and SM couplings are inversely proportional to the Higgs VEV), the correction is indeed $\delta g_{hZZ}/g_{hZZ} = v_{SM}/\tilde{v} - 1$. The numbers in Table 6.1 confirm that $g^{\rm RS}_{hZZ}$ gets more suppression w.r.t. SM as $\tilde{v}$ increase. The remaining part of the whole negative RS correction to g_{hZZ} comes from the direct KK gauge boson mixing effect on the Higgs coupling (numerator part). The $g^{\rm RS}_{hZZ}$ suppression is more effective for a larger KK gauge mixing effect on the coupling [i.e. larger $g_{Z'}$ or smaller M_{KK}] as illustrated in the same table and Fig.(6.2). In Fig.(6.2), we plot the ratio $g^{\rm RS}_{hZZ}/g^{\rm SM}_{hZZ}$ for RS parameters respecting the EWPT constraints (sets A and B of Table 6.1 with larger M_{KK}'s). It shows that RS corrections to the hVV vertex remain important in wide regions of the allowed parameter space.

6.4.2 Yukawa couplings

Yukawa couplings with KK mixings: The fermions mass matrices need to be studied as the Yukawa couplings induce mixing with the KK excitations. Moreover, the Yukawa terms have

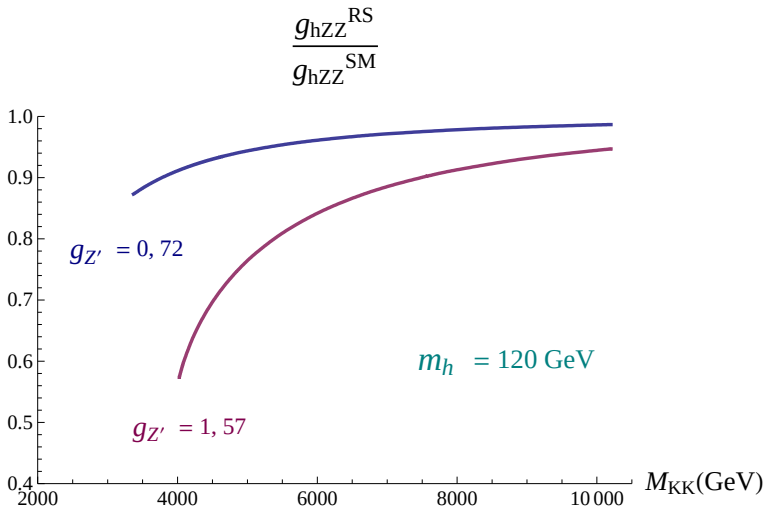

Figure 6.2: Value of the Higgs–ZZ coupling ratio $g_{hZZ}^{\rm RS}/g_{hZZ}^{\rm SM}$ as a function of M_{KK} [in GeV] for $g_{Z'} = 0.72$ and 1.57. The two minimum values of M_{KK}, where the curves stop respectively, are equal to the M_{KK} lower limits from EWPT obtained with $m_h = 120$ GeV (points A and B of Table 6.1).

to take an invariant form under the custodial symmetry as the Higgs field is embedded into a bidoublet of the $\mathrm{SU(2)_L \times SU(2)_R}$ gauge symmetry. As a consequence, fermions are promoted to higher gauge multiplets, the simplest realization being the right-handed fermion singlets promoted to $\mathrm{SU(2)_R}$ isodoublets, and new exotic quarks are expected. Since the $\mathrm{SU(2)_R}$ symmetry is broken by boundary conditions, these exotic quarks have $(-+)$ boundary conditions (BC), so that those have no zero–mode, in contrast with the SM fermions which have $(++)$ BC. Therefore, the first KK excitation of those exotic quarks can be relatively low depending on the value of the c_f parameter.

Defining $\mathcal{M}_f$ as the mass matrix of a specific chiral fermion $\Psi_{L/R}$ in the interaction basis (see e.g. Appendix B.3), this matrix can be diagonalized by unitary matrices $U_{L/R}$, through the transformation $\Psi'_{L/R} = U_{L/R}\Psi_{L/R}$:

$$\mathcal{M}'_f \equiv U_L \mathcal{M}_f U_R^\dagger = \mathrm{diag}\ (m_{f_1}, m_{f_2}, \dots) \tag{6.19}$$

where m_{f_1} corresponds to the measured value of the SM fermion mass (the unitary matrices being defined such that $m_{f_1} < m_{f_2} < ...$). The $\Psi'_{L/R}$ components are the mass eigenstates. Then, the Higgs couplings are given by the interaction Lagrangian

$$\mathcal{L}_{int} = \frac{h}{\tilde{v}} \bar{\Psi}'_L \mathcal{C}'_f \Psi'_R + \mathrm{h.c.} \tag{6.20}$$

where $\mathcal{C}'_f = U_L \mathcal{C}_f U_R^\dagger$ with $\mathcal{C}_f$ being the same matrix as $\mathcal{M}_f$ but with the KK masses set to zero (see for instance Appendix B.4). Hence, the 4D effective Higgs coupling to an eigenstate f_i (i.e. a component of Ψ') is given by $\lambda_{f_i}^{\rm RS} = (\mathcal{C}'_f|_{ii})/\tilde{v}$ in contrast to the usual m_f/v_{SM} Yukawa value within the SM.

Light fermion sector: For light fermions (other than the b- and t-quarks), the $c_{\rm light}$ parameters controlling each fermion multiplet localization along the fifth dimension need to be higher than 0.5 in order to reproduce the correct set of masses. As a consequence, wave function overlaps between light modes, and their KK excitations or exotic KK partners, induce negligible mixings (of order $(m_f/M_{KK})^2$) over the zero mode contribution. Hence, one can safely neglect the KK fermion contributions, inducing a 4D effective Yukawa coupling for light fermions being $\lambda^{\rm RS}_{f_{\rm light}} \simeq m_{f_{\rm light}}/\tilde{v}$.

In the end, the deviation of the Yukawa coupling in the RS scenario with respect to the SM for light fermions simplifies to the deviation of the Higgs boson VEV determined in Section 6.2.2. It gives:

$$\frac{\lambda^{\rm RS}_f}{\lambda^{\rm SM}_f} \simeq \frac{v_{SM}}{\tilde{v}} \quad \text{for every light fermions (other than the } b\text{- and } t\text{-quarks).} \tag{6.21}$$

Third quark generation sector: What differs greatly between the light fermion sector and the third quark generation sector is the $c_{b,t}$ parameters controlling the bottom/top localization. Indeed, in order to reproduce the top and bottom masses, one needs $c_{b,t}$ parameters smaller than 0.5. Having so, in particular, the wave function overlaps between the zero–modes and their KK excitations over the Higgs field on the TeV–brane can become quite large, inducing possibly large KK mixing effects in the Yukawa couplings.

The KK mixing depends on the mass matrix and hence on the quark representations under the gauge symmetry. In the sector of third generation quarks, the crucial EW constraints come from the precise measurements of the observables A^b_{FB} and R_b (ratio of the partial decay width into $b\bar{b}$ for the Z^0 boson). To be complete in our study of the Higgs boson phenomenology with regard to all the EWPT constraints, we will follow the previous work [28] where we have determined quark representations able to address the A^b_{FB} anomaly (i.e. improve significantly the global fit of R_b and the A^b_{FB} values at the Z^0 pole and outside resonance). Doing so, we consider the proposed choice of multiplets under the $\mathrm{SU(2)_L \times SU(2)_R \times U(1)_X}$ group for the bottom and top quarks:

$$\begin{aligned}
\{Q_{1L}\} \equiv (2,2)_{2/3} &= \begin{pmatrix} q'_{(5/3)L} & t_{1L} \\ t'_L & b_{1L} \end{pmatrix} \qquad \{t^c_R\} \equiv (1,3)_{2/3} = \begin{pmatrix} q^{c\prime}_{(5/3)R} & t^c_R & b^{c\prime}_R \end{pmatrix} \\
\{Q_{2L}\} \equiv (2,3)_{-5/6} &= \begin{pmatrix} t_{2L} & b'_L & q''_{(-4/3)L} \\ b_{2L} & q'_{(-4/3)L} & q'_{(-7/3)L} \end{pmatrix} \quad \{b^c_R\} \equiv (1,2)_{-5/6} = \begin{pmatrix} b^c_R & q^{c\prime}_{(-4/3)R} \end{pmatrix}
\end{aligned} \tag{6.22}$$

where the left bottom and top SM-like multiplets arise from a mixing mechanism between the two above left-handed multiplets (parametrized by a mixing angle θ) [6]. The heavy quarks indicated

[6] The precise description for the mentioned mechanism is left to the attention of the reader in our previous

with one or several primes (and an electric charge) are the mentioned fields with $(-+)$ BC [the so–called 'custodians']. For the rest of the work, all numerical values are based on this quark model.

In the field basis $\Psi_L^t \equiv (b_L^{(0)}, b_L^{(1)}, b_L^{c(1)}, b_L^{\prime\prime(1)}, b_L^{\prime c(1)})^t$, $\Psi_R^t \equiv (b_R^{c(0)}, b_R^{(1)}, b_R^{c(1)}, b_R^{\prime\prime(1)}, b_R^{\prime c(1)})^t$ where we have introduced the charge conjugated fields (indicated by the superscript c) in order to use only left-handed SM fields, the effective 4D bottom quark mass matrix and Yukawa coupling matrix induced by EWSB are given in Appendix B.3 and B.4. Similar structure can be found for the top quark mass and Yukawa coupling matrices.

Parameter space: Our choice of parameters in order to derive the deviation of the Yukawa couplings relies on a few considerations we discuss now.

First, numerically we consider only the first two fermionic custodian excitations, which gives rise to heaviest eigenvalues of $\mathcal{M}_f$ around $\sim 2M_{KK}$ in agreement with the NDA estimation of the cut–off scale of the effective field theory related to the perturbativity of Yukawa couplings: $\Lambda_{IR} \sim 2M_{KK}$.

Secondly, in order to derive the correct value of Yukawa couplings in the RS model, we need to implement in Eq.(6.19) the good value of the relevant fermion mass m_{f_1} and the exact unitary matrices $U_{L/R}$. In particular, the whole b- and t-quark mixings with the first two quark families are treated effectively through the parameters $\epsilon_{b,t}^{mixing}$ appearing in front of the first element of the mass matrices $\mathcal{M}_{b,t}$ (see Appendix B.3). As the Cabibbo-Kobayashi-Maskawa (CKM) quark mixing matrix $V_{CKM} = U_L^{up} U_L^{down\dagger}$ is close to unity, the simplest case corresponds to both rotation matrices for up and down fields being also close to unity. We thus estimate $\epsilon_{b,t}^{mixing}$ to be roughly of order $\cos\theta_{12}\cos\theta_{13} \sim \cos\theta_{12}\cos\theta_{23} \sim 0.97$ where θ_{ij} are the CKM mixing angles encoding its hierarchical structure. We then use the allowed range $\epsilon_{b,t}^{mixing} = [0.95, 1.05]$ for the numerical analysis.

A more important effect comes from the mass running and is also implemented into $\epsilon_{b,t} = \epsilon_{b,t}^{mixing} \times \epsilon_{b,t}^{running}$. The parameters $c_{b,t}$ and the dimensionful Yukawa coupling constants $\lambda_{b,t}^{5D}$, entering $\mathcal{M}_{b,t}$, are parameters appearing in the 5D Lagrangian and have thus to be considered e.g. at the effective 5D scale. Then, one has to consider the running of quark masses from M_{KK} typically down to the EWSB scale $\Lambda_{EW} \sim m_Z$ where the EWPT and light Higgs phenomenology are studied in the present work. The approximate effect of such a running can be estimated from the mass values at the two extreme scales:

$$m_b(m_Z) = [2.8, 3.0]\text{GeV}, \quad m_b(10\text{TeV}) = [2.1, 2.3]\text{GeV}$$
$$m_t(m_Z) = [168, 180]\text{GeV}, \quad m_t(10\text{TeV}) = [140, 148]\text{GeV}$$

where we have used the SM one loop renormalization group equations [52] to run the quark masses given in Ref. [53] from the scale m_Z to 10 TeV. At that point, one can neglect KK loop contributions

paper [28].

to the running which would correspond to higher order corrections. The running reduces at most the quark masses by about 21%-42% (13%-28%) for the bottom (top) mass and is taken into account through the considered allowed range for the whole factors $\epsilon_{b,t}$:

$$\epsilon_b = [1.15, 1.45] \quad , \quad \epsilon_t = [1.10, 1.35].$$

Anyway, the precise variation of the $\epsilon_{b,t}$ value has no important effects on the final Yukawa coupling, as the rotation matrices $U_{L/R}$ in Eq.(6.19) are systematically such that the smallest mass eigenvalue is equal to m_{f_1}, namely the measured fermion mass. Nevertheless, for completeness, we include these small possible variations of $\epsilon_{b,t}$. Those lead to several possible values of the parameters $c_{b,t}$, $\lambda_{b,t}^{5D}$ and the mixing angle θ which reproduce the correct $m_b(m_Z)$, $m_t(m_Z)$ and address the A_{FB}^b anomaly [the A_{FB}^b solution is fixed by $\mathcal{M}_b$ which determines b-b^{KK} mixings]. Here we are clearly thinking for a given value of M_{KK} which also enters $\mathcal{M}_{b,t}$ through the dependencies of KK fermion masses. Once all parameters are fixed, the Yukawa couplings are extracted through the method given in Eq.(6.20).

Results and discussion: The obtained values of the ratios $\lambda_{b,t}^{\rm RS}/\lambda_{b,t}^{\rm SM}$ are given in Table 6.1 for three characteristic points of the parameter space respecting the EWPT constraints in the light fermion and gauge boson sector. For these three fixed values of M_{KK}, the parameters $c_{b,t}$, $\lambda_{b,t}^{5D}$ and θ are varied as described above according to $m_{b,t}(m_Z)$ and A_{FB}^b. Those variations give rise to a certain range of 4D Yukawa coupling constants, for which the extremal values are given in Table 6.1.

The first conclusion about these numerical results is that the RS corrections of the Higgs couplings to fermions can be quite strong as was the case for the Higgs coupling to the EW gauge bosons (up to -23.8% for the example of point A). However, in contrast with the EW gauge boson couplings, comparing here RS corrections to the b- and t-quarks with light fermions, the table shows that the role of the Higgs VEV modification in the RS corrections to $\lambda_{b,t}$ is major in regard of KK mixing effects. At the same time, one can see that the KK mixing corrections also tend to decrease the coupling of the Higgs boson to a few more percents (up to -5.5% for the example of point B) which is what one can naively expect: for a given fermion mass value, the higher the KK mixing component is, the lower the Yukawa coupling is ('direct' mass contribution).

6.4.3 Effective coupling to gluons

Gluon fusion in the SM: The dominant production mode of the SM Higgs boson at the LHC is the reaction $gg \to h$ called the gluon–gluon fusion mechanism and mediated by triangular loops of SM quarks (noted as Q's here), as illustrated in Fig. (6.3). In the SM, mainly heavy quarks, namely the top quark and to a lesser extent the bottom quark, contribute to the amplitude. The decreasing Higgs form factor with rising loop mass is counterbalanced by the linear growth of the

Higgs coupling with the quark mass (Yukawa coupling).

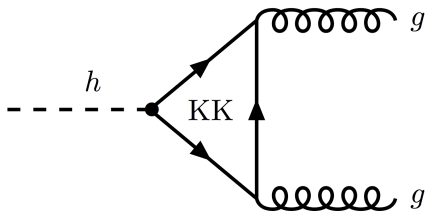

Figure 6.3: Feynman diagram for the loop-induced Higgs-gluon-gluon vertex. KK represents the exchanged zero–modes and KK towers of quarks.

To lowest order, the partonic cross section reads as

$$\sigma_h^{SM} = \frac{\alpha_s^2 m_h^2}{576\pi v_{SM}^2}\left|\sum_Q A_{1/2}^h(\tau_Q)\right|^2 \tag{6.23}$$

and it must be multiplied by $\delta(\hat{s}-m_h^2)$ where $\hat{s}$ is the gg invariant energy squared. The form factor for spin-$\frac{1}{2}$ particles is given by [33]:

$$A_{1/2}^h(\tau) = \frac{3}{2}[\tau+(\tau-1)f(\tau)]\tau^{-2}, \quad \text{where} \quad f(\tau) = \begin{cases} \arcsin^2\sqrt{\tau} & \tau \le 1 \\ -\frac{1}{4}\left[ln\,\frac{1+\sqrt{1-\tau^{-1}}}{1-\sqrt{1-\tau^{-1}}} - i\pi\right]^2 & \tau > 1 \end{cases} \tag{6.24}$$

The form factor $A_{1/2}^h(\tau_Q)$ with $\tau_Q = m_h^2/4m_Q^2$ is normalized such that for $m_h \ll m_Q$, it reaches unity while it approaches zero in the chiral limit $m_Q \to 0$.

The $g_{hgg}^{\rm RS}$ coupling: We now extend this result to the RS scenario. First, new loop contributions appear from the various KK excitations of usual SM quarks q, and the ones coming from possible exotic quarks q' with $(-+)$ or $(+-)$ BC, extending the sum in Eq.(6.23) as a consequence over all possible KK quarks coupled to the Higgs field (see Fig. (6.3) on the effective hgg coupling). Secondly, the decrease in the Yukawa couplings evaluated in previous section will tend to reduce the hgg effective coupling through the hqq vertex appearing in the loop. In contrast, the gqq ($gq'q'$) vertex couples universally all (KK) quarks with SM-like strength, due to the flat profile of the gluon fields along the fifth dimension.

Within this setup the production cross section is simply generalized to:

$$\sigma_h^{\rm RS} = \frac{\alpha_s^2 m_h^2}{576\pi v_{SM}^2}\left|\sum_{\{q\}}\frac{\lambda_q^{\rm RS} v_{SM}}{m_q}A_{1/2}^h(\tau_q) + \sum_{\{q'\}}\frac{\lambda_{q'}^{\rm RS} v_{SM}}{m_{q'}}A_{1/2}^h(\tau_{q'})\right|^2, \tag{6.25}$$

since e.g. $\lambda_q^{\rm RS}/\lambda_q^{\rm SM} = \lambda_q^{\rm RS} v_{SM}/m_q$. The sum over $\{q\}$ includes all SM quarks and their KK partner towers, whereas the sum over $\{q'\}$ includes all possible custodian quarks of KK type depending

on the model under consideration. λ_q^{RS} ($\lambda_{q'}^{RS}$) denotes the Yukawa coupling of the corresponding quark q (q') to the Higgs field in the mass eigenbasis. m_q ($m_{q'}$) is the mass of the corresponding quark q (q') running in the loop.

It is convenient to consider the ratio $\mathcal{R}_{hgg} = \sigma_h^{\rm RS}/\sigma_h^{\rm SM}$ of the $gg \to h$ cross sections in the RS and SM models which can be rewritten,

$$\mathcal{R}_{hgg} = \left(\frac{v_{SM}}{\tilde{v}}\right)^2 \left| \frac{\sum_{\{q\}} \frac{\lambda_q^{RS}\tilde{v}}{m_q} A_{1/2}^h(\tau_q) + \sum_{\{q'\}} \frac{\lambda_{q'}^{RS}\tilde{v}}{m_{q'}} A_{1/2}^h(\tau_{q'})}{\sum_Q A_{1/2}^h(\tau_Q)} \right|^2 . \tag{6.26}$$

Then the higher order QCD corrections, which are known to be rather large [54], are essentially the same for all quark species and, thus, drop in this ratio. From this ratio, one can also deduce the effective hgg loop-coupling deviation from the SM prediction by the straightforward relation:

$$\frac{g_{hgg}^{\rm RS}}{g_{hgg}^{\rm SM}} \equiv \sqrt{\mathcal{R}_{hgg}}. \tag{6.27}$$

We can use the formulas demonstrated in Appendix C.1, more precisely Eq.(C.7) and Eq.(C.8), in order to simplify our expression. The ratio $\mathcal{R}_{hgg}^{1/2}$ then simplifies to:

$$\frac{g_{hgg}^{\rm RS}}{g_{hgg}^{\rm SM}} = \frac{v_{SM}}{\tilde{v}} \left| \frac{\sum_Q \left(1 + \frac{\lambda_Q^{RS}\tilde{v}}{m_Q}[A_{1/2}^h(\tau_Q) - 1]\right)}{\sum_Q A_{1/2}^h(\tau_Q)} \right| \tag{6.28}$$

where the sum appearing in the numerator has been reduced to the SM quarks only. It is a remarkable feature that the contributions coming from all KK partners simplify to properties over the corresponding zero–mode. In the case of exotic quarks, the contribution vanishes due to the absence of zero–mode, even if these new quarks do couple to the Higgs field.

For light quarks, $A_{1/2}^h(\tau_Q) \to 0$ quickly and the ratio $\lambda_Q^{\rm RS}/m_Q \to 1/\tilde{v}$ as can be deduced from Eq.(6.21). Hence, their contributions to $\mathcal{R}_{hgg}^{1/2}$ tend to vanish as was already the case in the SM.

For heavy fermions (b- and t-quarks), overlaps between the zero–mode profile and KK wave functions can be quite large, as we have seen in the previous section, so that $\lambda_Q^{\rm RS}/m_Q \neq 1/\tilde{v}$. Besides, considering light Higgs masses of 120 GeV and 150 GeV, one check numerically that $|A_{1/2}^h(\tau_b)| \simeq 0.1$ which is negligible, but only as a first approximation, relatively to $|A_{1/2}^h(\tau_t)| \simeq 1.05$.

In the end, the deviation in the coupling simply reads:

$$\frac{g_{hgg}^{\rm RS}}{g_{hgg}^{\rm SM}} \simeq \frac{v_{SM}}{\tilde{v}} \left| \frac{2 - x_b(1 - A_b) - x_t(1 - A_t)}{A_b + A_t} \right| \tag{6.29}$$

where $A_Q \equiv A^h_{1/2}(\tau_Q)$ and $x_Q \equiv \tilde{v}\lambda^{\rm RS}_Q/m_Q$. Note that $x_Q \in [0,1]$. The limit $x_Q \to 1$ corresponds to the pure Higgs mass case when there is no mixing between the fermion zero–mode and its KK partners. x_Q tends to decrease as this mixing gets stronger. For a light Higgs mass, so that $m_h^2/4m_t^2 \ll 1$, in the limit where $|A^h_{1/2}(\tau_t)| \to 1$ and neglecting the bottom quark contribution: $|A^h_{1/2}(\tau_b)| \to 0$, our relation gets the following really simple structure,

$$\frac{g^{\rm RS}_{hgg}}{g^{\rm SM}_{hgg}} \approx \frac{v_{SM}}{\tilde{v}}(2 - x_b). \tag{6.30}$$

We present this final approximated relation to help the reader in getting an intuition on the main behavior of RS corrections to the Higgs coupling, but numerically, the complete formula (6.29) is used. As discussed in part 6.2.2, $v_{SM} < \tilde{v}$, systematically, which tends to reduce the production cross section of the Higgs field at LHC. This consequence is simply due to the fact that for a higher value of the Higgs VEV, one needs a smaller value of the Yukawa coupling to reproduce a given fermion mass. The second term in Eq.(6.30) is less trivial and encodes the whole b- and t-quark KK towers contribution minus the pure b-quark contribution. This contribution increases the deviation of the $g^{\rm RS}_{hgg}$ w.r.t. $g^{\rm SM}_{hgg}$ as the mixing between the bottom zero–mode with its KK excitations grows. On the contrary, when x_b decreases, the contribution from the bottom KK quarks becomes more and more crucial to the hgg coupling.

Results and discussion: We have derived the values of the ratio $g^{\rm RS}_{hgg}/g^{\rm SM}_{hgg}$ from Eq.(6.29) and given them in Table 6.1 for the same characteristic points of parameter space respecting all EWPT constraints (including the A^b_{FB} solution). The allowed variations of fundamental parameters give rise to some intervals of values for the Yukawa couplings and masses of the KK fermion towers. Based on those intervals, we have determined the maximum and minimum amplitudes for the loop-induced observable $g^{\rm RS}_{hgg}/g^{\rm SM}_{hgg}$.

Once more, we remark that the RS corrections to the effective Higgs boson coupling to two gluons are possibly quite strong (up to -22.4% for point A). Furthermore, comparing these RS corrections (obeying Eq.(6.30) in a good approximation) with the case of light fermion coupling to the Higgs boson (*c.f.* Eq.(6.21)), one concludes again on the major role of the Higgs VEV modification. Simultaneously, one can see that the KK mixing corrections combined with the new contributions from exchanges of KK states in the loop [synthesized in the $(2 - x_b)$ factor effect on Eq.(6.30)] tend to counter the effect of the Higgs VEV deviation, but at a smaller rate.

6.4.4 Effective coupling to photons

$\gamma\gamma$ channel in the SM: For low Higgs masses, the dominant decay mode $h \to b\bar{b}$ is swamped by a large QCD background and the Higgs boson can be searched for through more promising loop-induced decays. The decay channel into two photons is the most important one and is mediated

by triangular loops of charged fermions as well as massive vector bosons: see Fig. (6.4).

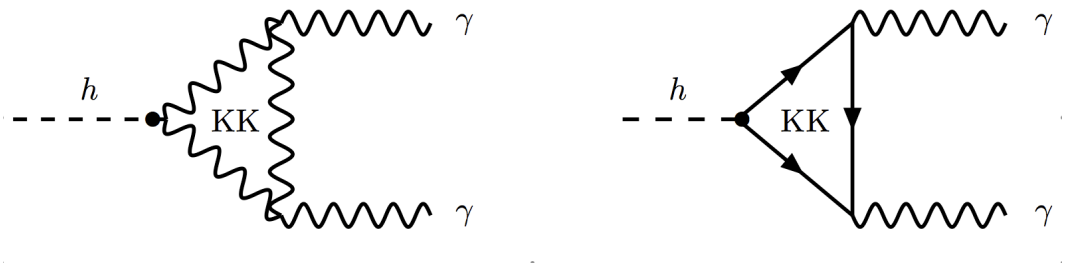

Figure 6.4: Feynman diagrams for the loop-induced Higgs-photon-photon vertex. KK stands for the exchanged zero–modes and KK towers of W gauge boson [left] or fermions [right].

The decay width of the Higgs in two photons reads [33]

$$\Gamma^{SM}_{h\to\gamma\gamma} = \frac{\alpha^2 m_h^3}{256\pi^3 v_{SM}^2}\left| A_1^h(\tau_W) + \frac{4}{3}\sum_f N_c Q_f^2 A_{1/2}^h(\tau_f)\right|^2 \tag{6.31}$$

where N_c is the number of color states (3 for quarks, 1 for leptons) and Q_f is the electric charge of the fermion in the loop. The form factor for spin-1/2 particles, $A^h_{1/2}$, is the one from Eq.(6.24), and the form factor for spin-1 particles is given by:

$$A_1^h(\tau) = -[2\tau^2 + 3\tau + 3(2\tau-1)f(\tau)]\tau^{-2}. \tag{6.32}$$

The form factor $A_1^h(\tau_V)$ with $\tau_V = m_h^2/4m_V^2$ is defined such that for large masses of the boson in the loop, $m_h \ll m_V$, it reaches $A_1^h(\tau_V \to 0) = -7$.

The $g^{\rm RS}_{h\gamma\gamma}$ coupling: Here we extend this result to RS case. This extension is similar to the one of the gluon fusion mechanism from previous section. New loop contributions appear from the various exchanged KK excitations of usual SM fermions, the exchanged custodians, but also the exchanged KK EW gauge bosons (see in Fig. (6.4) the diagram for the induced $h\gamma\gamma$ vertex). We have to take into account as well the deviations in the Yukawa couplings and in the Higgs coupling to the W boson. Finally, the $ff\gamma$, like the $WW\gamma$, vertex couples with an SM-like universal strength all fermion excitations, respectively all W bosons of the tower, due to the flat wave function of the electromagnetic field. The decay width becomes thus,

$$\Gamma^{\rm RS}_{h\to\gamma\gamma} = \frac{\alpha^2 m_h^3}{256\pi^3}\frac{1}{v_{SM}^2}\left|\sum_n \frac{g^{\rm RS}_{W^n} v_{SM}}{2m^2_{W^n}} A_1^h(\tau_{W^n}) + \frac{4}{3}\sum_{\{f\}}\frac{\lambda_f^{\rm RS} v_{SM}}{m_f} N_c Q_f^2 A^h_{1/2}(\tau_f)\right|^2 \tag{6.33}$$

as $g^{\rm RS}_{W^n}/g^{\rm SM}_{hWW} = g^{\rm RS}_{W^n} v_{SM}/2m^2_{W^n}$ with $g^{\rm RS}_{W^n} = g^{\rm RS}_{hW^nW^n} = 2(\mathcal{C}'_{\pm}|_{nn})/\tilde{v}$, following the notations of Section 6.4.1. We recall that m_{W^n} denotes the physical W state eigenmasses and we mention that the KK sum over n includes the zero–mode, namely the observed W boson.

We still consider the ratio $\mathcal{R}_{h\gamma\gamma} = \Gamma^{\rm RS}_{h\to\gamma\gamma}/\Gamma^{\rm SM}_{h\to\gamma\gamma}$:

$$\mathcal{R}_{h\gamma\gamma} = \left(\frac{v_{SM}}{\tilde{v}}\right)^2 \left| \frac{\frac{3}{4}\sum_n \frac{g^{\rm RS}_{W^n}\tilde{v}}{2m^2_{W^n}} A_1^h(\tau_{W^n}) + \sum_{\{f\}} \frac{\lambda_f^{\rm RS}\tilde{v}}{m_f} N_c Q_f^2 A_{1/2}^h(\tau_f)}{\frac{3}{4}A_1^h(\tau_W) + \sum_f N_c Q_f^2 A_{1/2}^h(\tau_f)} \right|^2 \tag{6.34}$$

from which one can deduce the $h\gamma\gamma$ coupling deviation,

$$\frac{g^{\rm RS}_{h\gamma\gamma}}{g^{\rm SM}_{h\gamma\gamma}} \equiv \sqrt{\mathcal{R}_{h\gamma\gamma}} \tag{6.35}$$

Combining now the formulas derived in Appendix C.1 and Appendix C.2, one easily find in a similar way for the bosonic part:

$$\frac{g^{\rm RS}_{h\gamma\gamma}}{g^{\rm SM}_{h\gamma\gamma}} \simeq \frac{v_{SM}}{\tilde{v}} \left| \frac{\frac{43}{4} - \frac{9}{4}x_W(A_W+7) + x_b(1-A_b) + 4x_t(1-A_t)}{\frac{9}{4}A_W + A_b + 4A_t} \right| \tag{6.36}$$

with $x_W \equiv \tilde{v} g^{\rm RS}_{hWW}/2m^2_W$. Similarly to the case of gluon fusion Higgs production, contributions from light quarks and charged leptons vanish, whereas the KK tower contributions for the W boson, quarks and charged leptons can be rewritten leaving only in the formula the explicit dependence on the W boson, bottom and top quark zero–modes.

Results and discussion: The extremal values of $g^{\rm RS}_{h\gamma\gamma}/g^{\rm SM}_{h\gamma\gamma}$ are also shown in Table 6.1. The $x_{W,b,t}$ values were obtained as discussed in previous sections. Due to the additional W mode effects, the deviation of this effective coupling can reach higher RS corrections (up to -25.1% e.g. with point A) than g_{hgg}. The principal RS deviation comes again from the modified value of the Higgs field VEV which is a general result of the present work.

6.5 RS variants

In this last part, we discuss qualitatively the implications of the Higgs VEV corrections on the EWPT and Higgs couplings that we have treated in detail above, but within the other versions of warped extra dimension models.

First, an alternative scenario to the one we have considered is that $\mathrm{SU}(2)_{\rm R}$ remains unbroken in the bulk ($\tilde{M} = 0$). Then the dominant contribution to $T_{\rm RS}$ comes from the exchange of (excited) t and b quarks at the one–loop level. The estimation of this radiatively generated $T_{\rm RS}$ relies on a sum over fermion/boson KK towers which depends on the choice of quark representations. In such a case, $\tilde{v}$ would no more depend on $\tilde{M}$ but the correlation between $S_{\rm RS}$ and $T_{\rm RS}$ through would still be modified by the dependence of the Higgs VEV corrections on these parameters. Indeed $T_{\rm RS}$ would still depend on $\tilde{v}$, M_{KK} and $g_{Z'}$. Besides, the increase of $\tilde{v}$ w.r.t. $v_{SM} = 245$ GeV would

imply an enhancement of $S_{\rm RS}$ which tends to increase the EWPT lower limit on M_{KK}, as we also find above.

Another possibility within the RS framework is to include large kinetic terms for the gauge fields on the IR brane [55], without bulk custodial symmetry. Such terms repel the KK mode wave functions from the brane so that the KK gauge mixing effect, coming from the coupling of KK gauge fields to the Higgs boson located at the IR brane, is reduced. Hence the Higgs VEV corrections are expected to be significantly weaker than here, and their effects on EWPT constraints as well as on Higgs couplings softer.

In the case of gauge–Higgs unification scenarios, where the extended bulk gauge symmetry generally contains the custodial group $\mathrm{SU(2)_L \times SU(2)_R \times U(1)_X}$, the KK gauge mixing effect [induced by EWSB] should be of the same order as in the present work since the Higgs profile is peaked on the TeV–brane (instead of being exactly confined as here). By consequence, comparable Higgs VEV corrections are expected and in turn similar EWPT bounds on M_{KK}.

Finally, we mention the so–called gaugephobic Higgs models where the Higgs VEV on the brane can be much larger than here, forcing then the lightest W and Z modes to move further from the brane [23, 24]. In the limit of an infinite VEV, where the couplings between the Higgs and gauge bosons vanish, one recovers the Higgsless gauge boundary conditions. In such models, to maintain compatibility with EWPT, one must render the corrections to the S parameter small. For that purpose, one has to allow all the light fermions to be spread in the bulk [56]. When their profile becomes approximately flat, their wave function being then orthogonal to the KK gauge boson ones, the contributions to S can be made arbitrarily small. Nevertheless, with such a fermion universality, one clearly looses the beauty of generating the mass hierarchy and flavor structure via the simple geometrical mechanism of wave function overlapping.

6.6 Conclusion

Within the RS framework, the corrections to the Higgs boson VEV induced by the KK gauge mixing can be large. Those imply an enhancement of the EWPT lower limit at $95.45\% C.L.$ on M_{KK} that can be larger than $+30\%$ for $m_h = 120$ GeV. Another important role of these RS corrections to the VEV is played in the calculation of the Higgs couplings. We find that the Higgs couplings can be significantly reduced w.r.t. SM. The large deviations to the Higgs couplings due to extra dimensions provide an indirect way of testing the RS model: the LHC precision in light Higgs rate measurements allow to explore KK boson mass ranges above 4 TeV (in agreement with EWPT) through Higgs production/decay channels involving the couplings g_{hgg} and g_{hVV}. With the higher accuracies expected at ILC, even more clear signatures of the RS scenario may arise in the precise measurement of g_{hZZ} deviations.

Bibliography

[1] L. Randall and R. Sundrum, Phys. Rev. Lett. **83** (1999) 3370. See also, M. Gogberashvili, Int. J. Mod. Phys. **D11** (2002) 1635.

[2] T. Gherghetta and A. Pomarol, Nucl. Phys. **B586** (2000) 141.

[3] S. J. Huber and Q. Shafi, Phys. Lett. **B498** (2001) 256; **B512** (2001) 365; Phys. Lett. B544 (2002) 295; Phys. Lett. B583 (2004) 293; S. Chang *et al.*, Phys. Rev. **D73** (2006) 033002; G. Moreau and J. I. Silva-Marcos, JHEP **0601** (2006) 048; **0603** (2006) 090; K. Agashe *et al.*, Phys. Rev. **D71** (2005) 016002; Phys. Rev. Lett. **93** (2004) 201804; Phys. Rev. **D75** (2007) 015002; Phys. Rev. **D74** (2006) 053011;

[4] T. Lari *et al.*, Report of Working Group 1 of the CERN Workshop "Flavour in the era of the LHC", Geneva, Switzerland, November 2005 – March 2007, Eur. Phys. J. **C57** (2008) 183; M. Raidal *et al.*, Report of Working Group 3 of the CERN Workshop "Flavour in the era of the LHC", Geneva, Switzerland, November 2005 – March 2007, Eur. Phys. J. **C57** (2008) 13.

[5] Y. Grossman and M. Neubert, Phys. Lett. **B474** (2000) 361; T. Appelquist *et al.*, Phys. Rev. **D65** (2002) 105019; T. Gherghetta, Phys. Rev. Lett. **92** (2004) 161601; G. Moreau, Eur. Phys. J. **C40** (2005) 539.

[6] A. Pomarol, Phys. Rev. Lett. **85** (2000) 4004; L. Randall and M. D. Schwartz, JHEP **0111** (2001) 003; Phys. Rev. Lett. **88** (2002) 081801; K. Agashe, A. Delgado and R. Sundrum, Annals Phys. **304** (2003) 145.

[7] See e.g. M. Carena, E. Ponton, J. Santiago and C. E. M. Wagner, Nucl. Phys. **B759** (2006) 202; Phys. Rev. **D76** (2007) 035006.

[8] C. Csáki, C. Grojean, H. Murayama, L. Pilo and J. Terning, Phys. Rev. **D69** (2004) 055006; C. Csáki, C. Grojean, L. Pilo and J. Terning, Phys. Rev. Lett. **92** (2004) 101802; G. Cacciapaglia, C. Csáki, C. Grojean and J. Terning, Phys. Rev. **D70** (2004) 075014.

[9] J. M. Maldacena, Adv. Theor. Math. Phys. **2** (1998) 231; Int. J. Theor. Phys. **38** (1999) 1113; S. S. Gubser, I. R. Klebanov and A. M. Polyakov, Phys. Lett. **B428** (1998) 105; E. Witten,

Adv. Theor. Math. Phys. **2** (1998) 253; N. Arkani-Hamed, M. Porrati and L. Randall, JHEP **0108** (2001) 017.

[10] R. Contino, Y. Nomura and A. Pomarol, Nucl. Phys. **B671** (2003) 148; K. Agashe, R. Contino and A. Pomarol, Nucl. Phys. **B719** (2005) 165; K. Agashe and R. Contino, Nucl. Phys. **B742** (2006) 59; R. Contino, L. Da Rold and A. Pomarol, Phys. Rev. **D75** (2007) 055014.

[11] M. E. Peskin and T. Takeuchi, Phys. Rev. Lett. **65** (1990) 964; Phys. Rev. **D46** (1992) 381.

[12] C. Csáki *et al.*, Phys. Rev. **D66** (2002) 064021; G. Burdman, Phys. Rev. **D66** (2002) 076003; J. Hewett, F. Petriello and T. Rizzo, JHEP **0209** (2002) 030.

[13] K. Agashe, A. Delgado, M. J. May and R. Sundrum, JHEP **0308** (2003) 050; A. Delgado and A. Falkowski, JHEP **0705** (2007) 097.

[14] K. Agashe *et al.*, Phys. Rev. **D76** (2007) 11505; `arXiv:0810.1497 [hep-ph]`; B. Lillie, J. Shu and T. M. P. Tait, Phys. Rev. **D76** (2007) 115016; B. Lillie, L. Randall and L.-T. Wang, JHEP **0709** (2007) 074; F. Ledroit, G. Moreau and J. Morel, JHEP **0709** (2007) 071; M. Guchait, F. Mahmoudi and K. Sridhar, Phys. Lett. **B666** (2008) 347; A. Djouadi, G. Moreau and R. K. Singh, Nucl. Phys. **B797** (2008) 1.

[15] A. Djouadi, G. Moreau and F. Richard, Nucl. Phys. **B773** (2007) 43; A. Djouadi *et al.*, `arXiv:0906.0604 [hep-ph]`.

[16] A. Djouadi, J. Kühn and P.M. Zerwas, Z. Phys. **C46** (1990) 411.

[17] R. Dermisek and J. F. Gunion, Phys. Rev. **D76** (2007) 095006; U. Ellwanger, J. F. Gunion and C. Hugonie, JHEP **0507** (2005) 041; `arXiv:hep-ph/0111179`.

[18] A. Falkowski, Phys. Rev. **D77** (2008) 055018.

[19] G. Bhattacharyya and T. S. Ray, Phys. Lett. **B675** (2009) 222.

[20] A. Djouadi and G. Moreau, Phys. Lett. **B660** (2008) 67.

[21] G. Cacciapaglia, A. Deandrea and J. Llodra-Perez, `arXiv:0901.0927 [hep-ph]`.

[22] G. F. Giudice, C. Grojean, A. Pomarol and R. Rattazzi, JHEP **0706** (2007) 045.

[23] B. Lillie, JHEP **0602** (2006) 019.

[24] G. Cacciapaglia, C. Csáki, G. Marandella and J. Terning, JHEP **0702** (2007) 036.

[25] M. Veltman, Nucl. Phys. **B123** (1977) 89; M. S. Chanowitz, M. A. Furman and I. Hinchliffe, Phys. Lett. **B78** (1978) 285; A. Djouadi and C. Verzegnassi, Phys. Lett. **B195** (1987) 265; J. J. van der Bij and F. Hoogeveen, Nucl. Phys. **B283** (1987) 477; A. Djouadi, Nuovo Cim. **A100** (1988) 357; B. Kniehl, Nucl. Phys. **B347** (1990) 86; R. Barbieri *et al.*, Phys. Lett. **B288** (1992) 95; A. Djouadi, P. Gambino and B. A. Kniehl, Nucl. Phys. **B523** (1998) 17.

[26] Tevatron Electroweak Working Group, arXiv:0808.0147 [hep-ex].

[27] Tevatron Electroweak Working Group, for the CDF Collaboration, the D0 Collaboration, arXiv:0903.2503 [hep-ex].

[28] C. Bouchart and G. Moreau, Nucl. Phys. **B810** (2009) 66.

[29] R. Barbieri, A. Pomarol, R. Rattazzi and A. Strumia, Nucl. Phys. **B703** (2004) 127.

[30] H. Davoudiasl, G. Perez and A. Soni, Phys. Lett. **B665** (2008) 67.

[31] G. Burdman and L. Da Rold, JHEP **0811** (2008) 025.

[32] Particle Data Group, J. Phys. **G33** (2006) 1 ; Phys. Lett. **B667** (2008) 1.

[33] A. Djouadi, Phys. Rept. **457** (2008) 1.

[34] ALEPH Collaboration, CDF Collaboration, D0 Collaboration, DELPHI Collaboration, L3 Collaboration, OPAL Collaboration, SLD Collaboration, LEP Electroweak Working Group, Tevatron Electroweak Working Group, SLD electroweak heavy flavour groups, arXiv:0811.4682 [hep-ex]; arXiv:0712.0929 [hep-ex].

[35] T. Appelquist and J. Carazzone, Phys. Rev. **D11** (1975) 2856.

[36] H. Burkhardt and B. Pietrzyk, Phys. Rev. **D72** (2005) 057501.

[37] F. Jegerlehner, Nucl. Phys. Proc. Suppl. **181** (2008) 135.

[38] K. Hagiwara *et al.*, Phys. Lett. **B649** (2007) 173.

[39] M. Davier, S. Eidelman, A. Hocker and Z. Zhang, Eur. Phys. J. **C27** (2003) 497; W. J. Marciano, Invited talks at SSI2004 SLAC Summer Institute, arXiv:hep-ph/0411179; M. Passera, W. J. Marciano and A. Sirlin, AIP Conf. Proc. **1078** (2009) 378.

[40] M. Davier *et al.*, arXiv:0908.4300 [hep-ph].

[41] M. Davier *et al.*, arXiv:0906.5443 [hep-ph].

[42] ALEPH, DELPHI, L3 and OPAL Collaborations, Phys. Lett. **B565** (2003) 61.

[43] M. Awramik, M. Czakon, A. Freitas and G. Weiglein, Phys. Rev. **D69** (2004) 053006.

[44] G. Degrassi and P. Gambino, Nucl. Phys. **B567** (2000) 3.

[45] M. Awramik, M. Czakon and A. Freitas, JHEP **0611** (2006) 048.

[46] The LEP Collaborations (ALEPH, DELPHI, L3 and OPAL), the LEP Electroweak Working Group and the SLD Heavy flavor Group, *A combination of preliminary Electroweak measurements and constraints on the Standard Model*, Phys. Rep. **427** (2006) 257, http://lepewwg.web.cern.ch/LEPEWWG.

[47] M. Davier, S. Descotes-Genon, A. Hocker, B. Malaescu and Z. Zhang, Eur. Phys. J. **C56** (2008) 305.

[48] ATLAS Collaboration, `arXiv:0901.0512 [hep-ex]`.

[49] G. L. Bayatian *et al.* [CMS Collaboration], *"CMS technical design report, volume II: Physics performance"*, J. Phys.**G34** (2007) 995.

[50] S. Dawson *et al.*, Working Group 1 (Higgs) Summary, Proceedings of the Workshop *"From the LHC to Future Colliders (LHC2FC)"*, February 2009, CERN.

[51] `https://twiki.cern.ch/twiki/bin/view/Atlas/AtlasResultsEcmDependence` ; `https://twiki.cern.ch/twiki/bin/view/CMS/HiggsAnalysisSummary2009FebCombinedLimits`

[52] H. Fusaoka and Y. Koide, Phys. Rev. **D57** (1998) 3986.

[53] H. Fritzsch and Z-Z. Xing, Prog. Part. Nucl. Phys. **45** (2000) 1.

[54] See e.g. M. Spira *et al.*, Nucl. Phys. **B453** (1995) 17.

[55] M. Carena, A. Delgado, E. Ponton, T. M. P. Tait and C. E. M. Wagner, Phys. Rev. **D68** (2003) 035010; Phys. Rev. **D71** (2005) 015010.

[56] G. Cacciapaglia, C. Csáki, C. Grojean and J. Terning, Phys. Rev. **D71**, (2005) 035015.

[57] K. Agashe and G. Servant, JCAP **0502** (2005) 002.

Chapter 7

The MSSM scenario after the Higgs boson discovery

Adapted from: *A. Djouadi, L. Maiani, G. Moreau, A. Polosa, J. Quevillon and V. Riquer*, Eur. Phys. J. **C73** (2013) 2650.

7.1 Introduction

The observation at the LHC of a Higgs particle with a mass of 125 GeV [1] has important implications for Supersymmetric (SUSY) and, in particular, for the Minimal Supersymmetric Standard Model (MSSM). In this extension, the Higgs sector consists of two scalar doublet fields H_u and H_d that lead, after electroweak symmetry breaking, to five Higgs states, two CP–even h and H, a CP–odd A and two charged $H^\pm$ bosons [2, 3]. At tree level, the masses of these particles and their mixings are described by only two parameters usually chosen to be the ratio of the vacuum expectations values of the two doublet fields $\tan\beta = v_d/v_u$ and the mass M_A of the pseudoscalar Higgs boson. However, as is well known, the radiative corrections play a very important role as their dominant component grows like the fourth power of the top quark mass, logarithmically with the supersymmetry breaking scale M_S and quadratically with the stop mixing parameter A_t; see e.g. Refs. [3–5].

The impact of the Higgs discovery is twofold. On the one hand, it gives support to the MSSM in which the lightest Higgs boson is predicted to have a mass below ≈ 130 GeV when the radiative corrections are included [3–5]. On the other hand, the fact that the measured value $M_h \approx 125$ GeV is close to this upper mass limit implies that the SUSY–breaking scale M_S might be rather high. This is backed up by the presently strong limits on supersymmetric particle masses from direct searches that indicate that the SUSY partners of the strongly interacting particles, the squarks and gluinos, are heavier than ≈ 1 TeV [6]. Hence, the MSSM that we currently have, and that we

call hMSSM (habemus MSSM?) in the subsequent discussion, appears to have $M_h \approx 125$ GeV and $M_S \gtrsim 1$ TeV.

It was pointed out in Refs. [7–9] that when the information $M_h = 125$ GeV is taken into account, the MSSM Higgs sector with solely the dominant radiative correction to the Higgs boson masses included, can be again described with only the two free parameters $\tan\beta$ and M_A as it was the case at tree–level. In other words, the dominant radiative corrections that involve the SUSY parameters are fixed by the value of M_h. In this study, we show that to a good approximation, this remains true even when the full set of radiative corrections to the Higgs masses at the two–loop level is included. This is demonstrated in particular by performing a full scan on the MSSM parameters that have an impact on the Higgs sector such as for instance $\tan\beta$ and the stop and sbottom mass and mixing parameters. The subleading radiative corrections are shown to have little impact on the mass and mixing of the heavier Higgs bosons when these SUSY parameters are varied in a reasonable range.

Nevertheless, there are also possibly large direct SUSY radiative corrections that modify the Higgs boson couplings and which might alter this simple picture. Among such corrections are, for instance, the stop contribution [10, 11] to the dominant Higgs production mechanism at the LHC, the gluon fusion process $gg \to h$, and to the important decay into two photons $h \to \gamma\gamma$, and the additional one–loop vertex corrections to the h couplings to b–quarks that grow with $\tan\beta$ [12]. In the most general case, besides M_h, seven couplings need to be considered to fully describe the properties of the observed h boson: those to gluons, photons, massive gauge bosons, t, b, c quarks and τ leptons. However, we show that given the accuracy that is foreseen at the LHC, a good approximation is to consider the three effective couplings to t, b quarks and to $V = W/Z$ bosons, c_t, c_b and c_V, as it was suggested in Ref. [13]. Following the approach of Ref. [14] for the inclusion of the current theoretical and experimental uncertainties, we perform a fit of these three couplings using the latest LHC data on the production and decay rates of the lighter h boson and the limits from the negative search of the heavier H, A and $H^\pm$ MSSM states.

The best fit points to low values of $\tan\beta$ and to M_A values of the order of 500 GeV, leading to a spectrum in the Higgs sector that can be fully explored at the 14 TeV LHC.

With the data obtained one year after the Higgs discovery at the LHC, these two aspects will be discussed in the next two sections. A brief discussion and a conclusion are given in Section 7.4 and the short Appendix D collects a set of formulae used in this analysis.

7.2 Post Higgs discovery parametrisation of radiative corrections

In the MSSM, the tree–level masses of the CP–even h and H bosons depend on M_A, $\tan\beta$ and the Z boson mass. However, many parameters of the MSSM such as the SUSY scale, taken to be the geometric average of the stop masses $M_S = \sqrt{m_{\tilde{t}_1} m_{\tilde{t}_2}}$, the stop/sbottom trilinear couplings $A_{t/b}$ or

the higgsino mass μ enter M_h and M_H through radiative corrections. In the basis (H_d, H_u), the CP–even Higgs mass matrix can be written as:

$$M_S^2 = M_Z^2 \begin{pmatrix} c_\beta^2 & -s_\beta c_\beta \\ -s_\beta c_\beta & s_\beta^2 \end{pmatrix} + M_A^2 \begin{pmatrix} s_\beta^2 & -s_\beta c_\beta \\ -s_\beta c_\beta & c_\beta^2 \end{pmatrix} + \begin{pmatrix} \Delta\mathcal{M}_{11}^2 & \Delta\mathcal{M}_{12}^2 \\ \Delta\mathcal{M}_{12}^2 & \Delta\mathcal{M}_{22}^2 \end{pmatrix} \tag{7.1}$$

where we use the short–hand notation $s_\beta \equiv \sin\beta$ etc... and have introduced the radiative corrections by a 2×2 general matrix $\Delta\mathcal{M}_{ij}^2$. One can then easily derive the neutral CP even Higgs boson masses and the mixing angle α that diagonalises the h, H states[1], $H = \cos\alpha H_d^0 + \sin\alpha H_u^0$ and $h = -\sin\alpha H_d^0 + \cos\alpha H_u^0$

$$M_{h/H}^2 = \frac{1}{2}\big(M_A^2 + M_Z^2 + \Delta\mathcal{M}_{11}^2 + \Delta\mathcal{M}_{22}^2 \mp \sqrt{M_A^4 + M_Z^4 - 2M_A^2 M_Z^2 c_{4\beta} + C}\big) \tag{7.2}$$

$$\tan\alpha = \frac{2\Delta\mathcal{M}_{12}^2 - (M_A^2 + M_Z^2)s_\beta}{\Delta\mathcal{M}_{11}^2 - \Delta\mathcal{M}_{22}^2 + (M_Z^2 - M_A^2)c_{2\beta} + \sqrt{M_A^4 + M_Z^4 - 2M_A^2 M_Z^2 c_{4\beta} + C}} \tag{7.3}$$

$$C = 4\Delta\mathcal{M}_{12}^4 + (\Delta\mathcal{M}_{11}^2 - \Delta\mathcal{M}_{22}^2)^2 - 2(M_A^2 - M_Z^2)(\Delta\mathcal{M}_{11}^2 - \Delta M_{22}^2)c_{2\beta} - 4(M_A^2 + M_Z^2)\Delta\mathcal{M}_{12}^2 s_{2\beta}$$

In previous analyses [7–9], we have assumed that in the 2×2 matrix for the radiative corrections, only the $\Delta\mathcal{M}_{22}^2$ entry which involves the by far dominant stop–top sector correction, is relevant, $\Delta\mathcal{M}_{22}^2 \gg \Delta\mathcal{M}_{11}^2, \Delta\mathcal{M}_{12}^2$. This occurs, for instance, in the so–called ϵ approximation [4] and its refinements [5] that are given in eqs. (A2) and (A3) of the Appendix D. In this case, one can simply trade $\Delta\mathcal{M}_{22}^2$ for the by now known M_h using

$$\Delta\mathcal{M}_{22}^2 = \frac{M_h^2(M_A^2 + M_Z^2 - M_h^2) - M_A^2 M_Z^2 c_{2\beta}^2}{M_Z^2 c_\beta^2 + M_A^2 s_\beta^2 - M_h^2} \tag{7.4}$$

In this case, one can simply write M_H and α in terms of $M_A, \tan\beta$ and M_h:

$$\text{hMSSM}: \quad \begin{aligned} M_H^2 &= \frac{(M_A^2+M_Z^2-M_h^2)(M_Z^2 c_\beta^2 + M_A^2 s_\beta^2) - M_A^2 M_Z^2 c_{2\beta}^2}{M_Z^2 c_\beta^2 + M_A^2 s_\beta^2 - M_h^2} \\ \alpha &= -\arctan\left(\frac{(M_Z^2+M_A^2)c_\beta s_\beta}{M_Z^2 c_\beta^2 + M_A^2 s_\beta^2 - M_h^2}\right) \end{aligned} \tag{7.5}$$

In this section, we will check the validity of the $\Delta\mathcal{M}_{11}^2 = \Delta\mathcal{M}_{12}^2 = 0$ approximation. To do so, we first consider the radiative corrections when the subleading contributions proportional to μ, A_t or A_b are included in the form of eqs. (A4–A6) of the Appendix D, that is expected to be a good approximation [3, 15], and in which one has $\Delta\mathcal{M}_{11}^2 \neq \Delta\mathcal{M}_{12}^2 \neq 0$.

As a first step we only consider the stop-top sector corrections which enter the $\Delta\mathcal{M}_{ij}^2$ terms and confront in Fig. 7.1, the values of $\Delta\mathcal{M}_{11}^2$, $\Delta\mathcal{M}_{12}^2$ to $\Delta\mathcal{M}_{22}^2$ for three different scenarios with

[1] A different definition for the mixing angle α, namely $\alpha \to \frac{\pi}{2} - \alpha$, has been adopted in Refs. [7, 8, 13].

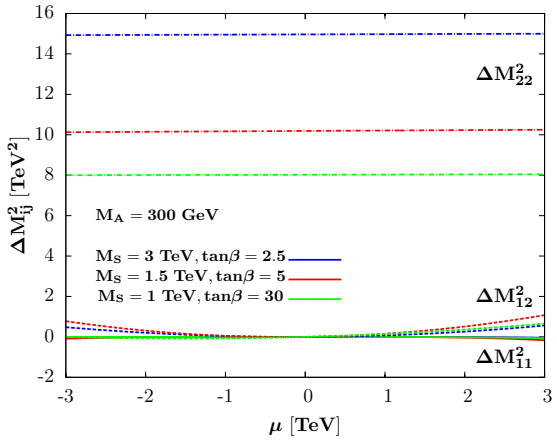

Figure 7.1: The entries $\Delta\mathcal{M}^2_{11}$ (solid), $\Delta\mathcal{M}^2_{12}$ (dashed), and $\Delta\mathcal{M}^2_{22}$ (dotted-dashed lines) of the radiative corrections matrix as functions of μ with a fixed $M_A = 300$ GeV for three different $(M_S, \tan\beta)$ sets and A_t such that it accommodates the mass range $M_h = 123$–129 GeV.

$M_A = 300$ GeV (i.e. before the onset of the decoupling regime $M_A \gg M_Z$): $M_S = 3$ TeV and $\tan\beta = 2.5$, $M_S = 1.5$ TeV and $\tan\beta = 5$, $M_S = 1$ TeV and $\tan\beta = 30$. The parameter A_t is adjusted in order to accommodate a light Higgs boson with a mass $M_h = 126 \pm 3$ GeV, including an expected theoretical and experimental uncertainty of 3 GeV [16]. One observes that for reasonable μ values, one obtains naturally $\Delta\mathcal{M}^2_{11}, \Delta\mathcal{M}^2_{12} \ll \Delta\mathcal{M}^2_{22}$.

We have verified that the situation is not very different if the corrections in the sbottom sector are also included: assuming $A_b = A_t$, we also obtain the hierarchy $\Delta\mathcal{M}^2_{11}, \Delta\mathcal{M}^2_{12} \ll \Delta\mathcal{M}^2_{22}$ for $\mu \lesssim 3$ TeV even for $\tan\beta = 30$ where contributions $\propto \mu \tan\beta$ become important.

Taking into account only the dominant top–stop radiative corrections in the approximations of eqs. (A4–A6), Fig. 7.2 displays the mass of the heavy CP–even Higgs state (left) and the mixing angle α (right) as a function of μ when $\Delta\mathcal{M}^2_{11}$ and $\Delta\mathcal{M}^2_{12}$ are set to zero (dashed lines) and when they are included (solid lines). We have assumed the same $(M_S, \tan\beta)$ sets as above and for each value of μ, we calculate "approximate" and 'exact" M_H and α values assuming $M_h = 126 \pm 3$ GeV. Even for large values of the parameter μ (but $\mu \lesssim 3$ TeV), the relative variation for M_H never exceeds the 0.5% level while the variation of the angle α is bounded by $\Delta\alpha \lesssim 0.015$. Hence, in this scenario for the radiative corrections, the approximation of determining the parameters M_H and α from $\tan\beta, M_A$ and the value of M_h is extremely good. We have again verified that it stays the case when the corrections in the sbottom sector, with $A_b = A_t$, are included.

We should note that for higher M_A values, $M_A \gtrsim 300$ GeV, the approximation is even better as we are closer to the decoupling limit in which one has $M_H = M_A$ and $\alpha = \frac{\pi}{2} - \beta$. Lower values, $M_A \lesssim 300$ GeV, are disfavored by the observed h rates [8,9] as seen later.

In order to check more thoroughly the impact of the subleading corrections $\Delta\mathcal{M}^2_{11}$, $\Delta\mathcal{M}^2_{12}$, we

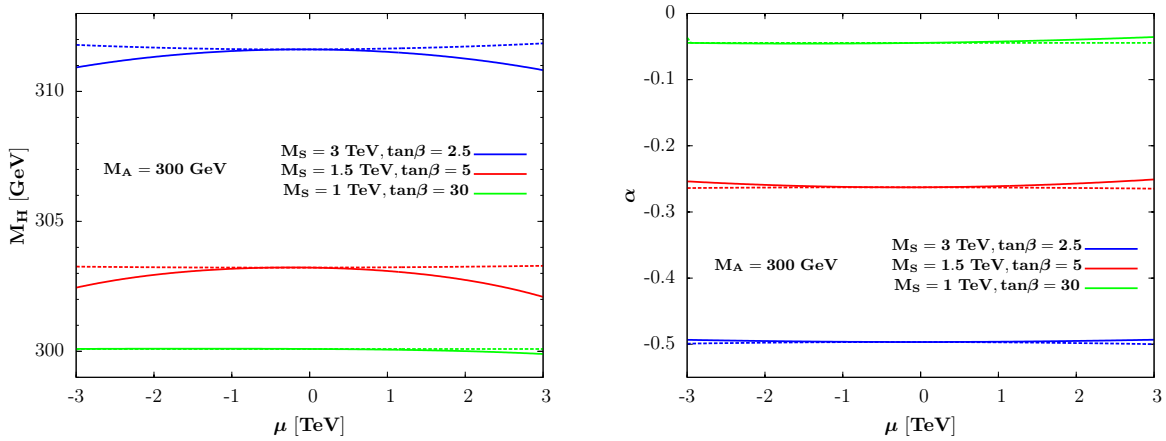

Figure 7.2: The mass of the heavier CP–even H boson (left) and the mixing angle α (right) as a function of μ with (solid lines) and without (dashed) the off–diagonal components components for $M_A = 300$ GeV and three $(M_S, \tan\beta)$ sets. A_t is such that $M_h = 123$–129 GeV and $A_b = 0$.

perform a scan of the MSSM parameter space using the program `SuSpect` [17] in which the full two–loop radiative corrections to the Higgs sector are implemented. For a chosen ($\tan\beta$,M_A) input set, the soft–SUSY parameters that play an important role in the Higgs sector are varied in the following ranges: $|\mu| \leq 3$ TeV, $|A_t, A_b| \leq 3M_S$, 1 TeV$\leq M_3 \leq 3$ TeV and 0.5 TeV$\leq M_S \leq 3$ TeV (≈ 3 TeV is the scale up to which programs such as `SuSpect` are expected to be reliable). We assume the usual relation between the weak scale gaugino masses $6M_1 = 3M_2 = M_3$ and set $A_u, A_d, A_\tau = 0$ (these last parameters have little impact).

We have computed the MSSM Higgs sector parameters all across the parameter space selecting the points which satisfy the constraint $123 \leq M_h \leq 129$ GeV. For each of the points, we have compared the Higgs parameters to those obtained in the simplified MSSM approximation, $\Delta\mathcal{M}^2_{11} = \Delta\mathcal{M}^2_{12} = 0$, with the lightest Higgs boson mass as input. We also required M_h to lie in the range 123–129 GeV, but allowed it to be different from the one obtained in the "exact" case $\Delta\mathcal{M}^2_{11}, \Delta\mathcal{M}^2_{12} \neq 0$.

For the mass M_H and the angle α, we display in Fig. 7.3 the difference between the values obtained when the two possibilities $\Delta\mathcal{M}^2_{11} = \Delta\mathcal{M}^2_{12} = 0$ and $\Delta\mathcal{M}^2_{11}, \Delta\mathcal{M}^2_{12} \neq 0$ are considered. This is shown in the plane $[M_S, X_t]$ with $X_t = A_t - \mu \cot\beta$ when all other parameters are scanned as above. Again, we have fixed the pseudoscalar Higgs mass to $M_A = 300$ GeV and used the two representative values $\tan\beta = 5$ and 30. We have adopted the conservative approach of plotting only points which maximize these differences.

In all cases, the difference between the two M_H values is very small (in fact, much smaller than the total decay width Γ_H), less than a few percent, while for α the difference does not exceed ≈ 0.025 for low values of $\tan\beta$ but at high $\tan\beta$ values, one can reach the level of ≈ 0.05 in some rare situations (large values of μ, which enhance the $\mu\tan\beta$ contributions). Nevertheless, at high enough $\tan\beta$, we are far in the decoupling regime already for $M_A \gtrsim 200$ GeV and such a difference

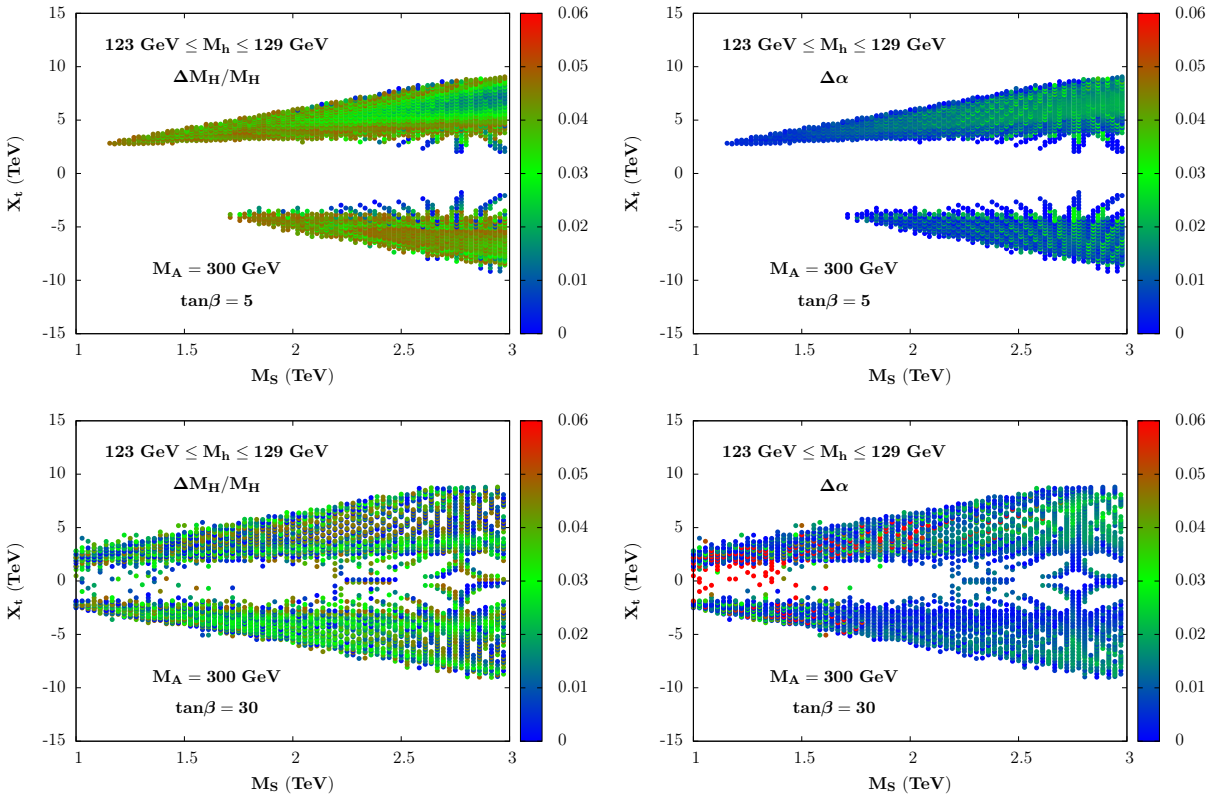

Figure 7.3: The variation of the mass M_H (left) and the mixing angle α (right), are shown as separate vertical colored scales, in the plane $[M_S, X_t]$ when the full two loop corrections are included with and without the subleading matrix elements $\Delta\mathcal{M}^2_{11}$ and $\Delta\mathcal{M}^2_{12}$. We take $M_A = 300$ GeV, $\tan\beta = 5$ (top) and 30 (bottom) and the other parameters are varied as described in the text.

does not significantly affect the couplings of the h and H bosons which, phenomenologically, are the main ingredients.

Hence, even when including the full set of radiative corrections up to two loops, it is a good approximation to use eqs. (7.5) to derive the parameters M_H and α in terms of the inputs $\tan\beta, M_A$ and the measured value of M_h. In the case of the charged Higgs boson mass, the radiative corrections are much smaller for large enough M_A and one has, at the few percent level (which is again smaller than the total $H^\pm$ decay width), $M_{H^\pm} \simeq \sqrt{M_A^2 + M_W^2}$ except in very rare situations[2] [18].

7.3 Determination of the h boson couplings in a generic MSSM

A second important issue is the MSSM Higgs couplings. In principle and as discussed earlier, knowing two parameters such as the pair of inputs $[\tan\beta, M_A]$ and fixing the value of M_h to its

[2]The physics of the charged boson, i.e the production and decay rates, can be accurately described by $\tan\beta, M_{H^\pm}$ (and eventually α if the subleading processes involving the h state are also considered).

measured value, the couplings of the Higgs bosons, in particular h, to fermions and gauge bosons can be derived, including the generally dominant radiative corrections that enter in the MSSM Higgs masses. Indeed, in terms of the angles β and α, one has for the reduced couplings (i.e. normalized to their SM values) of the lighter h state to third generation t, b fermions and gauge bosons $V = W/Z$,

$$c_V^0 = \sin(\beta - \alpha) \ , \quad c_t^0 = \frac{\cos\alpha}{\sin\beta} \ , \quad c_b^0 = -\frac{\sin\alpha}{\cos\beta} \tag{7.6}$$

However, outside the regime in which the pseudoscalar A boson and some supersymmetric particles are very heavy, there are also direct radiative corrections to the Higgs couplings not contained in the mass matrix of eq. (1). These can alter this simple picture.

First, in the case of b–quarks, additional one–loop vertex corrections modify the tree–level $hb\bar{b}$ coupling: they grow as $m_b \mu \tan\beta$ and are thus very large at high $\tan\beta$. The dominant component comes from the SUSY–QCD corrections with sbottom–gluino loops that can be approximated by $\Delta_b \simeq 2\alpha_s/(3\pi) \times \mu m_{\tilde{g}} \tan\beta / \max(m^2_{\tilde{g}}, m^2_{\tilde{b}_1}, m^2_{\tilde{b}_2})$ [12].

Outside the decoupling regime, the $hb\bar{b}$ coupling receives the possibly large correction

$$c_b \approx c_b^0 \times [1 - \Delta_b/(1+\Delta_b) \times (1 + \cot\alpha \cot\beta)] \ \text{ with } \ \tan\alpha \overset{M_A \gg M_Z}{\to} -1/\tan\beta \tag{7.7}$$

which would significantly alter the partial width of the decay $h \to b\bar{b}$ that is, in principle, by far the dominant one and, hence, affect the branching fractions of all other decay modes.

In addition, the $ht\bar{t}$ coupling is derived indirectly from the $gg \to h$ production cross section and the $h \to \gamma\gamma$ decay branching ratio, two processes that are generated via triangular loops. In the MSSM, these loops involve not only the top quark (and the W boson in the decay $h \to \gamma\gamma$) but also contributions from supersymmetric particles, if they are not too heavy. In the case of the $gg \to h$ process, only the contributions of stops is generally important. Including the later and working in the limit $M_h \ll m_t, m_{\tilde{t}_1}, m_{\tilde{t}_2}$, the hgg amplitude can be (very well) approximated by the expression [10]

$$c_t \approx c_t^0 \times \left[1 + \frac{m_t^2}{4 m^2_{\tilde{t}_1} m^2_{\tilde{t}_2}} (m^2_{\tilde{t}_1} + m^2_{\tilde{t}_2} - (A_t - \mu\cot\alpha)(A_t + \mu\tan\alpha) \ ) \right] \tag{7.8}$$

which shows that indeed, $\tilde{t}$ contributions can be very large for sufficiently light stops and in the presence of large stop mixing. In the $h \to \gamma\gamma$ decay rate, because the $t, \tilde{t}$ electric charges are the same, the $ht\bar{t}$ coupling is shifted by the same amount as above [11].

If one ignores the usually small $\tilde{b}$ contributions in the $gg \to h$ production and $h \to \gamma\gamma$ decay processes (in the latter case, it is suppressed by powers of the b electric charge $e_b^2/e_t^2 = \frac{1}{4}$ in addition) as well as the contributions of other SUSY particles such as charginos and stau's in the $h \to \gamma\gamma$

decay rate[3], the leading corrections to the $ht\bar{t}$ vertex can be simply accounted for by using the effective coupling given in eq. (7.8); see e.g. Ref. [8].

Note that in the case of associated production of the h boson with top quarks, $gg/q\bar{q} \to ht\bar{t}$, it is the parameter c_t^0 which should be considered for the direct $ht\bar{t}$ coupling. However, for the time being (and presumably for a long time), the constraints on the h properties from this process are very weak as the cross section has very large uncertainties.

One also should note that the couplings of the h boson to τ leptons and charm quarks do not receive the direct corrections of respectively eqs. (7.7) and (7.8) and one should still have $c_c = c_t^0$ and $c_\tau = c_b^0$. However, using $c_{t,b}$ or $c_{t,b}^0$ in this case has almost no impact in practice as these couplings appear only in the branching ratios for the decays $h \to c\bar{c}$ and $\tau^+\tau^-$ which are small, below 5%, and the direct corrections cannot be very large (these are radiative corrections after all). One can thus, in a first approximation, ignore them and assume that $c_c = c_t$ and $c_\tau = c_b$. Note that BR($h \to c\bar{c}$) cannot be measured at the LHC while the $h \to \tau^+\tau^-$ rate is presently measured only at the level of 40% or so [21].

Another caveat is that possible invisible decays (which at present are probed directly only for rates that are at the 50% to 100% level [23]), can also affect the properties of the observed h particle. However, a large invisible rate implies that the neutralinos that are considered as the lightest SUSY particles, are relatively light and couple significantly to the h boson, a situation that is rather unlikely (if the LSP is very light, $2m_{\chi_1^0} \lesssim M_h$, it should be mostly bino–like and, hence, has very suppressed couplings to the Higgs bosons that prefer to couple to mixtures of higgsinos and gauginos; see for instance Ref. [11]).

In the case of large direct corrections, the Higgs couplings cannot be described only by the parameters β and α as in eq. (7.6). One should consider at least three independent h couplings, namely $c_c = c_t$, $c_\tau = c_b$ and $c_V = c_V^0$ as advocated in Ref. [13]. This is equivalent to excluding the $h \to \tau\tau$ data from the global fit which, in practice, has no significant impact as the experimental error on the signal strength in this channel is presently large. Note that a future determination of the theoretically clean ratio of the $b\bar{b}$ and $\tau^+\tau^-$ signals in $pp \to hV$ gives a direct access to the Δ_b correction outside the decoupling regime [14].

To study the h state at the LHC, we thus define the following effective Lagrangian,

$$\begin{aligned} \mathcal{L}_h \;&=\; c_V\; g_{hWW}\; h\; W_\mu^+ W^{-\mu} + \; c_V\; g_{hZZ}\; h\; Z_\mu^0 Z^{0\mu} \\ &-\; c_t\; y_t\; h\bar{t}_L t_R - c_t\; y_c\; h\bar{c}_L c_R - c_b\; y_b\; h\bar{b}_L b_R - c_b\; y_\tau\; h\bar{\tau}_L \tau_R \;+\; \text{h.c.} \end{aligned} \tag{7.9}$$

where $y_{t,c,b,\tau} = m_{t,c,b,\tau}/v$ are the SM Yukawa coupling constants in the mass eigenbasis (L/R indicates the fermion chirality and we consider only the heavy fermions that have substantial couplings to the Higgs boson), $g_{hWW} = 2M_W^2/v$ and $g_{hZZ} = M_Z^2/v$ are the electroweak gauge

[3]The chargino contribution cannot exceed the 10% level even for very favorable gaugino-higgsino parameters [11], while the $\tilde{\tau}$ contributions are important only for extreme values of $\tan\beta$ and μ [19].

boson couplings and v is the Higgs vacuum expectation value.

We present the results for the fits of the Higgs signal strengths in the various channels

$$\mu_X \simeq \sigma(pp \to h) \times \text{BR}(h \to XX)/\sigma(pp \to h)_{\text{SM}} \times \text{BR}(h \to XX)_{\text{SM}} \tag{7.10}$$

closely following the procedure of Ref. [14] but in the case of the phenomenological MSSM. All the Higgs production/decay channels are considered and the data used are the latest ones [21] using the full ≈ 25 fb^{-1} statistics for the $\gamma\gamma, ZZ, WW$ channels as well as the $h \to b\bar{b}$ and $\tau\tau$ modes for CMS, but only ≈ 17 fb^{-1} data for the ATLAS fermionic channels.

We have performed the appropriate three-parameter fit in the three-dimensional space[4] $[c_t, c_b, c_V]$, assuming $c_c = c_t$ and $c_\tau = c_b$ as discussed above and of course the custodial symmetry relation $c_V = c_W = c_Z$ which holds in supersymmetric models. The results of this fit are presented in Fig. 7.4 for $c_t, c_b, c_V \geq 0$, as motivated by the supersymmetric structure of the Higgs couplings (there is also an exact reflection symmetry under, $c \to -c$ or equivalently $\beta \to \beta + \pi$, leaving the squared amplitudes of the Higgs rates unaffected). Again following Ref. [14], we have treated the theoretical uncertainty as a bias and not as if it were associated to a statistical distribution and have performed the fit for values of the signal strength $\mu_i|_{\text{exp}}[1 \pm \Delta\mu_i/\mu_i|_{\text{th}}]$ with the theoretical uncertainty $\Delta\mu_i/\mu_i|_{\text{th}}$ conservatively assumed to be 20% for both the gluon and vector boson fusion mechanisms (because of contamination) and $\approx 5\%$ for h production in association with $V = W/Z$ [20].

The best-fit value for the couplings, when the ATLAS and CMS data are combined, is $c_t = 0.89$, $c_b = 1.01$ and $c_V = 1.02$ with $\chi^2 = 64.8$ ($\chi^2 = 66.7$ in the SM).

In turn, in scenarios where the direct corrections in eqs. (7.7)-(7.8) are not quantitatively significant (i.e. considering either not too large values of $\mu \tan\beta$ or high stop/sbottom masses), one can use the MSSM relations of eq. (7.6) to reduce the number of effective parameters down to two. For instance, using $c_t = \cos\alpha/\sin\beta$ and $c_V = \sin(\beta - \alpha)$, one can derive the following relation, $c_b \equiv -\sin\alpha/\cos\beta = (1 - c_V c_t)/(c_V - c_t)$. This allows to perform the two-parameter fit in the plane $[c_V, c_t]$. Similarly, one can study the planes $[c_V, c_b]$ and $[c_t, c_b]$. The two-dimensional fits in these three planes are displayed in Fig. 7.5. As in the MSSM one has $\alpha \in [-\pi/2, 0]$ and $\tan\beta \in [1, \sim 50]$, one obtains the following variation ranges: $c_V \in [0, 1]$, $c_t \in [0, \sqrt{2}]$ and $c_b > 0$.

We also show on these figures the potential constraints obtained from fitting ratios of the Higgs signal strengths (essentially the two ratios $R_{\gamma\gamma} = \mu_{\gamma\gamma}/\mu_{ZZ}$ and $R_{\tau\tau} = \mu_{\tau\tau}/\mu_{WW}$) that are not or much less affected by the QCD uncertainties at the production level [14]. In this two–dimensional case, the best-fit points are located at ($c_t = 0.88$, $c_V = 1.0$), ($c_b = 0.97$, $c_V = 1.0$) and ($c_t = 0.88$, $c_b = 0.97$). Note that although for the best–fit point one has $c_b \lesssim 1$, actually $c_b \gtrsim 1$ in most of the 1σ region.

[4] Higgs coupling fits have been performed most often in the $[c_V, c_f]$ parameter space with $c_f = c_t = c_b \ldots$. Fits of the LHC data in SUSY scenarios including also the NMSSM can be found in Ref. [22] for instance.

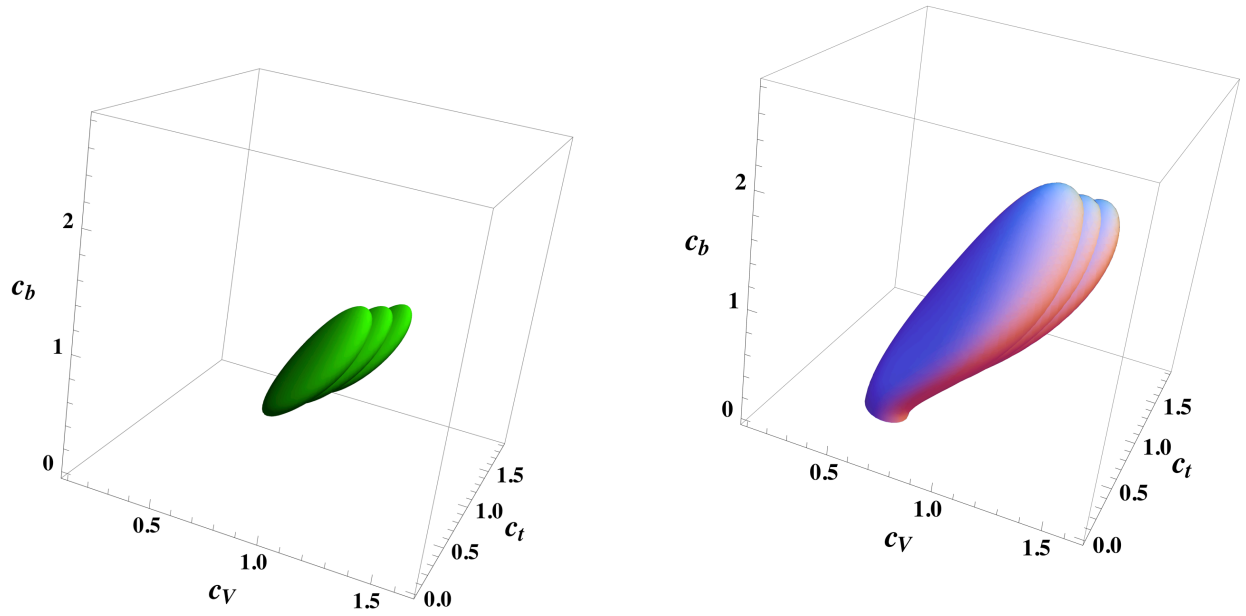

Figure 7.4: Best-fit regions at 68%CL (green, left) and 99%CL (light gray, right) for the Higgs signal strengths in the three–dimensional space $[c_t, c_b, c_V]$. The three overlapped regions are associated to central and two extreme choices of the theoretical prediction for the Higgs rates.

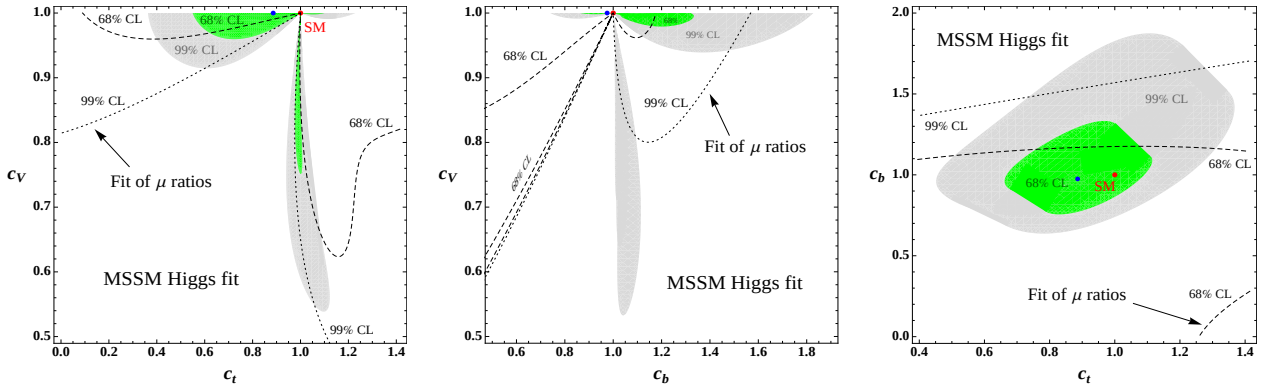

Figure 7.5: Best-fit regions at 68%CL (green) and 99%CL (light gray) for the Higgs signal strengths in the planes $[c_t, c_V]$ (left), $[c_b, c_V]$ (center) and $[c_t, c_b]$ (right). The theoretical uncertainty on the Higgs signal strengths is taken into account as a bias. The best-fit contours at 68%CL (dashed) and 99%CL (dotted) from the fit of signal strength ratios are superimposed as well. The SM points are indicated in red and the best-fit points in blue.

Alternatively, using the expressions of eq. (7.6), one can also realize a two-parameter fit in the $[\tan\beta, \alpha]$ plane[5]. However, using the expressions of eq. (7.5) for the mixing angle α and fixing

[5]This corresponds in fact to the case of a two–Higgs doublet model in which the direct corrections are expected to be small in contrast to the SUSY case: one can then parametrise the couplings of the h boson, that are given by eq. (7.6), by still two parameters α and β but with the angle α being a free input.

M_h to the measured value $M_h \approx 125$ GeV, one can perform a fit in the plane $[\tan\beta, M_A]$. This is shown in the left–hand side of Fig. 7.6 where the 68%CL, 95%CL and 99%CL contours from the signal strengths only are displayed when, again, the theoretical uncertainty is considered as a bias. We also display the best-fit contours for the signal strength ratios at the 68%CL and 95%CL. The best-fit point for the signal strengths when the theoretical uncertainty is set to zero, is obtained for the values $\tan\beta = 1$ and $M_A = 557$ GeV, which implies for the other parameters, when the radiative corrections entering the Higgs masses and the angle α are derived using the information $M_h = 125$ GeV : $M_H = 580$ GeV, $M_{H^\pm} = 563$ GeV and $\alpha = -0.837$ rad. Regarding this best-fit point, one should note that the χ^2 value is relatively stable all over the 1σ region shown in Fig. 7.6.

It is interesting to superimpose on these indirect limits in the $[\tan\beta, M_A]$ plane, the direct constraints on the heavy $H/A/H^\pm$ boson searches performed by the ATLAS and CMS collaborations as shown in the right–hand side of Fig. 7.6. As discussed in Ref. [9] (see also Ref. [24]), besides the limits from the $A/H \to \tau^+\tau^-$ and to a lesser extent $t \to bH^+ \to b\tau\nu$ searches which exclude high $\tan\beta$ values and which can be extended to very low $\tan\beta$ as well, there are also limits from adapting to the MSSM the high mass SM Higgs searches in the channels[6] $H \to WW$ and ZZ as well as the searches for heavy resonances decaying into $t\bar{t}$ final states that exclude low values of $\tan\beta$ and M_A. For values $250 \lesssim M_A \lesssim 350$ GeV, only the intermediate $\tan\beta \approx 2$–10 range is still allowed.

7.4 Conclusion

We have discussed the MSSM after the discovery of the Higgs boson that we identify with the lighter h state. The mass $M_h \approx 125$ GeV and the non–observation of SUSY particles, seems to indicate that the soft–SUSY breaking scale might be large, $M_S \gtrsim 1$ TeV. We have shown, using both approximate analytical formulae and a scan of the MSSM parameters, that the MSSM Higgs sector can be described to a good approximation by only the two parameters $\tan\beta$ and M_A if the information $M_h = 125$ GeV is used. One could then ignore the radiative corrections to the Higgs masses and their complicated dependence on the MSSM parameters and use a simple formula to derive the other parameters of the Higgs sector, α, M_H and $M_{H^\pm}$.

In a second step, we have shown that to describe accurately the h properties when the direct radiative corrections are also important, the three couplings c_t, c_b and c_V are needed besides the h mass. We have performed a fit of these couplings. In the limit of heavy sparticles (i.e. with small direct corrections), the best fit point turns out to be at low $\tan\beta$, $\tan\beta \approx 1$, and with a not too high CP–odd Higgs mass, $M_A \approx 560$ GeV.

For this particular point, the heavier Higgs particles will be accessible in the next LHC run at least in the channels $A, H \to t\bar{t}$ and presumably also in the modes $H \to WW, ZZ$ as the rates are

[6] At low $\tan\beta$, channels such as $A \to hZ$ and $H \to hh$ need also to be considered [9]. In the latter case, special care is needed in the treatment of the trilinear Hhh coupling.

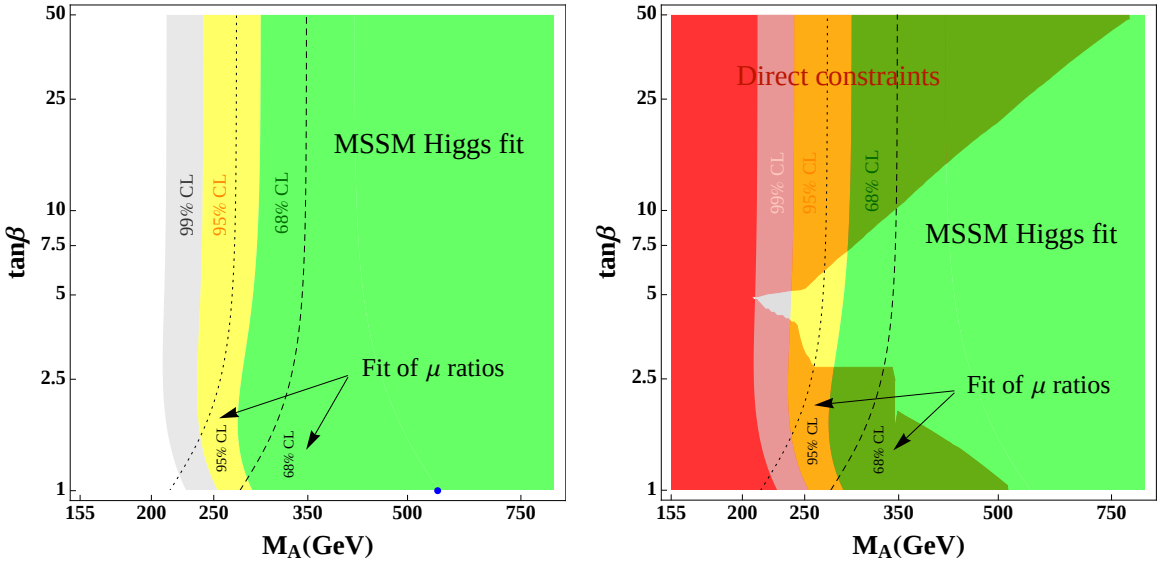

Figure 7.6: Left: best-fit regions at 68%CL (green), 95%CL (yellow) and 99%CL (light gray) for the Higgs signal strengths in the plane $[\tan\beta, M_A]$; the best–fit point is shown in blue and the theoretical uncertainty is taken into account as a bias as in the previous figures. The best-fit contours at 1σ (dashed) and 2σ (dotted) for the signal strength ratios are also shown. Right: we superimpose on these constraints the excluded regions (in red, and as a shadow when superimposed on the best-fit regions) from the direct searches of the heavier Higgs bosons at the LHC following the analysis of Ref. [9].

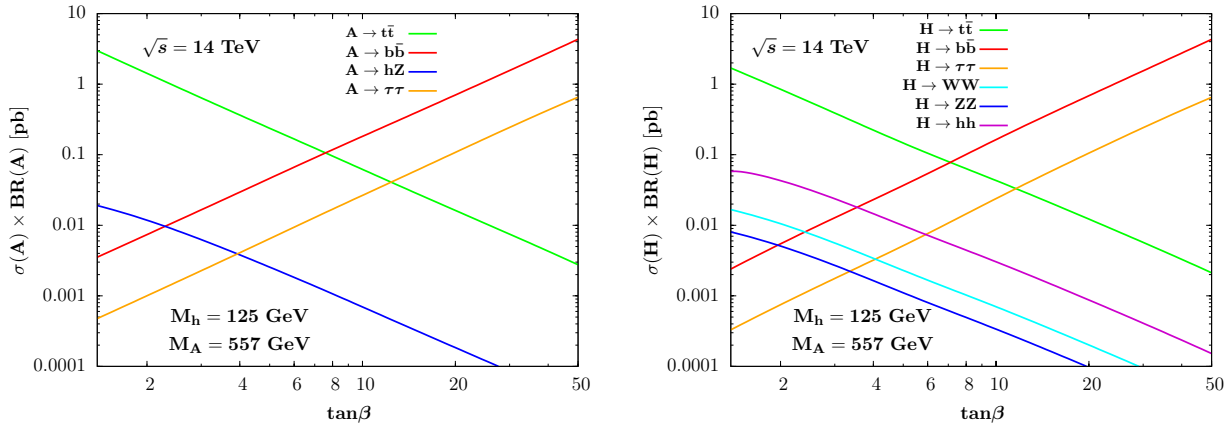

Figure 7.7: The cross section times branching fractions for the A (left) and H (right) MSSM Higgs bosons at the LHC with $\sqrt{s} = 14$ TeV as a function of $\tan\beta$ for the best–fit mass $M_A = 557$ GeV and with $M_h = 125$ GeV. For the production, we have taken into account only the gluon and bottom quark fusion processes and followed the analysis given in Ref. [9].

rather large for $\tan\beta \approx 1$. This is shown in Fig. 7.7 where the cross sections times decay branching ratios for A and H are displayed as a function of $\tan\beta$ for the choice $M_A = 557$ GeV for $\sqrt{s} = 14$

TeV[7].

[7]Furthermore, the correct relic abundance of the LSP neutralino can be easily obtained through $\chi_1^0\chi_1^0 \to A \to t\bar{t}$ annihilation by allowing the parameters μ and M_1 to be comparable and have an LSP mass close to the A–pole, $m_{\chi_1^0} \approx \frac{1}{2}M_A$.

Bibliography

[1] The ATLAS collaboration, Phys. Lett. B716 (2012) 1; the CMS collaboration, Phys. Lett. B716 (2012) 30.

[2] J. Gunion, H. Haber, G. Kane and S. Dawson, "The Higgs Hunter's Guide", Reading 1990; S. Heinemeyer, W. Hollik and G. Weiglein, Phys. Rept. 425 (2006) 265; A. Djouadi, Phys. Rept. 459 (2008) 1.

[3] M. Carena and H. Haber, Prog. Part. Nucl. Phys. 50 (2003) 63.

[4] Y. Okada, M. Yamaguchi and T. Yanagida, Prog. Theor. Phys. 85 (1991) 1; J. Ellis, G. Ridolfi and F. Zwirner, Phys. Lett. B257 (1991) 83; H.E. Haber and R. Hempfling, Phys. Rev. Lett. 66 (1991) 1815.

[5] M. Carena, J.R. Espinosa, M. Quiros and C.E. Wagner, Phys. Lett. B355 (1995) 209. See also, H. Haber, R. Hempfling and A. Hoang, Z. Phys. C75 (1997) 539.

[6] See the talk of A. Hoecker at the Lepton–Photon Conference, Stanford, June 2013.

[7] L. Maiani, A.D. Polosa and V. Riquier, New J. Phys. 14 (2012) 073029.

[8] L. Maiani, A.D. Polosa and V. Riquier, Phys. Lett. B718 (2012) 465.

[9] A. Djouadi and J. Quevillon, arXiv:1304.1787 [hep-ph].

[10] See e.g. A. Djouadi, Phys. Lett. B435 (1998) 101; A. Arvanitaki and G. Villadoro, JHEP 1202 (2012) 144; A. Delgado et al., Eur. Phys. J. C73 (2013) 2370.

[11] A. Djouadi, V. Driesen, W. Hollik and Jose Illana, Eur. Phys. J. C1 (1998) 149.

[12] See e.g. M. Carena, D. Garcia, U. Nierste and C. Wagner, Nucl. Phys. B577 (2000) 88.

[13] L. Maiani, A.D. Polosa and V. Riquier, arXiv:1305.2172 [hep-ph].

[14] A. Djouadi and G. Moreau, arXiv:1303.6591. The analysis is based on earlier work published in arXiv:1208.3436 [hep-ph] and Phys. Rev. D87 (2013) 015027.

[15] For the top–stop sector, formulae giving approximately the same results are given in G. Degrassi, P. Slavich and F. Zwirner, Nucl. Phys. B 611 (2001) 403.

[16] A. Arbey et al., Phys. Lett. B708 (2012) 162; S. Heinemeyer, O. Stal and G. Weiglein, Phys. Lett. B710 (2012) 201; M. Carena et al., arXiv:1302.7033 [hep-ph].

[17] A. Djouadi, J.L. Kneur and G. Moultaka, Comput. Phys. Commun. 176 (2007) 426. The parametrisation of the Higgs sector, including the radiative corrections is done in, B.C. Allanach et al., JHEP 0409 (2004) 044.

[18] For a recent account, see: M. Frank et al., arXiv:1306.1156 [hep-ph].

[19] See eg., M. Carena, S. Gori, N. R. Shah and C. E. M. Wagner, JHEP 1203 (2012) 014; G. Giudice, P. Paradisi and A. Strumia, JHEP 1210 (2012) 186.

[20] J. Baglio and A. Djouadi, JHEP 1103 (2011) 055. The total uncertainty for $gg \to h$ is slightly higher than the one assumed in, S. Dittmaier et al., arXiv:1101.0593 [hep-ph].

[21] See the summary talks given by Karl Jakobs (for ATLAS) and Albert de Roeck (for CMS) at the Lepton–Photon Conference, Stanford, June 2013.

[22] G. Belanger et al., arXiv:1306.2941 [hep-ph]; R. Barbieri et al., Phys. Rev. D87 (2013) 115018; D. Carmi et al., JHEP1210 (2012) 196; P. P. Giardino et al., JHEP 1206 (2012) 117; J. R. Espinosa et al., JHEP1212 (2012) 077; A. Azatov et al., Phys. Rev. D86 (2012) 075033; A. Arbey et al., JHEP 1209 (2012) 107; Phys. Lett. B720 (2013) 153.

[23] See e.g. A. Djouadi, A. Falkowski, Y. Mambrini and J. Quevillon, arXiv:1205.3169 [hep-ph].

[24] A. Arbey, M. Battaglia and F. Mahmoudi, arXiv:1303.7450 [hep-ph].

Chapter 8

A non-commutativity for the boundary-localized Higgs boson in 5D theories

Adapted from: *R. Barceló, S. Mitra and G. Moreau*, Eur. Phys. J. C75 (2015) 11, 527.

8.1 Introduction

The recent and historical discovery of a Higgs-like boson [1] around 125 GeV at the Large Hadron Collider (LHC) [2] of the CERN fulfills the last missing piece of the particle content of the Standard Model (SM). However, even with the discovery of the Brout-Englert-Higgs scalar field [3], the mechanism responsible for breaking the ElectroWeak (EW) symmetry is not fully understood ; there remain some questions unresolved like, for example, determining the range of validity of the SM. If the SM is valid all the way up to the Planck scale then one can wonder why the EW energy scale (close to the Higgs mass) is so much smaller than the Planck scale. The famous Randall-Sundrum (RS) proposition of an higher-dimensional background with the Higgs boson localized on a TeV or Infra-Red (IR) brane [4], besides addressing the gauge hierarchy problem of Higgs mass corrections, provides an aesthetic interpretation of this apparent discrepancy between fundamental scales of nature : the measured Planck scale would be an effective four-dimensional (4D) scale whereas the gravity scale on the TeV-brane would be reduced by a warp factor down to the EW scale order (the 5D gravity scale in the bulk being still of the order of the Planck scale). The later RS version with SM fields propagating in the bulk [5] even allows to explain the strong hierarchies among fermion masses.

At this special moment where the LHC is scrutinizing the Higgs boson properties [6,7] and exploring higher energy frontiers, it is crucial for the community to have a deep theoretical understanding of

the RS paradigm, in order to develop carefully phenomenological tests of such a scenario. These tests of the RS model can make use of the more and more precise experimental measurements in the Higgs sector [8–11] or of possible direct signatures from Kaluza-Klein (KK) excitations at colliders [12–16] (see Ref. [17] for a review).

Now, from the theoretical point of view, it turns out that recently there has been a debate in the literature on RS frameworks [18, 19]. A non-commutativity has appeared : different results were obtained for Higgs production/decay processes when taking $\epsilon \to 0$ and then $N_{KK} \to \infty$ [20] or the opposite order [21]. N_{KK} is the number of exchanged excited states at the level of the loop amplitude. ϵ is the infinitesimal parameter introduced to regularize the Dirac peak along the extra-dimension associated to the Higgs scalar stuck on the IR-brane ; indeed, this Higgs peak induces the so-called jump problem, for the wave functions of the fermion bulk fields, which must be regularized. It was clearly crucial for testing the Higgs sector of the RS model at LHC to shed light on those theoretical subtleties.

In this study, we show that there exists another type of non-commutativity in a 4D calculation (based on considering gradually KK tower effects) : the fermion mass spectrum expression relies on the arbitrary choice in ordering the limits $\epsilon \to 0$ and $N \to \infty$, where N is now the KK-index at the level of the calculation of mass eigenvalues. We point out this non-commutativity in a toy model with a brane-localized Higgs boson and fermionic matter propagating along a flat extra-dimension, but our main conclusions are expected to remain true in more realistic warped extra-dimension scenarios.
So once more, it is urgent to really understand this new non-commutativity and to determine which order of the limits on ϵ,N has to be followed to construct a consistent model before studying its phenomenology. For that purpose, we perform calculations of the fermion mass spectrum, in both the 4D and 5D (based on equations of motion with Yukawa terms) approaches, applying consecutively the two possible orders – assimilated to two kinds of Higgs regularization – for the above mentioned limits on ϵ,N. Those calculations allow effectively a better insight into the Higgs peak regularization features.
This 4D calculation of the mass spectrum reveals itself to be quite 'heavy', due to the rich texture of the infinite fermion mass matrices, but it has the further interest to demonstrate analytically the exact matchings with the 5D calculation results. Obtaining these 4D/5D matching results represents an opportunity to confirm again the 5D formalism for KK mixings often used.
Let us specify that in order to provide various illustrations of our calculations within the above two types of regularizations, we regularize the Higgs delta peak by shifting it away from the boundary as well as smoothing it into a square profile – which constitutes an equivalent alternative.
Last but not least, we show that the non-commutativity disappears in scenarios where the high-energy (ultra-violet) completion of the model leads to higher order operators with derivatives and localized at the Higgs brane.

The study is organized accordingly to the following simple plan. While the Section 2 is devoted

to the 5D approach of the fermion mass spectrum, Section 3 is focused on the 4D treatment and the two calculations are compared in the synthesis made in Section 4. We summarize and conclude in Section 5.

8.2 5D calculations

8.2.1 The model

We consider a toy model with an extra spatial dimension having a flat geometry and being parametrized by the coordinate, y. This extra-dimension constitutes an interval of length πR with two boundaries at $y = 0, \pi R$. The Higgs boson of the SM, embedded in a doublet under the $SU(2)_L$ gauge group, is strictly localized on the brane at $y = \pi R$ while some fermionic matter is spread out in the bulk. For illustration, let us consider the first quark generation [1] ; the down-quark fields denoted by Q and D are respectively a doublet component and a singlet under $SU(2)_L$, as in the SM. The dynamics for the up-quark sector fields, $\tilde{Q}$ and U, is dictated by an identical Lagrangian and thus we will not repeat such an analogous analysis throughout the present work. For our task, it is sufficient to concentrate on the kinetic terms for the down-quarks as well as their Yukawa interactions, whose fundamental 5D action can be written as usual (after the EW symmetry breaking),

$$\begin{aligned} S_{\text{fermion}} \;=\; & \int \mathrm{d}^4x\, \mathrm{d}y \,\Big[\, \frac{i}{2}(\bar{Q}\Gamma^M\partial_M Q \;-\; \partial_M\bar{Q}\Gamma^M Q \;+\{Q \leftrightarrow D\}) \\ & + \delta(y-\pi R)\,(Y_5\;\bar{Q}_L H D_R \;+\; Y_5'\;\bar{Q}_R H D_L \;+\; \text{H.c.})\,\Big]\,, \end{aligned} \tag{8.1}$$

where the index is $M = 0, 1, 2, 3, 5$ and the Higgs field is developed into the 4D scalar plus its vacuum expectation value as, $H = \frac{v+h(x)}{\sqrt{2}}$, x representing the usual four coordinates. It should be remarked that the coupling constants Y_5 and Y_5' are independent ; in order to avoid the introduction of a new scale in the theory, one can choose $Y_5 = yR$ and $Y_5' = y'R$, where y, y' are dimensionless coupling constants of $\mathcal{O}(1)$. In our notations, the 5D Dirac spinor, being the smallest irreducible representation of the Lorentz group, reads as,

$$Q = \begin{pmatrix} Q_L \\ Q_R \end{pmatrix} \quad \text{and} \quad D = \begin{pmatrix} D_L \\ D_R \end{pmatrix}\,, \tag{8.2}$$

in terms of the two two-component spinors, for the two down-quark fields.

[1] The third family of heavy SM quarks is generally expected to feel the largest mixings with KK modes, but our formalism is directly extendable to any quark generation as well as to leptons.

8.2.2 The KK decomposition and equations of motion

In this Section 8.2, we derive the fermion masses using the so-called exact or 5D approach. In this approach, one keeps the Yukawa mass terms that appear after EW symmetry breaking in the equations of motion for the fermion profiles along the extra-dimension [we will simply refer to those as Equations Of Motion (EOM)]. The advantage of this approach is that the mixing among *all* KK modes for any fermion is automatically taken care of when solving the EOM. Hence this method for deriving the masses is called a 5D calculation as it incorporates the full effect of the 5D theory in the EOM.

The first step is to perform a 'mixed' KK decomposition of the 5D fields in Eq. (8.2),

$$Q_L = \sum_{n=0}^{\infty} q_L^n(y)\; Q_L^n(x)\;, \tag{8.3a}$$

$$Q_R = \sum_{n=0}^{\infty} q_R^n(y)\; D_R^n(x)\;, \tag{8.3b}$$

$$D_L = \sum_{n=0}^{\infty} d_L^n(y)\; Q_L^n(x)\;, \tag{8.3c}$$

$$D_R = \sum_{n=0}^{\infty} d_R^n(y)\; D_R^n(x)\;, \tag{8.3d}$$

where $Q_L^n(x)$, $D_R^n(x)$ are the 4D fields and $q_{L,R}^n(y)$, $d_{L,R}^n(y)$ are the corresponding wave functions along the extra-dimension. Although not essential for our calculations, we note for completeness that with this KK decomposition, the profiles satisfy the following normalization condition,

$$\int_0^{\pi R} dy\, \left[|q_X(y)|^2 + |d_X(y)|^2\right] = 1\;; \quad \text{with } X = L, R\;.$$

Through a factorization of the 4D fields, the mixed KK decomposition allows to separate the Euler-Lagrange equations for the 5D fields into the 4D Dirac equations ($\mu = 0, 1, 2, 3$),

$$-i\bar{\sigma}^\mu \partial_\mu Q_L^n(x) + m\; D_R^n(x) \;=\; 0\;, \tag{8.4}$$

$$-i\sigma^\mu \partial_\mu D_R^n(x) + m\; Q_L^n(x) \;=\; 0\;, \tag{8.5}$$

and the equations of motion for any excited fermion profile after EW symmetry breaking,

$$-\ m\ q_L\ -\ q'_R\ +\ \delta(y-\pi R)\ \frac{vY_5}{\sqrt{2}}\ d_R\ =\ 0\ , \tag{8.6a}$$

$$-\ m\ q_R\ +\ q'_L\ +\ \delta(y-\pi R)\ \frac{vY'_5}{\sqrt{2}}\ d_L\ =\ 0\ , \tag{8.6b}$$

$$-\ m\ d_L\ -\ d'_R\ +\ \delta(y-\pi R)\ \frac{vY'_5}{\sqrt{2}}\ q_R\ =\ 0\ , \tag{8.6c}$$

$$-\ m\ d_R\ +\ d'_L\ +\ \delta(y-\pi R)\ \frac{vY_5}{\sqrt{2}}\ q_L\ =\ 0\ , \tag{8.6d}$$

where the ' $\prime$ ' exponent after any wave function denotes the derivative with respect to the fifth coordinate, y. We have assumed real Yukawa coupling constants and m masses for simplicity, but this kind of analysis is generalizable to cases with complex phases.

The variation of the action combined with the above EOM on the boundaries give rise either to the Dirichlet Boundary Conditions (BC) on both boundaries [i.e. vanishing profiles at the two endpoints], denoted $(--)$ and to be assigned to q_R and d_L, or to the Neumann BC [vanishing derivatives], noted $(++)$ and assigned to q_L and d_R. Now, due to the $\delta(y-\pi R)$-term in Eq. (8.6a), its infinitesimal integration around $y=\pi R$ leads to two distinct values of q_R at that point, which together with the unique q_R $(--)$ BC renders the value of this profile at $y=\pi R$ ambiguous : this is the 'jump' problem [22], first described on an interval in Ref. [23], which also arises of course for the d_L profile in Eq. (8.6d).
To avoid this ambiguity one has to regularize the Higgs peak [23] : this can be done via shifting the Dirac peak away from the boundary by a small (ϵR) amount, or, via smoothing the peak by giving it a narrow width (like a normalized square function of width ϵR). Then one imposes the $(--)$ BC's and solves the EOM (involving ϵ) to find the fermion masses, before finally taking the limit, $\epsilon \to 0$, in order to recover the wanted brane-localized Higgs situation. We are going to realize explicitly those two schemes of ϵ-regularization in the next two subsections.

8.2.3 Moving the Higgs peak

If one shifts the Higgs peak by a distance ϵR away from the πR-boundary,

$$\delta\left(y-\pi R\right) \to \delta\left(y-(\pi-\epsilon)R\right)\ , \tag{8.7}$$

then profile jumps move from the boundary to the bulk. The EOM that one needs to solve become,

$$-\ m\ q_L\ -\ q_R'\ +\ \delta\left(y-(\pi-\epsilon)R\right)\ \frac{vY_5}{\sqrt{2}}\ d_R=0\ , \tag{8.8a}$$

$$-\ m\ q_R\ +\ q_L'\ +\ \delta\left(y-(\pi-\epsilon)R\right)\ \frac{vY_5'}{\sqrt{2}}\ d_L=0\ , \tag{8.8b}$$

$$-\ m\ d_L\ -\ d_R'\ +\ \delta\left(y-(\pi-\epsilon)R\right)\ \frac{vY_5'}{\sqrt{2}}\ q_R=0\ , \tag{8.8c}$$

$$-\ m\ d_R\ +\ d_L'\ +\ \delta\left(y-(\pi-\epsilon)R\right)\ \frac{vY_5}{\sqrt{2}}\ q_L=0\ . \tag{8.8d}$$

Solving this set of equations is not very complicated since, for $0 \leq y < (\pi-\epsilon)R$ and $(\pi-\epsilon)R < y \leq \pi R$, the above equations become identical to the free equations, i.e. EOM without the Yukawa terms. For the q_R, d_L solutions satisfying the $(--)$ BC and the q_L, d_R solutions with $(++)$ BC, at $y=0$ [BC's still induced by the action variation combined with the new EOM (8.8a)-(8.8d) on the boundaries], we get the following physical profiles,

$$q_L(y)=\mathcal{C}\cos(my)\ ,\quad q_R(y)=-\mathcal{C}\sin(my)\ ,\quad d_R(y)=\mathcal{C}\cos(my)\ ,\quad d_L(y)=\mathcal{C}\sin(my)\ , \tag{8.9}$$

which are valid for $0 \leq y < (\pi-\epsilon)R$. $\mathcal{C}$ denotes the normalization factor. For $(\pi-\epsilon)R < y \leq \pi R$, we obtain the following general EOM solutions,

$$\begin{aligned}
&\hat{q}_L(y)=B_1\cos(my)+B_2\sin(my),\quad \hat{q}_R(y)=B_2\cos(my)-B_1\sin(my),\\
&\hat{d}_L(y)=B_3\cos(my)+B_4\sin(my),\quad \hat{d}_R(y)=B_4\cos(my)-B_3\sin(my),
\end{aligned} \tag{8.10}$$

where B_i's are arbitrary constants that are fixed by the normalizations. From Eq. (8.8a)-(8.8d), we see that the amount of jump that a field undergoes is proportional to the value of some other profile exactly at $y=(\pi-\epsilon)R$. Hence to connect the two sets of solutions in Eq. (8.9) and Eq. (8.10), one needs to assign some values for these profiles at the jump point. We use the following convention for a generic profile,

$$f\left((\pi-\epsilon)R\right)=\frac{1}{1+c}\left[f\left((\pi-\epsilon)R\right)+c\hat{f}\left((\pi-\epsilon)R\right)\right], \tag{8.11}$$

i.e. we take the weighted average of the limiting values of the function approaching from both sides, which, for $c = 1$, translates into the normal averaging. The continuity conditions read then as,

$$q_R\left((\pi-\epsilon)R\right) - \hat{q}_R\left((\pi-\epsilon)R\right) = \frac{-vY_5}{\sqrt{2}(1+c)}\left[d_R\left((\pi-\epsilon)R\right) + c\,\hat{d}_R\left((\pi-\epsilon)R\right)\right] , \tag{8.12a}$$

$$q_L\left((\pi-\epsilon)R\right) - \hat{q}_L\left((\pi-\epsilon)R\right) = \frac{vY_5'}{\sqrt{2}(1+c)}\left[d_L\left((\pi-\epsilon)R\right) + c\,\hat{d}_L\left((\pi-\epsilon)R\right)\right] , \tag{8.12b}$$

$$d_R\left((\pi-\epsilon)R\right) - \hat{d}_R\left((\pi-\epsilon)R\right) = \frac{-vY_5'}{\sqrt{2}(1+c)}\left[q_R\left((\pi-\epsilon)R\right) + c\,\hat{q}_R\left((\pi-\epsilon)R\right)\right] , \tag{8.12c}$$

$$d_L\left((\pi-\epsilon)R\right) - \hat{d}_L\left((\pi-\epsilon)R\right) = \frac{vY_5}{\sqrt{2}(1+c)}\left[q_L\left((\pi-\epsilon)R\right) + c\,\hat{q}_L\left((\pi-\epsilon)R\right)\right] . \tag{8.12d}$$

Injecting Eq. (8.9)-(8.10) in these four relations gives us the following constant expressions,

$$B_1 = B_4 = \frac{\mathcal{C}[(1+c)^2(X+X')\sin\left(2(\pi-\epsilon)mR\right) - 2((1+c)^2 + cXX')]}{2[c^2XX' - (1+c^2)]} , \tag{8.13}$$

$$B_3 = -B_2 = \frac{\mathcal{C}(1+c)^2[X - X' + (X+X')\cos\left(2(\pi-\epsilon)mR\right)]}{2[c^2XX' - (1+c^2)]} , \tag{8.14}$$

where $X = vY_5/\sqrt{2}$ and $X' = vY_5'/\sqrt{2}$. One can now apply the BC for the $(--)$ modes on the $y = \pi R$ brane,

$$\hat{q}_R(\pi R) = \hat{d}_L(\pi R) = 0 . \tag{8.15}$$

For small $\epsilon \to 0$, this requires,

$$\tan\left(\pi R\, m\right) = \frac{\sqrt{2}(1+c)^2 vY_5}{2(1+c)^2 + cv^2Y_5Y_5'} , \tag{8.16}$$

which for $c = 1$ becomes,

$$\tan\left(\pi R\, m\right) = \frac{4\sqrt{2}vY_5}{8 + v^2Y_5Y_5'} . \tag{8.17}$$

This relation gives directly the solutions for the fermion mass spectrum.

It is possible to choose another order of calculation. Indeed, one can first derive the BC for the 4 profiles at $y = 0, \pi R$ and thus take into account their effects on the EOM terms in Eq. (8.6a)-(8.6d). At this level, we can first show [as done in Appendix A] that the usual $(--)$ and $(++)$ BC exist in the case where the EOM (8.6a)-(8.6d), containing boundary terms, hold. Now the $(--)$ BC assigned to the d_L, q_R wave functions have the effect of eliminating the $\delta(y - \pi R)$ terms in Eq. (8.6b)-(8.6c).
Then the rest of the procedure to find the mass spectrum is identical to the previous order of calculation, except of course that the terms involving the Y_5' coupling constant are absent. At the

next step, one introduces a regularizing ϵ-shift in the EOM (8.6a)-(8.6d) [without Y_5' terms]. As above, integrating the obtained EOM leads to conditions at $y = (\pi - \epsilon)R$ which connect the d, q profiles defined in the interval, $[0, (\pi - \epsilon)R]$, with the $\hat{d}$, $\hat{q}$ profiles on, $[(\pi - \epsilon)R, \pi R]$. These are now conditions of continuity for the d_R, q_L profiles across $y = (\pi - \epsilon)R$,

$$q_R\left((\pi-\epsilon)R\right) - \hat{q}_R\left((\pi-\epsilon)R\right) = \frac{-vY_5}{\sqrt{2}} d_R\left((\pi-\epsilon)R\right) \ , \tag{8.18a}$$

$$q_L\left((\pi-\epsilon)R\right) - \hat{q}_L\left((\pi-\epsilon)R\right) = 0 \ , \tag{8.18b}$$

$$d_R\left((\pi-\epsilon)R\right) - \hat{d}_R\left((\pi-\epsilon)R\right) = 0 \ , \tag{8.18c}$$

$$d_L\left((\pi-\epsilon)R\right) - \hat{d}_L\left((\pi-\epsilon)R\right) = \frac{vY_5}{\sqrt{2}} q_L\left((\pi-\epsilon)R\right) \ , \tag{8.18d}$$

due to the absence of Y_5' terms on the right-hand side of Eq. (8.18b)-(8.18c). The consequence is that these profiles are well defined at $y = (\pi - \epsilon)R$, where $d_R = \hat{d}_R$, $q_L = \hat{q}_L$, which fixes uniquely the amounts of discontinuity in Eq. (8.18a) and Eq. (8.18d) ; there is thus no need to choose any c-prescription like in Eq. (8.12). One continues to follow the same steps of calculation as in the previous procedure, with the same BC as well. Replacing the d_L, q_R (d_R, q_L) profiles in Eq. (8.18a)-(8.18d) with their expressions dictated by the free EOM and the Dirichlet (Neumann) BC at $y = 0$, as well as $\hat{d}_{L,R}$, $\hat{q}_{L,R}$ with the general expressions for free profiles, gives rise to a system whose solutions for the constants once injected in the BC, $\hat{q}_R(\pi R) = \hat{d}_L(\pi R) = 0$, lead to the fermion mass spectrum,

$$\tan\left(\pi R\, m\right) = \frac{vY_5}{\sqrt{2}} \ , \tag{8.19}$$

in the $\epsilon \to 0$ limit. It turns out that this mass result can be obtained from Eq. (8.16) by setting $Y_5' = 0$, in which case indeed the c-dependence disappears.

8.2.4 Smoothing the Higgs peak

We can alternatively replace the Higgs Dirac peak at the boundary by a normalized square function, of width ϵR and height $1/\epsilon R$, so that the Dirac peak is recovered in the limit, $\epsilon \to 0$. With this smooth profile, one gets the following EOM,

$$-\, m\, q_L \,-\, q_R' \,+\, \frac{\Theta\left(y-(\pi-\epsilon)R\right)}{\epsilon R}\, \frac{vY_5}{\sqrt{2}}\, d_R = 0 \ , \tag{8.20a}$$

$$-\, m\, q_R \,+\, q_L' \,+\, \frac{\Theta\left(y-(\pi-\epsilon)R\right)}{\epsilon R}\, \frac{vY_5'}{\sqrt{2}} d_L = 0 \ , \tag{8.20b}$$

$$-\, m\, d_L \,-\, d_R' \,+\, \frac{\Theta\left(y-(\pi-\epsilon)R\right)}{\epsilon R}\, \frac{vY_5'}{\sqrt{2}}\, q_R = 0 \ , \tag{8.20c}$$

$$-\, m\, d_R \,+\, d_L' \,+\, \frac{\Theta\left(y-(\pi-\epsilon)R\right)}{\epsilon R}\, \frac{vY_5}{\sqrt{2}}\, q_L = 0 \ , \tag{8.20d}$$

where $\Theta(y) = 1$ for $y \geq 0$ and zero otherwise. In the range $0 \leq y < (\pi - \epsilon)R$, these equations correspond to the free EOM and have the same solutions as in Eq. (8.9) if we impose once more the $(--)$ and $(++)$ BC's at $y = 0$. Assuming $Y_5 = Y_5'$ for simplicity, the following generic ansatz solves the EOM (8.20a)-(8.20d) in the range $(\pi - \epsilon)R \leq y \leq \pi R$,

$$\hat{f}_X(y) \;=\; A_{f_X} \exp\left(\sqrt{\frac{v^2 Y_5^2 - 2m^2\epsilon^2 R^2}{2\epsilon^2 R^2}}\, y\right) + B_{f_X} \exp\left(-\sqrt{\frac{v^2 Y_5^2 - 2m^2\epsilon^2 R^2}{2\epsilon^2 R^2}}\, y\right) \;, \quad (8.21)$$

f_X standing for any profile and A_{f_X},B_{f_X} being normalization constants. Demanding that all the profiles are continuous across $y = (\pi - \epsilon)\, R$ and setting $\hat{q}_R(\pi R) = \hat{d}_L(\pi R) = 0$ [BC for the $(--)$ modes] gives us the following condition on the mass,

$$\tan(\pi R\, m) \;=\; \sqrt{\frac{vY_5 - \sqrt{2}m\epsilon R}{vY_5 + \sqrt{2}m\epsilon R}}\, \tanh\left(\sqrt{\frac{v^2 Y_5^2 - 2m^2\epsilon^2 R^2}{2}}\right) \;. \quad (8.22)$$

In the limit $\epsilon \to 0$ this simplifies to,

$$\tan(\pi R\, m) \;=\; \tanh\left(\sqrt{\frac{v^2 Y_5^2}{2}}\right) \;. \quad (8.23)$$

As in the case of the shifted delta function, if one first imposes instead the BC for the $(--)$ modes, $q_R(\pi R) = d_L(\pi R) = 0$, the Yukawa terms in the Eq. (8.6b)-(8.6c) are eliminated. Then solving the EOM (8.20a)-(8.20d) with an ϵR-square function but without those two Yukawa terms, one recovers, through the same steps of calculation, the simple mass spectrum of Eq. (8.19).

8.3 4D calculations

8.3.1 The KK decomposition and mass matrices

In this Section 8.3, considering the same model as the one defined by the Lagrangian (8.1), we calculate the fermion masses in the maybe more intuitive approach referred to as the perturbative or 4D calculation. To obtain the fermion profiles, here, one considers the free EOM, i.e. the equations without Yukawa mass terms. As a result, unlike the 5D point of view addressed in the previous Section 8.2, one needs to diagonalize the fermion mass matrices to include the whole KK mass mixing effect. The 4D approach denomination relies on the fact that one starts from a 4D model without KK modes and the entire KK tower is taken into account gradually, through the limit $N \to \infty$. It is also called a perturbative approach in the sense that the Yukawa interaction is incorporated via infinite series terms.

Now, these infinite numbers of KK excitations lead to infinite-dimensional mass matrices whose exact diagonalization can represent a challenging task. However, in certain cases it is possible

analytically as we shall illustrate in this Section 8.3. The aim being to compare the fermion masses obtained by diagonalizing the complete mass matrix with the ones obtained from the previous 5D approach.

We start by decomposing the 5D fields in KK towers like,

$$Q_L = \sum_{n=0}^{\infty} q_L^n(y)\; Q_L^n(x)\;, \tag{8.24a}$$

$$Q_R = \sum_{n=0}^{\infty} q_R^n(y)\; Q_R^n(x)\;, \tag{8.24b}$$

$$D_L = \sum_{n=0}^{\infty} d_L^n(y)\; D_L^n(x)\;, \tag{8.24c}$$

$$D_R = \sum_{n=0}^{\infty} d_R^n(y)\; D_R^n(x)\;, \tag{8.24d}$$

which gives rise to the following KK mass terms in the 4D effective Lagrangian,

$$\mathcal{L}_{\rm KK} = -\sum_{n=0}^{\infty} \left[M_{qn} \bar{Q}_L^n(x) Q_R^n(x) \;+\; M_{dn} \bar{D}_L^n(x) D_R^n(x) \right] + \text{H.c.}$$

where

$$M_{qn} = M_{dn} = \frac{n}{R}\;. \tag{8.25}$$

The complete quark mass matrix in the 4D effective picture, after EW symmetry breaking, reads as,

$$\mathcal{L}_{\rm mass} = -\bar{\Psi}_L \cdot [M] \cdot \Psi_R + \text{H.c.}$$

and can be expressed, in the 'combined' basis for the Left and Right-handed fields,

$$\begin{aligned} \Psi_L^t &= (Q_L^0, D_L^0, Q_L^1, D_L^1, Q_L^2, D_L^2, \cdots)\;, \\ \Psi_R^t &= (Q_R^0, D_R^0, Q_R^1, D_R^1, Q_R^2, D_R^2, \cdots)\;, \end{aligned} \tag{8.26}$$

by the following infinite matrix,

$$[M] \equiv \begin{pmatrix} M_{q0} & \alpha_{00} & 0 & \alpha_{01} & 0 & \alpha_{02} & \cdots \\ \beta_{00} & M_{d0} & \beta_{01} & 0 & \beta_{02} & 0 & \cdots \\ 0 & \alpha_{10} & M_{q1} & \alpha_{11} & 0 & \alpha_{12} & \cdots \\ \beta_{10} & 0 & \beta_{11} & M_{d1} & \beta_{12} & 0 & \cdots \\ 0 & \alpha_{20} & 0 & \alpha_{21} & M_{q2} & \alpha_{22} & \cdots \\ \beta_{20} & 0 & \beta_{21} & 0 & \beta_{22} & M_{d2} & \cdots \\ \vdots & \vdots & \vdots & \vdots & \vdots & \vdots & \ddots \end{pmatrix}, \tag{8.27}$$

with,

$$\alpha_{ij} = Y_5 \int_0^{\pi R} dy\ \delta(y-\pi R)\ \frac{v}{\sqrt{2}}\ q_L^i(y)\ d_R^j(y)\ , \tag{8.28}$$

$$\beta_{ij} = Y_5' \int_0^{\pi R} dy\ \delta(y-\pi R)\ \frac{v}{\sqrt{2}}\ d_L^i(y)\ q_R^j(y)\ . \tag{8.29}$$

To try to match the different regularizations performed in the 5D approach of Section 8.2, we will treat similarly the Higgs peak – by either moving or smoothing it – in the 4D calculations of next two subsections.

8.3.2 Moving the Higgs peak

The fields (8.26) undergo the unitary transformation matrices to the physical basis and the squared modulus of the quark masses, $|m|^2$, are the eigenvalues, noted λ, of the infinite-dimensional matrix, $\left[M^\dagger M\right]$. For a general Higgs profile, we present in the Appendix B one of the main results of the present work : the Characteristic Equation (CE), for the infinite $\left[M^\dagger M\right]$ matrix, whose solutions are the eigenvalues, $\lambda = |m|^2$. From the obtained expression of the CE terms shown there, a logical structure in series emerges for such a general case. The CE contains infinite series of various types which can be written using the generic structures, A_n and B_n, involving respectively, α_{ij} and β_{ij}.

Let us now focus on the case of a Higgs peak infinitesimally shifted at some point, $y = (\pi - \epsilon)R$, along the extra-dimension as in Eq. (8.7). Then the CE takes a much simpler form since the functions, α_{ij} and β_{ij}, are factorizable in, i and j,

$$\alpha_{ij} = \frac{vY_5}{\sqrt{2}}\ q_L^i((\pi-\epsilon)R) \times d_R^j((\pi-\epsilon)R)\ , \tag{8.30}$$

$$\beta_{ji} = \frac{vY_5'}{\sqrt{2}}\ q_R^i((\pi-\epsilon)R) \times d_L^j((\pi-\epsilon)R)\ , \tag{8.31}$$

so that accordingly to Eq. (F.3),

$$A_{n>1} = B_{n>1} = 0 \ , \tag{8.32}$$

due to the anti-symmetric constructions of A_n and B_n. As a result the generic CE of Eq. (F.1) simplifies to,

$$\begin{aligned}
1 \quad & + \sum_{q_1;d_1} (-\lambda) \frac{(\alpha_{q_1 d_1})^2 + (\beta_{d_1 q_1})^2}{(M_{q_1}^2 - \lambda)(M_{d_1}^2 - \lambda)} + \sum_{q_1,q_2;d_1,d_2} (-\lambda)^2 \frac{(\alpha_{q_1 d_1})^2 (\beta_{d_2 q_2})^2}{(M_{q_1}^2 - \lambda)(M_{d_1}^2 - \lambda)(M_{q_2}^2 - \lambda)(M_{d_2}^2 - \lambda)} \\
\times \quad & \left(1 - \delta_{q_1 q_2} \frac{M_{q_2}^2}{\lambda}\right) \left(1 - \delta_{d_1 d_2} \frac{M_{d_2}^2}{\lambda}\right) - \sum_{Q_1;D_1} 2 \, M_{Q_1} M_{D_1} \frac{\alpha_{Q_1 D_1} \beta_{D_1 Q_1}}{(M_{Q_1}^2 - \lambda)(M_{D_1}^2 - \lambda)} \\
+ \quad & \sum_{Q_1 < Q_2 : d_1, d_2} \frac{2(-\lambda) M_{Q_1} M_{Q_2}}{(M_{Q_1}^2 - \lambda)(M_{Q_2}^2 - \lambda)} \times \frac{\alpha_{Q_1 d_1} \alpha_{Q_2 d_1} \beta_{d_2 Q_1} \beta_{d_2 Q_2}}{(M_{d_1}^2 - \lambda)(M_{d_2}^2 - \lambda)} \times \left(1 - \delta_{d_1 d_2} \frac{M_{d_2}^2}{\lambda}\right) \\
+ \quad & \sum_{q_1,q_2 : D_1 < D_2} \frac{2(-\lambda) M_{D_1} M_{D_2}}{(M_{D_1}^2 - \lambda)(M_{D_2}^2 - \lambda)} \times \frac{\alpha_{q_1 D_1} \alpha_{q_1 D_2} \beta_{D_1 q_2} \beta_{D_2 q_2}}{(M_{q_1}^2 - \lambda)(M_{q_2}^2 - \lambda)} \times \left(1 - \delta_{q_1 q_2} \frac{M_{q_2}^2}{\lambda}\right) \\
+ \quad & \sum_{Q_1 < Q_2 ; D_1 < D_2} 2 \left(\prod_{i=1,2} \frac{M_{Q_i} M_{D_i}}{(M_{Q_i}^2 - \lambda)(M_{D_i}^2 - \lambda)} \right) \\
\times \quad & \left(\alpha_{Q_1 D_1} \alpha_{Q_2 D_2} \times \beta_{D_1 Q_1} \beta_{D_2 Q_2} + \alpha_{Q_1 D_2} \alpha_{Q_2 D_1} \times \beta_{D_2 Q_1} \beta_{D_1 Q_2} \right) = 0 \ .
\end{aligned} \tag{8.33}$$

Here and elsewhere, unless specified, a sum over any index is assumed to be running from 0 to ∞ ; in the above relation, the KK masses obey *e.g.*, $M_{q_1} = q_1/R$ where q_1 is a running integer [slightly different writing from Eq. (8.25) to ease notations]. We stress that to derive Eq. (8.33), no approximation has been made, or in other words this equation exhibits the complete CE in this case. Choosing the $(--)$ and $(++)$ BC's [from the action variation and free EOM on boundaries] for the quark profiles, to end up with a chiral theory, we get the following normalized solutions of the free EOM [2],

$$\begin{aligned}
q_L^n(y) = d_R^n(y) = \sqrt{\frac{2}{\pi R}} \cos\left(\frac{ny}{R}\right) \quad , \quad -q_R^n(y) = d_L^n(y) = \sqrt{\frac{2}{\pi R}} \sin\left(\frac{ny}{R}\right) \quad \text{for} \ \ n > 0 \\
q_L^0(y) = d_R^0(y) = \sqrt{\frac{1}{\pi R}} \quad , \quad -q_R^0(y) = d_L^0(y) = 0 \quad \text{for} \ \ n = 0 \ .
\end{aligned} \tag{8.34}$$

With these solutions, the α_{ij} and β_{ji} functions of Eq. (8.30)-(8.31) become,

$$\alpha_{ij} = \frac{\sqrt{2} v Y_5}{\pi R} \cos(i(\pi - \epsilon)) \cos(j(\pi - \epsilon)) \ , \quad \alpha_{00} = \frac{v Y_5}{\sqrt{2} \pi R} \ , \tag{8.35}$$

$$\beta_{ji} = \frac{-\sqrt{2} v Y_5'}{\pi R} \sin(i(\pi - \epsilon)) \sin(j(\pi - \epsilon)) \ , \quad \beta_{j0} = \beta_{0i} = \beta_{00} = 0 \ . \tag{8.36}$$

[2] Although we have kept β_{0j},β_{i0} in the matrix (8.27) to make its $(\alpha_{ij} \leftrightarrow \beta_{ji})$ symmetric texture explicit, we note that $\beta_{0j} = \beta_{i0} = 0$ since the zero-modes $q_R^0(y) = d_L^0(y) = 0$.

We are now in possession of all the necessary tools to simplify and solve the CE (8.33) in terms of the mass. Computing analytically all the involved infinite sums (over KK modes), we find the following compact form for the CE, in the final limit $\epsilon \to 0$,

$$1 + \frac{1}{4}v^2 Y_5 Y_5' + \frac{1}{64}v^4 (Y_5 Y_5')^2 = \frac{v^2 Y_5^2}{2} \cot^2\left(\pi R\sqrt{\lambda}\right) , \tag{8.37}$$

$$\text{or,} \quad \tan^2\left(\pi R\sqrt{|m|^2}\right) = \left(\frac{4\sqrt{2}vY_5}{8 + v^2 Y_5 Y_5'}\right)^2 . \tag{8.38}$$

Let us add a few comments, for the reader, about the methods used to derive that result. The term on the right hand side of Eq. (8.37) comes from (++) mode contributions only, in the sense that it follows from the series of Eq. (8.33) [second term of the whole expression],

$$\sum_{q_1;d_1} (-\lambda) \frac{(\alpha_{q_1 d_1})^2}{(M_{q_1}^2 - \lambda)(M_{d_1}^2 - \lambda)} , \tag{8.39}$$

if one invokes the following identity,

$$\sum_{n=0}^{\infty} \frac{1}{n^2 - x^2} = -\frac{1}{2x^2}\left[1 + (\pi x)\cot(\pi x)\right] ,$$

where x is some function of R and λ. All the other terms of Eq. (8.33), except the fifth one [last term of the second line] and the last one [two last lines], do not give contributions in the limit $\epsilon \to 0$. The non-vanishing terms of Eq. (8.33) can be re-expressed as combinations of the (Hurwitz) Lerch transcendent [3],

$$\begin{aligned} \Phi\left(e^{i\epsilon}, 1, x\right) &= \sum_{n=0}^{\infty} \frac{e^{in\epsilon}}{n + x} \\ &= -\gamma - \psi(x) - \log(-i\epsilon) + \mathcal{O}(\epsilon) , \end{aligned}$$

where γ is the Euler-Mascheroni constant and $\psi(x) = \Gamma'(x)/\Gamma(x)$ is the so-called digamma function (logarithmic derivative of the gamma function).

At this stage, we insist on the fact that in order to obtain Eq. (8.38) we have first written the CE of the mass matrix in Eq. (8.33) and calculated its KK summations up to $N \to \infty$, *before* imposing the limit $\epsilon \to 0$ on the obtained CE – as a last step. If, however, it is realized in the opposite order, i.e. first applying $\epsilon \to 0$ on the mass matrix (8.27) [so that the matrix elements $\beta_{ij} \to 0$ since $q_R^n(\pi R) = d_L^n(\pi R) = 0$], *before* writing the matrix CE and working out its infinite KK sums or in other words taking its limit for $N \to \infty$ [without β_{ij} series anymore], one would obtain,

$$\tan^2\left(\pi R\sqrt{|m|^2}\right) = \left(\frac{vY_5}{\sqrt{2}}\right)^2 , \tag{8.40}$$

[3] Due to cancellations among different terms, the Eq. (8.37) does depend ultimately neither on γ nor on $\log(-i\epsilon)$.

instead of Eq. (8.38). Eq. (8.40) originates solely from the series in Eq. (8.39). As already observed in the 5D approach, one would obtain the same result as in Eq. (8.40) by setting $Y_5' = 0$ in Eq. (8.38) ; this is logical since the β_{ij}'s are proportional to Y_5'.

8.3.3 Smoothing the Higgs peak

Alternatively, the Higgs Dirac peak at the boundary can be replaced by a normalized square function, of width ϵR, as in Eq. (8.20a)-(8.20d). Then, using the profiles from Eq. (8.34), we see that for $i, j > 0$,

$$\begin{aligned}
\alpha_{ij} &= \frac{vY_5}{\sqrt{2}\epsilon R}\int_{(\pi-\epsilon)R}^{\pi R} dy\; q_L^i(y)\; d_R^j(y) = \frac{-vY_5}{\sqrt{2}\epsilon R}\left(\frac{\sin[(i+j)(\pi-\epsilon)]}{i+j} + \frac{\sin[(i-j)(\pi-\epsilon)]}{i-j}\right) , \\
\beta_{ji} &= \frac{vY_5'}{\sqrt{2}\epsilon R}\int_{(\pi-\epsilon)R}^{\pi R} dy\; d_L^j(y)\; q_R^i(y) = \frac{-vY_5'}{\sqrt{2}\epsilon R}\left(\frac{\sin[(i+j)(\pi-\epsilon)]}{i+j} - \frac{\sin[(i-j)(\pi-\epsilon)]}{i-j}\right) ,
\end{aligned}$$

which means that the functions α_{ij} and β_{ji} are no longer factorizable in i, j – so that the simplification relation (F.3) does not hold anymore. As a result, the CE of Eq. (F.1)-(F.6)-(F.7), for the infinite $\left[M^\dagger M\right]$ matrix, contains multiple infinite series which render difficult its simplification. Now in the absence of a compact form, like the one in Eq. (8.33), it is tricky to solve the CE and work out the exact squared mass eigenvalues, $\lambda = |m|^2$.

8.4 Interpretation of the analytical results

8.4.1 A non-commutativity in the 4D approach

After having presented our analytical results, we now discuss their impacts, one by one. First, we have found that the 4D calculation gives rise to different fermion mass spectrum definitions in the two orderings of the calculation : first taking the limit $\epsilon \to 0$ (Higgs localization) in the mass matrix (8.27) before writing the characteristic equation and applying the limit $N \to \infty$ (here N refers generically to the various indices used in previous section for the KK summations), leads to the characteristic equation (8.40) [4], while the inverse order of taking $N \to \infty$ in the characteristic equation and $\epsilon \to 0$ in a second step, results in Eq. (8.38) – in the case of an Higgs profile regularized by a shifted Dirac peak where the characteristic equation can be derived analytically from the 4D point of view (dealing with infinite mass matrices). In the former order, the fermion $(--)$ wave functions play absolutely no rôle in the calculation since the β_{ij} off-diagonal terms of the matrix (8.27) vanish at the first step [$\epsilon \to 0$ limit]. In contrast, the infinite KK sum over these vanishing terms gives rise non-trivially to an additional contribution in Eq. (8.38) which is proportional to the Y_5' coupling (entering the β_{ij}'s). All this is summarized in the 4D line of Table 1.

[4] In a preliminary work [24] on the RS framework, an approximated mass spectrum was obtained in this ordering ($\epsilon \to 0$, $N \to \infty$) through an expansion in powers of v^2/M_{KK}^2.

This non-commutativity will be confirmed in Section 8.4.2 in the following sense: we will see that these two 4D calculation orderings correspond to two different 5D calculations.

Table 1 *(shifted Higgs)*	Regularization I	Regularization II
5D CALCULATION	$\boxed{\tan(\pi R\, m) = \dfrac{vY_5}{\sqrt{2}}}$ no δ-terms for $(--)$-profiles $(--)$ BC at πR, EOM with ϵ	$\boxed{\tan(\pi R\, m) = \dfrac{\sqrt{2}(1+c)^2 vY_5}{2(1+c)^2 + cv^2 Y_5 Y_5'}}$ δ-terms for $(--)$-profiles EOM with ϵ, $(--)$ BC at πR
4D CALCULATION	$\boxed{\tan^2(\pi R\sqrt{\lvert m\rvert^2}) = \left(\dfrac{vY_5}{\sqrt{2}}\right)^2}$ no $(--)$-profile rôle $\epsilon \to 0\ ,\ N \to \infty$	$\boxed{\tan^2(\pi R\sqrt{\lvert m\rvert^2}) = \left(\dfrac{vY_5/\sqrt{2}}{1 + v^2 Y_5 Y_5'/8}\right)^2}$ $(--)$-profile effect $N \to \infty\ ,\ \epsilon \to 0$

Table 1 : Quark mass spectrum for a shifted Higgs peak.

In the context with bulk fermions coupled to a brane Higgs, the non-commutativity pointed out here – the difference between the two orderings of the limits $\epsilon \to 0$ and $N \to \infty$ – differs from the non-commutativity discussed in the literature [18, 19] (in the RS framework) [5] : the latter one concerns the different results obtained from taking first $\epsilon \to 0$ and then $N_{KK} \to \infty$ as in Ref. [20], or, the opposite order as in Ref. [21]. Here, N_{KK} denotes the number of exchanged excited modes included at the level of the one-loop amplitude, when calculating the gluon-gluon fusion mechanism or the Higgs decay rate into two photons (the loop momentum integration is performed at the really first step).

While the 4D order $\epsilon \to 0$, $N_{KK} \to \infty$ matches the 5D calculation (avoiding the very notion of KK state) with a Higgs strictly stuck on the TeV-brane [where the $(--)$ KK modes vanish] [18], the opposite 4D order – with the brane-limit taken only at last – renders the Higgs sensitive to $(--)$ KK states and thus corresponds to the 5D approach with a narrow bulk-Higgs field localized towards the brane [18] (unsuppressed 'resonance contribution' from high-mass KK states which can resolve the Higgs wave function [26]). It was also found in Ref. [18] that the limit $\epsilon \to 0$, for the Higgs profile regulator, can be taken either before or after performing loop integrations.

The question [6] about the non-commutativity of $\epsilon \to 0$ and $N_{KK} \to \infty$ has a formal interest and

[5] See also Ref. [25].

[6] It was pointed out [27], based on a 4D calculation of the gluon-gluon fusion amplitude in RS, that some specific higher derivative operators allow to take into account a Ultra-Violet (UV) sensitivity.

was discussed for technical reasons since one has to impose anyway a Λ cut-off at the end of the day, due to the non-renormalizability of higher-dimensional theories (or their induced low gravity scale), so that N_{KK} is bounded from above. It was found in Ref. [18, 19] that once the loop calculation is performed in a realistic context with a consistent UV regulator such as dimensional regularization (or with a hard UV momentum cut-off on the 4D loop integral), the non-commutativity ambiguity disappears. The present non-commutativity of $\epsilon \to 0$ and $N \to \infty$ raises a new question, because the Λ cut-off must not be applied on N (see Section 8.4.4). This physical question about the interpretation of the non-commutativity will be addressed in Section 8.4.3.

8.4.2 Matching the 4D and 5D approaches

In the 5D approach, there are also two possible ways for calculating the fermion mass spectrum, as described in Section 8.2 and summarized in the 5D line of Table 1.
In one way, the BC at πR is imposed for the $(--)$ profiles in a first stage so that the two terms in Eq. (8.6b)-(8.6c) involving both the $\delta(y-\pi R)$ peak and a $(--)$ profile, $d_L(y)$ or $q_R(y)$, vanish (after integration). In a second stage, one solves the EOM system (8.6a)-(8.6d) with a regularized Higgs peak, *e.g.* shifted by an amount ϵR.
The other way consists of first solving the system (8.8a)-(8.8d) with an ϵR-shifted Higgs, so that the terms in Eq. (8.8b)-(8.8c) involving both $\delta(y-(\pi-\epsilon)R)$ and a $(--)$ profile, d_L or q_R, really contribute. Then one imposes the BC at πR for the $(--)$ profiles, which does not eliminate the above terms. The mass spectrum is dictated by those last conditions.
Those two calculation orderings result in two different mass spectrum definition given by Eq. (8.16) and Eq. (8.19), which are copied in the 5D line of Table 1 ; the angle of the tangent function is only defined modulo $n\pi$ which gives rise to the KK eigen-mass tower m_n [$n \in \mathbb{N}$ as in Eq. (8.3a)-(8.3d)]. The effect of the EW symmetry breaking is thus a shift of $\arctan(vY_5/\sqrt{2})/\pi R$ in the KK mass tower n/R, for the case of the left column in Table 1.

As expected [7], there is a mass spectrum matching between the 4D and 5D calculations that Table 1 exhibits. Although expected, this matching was not trivial to demonstrate analytically, especially due to the complexity of dealing with the infinite 4D mass matrix (8.27). Furthermore, it turns out that there are in fact two distinct 4D/5D matchings, for the two calculation orders performed in 4D (*c.f.* Section 8.4.1) and 5D (described in previous paragraph) that we thus commonly denote in the table as regularizations of type I and II – see later discussion in the next Section 8.4.3. The 4D/5D matching in the regularization of type I is explicit : the two equations obtained give rise to the same possible mass spectra. In the regularization of type II, the 4D/5D matching occurs exactly for $c = 1$ as show the two mass equations ; it means that other 5D c-prescriptions [i.e. $c \neq 1$] should not represent experimentally distinct regularizations [8] (as distinct

[7] In the 4D limit $N \to \infty$, the effect of the infinite KK tower is taken into account which is equivalent to consider rigorously the full 5D fields of Eq. (8.24a)-(8.24d).
[8] The precise notion of experimentally equivalent regularizations will be described at the beginning of Section 8.4.3.

4D approaches matching $c \neq 1$ do not exist).

The first implication of those two 4D/5D matchings is the existence of two different 4D calculations (confirming subsection 8.4.1) since there are two ways of calculating the mass spectrum from the 5D point of view as well. These two ways of calculating (regularizations I and II) differ in their brane-Higgs sensitivity to the tower of bulk $(--)$ profiles ; this can be described remarkably in both the 4D and 5D approaches. From the 5D point of view, in regularization II the terms in Eq. (8.8b)-(8.8c) coupling the VEV to $(--)$ profiles are not vanishing – in contrast with case I – as explained at the beginning of this subsection. Regarding the 4D treatment, in regularization II there is a non-vanishing contribution from the β_{ij} terms [*c.f.* Eq. (8.29)] which represent overlaps between the Higgs and $(--)$ profiles, whereas their contribution is absent in case I as discussed at the beginning of Subsection 8.4.1.

There is a second consequence ; the two 4D/5D matchings guarantee that the 5D mixed-formalism [*c.f.* Eq. (8.3a)-(8.3d)], followed usually in literature, represents a correct procedure to take into account mixing effects between all KK levels which are otherwise *explicitly* included via the off-diagonal elements of the 4D mass matrix (8.27).

Finally, the 4D/5D matching confirms that there exist two approaches for deriving the same mass spectrum and that in the 4D approach there is no inconsistency induced by the Higgs localization that should be regularized (as the so-called jump problem in the 5D approach). This can be interpreted by the fact that the exact 4D calculation proceeds by construction through a limit $(N \to \infty)$ to obtain 'softly' the fermion mass expressions in the wanted higher-dimensional scenario. This limit acts typically as the regularizing limit $\epsilon \to 0$ corresponding to a brane-Higgs, in the 5D framework.
The obtained 4D/5D matching also constitutes an additional confirmation of the validity of the field theory regularization usually applied in the 5D calculation (within this context of brane-localized Higgs scenarios), and leads to a global coherent picture. Now of course, to determine whether such a paradigm – relying on mathematical regularizations of an ill-defined peaked field – corresponds really to the physical model, one would have to confront it with experimental results [9].

8.4.3 On the two types of regularizations

It is mentioned at the end of Appendix C.2 in Ref. [23] (where description is limited to the simpler case $Y_5 = Y_5'$) that the regularizations, called I and II here, give at most two different interpretations of the $Y_5 v (= yvR)$ parameter combination [proportional to $M_D L$ in notations of Ref. [23]]. Let us discuss here this twofold feature more precisely. In fact, the two types of equations in Table 1 (both similar in 4D and 5D for $c = 1$) corresponding to the two regularizations constitute two different relations between the $Y_5^{(\prime)}$, v, R parameters and the physical mass solutions represented by m. A physical mass m having a unique value [the measured one], the difference between these

[9] As the renormalizations of quantum corrections were confronted (with success) to collider data.

two relations has to be either compensated by different values for Y_5, v, R (which do not constitute observables) in cases I and II, or, cancelled by setting Y_5' to zero (then Y_5, v, R can be identical in cases I and II). There exist thus two numerically equivalent definitions of the mass value m so that the regularizations I and II are experimentally equivalent [10] or even strictly identical [for vanishing Y_5'].

Indeed, concretely, today there exist two different sets of Y_5, v, R values (for $Y_5' \neq 0$) reproducing the measured values of the observed fermion masses through the two definitions, $f_n^{\rm I}$ and $f_n^{\rm II}$ (solutions from the two mass equations in Table 1), associated to the regularizations I and II :

$$\text{Regularization I} \left\{ \begin{array}{l} m_n = f_n^{\rm I}(R, v, Y_5) \\ \tilde{m}_n = f_n^{\rm I}(R, v, \tilde{Y}_5) \end{array} \right. \qquad \text{Regularization II} \left\{ \begin{array}{l} m_n = f_n^{\rm II}(R, v, Y_5, Y_5') \\ \tilde{m}_n = f_n^{\rm II}(R, v, \tilde{Y}_5, \tilde{Y}_5') \end{array} \right. \tag{8.41}$$

In other words, the two systems in Eq. (8.41) have solutions in terms of $Y_5^{(\prime)}$, v, R for the first mass eigenvalue $[m_{n=0}]$ and this is true including quarks/leptons (same formalism as here introducing parameters $m_{\ell n}$, $Y_{\ell 5}$, $Y_{\ell 5}'$) of down or up $\mathrm{SU(2)_L}$-isospin (notations trivially extended to $\tilde{m}_n$, $\tilde{Y}_5$, $\tilde{Y}_5'$, $\tilde{m}_{\ell n}$, $\tilde{Y}_{\ell 5}$, $\tilde{Y}_{\ell 5}'$) from the three generations (notations to be completed with flavor indices). The fact that there exist solutions to the systems of type (8.41) is also due to the individual dependences of the masses on the Yukawa parameters [11] and the higher number of Y_5-like parameters compared to the number of measured fermion masses. As for an overview of the other parameters, typically, the EW precision tests from the LEP collider would bound from above the R radius (imposing large KK masses to avoid dangerous corrections to the SM predictions for EW observables) while in the gauge boson sector m_Z, m_W, G_F would allow to determine the values of the bare parameters v, g, g' (through loop calculations as described *e.g.* in Ref. [11]), the recently measured Higgs mass fixing the quartic coupling λ [1] [12].

The experimental equivalence of the regularizations I and II is based on generic arguments and thus also applies to amplitudes induced by Flavor Changing Neutral Current (FCNC) effects. This leads to remarks on the FC Higgs couplings coming from misalignments between fermion masses and Yukawa couplings, in the RS framework with a brane Higgs [22]. This misalignment is quantified by a non-universal shift estimated to be, using notations of Ref. [22] except for down quark Yukawa

[10] The expression "experimentally equivalent", used here and throughout the present study, is motivated by the fact that the two regularizations can give rise to the same value of a measured mass m. Now it is clear that, formally speaking, the regularization II may generate values of a mass observable in a range different from the regularization I [as can be seen by comparing the mass spectra in Table 1], and, the degrees of freedom involved in the mass spectrum are also different [appearance or not of the Y_5' coupling constant] ; in this sense the regularizations I and II are not "physically equivalent".

[11] Basically different masses depend on different Y_5-like parameters (i.e. Y_5, $\tilde{Y}_5$, $Y_{\ell 5}$,...).

[12] Going from this toy model to RS [4], one should add the AdS_5 curvature parameter, k, but $kR \approx 11$ is fixed by the gauge hierarchy solution. For the RS custodially protected version [28] there can be an additional freedom from the $\tilde{M}$ parameter of explicit bulk custodial symmetry breaking, or even another one via the $g_{Z'}$ coupling [29] in case of no Left-Right parity [30]. One should also add basically the 5D mass parameters, $c_{u,d,\nu,l}^{L/R\ i}$ $(i = 1, 2, 3)$, in the RS extensions addressing the flavor problem [31].

parameters :

$$\begin{array}{l}\text{Regularization I} \\ \text{Regularization II}\end{array}\left\{\begin{array}{l}\Delta^d = 0 + \Delta_2^d = m_d|m_d|^2 R'^2\left(\frac{F(c_q)}{f(c_q)^2} + \frac{F(-c_d)}{f(-c_d)^2}\right) \\ \Delta^d = \Delta_1^d + \Delta_2^d = m_d|m_d|^2 R'^2\left(\frac{2}{3}\frac{Y_5'}{Y_5}\frac{1}{f(c_q)^2 f(-c_d)^2} + \frac{F(c_q)}{f(c_q)^2} + \frac{F(-c_d)}{f(-c_d)^2}\right)\end{array}\right. \tag{8.42}$$

where $F(c_q) = (2c_q - 1)/(2c_q + 1)$ and $\Delta_1^d = 0$ in case I due to vanishing contributions from Y_5' terms. Note that in these equations the physical condition to reproduce the (approximated) m_d mass has been used to fix the v parameter. Eq. (8.42) shows that there exist two sets of parameters [13] giving rise to the same value of Δ^d within the regularizations I (without terms proportional to Y_5', as included in Ref. [22]) and II (with such terms) so that these regularizations can be experimentally equivalent. There even exist such parameters (*e.g.* $f(c_q) \sim 1$, $f(-c_d) \ll 1$) for Y_5' and Y_5 of the same order of magnitude as might be wanted to not introduce new energy scales [22]. Notice that with more constraints on parameters from new experimental data and under the strong physical assumption $Y_5' \simeq Y_5$, it could happen that the two sets of input parameters in regularizations I and II cannot reproduce the same value of Δ^d : then precise FCNC data should be used to select the correct theoretical regularization by pinning down the real and unique Δ^d value. This experimental test is similar to the one discussed right below.

In the future, the upgraded 13 TeV LHC and other colliders will certainly provide more data. One can expect more precise measurements of the Yukawa and hVV $[V = Z, W]$ couplings (being functions of g, g', v [1] and R due to KK gauge boson mixings) or even the detection of Higgs pair production that would give information on the hVV, $hhVV$, hhh couplings (in turn on combinations of λ, g, g', v, R). The systems of Eq. (8.41) would thus have to be extended to include in particular the physical Y_{nm}, $\tilde{Y}_{nm}$ Yukawa couplings which depend on the same parameters $Y_5^{(\prime)}$, $\tilde{Y}_5^{(\prime)}$, v, R :

$$\text{Regularization I}\left\{\begin{array}{l} m_n = f_n^{\mathrm{I}}(R, v, Y_5) \\ \tilde{m}_n = f_n^{\mathrm{I}}(R, v, \tilde{Y}_5) \\ Y_{nm} = g_{nm}^{\mathrm{I}}(R, v, Y_5) \\ \tilde{Y}_{nm} = g_{nm}^{\mathrm{I}}(R, v, \tilde{Y}_5)\end{array}\right. \qquad \text{Regularization II}\left\{\begin{array}{l} m_n = f_n^{\mathrm{II}}(R, v, Y_5, Y_5') \\ \tilde{m}_n = f_n^{\mathrm{II}}(R, v, \tilde{Y}_5, \tilde{Y}_5') \\ Y_{nm} = g_{nm}^{\mathrm{II}}(R, v, Y_5, Y_5') \\ \tilde{Y}_{nm} = g_{nm}^{\mathrm{II}}(R, v, \tilde{Y}_5, \tilde{Y}_5')\end{array}\right. \tag{8.43}$$

Those couplings are involved in the action terms $Y_{nm} h(x) \bar{Q}_L^n(x) D_R^m(x)$ and $\tilde{Y}_{nm} h(x) \bar{\tilde{Q}}_L^n(x) U_R^m(x)$ expressed with 4D fields representing mass eigenstates [14]. KK mode discoveries would also add new entries (like m_n with $n > 0$) for the systems in Eq. (8.43).
With such new data coming it could happen at some point that there exist no more set of parameters satisfying one of the two types of system in Eq. (8.43) [more physical constraints without new degrees of freedom]. This would mean that the associated regularization is ruled out by experimental data. This uniquely ruled out regularization could only correspond to the system with less

[13] For instance with $f(c_q) \ll 1$, $f(-c_d) \ll 1$ and $Y_5' \ll Y_5$.
[14] In the 4D approach, this notation is coherent with previous notations if the $D_R^m(x)$ fields result from a mixing with the $Q_R^m(x)$ fields, and the $Q_L^n(x)$ include mixings with $D_L^n(x)$.

parameters : regularization I (no Y_5', $\tilde{Y}_5'$ parameters), since regularization II for $Y_5', \tilde{Y}_5' \to 0$ gives back regularization I so that excluding regularization II would also exclude regularization I. In a situation of this kind where the regularization I only is experimentally ruled out, the regularizations I and II would obviously not be experimentally equivalent.
Let us simply remark here that it is not trivial to conclude *intuitively* on the experimental equivalence of the two regularizations. Indeed in regularization II, from the 4D point of view, first taking $N \to \infty$ leads to have in a first step a full 5D theory with complete (i.e. infinite) 5D field KK decompositions. Then imposing the $\epsilon \to 0$ limit, in this non-truncated 5D framework, represents effectively a localization of the Higgs scalar on the brane. In contrast, for the regularization I, the physical sense of taking $\epsilon \to 0$ before having completed the 5D theory (i.e. having taken $N \to \infty$) is not clear anymore : it is not obvious that it corresponds to the geometric brane-localization along the extra-dimension as it is realized within an hybrid 5D scenario. In other words, this regularization may or may not be equivalent to regularization II. Therefore the experimental tests described above are really necessary to determine whether those two regularizations are experimentally equivalent or not.

The above considerations on the degrees of freedom added by the Y_5', $\tilde{Y}_5'$ parameters are expected to be similar with a warped extra-dimension. Therefore, one can invoke the previous discussion to make the following comments on the past and future literature about the RS scenario (or generally on higher-dimensional theories with a brane-localized Higgs scalar and bulk matter) [15].
As discussed at the beginning of this subsection, the regularizations I and II reproduce the present collider data and are thus experimentally equivalent. Hence, the constructions of RS realizations reproducing the fermion masses and mixings performed through the regularization I, as for instance in Ref. [29, 31], would have been possible as well using regularization II.
Concerning future data, one cannot be sure to predict theoretically all the possible physical values within regularization I [some can be inaccessible as discussed below Eq. (8.43)] whereas regularization II is clearly exhaustive in its predictions (it includes the parameter space of regularization I which is recovered for $Y_5' = \tilde{Y}_5' = 0$). This is the reason why the RS predictions on KK quark masses, FCNC rates or Higgs productions/decays (involving KK fermion mixings) made *e.g.* in Ref. [10, 11, 32–34] (4D calculation) [35] (5D calculation) [16] may not be complete in contrast with those of Ref. [9, 18–20, 22] (5D calculation).
Finally, our recommendations to treat the future experimental data within the RS model are as follows. One should perform the regularizations I and II to determine whether in both cases there exist parameters reproducing the whole set of observables [as in Eq. (8.43)]. If the regularization I cannot reproduce data then it is excluded, otherwise the two regularizations are experimentally equivalent [17]. This procedure is important to safely conclude on the validity of these Higgs regu-

[15] For constructions of RS scenarios with a brane-Higgs as a limit case of bulk-Higgs models, we refer to Ref. [21, 22].
[16] Let us also mention Ref. [24] in regularization I, which presents 4D/5D matching considerations via a numerical approach and for a truncated KK fermion tower.
[17] The last possible situation with both regularizations unable to reproduce data would mean that either another kind of regularization is necessary [as both previous regularizations would then not be correct] or the RS model itself

larizations and to avoid misleading interpretations. From a practical point of view, the question of the experimental equivalence of these regularizations is also important. Indeed, a systematic calculation of the fermion masses or Yukawa couplings is easier through regularization I than II, both in the 4D [less infinite sums to address cause some mass matrix elements vanish] and 5D [less $\delta(y-\pi R)$ terms in EOM] approaches. Therefore, one could benefit from a regularization equivalence by choosing to use the simpler regularization I.

8.4.4 The cut-off procedure

Generally speaking, the extra-dimensional backgrounds lead to non-renormalizable theories which are valid only up to a certain energy scale where starts the non-perturbative regime. For instance, in the RS model with bulk matter this scale is driven by the perturbativity of the top Yukawa coupling and is around 2-3M_{KK} ($M_{KK} \equiv$ first KK photon mass) [see *e.g.* Ref. [29]] so that a Λ cut-off satisfying, $\Lambda \lesssim$ 2-3M_{KK}, should be applied. Λ indicates the typical energy scale of the UV completion of the theory.

Based on the previous results and discussions, we are going to clarify here the correct and generic way to apply the Λ cut-off on scenarios with a Higgs scalar stuck at a brane. Without loss of generality, one should follow this two-step procedure,

(1) : *calculate the bulk fermion mass spectrum and Yukawa couplings including infinite KK tower contributions, as done automatically when manipulating 5D fields or considering infinite mass matrices [with $N \to \infty$ after/before $\epsilon \to 0$ accordingly to regularization I/II] in the 4D approach,*

(2) : *consider only the obtained mass eigenstates of the towers [masses and couplings derived at step* (1)*] which are lighter than the Λ cut-off, in the computation of physical observables and tree/loop-level amplitudes – with notations of Section 8.4.1, it means that N_{KK} must be finite* [18].

The reason for this rigorous order is that one should *first* build formally a consistent and pure 5D theory ($N \to \infty$) with full KK fermion mixings, *before* truncating this theory at the frontier of its validity domain indicated by Λ to get the physical effective low-energy model.
Notice that adopting the inverse order, i.e. (2)→(1), within regularization II, that is first applying the Λ cut-off and secondly calculating the fermion mass eigenvalues with a finite mass matrix (as the cut-off would prevent from taking $N \to \infty$) – ending with $\epsilon \to 0$ – would lead to incomplete eigen-mass expressions (even for the lightest modes) without the Y_5' term [*c.f.* Table 1]. Indeed, the non-vanishing contributions from the mass matrix elements involving Y_5' originate non-trivially from the fact that the limit $N \to \infty$ has been taken [see beginning of Section 8.4.1].

(in its minimal version with an Higgs boson strictly localized on the brane) is ruled out.

[18] Even if a cut-off should be applied on physical observables, it may be instructive to take the limit $N_{KK} \to \infty$ for technical purposes in formal discussions on the calculation itself [9, 18–21].

This cut-off procedure is analogous in supersymmetric RS extensions [36] where, at the first step, the 4D effective Lagrangian must be written including infinite KK tower effects : one can then regularize tree-level $\delta(0)$-inconsistencies, arising in the bulk sfermion couplings to two brane-Higgs bosons (from Yukawa and D-terms) [19], through cancellations with contributions from exchanges of infinite KK towers – treated via the completeness relation. In a second step, one can apply the Λ cut-off on tower eigenstates entering the computation *e.g.* of quantum corrections to the Higgs mass, based on the obtained couplings [36]. This procedure, which has been shown to be the correct one in supersymmetric RS frameworks [36], confirms that one should first elaborate a consistent and thus complete 5D theory (with infinite KK towers) *before* truncating it at the physical cut-off for calculating amplitudes – as justified in previous paragraph.

8.4.5 Discussion for the square Higgs profile

Let us finally discuss the regularization introduced in Section 8.2.4, which consists in smoothing the Higgs delta peak by a square function. In that case, depending on whether the $(--)$ BC at πR is applied before or after solving the EOM system (8.20a)-(8.20d) with a square Higgs profile, the mass spectrum is given by Eq. (8.19) [regularization I] or Eq. (8.23) [regularization II]. In the regularization I, there are no Θ-terms for $(--)$-profiles in Eq. (8.20b)-(8.20c). All this is summarized in Table 2 below, similarly to 5D part of previous Table 1 for the shifted Higgs regularization – except that here $Y_5 = Y_5'$ is assumed (case II) for simplicity in the calculation.

Table 2 *(square Higgs)*	Regularization I	Regularization II $[Y_5 = Y_5']$
5D CALCULATION	$\boxed{\tan(\pi R\, m) = \frac{vY_5}{\sqrt{2}}}$	$\boxed{\tan(\pi R\, m) = \tanh\left(\sqrt{\frac{v^2 Y_5^2}{2}}\right)}$
	no Θ-terms for $(--)$-profiles $(--)$ BC at πR, EOM with ϵ	Θ-terms for $(--)$-profiles EOM with ϵ, $(--)$ BC at πR

Table 2 : Quark mass spectrum for a square Higgs profile.

The Higgs regularizations via a square profile and a shifted delta peak are experimentally equivalent [20, 22, 23] for the same reasons as those presented in details at the beginning of Section 8.4.3 where regularizations I and II were compared. Note that in case of regularization I, these two profile regularizations are even formally equivalent as show the identical mass spectrum exhibited in Tables 1 and 2. Hence, the above discussion on the equivalence of regularizations I and II (Section 8.4.3) hold also for the square Higgs profile. In particular, the considerations on the counting of

[19] And in self couplings of the Higgs bosons as well.

degrees of freedom are the same : there are once more additional parameters (Y_5') in regularization II [even if those do not appear explicitly in Table 2 due to the $Y_5 = Y_5'$ hypothesis]. Finally, the discussion on the cut-off in Section 8.4.4 remains also valid with a square Higgs profile.

8.4.6 Higher order operators with derivatives

So far in our discussion, we have ignored the possibility that the UV completion of the considered model could induce some higher order operators in the low-energy effective description. In this section, we consider a scenario where higher order operators of the kind,

$$\delta(y-\pi R)\; Y_{\rm HO}\; \frac{\partial_y \overline{Q}_R\; H\; \partial_y D_L}{\Lambda^2} \quad \Leftrightarrow \quad \delta\left(y-\left[\pi R-\frac{1}{\Lambda}\right]\right)\; Y_{\rm HO}\; \bar{Q}_R\; H\; D_L\;, \tag{8.44}$$

would be present. The motivation is that these specific operators are allowed by the symmetries of the 5D action (8.1) and are relevant for the present discussion on the regularizations. The term (8.44) would add up to the 5D action of Eq. (8.1). Here Λ represents the cut-off energy scale, while the $Y_{\rm HO}$ coupling constant has the dimension and order of magnitude of R. The rewriting as a shifted Yukawa coupling was discussed at the end of Ref. [22] or in Ref. [27].

5D approach

We will show that in the scenario with an operator, like in Eq. (8.44), the regularizations I and II would become analytically equivalent. For that purpose, we will study the effects of such an operator on the fermion mass spectrum, going first through the 5D approach of the Higgs shift procedure. Let us first rewrite the EOM in the presence of such an operator,

$$-\,m\;q_L\;-\;q_R'\;+\;\delta(y-\pi R)\;\frac{vY_5}{\sqrt{2}}\;d_R\;=\;0\;, \tag{8.45a}$$

$$-\,m\;q_R\;+\;q_L'\;+\;\left\{\delta(y-\pi R)\;\frac{vY_5'}{\sqrt{2}}+\delta\left(y-\left[\pi R-\frac{1}{\Lambda}\right]\right)\frac{vY_{\rm HO}}{\sqrt{2}}\right\}\;d_L\;=\;0\;, \tag{8.45b}$$

$$-\,m\;d_L\;-\;d_R'\;+\;\left\{\delta(y-\pi R)\;\frac{vY_5'}{\sqrt{2}}+\delta\left(y-\left[\pi R-\frac{1}{\Lambda}\right]\right)\frac{vY_{\rm HO}}{\sqrt{2}}\right\}\;q_R\;=\;0\;, \tag{8.45c}$$

$$-\,m\;d_R\;+\;d_L'\;+\;\delta(y-\pi R)\;\frac{vY_5}{\sqrt{2}}\;q_L\;=\;0\;. \tag{8.45d}$$

Notice the two additional $Y_{\rm HO}$ terms with respect to the Eq. (8.6a)-(8.6d).

In case of the regularization I – following the steps described in Section 8.2.3 – the $(--)$ BC assigned to the d_L, q_R wave functions have first the effect of eliminating the $\delta(y-\pi R)$ terms in

Eq. (8.45b)-(8.45c). One is thus left with,

$$- m\, q_L - q'_R + \delta(y-(\pi-\epsilon)R)\,\frac{vY_5}{\sqrt{2}}\, d_R = 0\,, \tag{8.46a}$$

$$- m\, q_R + q'_L + \delta\left(y-\left[\pi R-\frac{1}{\Lambda}\right]\right)\frac{vY^I_{\rm HO}}{\sqrt{2}}\, d_L = 0\,, \tag{8.46b}$$

$$- m\, d_L - d'_R + \delta\left(y-\left[\pi R-\frac{1}{\Lambda}\right]\right)\frac{vY^I_{\rm HO}}{\sqrt{2}}\, q_R = 0\,, \tag{8.46c}$$

$$- m\, d_R + d'_L + \delta(y-(\pi-\epsilon)R)\,\frac{vY_5}{\sqrt{2}}\, q_L = 0\,, \tag{8.46d}$$

after introducing the regularizing ϵ-shift for the brane-Higgs field. At this level, one can view the inverse cut-off $1/\Lambda$ as the Higgs spatial shift ϵR, since the limit $\epsilon \to 0$ imposed by the regularization will then induce the limit $\Lambda \to \infty$ which must be taken as well – given the step **(1)** described in Section 8.4.4 (infinite KK tower, $N \to \infty$, to get a pure 5D theory). One thus ends up with the system of Eq. (8.8a)-(8.8d), with $Y^I_{\rm HO}$ instead of Y'_5. Hence, as in Section 8.2.3, combining the conditions at $(\pi-\epsilon)R$ (coming from the integrations of the EOM), the wave function expressions and the BC, $\hat{q}_R(\pi R) = \hat{d}_L(\pi R) = 0$, leads to the fermion mass spectrum of Eq. (8.16), with $Y^I_{\rm HO}$ instead of Y'_5,

$$\tan(\pi R\, m) = \frac{\sqrt{2}(1+c)^2 vY_5}{2(1+c)^2 + cv^2 Y_5 Y^I_{\rm HO}}\,. \tag{8.47}$$

In case of the regularization II, starting by shifting the brane-Higgs peak in Eq. (8.45b)-(8.45c), one first obtains the EOM,

$$- m\, q_L - q'_R + \delta(y-(\pi-\epsilon)R)\,\frac{vY_5}{\sqrt{2}}\, d_R = 0\,, \tag{8.48a}$$

$$- m\, q_R + q'_L + \left\{\delta(y-(\pi-\epsilon)R)\,\frac{vY'_5}{\sqrt{2}} + \delta\left(y-\left[\pi R-\frac{1}{\Lambda}\right]\right)\frac{vY^{II}_{\rm HO}}{\sqrt{2}}\right\} d_L = 0\,, \tag{8.48b}$$

$$- m\, d_L - d'_R + \left\{\delta(y-(\pi-\epsilon)R)\,\frac{vY'_5}{\sqrt{2}} + \delta\left(y-\left[\pi R-\frac{1}{\Lambda}\right]\right)\frac{vY^{II}_{\rm HO}}{\sqrt{2}}\right\} q_R = 0\,, \tag{8.48c}$$

$$- m\, d_R + d'_L + \delta(y-(\pi-\epsilon)R)\,\frac{vY_5}{\sqrt{2}}\, q_L = 0\,. \tag{8.48d}$$

Once again, taking the inverse cut-off $1/\Lambda$ as the Higgs shift ϵR, one ends up with the system of Eq. (8.8a)-(8.8d), with $Y'_5 + Y^{II}_{\rm HO}$ instead of Y'_5. Therefore, as in Section 8.2.3, combining the conditions at $(\pi-\epsilon)R$, the wave function expressions and the BC, $\hat{q}_R(\pi R) = \hat{d}_L(\pi R) = 0$ [Eq. (8.15)], we find the fermion mass spectrum of Eq. (8.16), with $Y'_5 + Y^{II}_{\rm HO}$ instead of Y'_5,

$$\tan(\pi R\, m) = \frac{\sqrt{2}(1+c)^2 vY_5}{2(1+c)^2 + cv^2 Y_5[Y'_5 + Y^{II}_{\rm HO}]}\,. \tag{8.49}$$

Therefore, the mass spectrum from Eq. (8.47) and Eq. (8.49) are equal after the parameter redefinition, $Y^I_{\rm HO} \equiv Y'_5 + Y^{II}_{\rm HO}$. This means that the regularizations I and II are identical in the presence of the higher order operator (8.44).

4D approach

Similarly, in the 4D approach, the mass matrix element β_{ji} of Eq. (8.31) becomes,

$$\beta_{ji} \;=\; \frac{vY'_5}{\sqrt{2}}\, q^i_R((\pi-\epsilon)R) \times d^j_L((\pi-\epsilon)R) + \frac{vY_{\rm HO}}{\sqrt{2}}\, q^i_R\left(\pi R - \frac{1}{\Lambda}\right) \times d^j_L\left(\pi R - \frac{1}{\Lambda}\right). \quad (8.50)$$

In the regularization I, first applying the regularization limit $\epsilon \to 0$ would only suppress the Y'_5 term of Eq. (8.50) [since $q^n_R(\pi R) = d^n_L(\pi R) = 0$] but not the whole matrix element β_{ji}. Then following the same calculations in terms of β_{ji} as in Section 8.3.2, one writes the matrix characteristic equation and works out its infinite KK sums ($N \to \infty$) leading to the same spectrum as obtained in Eq. (8.38), except that Y'_5 should be replaced there by $Y^I_{\rm HO}$,

$$\tan^2\left(\pi R\sqrt{|m|^2}\right) \;=\; \left(\frac{4\sqrt{2}vY_5}{8+v^2Y_5Y^I_{\rm HO}}\right)^2. \quad (8.51)$$

This is guaranteed by the fact that $\beta_{ji} \to 0$ as well in the limiting case $\Lambda \to \infty$ (step **(1)**, $N \to \infty$, of Section 8.4.4).

Within the regularization II, one is first writing the characteristic equation, calculating its KK summations up to $N \to \infty$. At this level, the β_{ji} element of Eq. (8.50) can be factorized with respect to $Y'_5 + Y^{II}_{\rm HO}$, given that the Higgs shift ϵR is non-vanishing yet and can be taken as the inverse cut-off $1/\Lambda$ (same arguments as in the 5D case). Then imposing the limit $\epsilon \to 0$, one finds the same spectrum as in Eq. (8.38), replacing Y'_5 by $Y'_5 + Y^{II}_{\rm HO}$,

$$\tan^2\left(\pi R\sqrt{|m|^2}\right) \;=\; \left(\frac{4\sqrt{2}vY_5}{8+v^2Y_5[Y'_5+Y^{II}_{\rm HO}]}\right)^2. \quad (8.52)$$

Once again, the mass spectrum from Eq. (8.51) and Eq. (8.52) are equal after the coupling redefinition, $Y^I_{\rm HO} \equiv Y'_5 + Y^{II}_{\rm HO}$. We thus recover, using the 4D calculations, that the regularizations I and II are identical in the presence of the derivative operator (8.44).

The conclusion of Sections 8.4.6 and 8.4.6 reads as follows. In the presence of the higher order operator (8.44), the non-commutativity disappears and the regularizations I and II give rise to the same analytical expression for the fermion mass spectrum. Obviously it is this unique mass spectrum which must be used for phenomenological studies. Notice that this spectrum is identical to the spectrum obtained within the regularization II in the absence of higher order operators (see

for instance Table 1).

8.5 Summary and conclusions

In the framework of a simple higher-dimensional model with bulk matter and a brane-localized Higgs boson [20], we have first pointed out a certain non-commutativity in the order of the 4D calculation for the fermion mass spectrum : applying first the limit $\epsilon \to 0$ and then $N \to \infty$ (so-called regularization I) leads to a different analytical expression from the inverse ordering (regularization II). The interpretation of this difference raises obviously a physical question : which order is the correct one?

Then the exact matching between the 4D and 5D calculations of the mass spectrum, which is expected, has been established analytically – for the first time and in both regularizations (I/II). This matching allows a deeper understanding of the regularizations of brane-Higgs models ; in particular, it turns out that the regularizations I and II differ in their brane-Higgs sensitivity to the tower of bulk $(--)$ profiles for the fermions. Besides, the obtained 4D/5D matching represents another confirmation that the usually applied 5D mixed-formalism [i.e. the mixed KK decomposition of Eq. (8.3a)-(8.3d)] is a correct way of including the whole KK mixing effect.

We have further worked out the interpretation of the existence of two types of Higgs peak regularization, which answers the question raised above about the new non-commutativity. The conclusion is that with the present experimental setup, the regularizations I and II are experimentally equivalent. Nevertheless, with future constraints from high-energy collider results, it could happen that only the regularization I is ruled out – as the regularization II involves more free parameters (like Y_5', $\tilde{Y}_5'$). Therefore, there is anyway no regularization-dependence of the model since either the regularizations I and II are experimentally equivalent or one of the two is simply excluded.

Our analysis has lead us to clarify the cut-off procedure in models with a brane-Higgs : one must *first* build a consistent 5D theory – i.e. calculate eigen-masses and Yukawa couplings accordingly to regularization I or II – with full KK fermion effects ($N \to \infty$), *before* restricting this theory (finite N_{KK}) to its validity domain delimited by the Λ UV cut-off for computing physical amplitudes. This is analogous to the cut-off process in supersymmetric extensions of the RS model [36].

We mention that even if the Higgs peak regularization used throughout the study was shifting the delta peak, regularizing the Higgs profile by a smooth square function is experimentally equivalent and has been performed as well. In particular, this square profile treatment has allowed to confirm our statements on the comparison between the regularizations I and II.

Besides, an important complementary result has been found : it has been shown, in the case of

[20] Our results are expected to be essentially similar (up to warp factors of course) in realistic warped extra-dimension scenarios.

the regularization through a Higgs shift, that the non-commutativity disappears in the presence of higher order derivative operators localized on the Higgs brane. In other terms, the regularizations I and II have been found to give mass spectra identical to each other – and analytically equivalent to the spectrum from the regularization II without higher order operators. Those results hold within both the 4D and 5D approaches.

Bibliography

[1] A. Djouadi, Phys. Rept. **457** (2008) 1; S. Heinemeyer, W. Hollik and G. Weiglein, Phys. Rept. **425** (2006) 265; J. Gunion, H. Haber, G. Kane and S. Dawson, "The Higgs Hunter's Guide", Reading 1990.

[2] The ATLAS collaboration, Phys. Lett. **B716** (2012) 1; the CMS collaboration, Phys. Lett. **B716** (2012) 30.

[3] S. Weinberg, Phys. Rev. Lett. **19** (1967) 1264; G. Guralnik, C. Hagen and T. Kibble, Phys. Rev. Lett. **13** (1964) 585; F. Englert and R. Brout, Phys. Rev. Lett. **13** (1964) 321; P. Higgs, Phys. Lett. **12** (1964) 132; Phys. Rev. Lett. **13** (1964) 506.

[4] L. Randall and R. Sundrum, Phys. Rev. Lett. **83** (1999) 3370.

[5] T. Gherghetta and A. Pomarol, Nucl. Phys. **B586** (2000) 141.

[6] G. Cacciapaglia et al., arXiv:1210.8120 [hep-ph]; T. Plehn and M. Rauch, arXiv:1207.6108 [hep-ph]; D. Carmi, A. Falkowski, E. Kuflik, T. Volansky and J. Zupan, arXiv:1207.1718 [hep-ph]; J. Espinosa, C. Grojean, M. Muhlleitner and M. Trott, arXiv:1207.1717 [hep-ph]; J. Ellis and T. You, arXiv:1207.1693 [hep-ph]; P. P. Giardino, K. Kannike, M. Raidal and A. Strumia, arXiv:1207.1347 [hep-ph]; G. Belanger et al., JHEP **1302** (2013) 053; A. Azatov and J. Galloway, Int. J. Mod. Phys. A Volume **28** (2013) 1330004; N. Bonne and G. Moreau, Phys. Lett. **B717** (2012) 409.

[7] J. Ellis and You, arXiv:1303.3879 [hep-ph]; T. Alanne, S. Di Chiara and K. Tuominen, arXiv:1303.3615 [hep-ph]; P. P. Giardino et al., arXiv:1303.3570 [hep-ph]; A. Falkowski, F. Riva and A. Urbano, arXiv:1303.1812 [hep-ph]; A. Djouadi et al., Eur. Phys. J. **C73** (2013) 2650; A. Djouadi et al., Eur. Phys. J. **C73** (2013) 2512; G. Moreau, Phys. Rev. **D87**, 015027 (2013).

[8] F. Goertz, U. Haisch and M. Neubert, Phys. Lett. **B713** (2012) 23.

[9] J. Hahn, C. Horner, R. Malm, M. Neubert, K. Novotny and C. Schmell, arXiv:1312.5731 [hep-ph].

[10] A. Djouadi and G. Moreau, Phys. Lett. **B660** (2008) 67.

[11] C. Bouchart and G. Moreau, Phys. Rev. **D80** (2009) 095022.

[12] K. Agashe et al., Phys. Rev. **D77** (2008) 015003; M. Guchait, F. Mahmoudi and K. Sridhar, Phys. Lett. **B666** (2008) 347; A. Djouadi, G. Moreau and R. K. Singh, Nucl. Phys. **B797** (2008) 1; B. Lillie, J. Shu and T. M. P. Tait, Phys. Rev. **D76** (2007) 115016; B. Lillie, L. Randall and L.-T. Wang, JHEP **0709** (2007) 074.

[13] A. Djouadi, G. Moreau and F. Richard, Phys. Lett. **B701** (2011) 458; A. Djouadi, G. Moreau, F. Richard and R. K. Singh, Phys. Rev. **D82** (2010) 071702; A. Djouadi, G. Moreau and F. Richard, Nucl. Phys. **B773** (2007) 43.

[14] K. Agashe et al., Phys.Rev. **D76** (2007) 115015; Phys. Rev. **D80** (2009) 075007; F. Ledroit, G. Moreau and J. Morel, JHEP **0709** (2007) 071.

[15] S. Gopalakrishna et al., arXiv:1306.2656 [hep-ph]; Phys. Rev. **D84** (2011) 055001.

[16] C. Y. Chen, H. Davoudiasl and D. Kim, Phys. Rev. **D89** (2014) 096007; K. Agashe, H. Davoudiasl, G. Perez and A. Soni, Phys. Rev. **D76** (2007) 036006; A. L. Fitzpatrick, J. Kaplan, L. Randall and L.-T. Wang, JHEP **0709** (2007) 013.

[17] H. Davoudiasl, S. Gopalakrishna, E. Ponton and J. Santiago, New J. Phys. **12** (2010) 075011.

[18] R. Malm, M. Neubert, K. Novotny and C. Schmell, arXiv:1303.5702 [hep-ph].

[19] M. Carena, S. Casagrande, F. Goertz, U. Haisch and M. Neubert, JHEP **1208** (2012) 156.

[20] S. Casagrande, F. Goertz, U. Haisch, M. Neubert and T. Pfoh, JHEP **1009** (2010) 014.

[21] A. Azatov, M. Toharia and L. Zhu, Phys. Rev. **D82** (2010) 056004.

[22] A. Azatov, M. Toharia and L. Zhu, Phys. Rev. **D80** (2009) 035016.

[23] C. Csaki, C. Grojean, J. Hubisz, Y. Shirman and J. Terning, Phys. Rev. **D70** (2004) 015012.

[24] F. Goertz and T. Pfoh, JHEP **0810** (2008) 035.

[25] M. Blanke, B. Shakya, P. Tanedo and Y. Tsai, JHEP **1208** (2012) 038; C. Csaki, Y. Grossman, P. Tanedo and Y. Tsai, Phys. Rev. **D83** (2011) 073002; K. Agashe, A. E. Blechman and F. Petriello, Phys. Rev. **D74** (2006) 053011.

[26] C. Delaunay, J. F. Kamenik, G. Perez and L. Randall, JHEP **1301** (2013) 027.

[27] M. Frank, N. Pourtolami and M. Toharia, Phys. Rev. **D87** no. 9 (2013) 096003.

[28] K. Agashe, A. Delgado, M. J. May and R. Sundrum, JHEP **0308** (2003) 050.

[29] C. Bouchart and G. Moreau, Nucl. Phys. **B810** (2009) 66.

[30] K. Agashe, R. Contino, L. Da Rold and A. Pomarol, Phys. Lett. **B641** (2006) 62.

[31] S. Chang et al., Phys. Rev. **D73** (2006) 033002; G. Moreau and J. I. Silva-Marcos, JHEP **0601** (2006) 048; JHEP **0603** (2006) 090; G. Moreau, Eur. Phys. J. **C40** (2005) 539; K. Agashe et al., Phys. Rev. Lett. **93** (2004) 201804; Phys. Rev. **D71** (2005) 016002; S. J. Huber and Q. Shafi, Phys. Lett. **B498** (2001) 256; Phys. Lett. **B512** (2001) 365; Phys. Lett. **B544** (2002) 295; Phys. Lett. **B583** (2004) 293.

[32] F. del Aguila and J. Santiago, Phys. Lett. **B493** (2000) 175.

[33] K. Agashe, A. E. Blechman and F. Petriello, Phys. Rev. **D74** (2006) 053011.

[34] K. Agashe, G. Perez and A. Soni, Phys. Rev. **D75** (2007) 015002.

[35] S. Casagrande, F. Goertz, U. Haisch, M. Neubert and T. Pfoh, JHEP **0810** (2008) 094.

[36] C. Bouchart, A. Knochel and G. Moreau, Phys. Rev. **D84** (2011) 015016.

Chapter 9

Discriminate 4D supersymmetry against its 5D warped version

Adapted from: *C. Bouchart, A. Knochel and G. Moreau*, Phys. Rev. **D84** (2011) 015016.

9.1 Introduction

Among the possible theories underlying the Standard Model (SM) of particle physics, the supersymmetric scenarios and the higher-dimensional models have several deep motivations. In particular, supersymmetry stabilizes the ElectroWeak Symmetry Breaking (EWSB) scale with respect to radiative corrections and when it is promoted to a local symmetry it provides a framework for the appearance of the graviton Lagrangian. On the other side, a warp extra-dimensional model has been proposed by Randall and Sundrum (RS) [1] [1] to explain the huge hierarchy between the EWSB energy scale and the gravity scale while some RS extensions [2] give rise to purely geometrical interpretations of the fermion structure in flavor space. Both supersymmetric and higher-dimensional scenarios can provide viable dark matter candidates (LSP, LKP) and allow for gauge unification. Since the physics beyond the SM is still unknown, one should consider the possibility of an effective low-energy hybrid theory with both SUperSYmmetry (SUSY) and extra dimension(s). More specifically, SUSY and extra dimensions could be crucial ingredients in a quantum description of gravity, as both indeed are in string theory. SUSY and extra dimensions could also be simultaneously involved in the origin of the electroweak symmetry breaking [7, 8]. The higher-dimensional framework even provides new and attractive ways of breaking supersymmetry, due to a more structured geometry of space-time; SUSY may be broken either in the bulk (i.e. whole space) or on a brane,

[1] The RS scenarios with a fundamental Higgs boson on the so-called TeV-brane, the alternative models of gauge-Higgs unification [3] and the Higgsless models [4] can be thought of as warped extra-dimension models constituting dual descriptions – through the AdS/CFT correspondence [5] – of four-dimensional (4D) strongly coupled gauge theories (in the limit of a large number of colors) predicting the effective Higgs scalar field as a composite state (see e.g. Ref. [6]).

playing the role of the necessary hidden sector, and then the breaking mediated to the brane where are living the SM particles [9]. A different approach towards the SUSY breaking [2] is to use specific Boundary Conditions (BC) for different fields (in the same supermultiplet) propagating along compactified extra dimensions [11]. A famous example is the Scherk-Schwarz mechanism [12] which can be applied to the minimal supersymmetric SM (see e.g. [13]) as well as to the Horava-Witten theory (see e.g. [14]) [3]. Finally, the supersymmetrization of extra-dimensional theories allows to have a realistic tension model [16], to alternatively achieve gauge unification at a low scale [17] and to address the so-called μ-problem in SUSY (see discussion below).
Hence, there exist several serious motivations for hybrid scenarios with both SUSY and (warped) extra dimensions. It was shown in [18] that an Anti-de Sitter (AdS) space is compatible with SUSY. Later [19], the supermultiplet mass-spectrum was derived in AdS_5, and then the analysis extended to the case of a fifth dimension compactified on an orbifold [2]. The RS SUSY scenario was initially studied with only gravity in the bulk [20] and finally with matter propagating in the bulk [2]. There exist also analyses of GUT theories within RS SUSY frameworks [21] and attempts of superstring realizations of the RS model [22].

In this work, we will study these supersymmetrized RS scenarios with matter/gauge fields in the bulk. Our first contributions are theoretical; we will write explicitly the complete 5D Lagrangian for a Higgs scalar field confined on the TeV-brane – as required to explain the discrepancy between EWSB and gravity scales and as motivated by the $SU(2)_R$ breaking from bulk Yukawa interactions (forbidden trilinear chiral superfield couplings in $N = 2$ 4D SUSY [23]) – and, when deriving the 4D effective action, we will take into account for the first time the mixing among the several Higgs bosons occuring in the minimal SUSY extensions.
In particular, the 4D effective Higgs couplings to two scalar fields (squarks/sleptons and their Kaluza-Klein excitations), originating from the so-called D-terms, are not trivial to derive due to the localized aspect of the Higgs boson and due to contributions to these effective couplings from the tree level exchange of Kaluza-Klein (KK) scalar modes of $(--)$ chiral superfields [4] (i.e. additional superfields with Dirichlet-Dirichlet boundary conditions which are characteristic of 5D theories). We derive these 4D couplings which do not appear in literature and explain why this specific KK $(--)$ tower must be taken into account without any cut-off (a non-natural task within a non-renormalizable 5D theory).
The derivation of Yukawa couplings between Higgs bosons and two scalars in the 4D effective Lagrangian is also subtle: singularities [Dirac peak functions taken at the origin, $\delta(0)$'s, due to the Higgs local aspect] appear in these couplings – after integrating out the auxiliary fields – but those are not the sign of an incomplete theory. Indeed, those singularities are cancelled out by the infinite sum of KK $(--)$ scalar contributions. A related kind of cancellation was pointed out for some loop

[2] It has been shown recently that in the limit of an infinite Majorana mass term on the infra-red brane [10], the gaugino mediation mechanism through the bulk is comparable to a SUSY breaking with twisted boundary conditions.
[3] In this context of extra dimensions, other new scenari of SUSY breaking have arisen [7] and in particular in the case of warped dimensions [15].
[4] We use a $N = 1$ 4D superfield formalism as in Ref. [24].

calculations in the string theory framework [25] using either the expression of $\delta(0)$ in terms of a sum over the fifth component of the momentum [9] (see Ref. [26] for the warped background case) or a Gaussian brane distribution [27]; in contrast, here we demonstrate the cancellation generally for the tree level couplings, using a simple method based on the completeness relation, by computing the Higgs couplings (including the Higgs-sfermion couplings and quartic Higgs interactions) in the flavor-motivated case of a warped extra dimension where only Higgs bosons are brane-localized [2]. In addition, in the present work we will derive the 4D effective scalar mass matrices induced, after EWSB, by the localized Higgs Vacuum Expectation Values (VEV). In contrast with the above 4D couplings, these 4D masses computed at tree level do not depend on the energy scale and must be derived consistently either through the integration out of heavy KK $(--)$ scalar modes or through the scalar mixing with KK $(--)$ states, as we will show here. We will finally combine at first order these KK $(--)$ scalar effects on the 4D zero-mode scalar masses with the scalar mixing effects of KK $(++)$ states (having Neumann-Neumann boundary conditions). Such a combination should have been done in Ref. [32] [where effects of KK scalar modes with even $\mathbb{Z}_2$ parity (i.e. $(++)$ BC) are studied in a 5D SUSY context with brane-localized Yukawa interactions, but the above effects of KK scalars with an odd parity ($(--)$ BC) are considered neither in squark/slepton masses nor in Higgs couplings].

We will then use the new 4D effective Lagrangian, that we will have derived in the RS SUSY framework, for several phenomenological applications.
The first application is an explicit and complete diagramatic computation of quantum corrections to the Higgs boson mass (δm_{Higgs}) at the one-loop level, including all kinds of KK contributions and each sector (Yukawa plus gauge couplings); we will show how the quadratically divergent parts can cancel each other due to 5D SUSY. This complete cancellation has not been shown before in warped SUSY models and it constitutes here an additional check of the obtained 4D effective Higgs couplings. More generically, we will clarify the connections between the cancellations of these 5D quadratic divergences and of the 5D triangular anomalies. Our way of finding the quadratic divergence cancellation brings some new light on the old debate about the validity of this cancellation in δm_{Higgs} within higher-dimensional SUSY models. In particular, the preliminary and complete calculation of 4D effective Higgs couplings allows a more clear overview of the subtle points and in turn allows to address the 'KK regularization' question and cut-off problems.
Our general results on the absence of quadratic divergences in δm_{Higgs} for 5D SUSY models [with a soft breaking] is important in the following sense: it seems to mean that hybrid scenarios – both higher-dimensional and supersymmetric – must not necessarily rely on a geometrical background reducing the gravity scale down to the TeV scale in order to protect the Higgs mass against its quantum corrections (i.e. to not reintroduce the gauge hierarchy problem). One can thus imagine a 5D SUSY scenario where the Higgs mass is only protected by SUSY (which allows to avoid the remaining little hierarchy problem of pure 5D models solving the gauge hierarchy) or a 5D SUSY scenario where in addition to SUSY protection the discrepancy between the fundamental gravity and EWSB energy scales is explained by some geometrical feature like the warp factor: those two

possible classes of higher-dimensional SUSY theories avoid to have two redundant solutions to the same Higgs mass instability problem [= fine-tuning problem].

The second application concerns the direct search at present and future high-energy colliders for the (necessary) physics standing beyond the SM; indeed, in the expected case where some signal for new physics would be discovered at the Large Hadron Collider (LHC) and then analyzed more precisely at the International Linear Collider (ILC), the primary phenomenological work would be to identify exactly the nature of the new physics detected. Based on the fact that today the two main types of new physics accessible at colliders are thought to be SUSY and the more recent paradigm of (warped) extra dimensions, three interesting possibilities might arise. The more optimistic is that both superpartners (squarks, gauginos...) and KK excitations would be produced on-shell and observed, proving then the existence of an higher-dimensional SUSY scenario. Another possibility is that only real KK excitations would be produced, however such a situation would represent a good indication for the existence of a higher-dimensional non-SUSY theory as (in)direct constraints and gauge hierarchy considerations favor the mass regions around 10^2 GeV for superpartners and higher mass regions above $\mathcal{O}(1)$ TeV for first KK states (of the warped models). The last possibility – among the cases of signals for new physics as it is predicted today – is that only superpartners would be produced on-shell (and maybe some additional Higgs bosons characteristic of SUSY). Then an important and non-trivial question (see e.g. the related Ref. [28]) would be: do the observed superpartners [either scalar or spinorial] belong to a pure SUSY theory or a (warped) higher-dimensional SUSY model ?

In the present work, we will propose and develop some tests allowing to answer this question which reads in a more compact form as: *how one can distinguish between pure SUSY and warped SUSY at colliders ?* A first kind of test would be to look at the measurement (at ILC or even at LHC) of the smuon masses: there are higher-dimensional minimal [5] SUperGRAvity (mSUGRA) scenarios where the mass splitting $m_{\tilde{\mu}_2} - m_{\tilde{\mu}_1}$ ($\tilde{\mu}_{1,2}$ are the two smuon eigenstates [6]) can be larger than in the 4D mSUGRA scenarios [29], allowing then a discrimination between those two types of scenarios. The reason is that in mSUGRA the off-diagonal elements of the 2×2 smuon mass matrix – partially responsible for the mixing and splitting – are proportional to the muon Yukawa coupling constant which is suppressed compared to the top quark one, while in some RS frameworks [2], the muon 5D Yukawa coupling is not suppressed relatively to the top one (the lightness of the muon originates from its wave function overlap with the Higgs boson). We will also show that RS SUSY models can lead to differences in the stop mass correlations ($m_{\tilde{t}_2}$ versus $m_{\tilde{t}_1}$) with respect to the pure SUSY case – differences which are here not restricted to the mSUGRA model.

Secondly, there exist well-motivated warped geometrical setups of SUSY breaking where the Higgs boson couplings to sleptons can be significantly increased with respect to the conventional 4D SUSY frameworks. Hence, in such warped scenarios, the decay channels of the heaviest neutral

[5] 'minimal' here means that the SUSY breaking masses and couplings are universal at the GUT scale.

[6] Strictly speaking, $\tilde{\mu}_{1,2}$ denote the two lightest mass eigenstates which are generally mainly composed of the left and right (w.r.t. gauge group $SU(2)_L$) smuon zero-modes while the heavier eigenstates are mainly made of their KK modes.

Higgs scalar (characteristic of SUSY and usually noted H) [7] into sleptons can have comparable or even larger branching ratios than the channels into (s)quarks and gauginos, leading to final states at LHC radically different from the 4D SUSY case. The produced H bosons could initiate slepton cascade decays more often than in 4D SUSY and in turn give rise to an increase number of events with leptonic final states. We will illustrate this study by giving numerically all the H boson branching ratios as a function of the mass, for characteristic parameter sets, and the cases of pseudo-scalar and charged Higgs fields will be briefly discussed.

At this level, one should mention related works. In fact, within the hybrid higher-dimensional SUSY context, while the literature on various SUSY breaking mechanisms is rich, there exist few papers on phenomenological aspects. Among those, we mention Ref. [32] where radiative corrections to scalar masses (excluding quadratically divergent parts) and to gauge/Yukawa couplings are calculated in order to *(i)* estimate the 5D MSSM upper limit on the lightest Higgs mass and *(ii)* constrain experimentally the universal scalar (m_0) and gaugino ($m_{1/2}$) masses. In Ref. [33], based on 4D superfield actions, the evolution of neutrino masses/mixings and confrontation with oscillation data were studied within a flat 5D MSSM. See also Ref. [34] for considerations on the proton decay suppression in SUSY grand unified theories with extra compact dimensions (and localized Yukawa couplings or not) as well as Ref. [35] for phenomenology in SUSY gauge-Higgs unification scenarios, Ref. [36] for SUSY composite Higgs models and finally Ref. [37] for SUSY warped Higgsless models.

The organization of the work is as follows. In Section 9.2, After a description of the general higher-dimensional SUSY framework considered, we derive the 4D effective couplings and mass matrices of sfermions and Higgs bosons, focusing on illustrative examples. In the first part of Section 9.3 (Subsection 9.3.1), the quadratic divergent contributions to the quantum corrections of the Higgs mass are calculated and the methods of calculation discussed. In the two following parts on collider phenomenology, various distinctive effects of RS SUSY models (Subsection 9.3.2), including effects in the Higgs sector (Subsection 9.3.3), are pointed out and quantified. Finally, we conclude in Section 9.4.

9.2 Theory

9.2.1 The model

Field content: In Appendix G, we give the full 5D field Lagrangian for a toy model with a U(1) gauge symmetry applying on two chiral superfields Φ_L, Φ_L^c (together with the associated $(--)$ superfields) and two 4D Higgs superfields H_u^0, H_d^0 localized on the TeV-brane within a warp background. With this appendix as a starting point, we will give throughout the work the 4D version of

[7] No deep modifications are expected for the branching ratios of the lightest neutral Higgs boson h, since its decays into two squarks/sleptons ($\tilde{q}/\tilde{\ell}$) are kinematically closed due to the upper theoretical mass bound on m_h GeV combined with the lower direct experimental bounds $m_{\tilde{q}/\tilde{\ell}} \gtrsim 10^2$ GeV [31].

this Lagrangian related to the Higgs boson or more precisely the parts which are not trivial/direct to derive from the 4D point of view. For these studied parts, we will extend the 4D Lagrangian to the phenomenological Minimal Supersymmetric Standard Model (pMSSM) [38] field content and gauge symmetry.

Energy scales: The RS framework is constituted by a 5D theory where the extra dimension is warped and compactified over a $S^1/\mathbb{Z}_2$ orbifold. The non-factorizable metric is of type AdS and the space-time, which is thus a slice of AdS_5, has two 4D boundaries: the Ultra-Violet (UV) boundary at the Planck scale and the Infra-Red (IR) brane with an exponentially suppressed scale in the vicinity of the TeV scale. The Higgs boson has to be localized at this so-called TeV-brane if the EW scale is to be stabilized by such a geometrical structure. We consider the attractive RS version with all other fields propagating in the bulk [2]: this allows to suppress higher dimensional operators, potentially troublesome with respect to Flavor-Changing Neutral Current effects, by energy scales larger than the TeV scale. This feature has also the advantage to possibly generate the fermion mass hierarchy and flavor structure by a simple geometrical mechanism [2, 39, 40].
More precisely, the gravity scale on the Planck-brane is $M_{\rm Planck} = 2.44 \times 10^{18}$ GeV, whereas the effective scale on the TeV-brane $M_\star = e^{-\sigma(\pi R_c)} M_{\rm Planck}$ (with $\sigma(y) = k|y|$) is suppressed by the warp factor which depends on the curvature radius $1/k$ of AdS_5 and the compactification radius R_c. For a product $kR_c \simeq 11$, $M_\star = \mathcal{O}(1)$ TeV allowing to address the gauge hierarchy problem. We will take $kR_c \simeq 10.11$ so that the maximum value of $M_{KK} \simeq 2.45 k e^{-\pi k R_c}$ [M_{KK} is the first KK photon mass], fixed by the theoretical consistency bound $k < 0.105 M_{\rm Planck}$, is ~ 10 TeV in agreement with the the typical indirect limits from EW precision tests (see below). The beauty of the RS model is to possess a unique fundamental energy scale $k \sim R_c^{-1} \sim M_{\rm Planck}$. Besides, the parameters noted c^ψ fix the 5D masses $m_\psi = c^\psi \partial_y \sigma$, affected to each fermion ψ, and thus control the field localizations in the bulk (and in turn the effective 4D masses). Those satisfy $|c^\psi| = \mathcal{O}(1)$ to avoid the introduction of new fundamental scales. The 5D masses for the scalar fields will be discussed throughout the work.

μ-problem: A usual problem of the supersymmetric theories is to explain why the μ parameter is of order of the EWSB scale, as imposed by the orders of magnitudes of the masses involved in the minimization conditions for the Higgs potential. In RS SUSY, there are two simple ways for generating a μ-term at the EWSB scale as we will discuss now [8]. The first way is simply to write the gauge invariant μ-term in the superpotential for pMSSM 5D Higgs superfields in the bulk:

$$\mu_{5D} H_u . H_d \in W, \text{ with } H_u = \begin{pmatrix} H_u^+ \\ H_u^0 \end{pmatrix}, \; H_d = \begin{pmatrix} H_d^0 \\ H_d^- \end{pmatrix} \text{ and } H_u . H_d = \epsilon_{ab} H_u^a H_d^b \tag{9.1}$$

[8] We will not discuss the type of possibility suggested in Ref. [41] which is characteristic of the Scherk-Schwarz mechanism not considered here. A related approach based on twisted BC for the Higgs fields was proposed in Ref. [42].

$H_{u,d}$ being $\mathrm{SU}(2)_\mathrm{L}$ doublets, a, b $\mathrm{SU}(2)_\mathrm{L}$ indices and ϵ_{ab} the antisymmetric tensor defined by $\epsilon_{12} = 1$. Such a term gives rise to the neutral Higgs scalar masses in the 4D effective potential (after field redefinition and inclusion of the metric warp factor)

$$|\mu^u_{eff}|^2|\phi_{H^0_u}|^2 + |\mu^d_{eff}|^2|\phi_{H^0_d}|^2 \in V_{4D}, \text{ with } |\mu^{u,d}_{eff}|^2 = \int_{-\pi R_c}^{\pi R_c} dy\ |\mu_{5D}|^2\ e^{-2\sigma(y)}\ |f_{H^0_{u,d}}(y)|^2$$

$f_{H^0_{u,d}}(y)$ being the Higgs wave functions along the fifth dimension parametrized by the coordinate y. It appears that $|f_{H^0_{u,d}}(y)|^2$ must approximately mimics the peak $\delta(y - \pi R_c)$ so that $\mu^{u,d}_{eff} \sim \mu_{5D} e^{-k\pi R_c} = \mathcal{O}(1)$ TeV since one must have a bulk parameter $\mu_{5D} \sim k \sim M_{\text{Planck}}$ to not reintroduce a new fundamental energy scale. In conclusion, in this setup with bulk Higgs fields, the effective μ parameter has the right order of magnitude around the TeV if the Higgs field wave functions are peaked at the TeV-brane. As an Higgs profile near this brane is motivated by the gauge hierarchy problem, one can claim that this warp setup solves the μ-problem.
The other way is to confine the Higgs fields on the TeV-brane. We thus start from the 5D superpotential coupling in terms of the 4D Higgs superfields,

$$[\mu H_u.H_d]\delta(y - \pi R_c) \in W. \tag{9.2}$$

In analogy with Eq.(G.12) for the U(1) model [equivalent to restrict the $\mathrm{SU}(2)_\mathrm{L}$ model to the neutral Higgs couplings] which leads to the expression of the μ terms written with the fields in Eq.(G.28), the term (9.2) gives rise to the 4D mass terms for the neutral Higgs scalar fields,

$$|\mu_{eff}|^2|\phi_{H^0_u}|^2 + |\mu_{eff}|^2|\phi_{H^0_d}|^2 \in V_{4D}, \text{ with } |\mu_{eff}|^2 = \int_{-\pi R_c}^{\pi R_c} dy\ |\mu|^2\ e^{-2\sigma(y)}\ \delta(y - \pi R_c) = |\mu e^{-\sigma(\pi R_c)}|^2,$$

so that the effective μ parameter reads as $\mu_{eff} = \mu e^{-k\pi R_c} \sim k e^{-k\pi R_c} \sim$ TeV. Note the absence of $\delta(0)$ factors in V_{4D} (or equivalently of $[\delta(y - \pi R_c)]^2$ terms in the 5D Lagrangian) after integration over y. In the work, we will consider this second setup with brane Higgs fields, while the first one is not deeply different as the bulk Higgs fields are localized towards the TeV-brane.

Custodial symmetry: In pure SUSY with $\tan\beta = 1$ [9], if the custodial symmetry $\mathrm{O}(3) \approx \mathrm{SU}(2)_\mathrm{V}$ – resulting after EWSB from the global symmetry $\mathrm{O}(4) \approx \mathrm{SU}(2)_\mathrm{L} \times \mathrm{SU}(2)_\mathrm{R}$ – was exactly respected it would protect the well known relation on gauge boson masses $\rho = m^2_W/(m^2_Z \cos^2\theta_W) = 1$ against quantum corrections, as in the SM. Indeed, the two Higgs $\mathrm{SU}(2)_\mathrm{L}$ doublets of the pMSSM can form a $(\mathbf{2}, \mathbf{2})$ representation under the $\mathrm{SU}(2)_\mathrm{L} \times \mathrm{SU}(2)_\mathrm{R}$ symmetry [43]:

$$\mathcal{H} \equiv (H_d\ H_u) = \begin{pmatrix} H^0_d & H^+_u \\ H^-_d & H^0_u \end{pmatrix}. \tag{9.3}$$

[9] We use the conventional notations for the pMSSM Higgs scalar fields: $\phi_{H^0_{u/d}} = (v_{u/d} + \phi_{h^0_{u/d}} + i\phi_{P^0_{u/d}})/\sqrt{2}$ ($\phi_{P^0_{u/d}}$ denoting the pseudo-scalars) with $\tan\beta = v_u/v_d$ and the squared VEV given by $v^2 = v^2_u + v^2_d \simeq (246\ GeV)^2$.

However, the custodial symmetry is broken in the gauge and Yukawa coupling sectors. Moreover, the deviations from $\tan\beta = 1$ and the presence of soft SUSY breaking terms for squarks/sleptons represent new sources of custodial symmetry (spontaneous) breaking if those differ for the up-type and down-type (w.r.t. $SU(2)_L$) scalars. Nevertheless, the loop level SUSY corrections to the precision EW observables (contributing to $\delta\rho$) can pass the constraints from precision measurements, even easily in the case of equal soft terms for up and down scalars [30, 31].
Concerning the tree level corrections to precision EW observables in warped models, the global fits of experimental data are satisfactory for large KK masses (reducing the KK mixing effects): $M_{KK} \gtrsim 10$ TeV [44].
In the present study where we study hybrid scenarios with both superpatners and KK excitations, we will take identical soft parameters for up/down scalars and KK masses just above ~ 10 TeV. We will not explore the whole parameter space and work out the precise global EW fits, but this realistic choice guarantees that the theoretical respective, and in turn total, corrections to SM observables have acceptable orders of magnitude given the experimental accuracy on these observables. There are (a priori) higher-order corrections involving both superpatners and KK modes, that we do not treat here.
Now one may wish to decrease the possible M_{KK} values in order to improve the situation with respect to considerations on the 'little hierarchy' problem related to the Higgs mass. In order to reduce the acceptable minimal M_{KK} value from ~ 10 TeV down to ~ 3 TeV, an attractive [46] possibility is to gauge the $SU(2)_L \times SU(2)_R \times U(1)_X$ symmetry in the bulk [45]. The SM gauge group is recovered after the breaking of the $SU(2)_R$ group into another $U(1)_R$, by boundary conditions.
The question arising here is whether it is possible to gauge the $SU(2)_L \times SU(2)_R$ symmetry within a SUSY context. First about the μ-term: can it be written in the case of a bulk gauge custodial symmetry ? The question arises as $SU(2)_L \times SU(2)_R$ must remain unbroken on the Higgs brane in order to protect precision EW observables. A simple possibility is to write down the following $SU(2)_R$ invariant term of the superpotential giving rise to the usual μ-term [possibly replacing μ_{5D} by μ and adding a localizing factor $\delta(y - \pi R_c)$ as in Eq.(9.2)],

$$-\frac{1}{2}\mu_{5D}\mathcal{H}.\mathcal{H} = -\frac{1}{2}\mu_{5D}(H_d.H_u - H_u.H_d) = \mu_{5D}H_u.H_d \ ,$$

accordingly to Eq.(9.1). Higgs couplings to matter invariant under $SU(2)_L \times SU(2)_R$ can also be written with the $\mathcal{H}$ bidoublet giving rise in particular to the usual Yukawa couplings in the superpotential, as usually in warped models by promoting matter (superfield) multiplets to $SU(2)_R$ representations (see e.g. [45, 46]). Finally, the gauge interaction sector of a SUSY theory as well as the soft breaking terms can also respect an additional $SU(2)_R$ gauge symmetry.
Hence, in this study we will also consider the case of a bulk gauge $SU(2)_L \times SU(2)_R$ symmetry with $M_{KK} \sim 3$ TeV and equal soft terms for up/down scalars, another setup which leads to realistic EW fits to data.

SUSY breaking: We adopt the classification of the three types of SUSY breaking framework where *(i)* the squark/slepton SUSY breaking masses are induced at loop level by SUSY breaking gaugino masses as in [2] *(ii)* there exist tree level squark/slepton masses [in the bulk and/or brane-localized] resulting directly from a 5D SUSY breaking mechanism *(iii)* the squark/slepton masses are of KK type like in the scenario à la Scherk-Schwarz with SUSY breaking BC [12]. This classification is motivated in particular by the fact that the framework with scalar SUSY breaking masses in the bulk leads to modifications of the wave functions and thus of the 4D effective couplings. Moreover this framework gives rise to an hard breaking of SUSY (reintroducing quadratic divergences in the Higgs mass corrections) which is acceptable in the present warped background where the Higgs mass is still protected by the reduced gravity scale. Finally, this framework with bulk scalar SUSY breaking masses has the attractive feature to generate scalar superpartner masses mainly through the Yukawa couplings like for SM fermions – as will be described in details.
We will consider the second class of SUSY breaking framework mentioned above, including the mSUGRA case where the SUSY breaking terms are universal and the soft trilinear scalar couplings (the A couplings) are proportional to the Yukawa couplings. The first class is typically restricted to the kind of model described in [2] (with SUSY breaking on the TeV-brane) while the third class has a SUSY breaking mechanism deeply related to BC. We will show that the second type of SUSY breaking allows to develop tests for distinguishing between pure SUSY and warped SUSY at colliders.

9.2.2 4D scalar couplings

In this section, we derive the 4D effective couplings of the brane-Higgs boson to two scalar superpartners (of type squark/slepton) in the RS SUSY framework, as well as the 4D Higgs self couplings.

Scalar Yukawa couplings to two Higgs bosons

In this first subsection, we calculate the 4D Yukawa-type coupling of a scalar field (e.g. ϕ_R) to an Higgs boson (of $\phi_{H_u^0}$ type, as an illustrative example) within our simple U(1) model defined in Appendix G.1 corresponding the superfield action given in Appendix G.2.

The obtained scalar Yukawa couplings are included in the following term of Eq.(G.26) in terms of the 5D fields,

$$\mathcal{L}_{5D} = -\sqrt{G}\left|\mathcal{Y}\delta(y-\pi R_c)\phi_{H_u^0}\phi_R - [\partial_y - (c_L + \frac{3}{2})(\partial_y\sigma)]\phi_L^c\right|^2 . \tag{9.4}$$

Developing over the KK decomposition (H.11) and integrating over the fifth dimension, the first

squared term gives rise to the 4D scalar Yukawa coupling (after field redefinition),

$$\begin{aligned}\frac{\delta^4 i\mathcal{L}_{4D}}{\delta\phi_{H_u^0}\bar{\phi}_{H_u^0}\phi_R^{(n)}\bar{\phi}_R^{(m)}} &= -i|\mathcal{Y}|^2\int_{-\pi R_c}^{\pi R_c} dy\delta^2(y-\pi R_c)\bar{f}_m^{++}(c_R;y)f_n^{++}(c_R;y)\\ &= -i|\mathcal{Y}|^2\delta(0)\bar{f}_m^{++}(c_R;\pi R_c)f_n^{++}(c_R;\pi R_c),\end{aligned} \tag{9.5}$$

whose corresponding diagram is drawn in Fig.(9.1).

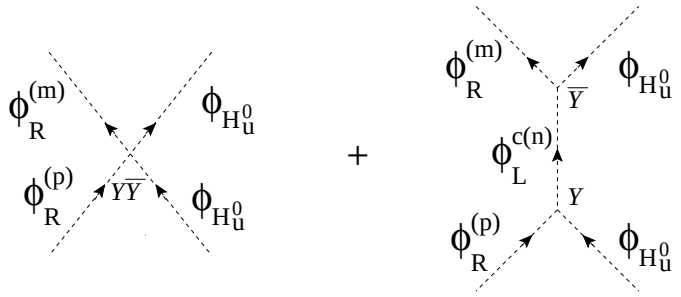

Figure 9.1: Feynman diagrams of the contributions to the 4D effective scalar Yukawa coupling $\frac{\delta^4\mathcal{L}_{4D}}{\delta\phi_{H_u^0}\bar{\phi}_{H_u^0}\phi_R^{(p)}\bar{\phi}_R^{(m)}}$. The second indirect contribution is induced by the exchange of the KK tower of $(--)$ scalar superpartners $\phi_L^{c(n)}$. The relevant coupling constants are described in details in text.

It turns out that the crossed products in Eq.(9.4) also bring a contribution to the 4D effective scalar Yukawa coupling, as we explain now; the crossed terms read as

$$\sqrt{G}\delta(y-\pi R_c)\left[\mathcal{Y}\phi_{H_u^0}\phi_R[\partial_y-(c_L+\frac{3}{2})(\partial_y\sigma)]\bar{\phi}_L^c+\bar{\mathcal{Y}}\bar{\phi}_{H_u^0}\bar{\phi}_R[\partial_y-(c_L+\frac{3}{2})(\partial_y\sigma)]\phi_L^c\right]\in\mathcal{L}_{5D}. \tag{9.6}$$

Combining the KK decomposition (H.12) of the 5D field ϕ_L^c together with the relation (H.16), which originates from the equation of motion, leads to

$$\begin{aligned}[\partial_y-(c_L+\frac{3}{2})(\partial_y\sigma)]\phi_L^c(x^\mu,y) &= \sum_{n=1}^{\infty}\phi_L^{c(n)}(x^\mu)[\partial_y-(c_L+\frac{3}{2})(\partial_y\sigma)]f_n^{--}(c_L;y)\\ &= -e^\sigma\sum_{n=1}^{\infty}m_L^{(n)}\phi_L^{c(n)}(x^\mu)f_n^{++}(c_L;y),\end{aligned} \tag{9.7}$$

$m_L^{(n)}$ being the nth KK scalar mass. Using this relation in Eq.(9.6) and developing ϕ_R over its KK tower gives the 4D couplings (taking into account field redefinitions):

$$\begin{aligned}-\Big[\quad &\mathcal{Y}\phi_{H_u^0}\sum_{m=0,n=1}^{\infty}m_L^{(n)}f_m^{++}(c_R;\pi R_c)\bar{f}_n^{++}(c_L;\pi R_c)\phi_R^{(m)}\bar{\phi}_L^{c(n)} \quad +\\ &\bar{\mathcal{Y}}\bar{\phi}_{H_u^0}\sum_{m=0,n=1}^{\infty}m_L^{(n)}\bar{f}_m^{++}(c_R;\pi R_c)f_n^{++}(c_L;\pi R_c)\bar{\phi}_R^{(m)}\phi_L^{c(n)}\quad\Big]\in\mathcal{L}_{4D}.\end{aligned} \tag{9.8}$$

These two types of 4D coupling to KK modes give rise to new contributions to scalar Yukawa couplings through the exchange of the KK tower states $\phi_L^{c(n)}$, as exhibits the second Feynman diagram of Fig.(9.1) [10]. The resulting new contributions to 4D scalar Yukawa couplings are given in the following, taking real wave functions,

$$\left.\frac{\delta^4 i\mathcal{L}_{4D}}{\delta\phi_{H_u^0}\bar{\phi}_{H_u^0}\phi_R^{(p)}\bar{\phi}_R^{(m)}}\right|_{indirect} = -|\mathcal{Y}|^2\sum_{n\geq 1}\frac{i\ m_L^{(n)2}}{k^2-m_L^{(n)2}}f_p^{++}(c_R;\pi R_c)f_m^{++}(c_R;\pi R_c)\left(f_n^{++}(c_L;\pi R_c)\right)^2 \tag{9.9}$$

k^μ being the $\phi_L^{c(n)}$ four-momentum. These couplings can be rewritten as follows, according to the completeness relation of Eq.(H.2) together with the 5D propagator definition $[G_5^f(k^2;y,y')]$ from Appendix I,

$$\begin{aligned}
&\left.\frac{\delta^4 i\mathcal{L}_{4D}}{\delta\phi_{H_u^0}\bar{\phi}_{H_u^0}\phi_R^{(p)}\bar{\phi}_R^{(m)}}\right|_{indirect}\\
=\ & -i|\mathcal{Y}|^2\sum_{n\geq 0}\left\{\frac{k^2}{k^2-m_L^{(n)2}}-1\right\}f_p^{++}(c_R;\pi R_c)f_m^{++}(c_R;\pi R_c)\left(f_n^{++}(c_L;\pi R_c)\right)^2\\
=\ & -i|\mathcal{Y}|^2 f_p^{++}(c_R;\pi R_c)f_m^{++}(c_R;\pi R_c)k^2 G_5^{f^{++}(c_L)}(k^2;\pi R_c,\pi R_c)\\
& +i|\mathcal{Y}|^2\delta(0)f_p^{++}(c_R;\pi R_c)f_m^{++}(c_R;\pi R_c)\\
=\ & i|\mathcal{Y}|^2 f_p^{++}(c_R;\pi R_c)f_m^{++}(c_R;\pi R_c)[\delta(0)-k^2 G_5^{f^{++}(c_L)}(k^2;\pi R_c,\pi R_c)].
\end{aligned} \tag{9.10}$$

Summing the two contributions, from Eq.(9.5) and Eq.(9.10), the divergent $\delta(0)$ terms cancel each other, and we obtain the 4D effective scalar Yukawa couplings:

$$\left.\frac{\delta^4 i\mathcal{L}_{4D}}{\delta\phi_{H_u^0}\bar{\phi}_{H_u^0}\phi_R^{(p)}\bar{\phi}_R^{(m)}}\right|_{total} = -i|\mathcal{Y}|^2 f_p^{++}(c_R;\pi R_c)f_m^{++}(c_R;\pi R_c)k^2 G_5^{f^{++}(c_L)}(k^2;\pi R_c,\pi R_c). \tag{9.11}$$

Hence, starting from couplings in a 5D SUSY theory, we have derived consistent 4D effective couplings. More precisely, at this level the Lagrangian of Eq.(9.11) given for any energy k^2 still describes a real 5D SUSY theory (the KK sum in $G_5^{f^{++}(c_L)}(k^2;\pi R_c,\pi R_c)$ is infinite) but its form is given from a 4D point of view (4D fields are used).

An interesting check of Eq.(9.11) is the following one. In the low–energy limit, $k^2 \ll m_L^{(n)2}$ $(n\geq 1)$, only the zero-mode in the 5D propagator survives at zero*th* order, so that the superpartner

[10] Note that the $\phi_L^{c(n)}$ fields, whose presence reflects the vectorial aspect of the 5D theory (like for the $\Sigma^{(n)}$ fields), enter indirectly – via some exchanges – the couplings in the 4D chiral Lagrangian.

coupling above simplifies to [11]:

$$\left.\frac{\delta^4 i\mathcal{L}_{4D}}{\delta\phi_{H_u^0}\bar{\phi}_{H_u^0}\phi_R^{(0)}\bar{\phi}_R^{(0)}}\right|_{total} \to -i|\mathcal{Y}|^2\left(f_0^{++}(c_R;\pi R_c)f_0^{++}(c_L;\pi R_c)\right)^2 = -i\ |\mathcal{Y}_{4D}|^2 \tag{9.12}$$

i.e. exactly the squared $\mathcal{Y}_{4D}$ Yukawa coupling of associated fermion zero-modes (with a brane-Higgs) [46], as one expects in a pure 4D SUSY theory (where all KK states decouple).

D-term couplings to two Higgs bosons

Now, we derive the 4D couplings, issued from D-terms, of scalar fields (continuing on the ϕ_R example) to the two $\phi_{H_u^0}$ bosons in the U(1) model of Appendices G.1 and G.2.

The obtained D-term couplings of ϕ_R, in terms of 5D fields, are included in Eq.(G.26):

$$\mathcal{L}_{5D} = -\frac{\sqrt{G}}{2}\left|[\partial_y - 2(\partial_y\sigma)]\Sigma - g\Big(q_R\Delta_{\phi_R} + q_{H_u^0}\phi_{H_u^0}\bar{\phi}_{H_u^0}\delta(y-\pi R_c)\Big)\right|^2. \tag{9.13}$$

The 4D effective D-term couplings are deduced from the above 5D Lagrangian (taking real gauge coupling constants):

$$\begin{aligned}\frac{\delta^4 i\mathcal{L}_{4D}}{\delta\phi_{H_u^0}\bar{\phi}_{H_u^0}\phi_R^{(n)}\bar{\phi}_R^{(m)}} &= -iq_{H_u^0}q_R|g|^2\int_{-\pi R_c}^{\pi R_c} dy\delta(y-\pi R_c)\bar{f}_m^{++}(c_R;y)f_n^{++}(c_R;y)\\ &= -iq_{H_u^0}q_R|g|^2\bar{f}_m^{++}(c_R;\pi R_c)f_n^{++}(c_R;\pi R_c).\end{aligned} \tag{9.14}$$

As for the Yukawa couplings, there are additional contributions to the 4D effective D-term couplings. Indeed, other couplings arising from Eq.(9.13) are

$$\sqrt{G}g(q_R\bar{\phi}_R\phi_R + q_{H_u^0}\bar{\phi}_{H_u^0}\phi_{H_u^0}\delta(y-\pi R_c))[\partial_y - 2(\partial_y\sigma)]\Sigma + h.c. \in \mathcal{L}_{5D}. \tag{9.15}$$

The KK decomposition of the 5D field Σ in Eq.(H.4) together with the relation (H.7) allow to write

$$[\partial_y - 2(\partial_y\sigma)]\Sigma(x^\mu,y) = \sum_{n=1}^{\infty}\Sigma^{(n)}(x^\mu)[\partial_y - 2(\partial_y\sigma)]g_n^{--}(y) = -e^{2\sigma}\sum_{n=1}^{\infty}M^{(n)}\Sigma^{(n)}(x^\mu)g_n^{++}(y) \tag{9.16}$$

$M^{(n)}$ being the nth KK gauge boson mass. Inserting this relation in Eq.(9.15) and developing ϕ_R

[11] The 5D Yukawa coupling constant $\mathcal{Y}$ has dimension -1 in energy for the simplified scheme with $\hbar = c = 1$, while $\mathcal{Y}_{4D}$ is dimensionless.

over its KK tower gives the 4D couplings for the redefined fields:

$$-q_R g \sum_{m,p=0;n=1}^{\infty} M^{(n)} \bar{\phi}_R^{(m)} \phi_R^{(p)} \Sigma^{(n)} \mathcal{F}_R^{mnp}$$
$$-q_{H_u^0} g \bar{\phi}_{H_u^0} \phi_{H_u^0} \sum_{n=1}^{\infty} M^{(n)} \Sigma^{(n)} g_n^{++}(\pi R_c) + h.c. \in \mathcal{L}_{4D} \tag{9.17}$$

with $\mathcal{F}_R^{mnp} = \int_{-\pi R_c}^{\pi R_c} dy \bar{f}_m^{++}(c_R; y) g_n^{++}(y) f_p^{++}(c_R; y)$. These 4D couplings induce new contributions to the D-term couplings via the exchange of the KK modes $\Sigma^{(n)}$, as shown in Fig.(9.2). These contributions read as,

$$\left. \frac{\delta^4 i\mathcal{L}_{4D}}{\delta\phi_{H_u^0}\bar{\phi}_{H_u^0}\phi_R^{(p)}\bar{\phi}_R^{(m)}} \right|_{indirect} = -q_R q_{H_u^0} |g|^2 \sum_{n\geq 1} \frac{i}{k^2 - M^{(n)2}} M^{(n)2} \mathcal{F}_R^{mnp} g_n^{++}(\pi R_c) \tag{9.18}$$

k^μ being the $\Sigma^{(n)}$ four-momentum. Let us rewrite these couplings with the help of the completeness relation (H.2) and 5D propagator,

$$\begin{aligned} \left. \frac{\delta^4 i\mathcal{L}_{4D}}{\delta\phi_{H_u^0}\bar{\phi}_{H_u^0}\phi_R^{(p)}\bar{\phi}_R^{(m)}} \right|_{indirect} &= -iq_R q_{H_u^0} |g|^2 \sum_{n\geq 0} \left\{ \frac{k^2}{k^2 - M^{(n)2}} - 1 \right\} \mathcal{F}_R^{mnp} g_n^{++}(\pi R_c) \\ &= -iq_R q_{H_u^0} |g|^2 \int_{-\pi R_c}^{\pi R_c} dy \bar{f}_m^{++}(c_R; y) f_p^{++}(c_R; y) k^2 G_5^{g^{++}}(k^2; y, \pi R_c) \\ &\quad + iq_R q_{H_u^0} |g|^2 f_m^{++}(c_R; \pi R_c) f_p^{++}(c_R; \pi R_c). \end{aligned} \tag{9.19}$$

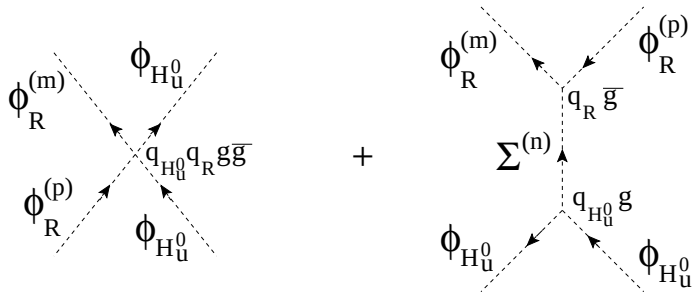

Figure 9.2: Feynman diagrams of the contributions to the 4D effective scalar gauge coupling $\frac{\delta^4 \mathcal{L}_{4D}}{\delta\phi_{H_u^0}\bar{\phi}_{H_u^0}\phi_R^{(p)}\bar{\phi}_R^{(m)}}$. The second indirect contribution is induced by the exchange of the KK tower of $(--)$ scalar modes $\Sigma^{(n)}$. The relevant coupling constants are described in details in text.

Then, the complete 4D couplings are of course obtained by summing the two contributions

(9.14) and (9.19),

$$\frac{\delta^4 i\mathcal{L}_{4D}}{\delta\phi_{H_u^0}\bar{\phi}_{H_u^0}\phi_R^{(p)}\bar{\phi}_R^{(m)}}\Big|_{total} = -iq_R q_{H_u^0}|g|^2 \int_{-\pi R_c}^{\pi R_c} dy \bar{f}_m^{++}(c_R;y) f_p^{++}(c_R;y) k^2 G_5^{g^{++}}(k^2;y,\pi R_c) \quad (9.20)$$

having taken into account the canceling terms. Once more, starting from couplings in a 5D SUSY theory, we have derived consistent 4D effective couplings; the Lagrangian (9.20) corresponds to a real 5D SUSY theory but written from the 4D point of view.

We finish this part by making the same check as in previous subsection. In the low–energy limit, $k^2 \ll M^{(n)2}$ $(n \geq 1)$, only the zero-mode in the 5D propagator survives at zero*th* order, so that the superpartner couplings (9.20) simplify to

$$\frac{\delta^4 i\mathcal{L}_{4D}}{\delta\phi_{H_u^0}\bar{\phi}_{H_u^0}\phi_R^{(0)}\bar{\phi}_R^{(0)}}\Big|_{total} \to -i\ q_R q_{H_u^0}\frac{|g|^2}{2\pi R_c} = -i\ q_R q_{H_u^0}|g_{4D}|^2 \quad (9.21)$$

since the gauge boson zero-mode profile encoded in $g_0^{++}(y) = 1/\sqrt{2\pi R_c}$ is flat along the fifth dimension. Thus the couplings in this limiting case correspond rigorously to the dimensionless $-iq_R q_{H_u^0}|g_{4D}|^2$ gauge coupling product of associated fermions, as expected in a pure 4D SUSY theory.

Comments on the obtained 4D couplings to Higgs bosons

It is interesting to note that in order to obtain the 4D effective couplings to two Higgs bosons [Yukawa couplings and D-terms] which are consistent (i.e. without the $\delta(0)$ divergences and recovering the 4D SUSY couplings in the limit $k^2 \ll m^{(n)2}, M^{(n)2}$), we had to use the completeness relation which relies on an infinite sum over the KK levels. The reason is that these couplings belong to the 4D effective Lagrangian of a fundamental 5D SUSY theory – the infinite KK tower reflects this 5D aspect.

Besides, no truncating cut-off must be applied when implementing the completeness relation (for the sum not involving KK masses in Eq.(9.10) and Eq.(9.19)), otherwise the consistent 4D effective couplings cannot be obtained while there is no reason why a non-renormalizable theory – as we are considering here – could not possess a 4D description. The reason for not applying a cut-off (due to the non-renormalizable aspect of the 5D SUSY theory) is that in Eq.(9.5)-(9.10) and Eq.(9.14)-(9.19) one is integrating the fifth dimension and summing *all* the exchanged heavy KK states to get an effective 4D vision of the *5D theory*. Only once the 4D effective couplings are obtained so that the 4D description is completed, the cut-off must be put, e.g. in Eq.(9.11) [on $G_5^{f^{++}(c_L)}(k^2;\pi R_c,\pi R_c)$], to take into account the non-renormalizable aspect of the 5D SUSY theory.

Final single couplings to the Higgs boson H

In this part, we deduce from the last three subsections the total 4D effective scalar couplings to the single Higgs boson H in the more realistic framework where the gauge symmetry group is as in the SM (EWSB has occurred) and the superfield content is extended to the pMSSM one. In particular, this framework is based on the coexistence of two complex Higgs $\mathrm{SU(2)_L}$ doublets H_u, H_d of superfields with opposite hypercharges ($Y_{H_u} = -Y_{H_d} = +1$) which guarantees the absence of chiral anomalies originating from triangular fermionic loops. The five scalar degrees of freedom, not absorbed in the longitudinal polarizations of the massive gauge bosons, constitute the five physical Higgs bosons: two CP-even neutral Higgs fields h (the lightest one) and H, one pseudo-scalar A boson and one pair of charged scalar particles $H^{\pm}$. We will give explicitly the H couplings in the RS SUSY framework, and similar couplings hold for the other Higgs fields. All Higgs bosons are assumed to be stuck on the TeV-brane.
We will focus on the top quark (t) superpartner couplings to H as an illustrative example, since the couplings of other scalar superpartners are analog. The nth KK level modes of the stop fields are denoted $\tilde{t}_L^{(n)}$ and $\tilde{t}_R^{(n)}$ respectively for the superpartners of the Left-handed (t_L) and Right-handed (t_R) top quarks. $\tilde{t}_L^{(n)}$ and $\tilde{t}_R^{(n)}$ are similar to the 4D (++) scalar fields $\phi_L^{(n)}$ and $\phi_R^{(n)}$ defined in Eq.(G.3), Eq.(G.6) and Eq.(H.11) for the U(1) model, except of course with respect to the gauge quantum numbers. In the interaction basis $\{\tilde{t}_L^{(0)}, \tilde{t}_R^{(0)}, \tilde{t}_L^{(1)}, \tilde{t}_R^{(1)}\}$ (generalization to higher KK states is straightforward), the stop-stop couplings to a single H boson appearing after EWSB are encoded in the matrix [in our notations H denotes the scalar field]:

$$i\,\mathcal{C}_{H\tilde{t}\tilde{t}} \equiv\ |\mathcal{Y}|^2 \sin\alpha\ v_u\ \times$$

$$\begin{pmatrix} (f_L^0)^2\, k^2\, G_5^{f^{++}(c_{\tilde{t}_R})}(k^2;\pi R_c,\pi R_c) & 0 & f_L^0 f_L^1 (f_R^0)^2 & 0 \\ 0 & (f_R^0)^2\, k^2\, G_5^{f^{++}(c_{\tilde{t}_L})}(k^2;\pi R_c,\pi R_c) & 0 & f_R^0 f_R^1 (f_L^0)^2 \\ f_L^0 f_L^1 (f_R^0)^2 & 0 & (f_L^1 f_R^0)^2 & 0 \\ 0 & f_R^0 f_R^1 (f_L^0)^2 & 0 & (f_L^0 f_R^1)^2 \end{pmatrix}$$

$$-\ \frac{\mathcal{Y}\cos\alpha\ \mu_{eff}}{\sqrt{2}} \begin{pmatrix} 0 & f_L^0 f_R^0 & 0 & f_L^0 f_R^1 \\ f_L^0 f_R^0 & 0 & f_L^1 f_R^0 & 0 \\ 0 & f_L^1 f_R^0 & 0 & f_L^1 f_R^1 \\ f_L^0 f_R^1 & 0 & f_L^1 f_R^1 & 0 \end{pmatrix} \ +\ g_Z^2\ \pi R_c\ \cos(\alpha+\beta)\ v\ \times$$

$$\begin{pmatrix} Q_Z^{t_L} \int dy f_L^0(y)^2\, k^2\, G_5^{g^{++}}(k^2;y,\pi R_c) & 0 & 0 & 0 \\ 0 & -Q_Z^{t_R} \int dy f_R^0(y)^2\, k^2\, G_5^{g^{++}}(k^2;y,\pi R_c) & 0 & 0 \\ 0 & 0 & Q_Z^{t_L}/2\pi R_c & 0 \\ 0 & 0 & 0 & -Q_Z^{t_R}/2\pi R_c \end{pmatrix}$$

$$+\frac{Ae^{-k\pi R_c}\sin\alpha}{\sqrt{2}}\begin{pmatrix} 0 & f_L^0 f_R^0 & 0 & f_L^0 f_R^1 \\ f_L^0 f_R^0 & 0 & f_L^1 f_R^0 & 0 \\ 0 & f_L^1 f_R^0 & 0 & f_L^1 f_R^1 \\ f_L^0 f_R^1 & 0 & f_L^1 f_R^1 & 0 \end{pmatrix}, \tag{9.22}$$

where we have used the compact notation e.g. $f^n_{L/R} = f^{++}_n(c_{\tilde{t}_{L/R}}; \pi R_c)$. Besides, based on the 5D superpotential of Eq.(G.12) and on the deduced field Lagrangian in Eq.(G.28), the 4D effective μ parameter appearing above reads as (after field redefinition and inclusion of the metric warp factor):

$$\mu_{eff} = \mu e^{-k\pi R_c} \sim k e^{-k\pi R_c} \sim \text{TeV}. \tag{9.23}$$

No $\delta(0)$ factors appear after integration over y. The soft trilinear scalar coupling constant in Eq.(9.22) is taken at $A \sim 1$ to avoid the introduction of a new scale in the bulk. This 4D effective coupling matrix is deduced from Eq.(9.11) for the Yukawa couplings and from Eq.(9.20) for the D-term couplings (where the effects of the $(--)$ KK towers of $\phi^c_{L/R}$ and Σ type fields, as defined in Eq.(G.5)-(G.7) and Eq.(G.9), have been taken into account). This coupling matrix, that will be taken at the energy $k^2 = m_H^2$ (for the Z coupling constant $g_Z = g_{4D}/\cos\theta_W$ and top charges to the Z gauge boson: $Q_Z^{t_{L/R}} = I_{3L}^{t_{L/R}} - Q_{e.m.}^{t_{L/R}} \sin^2\theta_W$), can be easily generalized e.g. to sbottoms.

Let us comment more precisely on the 5D effects. The Higgs mixing between $\phi_{H_d^0}$ and $\phi_{H_u^0}$ into the mass eigenstates h and H is parametrized by the mixing angle noted here, as usually, α [30]. $\sin\alpha$, which enters the above coupling matrix, receives some corrections in the present 5D framework, as the $|\phi_{H_u^0}|^2|\phi_{H_d^0}|^2$ and $|\phi_{H^0_{u,d}}|^4$ couplings do so (see next subsection).
Moreover, the stop-stop-Higgs couplings are affected by the mixing between the stops and their KK $(++)$ excitations. The $H\tilde{t}_i\tilde{t}_j$ couplings, where $\tilde{t}_i$ $[i = 1, \ldots, 4]$ are the stop mass eigenstates, are obtained after transformation from the basis $\{\tilde{t}_L^{(0)}, \tilde{t}_R^{(0)}, \tilde{t}_L^{(1)}, \tilde{t}_R^{(1)}\}$ to the stop mass basis (rotation matrices being obtained from diagonalizing the stop mass matrix given later).
The third effect is the exchange of KK $(--)$ modes, encoded in the 5D propagators G_5 appearing in the matrix (9.22). Such KK $(--)$ contributions to couplings between H and KK stops would represent higher-order corrections to the $H\bar{\tilde{t}}^{(0)}_{L/R}\tilde{t}^{(0)}_{L/R}$ couplings and are thus not written in matrix (9.22).
All these heavy KK mixing and KK exchange effects will not be computed numerically as they are sub-leading compared to other direct 5D effects in the structure of zero-mode $H\bar{\tilde{f}}^{(0)}_{L/R}\tilde{f}^{(0)}_{L/R}$ couplings ($\tilde{f} \equiv$ sfermion), that will be studied in details in Section 9.3.3.

Self couplings of the Higgs boson

Finally, we derive the non-trivial 4D quartic couplings e.g. of the Higgs boson $\phi_{H_u^0}$, still within the context of the toy model defined in Appendix G. A totally similar study could be made for

the $\phi_{H_u^0}\bar{\phi}_{H_u^0}\phi_{H_d^0}\bar{\phi}_{H_d^0}$ couplings (without combinatorial factor neither the additional $\Sigma^{(n)}$ exchange in the t-channel discussed below).

As above we start from the 5D couplings included in Eq.(G.26):

$$\mathcal{L}_{5D} = -\frac{\sqrt{G}}{2}\left|[\partial_y - 2(\partial_y\sigma)]\Sigma - g\Big(q_{H_u^0}\phi_{H_u^0}\bar{\phi}_{H_u^0}\delta(y-\pi R_c)\Big)\right|^2. \tag{9.24}$$

The 4D quartic couplings directly deduced from this Lagrangian are:

$$\frac{\delta^4 i\mathcal{L}_{4D}}{\delta\phi^2_{H_u^0}\bar{\phi}^2_{H_u^0}} = -\frac{i}{2}q^2_{H_u^0}|g|^2\delta(0)\times 4. \tag{9.25}$$

We have included the combinatorial factor 4 as we consider a process rather than a coupling here since Eq.(9.25) will be combined with other contributions.

Indeed, here again, there exist additional contributions to the 4D couplings as Eq.(9.24) also induces the $\phi_{H_u^0}$ couplings of Eq.(9.15) and in turn of Eq.(9.17). These later 4D couplings induce the two following new contributions to the quartic terms, via two possible exchanges of the KK $\Sigma^{(n)}$ [see Fig.(9.3)],

$$\begin{aligned}\left.\frac{\delta^4 i\mathcal{L}_{4D}}{\delta\phi^2_{H_u^0}\bar{\phi}^2_{H_u^0}}\right|_{indirect} = &- q^2_{H_u^0}|g|^2\sum_{n\geq 1}\frac{i}{k^2-M^{(n)2}}M^{(n)2}\Big(g_n^{++}(\pi R_c)\Big)^2 \\ &- q^2_{H_u^0}|g|^2\sum_{m\geq 1}\frac{i}{q^2-M^{(m)2}}M^{(m)2}\Big(g_m^{++}(\pi R_c)\Big)^2\end{aligned} \tag{9.26}$$

k^μ being the $\Sigma^{(n)}$ four-momentum in the s-channel while q^μ represents the $\Sigma^{(n)}$ momentum in the t-channel. Rewriting these couplings with the completeness relation in mind gives,

$$\begin{aligned}&\left.\frac{\delta^4 i\mathcal{L}_{4D}}{\delta\phi^2_{H_u^0}\bar{\phi}^2_{H_u^0}}\right|_{indirect} \\ =\ & -iq^2_{H_u^0}|g|^2\sum_{n\geq 0}\left\{\frac{k^2}{k^2-M^{(n)2}}-1\right\}\Big(g_n^{++}(\pi R_c)\Big)^2 - iq^2_{H_u^0}|g|^2\sum_{m\geq 0}\left\{\frac{q^2}{q^2-M^{(m)2}}-1\right\}\Big(g_m^{++}(\pi R_c)\Big)^2 \\ =\ & iq^2_{H_u^0}|g|^2[2\delta(0) - k^2G_5^{g^{++}}(k^2;\pi R_c,\pi R_c) - q^2G_5^{g^{++}}(q^2;\pi R_c,\pi R_c)].\end{aligned} \tag{9.27}$$

Adding the contributions (9.25) and (9.27) gives the complete 4D quartic terms:

$$\left.\frac{\delta^4 i\mathcal{L}_{4D}}{\delta\phi^2_{H_u^0}\bar{\phi}^2_{H_u^0}}\right|_{total} = -iq^2_{H_u^0}|g|^2k^2G_5^{g^{++}}(k^2;\pi R_c,\pi R_c) - iq^2_{H_u^0}|g|^2q^2G_5^{g^{++}}(q^2;\pi R_c,\pi R_c). \tag{9.28}$$

Note the cancellation of $\delta(0)$ terms which leads to consistent 4D effective couplings.

In the check of the low–energy limit, $k^2, q^2 \ll M^{(n)2}$ $[n\neq 0]$, the Higgs coupling (9.28) is reduced

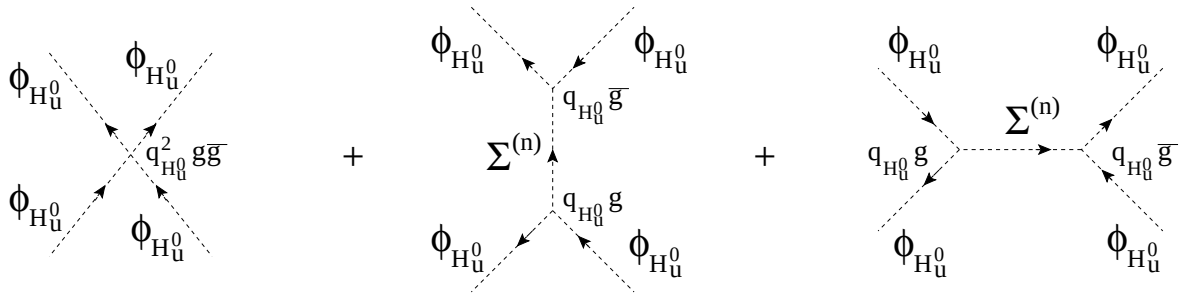

Figure 9.3: Feynman diagrams of the contributions to the 4D effective self scalar gauge coupling $\frac{\delta^4 \mathcal{L}_{4D}}{\delta \phi^2_{H_u^0} \bar{\phi}^2_{H_u^0}}$. The second and third indirect contributions are induced by the exchanges of the KK tower of $(--)$ scalar modes $\Sigma^{(n)}$ in the s-channel and t-channel, respectively (the choice of calling 's-channel' or 't-channel' a given diagram depends on which final state is considered). The relevant coupling constants are described in details in text.

to the following form (the combinatorial factor 4 is taken off to get the pure quartic Lagrangian coupling),

$$\left.\frac{\delta^4 i\mathcal{L}_{4D}}{\delta\phi^2_{H_u^0}\bar{\phi}^2_{H_u^0}}\right|_{total} \to -\frac{i}{2} q^2_{H_u^0} \frac{|g|^2}{2\pi R_c} = -\frac{i}{2}\, q^2_{H_u^0} |g_{4D}|^2 \tag{9.29}$$

recalling that $g_0^{++}(y) = 1/\sqrt{2\pi R_c}$. The quartic Higgs coupling in this limit corresponds thus well to the exact squared gauge coupling expected in a pure 4D SUSY theory.

For completeness (and it will prove to be useful for the following), we give the result for the $\phi_{H_u^0}\bar{\phi}_{H_u^0}\phi_{H_d^0}\bar{\phi}_{H_d^0}$ coupling, obtained through the same method,

$$\left.\frac{\delta^4 i\mathcal{L}_{4D}}{\delta\phi_{H_u^0}\bar{\phi}_{H_u^0}\phi_{H_d^0}\bar{\phi}_{H_d^0}}\right|_{total} = -i q_{H_u^0} q_{H_d^0} |g|^2 k^2 G_5^{g^{++}}(k^2; \pi R_c, \pi R_c). \tag{9.30}$$

This coupling is obtained from the two contributions drawn in Fig.(9.4).

9.2.3 Scalar mass matrix

We now calculate the 4D effective mass matrix for sfermions induced by brane-Higgs bosons within RS SUSY. One must develop different methods than in the above approach of 4D Higgs couplings.

Effect of the ϕ^c KK tower on $\phi^{(0)}$ masses through mixing

In this subsection, we derive the 4D masses coming from Yukawa interactions for the ϕ_R scalar field [the same analysis can be done for ϕ_L] in the toy model of Appendices G.1 and G.2, assuming that the $\phi_{H_u^0}$ boson acquires a VEV $v_u = \sqrt{2}\langle\phi_{H_u^0}\rangle \sim 10^2$ GeV.

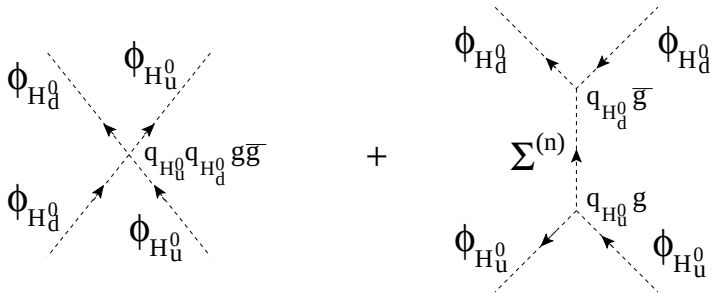

Figure 9.4: Feynman diagrams of the contributions to the 4D effective scalar gauge coupling $\frac{\delta^4 i\mathcal{L}_{4D}}{\delta\phi_{H_u^0}\bar{\phi}_{H_u^0}\phi_{H_d^0}\bar{\phi}_{H_d^0}}$. The second indirect contribution is induced by the exchange of the KK tower of $(--)$ scalar modes $\Sigma^{(n)}$.

In addition to the $\bar{\phi}_R^{(0)}\phi_R^{(0)}$ mass, proportional to $(\mathcal{Y}v_u)^2$, which is obtained directly from the Lagrangian (G.26), the exchanges of the KK modes $\phi_L^{c(n)}$ also contribute to this mass as illustrates Fig.(9.1) in the case where $\phi_{H_u^0}$ acquires a VEV. In order to compute the whole zero-mode mass, one needs to estimate the mixing between $\phi_R^{(0)}$ and $\phi_L^{c(n)}$, a mixing induced by the VEV at the origin of the additional contributions as shows Fig.(9.1) – analogously to the mixing with the heavy Majorana neutrino in the type I See-saw model [47]. For that purpose, we write down the complete 4D mass matrix in the infinite basis $\vec{\phi} = (\phi_R^{(0)}, \phi_L^{c(1)}, \phi_L^{c(2)}, \dots)$ and search for the smallest eigenvalue. Indeed, the lightest eigenstate is typically mainly composed by the $\phi_R^{(0)}$ state, given usually the realistic KK $\phi_L^{c(n)}$ masses which are around a few TeV at least and hence much larger than the VEV-induced $\phi_R^{(0)}$ mass. From Lagrangian (G.26), this 4D mass matrix reads as $-\vec{\bar{\phi}}\mathcal{M}_{RR}^2\vec{\phi}^t \in \mathcal{L}_{4D}$ with [12]

$$\mathcal{M}_{RR}^2 =$$

$$\begin{pmatrix} \mathcal{Y}^2\hat{v}_u^2\int dy\delta^2 f_R^0(y)^2 & \mathcal{Y}\hat{v}_u m_L^{(1)}\int dy'\delta f_R^0(y')f_L^1(y') & \mathcal{Y}\hat{v}_u m_L^{(2)}\int dy'\delta f_R^0(y')f_L^2(y') & \dots \\ \mathcal{Y}\hat{v}_u m_L^{(1)}\int dy'\delta f_R^0(y')f_L^1(y') & m_L^{(1)2} & 0 & \dots \\ \mathcal{Y}\hat{v}_u m_L^{(2)}\int dy'\delta f_R^0(y')f_L^2(y') & 0 & m_L^{(2)2} & \dots \\ \vdots & \vdots & \vdots & \ddots \end{pmatrix} \tag{9.31}$$

where we have used again the compact notation $f_{L/R}^n(y) = f_n^{++}(c_{L/R}; y)$, $f_{L/R}^{cn}(y) = f_n^{--}(c_{L/R}; y)$ and $\hat{v}_u = v_u/\sqrt{2}$, $\delta = \delta(y - \pi R_c)$. For writing the off-diagonal elements, we have made use of relation (H.16) which can be written in a compact form as $D_5' f_L^{c\,n}(y) = -m_L^{(n)} e^{\sigma} f_L^n(y)$ and then have redefined the scalar wave functions with e^{σ} factors as usual in RS.
The generalized characteristic equation, of which the (squared mass) eigenvalues m^2 are solutions,

[12] Note that taking purely real wave functions and Yukawa coupling constants simplifies the approach by avoiding a *bi*-diagonalization, as it renders the mass matrix fully real and symmetric.

reads as

$$\left(\mathcal{Y}^2\hat{v}_u^2\int dy\delta^2 f_R^0(y)^2 - m^2 - \sum_{n=1}^{\infty}\frac{[\mathcal{Y}\hat{v}_u m_L^{(n)}\int dy'\delta f_R^0(y')f_L^n(y')]^2}{m_L^{(n)2}-m^2}\right)\Pi_{n=1}^{\infty}(m_L^{(n)2}-m^2)=0. \quad (9.32)$$

As $m^2 = m_L^{(n)2}$ leads to divergences in the above equality, those are not solutions. Hence Eq.(9.32) simplifies to

$$\mathcal{Y}^2\hat{v}_u^2\int dy\delta^2 f_R^0(y)^2 - m^2 + \sum_{n=1}^{\infty}\frac{[\mathcal{Y}\hat{v}_u m_L^{(n)}\int dy'\delta f_R^0(y')f_L^n(y')]^2}{m^2-m_L^{(n)2}}=0. \quad (9.33)$$

Using here also the equality $m_L^{(n)2}/(m^2-m_L^{(n)2}) = -1 + m^2/(m^2-m_L^{(n)2})$ together with the completeness relation applied as $\sum_{n=0}^{\infty} f_L^n(y)f_L^n(y') = \delta(y-y')$, one can rewrite

$$\mathcal{Y}^2\hat{v}_u^2\delta(0)f_R^0(\pi R_c)^2 - m^2 - \mathcal{Y}^2\hat{v}_u^2 f_R^0(\pi R_c)^2\delta(0) + \mathcal{Y}^2\hat{v}_u^2 m^2 f_R^0(\pi R_c)^2 G_5^{f^{++}(c_L)}(m^2;\pi R_c,\pi R_c)=0$$

$$m^2\left(1-\mathcal{Y}^2\hat{v}_u^2 f_R^0(\pi R_c)^2 G_5^{f^{++}(c_L)}(m^2;\pi R_c,\pi R_c)\right)=0. \quad (9.34)$$

Since $m^2=0$ is not a physically acceptable solution,

$$m^2 = \frac{f_L^0(\pi R_c)^2}{\frac{1}{\mathcal{Y}^2\hat{v}_u^2 f_R^0(\pi R_c)^2} - \sum_{n=1}^{\infty}\frac{f_L^n(\pi R_c)^2}{m^2-m_L^{(n)2}}}. \quad (9.35)$$

The check at this level is that in the decoupling limit $m_L^{(n)}\to\infty$ for any $n\geq 1$, we recover the equality between the Yukawa mass for (zero-mode) fermions and their scalar superpartner, as expected in a 4D SUSY theory:

$$m^2 \to \mathcal{Y}^2\hat{v}_u^2 f_R^0(\pi R_c)^2 f_L^0(\pi R_c)^2 = \mathcal{Y}_{4D}^2\hat{v}_u^2 = m_{fermion}^2. \quad (9.36)$$

The divergence cancellation in Eq.(9.34) and this 4D SUSY limiting case confirm that our solution for the smallest eigenvalue will be consistent. This consistency is due to the infinite aspect of the $\phi_L^{c(n)}$ basis considered here, in analogy to the calculation of Yukawa couplings in Section 9.2.2. Now in the case (of realistic scenarios) where the eigenvalue of the lightest eigenstate $m_{lightest}^2$ is much smaller than $m_L^{(1)2}$, one obtains at leading order from Eq.(9.35):

$$m_{lightest}^2 \simeq \frac{f_L^0(\pi R_c)^2}{\frac{1}{\mathcal{Y}^2\hat{v}_u^2 f_R^0(\pi R_c)^2} + \sum_{n=1}^{\infty}\frac{f_L^n(\pi R_c)^2}{m_L^{(n)2}}}. \quad (9.37)$$

An eigenvalue m^2 much smaller than $m_L^{(1)2}$ can only be the smallest one since all the others are larger than $m_L^{(1)2}$. As a matter of fact, at leading order in $f_L^0(\pi R_c)^2/f_L^n(\pi R_c)^2$ for $n\geq 1$, Eq.(9.35)

can be rewritten as

$$m^2\Big(-\frac{1}{\mathcal{Y}^2\hat{v}_u^2 f_R^0(\pi R_c)^2}+\sum_{n=1}^{\infty}\frac{f_L^n(\pi R_c)^2}{m^2-m_L^{(n)2}}\Big)\simeq 0. \tag{9.38}$$

Here the solution $m^2\simeq 0$, at leading order in $f_L^0(\pi R_c)^2/f_L^n(\pi R_c)^2$, corresponds to the lightest solution (9.37). Concentrating on the other solutions, those satisfy

$$1=\mathcal{Y}^2\hat{v}_u^2 f_R^0(\pi R_c)^2\sum_{n=1}^{\infty}\frac{f_L^n(\pi R_c)^2}{m^2-m_L^{(n)2}}. \tag{9.39}$$

For this sum to be equal to unity, at least one of the terms must be positive, that is to say that $m^2-m_L^{(n)2}>0$ for at least one value of $n\geq 1$. Even if it occurs for $n=1$, one would obtain that $m^2>m_L^{(1)2}$ which means that all the solutions m^2 of Eq.(9.39) have to be larger than $m_L^{(1)2}$ at least. The above method was inspired from an higher-dimensional analysis performed in [48].

Effect of the Σ KK tower on $\phi^{(0)}$ masses through integration out

Let us calculate the 4D zero-mode masses due to SUSY D-terms for ϕ_L (to vary our examples), still in the context of Appendix G. There exist contributions from the exchange of the KK modes $\Sigma^{(n)}$ if $\phi_{H_u^0}$ acquires a VEV, as is illustrated in Fig.(9.2) replacing ϕ_R by ϕ_L. Such contributions to the $\bar{\phi}_L^{(0)}\phi_L^{(0)}$ mass are not arising from a mixing between $\phi_L^{(0)}$ and some KK excitations (as happens in previous subsection for Yukawa terms). These low-energy contributions must instead be calculated by integrating out the $\Sigma^{(n)}$ fields, exactly like the heavy triplet scalar is integrated out within the type II See-saw scenario [47]. Hence we derive here the complete $|\phi_{H_u^0}|^2\bar{\phi}_L^{(i)}\phi_L^{(j)}$ couplings induced by integrating out all the $\Sigma^{(n)}$ modes, which contribute to the $\bar{\phi}_L^{(0)}\phi_L^{(0)}$ mass after $\phi_{H_u^0}$ gets its VEV.

As we are going to concentrate on the explicit derivation of the various contributions to the $|\phi_{H_u^0}|^2\bar{\phi}_L^{(i)}\phi_L^{(j)}$ couplings, we will consider a Lagrangian part depending only on the fields $\phi_{H_u^0}$, ϕ_L and Σ. This Lagrangian is obtained from Eq.(G.28) and Eq.(G.30) in terms of the 5D fields:

$$-e^{4\sigma}\mathcal{L}_{5D}^{D-terms}=-\frac{e^{2\sigma}}{2}\partial_\mu\Sigma\partial^\mu\Sigma+\frac{1}{2}\Big|D_5^k\Sigma\Big|^2-g\Big(q_L\overline{\phi}_L\phi_L+q_{H_u^0}\delta\overline{\phi}_{H_u^0}\phi_{H_u^0}\Big)D_5^k\Sigma+g^2q_Lq_{H_u^0}|\phi_L\phi_{H_u^0}|^2\delta.$$

Using once more Eq.(9.16), replacing the 5D fields by their KK decomposition, redefining them with warp factors (to recover the canonical 4D kinetic terms) and applying the orthonormalization

condition (H.1), one gets the 4D Lagrangian

$$\mathcal{L}_{4D}^{D-terms} = \frac{1}{2}\sum_{n=1}^{\infty}\left|\partial_\mu \Sigma^{(n)}\right|^2 - \frac{1}{2}\sum_{n=1}^{\infty} M^{(n)2}\Sigma^{(n)2} - q_L g\sum_{i,j=0}^{\infty}\sum_{n=1}^{\infty}\mathcal{T}_L^{ijn} M^{(n)}\Sigma^{(n)}\overline{\phi}_L^{(i)}\phi_L^{(j)}$$
$$-q_{H_u^0} g\sum_{n=1}^{\infty} g_n^{++}(\pi R_c) M^{(n)}\Sigma^{(n)}\overline{\phi}_{H_u^0}\phi_{H_u^0} - q_L q_{H_u^0} g^2\sum_{i,j=0}^{\infty}\overline{\phi}_L^{(i)}\phi_L^{(j)} f_i^{++}(c_L;\pi R_c) f_j^{++}(c_L;\pi R_c)\overline{\phi}_{H_u^0}\phi_{H_u^0} \tag{9.40}$$

with $\mathcal{T}_L^{ijn} = \int_{-\pi R_c}^{\pi R_c} dy f_i^{++}(c_L;y) f_j^{++}(c_L;y) g_n^{++}(y)$.

The equation of motion for each field $\Sigma^{(n)}$ $(n \geq 1)$ is then given by,

$$-\left(\partial_\mu\partial^\mu + M^{(n)2}\right)\Sigma^{(n)} = q_L g\sum_{i,j=0}^{\infty}\mathcal{T}_L^{ijn} M^{(n)}\overline{\phi}_L^{(i)}\phi_L^{(j)} + q_{H_u^0} g g_n^{++}(\pi R_c) M^{(n)}\overline{\phi}_{H_u^0}\phi_{H_u^0}, \tag{9.41}$$

which can be rewritten at second order in $\partial_\mu\partial^\mu/M^{(n)2}$,

$$\Sigma^{(n)} \simeq -\frac{g}{M^{(n)}}\left[1 - \frac{\partial_\mu\partial^\mu}{M^{(n)2}} + \left\{\frac{\partial_\mu\partial^\mu}{M^{(n)2}}\right\}^2\right]\left(q_L\sum_{i,j=0}^{\infty}\mathcal{T}_L^{ijn}\overline{\phi}_L^{(i)}\phi_L^{(j)} + q_{H_u^0} g_n^{++}(\pi R_c)\overline{\phi}_{H_u^0}\phi_{H_u^0}\right). \tag{9.42}$$

Now we integrate out all the $\Sigma^{(n)}$ fields by inserting Eq.(9.42) into Eq.(9.40) which gives rise to the following terms in the Lagrangian, restricting ourselves to the first order in $\partial_\mu\partial^\mu/M^{(n)2}$,

$$\begin{aligned}
& q_{H_u^0} q_L g^2\sum_{n=1}^{\infty} g_n^{++}(\pi R_c)\overline{\phi}_{H_u^0}\phi_{H_u^0}\sum_{i,j=0}^{\infty}\mathcal{T}_L^{ijn}\overline{\phi}_L^{(i)}\phi_L^{(j)} \\
- \;& q_L q_{H_u^0} g^2\sum_{i,j=0}^{\infty}\overline{\phi}_L^{(i)}\phi_L^{(j)} f_i^{++}(c_L;\pi R_c) f_j^{++}(c_L;\pi R_c)\overline{\phi}_{H_u^0}\phi_{H_u^0} \\
+ \;& q_{H_u^0} q_L g^2\sum_{i,j=0;n=1}^{\infty} g_n^{++}(\pi R_c)\mathcal{T}_L^{ijn}\frac{\partial_\mu(\overline{\phi}_{H_u^0}\phi_{H_u^0})\partial^\mu(\overline{\phi}_L^{(i)}\phi_L^{(j)})}{M^{(n)2}} \quad \in \mathcal{L}_{4D}^{D-terms}.
\end{aligned} \tag{9.43}$$

The first term in this Lagrangian part can be rewritten, according to the orthonormalization condition (H.1) and completeness relation (H.2), as

$$\begin{aligned}
& q_{H_u^0} q_L g^2\sum_{n=1}^{\infty} g_n^{++}(\pi R_c)\overline{\phi}_{H_u^0}\phi_{H_u^0}\sum_{i,j=0}^{\infty}\mathcal{T}_L^{ijn}\overline{\phi}_L^{(i)}\phi_L^{(j)} \\
&= q_{H_u^0} q_L g^2\int_{-\pi R_c}^{\pi R_c} dy[\delta(y-\pi R_c) - g_0^{++}(\pi R_c) g_0^{++}(y)]\overline{\phi}_{H_u^0}\phi_{H_u^0}\sum_{i,j=0}^{\infty} f_i^{++}(c_L;y) f_j^{++}(c_L;y)\overline{\phi}_L^{(i)}\phi_L^{(j)} \\
&= q_{H_u^0} q_L g^2\sum_{i,j=0}^{\infty} f_i^{++}(c_L;\pi R_c) f_j^{++}(c_L;\pi R_c)\overline{\phi}_{H_u^0}\phi_{H_u^0}\overline{\phi}_L^{(i)}\phi_L^{(j)} - q_{H_u^0} q_L\frac{g^2}{2\pi R_c}\overline{\phi}_{H_u^0}\phi_{H_u^0}\sum_{i=0}^{\infty}\overline{\phi}_L^{(i)}\phi_L^{(i)}.
\end{aligned} \tag{9.44}$$

Then plugging this expression into Eq.(9.43) brings,

$$
\begin{aligned}
- \quad & q_{H_u^0} q_L \frac{g^2}{2\pi R_c} \overline{\phi}_{H_u^0} \phi_{H_u^0} \sum_{i=0}^{\infty} \overline{\phi}_L^{(i)} \phi_L^{(i)} \\
+ \quad & q_{H_u^0} q_L g^2 \sum_{i,j=0;n=1}^{\infty} g_n^{++}(\pi R_c) \mathcal{T}_L^{ijn} \frac{\partial_\mu (\overline{\phi}_{H_u^0} \phi_{H_u^0}) \partial^\mu (\overline{\phi}_L^{(i)} \phi_L^{(j)})}{M^{(n)2}} \quad \in \mathcal{L}_{4D}^{D-terms}.
\end{aligned} \tag{9.45}
$$

At this stage, a useful check is to recover the 4D SUSY Lagrangian – in our simple toy model with a U(1) gauge symmetry and a minimal matter content – by taking the limiting case $M^{(n)}, m_{L/R}^{(n)} \to \infty$ ($n \geq 1$). Indeed, in this case Eq.(9.45) simplifies to the 4D SUSY Lagrangian

$$
\mathcal{L}_{4D}^{D-terms} \quad \to \quad -q_{H_u^0} q_L \frac{g^2}{2\pi R_c} \overline{\phi}_{H_u^0} \phi_{H_u^0} \overline{\phi}_L^{(0)} \phi_L^{(0)} = -q_{H_u^0} q_L g_{4D}^2 \overline{\phi}_{H_u^0} \phi_{H_u^0} \overline{\phi}_L^{(0)} \phi_L^{(0)} \tag{9.46}
$$

where g_{4D} represents the 4D effective gauge coupling constant. This test confirms the consistency of the obtained 4D couplings in Eq.(9.45). This consistency relies on the full summation over the infinite Σ KK tower in Eq.(9.44), similarly to the derivation of D-term couplings in Section 9.2.2.

In conclusion, the KK corrections with respect to the 4D SUSY $|\phi_{H_u^0}|^2 |\phi_L^{(0)}|^2$ coupling arise at the order $1/M^{(n)2}$. At this order $1/M^{(n)2}$ (and above) the corrections in Eq.(9.45) affect the $|\phi_{H_u^0}|^2 |\phi_L^{(0)}|^2$ coupling but not the consequent masses as the '∂_μ' acting on the constant $\phi_{H_u^0}$ VEV vanishes. This means that there are no KK tower-induced corrections to any D-term mass at order $1/M^{(n)2}$ with respect to 4D SUSY.

Complete scalar mass matrices

We have done all the necessary preliminary calculations to obtain different 4D mass contributions so that we can now write the whole 4D effective scalar mass matrix within the pMSSM. We will give the stop mass matrix as an example, the other scalar superpartner masses being easily deducible from it. This $\tilde{t}$ mass matrix in the interaction basis $\vec{\tilde{t}} = \{\tilde{t}_L^{(0)}, \tilde{t}_R^{(0)}, \tilde{t}_L^{(1)}, \tilde{t}_R^{(1)}\}$ reads as $-\vec{\bar{\tilde{t}}} \mathcal{M}_{\tilde{t}\tilde{t}}^2 \vec{\tilde{t}} \in \mathcal{L}_{4D}$ with,

$$
\mathcal{M}_{\tilde{t}\tilde{t}}^2 \quad \equiv \quad \begin{pmatrix} 0 & 0 & 0 & 0 \\ 0 & 0 & 0 & 0 \\ 0 & 0 & m_L^{(1)2} & 0 \\ 0 & 0 & 0 & m_R^{(1)2} \end{pmatrix} + \mathcal{Y}^2 \hat{v}_u^2
$$

$$
\times \begin{pmatrix} (f_L^0 f_R^0)^2 [1 - \mathcal{Y}^2 \hat{v}_u^2 (f_L^0)^2 \sum_{n=1}^{\infty} \frac{(f_R^n)^2}{m_R^{(n)2}}] & 0 & f_L^0 f_L^1 (f_R^0)^2 & 0 \\ 0 & (f_L^0 f_R^0)^2 [1 - \mathcal{Y}^2 \hat{v}_u^2 (f_R^0)^2 \sum_{n=1}^{\infty} \frac{(f_L^n)^2}{m_L^{(n)2}}] & 0 & f_R^0 f_R^1 (f_L^0)^2 \\ f_L^0 f_L^1 (f_R^0)^2 & 0 & (f_L^1 f_R^0)^2 & 0 \\ 0 & f_R^0 f_R^1 (f_L^0)^2 & 0 & (f_L^0 f_R^1)^2 \end{pmatrix}
$$

$$
- \quad \frac{\mu_{eff}\mathcal{Y}\,\hat{v}_u}{\tan\beta}\begin{pmatrix} 0 & f_L^0 f_R^0 & 0 & f_L^0 f_R^1 \\ f_L^0 f_R^0 & 0 & f_L^1 f_R^0 & 0 \\ 0 & f_L^1 f_R^0 & 0 & f_L^1 f_R^1 \\ f_L^0 f_R^1 & 0 & f_L^1 f_R^1 & 0 \end{pmatrix} \quad + \quad \cos 2\beta\; m_Z^2 \begin{pmatrix} Q_Z^{t_L} & 0 & 0 & 0 \\ 0 & -Q_Z^{t_R} & 0 & 0 \\ 0 & 0 & Q_Z^{t_L} & 0 \\ 0 & 0 & 0 & -Q_Z^{t_R} \end{pmatrix}
$$

$$
+ \quad \tilde{m}e^{-2k\pi R_c}\begin{pmatrix} f_L^0 f_L^0 & 0 & f_L^0 f_L^1 & 0 \\ 0 & f_R^0 f_R^0 & 0 & f_R^0 f_R^1 \\ f_L^0 f_L^1 & 0 & f_L^1 f_L^1 & 0 \\ 0 & f_R^0 f_R^1 & 0 & f_R^1 f_R^1 \end{pmatrix} \quad + \quad Ae^{-k\pi R_c}\,\hat{v}_u \begin{pmatrix} 0 & f_L^0 f_R^0 & 0 & f_L^0 f_R^1 \\ f_L^0 f_R^0 & 0 & f_L^1 f_R^0 & 0 \\ 0 & f_L^1 f_R^0 & 0 & f_L^1 f_R^1 \\ f_L^0 f_R^1 & 0 & f_L^1 f_R^1 & 0 \end{pmatrix}, \tag{9.47}
$$

with the notation $f_{L/R}^n = f_n^{++}(c_{\tilde{t}_{L/R}}; \pi R_c)$. m_Z is the Z^0 gauge boson mass, $\mu_{eff} = \mu e^{-k\pi R_c} \sim$ TeV [*c.f.* Eq.(9.23)], $A \sim 1$ as above and to not introduce a new bulk scale, the soft mass localized on the TeV-brane for bulk stops (see later discussion for the alternative possibilities of SUSY breaking masses either on the Planck-brane or in the bulk) is taken at $\tilde{m} \sim k$. We have taken a unique soft mass $\tilde{m}$ for having a more simple matrix here but the above mass matrix is easily extended to the case $\tilde{m}_L \neq \tilde{m}_R$ (respective soft masses for $\tilde{t}_L^{(0)}$ and $\tilde{t}_R^{(0)}$).

The fourth mass matrix of Eq.(9.47) originates from the D-terms while the Yukawa masses (second matrix) have been generalized from Eq.(9.37). We have noted $\tilde{t}_L^{(0)}$ and $\tilde{t}_R^{(0)}$ the first two states of the basis but one should clarify the point that $\tilde{t}_{L/R}^{(0)}$ possess in fact small admixtures of the $\tilde{t}_{L/R}^{c(n)}$ KK states (identical to the fields noted $\phi_{L/R}^{c(n)}$ defined in the KK decomposition (H.12)), a kind of mixing described in the study of mass matrix (9.31) and at the origin of the two corrections to the first elements in the second matrix of Eq.(9.47). The KK sum in these corrections for the stop, typically localized near the TeV-brane, must be cut at $\sim 2M_{KK}^{(1)}$ as is usual in this 5D framework (see the perturbativity considerations on the top Yukawa coupling e.g. in [46]).

In conclusion, the effect of $(--)$ KK towers on the $\tilde{t}^{(0)}$ mass is taken into account at first order in $1/M^{(n)2}$ (or $1/m_{L/R}^{(n)2}$) via the corrective terms in the second matrix of Eq.(9.47), whereas the $(--)$ KK effects in D-term masses have been shown above to vanish at this first order (see Eq.(9.45)). The mixing effect of $(++)$ KK towers on the $\tilde{t}^{(0)}$ mass is taken into account at first order by diagonalizing the mass matrix (9.47) which includes the first KK modes.

9.3 Phenomenology

9.3.1 Quantum corrections to the Higgs mass

In this section, we compute explicitly the quantum corrections – at the one-loop level – to the $\phi_{H_u^0}$ Higgs mass (similar corrections hold for the complex $\phi_{H_d^0}$ boson) in the model defined in Appendix G without μ-term for simplification reason and without introducing any (soft) SUSY breaking mechanism. Indeed, our goal in this part is to study generically the possible re-introduction, due to the existence of warped extra dimensions, of the gauge hierarchy problem in a SUSY framework. For that purpose, we focus on the quadratic divergent contributions exclusively, using the 4D effective couplings derived in previous sections.

Before starting let us discuss the general aspect of this loop analysis, through an overview of the assumptions made. First, our results on the cancellation of quadratic divergences and on the necessity for some cancellation conditions in certain cases, although obtained within a minimal SUSY model, also apply to the pMSSM gauge group, Lagrangian and field content. Indeed those results rely (partially) on the gauge symmetry structure whatever gauge group it is [in particular abelian or not].
Secondly, there are no masses for the Higgs bosons in our framework (as neither μ-terms nor soft scalar masses) and in turn the Higgs fields do not acquire VEV. Nevertheless, all our conclusions on quadratic cancellations still hold, for example, in the pMSSM after spontaneous EWSB. The vanishing mass hypothesis also allows us to work in the Higgs rest frame where the external four-momentum are exactly equal to zero, a Lorentz transformation choice which does not affect our conclusions due to the invariant nature of the (Higgs) mass.
Finally, we work generically without choosing a specific gauge; the gauge choice will be parametrized by the non-fixed λ quantity entering the nth KK gauge boson propagator:

$$\frac{-i}{k^2 - M^{(n)2}} \left[\eta_{\mu\nu} + \frac{1-\lambda}{\lambda} \frac{k_\mu k_\nu}{k^2 - \frac{1}{\lambda} M^{(n)2}} \right].$$

Recall that for instance $\lambda = 0$ ($\lambda = 1$) corresponds to the Landau (Feynman) gauge which is characterized by $\partial^\mu A_\mu = 0$ as considered in the other parts of this study together with $A_5 = 0$ – for a gauge boson field A_M. We thus find that the λ-dependent terms vanish which means that the physical result on Higgs mass corrections is not gauge-dependent, as expected. This approach confers to the analysis, and a fortiori to the result, a general character. Although we do not fix λ, or equivalently $Im(z)$ (which determines the A_μ field in Eq.(G.8)), we choose to work in the Wess-Zumino gauge where the extra fields that generically appear in the V expression have been transformed to zero (see Eq.(G.8)) due to the specific choices of $Re(z)$, η, f – if a gauge transformation on generic vectorial (chiral) superfields V (Ω) is defined by $V \to V + \mathcal{Z} + \bar{\mathcal{Z}}$ ($\Omega \to \Omega + \sqrt{2}\partial_y \mathcal{Z}$), the chiral superfield $\mathcal{Z}$ involving the scalar field z, spinor η and auxiliary f. We choose the Wess-Zumino gauge for simplicity in the loop calculation but the physical result that we obtain would clearly be the same in another gauge.

Yukawa coupling sector

Starting with the fermion contributions, the first step is to get the 4D effective Yukawa couplings of the fermions to the Higgs boson $\phi_{H_u^0}$; from the Lagrangian obtained in Eq.(G.29), we know that those couplings after field redefinition (absorbing the $\sqrt{G}$ factor) are $\lambda_{nm} \equiv -\int dy \mathcal{Y} f_L^n(y) f_R^m(y) \delta(y - \pi R_c)$, assuming a real Yukawa coupling for simplicity.
The loop diagrams involving Yukawa couplings and resulting in quadratic divergences are those drawn in Fig.(9.5) and Fig.(9.6). From the formal point of view, for a loop having fermions of different masses as in Fig.(9.5), say m_{f^1} and m_{f^2}, running in, one can write the loop integral as (calling λ the Yukawa coupling constants):

$$\begin{aligned} &-\int \frac{d^4k}{(2\pi)^4} \mathrm{Tr} \left[(-i\lambda) \left(\frac{1-\gamma_5}{2} \right) \left(\frac{i}{\not{k} - m_{f^1}} \right) (-i\lambda) \left(\frac{1+\gamma_5}{2} \right) \left(\frac{i}{\not{k} - m_{f^2}} \right) \right] \\ &= -2\lambda^2 \int \frac{d^4k}{(2\pi)^4} \left[\frac{k^2}{(k^2 - m_{f^1}^2)(k^2 - m_{f^2}^2)} \right] \end{aligned} \tag{9.48}$$

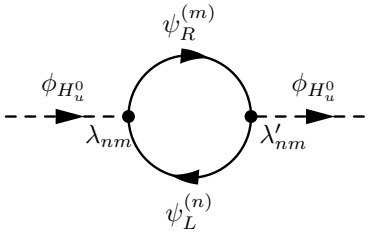

Figure 9.5: Quadratically divergent quantum corrections at one-loop to the $\phi_{H_u^0}$ mass due to the exchange of KK Dirac fermions $\psi_{L/R}^{(n)}$. Couplings are described in text.

The four-momentum of the fields exchanged in the loop is generically noted k^μ. Note the presence of the $\frac{1\pm\gamma_5}{2}$ chirality projectors, since such scalar couplings flip the fermion chirality, as well as the overall minus sign due to the Fermi-Dirac statistics which is crucial for the SUSY cancellation of divergences. Now expanding over different KK fermion towers results in the following contribution to the $\phi_{H_u^0}$ Higgs mass, respecting the correct order between the discrete KK sum and the four-momentum loop integral,

$$\mathcal{I}_F = -2 \sum_{\{n,m\}=0,0}^{N,M} \int \frac{d^4k}{(2\pi)^4} \left[\frac{k^2}{(k^2 - m_L^{(n)\,2})(k^2 - m_R^{(m)\,2})} \right] \lambda_{nm} \lambda'_{nm} \tag{9.49}$$

where $\lambda'_{nm} \equiv -\int dy' \mathcal{Y} f_L^n(y') f_R^m(y') \delta(y' - \pi R_c)$ and $m_{L/R}^{(n)}$ [with $m_{L/R}^{(0)} = 0$] are the KK fermion masses. We have truncated the KK summation at the indices N, M such that $m_L^{(N)}, m_R^{(M)} \sim \Lambda$ and consistently the momentum integration at the cut-off of the 5D theory Λ (one has typically $\Lambda \sim M_{KK}^{(2)}$, the second KK gauge mass). The reason being that the non-renormalizable 5D SUSY theory is only valid below this cut-off. The integral gives us :

$$\begin{aligned}
\mathcal{I}_F &= -2\mathcal{Y}^2 \sum_{\{n,m\}=0,0}^{N,M} \int \frac{d^4k}{(2\pi)^4} k^2 \int dy \int dy' \left[\frac{f_L^n(y) f_L^n(y')}{k^2 - m_L^{(n)\,2}} \frac{f_R^m(y) f_R^m(y')}{k^2 - m_R^{(m)\,2}} \right] \delta(y - \pi R_c)\ \delta(y' - \pi R_c) \\
&= -2\mathcal{Y}^2 \sum_{\{n,m\}=0,0}^{N,M} \int \frac{d^4k}{(2\pi)^4} k^2 \frac{f_L^n(\pi R_c) f_L^n(\pi R_c)}{k^2 - m_L^{(n)\,2}} \frac{f_R^m(\pi R_c) f_R^m(\pi R_c)}{k^2 - m_R^{(m)\,2}}.
\end{aligned} \tag{9.50}$$

We now calculate the scalar superpartner contributions. First one has to derive the 4D effective Yukawa coupling of the matter scalars to the Higgs boson $\phi_{H_u^0}$; we have obtained it in Eq.(9.11) renaming it now for commodity as $\tilde{\lambda}_n|_{L/R} = -i\mathcal{Y}^2 \left[f_{L/R}^n(\pi R_c) \right]^2 k^2\, G_5^{f_{c_{R/L}}^{++}}(k^2; \pi R_c, \pi R_c)$; the KK scalar contributions to the $\phi_{H_u^0}$ mass only come from these 'diagonal' nn Yukawa couplings as shows Fig.(9.6). As explained at the end of the part commenting the scalar 4D couplings to two Higgs bosons in Section 9.2.2, the KK summation in $G_5^{f_{c_{R/L}}^{++}}(k^2; \pi R_c, \pi R_c)$ has to be truncated and we truncate it consistently at the index N such that $m_L^{(N)} \sim \Lambda$.

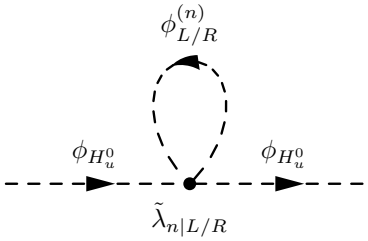

Figure 9.6: Quadratically divergent quantum corrections at one-loop to the $\phi_{H^0_u}$ mass due to the exchange of KK scalar superpartners $\phi^{(n)}_{L/R}$. Couplings are described in text.

From Fig.(9.6), we see that expanding over different KK scalar towers results in the contribution:

$$\mathcal{I}_S = \sum_{n=0}^{N} \int \frac{d^4k}{(2\pi)^4} \left\{ \frac{i\tilde{\lambda}_n|_L}{k^2 - m_L^{(n)\,2}} + \frac{i\tilde{\lambda}_n|_R}{k^2 - m_R^{(n)\,2}} \right\} \tag{9.51}$$

where $m^{(n)}_{L/R}$ are the KK scalar masses. As there is no SUSY breaking here the fermions and their scalar superpartners have identical KK masses and wave functions. We have cut the KK tower and momentum integration at Λ ($\sim M^{(2)}_{KK}$) as for the fermion contribution. We get

$$\begin{aligned} \mathcal{I}_S &= \mathcal{Y}^2 \sum_{n=0}^{N} \int \frac{d^4k}{(2\pi)^4} \left[\frac{[f^n_L(\pi R_c)]^2}{k^2 - m_L^{(n)\,2}} k^2\, G_5^{f^{++}_{c_R}}(k^2; \pi R_c, \pi R_c) + \frac{[f^n_R(\pi R_c)]^2}{k^2 - m_R^{(n)\,2}} k^2\, G_5^{f^{++}_{c_L}}(k^2; \pi R_c, \pi R_c) \right] \\ &= 2\mathcal{Y}^2 \sum_{\{n,m\}=0,0}^{N,M} \int \frac{d^4k}{(2\pi)^4} k^2 \frac{[f^n_R(\pi R_c)]^2}{k^2 - m_R^{(n)\,2}} \frac{[f^m_L(\pi R_c)]^2}{k^2 - m_L^{(m)\,2}} \end{aligned} \tag{9.52}$$

after inverting a *finite* summation (in 5D propagators) with the *cut* integration over k.

One thus finds $\mathcal{I}_F + \mathcal{I}_S = 0$ due to SUSY. Strictly speaking, we have in fact obtained this quadratic divergence cancellation analytically in the generic case of any cut-off (i.e. for any Λ value). Was this result predictable ? In the limiting case $\Lambda < M_{KK}$ – the first KK gauge mass M_{KK} is the smallest KK mass among bosons and fermions – where $n = m = 0$, one recovers the 4D SUSY model (with a cut-off) so that the above result of quadratic cancellation constitutes only a good check. On the opposite side, for $\Lambda \to \infty$ assuming a known UV completion for the 5D theory (or more realistically $\Lambda \simeq M_\star$ in our RS context) so that the theory is totally 5D (or only up to the effective gravity scale), it is not surprising to find that the pure 5D SUSY guarantees the quadratic cancellation. Finally, for any intermediate cut-off truncating KK sums and loop integrations, our generic result is that the cancellation systematically occurs [the same cut-off Λ must be applied on Eq.(9.50) and Eq.(9.52) so that these expressions remain exactly opposite] in what could be called a 'truncated 5D theory'; this constitutes the proof of a supersymmetric cancellation KK level by KK level (i.e. the n*th* KK scalar contribution compensates the n*th* KK fermion contribution), a non-obvious result. A similar result holds for the quadratic divergence cancellation in the gauge coupling sector treated below.

Comments about the cancellation of quadratic divergences

Based on the above example of cancellation of quadratic divergences in the Yukawa coupling sector (compensation between fermions and their scalar superpartner), we discuss here why our approach brings some new light on the old debate about this cancellation in Higgs mass quantum corrections in higher-dimensional SUSY theories (the SUSY breaking aspect is not considered here) with localized Higgs interactions.

First there were questions [49, 50] on the sense of the "KK regularization" [51] in higher-dimensional SUSY theories. The KK regularization is the divergence cancellation which relies on performing first the infinite summation of loop-exchanged KK states and secondly the infinite four-momentum loop-integral; this order corresponds to a non-justified inversion in the analytical computation of an *infinite* number of KK contributions at the one-loop level to the Higgs mass.
We have shown, in the part commenting the scalar 4D couplings to two Higgs bosons in Section 9.2.2, that writing the scalar effective 4D couplings requires to perform an infinite summation on KK tower without applying any cut-off. Only once one has derived these scalar effective 4D couplings, the analytical loop computation – in a 4D framework – of KK scalar contributions to the Higgs mass can be started: that is the correct order. Hence, the loop four-momentum integration must be performed *after* the aforementioned infinite KK summation, as exhibits Eq.(9.51) (where an infinite summation has already been calculated to obtain $\tilde{\lambda}_n|_{L/R}$), even if this is in contrast with a naive thinking. In Eq.(9.52), the summations in G_5 – which originate from the remaining summation in $\tilde{\lambda}_n|_{L/R}$ – are finite so it makes sense to invert those with the cut integration, in order to obtain the quadratic divergence cancellation with Eq.(9.50) [13].

Related doubts pointed out in Ref. [49] concerned the effect of the necessary cut-off, due to the non-renormalizable aspect of 5D SUSY models, which prevents from making any infinite KK summation and in turn to find the quadratic cancellation: indeed, the authors of [49] have demonstrated that the cancellation results partially from SUSY and partially from a compensation between the quadratic terms of a finite number of KK modes with masses below the cut-off and the logarithmic terms of an infinite number of KK states above it. It was believed that the procedure in Ref. [49] based on a sharp cut of the KK tower, spoiling the supersymmetry of the underlying theory, could prevent from quadratic cancellations. However, the proper time cut-off (made separately from the KK level truncation) not spoiling four-dimensional symmetries can be applied [52] and similar problems arise: quantum corrections to the Higgs mass become insensitive to details of physics at the UltraViolet (UV) scale only under certain conditions. Another alternative to the sharp KK tower truncation is the suppression by a Gaussian brane distribution [27] (the couplings of high KK modes are suppressed by a finite width of the brane) which indeed allows to recover a finite Higgs mass – including the cut-off effect but keeping an infinite sum so evading the drawbacks outlined in [49]. Nevertheless, it appears also in Ref. [27] that other distributions leading to a linear sensitivity on the momentum cut-off exist, a remark forbidding a general conclusion [14]. These two works [27, 52] have thus not really solved the problems raised in [49] on a general justification of the finiteness of the Higgs mass.
The way to describe the cut-off problem of Ref. [49] within our framework is as follows. An infinite KK summation has to be computed for applying the completeness relation and hence for finding the $\tilde{\lambda}_n|_{L/R}$ form obtained in Eq.(9.11) and used in Eq.(9.51) to give rise to the quadratic cancellation (between $\mathcal{I}_S$ and $\mathcal{I}_F$),

[13] In fact, within our approach we don't have to make *abnormally* an infinite KK summation before a loop integration.

[14] The approach developed in Ref. [27] also shows that the Higgs mass corrections at higher order (two loops) potentially give rise to linear divergences which are in fact cancelled by linear threshold effects of Yukawa and gauge couplings [53].

however, the infinite character seems meaningless as the KK states with masses above Λ make no sense in a theory valid only up to the cut-off scale. In fact it turns out, as we have discussed in the part commenting the scalar 4D couplings (Section 9.2.2), that an infinite KK summation must really be calculated in order to write down a consistent 4D Lagrangian for the fundamental 5D SUSY theory; the cut-off is indeed applied but only after the 4D couplings have been derived (which requires an infinite summation computation) and it is applied on the remaining not-computed sums in the coherent 4D framework [15].

We have not brought arguments against the claims of Ref. [49] but we have proposed a different approach avoiding their problems (for the KK regularization) and we have justified the required infinite KK summation (including the cut-off aspect). Therefore the quadratic cancellation appears to be well treated in our context and thus to be meaningful. Similar arguments hold for the independent quadratic cancellation in the gauge coupling sector (involving also Higgs boson, higgsino, gauge boson and gaugino contributions to the Higgs mass) that will be treated in the following subsection.
There exist other approaches like the Pauli-Villars regularization [54] or the elegant 5D (mixed position-momentum space) framework [55], based on formally correct treatments of the divergences avoiding subtleties on KK excitations and 4D Lagrangians, which also conclude positively on the validity of quadratic cancellations.

Gauge coupling sector

First, the exchange of U(1) gauge boson KK modes contributes (*c.f.* Fig.(9.7)), via the gauge couplings derived in Eq.(G.30), to the quadratic divergences appearing in the $\phi_{H_u^0}$ mass corrections. This contribution reads as,

$$\begin{aligned}\mathcal{I}_A &= \sum_{n=0}^{N}\int\frac{d^4k}{(2\pi)^4}\int dy\; i\; q_{H_u^0}^2 g^2\,[g_n^{++}(y)]^2\,\eta^{\mu\nu}\,\delta(y-\pi R_c)\frac{-i}{k^2-M^{(n)2}}\left[\eta_{\mu\nu}+\frac{1-\lambda}{\lambda}\frac{k_\mu k_\nu}{k^2-\frac{1}{\lambda}M^{(n)2}}\right]\\ &= q_{H_u^0}^2 g^2\sum_{n=0}^{N}\int\frac{d^4k}{(2\pi)^4}\frac{[g_n^{++}(\pi R_c)]^2}{k^2-M^{(n)2}}\left[4+\frac{1-\lambda}{\lambda-M^{(n)2}/k^2}\right],\end{aligned} \tag{9.53}$$

where we have used the 4D effective gauge coupling obtained from Eq.(G.30). As for the Yukawa sector, the KK summation and momentum integration are truncated at the 5D cut-off Λ.

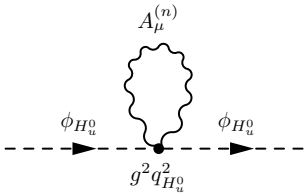

Figure 9.7: Quadratically divergent quantum corrections at one-loop to the $\phi_{H_u^0}$ mass due to the exchange of KK gauge bosons $A_\mu^{(n)}$. Couplings are described in text.

[15] Hence, our approach to the cut-off problem (w.r.t. divergence cancellations) is different from Ref. [27, 52]: we do not deal with the kind of cut-off that is applied but instead we justify why this cut-off must not be applied systematically on KK sums.

The exchanges of $A_\mu^{(n)}$ states together with the Higgs boson also contribute as drawn in Fig.(9.8). Still truncating the sum and integration at Λ, we obtain [see again Eq.(G.30)]

$$\begin{aligned}
\mathcal{I}'_A &= \sum_{n=0}^{N} \int \frac{d^4k}{(2\pi)^4} \int dy \int dy' \left(-i\, q_{H_u^0} g k^\mu\, g_n^{++}(y)\, \delta(y-\pi R_c)\right) \left(-i\, q_{H_u^0} g k^\nu\, g_n^{++}(y')\, \delta(y'-\pi R_c)\right) \\
&\qquad \times \frac{i}{k^2}\, \frac{-i}{k^2 - M^{(n)2}} \left[\eta_{\mu\nu} + \frac{1-\lambda}{\lambda}\, \frac{k_\mu k_\nu}{k^2 - \frac{1}{\lambda} M^{(n)2}}\right] \\
&= -q_{H_u^0}^2 g^2 \sum_{n=0}^{N} \int \frac{d^4k}{(2\pi)^4}\, \frac{[g_n^{++}(\pi R_c)]^2}{k^2 - M^{(n)2}} \left[1 + \frac{1-\lambda}{\lambda - M^{(n)2}/k^2}\right]. \qquad (9.54)
\end{aligned}$$

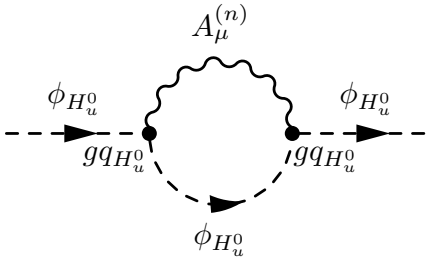

Figure 9.8: Quadratically divergent quantum corrections at one-loop to the $\phi_{H_u^0}$ mass due to the exchange of KK gauge bosons $A_\mu^{(n)}$ together with the Higgs boson itself. Couplings are described in text.

Similarly, the exchanges of $\psi_{\lambda_1}^{(n)}$ gaugino states (four-component spinorial notation) and higgsinos ($\psi_{H_u^0}$) contribute as in Fig.(9.9). Deducing the 4D effective gaugino couplings from the superfield action (G.12) [as done exactly in Eq.(G.29)], one finds the mass contribution

$$\begin{aligned}
\mathcal{I}_G &= -\sum_{n=0}^{N} \int \frac{d^4k}{(2\pi)^4} \int dy \int dy' \left(-\sqrt{2} q_{H_u^0} g g_n^{++}(y)\, \delta(y-\pi R_c)\right) \left(\sqrt{2} q_{H_u^0} g g_n^{++}(y')\, \delta(y'-\pi R_c)\right) \\
&\qquad \times \mathrm{Tr}\left[\frac{i(\not{k} + M^{(n)})}{k^2 - M^{(n)2}}\, \frac{1-\gamma_5}{2}\, \frac{i\not{k}}{k^2}\, \frac{1+\gamma_5}{2}\right] \\
&= -4 q_{H_u^0}^2 g^2 \sum_{n=0}^{N} \int \frac{d^4k}{(2\pi)^4}\, \frac{[g_n^{++}(\pi R_c)]^2}{k^2 - M^{(n)2}}. \qquad (9.55)
\end{aligned}$$

This loop contribution carries a minus sign in front of the sum due to the Fermi-Dirac statistics. Since there is no SUSY breaking, the gauge boson modes have the same KK masses and wave functions as their fermionic superpartners.
Other divergences arise from the Higgs exchange itself; see Fig.(9.10). The preliminary 4D result of Eq.(9.30)

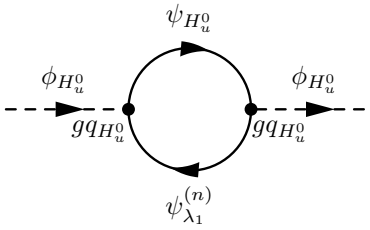

Figure 9.9: Quadratically divergent quantum corrections at one-loop to the $\phi_{H_u^0}$ mass due to the exchange of KK gaugino modes $\psi^{(n)}_{\lambda_1}$ with the higgsino state $\psi_{H_u^0}$. Couplings are described in text.

and Eq.(9.28) allow us to write down these two mass corrections, respectively, as:

$$\begin{aligned}
\mathcal{I}_{H_d^0} &= \int \frac{d^4k}{(2\pi)^4}\left(-iq_{H_u^0}q_{H_d^0}g^2p^2G_5^{g^{++}}(p^2;\pi R_c,\pi R_c)\right)\frac{i}{k^2} \\
&\to q_{H_u^0}q_{H_d^0}g^2\int\frac{d^4k}{(2\pi)^4}\frac{[g_0^{++}(\pi R_c)]^2}{k^2} = \frac{q_{H_u^0}q_{H_d^0}g^2}{2\pi R_c}\int\frac{d^4k}{(2\pi)^4}\frac{1}{k^2}, \qquad (9.56) \\
\mathcal{I}_{H_u^0} &= \int \frac{d^4k}{(2\pi)^4}\left(-iq_{H_u^0}^2g^2p^2G_5^{g^{++}}(p^2;\pi R_c,\pi R_c)\right)\frac{i}{k^2} + \int \frac{d^4k}{(2\pi)^4}\left(-iq_{H_u^0}^2g^2k^2G_5^{g^{++}}(k^2;\pi R_c,\pi R_c)\right)\frac{i}{k^2} \\
&\to \frac{q_{H_u^0}^2g^2}{2\pi R_c}\int\frac{d^4k}{(2\pi)^4}\frac{1}{k^2} + q_{H_u^0}^2g^2\int\frac{d^4k}{(2\pi)^4}G_5^{g^{++}}(k^2;\pi R_c,\pi R_c) \\
&= \frac{q_{H_u^0}^2g^2}{2\pi R_c}\int\frac{d^4k}{(2\pi)^4}\frac{1}{k^2} + q_{H_u^0}^2g^2\sum_{n=0}^{N}\int\frac{d^4k}{(2\pi)^4}\frac{[g_n^{++}(\pi R_c)]^2}{k^2-M^{(n)2}}. \qquad (9.57)
\end{aligned}$$

In Eq.(9.56), the limit $p^2 \to 0$ has been performed (using Eq.(I.6)) since the effective coupling involved in Fig.(9.10) confers to this loop diagram a tadpole-form contribution; indeed the effective diagram in Fig.(9.10) may be obtained by summing the two diagrams of Fig.(9.4) after joining the two $\phi_{H_d^0}$ legs and affecting respectively to the $\phi_{H_d^0}$, $\Sigma^{(n)}$, $\phi_{H_u^0}$ fields the momentum k^2 (integrated loop momentum), $p^2 = 0$ and 0 (chosen external momentum). In Eq.(9.57), the limit $p^2 \to 0$ has also been performed since the effective coupling involved in Fig.(9.10) for an internal $\phi_{H_u^0}$ field also confers to this loop diagram a tadpole-form contribution. Here there is even an additional contribution from the exchange of $\Sigma^{(n)}$ with the same momentum k^2 as in the loop. All this can be seen from generating Fig.(9.10) by summing the three diagrams of Fig.(9.3) after joining the two upper $\phi_{H_u^0}$ legs in each diagram. We have also truncated the KK summation by the 5D cut-off Λ (like the integration), in the 5D propagator $G_5^{g^{++}}(k^2;\pi R_c,\pi R_c)$, and then inverted it with the integral.

The last contributions to quadratic divergences generated by gauge couplings are the scalar exchanges in Fig.(9.11)-(9.12). In the same way as just above, the 4D D-term coupling previously obtained in Eq.(9.20)

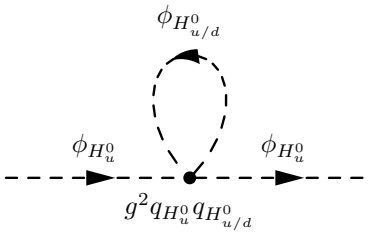

Figure 9.10: Quadratically divergent quantum corrections at one-loop to the $\phi_{H^0_u}$ mass due to self-couplings and couplings with the scalar field $\phi_{H^0_d}$ (described in text).

leads to the corresponding mass corrections:

$$\begin{aligned}
\mathcal{I}_{L/R} &= \sum_{n=0}^{N} \int \frac{d^4k}{(2\pi)^4} \left(-iq_{L/R} q_{H^0_u} g^2 \int dy [f^n_{L/R}(y)]^2 p^2 G_5^{g^{++}}(p^2; y, \pi R_c) \right) \frac{i}{k^2 - m^{(n)2}_{L/R}} \\
&\to \frac{q_{L/R} q_{H^0_u} g^2}{2\pi R_c} \sum_{n=0}^{N} \int \frac{d^4k}{(2\pi)^4} \int dy [f^n_{L/R}(y)]^2 \frac{1}{k^2 - m^{(n)2}_{L/R}} \\
&= \frac{q_{L/R} q_{H^0_u} g^2}{2\pi R_c} \sum_{n=0}^{N} \int \frac{d^4k}{(2\pi)^4} \frac{1}{k^2 - m^{(n)2}_{L/R}}.
\end{aligned} \tag{9.58}$$

in the limit $p^2 \to 0$ and using the orthonormalization condition for wave functions.
Similarly, the 4D effective couplings of two $\phi^{c(m)}_{L/R}$ [defined in Eq.(H.12)] to two Higgs bosons – induced by $\Sigma^{(n)}$ exchanges – can be directly derived from the scalar field Lagrangian (G.26), by using relation (H.7), and lead to the respective tadpole contributions of Fig.(9.12):

$$\mathcal{I}^c_{L/R} = \sum_{m=1}^{M} \int \frac{d^4k}{(2\pi)^4} \left(q_{L/R} q_{H^0_u} g^2 \int dy [f^{cm}_{L/R}(y)]^2 \sum_{n=1}^{N} M^{(n)2} \frac{g_n^{++}(y)\ i\ g_n^{++}(\pi R_c)}{p^2 - M^{(n)2}} \right) \frac{i}{k^2 - m^{(m)2}_{L/R}},$$

reminding that $f^{cm}_{L/R}(y) = f^{--}_m(c_{L/R}; y)$. Applying now the completeness relation and the equality $M^{(n)2}/(p^2 - M^{(n)2}) = \{p^2/(p^2 - M^{(n)2})\} - 1$, one can recast this contribution into the expression

$$\begin{aligned}
\mathcal{I}^c_{L/R} &= -\sum_{m=1}^{M} \int \frac{d^4k}{(2\pi)^4} \left(q_{L/R} q_{H^0_u} g^2 \int dy [f^{cm}_{L/R}(y)]^2 p^2 G_5^{g^{++}}(p^2; y, \pi R_c) \right) \frac{1}{k^2 - m^{(m)2}_{L/R}} \\
&\to -\sum_{m=1}^{M} \int \frac{d^4k}{(2\pi)^4} \frac{q_{L/R} q_{H^0_u} g^2}{2\pi R_c} \int dy [f^{cm}_{L/R}(y)]^2 \frac{1}{k^2 - m^{(m)2}_{L/R}} \\
&= -\frac{q_{L/R} q_{H^0_u} g^2}{2\pi R_c} \sum_{m=1}^{M} \int \frac{d^4k}{(2\pi)^4} \frac{1}{k^2 - m^{(m)2}_{L/R}}
\end{aligned} \tag{9.59}$$

in the limit $p^2 \to 0$.

At this stage where all quadratically divergent contributions have been estimated, a useful check is to take the 4D SUSY limit: $k^2/m^{(n)2}_{L/R} \ll 1$ and $k^2/M^{(n)2} \ll 1$ $[n \geq 1]$ at the zero*th* order. Doing so, one recovers indeed the whole quadratically divergent mass correction for the gauge coupling sector of the 4D

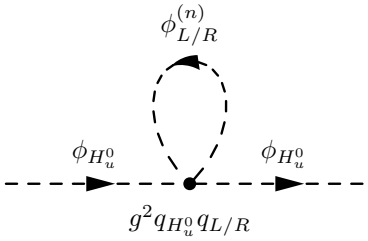

Figure 9.11: Quadratically divergent quantum corrections at one-loop to the $\phi_{H^0_u}$ mass due to gauge couplings with KK scalar superpartners $\phi^{(n)}_{L/R}$ (described in text).

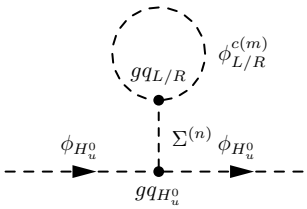

Figure 9.12: Quadratically divergent quantum corrections at one-loop to the $\phi_{H^0_u}$ mass due to the exchange of KK $(--)$ scalar superpartners $\phi^{c(m)}_{L/R}$ and KK $(--)$ scalar modes $\Sigma^{(n)}$ (couplings discussed in text).

SUSY theory:

$$\mathcal{I}_A + \mathcal{I}'_A + \mathcal{I}_G + \mathcal{I}_{H^0_u} + \mathcal{I}_{H^0_d} + \mathcal{I}_L + \mathcal{I}_R + \mathcal{I}^c_L + \mathcal{I}^c_R \to q_{H^0_u}\Big(q_{H^0_u} + q_{H^0_d} + q_L + q_R\Big) g^2_{4D} \int \frac{d^4k}{(2\pi)^4}\frac{1}{k^2},$$

with $g_{4D} = g/\sqrt{2\pi R_c}$ as already defined. Indeed, in 4D SUSY the quadratically divergent Higgs mass corrections cancel each other only if the anomaly cancellation condition $q_{H^0_u} + q_{H^0_d} + q_L + q_R = 0$ is verified, recalling that the quadratic divergence cancellation is induced by the simultaneous presence of SUSY and a gauge symmetry (which relies on the absence of Adler-Bardeen-Jackiw anomalies [56] originating from triangular loops of fermions).

In the present RS SUSY context with localized Higgs fields, we thus have first to wonder what is the global 5D anomaly cancellation condition. The contributions to triangular loops, of the fermions belonging to the chiral matter superfields Φ_L and Φ^{--}_L, should vanish due to the vectorial nature of the 5D theory [i.e. presence of Φ^{--}_L]. Same comment holds for the Φ^c_L and Φ^{c--}_L superfields. The orbifolding apparently spoils this 5D vectorial nature [i.e. no zero-mode for Φ^{--}_L] but the anomaly cancellation is recovered in the matter sector through certain tree level contributions (see e.g. Ref. [57]) induced by the Chern-Simons term (see Ref. [58] for the case of warped orbifolds) together with mixings generated by the Stückelberg term (for instance, see Ref. [59]). For intervals in AdS_5, anomalies might lead to some constraints on the consistent effective field theory description [60]. Finally, one must recall here that the whole 5D anomaly cancellation condition includes the anomaly cancellation condition of the low-energy 4D chiral theory whose role is to insure the anomaly cancellation for the contributions of the zero-modes and possibly fields of the considered model confined on 3-branes (in other words for all states except the KK excitations).

Coming back to our 5D SUSY model, we see that one gets (whatever are the KK masses)

$$\mathcal{I}_A + \mathcal{I}'_A + \mathcal{I}_G + \mathcal{I}_{H_u^0} + \mathcal{I}_{H_d^0} + \mathcal{I}_L + \mathcal{I}_R + \mathcal{I}_L^c + \mathcal{I}_R^c = q_{H_u^0}\Big(q_{H_u^0} + q_{H_d^0} + q_L + q_R\Big)\frac{g^2}{2\pi R_c}\int \frac{d^4k}{(2\pi)^4}\frac{1}{k^2},$$

so that the quadratic divergence cancellation for the Higgs mass in the gauge sector (and hence in all sectors) is guaranteed by the 4D condition $q_{H_u^0}+q_{H_d^0}+q_L+q_R=0$ for the chiral zero-modes and 4D higgsinos (localized on the TeV-brane) which is part of the 5D anomaly cancellation condition. On the other side, the vectorial nature of the 5D SUSY theory, which induces the cancellation of 5D anomalies, is also responsible for the cancellation of the KK $\phi_{L/R}^{(n)}$ contributions to the Higgs mass quadratic divergences (entering Eq.(9.58)) with the KK $\phi_{L/R}^{c(m)}$ contributions (see Eq.(9.59)). This cancellation results from a compensation KK level by KK level and remains thus true for any 5D cut-off value.
As a general conclusion (the present analysis being not based on arguments restricted to warped geometries), in higher-dimensional SUSY models, the quadratic divergence cancellation in the Higgs mass is insured by the higher-dimensional anomaly cancellation condition (as occurs in 4D with the difference that the higher-dimensional anomaly condition can be more complex than the 4D one since it may include the adjustment of the Chern-Simons term to restore the vectorial behavior [16]).

We finish this part by a comment, for completeness. While the condition $q_{H_u^0}+q_{H_d^0}+q_L+q_R=0$ is issued from anomalies of type U(1)−Gravity−Gravity, there is a second condition, namely $q_{H_u^0}^3+q_{H_d^0}^3+q_L^3+q_R^3=0$, coming from the cubic $\mathrm{U}(1)-\mathrm{U}(1)-\mathrm{U}(1)$ anomalies. Let us mention here the third condition on U(1) charges in our toy model: $q_{H_u^0}+q_L+q_R=0$ related to the existence of a Yukawa interaction for $\Phi_{L/R}$ (see Eq.(G.12)). Our motivation for writing an interaction of this type was clearly to consider all the quadratically divergent contributions to the Higgs mass and in particular those involving Yukawa couplings (discussed above).

9.3.2 Sfermion mass splitting

Phenomenological framework

We first describe in more details the phenomenological framework of this Section 9.3.2. We consider the class of SUSY breaking scenario where (soft) squark/slepton masses appear in the bulk and on the boundaries [see SUSY breaking classification of Section 9.2.1]. The model studied is the warped 5D pMSSM. We do not compute numerically the heavy KK state mixing effects since we focus on dominant low-energy structural effects on scalar couplings induced by the SUSY breaking scenario discussed below.

Let us thus discuss what are the favored geometrical setups concerning the SUSY breaking scalar mass locations. First, to have a generic approach, we assume that all bulk sfermions have additional (i.e. SUSY breaking) 5D mass terms of course invariant under the $\mathbb{Z}_2$ parity: those are also taken of the type shown in Eq.(G.27) but with other c parameters. We have shown in Appendix H.3 that adding such masses is equivalent to introduce new 5D scalar parameters, say $c_{\tilde{f}_{L/R}}$, completely independent from the fermion (or superfield) parameters $c_{f_{L/R}}$ and thus affects the scalar localizations. In analogy with RS flavor models for fermions, we will generally make the hypothesis that the first generations of sfermions are typically localized towards the UV boundary (large $c_{\tilde{f}_{L/R}}$) whereas last families are rather located near the IR boundary (small

[16] This Chern-Simons term has anyway no effects on the quadratic divergences of the Higgs mass.

$c_{\tilde{f}_{L/R}}$). Remaining general, the first scalar generations have also SUSY breaking masses localized on the two boundaries and the large soft masses on the Planck-brane are thus not reduced by wave functions overlaps. These Planckian masses mimic $(-+)$ BC so that the first generation sfermion zero-modes decouple from the low-energy theory as occurs in the model of Ref. [42]. This class of scenario represents thus a realization of partially split SUSY models which allow to improve the situation [61] with respect to Flavor Changing Neutral Currents (FCNC). In contrast, the last sfermion generations have soft masses on the TeV-brane which are not suppressed by wave function overlaps. These soft masses enlarge the parameter space that we will explore. Having typically small $c_{\tilde{f}_{L/R}}$ for last sfermion families is also an attractive possibility as it leads to sfermion masses which are mainly generated by the Yukawa interactions after EWSB, as for SM fermions, and to specific collider signatures as discussed in the following subsections.
For the considered case $c_{\tilde{f}_{L/R}} < c_{f_{L/R}}$, the Yukawa-like couplings of these last generation sfermions to Higgs bosons [first coupling matrix in Eq.(9.22)] are increased – modulo a square and a Higgs rotation angle/VEV – relatively to the effective 4D fermion Yukawa couplings [see Eq.(9.12)] which are themselves equal to the 4D SUSY scalar Yukawa couplings (forgetting small KK corrections). A same comparison holds for the interactions proportional to μ_{eff} [second coupling matrix of Eq.(9.22)]. Since the RS SUSY scenario considered increases globally sfermion couplings to Higgs bosons compared to the usual 4D SUSY case, which brings new significant contributions to the (s)quark triangular loop of the gluon-gluon fusion mechanism for Higgs production at hadron colliders [= main production channel] [62] [17], one might wonder whether such a model is not excluded by present experimental searches [64] at Tevatron Run II for 4D SUSY Higgs fields (or estimated results from SM Higgs searches [65] e.g. in the decoupling limit). First it must be remarked that the Tevatron production cross sections and decay branching ratios as well as various theoretical uncertainties have been recently re-evaluated for SUSY Higgs bosons [66], also that 4D SUSY Higgs searches were not exhaustive in the parameter space exploration [64] and that other effects could appear in 5D SUSY Higgs productions. Secondly, the obtained lower limit of the lightest neutral Higgs (noted h) mass is not so close to the 4D SUSY theoretical upper bound which furthermore can be enhanced in the 5D SUSY context [32] enlarging the allowed mass range. In fact, the main 4D SUSY contribution to the gluon-fusion mechanism is the stop exchange in the loop, due to its large Yukawa coupling. In the above RS SUSY setup, the only additional new contribution is the sbottom exchange as we assume the decoupling of the first two generations of squarks to avoid constraints from the $K^0 - \bar{K}^0$ mixing (one could even assume the decoupling of the squark doublet $\tilde{Q}_L$ and sbottom singlet $\tilde{b}_R$). Since we take masses $m_{\tilde{b}} \sim 10^2$ GeV (from little hierarchy arguments), the sbottom Yukawa couplings are of the same order as the (s)top Yukawa interactions and hence comparable Higgs production rates are expected in 4D versus RS SUSY, which is realistic. Concerning sleptons, we assume that only the first generation decouples since these non-colored scalar fields only affect 4D SUSY Higgs searches through the radiative Higgs decay into two photons, a decay representing only one of the various channels investigated. Going into the details of the calculation of the Higgs production/decays, different sfermion exchanges might suppress each other by destructive interferences of the triangular loops [62] depending on the signs of various 4D effective couplings over parameter ranges, and some more freedom might even arise from 5D SUSY model building.

Concerning bulk gauginos, their 4D soft masses are taken effectively i.e. without specifying the higher-dimensional geometry (as we do not study possible 4D/5D SUSY differences in that sector). For example these masses could be localized on the TeV-brane – without suffering from large overlap suppression like light generations.

[17] KK contributions to this gluon-gluon fusion mechanism have been studied e.g. in Ref. [63].

Charge and color breaking minima

Before presenting numerical results, we need to discuss another SUSY aspect which is significantly modified in this RS context: the Charge and Color Breaking (CCB) minima. We will show that no drastic constraints arise on the parameter space and even that no SUGRA-like scenario – in the sense where trilinear soft scalar terms are proportional to the Yukawa coupling constants (reducing effectively the trilinear scale A) – needs to be assumed [as usually required in 4D SUSY] in order to satisfy those constraints.

In 4D mSUGRA, the constraints coming from imposing the absence of CCB global minima for the potential of squark/slepton VEV's read typically as [67] (see [68] for the NMSSM case), taking the example of the usually dangerous selectron direction,

$$(\mathcal{Y}^e_{4D}A^e)^2 < 3\Big((\tilde{m}^e_R)^2 + (\tilde{m}^e_L)^2 + \hat{m}_d^2\Big)(\mathcal{Y}^e_{4D})^2 \tag{9.60}$$

where $\tilde{m}^e_L$, $\tilde{m}^e_R$ denote the selectron soft masses and $\hat{m}_d^2 = m_{H_d}^2 + \mu^2$ with m_{H_d} being the down Higgs soft mass. $\mathcal{Y}^e_{4D} \sim 10^{-5}$ is the Yukawa coupling constant for the electron and $A^e \sim 10^2$ GeV. Since the Yukawa couplings simplify each other in the above inequality, there are often not written in the literature, but here we keep them for the 5D discussion below. The general conclusion on the 4D case is that the CCB constraints, as illustrates the one above, remain respected if the soft parameters A, $\tilde{m}$, m_{H_d} and also μ are all of order the EWSB scale (which is compatible with both the Higgs fine-tuning considerations and electroweak potential minimization relations).

For mSUGRA models in a warped background, the CCB constraint (9.60) is replaced by (neglecting the KK mixing corrections),

$$(\mathcal{Y}^e A^e e^{-\sigma(\pi R_c)} f^0_L f^0_R)^2 < 3\Big(\tilde{m}^e_R (f^0_R e^{-\sigma(\pi R_c)})^2 + \tilde{m}^e_L (f^0_L e^{-\sigma(\pi R_c)})^2 + \hat{m}_d|^2_{eff}\Big)(\mathcal{Y}^e f^0_L f^0_R)^2 \tag{9.61}$$

as deduced from the form of 4D Higgs couplings (9.22) – of type $\mathcal{Y}^2$ and A – and the form of 4D soft scalar masses on TeV-brane in Eq.(9.47). Here $f^0_{L/R} = f_0^{++}(c_{\tilde{e}_{L/R}}; \pi R_c)$; $A^e\mathcal{Y}^e = \mathcal{O}(1)$ (as discussed in the next subsection on slepton masses in mSUGRA) and $\hat{m}_d|^2_{eff} = m^2_{H_d} + \mu^2_{eff}$ [see the discussion on μ_{eff} in Section 9.2.1]. Now, the RS CCB criteria of type Eq.(9.61) simplifies to

$$(A^e e^{-\sigma(\pi R_c)})^2 < 3\Big(\tilde{m}^e_R (f^0_R e^{-\sigma(\pi R_c)})^2 + \tilde{m}^e_L (f^0_L e^{-\sigma(\pi R_c)})^2 + \hat{m}_d|^2_{eff}\Big) \tag{9.62}$$

where $A^e e^{-\sigma(\pi R_c)} \sim 10^2$ GeV so that this condition is as natural as in 4D mSUGRA for effective soft masses at the EWSB scale, which is the case since $\hat{m}_d|_{eff} \sim 10^2$ GeV and e.g. $\tilde{m}_R (f^0_R e^{-\sigma(\pi R_c)})^2 \sim k^2 e^{-2\sigma(\pi R_c)} \sim (10^2 \text{ GeV})^2$ [$\tilde{m}_R \sim k$ from discussion below Eq.(9.47) and see Eq.(H.13) for the wave function order of magnitude] as confirmed by all the values obtained in next subsections.

In an RS framework with a SUSY breaking not specifically of the type SUGRA, the CCB constraint of Eq.(9.61) simply becomes

$$(A^e e^{-\sigma(\pi R_c)} f^0_L f^0_R)^2 < 3\Big(\tilde{m}^e_R (f^0_R e^{-\sigma(\pi R_c)})^2 + \tilde{m}^e_L (f^0_L e^{-\sigma(\pi R_c)})^2 + \hat{m}_d|^2_{eff}\Big)(\mathcal{Y}^e f^0_L f^0_R)^2 \tag{9.63}$$

with now $A^e = \mathcal{O}(1)$ being dimensionless [*c.f.* Eq.(9.47)]. After simplification, it reads as

$$(A^e e^{-\sigma(\pi R_c)})^2 < 3\Big(\tilde{m}^e_R (f^0_R e^{-\sigma(\pi R_c)})^2 + \tilde{m}^e_L (f^0_L e^{-\sigma(\pi R_c)})^2 + \hat{m}_d|^2_{eff}\Big)(\mathcal{Y}^e)^2 \ , \tag{9.64}$$

a condition which is also systematically fulfilled in orders of magnitudes since $(\mathcal{Y}^e)^{-1}e^{-\sigma(\pi R_c)} \sim ke^{-\sigma(\pi R_c)} \sim 10^2$ GeV. Hence, we conclude that within RS SUSY the CCB constraint is generically satisfied, with respect to the orders of magnitude, even without assuming a SUGRA-like breaking.

Strictly speaking, the CCB induced conditions must be imposed at the energy scale $Q \sim \langle \tilde{f} \rangle$ but the running of soft parameters in the RS SUSY framework is beyond our scope.

There exists a related kind of bound which originates from forbidding true minima along scalar potential directions Unbounded From Below (UFB) [69] (*c.f.* [68] for the NMSSM). The condition for such minima not to be deeper than the standard EWSB minimum implies the following bound, $m_0/m_{1/2} > \mathcal{O}(1)$ (in case one assumes universal soft terms). This typical UFB bound should also be quite easily satisfied in an RS SUSY context, applying it for simplicity on the 4D effective soft masses.

Finally, one must recall that the actual relevance of these CCB and UFB bounds is not entirely evident in general because even if e.g. an existing CCB minimum is deeper than the standard EWSB one, it can be acceptable if the tunneling rate out of the standard minimum is small relatively to the age of the universe. The various analyses in literature lead to the conclusion that these tunneling rates are often quite small (the original paper is the third one of Ref. [67]). The relevance of the CCB and UFB bounds is thus model-dependent as it depends on cosmology, and in particular on which minimum we drop after inflation [70].

Numerical results for stop masses: a first discrimination test

First, we investigate the heavy quark superpartner (namely the stop denoted $\tilde{t}$) sector. The flavor context of the pMSSM, considered in this study, will be reminded in Section 9.3.3 where all flavors are potentially involved. In the present analysis, we propose a test to discriminate the 4D pMSSM w.r.t. 5D warped pMSSM by looking at the different ways to generate stop masses in these two setups. To be general, we consider here within 4D and 5D SUSY the case where the soft breaking parameters are chosen effectively, only constrained from the experimental data.

In Fig.(9.13), we have represented the domains possibly explored in 4D or warped SUSY in the plan of the two stop mass eigenstates. The blue lines represent the lower limit on $m_{\tilde{t}_2}$ obtained in 4D SUSY (see discussion below). The two plots showed correspond to scans of the fundamental parameters in the case where SUSY breaking occurs in the bulk (see Appendix H.3), and for the right plot, soft SUSY breaking terms (stop masses and trilinear couplings) have been added on the TeV-brane. For the left plot, the only parameters entering the scan are the SUSY parameters $\tan\beta$, μ (or μ_{eff} [see Eq.(9.23)]), the 5D stop parameters $c_{\tilde{t}_{L/R}}$ and the soft masses $\tilde{m}_{L/R}$ (for 4D SUSY), whereas for the right scan we have further considered the 4D trilinear coupling A_t as well as the TeV-brane SUSY breaking parameters $\tilde{m}_{L/R}|^2_{eff} = \tilde{m}_{L/R}ke^{-2k\pi R_c}$ and $A_t|_{eff} = A_t ke^{-k\pi R_c}$ appearing in the stop mass matrix of warped SUSY models (as seen from Eq.(9.47) and Eq.(H.13)). The $A_t|_{eff}$ term is localized on the TeV-brane due to the Higgs localization. In case of the absence of soft stop mass terms on the TeV-brane (left plot), the stop mass is generated in particular by its coupling with the Higgs boson – which can itself be increased through the stop-Higgs wave function overlap controlled by the SUSY breaking stop mass term in the bulk.
The parameters are scanned over the following ranges, $\tan\beta \in [2;50]$, $\mu, \mu_{eff} \in [100;1000]$ GeV, $c_{\tilde{t}_{L/R}} \in [-1,1]$, $\tilde{m}_{L/R}, \tilde{m}_{L/R}|_{eff} \in [0;1000]$ GeV and $A_t, A_t|_{eff} \in [0;1000]$ GeV. The interval on $\tan\beta$ is conservative given present constraints [30,74]. The μ or μ_{eff} ($|c_{\tilde{t}_{L/R}}|$) interval is justified by its required order of magnitude at the EWSB scale (around ~ 1) as discussed in Section 9.2.1. The $\tilde{m}_{L/R}$ range is motivated by the usual

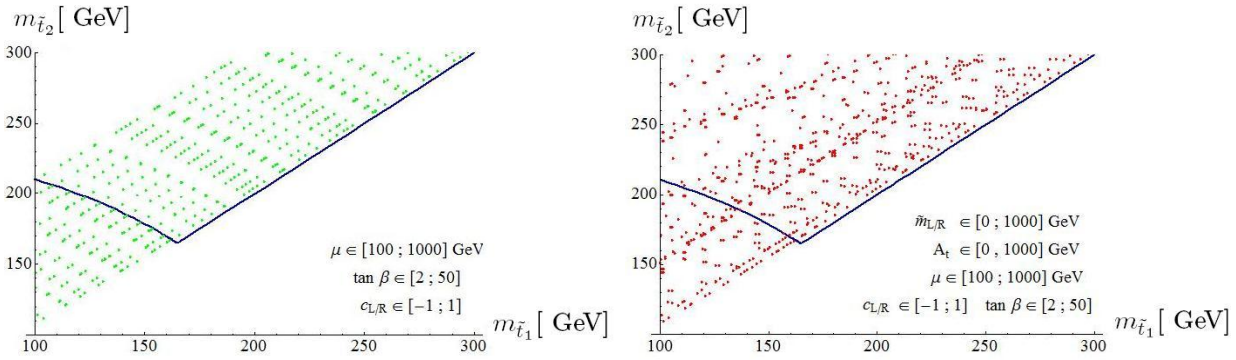

Figure 9.13: Allowed regions in the plan $m_{\tilde{t}_2}$ versus $m_{\tilde{t}_1}$ (in GeV) within 4D SUSY [demarcated by the blue lines] and RS SUSY [green/red points]. The plot on the left side corresponds to the situation where there are no more SUSY breaking terms on the TeV-brane (for the 5D case). The thick blue lines represent a lower limit on $m_{\tilde{t}_2}$ obtained analytically. The parameters are scanned in the intervals indicated on the plot. $c_{L/R} = c_{\tilde{t}_{L/R}}$ are the 5D stop parameters. In the RS case, the so-called effective parameter μ_{eff} is the equivalent of the μ parameter in 4D SUSY [*c.f.* Eq.(9.23)]. The interval indicated on $\tilde{m}$ (A_t) corresponds to the scan interval for the soft stop masses $\tilde{m}_{L/R}$ (trilinear coupling A_t) in 4D SUSY and $\tilde{m}_{L/R}|_{eff} = \sqrt{\tilde{m}_{L/R} k e^{-2k\pi R_c}}$ ($A_t|_{eff} = A_t k e^{-k\pi R_c}$) in the RS SUSY case.

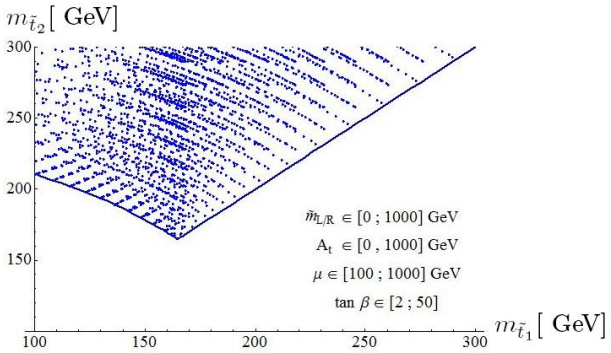

Figure 9.14: Allowed regions in the plan $m_{\tilde{t}_2}$ versus $m_{\tilde{t}_1}$ (in GeV) within 4D SUSY. These regions have been obtained for parameters scanned in the intervals indicated on the plot itself.

effective scale of 4D SUSY breaking scenarios limiting the Higgs mass fine-tuning and the $\tilde{m}_{L/R}|_{eff}$ range is motivated by the energy scale orders in RS: $\tilde{m}_{L/R}|_{eff} = (\tilde{m}_{L/R} k e^{-2k\pi R_c})^{1/2} \sim (k^2 e^{-2k\pi R_c})^{1/2} \sim 10^2$ GeV [see discussion below Eq.(9.23)]. Finally, The chosen A_t interval is based on usual 4D SUSY breaking scenarios and the considered $A_t|_{eff}$ range comes from the scales characteristic of RS: $A_t|_{eff} = A_t k e^{-k\pi R_c} \sim 1 \times k e^{-k\pi R_c} \sim 10^2$ GeV [see again below Eq.(9.23)]. In order to have a consistent comparison between 4D and 5D models, we have chosen the same ranges in both setups. The scans in the plots are not performed on negative values of the A_t (or $A_t|_{eff}$) neither of the μ (or μ_{eff}) terms but taking the opposite signs does not change the conclusions. The last remark on the scans is that having chosen slightly larger parameter ranges – but remaining with the same orders of magnitude as above since those are physically motivated –

would have not affected significantly the obtained numerical results presented here.

Let us now explain the differences arising between the 4D and 5D models in plots of Fig.(9.13). For that purpose, we need to start from the stop mass matrix structure. The stop mass matrix within the RS scenario has been derived in Eq.(9.47). Moving to 4D SUSY, we recall the general form of the stop mass matrix in the $\{\tilde{t}_L, \tilde{t}_R\}$ basis,

$$\mathcal{M}^2_{\tilde{t}\tilde{t}}|_{\text{4D SUSY}} = \begin{pmatrix} m_t^2 + Q_Z^{t_L} \cos 2\beta \, m_Z^2 + \tilde{m}_L^2 & A_t - \frac{\mu \, m_t}{\tan\beta} \\ A_t - \frac{\mu \, m_t}{\tan\beta} & m_t^2 - Q_Z^{t_R} \cos 2\beta \, m_Z^2 + \tilde{m}_R^2 \end{pmatrix} \tag{9.65}$$

where $Q_Z^{t_L} \equiv \frac{1}{2} - \frac{2}{3}\sin^2\theta_W$, $Q_Z^{t_R} \equiv -\frac{2}{3}\sin^2\theta_W$ and m_t is the top quark mass. One can note at this level that the SM top mass entering this mass matrix (and taken in agreement with recent Tevatron measurements [71]) is larger than the experimental lower bound on the stop mass, $m_{\tilde{t}_1} > 95.7$ GeV [31, 74]. The mass matrix (9.65) can be diagonalized by 2×2 orthogonal matrices, resulting in the following mass eigenvalues for the stop eigenstates $\tilde{t}_{1,2}$,

$$\begin{aligned} m^2_{\tilde{t}_{1,2}} = \frac{1}{2}\Bigg(& 2m_t^2 + \frac{1}{2}\cos 2\beta \, m_Z^2 + \tilde{m}_L^2 + \tilde{m}_R^2 \\ & \mp \sqrt{\left((Q_Z^{t_L} + Q_Z^{t_R})\cos 2\beta \, m_Z^2 + \tilde{m}_L^2 - \tilde{m}_R^2\right)^2 + 4\left(A_t - \frac{\mu \, m_t}{\tan\beta}\right)^2} \Bigg). \end{aligned} \tag{9.66}$$

For 4D SUSY, in Fig.(9.13), we observe that $m_{\tilde{t}_2}$ has a lower limit (blue line) depending on $m_{\tilde{t}_1}$: this limit is due to the structure of matrix (9.65) and it has thus been possible to obtain it analytically. Indeed, from Eq.(9.66), summing the two squared masses, we get

$$m^2_{\tilde{t}_2} + m^2_{\tilde{t}_1} = 2m_t^2 + \frac{1}{2}\cos 2\beta \, m_Z^2 + \tilde{m}_L^2 + \tilde{m}_R^2. \tag{9.67}$$

For arbitrary large soft masses, $\tilde{m}_L^2$ and $\tilde{m}_R^2$, there is no constraint on how high can $m_{\tilde{t}_2}$ be compared to $m_{\tilde{t}_1}$ as illustrated in Fig.(9.13). We are thus interested in how low can $m_{\tilde{t}_2}$ be w.r.t. $m_{\tilde{t}_1}$ in the low soft mass region (where it appears on the plot to exist a non-trivial lower limit on $m_{\tilde{t}_2}$). Obviously, one must have $m_{\tilde{t}_2} \geq m_{\tilde{t}_1} \gtrsim 100$ GeV from definition together with the experimental constraint on stop searches mentioned above. The $m_{\tilde{t}_2}$ lowest value thus corresponds to $\tilde{m}_{L/R} = 0$ together with a vanishing $\tilde{t}_L - \tilde{t}_R$ mixing, resulting in $m^{lowest}_{\tilde{t}_2} = m_{\tilde{t}_1} = \sqrt{m_t^2 + \frac{1}{4}\cos 2\beta \, m_Z^2} \sim m_t$. When there is a non-vanishing mixing, for $m_{\tilde{t}_1} \leq m^{lowest}_{\tilde{t}_2}$, we have from Eq.(9.67)

$$m_{\tilde{t}_2} \geq \sqrt{2m_t^2 + \frac{1}{2}\cos 2\beta \, m_Z^2 - m^2_{\tilde{t}_1}} \quad \text{for} \quad m_{\tilde{t}_1} \leq \sqrt{m_t^2 + \frac{1}{4}\cos 2\beta \, m_Z^2} \tag{9.68}$$

which corresponds to the first branch of the blue line in both plots of Fig.(9.13) – fitting perfectly the lower limit of the 4D SUSY scan point domain that we have also generated for checking [it is shown on Fig.(9.14)]. The second branch, as mentioned above, simply reveals the constraint

$$m_{\tilde{t}_2} \geq m_{\tilde{t}_1} \quad \text{for} \quad m_{\tilde{t}_1} \geq \sqrt{m_t^2 + \frac{1}{4}\cos 2\beta \, m_Z^2}. \tag{9.69}$$

The minimum $m_{\tilde{t}_2}$ value is thus

$$m_{\tilde{t}_2}^{lowest} = m_{\tilde{t}_1} \quad \text{for} \quad m_{\tilde{t}_1} = \sqrt{m_t^2 + \frac{1}{4}\cos 2\beta\, m_Z^2} \;\sim\; m_t. \tag{9.70}$$

Note that this result is a quite general result for 4D SUSY models.

Having determined explicitly the 4D SUSY structural limit on $m_{\tilde{t}_2}$ as a function of $m_{\tilde{t}_1}$, we now turn our attention to the results in the context of RS SUSY shown in Fig.(9.13). Looking at those two plots, we observe an important difference between the 4D and 5D SUSY models; $m_{\tilde{t}_2}$ can now reach smaller values (for a given $m_{\tilde{t}_1}$ value) than those in 4D SUSY [limited by the blue line] and is now only constrained by

$$m_{\tilde{t}_2} \geq m_{\tilde{t}_1} \gtrsim 100 \text{ GeV}. \tag{9.71}$$

This difference with the 4D case can be understood as follows. The 4D SUSY conservative constraint of Eq.(9.70) is changed in RS to the global constraint $m_{\tilde{t}_2} \gtrsim \mathcal{Y}\hat{v}_u f_0^{++}(c_{\tilde{t}_L};\pi R_c) f_0^{++}(c_{\tilde{t}_R};\pi R_c)$ as deduced from Eq.(9.47). If there were no SUSY breaking in the bulk, one would have $c_{\tilde{t}_{L/R}} = c_{t_{L/R}}$ and by consequence $\mathcal{Y}\hat{v}_u f_0^{++}(c_{\tilde{t}_L};\pi R_c) f_0^{++}(c_{\tilde{t}_R};\pi R_c) = m_t$ [neglecting the KK (s)top mixing effect as already mentioned] so that the constraint (9.70) would be recovered. However, when SUSY is broken in the bulk, $c_{\tilde{t}_{L/R}}$ are now effectively free parameters that can lead to either larger or smaller values of $\mathcal{Y}\hat{v}_u f_0^{++}(c_{\tilde{t}_L};\pi R_c) f_0^{++}(c_{\tilde{t}_R};\pi R_c)$ relatively to m_t. In particular, the lower limit in Eq.(9.68) materialized by the first branch in plots is relaxed down to the bound (9.71) in RS SUSY, thus explaining the RS scanned points going beyond the blue line.

Hence a measurement of $m_{\tilde{t}_2}$ at high energy colliders in the lower-left region of the RS scans shown here (below the blue line) would greatly disfavor 4D SUSY models in their minimal form while constituting possible signatures of RS SUSY scenarios. Such a discrimination test should be already possible before a future precision ILC physics, at LHC, given the experimental accuracies expected on squark mass reconstructions. Indeed, an uncertainty of $\sim 5\% - 10\%$ on stop masses should be reachable at LHC [72] which is clearly sufficient for the potential test suggested here, given the large stop mass deviations in RS with respect to the pure 4D SUSY scenario shown in Fig.(9.13). This typically expected accuracy of $\sim 5\% - 10\%$ on stop masses corresponds to illustrative examples studied in Ref. [72] but of course the exact performance would rely on effectively observed events at LHC as well as on the realized SUSY model/parameters chosen by nature. Note finally that for the values taken throughout this study, $m_{\tilde{\nu}_1} > 120$ GeV and $m_{\tilde{\chi}_1^0} > 150$ GeV, the conservative experimental lower bound on the stop mass is exactly $m_{\tilde{t}_1} > 95.7$ GeV [31, 74] so that the region only accessible in RS SUSY on Fig.(9.13) is not yet excluded and could be revealed by an LHC discovery.

The last comment – which is interesting for understanding the formal RS SUSY construction – is about the difference between the two plots of Fig.(9.13). In the first scenario (left plot) where breaking only occurs in the bulk, while, as discussed, $m_{\tilde{t}_2}$ can reach any values $\gtrsim 100$ GeV, on the other side we observe that the scan reaches a maximum value of $m_{\tilde{t}_2}$ depending on $m_{\tilde{t}_1}$. This is due to the chosen usual range for the $c_{\tilde{t}_{L/R}}$ parameters spanning from -1 to $+1$, together with the absence of soft mass terms on the TeV-brane. Indeed, in the absence of such mass terms, high values of $m_{\tilde{t}_2}$ are limited by the diagonal Yukawa-type mass contributions and thus by the largest allowed overlap of the stop wave functions with the Higgs boson, an overlap being limited from above by the minimal $c_{\tilde{t}_{L/R}}$ values. In contrast, the scan is not limited from above for the second RS scenario (right plot) due to the presence of soft mass terms on the TeV-brane (and even of trilinear scalar couplings).

Numerical results for smuon masses in mSUGRA

In this part, we consider within 4D SUSY the subcase of the mSUGRA scenario where the soft breaking parameters have universal values at the Grand Unified Theory (GUT) scale, m_0, $m_{1/2}$, A_0, the whole trilinear scalar couplings $A_0\mathcal{Y}$ being proportional to Yukawa coupling constants $\mathcal{Y}$. The two other input (SUSY) parameters are $\tan\beta$ and $sign(\mu)$. The soft masses $\tilde{m}_{L/R}$ will be run here [18] from their GUT value m_0 down to low-energy, where we study collider physics, and the obtained values included into the mass matrix form (9.65). To adopt a general approach, we will take the low-energy $|A|$ parameter to be between zero and the TeV scale. This maximum scale is justified, in 4D mSUGRA, by the order of effective SUSY breaking scales and by the condition of absence of CCB minima [see typically Eq.(9.60)].

In a minimal RS version of the mSUGRA scenario, the set of parameters entering the scalar mass matrices can be taken as follows. First, the parameter μ_{eff} (see Eq.(9.23)), which enters the mass matrix form (9.47), is taken at the μ value one gets in 4D mSUGRA since it is the equivalent parameter. The possible kind of differences arising between 4D and 5D models in the running necessary to derive the μ parameter is not studied here; this is a potential source of additional differences that could lead to new tests for distinguishing between 4D and 5D SUSY. Similarly, for the diagonal scalar mass matrix elements, we take the same values as the ones obtained from the 4D mSUGRA running, motivated by the fact that we will focus on differences between 4D and 5D mSUGRA arising in the off-diagonal mass matrix elements. Last but not least, in a mSUGRA like scenario, one would have a new [compared to Eq.(9.47)] trilinear coupling constant $A\mathcal{Y} = \mathcal{O}(1)$ with $A \sim (1/\mathcal{Y}) \sim k$ to not introduce new scales. The quantity $A|_{eff} = A\mathcal{Y}ke^{-k\pi R_c} \sim$ TeV ($A = 0$ could also be an acceptable scale) appearing now in the A terms of Eq.(9.47), namely in $A\mathcal{Y}e^{-k\pi R_c}\hat{v}_u f_L^0 f_R^0$, is taken equal numerically to the 4D SUSY breaking parameter A introduced just above, neglecting once again possible differences arising in the 5D running.

Let us now emphasize 4D versus 5D differences in the smuon mass matrix (studying the example of the smuon is motivated by the theoretical framework described above and the experimental performances discussed below) within this context.
In 4D mSUGRA, the off-diagonal entry to squared smuon mass $A_\mu\mathcal{Y}_\mu\hat{v}_d$, driven by the muon mass (m_μ), is typically around 10^2 GeV^2 at most which leads to a $\bar{\tilde{\mu}}_L\tilde{\mu}_R$ smuon mass term induced by the Higgs VEV much smaller than the diagonal soft mass terms $\tilde{m}_L^2\bar{\tilde{\mu}}_L\tilde{\mu}_L$ and $\tilde{m}_R^2\bar{\tilde{\mu}}_R\tilde{\mu}_R$ [see the matrix form (9.65)]. Indeed, one should typically have $\tilde{m}_{L,R}^2 \gtrsim 10^4$ GeV^2 so that smuon mass eigenvalues are not excluded by the conservative current experimental lower bound $m_{\tilde{\mu}_1} > 94$ GeV [31, 74].
The other off-diagonal $\bar{\tilde{\mu}}_L\tilde{\mu}_R$ contribution to the smuon mass is at most $m_\mu\mu\tan\beta \sim 5\ 10^3$ GeV^2, for extremely optimized parameter values, so that this contribution remains also systematically smaller than $\tilde{m}_{L,R}^2 \gtrsim 10^4$ GeV^2. Hence the two Left-Right mass mixing terms are limited in 4D mSUGRA, relatively to the complete diagonal elements of the 2×2 smuon squared mass matrix.

In the RS version of mSUGRA, one has a trilinear-induced mass term $A_\mu\mathcal{Y}_\mu e^{-k\pi R_c}\hat{v}_d f_L^0 f_R^0$ where the $f_{L/R}^0$ wave function values at $y = \pi R_c$ are not constrained from above by the muon mass because $f_{L/R}^0 = f_0^{++}(c_{\tilde{\mu}_{L/R}}; \pi R_c)$ whereas the muon mass is controlled by independent fermionic 5D parameters $c_{\mu_{L/R}}$ in the present SUSY breaking scheme.
Similarly, the off-diagonal Left-Right smuon squared mass $\mu_{eff}\mathcal{Y}_\mu\hat{v}_d\tan\beta f_L^0 f_R^0$ of Eq.(9.47) can take benefit from large factors from the scalar wave function overlaps with the Higgs brane, while $\tan\beta$ takes comparable values as in 4D SUSY and $\mathcal{Y}_\mu \sim 1/k$ is compensated by $f_L^0 f_R^0 \propto k$ (*c.f.* Eq.(H.13)). Therefore, in contrast

[18] We use the standard RGE evolution to the weak scale at one-loop for the studied smuon masses.

to the 4D mSUGRA case, the off-diagonal mixing smuon mass terms are not constrained by the muon mass and can thus get higher values.

In consequence, the Left-Right mass mixing for smuon masses can reach higher amounts within RS mSUGRA than in 4D mSUGRA. In turn (having a universal mass m_0 tends to have a configuration with identical diagonal squared masses), the splitting between the mass eigenvalues $m_{\tilde{\mu}_1}$ and $m_{\tilde{\mu}_2}$ can be much larger as illustrates Fig.(9.15).
In order to obtain this figure, we have scanned the input parameters over these ranges: $\tan\beta \in [1;60]$, $m_0 \in [300;2000]$ GeV, $m_{1/2} \in [150;600]$ GeV, $c_{\tilde{t}_{L/R}} \in [-1,1]$ and $A_\mu, A_\mu|_{eff} \in [0;1000]$ GeV (see above discussion). The interval on $\tan\beta$ corresponds to the domain allowed by the Higgs potential minimization conditions in mSUGRA [30]. The choice of m_0 and $m_{1/2}$ ranges is based on the constraints coming from SUSY searches at colliders combined with the requirement that the Lightest Supersymmetric Particle (LSP) is not the tau lepton superpartner (the stau) [73, 74]; taking higher m_0 and $m_{1/2}$ values does not modify significantly the scan presented in Fig.(9.15). The output smuon mass ranges (i.e. the shown plot domain in Fig.(9.15)) is motivated by the order of magnitude of usual effective 4D SUSY breaking scale – near the EWSB scale – allowing to protect the Higgs boson against too dramatic mass fine-tuning. The scans here are not done for negative values of the A_μ (or $A_\mu|_{eff}$) terms and the μ (or μ_{eff}) terms are neither taken negatively but choosing the opposite signs would not change the present conclusions. Besides, only values in the range $[100;1000]$ GeV have been kept for the $|\mu|$ (or $|\mu_{eff}|$) quantity; this is imposed by the orders of experimental bounds and the Higgs potential minimization conditions already mentioned. The last remark, as before, is that having chosen slightly larger parameter ranges – staying with the same orders of magnitude physically motivated – would have not affected significantly the obtained numerical results shown in this part.
In conclusion, if a $m_{\tilde{\mu}_2}$ measurement is obtained at ILC or even at LHC at a value larger – including the experimental uncertainty in this comparison – than the 4D SUSY upper limit appearing on Fig.(9.15) for a given $m_{\tilde{\mu}_1}$ value (assumed to be measured also), this result would rule out the 4D mSUGRA scenario [at least in its simplest form] and constitute a good indication for an RS mSUGRA model. Indeed all $m_{\tilde{\mu}_2}$ values above the upper 4D mSUGRA limit can be reached within RS mSUGRA as shown by the scan over parameters. Such a discrimination should be already possible at LHC given the accuracies expected on slepton mass reconstructions: a $\sim 5\% - 10\%$ uncertainty is reasonable to expect [72] and clearly sufficient in a large part of parameter space (at high $m_{\tilde{\mu}_2}$) for the proposed potential test – given the large mass splitting reachable theoretically in RS mSUGRA [illustrated in Fig.(9.15)]. This typical uncertainty of $\sim 5\% - 10\%$ on the smuon mass corresponds to illustrative examples studied in Ref. [72] but of course this performance will be quite model/parameter-dependent and can be improved by combining different related mass measurements. Note that the present experimental bound $m_{\tilde{\mu}_1} > 94$ GeV [31, 74] is respected on the plot of Fig.(9.15).

9.3.3 H boson decays

The phenomenological framework of this Section 9.3.3 is the same as the one described in Section 9.3.2. We have seen that in this RS framework the interactions between Higgs bosons and sfermions can be significantly increased with respect to the 4D SUSY case. This is mainly due to the fact that the 5D $c_{\tilde{f}_{L/R}}$ parameters involved in these Higgs interactions are quite free (more precisely $c_{\tilde{f}_{L/R}}$ only affect squark/slepton masses) in RS SUSY whereas the same Higgs interactions are fixed by SM Yukawa coupling constants (related to SM fermion masses) in 4D SUSY. In this section, we will look at the effects of these increases on Higgs decay

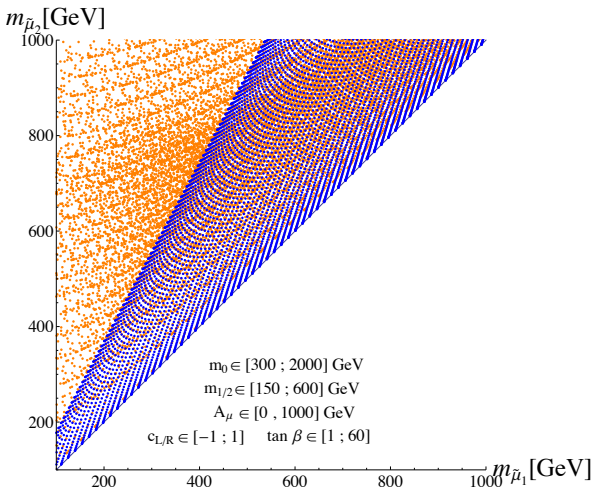

Figure 9.15: Points obtained in the plan $m_{\tilde{\mu}_2}$ versus $m_{\tilde{\mu}_1}$ (in GeV), for an mSUGRA type scenario within 4D SUSY [blue points] and RS SUSY [orange points], from a scan performed in the intervals indicated on the plot. The interval indicated on A_μ corresponds to the range for the soft trilinear coupling A_μ in 4D SUSY and for the $A_\mu|_{eff}$ effective dimension-one parameter defined in RS SUSY (see text). $c_{L/R} = c_{\tilde{\mu}_{L/R}}$ denote now the 5D smuon parameters.

branching ratios. The analysis emphasis will be put on the example of the heaviest neutral Higgs boson H as, kinematically, the lightest h field (being heavier than ~ 91 GeV from LEP results but smaller than ~ 140 GeV from SUSY Higgs structure [30]) cannot decay into pairs of on-shell sfermions (having lower experimental limits of $\sim 10^2$ GeV [31, 74]) and hence does not feel optimal RS effects, except of course if the theoretical upper limit on its mass m_h can really be sufficiently relaxed in warped SUSY [32]. The pseudo-scalar field A and charged Higgs boson $H^\pm$ can similarly have increased decay widths into sleptons, as we will show it occurs for H in RS SUSY.

Technically, the branching ratio formulas for Higgs bosons can be found in [30] together with EW and NLO radiative corrections. We have included the leading corrections involved: the b quark running mass, the radiative corrections to the neutral Higgs boson masses m_h and m_H as well as the corrections to the trilinear Higgs coupling $\Delta\lambda_{Hhh}$ within the ϵ approximation (see Ref. [30], Section 1.3.3, for details).
These branching ratios depend on the various Higgs couplings; in RS SUSY, the H boson couplings to SM fermions, Higgs/gauge bosons and higgsinos/gauginos are taken as in 4D SUSY (since heavy KK mixing/exchange effects are neglected as mentioned above) while the H couplings to squarks/sleptons are deduced from stop couplings in Eq.(9.22) – and rotation to the sfermion mass basis.
The higher-dimensional parameters entering these effective H couplings to squarks/sleptons are $c_{\tilde{q}_{L/R}}$, $c_{\tilde{\ell}_{L/R}}$ (with absolute values around unity), μ_{eff} [see Eq.(9.23)] and $A|_{eff} = Ake^{-k\pi R_c} \sim$ TeV which appears in the scalar coupling matrix of Eq.(9.22). The TeV scale parameter μ_{eff} ($A|_{eff}$) will be taken numerically as μ (A) in 4D SUSY. Similarly, the effective quantity $\tilde{m}_{L/R}|_{eff} = (\tilde{m}_{L/R}ke^{-2k\pi R_c})^{1/2} \sim$ TeV that shows up in scalar mass matrices of type (9.47) is taken numerically approximately equal to the 4D soft mass $\tilde{m}_{L/R} \sim$ TeV [see Eq.(9.65)]. We denote as usual the effective 4D soft gaugino masses for the bino and wino respectively M_1 and M_2.

In Fig.(9.16), we show the branching ratios for the main decay channels of the H boson as a function

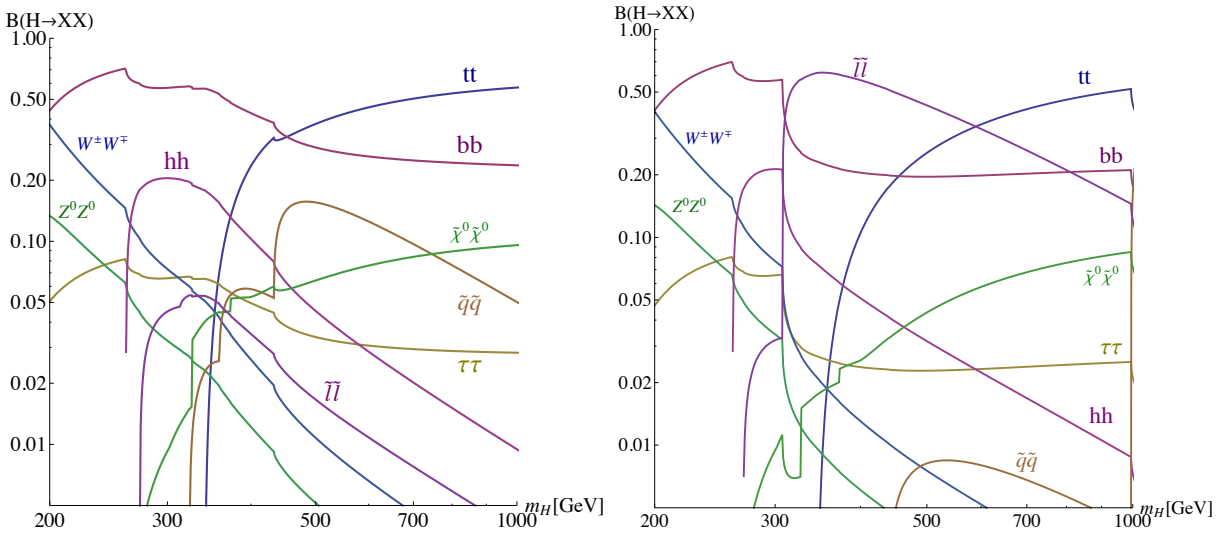

Figure 9.16: Branching ratios of the H boson decays as a function of its mass m_H (in GeV) within pure SUSY [left] and RS SUSY [right]. The types of final states are indicated directly on the plot; all kinematically allowed channels for neutralinos (among $\bar{\tilde{\chi}}_i^0\tilde{\chi}_j^0$, with $i,j = \{1,2,3,4\}$) and squarks/sleptons are summed. The τ lepton channel is included but not the ones with branching ratios below $\sim 10^{-2}$ in this m_H range (like the triangular-loop induced decays into photons and gluons). The values for the gaugino sector parameters in the two plots are: $\mu = \mu_{eff} = 170$ GeV, $\tan\beta = 6$ and $M_1 = 160$ GeV, $M_2 = 1000$ GeV, leading to the neutralino masses $m_{\tilde{\chi}_1^0} \simeq 128$ GeV, $m_{\tilde{\chi}_2^0} \simeq 174$ GeV and lightest chargino mass $m_{\tilde{\chi}_1^\pm} \simeq 167$ GeV. The other common parameters are taken at $A_t|_{eff} = A_t = A_b = A_\nu = A_{\ell^\pm} = -500$ GeV. The soft masses in 4D SUSY are: $\tilde{m}_L^q = 170$ GeV, $\tilde{m}_R^q = 1000$ GeV for the squarks and $\tilde{m}_L^\ell = 180$ GeV, $\tilde{m}_R^\ell = 1000$ GeV for the sleptons. For this set of parameters, the smallest mass eigenvalues obtained are: $m_{\tilde{\nu}_{\mu 1}} \simeq m_{\tilde{\nu}_{\tau 1}} \simeq 169$ GeV for sneutrinos, $m_{\tilde{\mu}_1} \simeq m_{\tilde{\tau}_1} \simeq 186$ GeV for charged sleptons, $m_{\tilde{t}_1} \simeq 216$ GeV for the stop and $m_{\tilde{b}_1} \simeq 179$ GeV for the sbottom quark. In RS SUSY, the effective soft masses are: $\tilde{m}_L^q|_{eff} = 275$ GeV, $\tilde{m}_R^q|_{eff} = 1000$ GeV, $\tilde{m}_L^\ell|_{eff} = 105$ GeV, $\tilde{m}_R^\ell|_{eff} = 1000$ GeV leading to $m_{\tilde{\nu}_{\mu 1}} \simeq m_{\tilde{\nu}_{\tau 1}} \simeq 135$ GeV, $m_{\tilde{\mu}_1} \simeq m_{\tilde{\tau}_1} \simeq 154$ GeV and $m_{\tilde{t}_1} \simeq m_{\tilde{b}_1} \simeq 218$ GeV while the 5D parameters are $c_{\tilde{q}_L} = c_{\tilde{q}_R} = 0.2$ for squarks and $c_{\tilde{\ell}_L} = c_{\tilde{\ell}_R} = -0.5$ for sleptons (for all flavors).

of its mass for a given set of parameters. Both 4D and 5D SUSY scenarios are represented. The tree level Higgs mass m_H (like m_h and the neutral Higgs mixing angle α) depends on the parameter $\tan\beta$ and on m_A (pseudo-scalar mass) which has been varied (above ~ 200 GeV) to span the m_H interval in Fig.(9.16). The modifications of radiative corrections due to heavy KK modes are expected to raise Higgs masses by an amount of at most $\mathcal{O}(10)$ GeV [32] so that Fig.(9.16) would not be significantly affected by those. The heavy Higgs mass and $\tan\beta$ ranges considered in Fig.(9.16) and in the following Higgs branching ratio plots, namely $m_H \in [200, 1000]$ GeV and $\tan\beta \in [6, 30]$ [19], are clearly in agreement with the several constraints coming from direct charged/neutral Higgs boson searches at LEP [30] or Tevatron Run II [74] within a SUSY framework. The modifications of these constraints due to KK mode effects should not be significant here for $M_{KK} \gtrsim 3$ TeV (*c.f.* Section 9.2.1).

For the sake of convenience, in this section, we only write the sets of parameter values in the captions of Higgs branching ratio plots. But let us give here some general comments about these sets chosen in the plots. First, the branching ratios are shown for either positive or negative values of the A (or $A|_{eff}$) and

[19] More precisely, we will only take $\tan\beta = 6$ and $\tan\beta = 30$ in order to illustrate the main characteristic behaviours.

μ (or μ_{eff}) terms as these signs do not affect the main ratio behaviors. Secondly, all the superpartner mass eigenvalues considered respect their last conservative/combined experimental lower limits derived from direct SUSY searches at colliders [31, 74] some of which we quote here for comparison: $m_{\tilde{\chi}_1^0} > 120$ GeV, $m_{\tilde{\chi}_2^0} > 116$ GeV, $m_{\tilde{\chi}_1^\pm} > 164$ GeV, $m_{\tilde{\nu}_1} > 120$ GeV, $m_{\tilde{\ell}_1} > 107$ GeV, $m_{\tilde{t}_1} > 95$ GeV and $m_{\tilde{b}_1} > 89$ GeV. In order to compare the Higgs couplings via its branching ratios, we have chosen the parameters so that the superpartner mass eigenvalues are approximately identical in the 4D and 5D pMSSM (KK corrections might be up to a few percents and are irrelevant in this analysis); this is also motivated by the present philosophy of developing tests of discrimination between the two SUSY scenarios (4D versus 5D) for a situation where light SUSY particles would have been discovered [and thus their masses at least approximately estimated]. Note also that the lightest neutralino is systematically the LSP in our choices of parameters so that $\tilde{\chi}_1^0$ represents the potential candidate for dark matter as in usual 4D SUSY theories. In order to minimize the corrections to EW observables, we have further imposed $A_t = A_b$, $A_\nu = A_\ell$, $\tilde{m}^u_{L/R} = \tilde{m}^d_{L/R}$ for soft squark masses and $\tilde{m}^\nu_L = \tilde{m}^e_L$ for the slepton ones (in the RS case as well). Finally, the sfermion mass matrices as well as soft trilinear scalar couplings are taken universal for all families and diagonal in the flavor basis (which guarantees the absence of FCNC at tree level) as motivated by the SUSY flavor problem. Note that these hypotheses imply the absence of flavor mixing in the scalar sector which allows a better identification of the smuon and stop studied in Section 9.3.2. We also assume that all phases in the soft SUSY breaking potential are zero to eliminate all new sources of CP-violation. Those assumptions are characteristic of the pMSSM [38].

For simplifying the discussion on this first Fig.(9.16), we have chosen large effective TeV-brane soft masses $\tilde{m}^{q,\ell}_R, \tilde{m}^{q,\ell}_R|_{eff}$ so that the heaviest sfermion mass eigenvalues become large enough to close the associated channels $H \to \tilde{f}_1\tilde{f}_2, \tilde{f}_2\tilde{f}_2$. We see on Fig.(9.16) that starting from a 4D SUSY regime where the $W^\pm$ boson, top quark and lightest neutral Higgs channels are dominant (the top dominance is due, in particular, to the low $\tan\beta$ regime increasing the top-Higgs coupling), and then moving to the RS case with small $c_{\tilde{\ell}_{L/R}}$ values, the slepton channel is globally increased and even becomes dominant at intermediate m_H values. This slepton channel has a width decreasing with the third power of the H mass which explains its branching behavior on the plot. The first reason for having larger slepton branching ratios in that RS case is that the slepton-Higgs couplings are favored by the large wave function overlaps between sleptons and the localized Higgs boson induced by the small $c_{\tilde{\ell}_{L/R}}$ values taken. The other reason, of same kind, is the choice of large $c_{\tilde{q}_{L/R}}$ reducing the squark overlaps with Higgs bosons relatively to the 4D SUSY case. Indeed, one can clearly observe, by comparing the two plots of Fig.(9.16), the decrease of the branching ratio $B(H \to \bar{\tilde{q}}\tilde{q})$ in RS which leads to an increase of $B(H \to \bar{\tilde{\ell}}\tilde{\ell})$.

We now present in Fig.(9.17) the branching ratios for the main decay channels of the H boson as a function of m_H for another set of parameters [specified in the caption]. The soft masses $\tilde{m}^q_R$, in particular, are smaller than in the previous figure so that the stop masses are smaller and channels into the heaviest state $\tilde{q}_2$ open up, leading to a dominant squark channel at intermediate m_H in the 4D SUSY case. The $M_{1,2}$ parameters are also typically lower than in Fig.(9.16), so that channels into charginos open up and neutralino channels have larger phase space factors, which modifies the branching profiles rendering in particular the various gaugino channels dominant above $m_H \simeq 800$ GeV in 4D SUSY. We see as well on Fig.(9.17) that compared to this new 4D SUSY regime with alternatively dominant squark and bottom channels, in RS the slepton channel rates can again be greatly enhanced (and still become dominant at intermediate m_H) for small enough $c_{\tilde{\ell}_{L/R}}$ values increasing the slepton-Higgs couplings. This enhancement of $B(H \to \bar{\tilde{\ell}}\tilde{\ell})$ is also correlated with the large $c_{\tilde{q}_{L/R}}$ values allowing to have small squark-Higgs couplings relatively to 4D SUSY,

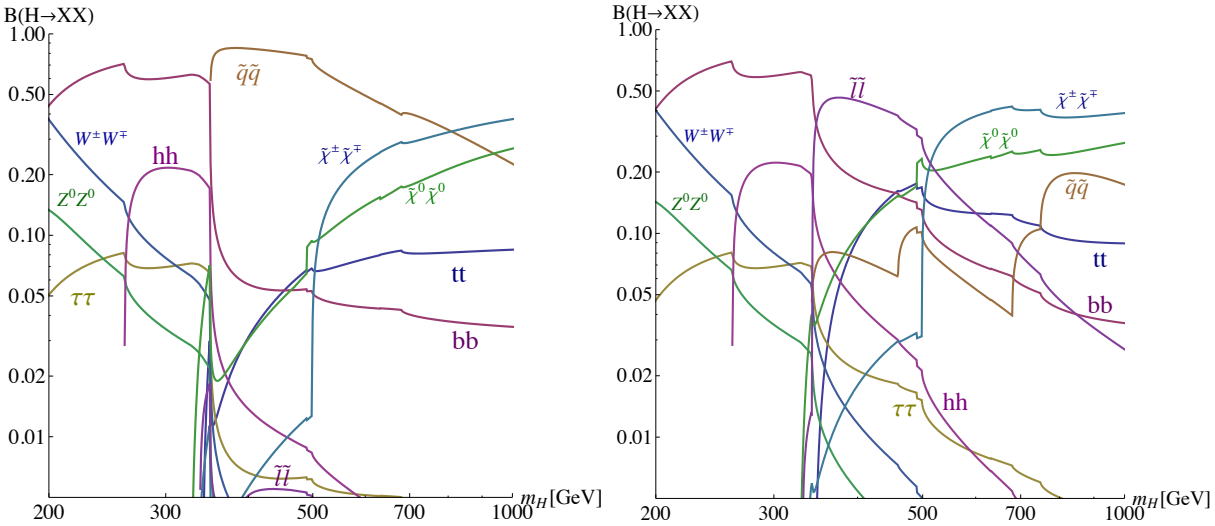

Figure 9.17: Branching ratios of the H boson decays as a function of its mass m_H (in GeV) within pure SUSY [left] and RS SUSY [right]. The types of final states are indicated directly on the plot; all kinematically allowed channels for neutralinos (among $\bar{\tilde{\chi}}_i^0\tilde{\chi}_j^0$, with $i,j=\{1,2,3,4\}$), charginos (among $\tilde{\chi}_k^\pm\tilde{\chi}_l^\mp$, with $k,l=\{1,2\}$) and squarks/sleptons are summed, as in Fig.(9.16). The values for the gaugino sector parameters are: $\mu=\mu_{eff}=300$ GeV, $\tan\beta=6$, $M_1=600$ GeV and $M_2=190$ GeV leading to $m_{\tilde{\chi}_1^0}\simeq 163$ GeV, $m_{\tilde{\chi}_2^0}\simeq 305$ GeV and $m_{\tilde{\chi}_1^\pm}\simeq 164$ GeV. The other common parameters are $A_t|_{eff}=A_t=A_b=-200$ GeV and $A_\nu|_{eff}=A_\nu=A_{\ell^\pm}=-300$ GeV. The soft masses in 4D SUSY are: $\tilde{m}_L^q=210$ GeV, $\tilde{m}_R^q=220$ GeV and $\tilde{m}_{L/R}^\ell=180$ GeV which give rise to $m_{\tilde{\nu}_{\mu 1}}\simeq m_{\tilde{\nu}_{\tau 1}}\simeq 169$ GeV, $m_{\tilde{\mu}_1}\simeq m_{\tilde{\tau}_1}\simeq 175$ GeV, $m_{\tilde{t}_1}\simeq 175$ GeV and $m_{\tilde{b}_1}\simeq 206$ GeV. In RS SUSY, the effective soft masses are: $\tilde{m}_L^q|_{eff}=500$ GeV, $\tilde{m}_R^q|_{eff}=260$ GeV, $\tilde{m}_L^\ell|_{eff}=125$ GeV and $\tilde{m}_R^\ell|_{eff}=1000$ GeV giving $m_{\tilde{\nu}_{\mu 1}}\simeq m_{\tilde{\nu}_{\tau 1}}\simeq 165$ GeV, $m_{\tilde{\mu}_1}\simeq m_{\tilde{\tau}_1}\simeq 171$ GeV, $m_{\tilde{t}_1}\simeq 171$ GeV and $m_{\tilde{b}_1}\simeq 229$ GeV while the 5D parameters are $c_{\tilde{q}_L}=c_{\tilde{b}_R}=0$, $c_{\tilde{t}_R}=0.3$ and $c_{\tilde{\ell}_{L/R}}=-0.5$.

and in turn to have small amounts of $B(H\to\bar{\tilde{q}}\tilde{q})$. We note from the RS plot that $B(H\to\bar{\tilde{\ell}}\tilde{\ell})$ reaches values a bit smaller than $\sim 50\%$ whereas it was above $\sim 60\%$ in Fig.(9.16), which is due to the $\tilde{m}_L^\ell|_{eff}$ value taken larger here.

We present in Fig.(9.18) the branching ratios for the main H decay channels as a function of m_H in the high $\tan\beta$ regime. We see on this figure that starting from such a 4D SUSY regime where the bottom channel is extremely dominant and going to the RS case, the Higgs-to-slepton branching ratio is largely enhanced – once again due to the small $c_{\tilde{\ell}_{L/R}}$ values – reaching significant levels around 20% and even dominantly at $\sim 40\%$ for a large m_H (thanks to the $H\to\bar{\tilde{\ell}}_1\tilde{\ell}_2$ opening). This $B(H\to\bar{\tilde{\ell}}\tilde{\ell})$ enhancement is also due to the large $c_{\tilde{q}_{L/R}}$ values which tend to suppress $B(H\to\bar{\tilde{q}}\tilde{q})$ relatively to the 4D SUSY configuration. The reasons why the H decay width into sleptons cannot be comparable in size to the one for bottom quark final states, at $m_H\lesssim 800$ GeV in RS, are the large $\tan\beta$, phase space and color factor.

Of course in the different configuration of relatively high $c_{\tilde{\ell}_{L/R}}$ values, the slepton-Higgs couplings, and in turn the associated Higgs channels, are not significantly increased with respect to the 4D pMSSM, as illustrated in Fig.(9.19) in a low $\tan\beta$ example; note that in the RS case the sneutrino channel opens up at a larger m_H due to sneutrinos being a bit heavier than in the 4D case. The main difference between the two plots of Fig.(9.19) is the decrease of the squark channel in RS due to still quite large $c_{\tilde{q}_{L/R}}$ parameters (for

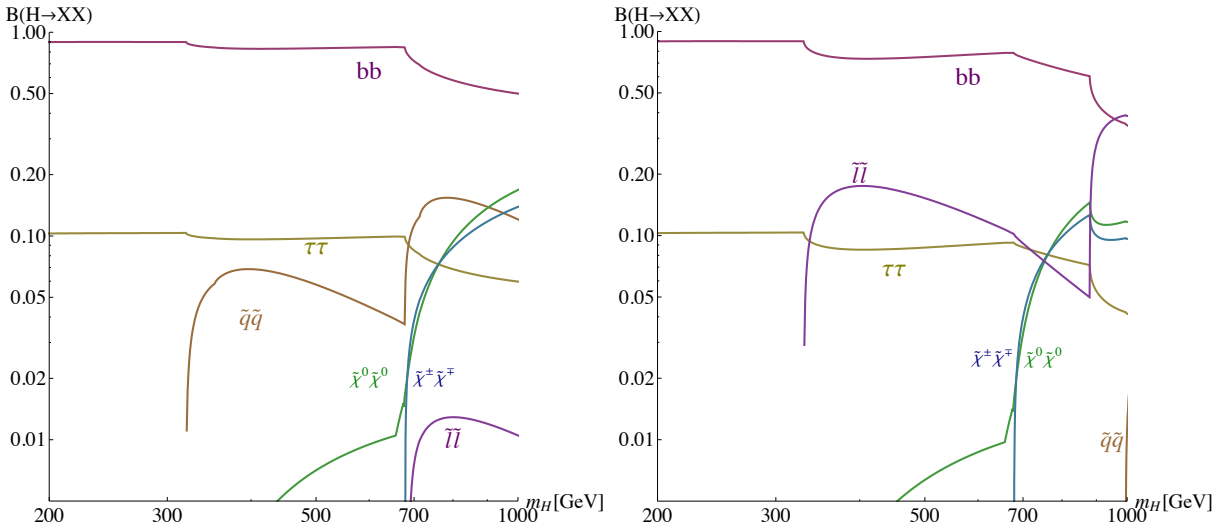

Figure 9.18: Branching ratios for the H boson decays as a function of m_H (in GeV) within pure SUSY [left] and RS SUSY [right]. The types of final states are indicated directly on the plot; all kinematically allowed channels for neutralinos, charginos and squarks/sleptons are summed, as in previous figures. The values for the gaugino sector parameters are: $\mu = \mu_{eff} = 170$ GeV, $\tan\beta = 30$, $M_1 = M_2 = 500$ GeV leading to $m_{\tilde{\chi}_1^0} \simeq 157$ GeV, $m_{\tilde{\chi}_2^0} \simeq 176$ GeV and $m_{\tilde{\chi}_1^\pm} \simeq 164$ GeV. The trilinear couplings read as $A_t|_{eff} = A_t = A_b = -A_\nu = -A_{\ell^\pm} = -500$ GeV. The 4D soft masses are: $\tilde{m}_L^q = 170$ GeV, $\tilde{m}_R^q = 500$ GeV, $\tilde{m}_L^\ell = 180$ GeV and $\tilde{m}_R^\ell = 500$ GeV which give $m_{\tilde{\nu}_{\mu 1}} \simeq m_{\tilde{\nu}_{\tau 1}} \simeq 168$ GeV, $m_{\tilde{\mu}_1} \simeq m_{\tilde{\tau}_1} \simeq 185$ GeV, $m_{\tilde{t}_1} \simeq 160$ GeV and $m_{\tilde{b}_1} \simeq 177$ GeV. In RS SUSY, the effective soft masses are: $\tilde{m}_L^q|_{eff} = 275$ GeV, $\tilde{m}_R^q|_{eff} = 1000$ GeV, $\tilde{m}_L^\ell|_{eff} = 130$ GeV and $\tilde{m}_R^\ell|_{eff} = 500$ GeV giving $m_{\tilde{\nu}_{\mu 1}} \simeq m_{\tilde{\nu}_{\tau 1}} \simeq 172$ GeV, $m_{\tilde{\mu}_1} \simeq m_{\tilde{\tau}_1} \simeq 165$ GeV and $m_{\tilde{t}_1} \simeq m_{\tilde{b}_1} \simeq 219$ GeV while the 5D parameters are $c_{\tilde{q}_{L/R}} = 0.2$ and $c_{\tilde{\ell}_{L/R}} = -0.5$.

smaller $c_{\tilde{q}_{L/R}}$ one would recover branching profiles similar to those in 4D SUSY). This leads in particular to an increase of $B(H \to \tilde{\chi}^\pm\tilde{\chi}^\mp, \bar{\tilde{\chi}}^0\tilde{\chi}^0)$. Finally, for a better understanding of Fig.(9.19), we remark that in RS the slepton masses are mainly generated through large TeV-brane soft masses (reduced to the EWSB scale by wave function overlap factors) since the masses induced by Yukawa-type couplings to the Higgs VEV are suppressed by the present high $c_{\tilde{\ell}_{L/R}}$ values. For comparison, within 4D SUSY, the soft masses in Fig.(9.19) are smaller (roughly at the EWSB scale) since those are not suppressed by overlap factors, while the masses induced by Yukawa coupling constants are negligible due to the tiny lepton masses.

Let us summarize this part on Higgs decays and conclude. In order to maximize the H couplings to sleptons in 4D SUSY, the A terms have been taken of the order of the TeV, and not at zero. The slepton masses have also been taken close to their lower experimental limits to maximize the branching ratios of the slepton channel in 4D SUSY. However we have found that even in these optimal cases the slepton channel branchings cannot reach amounts above $\sim 5\%$ (in agreement with Ref. [30]) while important slepton branchings can arise in RS – where $B(H \to \bar{\tilde{\ell}}\tilde{\ell})$ can reach up to $\sim 60\%$ (even larger ratios are accessible for instance by decreasing again $c_{\tilde{\ell}_{L/R}}$ w.r.t. present values, or by introducing a Right-handed (s)neutrino). Besides, the other way to try to increase the slepton channel branching ratio in 4D SUSY is to decrease the other branching ratios: for that purpose, we have explored – keeping trilinear couplings at the TeV scale – the main typical domains of 4D SUSY (breaking) parameter space characterized by different types of dominant H decay channels. The conclusion was still that the slepton channel rate can never be as important as it can

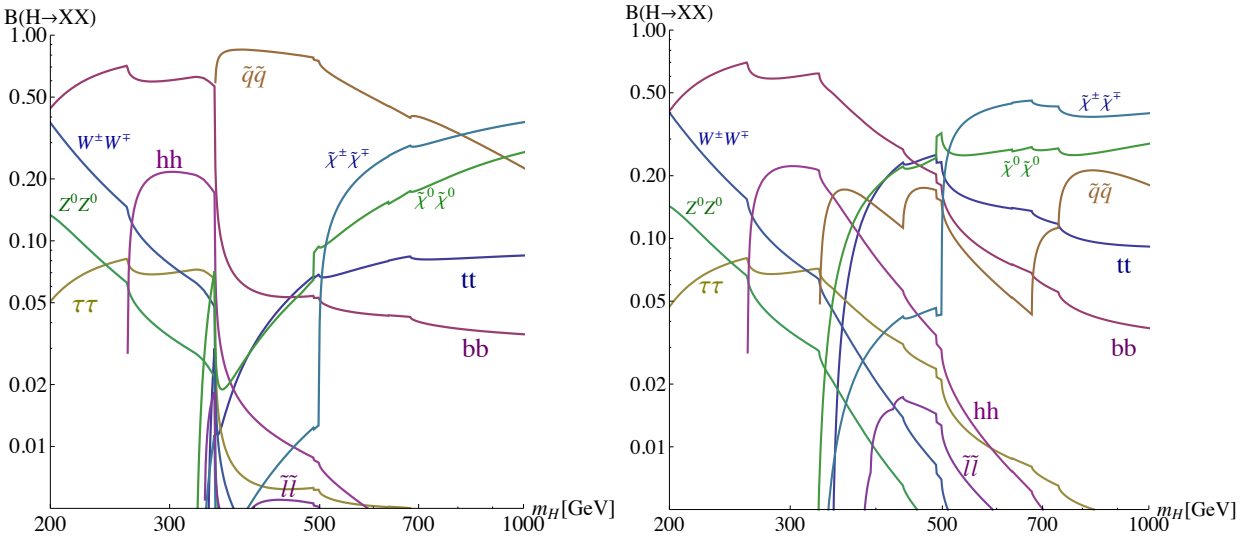

Figure 9.19: Branching ratios for the H boson decays as a function of m_H (in GeV) within pure SUSY [left] and RS SUSY [right]. The types of final states are indicated directly on the plot. The parameters in the higgsino/gaugino sector, the scalar trilinear couplings and the soft masses in 4D SUSY are the same as in Fig.(9.17) so that the left plot here is identical to the left plot of Fig.(9.17). In RS SUSY, the effective soft masses are: $\tilde{m}^q_L|_{eff} = 500$ GeV, $\tilde{m}^q_R|_{eff} = 250$ GeV, $\tilde{m}^\ell_L|_{eff} = 1000$ GeV and $\tilde{m}^\ell_R|_{eff} = 800$ GeV giving $m_{\tilde{\nu}_{\mu 1}} \simeq m_{\tilde{\nu}_{\tau 1}} \simeq 197$ GeV, $m_{\tilde{\mu}_1} \simeq m_{\tilde{\tau}_1} \simeq 169$ GeV, $m_{\tilde{t}_1} \simeq 165$ GeV and $m_{\tilde{b}_1} \simeq 219$ GeV while the 5D parameters are $c_{\tilde{q}_L} = c_{\tilde{b}_R} = 0$, $c_{\tilde{t}_R} = 0.3$ and $c_{\tilde{\ell}_{L/R}} = +0.49$.

be in RS. Furthermore, the case of a dominant slepton channel can occur in RS (see e.g. Fig.(9.17)) whereas it is impossible in 4D SUSY. This is due to the fact that in 4D SUSY slepton-Higgs couplings are severely constrained by the small Yukawa coupling constants of SM leptons. Therefore the experimental observation of either a dominant slepton channel or a slepton channel with say e.g. $B(H \to \bar{\tilde{\ell}}\tilde{\ell}) \simeq 50\%$ would exclude the 4D pMSSM and indicate the possible existence of a warped version of the pMSSM. Such a potential test should in principle be doable at colliders; a four-momentum reconstruction of slepton cascade decays based on measured slepton masses could allow to identify the decay channel $H \to \bar{\tilde{\ell}}\tilde{\ell}$ which is necessary to estimate its branching ratio – or (it would be sufficient here) a lower bound on this ratio. This kinematics approach being experimentally challenging, one could also use the clean leptonic event topology to identify the slepton channel. Indeed, the decay $H \to \bar{\tilde{\ell}}\tilde{\ell}$ would lead to final states with an higher lepton multiplicity due to the decay $\tilde{\ell} \to \ell\tilde{\chi}^0_i$ (recall that $\tilde{\chi}^0_1$ is the LSP).

9.4 Conclusion

If the fundamental theory of nature is of string theory kind, the effective low-energy model manifesting itself at present and future particle colliders would probably be an higher-dimensional SUSY model. In this study, we have studied the theory and phenomenology of such models entering the class of particularly well-motivated frameworks with a warped space-time.

First, we have derived in a consistent analytical way, within the realistic 5D pMSSM context, the effective 4D Lagrangian for the brane-Higgs interactions as well as the complete sfermion mass matrices (illustrating

explicitly the example of the stop quark) induced partially by such interactions.

Those theoretical investigations have provided us with the necessary tools to perform concrete phenomenological studies of the RS SUSY models. In this respect, we have first demonstrated that the cancellation of quadratic divergences in the one-loop corrections to the Higgs mass is deeply related to the 5D anomaly cancellation (similarly to 4D). We have also found that the quadratic divergence cancellation occurs for any 5D cut-off, which means possibly for a 'truncated' 5D SUSY theory (as it must be due to its non-renormalizable aspect). In these loop calculations, the accent was also put on the justification of the infinite KK summation required in the KK regularization which has open up a rich debate in the literature a decade ago. Possible perspectives are the extensions of these calculations to the sfermion masses.
Concerning collider physics, we have tried to answer a crucial question: in the hypothetical situation where some superpartners were discovered whereas all KK modes were outside the reach of direct detection (at LHC and/or ILC), how one could distinguish experimentally between a pure 4D SUSY scenario and a warped 5D SUSY model ? In particular, the virtual effects of KK gluon excitations on the stop pair production at LHC might certainly be at least as tricky to detect as the similar effects for the top pair final state [79]. We have developed series of tests that could be more clear or at least complementary. For instance, we have shown that the heaviest stop eigenstate can reach lower mass values in RS SUSY than in 4D SUSY. Other clear 4D/5D SUSY differences, that may be used for data-based discriminations, are those arising from the slepton mass sector of mSUGRA scenarios where larger mass splittings can occur in 5D setups. Finally, in the same philosophy applied to the SUSY Higgs sector, it has been shown in particular that branching ratios of H decay channels into sleptons can reach dominant levels in the RS pMSSM, a feature absent of the conventional 4D SUSY models. In the future, it will be interesting to explore a related direction: the search at hadron colliders for the SM Higgs boson – or the lightest neutral 4D SUSY Higgs field h – could be affected by new significant contributions to the gluon-fusion mechanism induced by 5D effects [if not too much constrained by present experimental data], effects representing other potential distinctive signatures of 5D SUSY scenarios.

In the complete study performed in Ref. [80], we further study the stop pair production at ILC and show how it can be used to pin down the presence of soft terms on the IR boundary, and in turn, to discriminate between different types of SUSY breaking in the RS context: bulk versus brane SUSY breaking.

Bibliography

[1] L. Randall and R. Sundrum, Phys. Rev. Lett. **83** (1999) 3370. See also, M. Gogberashvili, Int. J. Mod. Phys. **D11** (2002) 1635.

[2] T. Gherghetta and A. Pomarol, Nucl. Phys. **B586** (2000) 141.

[3] See e.g. M. Carena, E. Ponton, J. Santiago and C. E. M. Wagner, Nucl. Phys. **B759** (2006) 202; Phys. Rev. **D76** (2007) 035006.

[4] C. Csáki, C. Grojean, H. Murayama, L. Pilo and J. Terning, Phys. Rev. **D69** (2004) 055006; C. Csáki, C. Grojean, L. Pilo and J. Terning, Phys. Rev. Lett. **92** (2004) 101802; G. Cacciapaglia, C. Csáki, C. Grojean and J. Terning, Phys. Rev. **D70** (2004) 075014.

[5] J. M. Maldacena, Adv. Theor. Math. Phys. **2** (1998) 231; Int. J. Theor. Phys. **38** (1999) 1113; S. S. Gubser, I. R. Klebanov and A. M. Polyakov, Phys. Lett. **B428** (1998) 105; E. Witten, Adv. Theor. Math. Phys. **2** (1998) 253; N. Arkani-Hamed, M. Porrati and L. Randall, JHEP **0108** (2001) 017.

[6] R. Contino, Y. Nomura and A. Pomarol, Nucl. Phys. **B671** (2003) 148; K. Agashe, R. Contino and A. Pomarol, Nucl. Phys. **B719** (2005) 165; K. Agashe and R. Contino, Nucl. Phys. **B742** (2006) 59; R. Contino, L. Da Rold and A. Pomarol, Phys. Rev. **D75** (2007) 055014.

[7] I. Antoniadis Phys. Lett. **B246** (1990) 377; G. Dvali and M. Shifman Nucl. Phys. **B**504 (1997) 127.

[8] A. Delgado, M. Quirós, Nucl. Phys. **B607** (2001) 99.

[9] E. A. Mirabelli, M. E. Peskin, Phys. Rev. **D58** (1998) 065002; W. D. Goldberger, Y. Nomura, D. R. Smith, Phys. Rev. **D67** (2003) 075021; H.P. Nilles, TASI97 lectures as published in Supersymmetry, Supergravity and Supercolliders, World Scientific, Ed. J. A. Bagger.

[10] S. Abel and T. Gherghetta, JHEP **1012** (2010) 091.

[11] T. Gherghetta, A. Pomarol, Nucl. Phys. **B602** (2001) 3.

[12] J. Scherk and J. H. Schwarz, Phys. Lett. **B82** (1979) 60; Nucl. Phys. **B153** (1979) 61.

[13] I. Antoniadis, Phys. Lett. **B246** (1990) 377.

[14] E. Dudas and C. Grojean, Nucl. Phys. **B507** (1997) 553.

[15] C. P. Burgess, P. G. Camara, S. P. de Alwis, S. B. Giddings, A. Maharana, F. Quevedo, K. Suruliz, JHEP **0804** (2008) 053; H. Abe, Y. Sakamura, JHEP **0703** (2007) 106; M. R. Douglas, J. Shelton, G. Torroba, `arXiv: hep-th/0704.4001`; N. Uekusa, Mod. Phys. Lett. **A23** (2008) 603.

[16] J. Casas, J. R. Espinosa, I. Navarro, Nucl. Phys. **B620** (2002) 195; R. C. Myers, O. Tafjord, JHEP **0111** (2001) 009.

[17] K. R. Dienes, E. Dudas, T. Gherghetta, Phys. Lett. **B436** (1998) 55; Nucl. Phys. **B537** (1999) 47.

[18] P. K. Townsend, Phys. Rev. **D15** (1977) 2802; S. Deser and B. Zumino, Phys. Rev. Lett. **38** (1977) 1433.

[19] E. Shuster, Nucl. Phys. **B554** (1999) 198.

[20] R. Altendorfer, J. Bagger, D. Nemeschansky, Phys. Rev. **D63** (2001) 125025; N. Alonso-Alberca, P. Meessen, T. Ortin, Phys. Lett. **B482** (2000) 400.

[21] A. Pomarol, Phys. Rev. Lett. **85** (2000) 4004; W. D. Goldberger, Y. Nomura, D.R. Smith, Phys. Rev. **D67** (2003) 075021; H.-Y. Guo, C.-G. Huang, Z. Xu, B. Zhou, Phys. Lett. **A331** (2004) 1; Y. Nomura, D.R. Smith, Phys. Rev. **D68** (2003) 075003; O. Saremi, A. W. Peet, Phys. Rev. **D70** (2004) 026008.

[22] H. Verlinde, Nucl. Phys. **B580** (2000) 264; A. Bacchetta, P. J. Mulders, Phys. Rev. **D62** (2000) 114004; J.Perez-Peraza, J. Velasco, A. Gallegos-Cruz, M. Alvarez-Madrigal, A. Faus-Golfe, A. Sanchez-Hertz, `arXiv: hep-th/0011167`; A. Falkowski, Z. Lalak, S. Pokorski, Phys. Lett. **B491** (2000) 172; R. N. Faustov, A.P.Martynenko, Phys. Atom. Nucl. **65** (2002) 265, Yad. Fiz. **65** (2002) 291; E. Bergshoeff, R. Kallosh, A. Van Proeyen, JHEP **0010** (2000) 033; J. R. Pelaez, A. Gomez Nicola, AIP Conf. Proc. **602** (2001) 34; H. Päs, T.W. Kephart, Phys. Rev. **D70** (2004) 086009; G. A. Diamandis, B. C. Georgalas, P. Kouroumalou, A. B. Lahanas, Phys. Lett. **B602** (2004) 112.

[23] J. A. Strathdee, Int. J. Mod. Phys. **A2** (1987) 273.

[24] D. Martí and A. Pomarol, Phys. Rev. **D64** (2001) 105025.

[25] E. Sharpe, Nucl. Phys. **B523** (1998) 211.

[26] M. McGarrie and R. Russo, `arXiv:1004.3305 [hep-ph]`; M. McGarrie and D. C. Thompson, `arXiv:1009.4696 [hep-th]`.

[27] A. Delgado, G. v. Gersdorff, P. John, M. Quiros, Phys. Lett. **B517** (2001) 445; G. Grignani, M. Orselli, G. W. Semenoff, JHEP **0107** (2001) 004.

[28] J. L. Hewett and D. Sadri, Phys. Rev. **D69** (2004) 015001.

[29] H. P. Nilles, Phys. Rept. **110** (1984) 1.

[30] A. Djouadi, Phys. Rept. **459** (2008) 1.

[31] Particle Data Group, Phys. Lett. **B667** (2008) 1; J. Phys. **G37** (2010) 075021.

[32] G. Bhattacharyya, S. K. Majee, A. Raychaudhuri, Nucl. Phys. **B793** (2008) 114; G. Bhattacharyya, S. K. Majee, T.S. Ray, Phys. Rev. **D78** (2008) 071701; G. Bhattacharyya, T. S. Ray, JHEP **1005** (2010) 040.

[33] A. Deandrea, P. Hosteins, M. Oertel, J. Welzel, Phys. Rev. **D75** (2007) 113005.

[34] K. R. Dienes, E. Dudas, T. Gherghetta, Phys. Lett. **B436** (1998) 55; Nucl. Phys. **B537** (1999) 47; G. Altarelli, F. Feruglio, Phys. Lett. **B511** (2001) 257; G. Bhattacharyya, K. Sridhar, J. Phys. **G29** (2003) 993; Y. Nomura, D. Poland, B. Tweedie, JHEP **0612** (2006) 002.

[35] F. Brümmer, S. Fichet, A. Hebecker, S. Kraml, JHEP **0908** (2009) 011; F. Brümmer, S. Fichet, S. Kraml, R.K. Singh, arXiv:1007.0321 [hep-ph].

[36] M. Redi and B. Gripaios, arXiv:1004.5114 [hep-ph].

[37] A. Knochel and T. Ohl, Phys. Rev. **D78** (2008) 045016; arXiv:0909.5330 [hep-ph]; A. Knochel, to appear in conference proceedings of Rencontres de Moriond 2010 (Electroweak), arXiv:1005.2103 [hep-ph].

[38] A. Djouadi and S. Rosier-Lees (conv.), The Minimal Supersymmetric Standard Model: Group Summary Report, arXiv: hep-ph/9901246.

[39] S. J. Huber and Q. Shafi, Phys. Lett. **B498** (2001) 256; **B512** (2001) 365; **B544** (2002) 295; **B583** (2004) 293; S. Chang *et al.*, Phys. Rev. **D73** (2006) 033002; G. Moreau and J. I. Silva-Marcos, JHEP **0601** (2006) 048; **0603** (2006) 090; K. Agashe *et al.*, Phys. Rev. **D71** (2005) 016002; Phys. Rev. Lett. **93** (2004) 201804; Phys. Rev. **D75** (2007) 015002; Phys. Rev. **D74** (2006) 053011.

[40] T. Lari *et al.*, Eur. Phys. J. **C57** (2008) 183; M. Raidal *et al.*, Eur. Phys. J. **C57** (2008) 13.

[41] A. Delgado, A. Pomarol, M. Quiros, Phys. Rev. **D60** (1999) 095008.

[42] T. Gherghetta and A. Pomarol, Phys. Rev. **D67** (2003) 085018.

[43] M. Drees, K. Hagiwara, Phys. Rev. **D42** (1990) 1709.

[44] C. Csáki *et al.*, Phys. Rev. **D66** (2002) 064021; G. Burdman, Phys. Rev. **D66** (2002) 076003; J. Hewett, F. Petriello and T. Rizzo, JHEP **0209** (2002) 030.

[45] K. Agashe, A. Delgado, M. J. May and R. Sundrum, JHEP **0308** (2003) 050; A. Delgado and A. Falkowski, JHEP **0705** (2007) 097.

[46] C. Bouchart and G. Moreau, Nucl. Phys. **B810** (2009) 66; Phys. Rev. **D80** (2009) 095022; A. Djouadi, G. Moreau and F. Richard, Nucl. Phys. **B773** (2007) 43.

[47] A. Abada, C.Biggio, F. Bonnet, M.B. Gavela, T. Hambye, JHEP **0712** (2007) 061.

[48] G. Moreau, Eur. Phys. J. **C40** (2005) 539.

[49] D. Ghilencea, H.P. Nilles, Phys. Lett. **B507** (2001) 327; E.M. Prodanov, Phys. Lett. **B530** (2002) 210.

[50] H. Do Kim, arXiv: hep-ph/0106072; B. Morariu, A.P. Polychronakos, JHEP **0107** (2001) 006.

[51] I. Antoniadis, S. Dimopoulos, A. Pomarol, M. Quiros, Nucl. Phys. **B544** (1999) 503; A. Delgado, A. Pomarol, M. Quiros, Phys. Rev. **D60** (1999) 095008; N. Arkani-Hamed, L. J. Hall, Y. Nomura, D. Smith, N. Weiner, Nucl. Phys. **B605** (2001) 81; R. Barbieri, L. J. Hall, Y. Nomura, Phys. Rev. **D63** (2001) 105007.

[52] T. Kobayashi, H. Terao, Prog. Theor. Phys. **107** (2002) 785; Sunil Mukhi, Pramana **58** (2002) 21.

[53] A. Delgado, G. V. Gersdorff, M. Quiros, Nucl. Phys. **B613** (2001) 49; M. Giovannini, Phys. Rev. **D64** (2001) 124004.

[54] R. Contino, L. Pilo, Phys. Lett. **B523** (2001) 347; T. Fujita, K. Ohashi, Prog. Theor. Phys. **106** (2001) 221; A. Masiero, C.A. Scrucca, M. Serone, L. Silvestrini, Phys. Rev. Lett. **87** (2001) 251601; A. Nayeri, A. Reynolds, e-print: hep-ph/0107201; V. Di Clemente, S. F. King, D. A. J. Rayner, Nucl. Phys. **B617** (2001) 71.

[55] K. Goeke, M. V. Polyakov, M. Vanderhaeghen, Prog. Part. Nucl. Phys. **47** (2001) 401; R. Emparan, D. Mateos, P. Townsend, JHEP **0107** (2001) 011; T. Ueda, T. Uematsu, K. Sasaki, Phys. Lett. **B640** (2006) 188; E. Álvarez, A. F. Faedo, Phys. Rev. **D74** (2006) 124029; G. F. Giudice, R. Rattazzi, J. D. Wells, Nucl. Phys. **B630** (2002) 293; R. Contino, A. Gambassi, J. Math. Phys. **44** (2003) 570.

[56] S. L. Adler and W. A. Bardeen, Phys. Rev. **182** (1969) 1517; R. Jackiw, Lectures on Current Algebra and its Applications, Princeton University Press, 1972.

[57] A. Djouadi, G. Moreau, R.K. Singh, Nucl. Phys. **B797** (2008) 1.

[58] T. Hirayama and K. Yoshioka, JHEP **0401** (2004) 032.

[59] C. T. Hill, Phys. Rev. **D73** (2006) 085001; P. Anastasopoulos, M. Bianchi, E. Dudas and E. Kiritsis, JHEP **0611** (2006) 057.

[60] B. Gripaios, Phys. Lett. **B663** (2008) 419.

[61] See e.g. L. Senatore, Phys. Rev. **D71** (2005) 103510; D. A. Demir, `arXiv:0410056 [hep-ph]`.

[62] A. Djouadi, Phys. Lett. **B435** (1998) 101.

[63] A. Djouadi and G. Moreau, Phys. Lett. **B660** (2008) 67.

[64] L. Scodellaro, the CDF, D0 Collaborations, `arXiv:0905.2554 [hep-ex]`.

[65] Tevatron New Phenomena, Higgs working group, for the CDF collaboration, DZero collaboration, `arXiv:0903.4001 [hep-ex]`.

[66] J. Baglio and A. Djouadi, `arXiv:1012.2748 [hep-ph]`.

[67] J.-M. Frère, D. R. T. Jones and S. Raby, Nucl. Phys. **B222** (1983) 11; L. Alvarez-Gaumé, J. Polchinski and M. Wise, Nucl. Phys. **B221** (1983) 495; M. Claudson, L. Hall and I. Hinchliffe, Nucl. Phys. **B228** (1983) 501.

[68] U. Ellwanger and C. Hugonie, Phys. Lett. **B457** (1999) 299.

[69] H. Komatsu, Phys. Lett. **B215** (1988) 323.

[70] A. Strumia, Nucl. Phys. **B482** (1996) 24; T. Falk, K. A. Olive, L. Koszkowski, A. Singh and M. Srednicki, Phys. Lett. **B396** (1997) 50.

[71] See last results/references on `http://lepewwg.web.cern.ch/LEPEWWG/` .

[72] ATLAS detector and physics performance, Technical Design Report, Volume II, 25 May 1999; CMS Physics TDR: Volume II (PTDR2), Physics Performance, 25 June 2006.

[73] CMS Collaboration, `arXiv:1101.1628 [hep-ex]`.

[74] CDF and D0 experiment webpages: `http://www-cdf.fnal.gov/` and `http://www-d0.fnal.gov/` .

[75] N. Marcus, A. Sagnotti and W. Siegel, Nucl. Phys. **B224** (1983) 159.

[76] N. Arkani-Hamed, T. Gregoire and J. Wacker, JHEP **0203** (2002) 055.

[77] A. Falkowski, Phys. Rev. **D77** (2008) 055018.

[78] S. Chang *et al.*, Phys. Rev. **D62** (2000) 084025.

[79] K. Agashe *et al.*, Phys. Rev. **D77** (2008) 015003; B. Lillie, J. Shu and T. M. P. Tait, Phys. Rev. **D76** (2007) 115016; B. Lillie, L. Randall and L.-T. Wang, JHEP **0709** (2007) 074; M. Guchait, F. Mahmoudi and K. Sridhar, Phys. Lett. **B666** (2008) 347; A. Djouadi, G. Moreau and R. K. Singh, Nucl. Phys. **B797** (2008) 1.

[80] C. Bouchart, A. Knochel and G. Moreau, Phys. Rev. **D84** (2011) 015016.

Appendix A

Updated results

In Fig.(A.1)-(A.2)-(A.3)-(A.4)-(A.5), we present the numerical results of the study updated to the experimental data about the various Higgs boson rates provided by the two LHC Collaborations after the Moriond 2013 winter conference [105]. Most of the Higgs channels have been updated.

Let us summarize here the references per channel and experiment; Regarding the ATLAS data, the diphoton final state results are taken from Ref. [106], the ZZ channel is from Ref. [107], the WW channel from Ref. [108], the $b\bar{b}$ from Ref. [109] and the $\tau\bar{\tau}$ from Ref. [110] (see also the combined channels in Ref. [111, 112]).
As for the CMS results, the diphoton final state has just been presented in Ref. [113], the ZZ channel measurements are provided in Ref. [114], the WW channel ones in Ref. [115], the $b\bar{b}$ in Ref. [99, 116] and the $\tau\bar{\tau}$ in Ref. [117] (combined analyses in Ref. [116]).
Finally, the latest results from the Tevatron (D0 and CDF Collaborations) can be found in Ref. [93].

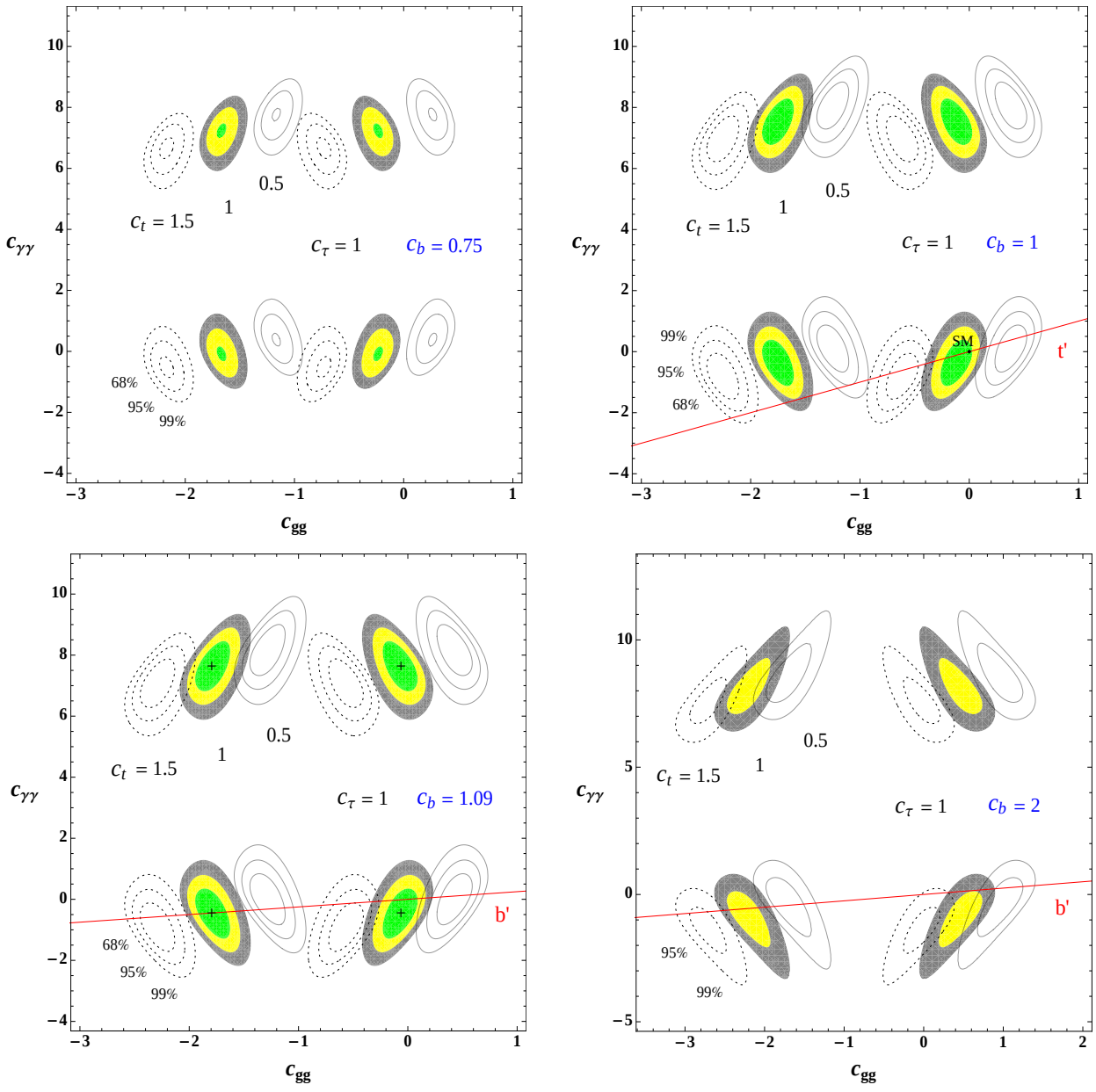

Figure A.1: Update of Fig.(4.1).

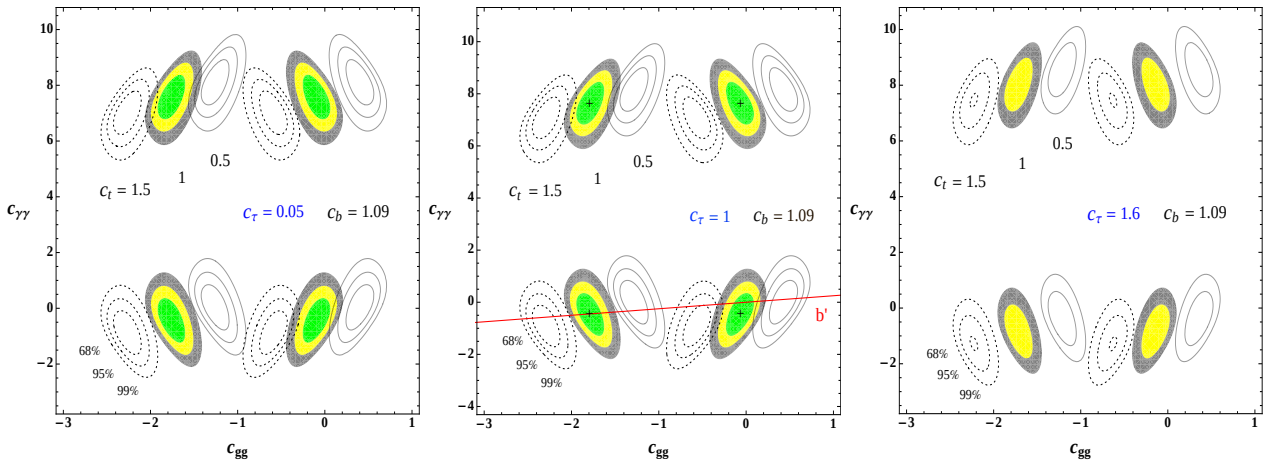

Figure A.2: Update of Fig.(4.2).

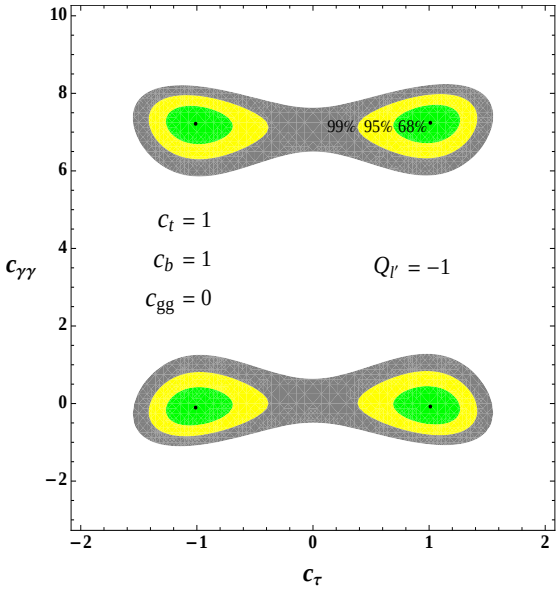

Figure A.3: Update of Fig.(4.3).

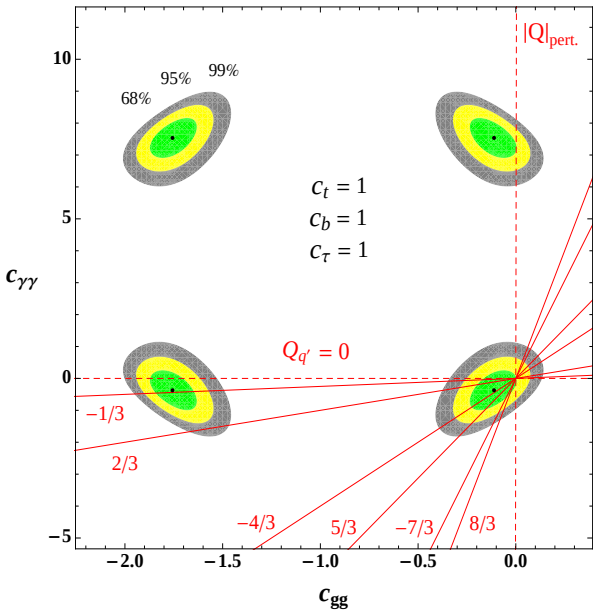

Figure A.4: Update of Fig.(4.4).

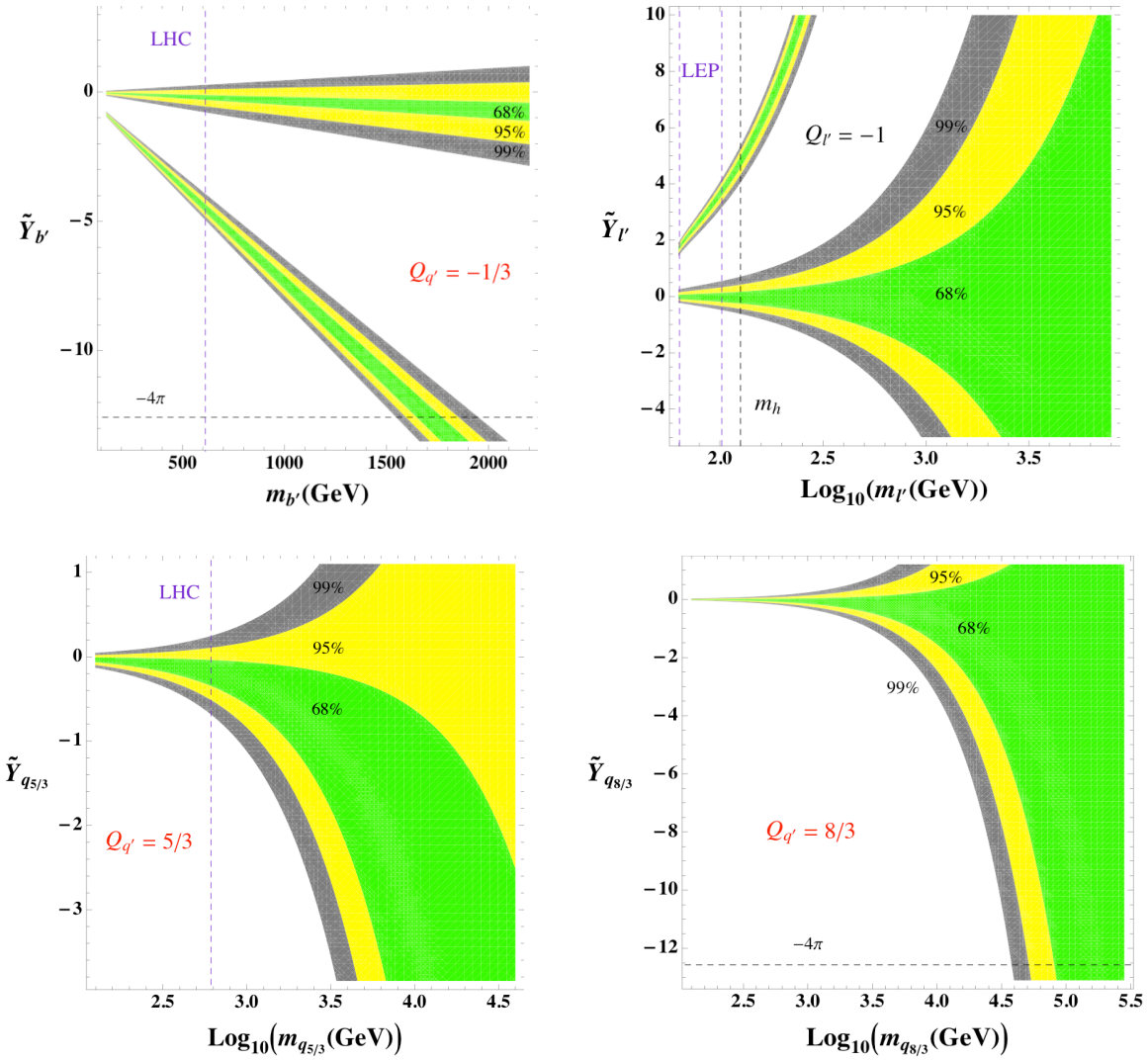

Figure A.5: Update of Fig.(4.5).

Appendix B

Mass and coupling matrices

B.1 Gauge boson mass matrices

The neutral gauge boson mass matrix reads as (writing only the first KK mode contributions),

$$\mathcal{M}_0^2 = \begin{pmatrix} g_Z^2\frac{\tilde{v}^2}{4} + \delta^{\rm SM} m_Z^2 & g_Z^2\frac{\tilde{v}^2}{4}\sqrt{2k\pi R_c} & -g_Z^2\frac{\tilde{v}^2}{4}\sqrt{2k\pi R_c}\frac{g_{Z'}}{g_Z}\cos^2\theta' \\ g_Z^2\frac{\tilde{v}^2}{4}\sqrt{2k\pi R_c} & M_{KK}^2 + g_Z^2\frac{\tilde{v}^2}{4}(2k\pi R_c) & -g_Z^2\frac{\tilde{v}^2}{4}(2k\pi R_c)\frac{g_{Z'}}{g_Z}\cos^2\theta' \\ -g_Z^2\frac{\tilde{v}^2}{4}\sqrt{2k\pi R_c}\frac{g_{Z'}}{g_Z}\cos^2\theta' & -g_Z^2\frac{\tilde{v}^2}{4}(2k\pi R_c)\frac{g_{Z'}}{g_Z}\cos^2\theta' & M_{KK}'^2 + g_Z^2\frac{\tilde{v}^2}{4}(2k\pi R_c)\frac{g_{Z'}^2}{g_Z^2}\cos^4\theta' \end{pmatrix}, \tag{B.1}$$

with $g_Z^2 = g^2 + g'^2$. The increasing factor $\sqrt{2k\pi R_c}$ is the ratio of the $Z^{(1)}$ over Z^0 wave function amounts at the TeV–brane (where is stuck the Higgs boson). We have checked that numerically this ratio is not significantly different for the three first KK states (independently of the BC: $(++)$ or $(-+)$). However, the sign of the nth KK gauge wave function at the IR boundary goes like $(-1)^{n-1}$. The three first KK masses are respectively $M_{KK} \simeq (2.45; 5.57; 8.70)ke^{-\pi kR_c}$ and $M'_{KK} \simeq (2.40; 5.52; 8.65)ke^{-\pi kR_c}$.

The charged gauge boson mass matrix is (note the presence of the $\tilde{M}^2$ term):

$$\mathcal{M}_\pm^2 = \begin{pmatrix} g^2\frac{\tilde{v}^2}{4} + \delta^{\rm SM} m_W^2 & g^2\frac{\tilde{v}^2}{4}\sqrt{2k\pi R_c} & -g^2\frac{\tilde{v}^2}{4}\sqrt{2k\pi R_c}\frac{\tilde{g}}{g} \\ g^2\frac{\tilde{v}^2}{4}\sqrt{2k\pi R_c} & M_{KK}^2 + g^2\frac{\tilde{v}^2}{4}(2k\pi R_c) & -g^2\frac{\tilde{v}^2}{4}(2k\pi R_c)\frac{\tilde{g}}{g} \\ -g^2\frac{\tilde{v}^2}{4}\sqrt{2k\pi R_c}\frac{\tilde{g}}{g} & -g^2\frac{\tilde{v}^2}{4}(2k\pi R_c)\frac{\tilde{g}}{g} & (M'_{KK} + \frac{\tilde{M}^2}{4k}e^{-\pi kR_c})^2 + g^2\frac{\tilde{v}^2}{4}(2k\pi R_c)\frac{\tilde{g}^2}{g^2} \end{pmatrix}. \tag{B.2}$$

B.2 Gauge boson couplings

The neutral gauge boson couplings to the Higgs boson are given by the following matrix (see Section 6.4),

$$\mathcal{C}_0 = \begin{pmatrix} g_Z^2\frac{\tilde{v}^2}{4} + \delta^{\rm SM} g_{hZZ} & g_Z^2\frac{\tilde{v}^2}{4}\sqrt{2k\pi R_c} & -g_Z^2\frac{\tilde{v}^2}{4}\sqrt{2k\pi R_c}\frac{g_{Z'}}{g_Z}\cos^2\theta' \\ g_Z^2\frac{\tilde{v}^2}{4}\sqrt{2k\pi R_c} & g_Z^2\frac{\tilde{v}^2}{4}(2k\pi R_c) & -g_Z^2\frac{\tilde{v}^2}{4}(2k\pi R_c)\frac{g_{Z'}}{g_Z}\cos^2\theta' \\ -g_Z^2\frac{\tilde{v}^2}{4}\sqrt{2k\pi R_c}\frac{g_{Z'}}{g_Z}\cos^2\theta' & -g_Z^2\frac{\tilde{v}^2}{4}(2k\pi R_c)\frac{g_{Z'}}{g_Z}\cos^2\theta' & g_Z^2\frac{\tilde{v}^2}{4}(2k\pi R_c)\frac{g_{Z'}^2}{g_Z^2}\cos^4\theta' \end{pmatrix} \tag{B.3}$$

where the irreducible quantum correction to the hZZ vertex is,

$$\delta^{\rm SM} g_{hZZ} = -\frac{3(g^2+g'^2)}{16\pi^2}\frac{m_b^2+m_t^2}{2}. \tag{B.4}$$

We do not include explicitly the SM radiative corrections due to the Higgs boson self–energy as those constitute a common factor in the RS and SM coupling hZZ, thus disappearing in their ratio that we will compute here.

The charged gauge boson couplings to the Higgs boson are alternatively determined by

$$\mathcal{C}_\pm = \begin{pmatrix} g^2\frac{\tilde{v}^2}{4} + \delta^{\rm SM} g_{hWW} & g^2\frac{\tilde{v}^2}{4}\sqrt{2k\pi R_c} & -g^2\frac{\tilde{v}^2}{4}\sqrt{2k\pi R_c}\frac{\tilde{g}}{g} \\ g^2\frac{\tilde{v}^2}{4}\sqrt{2k\pi R_c} & g^2\frac{\tilde{v}^2}{4}(2k\pi R_c) & -g^2\frac{\tilde{v}^2}{4}(2k\pi R_c)\frac{\tilde{g}}{g} \\ -g^2\frac{\tilde{v}^2}{4}\sqrt{2k\pi R_c}\frac{\tilde{g}}{g} & -g^2\frac{\tilde{v}^2}{4}(2k\pi R_c)\frac{\tilde{g}}{g} & g^2\frac{\tilde{v}^2}{4}(2k\pi R_c)\frac{\tilde{g}^2}{g^2} \end{pmatrix} \tag{B.5}$$

the irreducible quantum correction to the hWW vertex being:

$$\delta^{\rm SM} g_{hWW} = -\frac{3g^2}{16\pi^2}\left(\frac{m_b^2+m_t^2}{4} - \frac{m_b^4\, ln(m_b^2/m_t^2)}{2(m_t^2-m_b^2)}\right). \tag{B.6}$$

B.3 Bottom and top quark mass matrices

In the field basis $\Psi_L^t \equiv (b_L^{(0)}, b_L^{(1)}, b_L^{c(1)}, b_L^{\prime\prime(1)}, b_L^{\prime c(1)})^t$, $\Psi_R^t \equiv (b_R^{c(0)}, b_R^{(1)}, b_R^{c(1)}, b_R^{\prime\prime(1)}, b_R^{\prime c(1)})^t$, the 4D bottom quark mass matrix, up to the first KK modes (numerical analysis includes first and second KK modes) for our model is,

$$\mathcal{M}_b = \begin{pmatrix} \epsilon_b \tilde{v}_b c_\theta f_{c_2}^{(0)*} f_{c_{b_R}}^{(0)} & 0 & \tilde{v}_b c_\theta f_{c_2}^{(0)*} f_{c_{b_R}}^{(1)} & 0 & \sqrt{2}\tilde{v}_t s_\theta f_{c_1}^{(0)*} g_{c_{t_R}}^{(1)} \\ \tilde{v}_b c_\theta f_{c_2}^{(1)*} f_{c_{b_R}}^{(0)} & s_\theta^2 m_{c_1}^{(1)} + c_\theta^2 m_{c_2}^{(1)} & \tilde{v}_b c_\theta f_{c_2}^{(1)*} f_{c_{b_R}}^{(1)} & 0 & \sqrt{2}\tilde{v}_t s_\theta f_{c_1}^{(1)*} g_{c_{t_R}}^{(1)} \\ 0 & 0 & m_{c_{b_R}}^{(1)} & 0 & 0 \\ \frac{1}{\sqrt{2}}\tilde{v}_b g_{c_2}^{(1)*} f_{c_{b_R}}^{(0)} & 0 & \frac{1}{\sqrt{2}}\tilde{v}_b c_\theta g_{c_2}^{(1)*} f_{c_{b_R}}^{(1)} & m_{c_2}^{\prime(1)} & 0 \\ 0 & 0 & 0 & 0 & m_{c_{t_R}}^{\prime(1)} \end{pmatrix}. \tag{B.7}$$

In the field basis $\Phi_L^t \equiv (t_L^{(0)}, t_L^{(1)}, t_L^{c(1)}, t_L^{\prime(1)})^t$, $\Phi_R^t \equiv (t_R^{c(0)}, t_R^{(1)}, t_R^{c(1)}, t_R^{\prime(1)})^t$, the top quark mass matrix up

to the first KK states (same comment for the numerical analysis) is given by:

$$\mathcal{M}_t = \begin{pmatrix} \epsilon_t \tilde{v}_t s_\theta f_{c_1}^{(0)*} f_{c_{t_R}}^{(0)} & 0 & \tilde{v}_t s_\theta f_{c_1}^{(0)*} f_{c_{t_R}}^{(1)} & 0 \\ \tilde{v}_t s_\theta f_{c_1}^{(1)*} f_{c_{t_R}}^{(0)} & s_\theta^2 m_{c_1}^{(1)} + c_\theta^2 m_{c_2}^{(1)} & \tilde{v}_t s_\theta f_{c_1}^{(1)*} f_{c_{t_R}}^{(1)} & 0 \\ 0 & 0 & m_{c_{t_R}}^{(1)} & 0 \\ \tilde{v}_t s_\theta g_{c_1}^{(1)*} f_{c_{t_R}}^{(0)} & 0 & \tilde{v}_t s_\theta g_{c_1}^{(1)*} f_{c_{t_R}}^{(1)} & m_{c_1}^{\prime(1)} \end{pmatrix}. \tag{B.8}$$

$\epsilon_{b,t}$ is described in Section 6.4.2. Besides, in our notations, $\tilde{v}_{b,t} = \lambda_{b,t}^{5D}\tilde{v}/\sqrt{2}kR_c$, $m_c^{(n)}$ ($m_c^{\prime(n)}$) is the n–th KK mass for $(++)$ ($(-+)$) BC fields, $c_\theta = \cos\theta$ ($s_\theta = \sin\theta$) and θ is the effective angle of the mixing between the two left multiplets. $f_c^{(n)}$ and $g_c^{(n)}$ are respectively the fermion wave functions along the 5–th dimension with $(++)$ and $(-+)$ BC, whose values are taken at the position of the TeV–brane, $x_5 = \pi R_c$ (where the Higgs boson is confined). For instance (see e.g. [57] for excited profiles):

$$f_c^{(0)}(x_5) \equiv \sqrt{\frac{(1-2c)kR_c}{e^{(1-2c)\pi kR_c}-1}} e^{(\frac{1}{2}-c)kx_5}. \tag{B.9}$$

The zeroes in the bottom mass matrix originate from the fact that the fields $b_L^{c(1)}$, $b_L^{\prime c(1)}$, $b_R^{(1)}$ and $b_R^{\prime\prime(1)}$ (with $n = 1, 2$) have Dirichlet BC on the TeV–brane and thus, do not couple to the Higgs boson. For the top mass matrix, it originates from the fact that $t_L^{c(1)}$, $t_R^{(1)}$ and $t_R^{\prime(1)}$ have Dirichlet BC on the TeV-brane.

B.4 Bottom and top quark couplings

The bottom quark Yukawa coupling matrix reads as,

$$\mathcal{C}_b = \begin{pmatrix} \epsilon_b \tilde{v}_b c_\theta f_{c_2}^{(0)*} f_{c_{b_R}}^{(0)} & 0 & \tilde{v}_b c_\theta f_{c_2}^{(0)*} f_{c_{b_R}}^{(1)} & 0 & \sqrt{2}\tilde{v}_t s_\theta f_{c_1}^{(0)*} g_{c_{t_R}}^{(1)} \\ \tilde{v}_b c_\theta f_{c_2}^{(1)*} f_{c_{b_R}}^{(0)} & 0 & \tilde{v}_b c_\theta f_{c_2}^{(1)*} f_{c_{b_R}}^{(1)} & 0 & \sqrt{2}\tilde{v}_t s_\theta f_{c_1}^{(1)*} g_{c_{t_R}}^{(1)} \\ 0 & 0 & 0 & 0 & 0 \\ \frac{1}{\sqrt{2}}\tilde{v}_b g_{c_2}^{(1)*} f_{c_{b_R}}^{(0)} & 0 & \frac{1}{\sqrt{2}}\tilde{v}_b c_\theta g_{c_2}^{(1)*} f_{c_{b_R}}^{(1)} & 0 & 0 \\ 0 & 0 & 0 & 0 & 0 \end{pmatrix}, \tag{B.10}$$

It is obtained from the bottom mass matrix defined in previous appendix, but with the KK mass terms set to zero. Hence, it can be defined through the relation:

$$\mathcal{C}_b \equiv \tilde{v}\frac{\partial \mathcal{M}_b}{\partial \tilde{v}}, \tag{B.11}$$

as may be useful.

The dimensionful top quark Yukawa couplings can be derived from the matrix:

$$\mathcal{C}_t = \begin{pmatrix} \epsilon_t \tilde{v}_t s_\theta f_{c_1}^{(0)*} f_{c_{t_R}}^{(0)} & 0 & \tilde{v}_t s_\theta f_{c_1}^{(0)*} f_{c_{t_R}}^{(1)} & 0 \\ \tilde{v}_t s_\theta f_{c_1}^{(1)*} f_{c_{t_R}}^{(0)} & 0 & \tilde{v}_t s_\theta f_{c_1}^{(1)*} f_{c_{t_R}}^{(1)} & 0 \\ 0 & 0 & 0 & 0 \\ \tilde{v}_t s_\theta g_{c_1}^{(1)*} f_{c_{t_R}}^{(0)} & 0 & \tilde{v}_t s_\theta g_{c_1}^{(1)*} f_{c_{t_R}}^{(1)} & 0 \end{pmatrix}. \tag{B.12}$$

Appendix C

Sum rules

C.1 Fermion sum rule

In this Appendix, we demonstrate analytically some useful theoretical relations which allow to take into account the full KK quark tower in the calculation of the gluon–gluon fusion mechanism amplitude, within the RS scenario. This generalizes results obtained in the case of a bulk Higgs boson within the framework of gauge–Higgs unification [18]. These relations also allow to implement the full KK charged fermion tower when calculating the loop-induced $h\gamma\gamma$ coupling.

For that, we use the same conventions/notations as in the Section 6.4.2: $\mathcal{M}_f$ is defined as the mass matrix of a particular fermion $\Psi_{L/R}$ in the interaction basis. We have obtained $\mathcal{C}'_f/\tilde{v}$ to be the Yukawa matrix in the mass eigenbasis, where $\mathcal{C}'_f = U_L \mathcal{C}_f U_R^\dagger$; $\mathcal{C}_f$ being the same matrix as $\mathcal{M}_f$ but with the KK masses set to zero.

The matrices $\mathcal{M}_f$ and $\mathcal{C}'_f$ are thus linked through the relation (see for instance Eq.(B.11)):

$$\mathcal{C}'_f \equiv U_L . \tilde{v} \frac{\partial \mathcal{M}_f}{\partial \tilde{v}} . U_R^\dagger \tag{C.1}$$

Let us define here, for simplicity about the subscript notation, $m_i \equiv \mathcal{M}'_f|_{ii}$ and $\lambda_i^{\rm RS} \equiv (\mathcal{C}'_f|_{ii})/\tilde{v}$ for a given fermion within RS. Then we have

$$\sum_i \frac{\lambda_i^{\rm RS}\, \tilde{v}}{m_i} \equiv \mathrm{Tr}\left(\mathcal{M'}_f^{-1} . \mathcal{C'}_f \right) \quad \text{where} \quad \mathcal{M'}_f^{-1} . \mathcal{M'}_f = 1. \tag{C.2}$$

and can rewrite this trace as (accordingly to Eq.(6.19)):

$$\sum_i \frac{\lambda_i^{\rm RS}\, \tilde{v}}{m_i} = \mathrm{Tr}\left(U_R \mathcal{M}_f^{-1} U_L^\dagger . U_L \tilde{v} \frac{\partial \mathcal{M}_f}{\partial \tilde{v}} U_R^\dagger \right) = \mathrm{Tr}\left(\tilde{v} \frac{\partial \mathcal{M}_f}{\partial \tilde{v}} . \mathcal{M}_f^{-1} \right) \tag{C.3}$$

$$\sum_i \frac{\lambda_i^{\rm RS}\, \tilde{v}}{m_i} = \tilde{v} \frac{\partial}{\partial \tilde{v}} \mathrm{Tr}\left(ln\ \mathcal{M}_f \right) = \tilde{v} \frac{\partial}{\partial \tilde{v}}\ ln\left(\mathrm{Det} \mathcal{M}_f \right) \tag{C.4}$$

Applying this result to SM fermion mass matrices such as the ones in the Appendix B.3 (including even possibly the entire KK tower contribution),

$$\sum_i \frac{\lambda_i^{\rm RS}\,\tilde{v}}{m_i} = \tilde{v}\frac{\partial}{\partial\tilde{v}}\sum_i\; ln\;\mathcal{M}_f|_{ii} = \tilde{v}\frac{\partial}{\partial\tilde{v}}\;ln\;\mathcal{M}_f|_{11} = 1 \tag{C.5}$$

and for exotic fermions without zero–mode, as for instance the $q'_{(-7/3)}$ field appearing in a multiplet of Eq.(6.22),

$$\sum_i \frac{\lambda_i^{\rm RS}\,\tilde{v}}{m_i} = \tilde{v}\frac{\partial}{\partial\tilde{v}}\sum_i\; ln\;\mathcal{M}_f|_{ii} = 0. \tag{C.6}$$

Application to the KK fermionic contributions of the effective hgg and $h\gamma\gamma$ couplings:

In both Eq.(6.26) and Eq.(6.34), the fermionic contribution to the amplitude reads, for each independent KK tower, $\sum_{\{f\}}\frac{\lambda_f^{\rm RS}\tilde{v}}{m_f}A^h_{1/2}(\tau_f)$, up to irrelevant global color and electric charge factors. The sum over $\{f\}$ denotes the sum for a corresponding fermion f, of its zero–mode and all KK excitations it couples to through the Higgs field.

Using the properties of the spin–1/2 form factor, one can set that for all KK excitations, $A^h_{1/2}(\tau_{f^{KK}})\simeq 1$ with a high precision (up to 1 per 1000). Having so, one can separate the contribution in the tower of the first fermion eigenstate (generally mainly composed by the zero–mode component) noted f^0 from the heavier eigenstates (mainly made of KK modes) noted f^{KK}'s for simplicity here:

$$\begin{aligned}
\sum_{\{f\}}\frac{\lambda_f^{\rm RS}\tilde{v}}{m_f}A^h_{1/2}(\tau_f) &\equiv \frac{\lambda_{f^0}^{\rm RS}\tilde{v}}{m_{f^0}}A^h_{1/2}(\tau_{f^0}) + \sum_{KK}\frac{\lambda_{f^{KK}}^{\rm RS}\tilde{v}}{m_{f^{KK}}}A^h_{1/2}(\tau_{f^{KK}}) = \frac{\lambda_{f^0}^{\rm RS}\tilde{v}}{m_{f^0}}A^h_{1/2}(\tau_{f^0}) + \sum_{KK}\frac{\lambda_{f^{KK}}^{\rm RS}\tilde{v}}{m_{f^{KK}}}\\
\sum_{\{f\}}\frac{\lambda_f^{\rm RS}\tilde{v}}{m_f}A^h_{1/2}(\tau_f) &= \frac{\lambda_{f^0}^{\rm RS}\tilde{v}}{m_{f^0}}A^h_{1/2}(\tau_{f^0}) + \left(1-\frac{\lambda_{f^0}^{\rm RS}\tilde{v}}{m_{f^0}}\right) = 1 + \frac{\lambda_{f^0}^{\rm RS}\tilde{v}}{m_{f^0}}\left(A^h_{1/2}(\tau_{f^0})-1\right),
\end{aligned} \tag{C.7}$$

where we have used the relation (C.5). It is a remarkable feature that the KK sum can be reflected in a few properties from the lightest mode.

Note that for an exotic fermion f', with no zero–mode, the sum even cancels:

$$\sum_{\{f'\}}\frac{\lambda_{f'}^{\rm RS}\tilde{v}}{m_{f'}}A^h_{1/2}(\tau_{f'}) \equiv \sum_{KK}\frac{\lambda_{f^{KK}}^{\rm RS}\tilde{v}}{m_{f^{KK}}}A^h_{1/2}(\tau_{f^{KK}}) = \sum_{KK}\frac{\lambda_{f^{KK}}^{\rm RS}\tilde{v}}{m_{f^{KK}}} = 0 \tag{C.8}$$

according to the relation (C.6).

C.2 Boson sum rule

Here are shown some theoretical sum rules for the bosons, similarly to the fermion case of previous appendix, but which apply now to the computation of the effective $h\gamma\gamma$ vertex.

The coupling matrix $\mathcal{C}'_{\pm}$ and mass matrix $\mathcal{M}^2_{\pm}$ for the charged gauge bosons are linked via,

$$\mathcal{C}'_{\pm} \equiv V.\tilde{v}^2 \frac{\partial \mathcal{M}^2_{\pm}}{\partial \tilde{v}^2}.V^{\dagger} \tag{C.9}$$

Reminding $m^2_{W^n} = \mathcal{M}'^2_{\pm}|_{nn}$ and $g^{\rm RS}_{hW^nW^n} = 2(\mathcal{C}'_{\pm}|_{nn})/\tilde{v}$ from Section 6.4.1, the loop part from the gauge boson KK tower can then be written as [see Eq.(6.16)]:

$$\begin{aligned}
\sum_n \frac{g^{\rm RS}_{W^n}\tilde{v}}{2m^2_{W^n}} &= \sum_n \frac{\mathcal{C}'_{\pm}|_{nn}}{\mathcal{M}'^2_{\pm}|_{nn}} = {\rm Tr}\left([\mathcal{M}'^2_{\pm}]^{-1}.\mathcal{C}'_{\pm}\right) = {\rm Tr}\left(V[\mathcal{M}^2_{\pm}]^{-1}V^{\dagger}.V\tilde{v}^2\frac{\partial \mathcal{M}^2_{\pm}}{\partial \tilde{v}^2}V^{\dagger}\right) \\
\sum_n \frac{g^{\rm RS}_{W^n}\tilde{v}}{2m^2_{W^n}} &= {\rm Tr}\left(\tilde{v}^2\frac{\partial \mathcal{M}^2_{\pm}}{\partial \tilde{v}^2}.[\mathcal{M}^2_{\pm}]^{-1}\right) = \tilde{v}^2\frac{\partial}{\partial \tilde{v}^2}{\rm Tr}\left(ln\ \mathcal{M}^2_{\pm}\right) = \tilde{v}^2\frac{\partial}{\partial \tilde{v}^2}\ ln\left({\rm Det}\mathcal{M}^2_{\pm}\right).
\end{aligned} \tag{C.10}$$

Obviously, this relation also holds for the neutral gauge boson KK tower, and one can check that

$${\rm Det}\mathcal{M}^2_{\pm} = g^2\frac{\tilde{v}^2}{4}\prod_n\ M^{(n)2}_{KK}\ \bar{M}'^{(n)2}_{KK}, \tag{C.11}$$

where $\bar{M}'^{(n)2}_{KK} = (M'^{(n)}_{KK} + \frac{\tilde{M}^2}{4k}e^{-\pi kR_c})^2$, so that, at the end:

$$\sum_n \frac{g^{\rm RS}_{W^n}\tilde{v}}{2m^2_{W^n}} = \tilde{v}^2\frac{\partial}{\partial \tilde{v}^2}\ ln(g^2\frac{\tilde{v}^2}{4}) = 1. \tag{C.12}$$

Application to the KK W contributions of the effective $h\gamma\gamma$ coupling:

Applying the above result to the EW gauge boson KK tower contribution in the $h\gamma\gamma$ effective coupling allows one to rewrite:

$$\begin{aligned}
\sum_n \frac{\mathcal{C}'_{\pm}|_{nn}}{\mathcal{M}'^2_{\pm}|_{nn}}A^h_1(\tau_{W^n}) &\equiv \frac{g^{\rm RS}_{hWW}\tilde{v}}{2m^2_W}A^h_1(\tau_W) + \sum_{n\geq 1}\frac{\mathcal{C}'_{\pm}|_{nn}}{\mathcal{M}'^2_{\pm}|_{nn}}A^h_1(\tau_{W^n}) \\
\sum_n \frac{\mathcal{C}'_{\pm}|_{nn}}{\mathcal{M}'^2_{\pm}|_{nn}}A^h_1(\tau_{W^n}) &= \frac{g^{\rm RS}_{hWW}\tilde{v}}{2m^2_W}A^h_1(\tau_W) - 7\sum_{n\geq 1}\frac{\mathcal{C}'_{\pm}|_{nn}}{\mathcal{M}'^2_{\pm}|_{nn}} = \frac{g^{\rm RS}_{hWW}\tilde{v}}{2m^2_W}A^h_1(\tau_W) - 7\left(1 - \frac{g^{\rm RS}_{hWW}\tilde{v}}{2m^2_W}\right) \\
\sum_n \frac{\mathcal{C}'_{\pm}|_{nn}}{\mathcal{M}'^2_{\pm}|_{nn}}A^h_1(\tau_{W^n}) &= -7 + \frac{g^{\rm RS}_{hWW}\tilde{v}}{2m^2_W}\left(7 + A^h_1(\tau_W)\right),
\end{aligned} \tag{C.13}$$

where we have used the properties of the spin–1 form factor, so one can set that for all KK excitations, $A^h_1(\tau_{W^n}) = -7$ again at a high accuracy level (up to 1 per 1000).

Appendix D

Approximating the radiative corrections

The radiative corrections to the CP–even Higgs boson mass matrix can be written as

$$\mathcal{M}^2 = \begin{bmatrix} \mathcal{M}^2_{11} + \Delta\mathcal{M}^2_{11} & \mathcal{M}^2_{12} + \Delta\mathcal{M}^2_{12} \\ \mathcal{M}^2_{12} + \Delta\mathcal{M}^2_{12} & \mathcal{M}^2_{22} + \Delta\mathcal{M}^2_{22} \end{bmatrix} \tag{D.1}$$

The leading one–loop radiative corrections $\Delta\mathcal{M}^2_{ij}$ to the mass matrix are controlled by the top Yukawa coupling $\lambda_t = m_t/v \sin\beta$ which appears with the fourth power. One can obtain a very simple analytical expression if only this contribution is taken into account [4]

$$\begin{aligned} \Delta\mathcal{M}^2_{11} &\sim \Delta\mathcal{M}^2_{12} \sim 0 \, , \\ \Delta\mathcal{M}^2_{22} &\sim \epsilon = \frac{3\,\bar{m}_t^4}{2\pi^2 v^2 \sin^2\beta} \left[\log\frac{M_S^2}{\bar{m}_t^2} + \frac{X_t^2}{M_S^2}\left(1 - \frac{X_t^2}{12\,M_S^2}\right)\right] \end{aligned} \tag{D.2}$$

where M_S is the geometric average of the stop masses $M_S = \sqrt{m_{\tilde{t}_1} m_{\tilde{t}_2}}$, X_t is the stop mixing parameter given by $X_t = A_t - \mu/\tan\beta$ and $\bar{m}_t$ is the running $\overline{\rm MS}$ top quark mass to account for the leading two–loop QCD corrections in a renormalisation–group improvement.

A better approximation, with some more renormalisation–group improved two–loop QCD and electroweak corrections included is given by [5]

$$\Delta\mathcal{M}^2_{22} = \frac{3}{2\pi^2}\frac{m_t^4}{v^2\sin^2\beta}\left[\frac{1}{2}\tilde{X}_t + \ell_S + \frac{1}{16\pi^2}\left(\frac{3}{2}\frac{m_t^2}{v^2} - 32\pi\alpha_s\right)\left(\tilde{X}_t\ell_S + \ell_S^2\right)\right] , \tag{D.3}$$

where $\ell_S = \log(M_S^2/m_t^2)$ and using $x_t = X_t/M_S = (A_t - \mu\cot\beta)/M_S$ one has $\tilde{X}_t = 2x_t^2(1 - x_t^2/12)$ with A_t the trilinear Higgs-stop coupling and μ the higgsino mass parameter.

Other soft SUSY–breaking parameters, in particular μ and A_b (and in general the corrections controlled by the bottom Yukawa coupling $\lambda_b = m_b/v\cos\beta$ which at large value of the product $\mu\tan\beta$, provide a non–negligible correction to $\mathcal{M}^2_{ij}$) can also have an impact on the loop corrections. Including these subleading contributions at one–loop, plus the leading logarithmic contributions at two–loops, the radiative corrections

to the CP–even mass matrix elements can still be written in a compact form [3]

$$\begin{aligned}
\Delta\mathcal{M}^2_{11} &= -\frac{v^2\sin^2\beta}{32\pi^2}\bar{\mu}^2\Big[x_t^2\lambda_t^4(1+c_{11}\ell_S)+a_b^2\lambda_b^4(1+c_{12}\ell_S)\Big] \\
\Delta\mathcal{M}^2_{12} &= -\frac{v^2\sin^2\beta}{32\pi^2}\bar{\mu}\Big[x_t\lambda_t^4(6-x_ta_t)(1+c_{31}\ell_S)-\bar{\mu}^2a_b\lambda_b^4(1+c_{32}\ell_S)\Big] \\
\Delta\mathcal{M}^2_{22} &= \frac{v^2\sin^2\beta}{32\pi^2}\Big[6\lambda_t^4\ell_S(2+c_{21}\ell_S)+x_ta_t\lambda_t^4(12-x_ta_t)(1+c_{21}\ell_S)-\bar{\mu}^4\lambda_b^4(1+c_{22}\ell_S)\Big]
\end{aligned} \tag{D.4}$$

where the additional abbreviations $\bar{\mu}=\mu/M_S$ and $a_{t,b}=A_{t,b}/M_S$ have been used. The factors c_{ij} take into account the leading two–loop corrections due to the top and bottom Yukawa couplings and to the strong coupling constant $g_s=\sqrt{4\pi\alpha_s}$; they read

$$c_{ij}=\frac{1}{32\pi^2}(t_{ij}\lambda_t^2+b_{ij}\lambda_b^2-32g_s^2) \tag{D.5}$$

with the various coefficients given by,

$$(t_{11},t_{12},t_{21},t_{22},t_{31},t_{32})=(12,-4,6,-10,9,7) \text{ and } (b_{11},b_{12},b_{21},b_{22},b_{31},b_{32})=(-4,12,2,18,-1,15).$$

The expressions eq. (D.4) provide a good approximation of the bulk of the radiative corrections [3]. However, one needs to include the full set of corrections to have precise predictions for the Higgs boson masses and couplings as discussed at the end of Section 7.2.

Appendix E

The boundary conditions with boundary terms

In this Appendix, we derive BC for the fermions obeying the action of Eq. (8.1) which contains boundary interactions. Expanding this action, to isolate the terms involving derivatives along the fifth dimension, and integrating by part the second term over the 4 usual dimensions, one gets,

$$\begin{aligned} S_{\text{fermion}} \;=\; & \int \mathrm{d}^4x\;\mathrm{d}y\;\Big[\; i\Big(\bar{Q}\gamma^\mu\partial_\mu Q \;+\frac{1}{2}\;(\bar{Q}\gamma^5\partial_5 Q - \partial_5\bar{Q}\gamma^5 Q) \;+\; \{Q\leftrightarrow D\}\Big) \\ & +\;\delta(y-\pi R)\;(Y_5\;\bar{Q}_L H D_R \;+\; Y_5'\;\bar{Q}_R H D_L \;+\text{H.c.})\;\Big]\;. \end{aligned} \tag{E.1}$$

Now integrating by part the third term of this action over the extra dimension and considering the EW symmetry breaking that will affect the mass spectrum, one obtains,

$$\begin{aligned} S_{\text{fermion}} \;=\; & \int \mathrm{d}^4x\;\mathrm{d}y\;\Big[\; i\Big(\bar{Q}\gamma^\mu\partial_\mu Q \;+\;\bar{Q}\gamma^5\partial_5 Q \;-\frac{1}{2}\;\partial_5(\bar{Q}\gamma^5 Q) \;+\; \{Q\leftrightarrow D\}\Big) \\ & +\;(X_5\;\bar{Q}_L D_R \;+\; X_5'\;\bar{Q}_R D_L \;+\text{H.c.})\;\Big]\;, \end{aligned} \tag{E.2}$$

with the compact notation, $X_5^{(\prime)} = Y_5^{(\prime)}\,\frac{v}{\sqrt{2}}\,\delta(y-\pi R)$. Expressing the action in terms of the two-component spinors defined in Eq. (8.2), the Eq. (E.2) becomes,

$$\begin{aligned} S_{\text{fermion}} \;=\; & \int \mathrm{d}^4x\;\mathrm{d}y\;\Big[\;\Big(-i\;\bar{Q}_R\sigma^\mu\partial_\mu Q_R \;-i\;\bar{Q}_L\bar{\sigma}^\mu\partial_\mu Q_L \;+\;\bar{Q}_R\partial_5 Q_L \;-\;\bar{Q}_L\partial_5 Q_R \\ & +\frac{1}{2}\;\partial_5(\bar{Q}_L Q_R - \bar{Q}_R Q_L) \;+\; \{Q\leftrightarrow D\}\Big) \;+\; (X_5\;\bar{Q}_L D_R \;+\; X_5'\;\bar{Q}_R D_L \;+\text{H.c.})\;\Big]\;. \end{aligned} \tag{E.3}$$

The variation of the action with respect to the $\bar{Q}_{L,R}$ fields reads as,

$$\begin{cases} \delta_{\bar{Q}_L} S_{\text{fermion}} = \int \mathrm{d}^4x\;\mathrm{d}y\;\big[\;\delta\bar{Q}_L\;(-i\;\bar{\sigma}^\mu\partial_\mu Q_L \;-\;\partial_5 Q_R \;+\; X_5\;D_R) \;+\frac{1}{2}\;\partial_5(\delta\bar{Q}_L Q_R)\;\big] \\ \delta_{\bar{Q}_R} S_{\text{fermion}} = \int \mathrm{d}^4x\;\mathrm{d}y\;\big[\;\delta\bar{Q}_R\;(-i\;\sigma^\mu\partial_\mu Q_R \;+\;\partial_5 Q_L \;+\; X_5'\;D_L) \;-\frac{1}{2}\;\partial_5(\delta\bar{Q}_R Q_L)\;\big] \end{cases} \tag{E.4}$$

Analogous equations hold for the $\bar{D}_{L,R}$ spinors [obtained from Eq. (E.4) by the replacements $Q\leftrightarrow D$ and $X_5\leftrightarrow X_5'$]. The vanishing for any $\delta\bar{Q}_L$ of the action variation in first line of Eq. (E.4) is realized, as in the

absence of Yukawa interactions, via the separate vanishing of two distinct parts,

$$-i\ \bar{\sigma}^\mu \partial_\mu Q_L - \partial_5 Q_R + X_5\ D_R \ = \ 0\ , \tag{E.5}$$

$$\int \mathrm{d}y\ \partial_5(\delta\bar{Q}_L Q_R) \ = \ [\delta\bar{Q}_L Q_R]_{y=0}^{y=\pi R} \ = \ 0\ , \tag{E.6}$$

the first equation leading to the EOM while the second one defines the BC. By inserting the KK decompositions (8.3a)-(8.3d) into Eq. (E.5), and the three similar equations obtained from variations with respect to the 5D fields, $\bar{Q}_R$, $\bar{D}_{L,R}$, one obtains the EOM (8.6a)-(8.6d) for the profiles – if one uses the 4D Dirac equations (8.4)-(8.5). The condition (E.6) should be satisfied for any $\delta\bar{Q}_L$ so that it can be written as, together with all the similar conditions for the other 5D fields,

$$\begin{aligned} &\delta\bar{Q}_L Q_R\big|_{\pi R} = \delta\bar{Q}_L Q_R\big|_0 = \delta\bar{Q}_R Q_L\big|_{\pi R} = \delta\bar{Q}_R Q_L\big|_0 = 0\ , \\ &\delta\bar{D}_L D_R\big|_{\pi R} = \delta\bar{D}_L D_R\big|_0 = \delta\bar{D}_R D_L\big|_{\pi R} = \delta\bar{D}_R D_L\big|_0 = 0\ . \end{aligned} \tag{E.7}$$

The condition, $d_L(0) = q_R(0) = 0$, is compatible with Eq. (E.7) – involving the 5D fields (8.3a)-(8.3d) – and once inserted into the EOM (8.6b)-(8.6c), taken at $y = 0$, leads to the additional condition, $d'_R(0) = q'_L(0) = 0$ [as the EOM boundary terms are not at $y = 0$]. Similarly, the condition, $d_L(\pi R) = q_R(\pi R) = 0$, respects Eq. (E.7) and after injection in the EOM (8.6b)-(8.6c) at $y = \pi R$ gives rise to, $d'_R(\pi R) = q'_L(\pi R) = 0$ [here the EOM Yukawa terms are removed by the condition, $d_L(\pi R) = q_R(\pi R) = 0$]. In summary, the $(--)$ and $(++)$ BC for d_L, q_R and d_R, q_L, respectively, fulfill the conditions (E.7) [1] together with the EOM at the boundaries and thus constitute satisfactory BC.

We notice that, in order to cancel the action variation, grouping together the terms of the first line of Eq. (E.4) in the following way,

$$-i\ \bar{\sigma}^\mu \partial_\mu Q_L - \partial_5 Q_R \ = \ 0\ , \tag{E.8}$$

$$\int \mathrm{d}y\ [X_5\ \delta\bar{Q}_L D_R + \frac{1}{2}\ \partial_5(\delta\bar{Q}_L Q_R)] \ = \ \frac{vY_5}{\sqrt{2}}\ \delta\bar{Q}_L D_R\big|_{\pi R} + \frac{1}{2}\ [\delta\bar{Q}_L Q_R]_{y=0}^{y=\pi R} \ = \ 0\ , \tag{E.9}$$

is different from Eq. (E.5)-(E.6) : here, all the boundary terms appear in the same equality (E.9). The Eq. (E.8), and similar equations for the other fields, would lead to the EOM of Eq. (8.4)-(8.5) and Eq. (8.6a)-(8.6d) without Yukawa interactions. Those interaction terms would now be included in the Eq. (E.9) which is at the origin of the fermion BC. We see clearly that when one would then try to regularize the Higgs peak, through a shift or a smearing, it would not be possible anymore to write the Yukawa interaction as a boundary term in Eq. (E.9). It means that it is more tricky to follow a regularization procedure when the Yukawa interaction is included in the BC equation (whichever regularization I or II is invoked as the Y_5 coupling has to be regularized in both). This is the reason why the brane-localized Yukawa interactions are usually (see for instance Ref. [20, 22]) taken into account instead in the EOM, like in our Eq. (E.5). There a shift or a smearing of the Dirac peak contained in X_5 does not make the Yukawa coupling disappear from the EOM, since the latter is defined over the whole interval.

[1] Note that all the conditions of Eq. (E.7) are induced by the $(--)$ BC only.

Appendix F

The generic characteristic equation

From the infinite quark mass matrix, $[M]$, defined in Eq. (8.27), we first get the symmetric matrix, $\left[M^{\dagger}M\right]$, which can be written without loss of generality as,

$$\begin{pmatrix} M_{q_0}^2+\sum_n \beta_{n0}^2 & \alpha_{00}M_{q0}+\beta_{00}M_{d0} & \sum_n \beta_{n0}\beta_{n1} & \alpha_{01}M_{q0}+\beta_{10}M_{d1} & \sum_n \beta_{n0}\beta_{n2} & \cdots \\ \vdots & M_{d_0}^2+\sum_n \alpha_{n0}^2 & \alpha_{10}M_{q1}+\beta_{01}M_{d0} & \sum_n \alpha_{n0}\alpha_{n1} & \alpha_{20}M_{q2}+\beta_{02}M_{d0} & \cdots \\ \vdots & \vdots & M_{q_1}^2+\sum_n \beta_{n1}^2 & \alpha_{11}M_{q1}+\beta_{11}M_{d1} & \sum_n \beta_{n1}\beta_{n2} & \cdots \\ \vdots & \vdots & \vdots & M_{d_1}^2+\sum_n \alpha_{n1}^2 & \alpha_{21}M_{q2}+\beta_{12}M_{d1} & \cdots \\ \vdots & \vdots & \vdots & \vdots & M_{q_2}^2+\sum_n \beta_{n2}^2 & \cdots \\ \vdots & \vdots & \vdots & \vdots & \vdots & \ddots \end{pmatrix}$$

where the discrete sums are taken from $n=0$ to infinity.

For the characteristic equation of this infinite matrix, $\left[M^{\dagger}M\right]$, we find the following analytical expression,

$$1+\mathcal{P}_0+\mathcal{P}_1=0 \tag{F.1}$$

where $\mathcal{P}_0$ and $\mathcal{P}_1$ are both series of infinite number of terms. In the limit where all the KK mass ($M's$) terms go to zero, $\mathcal{P}_1$ vanishes but $\mathcal{P}_0$ does not. In order to describe the parts, $\mathcal{P}_0$ and $\mathcal{P}_1$, we have to first define the following structures depending on the α_{qd} [defined in Eq. (8.28)],

$$A_n\left(q_1,\cdots,q_n;d_1,\cdots,d_n\right) \equiv \sum_{r_1,\cdots,r_n(\in\{d_1,\cdots,d_n\})} \varepsilon^{i(r_1)\ldots i(r_n)}\ \varepsilon_{i(d_1)\ldots i(d_n)}\ \alpha_{q_1r_1}\cdots\alpha_{q_nr_n}\ , \tag{F.2}$$

such that $\varepsilon^{abc\cdots}$ is the anti-symmetric tensor, with for instance the index $i(r_3)=i(d_2)\hat{=}2$, and the three first structures can be written explicitly as [notice the specific definition for $A_1\left(q_1;d_1\right)$],

$$\begin{aligned} A_1\left(q_1;d_1\right) &= \alpha_{q_1d_1}\ , \\ A_2\left(q_1,q_2;d_1,d_2\right) &= \alpha_{q_1d_1}\alpha_{q_2d_2}-\alpha_{q_1d_2}\alpha_{q_2d_1}\ , \\ A_3\left(q_1,q_2,q_3;d_1,d_2,d_3\right) &= \alpha_{q_1d_1}\alpha_{q_2d_2}\alpha_{q_3d_3}+\alpha_{q_1d_2}\alpha_{q_2d_3}\alpha_{q_3d_1}+\alpha_{q_1d_3}\alpha_{q_2d_1}\alpha_{q_3d_2} \\ &\quad -\alpha_{q_1d_1}\alpha_{q_2d_3}\alpha_{q_3d_2}-\alpha_{q_1d_3}\alpha_{q_2d_2}\alpha_{q_3d_1}-\alpha_{q_1d_2}\alpha_{q_2d_1}\alpha_{q_3d_3}\ . \end{aligned}$$

Note that because of the anti-symmetric nature of these structures, in a factorizable case where $\alpha_{qd} = f_q \times f_d$, one has simply,

$$A_{n\geq 2} = 0. \tag{F.3}$$

Analogous structures can be introduced for the β_{dq} [defined in Eq. (8.29)] :

$$B_n\left(d_1,\cdots,d_n;q_1,\cdots,q_n\right) \equiv \sum_{r_1,\cdots,r_n(\in\{d_1,\cdots,d_n\})} \varepsilon^{i(r_1)\ldots i(r_n)}\ \varepsilon_{i(d_1)\ldots i(d_n)}\ \beta_{r_1q_1}\cdots\beta_{r_nq_n}\ . \tag{F.4}$$

One has similarly, $B_{n\geq 2} = 0$, for factorizable cases with, $\beta_{dq} = f_d \times f_q$. Now, with the conditions

$$q_i \neq q_j \neq Q_k \quad ; \quad d_i \neq d_j \neq D_k \tag{F.5}$$

where $i,j,k = 0,1,2,\cdots$, the first few terms (sufficient to deduce the rest of the infinite series) in the $\mathcal{P}_0$ and $\mathcal{P}_1$ parts can be expressed as,

$$\begin{aligned}
\mathcal{P}_0 \;=\;& \sum_{q_1;d_1}(-\lambda)\left(\frac{\left(A_1(q_1;d_1)\right)^2}{(M_{q_1}^2-\lambda)(M_{d_1}^2-\lambda)} + (\alpha\leftrightarrow\beta)\right)\\
&+\sum_{q_1<q_3;d_1<d_3}(-\lambda)^2\left(\frac{\left(A_2(q_1,q_3;d_1,d_3)\right)^2}{(M_{q_1}^2-\lambda)(M_{d_1}^2-\lambda)(M_{q_3}^2-\lambda)(M_{d_3}^2-\lambda)} + (\alpha\leftrightarrow\beta)\right)\\
&+\sum_{q_1,q_2;d_1,d_2}(-\lambda)^2\ \frac{\left(A_1(q_1;d_1)\right)^2}{(M_{q_1}^2-\lambda)(M_{d_1}^2-\lambda)}\times\frac{\left(B_1(d_2;q_2)\right)^2}{(M_{q_2}^2-\lambda)(M_{d_2}^2-\lambda)}\\
&\quad\times\left(1-\delta_{q_1q_2}\frac{M_{q_2}^2}{\lambda}\right)\left(1-\delta_{d_1d_2}\frac{M_{d_2}^2}{\lambda}\right)\\
&+\sum_{q_1<q_3,q_2;d_1<d_3,d_2}(-\lambda)^3\left\{\frac{\left(A_2(q_1,q_3;d_1,d_3)\right)^2}{\prod_{i=1,3}(M_{q_i}^2-\lambda)(M_{d_i}^2-\lambda)}\times\frac{\left(B_1(d_2;q_2)\right)^2}{(M_{q_2}^2-\lambda)(M_{d_2}^2-\lambda)}\right.\\
&\quad\left.\times\left(1-\delta_{q_1q_2}\frac{M_{q_2}^2}{\lambda}\right)\left(1-\delta_{d_1d_2}\frac{M_{d_2}^2}{\lambda}\right)\left(1-\delta_{q_3q_2}\frac{M_{q_2}^2}{\lambda}\right)\left(1-\delta_{d_3d_2}\frac{M_{d_2}^2}{\lambda}\right)+(\alpha\leftrightarrow\beta)\right\}\\
&+\sum_{q_1<q_3,q2<q_4;d_1<d_3,d_2<d_4}(-\lambda)^4\ \frac{\left(A_2(q_1,q_3;d_1,d_3)\right)^2}{\prod_{i=1,3}(M_{q_i}^2-\lambda)(M_{d_i}^2-\lambda)}\times\frac{\left(B_2(d_2,d_4;q_2,q_4)\right)^2}{\prod_{j=2,4}(M_{q_j}^2-\lambda)(M_{d_j}^2-\lambda)}\\
&\quad\times\left(1-\delta_{q_1q_2}\frac{M_{q_2}^2}{\lambda}\right)\left(1-\delta_{q_3q_2}\frac{M_{q_2}^2}{\lambda}\right)\left(1-\delta_{q_1q_4}\frac{M_{q_4}^2}{\lambda}\right)\left(1-\delta_{q_3q_4}\frac{M_{q_4}^2}{\lambda}\right)\\
&\quad\times\left(1-\delta_{d_1d_2}\frac{M_{d_2}^2}{\lambda}\right)\left(1-\delta_{d_3d_2}\frac{M_{d_2}^2}{\lambda}\right)\left(1-\delta_{d_1d_4}\frac{M_{d_4}^2}{\lambda}\right)\left(1-\delta_{d_3d_4}\frac{M_{d_4}^2}{\lambda}\right)\\
&+\ \mathcal{O}(\alpha^6,\beta^6)\ ,
\end{aligned} \tag{F.6}$$

and,

$$
\begin{aligned}
\mathcal{P}_1 \;=\; & \sum_{Q_1;D_1} \frac{-2M_{Q_1}M_{D_1}}{(M_{Q_1}^2-\lambda)(M_{D_1}^2-\lambda)} \times \Bigg[A_1(Q_1;D_1) \times B_1(D_1;Q_1) \\
& + \sum_{q_1;d_1} (-\lambda) \left\{ \frac{A_2(Q_1,q_1;D_1,d_1)A_1(q_1;d_1)}{(M_{q_1}^2-\lambda)(M_{d_1}^2-\lambda)} \times B_1(D_1;Q_1) + (\alpha \leftrightarrow \beta) \right\} \\
& + \sum_{q_1 q_2;d_1,d_2} (-\lambda)^2 \times \frac{A_2(Q_1,q_1;D_1,d_1)A_1(q_1;d_1)}{(M_{q_1}^2-\lambda)(M_{d_1}^2-\lambda)} \times \frac{B_2(D_1,d_2;Q_1,q_2)B_1(d_2;q_2)}{(M_{q_2}^2-\lambda)(M_{d_2}^2-\lambda)} \\
& \times \left(1-\delta_{q_1q_2}\frac{M_{q_2}^2}{\lambda}\right)\left(1-\delta_{d_1d_2}\frac{M_{d_2}^2}{\lambda}\right) + \mathcal{O}\left(\alpha^5,\beta^5\right) \Bigg] \\
+ \; & \Bigg\{ \sum_{Q_1<Q_2} \frac{2M_{Q_1}M_{Q_2}}{(M_{Q_1}^2-\lambda)(M_{Q_2}^2-\lambda)} \times \Bigg[\sum_{d_1,d_2} (-\lambda) \times \frac{A_1(Q_1;d_1)A_1(Q_2;d_1)}{(M_{d_1}^2-\lambda)} \\
& \times \frac{B_1(d_2;Q_1)B_1(d_2;Q_2)}{(M_{d_2}^2-\lambda)} \left(1-\delta_{d_1d_2}\frac{M_{d_2}^2}{\lambda}\right) \\
& + \sum_{q_1;d_1,d_2,d_3} (-\lambda)^2 \left\{ \frac{A_2(Q_1,q_1;d_1,d_3)A_2(Q_2,q_1;d_1,d_3)}{(M_{q_1}^2-\lambda)(M_{d_1}^2-\lambda)} \times \frac{B_1(d_2;Q_1)B_1(d_2;Q_2)}{(M_{d_3}^2-\lambda)} \right. \\
& \left. \times \left(1-\delta_{d_1d_2}\frac{M_{d_2}^2}{\lambda}\right)\left(1-\delta_{d_3d_2}\frac{M_{d_2}^2}{\lambda}\right) + (\alpha \leftrightarrow \beta) \right\} \\
& + \sum_{q_1,q_2;d_1,d_2,d_3,d_4} (-\lambda)^3 \times \frac{A_2(Q_1,q_1;d_1,d_3)A_2(Q_2,q_1;d_1,d_3)}{(M_{q_1}^2-\lambda)(M_{d_1}^2-\lambda)(M_{d_3}^2-\lambda)} \\
& \times \frac{B_2(d_2,d_4;Q_1,q_2)B_2(d_2,d_4;Q_2,q_2)}{(M_{q_2}^2-\lambda)(M_{d_2}^2-\lambda)(M_{d_4}^2-\lambda)} \left(1-\delta_{q_1q_2}\frac{M_{q_2}^2}{\lambda}\right)\left(1-\delta_{d_1d_2}\frac{M_{d_2}^2}{\lambda}\right) \\
& \times \left(1-\delta_{d_1d_4}\frac{M_{d_4}^2}{\lambda}\right)\left(1-\delta_{d_3d_2}\frac{M_{d_2}^2}{\lambda}\right)\left(1-\delta_{d_3d_4}\frac{M_{d_4}^2}{\lambda}\right) + \mathcal{O}\left(\alpha^6,\beta^6\right) \Bigg] \\
& + [(Q_1,Q_2) \to (D_1,D_2)] \Bigg\} \\
+ \; & \sum_{Q_1<Q_2;D_1<D_2} 2\left(\prod_{i=1,2} \frac{M_{Q_i}M_{D_i}}{(M_{Q_i}^2-\lambda)(M_{D_i}^2-\lambda)}\right) \\
& \times \Bigg[A_2(Q_1,Q_2;D_1,D_2) \times B_2(D_1,D_2;Q_1,Q_2) \\
& + A_1(Q_1;D_1)A_1(Q_2;D_2) \times B_1(D_1;Q_1)B_1(D_2;Q_2) \\
& + A_1(Q_1;D_2)A_1(Q_2;D_1) \times B_1(D_2;Q_1)B_1(D_1;Q_2) + \mathcal{O}\left(\alpha^4,\beta^4\right) \Bigg]
\end{aligned}
$$

$$
\begin{aligned}
+ \quad & \left\{ \sum_{Q_1<Q_2<Q_3;D_1} (-2) \left(\prod_{i=1,3} \frac{M_{Q_i}}{(M_{Q_i}^2-\lambda)} \right) \frac{M_{D_1}}{(M_{D_1}^2-\lambda)} \right. \\
& \times \left[\sum_{d_1,d_2} (-\lambda) \left(\frac{A_2(Q_1,Q_2;D_1,d_1)A_1(Q_3;d_1)}{(M_{d_1}^2-\lambda)} \times \frac{B_2(D_1,d_2;Q_1,Q_2)B_1(d_2;Q_3)}{(M_{d_2}^2-\lambda)} \right. \right. \\
& + \frac{A_2(Q_1,Q_3;D_1,d_1)A_1(Q_2;d_1)}{(M_{d_1}^2-\lambda)} \times \frac{B_2(D_1,d_2;Q_1,Q_3)B_1(d_2;Q_3)}{(M_{d_2}^2-\lambda)} \\
& \left. \left. + \frac{A_2(Q_2,Q_3;D_1,d_1)A_1(Q_1;d_1)}{(M_{d_1}^2-\lambda)} \times \frac{B_2(D_1,d_2;Q_2,Q_3)B_1(d_2;Q_1)}{(M_{d_2}^2-\lambda)} \right) \right. \\
& \left. \left. \times \left(1-\delta_{d_1 d_2} \frac{M_{d_2}^2}{\lambda} \right) + \mathcal{O}\left(\alpha^5,\beta^5\right) \right] + (M_Q \leftrightarrow M_D, \alpha \leftrightarrow \beta) \right\} \\
+ \quad & \left\{ \sum_{Q_1<Q_2<Q_3<Q_4} 2 \left(\prod_{i=1,4} \frac{M_{Q_i}}{(M_{Q_i}^2-\lambda)} \right) \right. \\
& \times \left[\sum_{d_1,d_2} (-\lambda)^2 \left(\frac{A_2(Q_1,Q_2;d_1,d_3)A_2(Q_3,Q_4;d_1,d_3)}{(M_{d_1}^2-\lambda)(M_{d_3}^2-\lambda)} \right. \right. \\
& \times \frac{B_2(d_2,d_4;Q_1,Q_2)B_2(d_2,d_4;Q_3,Q_4)}{(M_{d_2}^2-\lambda)(M_{d_4}^2-\lambda)} + \frac{A_2(Q_1,Q_3;d_1,d_3)A_2(Q_2,Q_4;d_1,d_3)}{(M_{d_1}^2-\lambda)(M_{d_3}^2-\lambda)} \\
& \times \frac{B_2(d_2,d_4;Q_1,Q_3)B_2(d_2,d_4;Q_2,Q_4)}{(M_{d_2}^2-\lambda)(M_{d_4}^2-\lambda)} + \frac{A_2(Q_1,Q_4;d_1,d_3)A_2(Q_2,Q_3;d_1,d_3)}{(M_{d_1}^2-\lambda)(M_{d_3}^2-\lambda)} \\
& \left. \left. \times \frac{B_2(d_2,d_4;Q_1,Q_4)B_2(d_2,d_4;Q_2,Q_3)}{(M_{d_2}^2-\lambda)(M_{d_4}^2-\lambda)} \right) \right. \\
& \left. \times \left(1-\delta_{d_1 d_2} \frac{M_{d_2}^2}{\lambda} \right) \left(1-\delta_{d_1 d_4} \frac{M_{d_4}^2}{\lambda} \right) \left(1-\delta_{d_3 d_2} \frac{M_{d_2}^2}{\lambda} \right) \left(1-\delta_{d_3 d_4} \frac{M_{d_4}^2}{\lambda} \right) + \mathcal{O}\left(\alpha^6,\beta^6\right) \right] \\
& \left. + (M_Q \leftrightarrow M_D, \alpha \leftrightarrow \beta) \right\}, \qquad \text{(F.7)}
\end{aligned}
$$

where all the discrete sums are taken from zero to infinity and λ represents the eigenvalues of the $\left[M^\dagger M\right]$ matrix.

Appendix G

The supersymmetric 5D Lagrangian

We consider the usual warped space-time based on the 5D metric G_{AB}:

$$ds^2 = G_{AB}\, dx^A dx^B = e^{-2\sigma(y)} \eta_{\mu\nu} dx^\mu dx^\nu - dy^2 \quad , \quad y \in [-\pi R_c; +\pi R_c] \tag{G.1}$$

$$\sqrt{+G} \equiv \sqrt{\det[G_{AB}]} = \sqrt{(-1)^4 (e^{-2\sigma(y)})^4} = e^{-4\sigma(y)} \tag{G.2}$$

where capital latin letters A, B are 5D Lorentz indices, $\eta_{\mu\nu}$ is the 4D flat $(+,-,-,-)$ Minkowski metric and x^μ denote the usual coordinates ($\mu = 0, 1, 2, 3$) while y parametrizes the fifth dimension.

G.1 Superfield content

Writing higher-dimensional SUSY Lagrangians with ordinary $N = 1$ 4D superfields only allows to make the $N = 1$ 4D SUSY invariance manifest and it prevents from explicitly covariant forms. In spite of these limitations, it allows for a more compact form than when using the component fields themselves and also to easily get the bulk-boundary couplings. We thus adopt this formalism. This approach was first developed for theories with 10 dimensions [75], then extended to other dimensions [76] and to incorporate the radion superfield [24].

In this Appendix G, we derive explicitly in terms of the fields, within the RS SUSY framework with a bulk U(1) gauge symmetry, the whole Lagrangian encoding the Yukawa and gauge couplings of the two $N = 1$ 5D (or $N = 2$ 4D) bulk hypermultiplets $\{\Phi_L, \Phi_L^{--}\}$ and $\{\Phi_L^c, \Phi_L^{c--}\}$ to two $N = 1$ 4D complex chiral superfields localized on the TeV-brane called H_u^0 (as it will play the role of the 'up-type' neutral Higgs superfield when extending this toy model to the pMSSM) and H_d^0 (for 'down-type'). The $N = 1$ chiral superfield Φ_L [the subscript L corresponds to the chirality of the contained fermion field once promoted to a four-component spinor: see just below [1]] with Neumann BC at $y = 0, \pi R_c$ (noted $(++)$ in the main text)

[1] Note that L/R would be seen as a gauge index within the pMSSM, corresponding to a doublet/singlet under $SU(2)_L$.

reads as

$$\Phi_L(x^\mu,y;\theta,\overline{\theta}) \equiv \phi_L(x^\mu,y)+\sqrt{2}\theta\zeta_L(x^\mu,y)e^{-\frac{1}{2}\sigma(y)}-\theta\theta F_L(x^\mu,y)+i\theta\sigma^\mu\overline{\theta}\partial_\mu\phi_L(x^\mu,y) +\frac{i}{\sqrt{2}}\theta\theta\overline{\theta}\overline{\sigma}^\mu\partial_\mu\zeta_L(x^\mu,y)e^{-\frac{1}{2}\sigma(y)}-\frac{1}{4}\theta\theta\overline{\theta}\overline{\theta}\partial_\mu\partial^\mu\phi_L(x^\mu,y), \quad (G.3)$$

ζ_L being the two-component spinorial field, ϕ_L its scalar superpartner and F_L the auxiliary field, whereas its complex conjugated develops according to

$$\overline{\Phi}(x^\mu,y;\theta,\overline{\theta}) \equiv \overline{\phi}_L(x^\mu,y)+\sqrt{2\theta\zeta}_L(x^\mu,y)e^{-\frac{1}{2}\sigma(y)}-\overline{\theta\theta F}_L(x^\mu,y)-i\theta\sigma^\mu\overline{\theta}\partial_\mu\overline{\phi}_L(x^\mu,y) +\frac{i}{\sqrt{2}}\overline{\theta\theta}\theta\sigma^\mu\partial_\mu\overline{\zeta}_L(x^\mu,y)e^{-\frac{1}{2}\sigma(y)}-\frac{1}{4}\overline{\theta\theta}\theta\theta\partial_\mu\partial^\mu\overline{\phi}_L(x^\mu,y) \quad (G.4)$$

and its charge conjugated superfield with Dirichlet BC at $y=0,\pi R_c$ (noted $(--)$) is

$$\Phi_L^{--}(x^\mu,y;\theta,\overline{\theta}) \equiv \phi_L^c(x^\mu,y)+\sqrt{2}\theta\chi_L(x^\mu,y)e^{-\frac{1}{2}\sigma(y)}-\theta\theta F_L^c(x^\mu,y)+i\theta\sigma^\mu\overline{\theta}\partial_\mu\phi_L^c(x^\mu,y) +\frac{i}{\sqrt{2}}\theta\theta\overline{\theta}\overline{\sigma}^\mu\partial_\mu\chi_L(x^\mu,y)e^{-\frac{1}{2}\sigma(y)}-\frac{1}{4}\theta\theta\overline{\theta}\overline{\theta}\partial_\mu\partial^\mu\phi_L^c(x^\mu,y). \quad (G.5)$$

We define another superfield Φ_L^c through its charge conjugated state [this will allow us to introduce only Left-handed chiral superfields, as usually in the 4D pMSSM]:

$$\Phi_L^c(x^\mu,y;\theta,\overline{\theta}) \equiv \phi_R(x^\mu,y)+\sqrt{2}\theta\chi_R(x^\mu,y)e^{-\frac{1}{2}\sigma(y)}-\theta\theta F_R(x^\mu,y)+i\theta\sigma^\mu\overline{\theta}\partial_\mu\phi_R(x^\mu,y) +\frac{i}{\sqrt{2}}\theta\theta\overline{\theta}\overline{\sigma}^\mu\partial_\mu\chi_R(x^\mu,y)e^{-\frac{1}{2}\sigma(y)}-\frac{1}{4}\theta\theta\overline{\theta}\overline{\theta}\partial_\mu\partial^\mu\phi_R(x^\mu,y) \quad (G.6)$$

and the opposite BC superfield is:

$$\Phi_L^{c--}(x^\mu,y;\theta,\overline{\theta}) \equiv \phi_R^c(x^\mu,y)+\sqrt{2}\theta\zeta_R(x^\mu,y)e^{-\frac{1}{2}\sigma(y)}-\theta\theta F_R^c(x^\mu,y)+i\theta\sigma^\mu\overline{\theta}\partial_\mu\phi_R^c(x^\mu,y) +\frac{i}{\sqrt{2}}\theta\theta\overline{\theta}\overline{\sigma}^\mu\partial_\mu\zeta_R(x^\mu,y)e^{-\frac{1}{2}\sigma(y)}-\frac{1}{4}\theta\theta\overline{\theta}\overline{\theta}\partial_\mu\partial^\mu\phi_R^c(x^\mu,y). \quad (G.7)$$

In our notations, the four-component fermions $\psi_{L/R}$ (L/R indicating the Lorentz chirality) read in terms of the two-component fields as

$$\psi^t\equiv(\zeta,\bar{\chi}),\quad \psi_L^t\equiv(\zeta,0),\quad \psi^{c\ t}\equiv(\chi,\bar{\zeta}).$$

We consider a U(1) gauge symmetry whose $N=1$ 5D (or $N=2$ 4D) gauge supermultiplet is known to have the same field content as **one** $N=1$ vector supermultiplet with $(++)$ BC, for which we write the decomposition as (in the Wess-Zumino gauge)

$$V(x^\mu,y;\theta,\overline{\theta}) \equiv \theta\sigma^\mu\overline{\theta}A_\mu(x^\mu,y)-i\overline{\theta\theta}\theta\lambda_1(x^\mu,y)e^{-\frac{3}{2}\sigma(y)}+i\theta\theta\overline{\theta\lambda}_1(x^\mu,y)e^{-\frac{3}{2}\sigma(y)}+\frac{1}{2}\theta\theta\overline{\theta}\overline{\theta}D(x^\mu,y) \quad (G.8)$$

A_μ denoting the gauge boson, λ_1 the Weyl gaugino field and D the complex auxiliary field, plus **one** $(--)$

$N=1$ chiral superfield, that we write

$$\begin{aligned}\Omega(x^\mu,y;\theta,\overline{\theta}) \;\equiv\; & \frac{1}{\sqrt{2}}[\Sigma(x^\mu,y)-iA_5(x^\mu,y)]-i\sqrt{2}\theta\lambda_2(x^\mu,y)e^{-\frac{1}{2}\sigma(y)}-\theta\theta F_\Omega(x^\mu,y)\\ & +i\theta\sigma^\mu\overline{\theta}\partial_\mu\frac{1}{\sqrt{2}}[\Sigma(x^\mu,y)-iA_5(x^\mu,y)]+\frac{1}{\sqrt{2}}\theta\theta\overline{\theta}\overline{\sigma}^\mu\partial_\mu\lambda_2(x^\mu,y)e^{-\frac{1}{2}\sigma(y)}\\ & -\frac{1}{4}\theta\theta\overline{\theta}\overline{\theta}\partial_\mu\partial^\mu\frac{1}{\sqrt{2}}[\Sigma(x^\mu,y)-iA_5(x^\mu,y)] \end{aligned} \tag{G.9}$$

Σ being a real scalar field.

G.2 Superfield action

The field content described in previous subsection G.1 together with the following action $\mathcal{S}_{5D}$ define the toy model analyzed in this part G. This action is given by $\mathcal{S}_{5D}=\mathcal{S}_{gauge}+\mathcal{S}_{Higgs}\Big|_{brane}+\mathcal{S}_{matter}$ with, following the formalism of Ref. [24],

$$\mathcal{S}_{gauge} = \frac{1}{4}\int d^5x\int d^2\theta\ (W^\alpha W_\alpha+h.c.)+\int d^5x\int d^4\theta\ e^{-2\sigma(y)}\left(\partial_y V-\frac{1}{\sqrt{2}}(\Omega+\overline{\Omega})\right)^2 \tag{G.10}$$

$$\begin{aligned}\mathcal{S}_{matter} &= \int d^5x\int d^4\theta\ e^{-2\sigma(y)}\left(\overline{\Phi}_L e^{-2gq_LV}\Phi_L+\Phi_L^{--}e^{2gq_LV}\overline{\Phi}_L^{--}+\overline{\Phi}_L^c e^{-2gq_RV}\Phi_L^c+\Phi_L^{c--}e^{2gq_RV}\overline{\Phi}_L^{c--}\right)\\ &+\int d^5x\int d^2\theta\ e^{-3\sigma(y)}\left(\Phi_L^{--}[D_5-\sqrt{2}gq_L\Omega]\Phi_L+\Phi_L^{c--}[D_5-\sqrt{2}gq_R\Omega]\Phi_L^c\right)+h.c.\end{aligned} \tag{G.11}$$

$$\begin{aligned}\mathcal{S}_{Higgs}\Big|_{brane} &= \int d^5x\int d^4\theta\ e^{-2\sigma(y)}\left(\overline{H_u^0}e^{-(2gq_{H_u^0})V}H_u^0+\overline{H_d^0}e^{-(2gq_{H_d^0})V}H_d^0\right)\delta(y-\pi R_c)\\ &+\int d^5x\int d^2\theta\ e^{-3\sigma(y)}\left(\mu\, H_u^0H_d^0+\mathcal{Y}H_u^0\Phi_L\Phi_L^c\right)\delta(y-\pi R_c)+h.c.\end{aligned} \tag{G.12}$$

where g ($\mathcal{Y}$) is the 5D gauge (Yukawa) coupling constant, $D_5=\partial_y-(\frac{3}{2}-c_{L/R})\sigma'$ [with $\sigma'=\partial_y\sigma(y)=sign(y)\times k$, $sign(y)$ being a step function] and the U(1) charges of the superfields $H^0_{u,d}$, Φ_L, Φ_L^c must obey $q_{H_u^0}+q_L+q_R=0$, $q_{H_u^0}+q_{H_d^0}=0$. The above $c_{L/R}$ terms represent 5D mass terms in the superpotential of the superfields Φ_L/Φ_L^c that will lead to 5D fermion and 5D scalar mass terms, as will appear soon. In the above action, the fundamental parameter μ is of order k.

G.3 Auxiliary field Lagrangians

The 5D Lagrangian for the gauge auxiliary field D is given by (from now on, σ stands for $\sigma(y)$):

$$\begin{aligned}\mathcal{L}_D &= \frac{1}{2}D^2+e^{-2\sigma}D\left(\partial_y-2\sigma'\right)\Sigma\\ &- ge^{-2\sigma}D\left(q_L(\overline{\phi}_L\phi_L-\phi_L^c\overline{\phi}_L^c)+q_R(\overline{\phi}_R\phi_R-\phi_R^c\overline{\phi}_R^c)\right)\\ &- ge^{-2\sigma}D\left(q_{H_u^0}\overline{\phi}_{H_u^0}\phi_{H_u^0}+q_{H_d^0}\overline{\phi}_{H_d^0}\phi_{H_d^0}\right)\delta(y-\pi R_c)\end{aligned} \tag{G.13}$$

$\phi_{H_u^0}$ and $\phi_{H_d^0}$ being the scalar field components of the superfields H_u^0 and H_d^0, respectively.

The 5D Lagrangian for the auxiliary field F_Ω is given by:

$$\mathcal{L}_\Omega = e^{-2\sigma}\overline{F}_\Omega F_\Omega - \sqrt{2}ge^{-3\sigma}\left((q_L\,\phi_L^c\phi_L + q_R\,\phi_R^c\phi_R)F_\Omega + h.c.\right). \tag{G.14}$$

The 5D Lagrangian for the matter auxiliary fields, namely F_L, F_R, F_L^c, F_R^c, is given by:

$$\begin{aligned}
\mathcal{L}_F &= e^{-2\sigma}\left(\overline{F}_L F_L + F_L^c\overline{F}_L^c + \overline{F}_R F_R + F_R^c\overline{F}_R^c\right) \\
&- e^{-3\sigma}\left(F_L^c D_5\phi_L - F_L D_5'\phi_L^c + F_R^c D_5\phi_R - F_R D_5'\phi_R^c\right) + h.c. \\
&+ e^{-3\sigma}2g\left(q_L(\phi_L^c F_L + F_L^c\phi_L) + q_R(\phi_R^c F_R + F_R^c\phi_R)\right)\Sigma + h.c. \\
&- e^{-3\sigma}\mathcal{Y}\left(\phi_{H_u^0}\phi_R F_L + \phi_{H_u^0}\phi_L F_R\right)\delta(y-\pi R_c) + h.c.
\end{aligned} \tag{G.15}$$

where $D_5' = \partial_y - (\frac{3}{2} + c_{L/R})\sigma'$. This Lagrangian is obtained after integrating by part (for convenience).

The 5D Lagrangian for the Higgs auxiliary fields, $F_{H_u^0}, F_{H_d^0}$, is given by:

$$\begin{aligned}
\mathcal{L}_H &= e^{-2\sigma}\left(\overline{F}_{H_u^0}F_{H_u^0} + \overline{F}_{H_d^0}F_{H_d^0}\right)\delta(y-\pi R_c) \\
&- e^{-3\sigma}\left(\mu\,F_{H_u^0}\phi_{H_d^0} + \mu\,\phi_{H_u^0}F_{H_d^0} + \mathcal{Y}\,F_{H_u^0}\phi_L\phi_R\right)\delta(y-\pi R_c) + h.c.
\end{aligned} \tag{G.16}$$

G.4 Auxiliary field solutions

The solutions of the equations of motion for the auxiliary fields are the following ones,

$$\begin{aligned}
D = -e^{-2\sigma}\Big\{&(\partial_y - 2\sigma')\Sigma - g\left(q_L(\overline{\phi}_L\phi_L - \phi_L^c\overline{\phi}_L^c) + q_R(\overline{\phi}_R\phi_R - \phi_R^c\overline{\phi}_R^c)\right) \\
&-g\left(q_{H_u^0}\overline{\phi}_{H_u^0}\phi_{H_u^0} + q_{H_d^0}\phi_{H_d^0}\overline{\phi}_{H_d^0}\right)\delta(y-\pi R_c)\Big\}
\end{aligned} \tag{G.17}$$

$$F_\Omega = -\sqrt{2}ge^{-\sigma}\left(q_L\,\overline{\phi}_L^c\overline{\phi}_L + q_R\,\overline{\phi}_R^c\overline{\phi}_R\right) \tag{G.18}$$

$$F_L = -e^{-\sigma}\left((D_5' + g\Sigma)\overline{\phi}_L^c - \bar{\mathcal{Y}}\delta(y-\pi R_c)\,\overline{\phi}_{H_u^0}\overline{\phi}_R\right) \quad , \quad \overline{F}_L^c = e^{-\sigma}(D_5 - g\Sigma)\phi_L \tag{G.19}$$

$$F_R = -e^{-\sigma}\left((D_5' + g\Sigma)\overline{\phi}_R^c - \bar{\mathcal{Y}}\delta(y-\pi R_c)\,\overline{\phi}_{H_u^0}\overline{\phi}_L\right) \quad , \quad \overline{F}_R^c = e^{-\sigma}(D_5 - g\Sigma)\phi_R \tag{G.20}$$

$$F_{H_u^0} = e^{-\sigma}\left(\bar{\mu}\,\overline{\phi}_{H_d^0} + \bar{\mathcal{Y}}\,\overline{\phi}_L\overline{\phi}_R\right) \quad , \quad F_{H_d^0} = e^{-\sigma}\bar{\mu}\,\overline{\phi}_{H_u^0}. \tag{G.21}$$

Plugging those back into the above Lagrangians, we get:

$$\mathcal{L}_D = -\frac{1}{2}D^2 \qquad , \qquad \mathcal{L}_\Omega = -e^{-2\sigma}\overline{F}_\Omega F_\Omega \tag{G.22}$$

$$\mathcal{L}_F = -e^{-2\sigma}\left(\overline{F}_L F_L + F_L^c\overline{F}_L^c + \overline{F}_R F_R + F_R^c\overline{F}_R^c\right) \tag{G.23}$$

$$\mathcal{L}_H = -e^{-2\sigma}\left(\overline{F}_{H_u^0}F_{H_u^0} + \overline{F}_{H_d^0}F_{H_d^0}\right)\delta(y-\pi R_c). \tag{G.24}$$

G.5 Scalar field Lagrangian

The whole 5D Lagrangian – all SUSY Lagrangians given in terms of 5D fields in this Appendix G are provided before field redefinition through warp factors – for scalar fields, $\mathcal{L}_{kin.} + \mathcal{L}_{scalar}$ with $\mathcal{L}_{scalar} = \mathcal{L}_D + \mathcal{L}_\Omega + \mathcal{L}_F + \mathcal{L}_H$, can be rewritten in explicit forms as:

$$\begin{aligned}\mathcal{L}_{kin.} &= e^{-2\sigma}\partial_\mu\bar{\phi}_{H_u^0}\partial^\mu\phi_{H_u^0}\delta(y-\pi R_c) + e^{-2\sigma}\partial_\mu\bar{\phi}_{H_d^0}\partial^\mu\phi_{H_d^0}\delta(y-\pi R_c)\\ &+ e^{-2\sigma}\partial_\mu\bar{\phi}_L\partial^\mu\phi_L + e^{-2\sigma}\partial_\mu\bar{\phi}_L^c\partial^\mu\phi_L^c + e^{-2\sigma}\partial_\mu\bar{\phi}_R\partial^\mu\phi_R + e^{-2\sigma}\partial_\mu\bar{\phi}_R^c\partial^\mu\phi_R^c, \end{aligned} \tag{G.25}$$

$$\begin{aligned}-\sqrt{G}^{-1}\mathcal{L}_{scalar} &= D_5\overline{\phi}_L D_5\phi_L + D_5\overline{\phi}_R D_5\phi_R + |\mu|^2\,\overline{\phi}_{H_u^0}\phi_{H_u^0}\,\delta(y-\pi R_c)\\ &+ \left|\mathcal{Y}\delta(y-\pi R_c)\,\phi_{H_u^0}\phi_L - D_5'\phi_R^c\right|^2 + \left|\mathcal{Y}\delta(y-\pi R_c)\,\phi_{H_u^0}\phi_R - D_5'\phi_L^c\right|^2\\ &+ \left|\mu\,\phi_{H_d^0} + \mathcal{Y}\,\phi_L\phi_R\right|^2\delta(y-\pi R_c) + 2g^2\left|q_L\,\phi_L^c\phi_L + q_R\,\phi_R^c\phi_R\right|^2\\ &+ \frac{1}{2}\left|(\partial_y - 2\sigma')\Sigma - g\Big(q_L\Delta_{\phi_L} + q_R\Delta_{\phi_R} + [q_{H_d^0}\overline{\phi}_{H_d^0}\phi_{H_d^0} + q_{H_u^0}\overline{\phi}_{H_u^0}\phi_{H_u^0}]\delta(y-\pi R_c)\Big)\right|^2\end{aligned} \tag{G.26}$$

where e.g. $\Delta_{\phi_R} \equiv \overline{\phi}_R\phi_R - \phi_R^c\overline{\phi}_R^c$. By developing the $|D_5\phi|^2$, $|D_5'\phi|^2$ and $|(\partial_y - 2\sigma')\Sigma|^2$ terms from above, one finds the 5D scalar masses:

$$m^2_{\phi_{L/R},\phi^c_{L/R}} \equiv (c^2_{L/R} \pm c_{L/R} - \frac{15}{4})k^2 + (\frac{3}{2} \mp c_{L/R})\partial_y(\partial_y\sigma) \quad , \quad m^2_\Sigma \equiv -4k^2 + 2\partial_y(\partial_y\sigma). \tag{G.27}$$

If one now develops the last two lines proportional to the g gauge coupling in the above Lagrangian, one finds (after few simplifications):

$$\begin{aligned}-\sqrt{G}^{-1}\mathcal{L}_{scalar} &= D_5\overline{\phi}_L D_5\phi_L + D_5\overline{\phi}_R D_5\phi_R + |\mu|^2\,\overline{\phi}_{H_u^0}\phi_{H_u^0}\,\delta(y-\pi R_c)\\ &+ \left|\mathcal{Y}\delta(y-\pi R_c)\,\phi_{H_u^0}\phi_L - D_5'\phi_R^c\right|^2 + \left|\mathcal{Y}\delta(y-\pi R_c)\,\phi_{H_u^0}\phi_R - D_5'\phi_L^c\right|^2\\ &+ \left|\mu\,\phi_{H_d^0} + \mathcal{Y}\,\phi_L\phi_R\right|^2\delta(y-\pi R_c) + \frac{1}{2}\left|D_5^k\Sigma\right|^2\\ &- g\Big(q_L(\overline{\phi}_L\phi_L - \phi_L^c\overline{\phi}_L^c) + q_R(\overline{\phi}_R\phi_R - \phi_R^c\overline{\phi}_R^c) + \delta(y-\pi R_c)(q_{H_u^0}\overline{\phi}_{H_u^0}\phi_{H_u^0} + q_{H_d^0}\overline{\phi}_{H_d^0}\phi_{H_d^0})\Big)D_5^k\Sigma\\ &+ \frac{g^2}{2}\Big(q_L^2(|\phi_L|^4 + |\phi_L^c|^4) + q_R^2(|\phi_R|^4 + |\phi_R^c|^4) + \delta^2(y-\pi R_c)(q_{H_u^0}^2|\phi_{H_u^0}|^4 + q_{H_d^0}^2|\phi_{H_d^0}|^4)\Big)\\ &+ g^2\Big(q_L^2|\phi_L^c\phi_L|^2 + q_R^2|\phi_R^c\phi_R|^2 + q_{H_u^0}q_{H_d^0}\delta^2(y-\pi R_c)|\phi_{H_u^0}\phi_{H_d^0}|^2\Big)\\ &+ g^2 q_L q_R\Big(|\phi_L\phi_R|^2 - |\phi_L\phi_R^c|^2 - |\phi_L^c\phi_R|^2 + |\phi_L^c\phi_R^c|^2 + 2(\phi_L^c\phi_L\overline{\phi}_R^c\overline{\phi}_R + \phi_R^c\phi_R\overline{\phi}_L^c\overline{\phi}_L)\Big)\\ &+ g^2\Big(q_L(q_{H_u^0}|\phi_L\phi_{H_u^0}|^2 + q_{H_d^0}|\phi_L\phi_{H_d^0}|^2) + q_R(q_{H_u^0}|\phi_R\phi_{H_u^0}|^2 + q_{H_d^0}|\phi_R\phi_{H_d^0}|^2)\Big)\delta(y-\pi R_c)\end{aligned} \tag{G.28}$$

with $D_5^k = \partial_y - 2\sigma'$.

One can also simply add the soft bilinear terms for the Higgs fields on the TeV-brane and having, as usually in RS, soft squared Higgs masses and $B\mu$ (Higgs mixing) scales of order k squared leads to 4D effective soft terms with a scale at the TeV. The soft scalar trilinear A couplings are discussed in details in the main text.

G.6 Fermion field Lagrangian

We now derive the fermionic part of the 5D Lagrangian issued from the actions in Eq.(G.10)-(G.12):

$$\begin{aligned}
\mathcal{L}_{fermion} &= -e^{-4\sigma}\left(\chi_L D_5'' \zeta_L + \overline{\chi}_L D_5'' \overline{\zeta}_L + \chi_R D_5'' \zeta_R + \overline{\chi}_R D_5'' \overline{\zeta}_R\right) \\
&- ie^{-3\sigma}\left(\zeta_L \sigma^\mu \partial_\mu \overline{\zeta}_L + \zeta_R \sigma^\mu \partial_\mu \overline{\zeta}_R\right) - ie^{-3\sigma}\left(\chi_L \sigma^\mu \partial_\mu \overline{\chi}_L + \chi_R \sigma^\mu \partial_\mu \overline{\chi}_R\right) \\
&- ie^{-3\sigma}\left(\zeta_{H_u^0} \sigma^\mu \partial_\mu \overline{\zeta}_{H_u^0} + \zeta_{H_d^0} \sigma^\mu \partial_\mu \overline{\zeta}_{H_d^0}\right)\delta(y-\pi R_c) \\
&- e^{-4\sigma}\left(\lambda_2(\partial_y - \frac{3}{2}k)\lambda_1 + \overline{\lambda}_2(\partial_y - \frac{3}{2}k)\overline{\lambda}_1\right) - ie^{-3\sigma}\left(\lambda_1 \sigma^\mu \partial_\mu \overline{\lambda}_1 + \lambda_2 \sigma^\mu \partial_\mu \overline{\lambda}_2\right) \\
&- e^{-4\sigma}\left(\mu\, \zeta_{H_u^0}\zeta_{H_d^0} + \mathcal{Y}\phi_{H_u^0}\zeta_L\zeta_R + \mathcal{Y}\phi_L \zeta_{H_u^0}\zeta_R + \mathcal{Y}\phi_R \zeta_{H_u^0}\zeta_L\right)\delta(y-\pi R_c) \\
&- i\sqrt{2}e^{-4\sigma} g\left(q_{H_u^0}(\overline{\phi}_{H_u^0}\lambda_1\zeta_{H_u^0} - \phi_{H_u^0}\overline{\zeta}_{H_u^0}\overline{\lambda}_1) + q_{H_d^0}(\overline{\phi}_{H_d^0}\lambda_1\zeta_{H_d^0} - \phi_{H_d^0}\overline{\zeta}_{H_d^0}\overline{\lambda}_1)\right)\delta(y-\pi R_c) \\
&- i\sqrt{2}e^{-4\sigma} g\Big(q_L(\overline{\phi}_L\lambda_1\zeta_L - \phi_L\overline{\zeta}_L\overline{\lambda}_1) + q_R(\overline{\phi}_R\lambda_1\zeta_R - \phi_R\overline{\zeta}_R\overline{\lambda}_1)\Big) \\
&+ i\sqrt{2}e^{-4\sigma} g\Big(q_L(\overline{\phi}^c_L\lambda_1\chi_L - \phi^c_L\overline{\chi}_L\overline{\lambda}_1) + q_R(\overline{\phi}^c_R\lambda_1\chi_R - \phi^c_R\overline{\chi}_R\overline{\lambda}_1)\Big) \\
&- i\sqrt{2}e^{-4\sigma} g\Big(q_L(\phi^c_L\lambda_2\zeta_L + \phi_L\chi_L\lambda_2) + q_R(\phi^c_R\lambda_2\zeta_R + \phi_R\chi_R\lambda_2)\Big) + h.c.
\end{aligned} \tag{G.29}$$

where $D_5'' = \partial_y - (2 - c_{L/R})\sigma'$ and $\zeta_{H^0_{u,d}}$ are the higgsino two-component spinors.

G.7 Gauge field Lagrangian

Finally, the gauge interactions encoded in the superfield actions of Eq.(G.10)-(G.12) read in terms of the 5D gauge fields as,

$$\begin{aligned}
\mathcal{L}_{gauge} &= -\frac{1}{4}F_{\mu\nu}F^{\mu\nu} + \frac{1}{2}e^{-2\sigma}\partial_y A_\mu \partial_y A^\mu + \frac{1}{2}e^{-2\sigma}\partial_\mu \Sigma \partial^\mu \Sigma \\
&+ e^{-2\sigma}\left(\overline{D_\mu \phi}_L D^\mu \phi_L + \overline{D_\mu \phi}^c_L D^\mu \phi^c_L + \overline{D_\mu \phi}_R D^\mu \phi_R + \overline{D_\mu \phi}^c_R D^\mu \phi^c_R\right) \\
&- e^{-3\sigma}\left(i\zeta_L \sigma^\mu D_\mu \overline{\zeta}_L + i\chi_L \sigma^\mu D_\mu \overline{\chi}_L + i\zeta_R \sigma^\mu D_\mu \overline{\zeta}_R + i\chi_R \sigma^\mu D_\mu \overline{\chi}_R\right) \\
&+ e^{-2\sigma}\left(\overline{D_\mu \phi}_{H_u^0} D^\mu \phi_{H_u^0} + \overline{D_\mu \phi}_{H_d^0} D^\mu \phi_{H_d^0}\right)\delta(y-\pi R_c) \\
&- e^{-3\sigma}\left(i\zeta_{H_u^0}\sigma^\mu D_\mu \overline{\zeta}_{H_u^0} + i\zeta_{H_d^0}\sigma^\mu D_\mu \overline{\zeta}_{H_d^0}\right)\delta(y-\pi R_c)
\end{aligned} \tag{G.30}$$

where

$$\begin{aligned}
D_\mu &\equiv \partial_\mu + igq_{L/R}A_\mu \;/\; \partial_\mu + igq_{H^0_{u,d}}A_\mu \\
\overline{D_\mu \phi} D^\mu \phi &\equiv \partial_\mu \bar{\phi}\partial^\mu \phi + igq\left(\phi \partial_\mu \overline{\phi} - \overline{\phi}\partial_\mu \phi\right)A^\mu + g^2 q^2 \overline{\phi}\phi A_\mu A^\mu \\
i\zeta\sigma^\mu D_\mu \overline{\zeta} &\equiv i\zeta\sigma^\mu \partial_\mu \overline{\zeta} - gq\zeta\sigma^\mu \overline{\zeta} A_\mu.
\end{aligned}$$

To compare with another parametrization often found in literature, one can rewrite the second term of Eq.(G.30) in terms of the new coordinate $z = \frac{e^{\sigma(y)}}{k}$ ($y = 0 \Leftrightarrow z = \frac{1}{k} \equiv R$ and $y = \pi R_c \Leftrightarrow z = \frac{e^{k\pi R_c}}{k} \equiv R'$):

$$\frac{1}{2}e^{-2\sigma}\left(\partial_y A_\mu\right)^2 = -\frac{1}{2}A_\mu\left(\partial_z^2 - \frac{1}{z}\partial_z\right)A^\mu. \tag{G.31}$$

Appendix H

Wave functions

H.1 Generic relations

Any wave function $f_n(y)$, for a nth KK state along the fifth dimension y, satisfies the orthonormalization condition (after the usual RS field redefinition)

$$\int_{-\pi R_c}^{\pi R_c} \bar{f}_n(y) f_m(y) dy = \delta_{nm}, \tag{H.1}$$

showing that $f_n(y)$ has dimension 1/2, and the completeness relation (see for instance Ref. [77])

$$\sum_{n=0}^{\infty} \bar{f}_n(y) f_n(y') = \delta(y - y'). \tag{H.2}$$

H.2 Solutions for free vectorial fields

For the equations of motion in the warped SUSY background, the solutions for the wave functions along the fifth dimension of the free 5D vectorial field in Eq.(G.8), with KK decomposition

$$A_\mu(x^\mu, y) = \sum_{n=0}^{\infty} A_\mu^{(n)}(x^\mu) g_n^{++}(y),$$

are [2] for $n \geq 1$:

$$\begin{aligned} g_n^{++}(y) &= \frac{1}{\sqrt{2\pi R_c}} \frac{e^\sigma}{N_n} \left[J_1\left(\frac{M^{(n)} e^\sigma}{k}\right) + b_1^{++}(M^{(n)}) Y_1\left(\frac{M^{(n)} e^\sigma}{k}\right) \right], \\ b_1^{++}(M^{(n)}) &= -\frac{J_1(M^{(n)}/k) + (M^{(n)}/k) J_1'(M^{(n)}/k)}{Y_1(M^{(n)}/k) + (M^{(n)}/k) Y_1'(M^{(n)}/k)} \end{aligned} \tag{H.3}$$

where $\sigma = \sigma(y) = k|y|$, J_1, Y_1 (J_1', Y_1') are the (differentiated) Bessel functions, $M^{(n)} = M_{KK}^{(n)}$ is the n-*th* KK gauge mass and N_n is the normalization constant. Note that these wave functions are given here before the field redefinition usually done in the RS model. The solutions for the wave functions of the associated 5D

scalar field in Eq.(G.9), with KK decomposition

$$\Sigma(x^\mu, y) = \sum_{n=1}^{\infty} \Sigma^{(n)}(x^\mu) g_n^{--}(y), \tag{H.4}$$

are [2] for $n \geq 1$:

$$g_n^{--}(y) = sign(y) \frac{1}{\sqrt{2\pi R_c}} \frac{e^{2\sigma}}{N_n} \left[J_0\left(\frac{M^{(n)} e^{\sigma}}{k}\right) + b_0^{--}(M^{(n)}) Y_0\left(\frac{M^{(n)} e^{\sigma}}{k}\right) \right],$$
$$b_0^{--}(M^{(n)}) = -\frac{J_0(M^{(n)}/k)}{Y_0(M^{(n)}/k)} = b_1^{++}(M^{(n)}). \tag{H.5}$$

For completeness, we present the wave functions of the would-be A_5 component, even if we work in the gauge where $A_5 = 0$ together with the constraint $\partial^\mu A_\mu = 0$,

$$A_5(x^\mu, y) = \sum_{n=1}^{\infty} A_5^{(n)}(x^\mu) a_n^{--}(y),$$

with, for $n \geq 1$,

$$a_n^{--}(y) = e^{-\sigma}\ g_n^{--}(y). \tag{H.6}$$

Using the various relations on Bessel function derivatives, one obtains the useful following relation:

$$(\partial_y - 2\sigma') g_n^{--}(y) = -M^{(n)} e^{2\sigma} g_n^{++}(y). \tag{H.7}$$

There is also a term $-(\sigma''/\sigma') g_n^{--}$ but this term gives rise to a vanishing contribution when replaced in couplings and integrated over y cause $\sigma'' = 2k[\delta(y) - \delta(y - \pi R_c)]$ and g_n^{--} vanishes at $y = 0, \pi R_c$. One finds also the relation

$$\partial_y g_n^{++}(y) = M^{(n)} g_n^{--}(y). \tag{H.8}$$

Eq.(H.7)-(H.8) allow to recover the differential equations [78]

$$\partial_y \left(\frac{1}{e^{2\sigma}} \partial_y g_n^{++}(y) \right) = -(M^{(n)})^2 g_n^{++}(y) \tag{H.9}$$

and [2]

$$-e^{-4\sigma} \partial_y \left(\frac{1}{e^{4\sigma}} \partial_y g_n^{--}(y) \right) - 4k^2 g_n^{--}(y) = (M^{(n)})^2 e^{2\sigma} g_n^{--}(y). \tag{H.10}$$

H.3 Scalar/fermion fields and SUSY breaking

Similarly, the solutions for the wave functions along the fifth dimension of the 5D scalar fields introduced in Appendix G, with KK decomposition

$$\phi_{L/R}(x^\mu, y) = \sum_{n=0}^{\infty} \phi_{L/R}^{(n)}(x^\mu) f_n^{++}(c_{L/R}; y), \tag{H.11}$$

$$\phi_{L/R}^{c}(x^\mu, y) = \sum_{n=1}^{\infty} \phi_{L/R}^{c(n)}(x^\mu) f_n^{--}(c_{L/R}; y), \tag{H.12}$$

read as [2]

$$f_0^{++}(c_{L/R}; y) = \sqrt{\frac{k}{2}} \sqrt{\frac{1-2c_{L/R}}{1-e^{-(1-2c_{L/R})k\pi R_c}}}\, e^{k(\frac{1}{2}-c_{L/R})(y-\pi R_c)} \tag{H.13}$$

for the unique zero-mode and as [defining $\alpha_{L/R}^{\pm} = |c_{L/R} \pm 1/2|$]

$$\begin{aligned} f_n^{++}(c_{L/R}; y) &= \frac{1}{\sqrt{2\pi R_c}} \frac{e^{2\sigma}}{\mathcal{N}_n} \left[J_{\alpha_{L/R}^+}\left(\frac{m_{L/R}^{(n)} e^{\sigma}}{k}\right) + b_{\alpha_{L/R}^+}^{++}(m_{L/R}^{(n)}) Y_{\alpha_{L/R}^+}\left(\frac{m_{L/R}^{(n)} e^{\sigma}}{k}\right)\right], \\ b_{\alpha_{L/R}^+}^{++}(m_{L/R}^{(n)}) &= -\frac{[2-(3/2-c_{L/R})] J_{\alpha_{L/R}^+}(m_{L/R}^{(n)}/k) + (m_{L/R}^{(n)}/k) J'_{\alpha_{L/R}^+}(m_{L/R}^{(n)}/k)}{[2-(3/2-c_{L/R})] Y_{\alpha_{L/R}^+}(m_{L/R}^{(n)}/k) + (m_{L/R}^{(n)}/k) Y'_{\alpha_{L/R}^+}(m_{L/R}^{(n)}/k)} \end{aligned} \tag{H.14}$$

$$\begin{aligned} f_n^{--}(c_{L/R}; y) &= sign(y) \frac{1}{\sqrt{2\pi R_c}} \frac{e^{2\sigma}}{\mathcal{N}_n} \left[J_{\alpha_{L/R}^-}\left(\frac{m_{L/R}^{(n)} e^{\sigma}}{k}\right) + b_{\alpha_{L/R}^-}^{--}(m_{L/R}^{(n)}) Y_{\alpha_{L/R}^-}\left(\frac{m_{L/R}^{(n)} e^{\sigma}}{k}\right)\right], \\ b_{\alpha_{L/R}^-}^{--}(m_{L/R}^{(n)}) &= -\frac{J_{\alpha_{L/R}^-}(m_{L/R}^{(n)}/k)}{Y_{\alpha_{L/R}^-}(m_{L/R}^{(n)}/k)} \end{aligned} \tag{H.15}$$

for KK modes ($n \geq 1$), where $m_{L/R}^{(n)} = m_{KK}^{(n)}(c_{L/R})$ is the n-*th* KK scalar mass (the KK fermion spectrum is identical as we do not consider Sherk-Schwarz like mechanisms of SUSY breaking) and $\mathcal{N}_n$ is the normalization constant. At this level, the field redefinition has not been performed for the n*th* wave functions.

From the above wave function expressions, we deduce the useful relations

$$(\partial_y - (c_{L/R} + \frac{3}{2})\sigma') f_n^{--}(c_{L/R}; y) = -m_{KK}^{(n)}(c_{L/R})\; e^{\sigma} f_n^{++}(c_{L/R}; y), \tag{H.16}$$

$$(\partial_y - (-c_{L/R} + \frac{3}{2})\sigma') f_n^{++}(c_{L/R}; y) = m_{KK}^{(n)}(c_{L/R})\; e^{\sigma} f_n^{--}(c_{L/R}; y). \tag{H.17}$$

Concerning fermions, an example of KK decomposition is (in the two-component notation),

$$\zeta_L(x^\mu, y) = \sum_{n=0}^{\infty} \zeta_L^{(n)}(x^\mu)\omega_n^{++}(c_L; y), \tag{H.18}$$

$$\chi_L(x^\mu, y) = \sum_{n=1}^{\infty} \chi_L^{(n)}(x^\mu)\omega_n^{--}(c_L; y), \tag{H.19}$$

where c_L parametrizes the 5D mass of the Φ_L superfield in Eq.(G.11). The wave function $\omega_n^{++}(c_L; y)$ (respectively $\omega_n^{--}(c_L; y)$) is exactly equal [after the RS field redefinition] to the scalar superpartner wave function $f_n^{++}(c_L; y)$ (respectively $f_n^{--}(c_L; y)$) as imposed by SUSY. This remains true as long as the SUSY breaking does not occur through the Scherk-Schwarz mechanism. In fact, these scalar wave functions $f_n^{++/--}$ depend on the scalar bulk mass a and boundary mass b which are imposed by 5D SUSY to be the following functions of the fermionic superpartner bulk mass $c_L\sigma'$ [*c.f.* Eq.(G.29)], $a(c_L) = c_L^2 \pm c_L - 15/4$, $b(c_L) = 3/2 \mp c_L$ [*c.f.* Eq.(G.27)], relations rendering the scalar and fermion wave functions identical in terms of the c_L parameter. Analog remarks hold for the c_R case as well as for the KK masses $m_{KK}^{(n)}(c_{L/R})$.

A possible SUSY breaking framework – that we consider in this study without specifying the underlying breaking mechanism – is that additional bulk/brane masses arise for the scalar fields, encoded e.g. in $a(c_L) + \delta a$ and $b(c_L) + \delta b$: these corrective masses spoil the SUSY relations between scalar and fermion bulk/brane masses and in turn break SUSY. It is more convenient for the numerical calculation parts to define e.g. a new c_L^s parameter for scalars such that $a(c_L) + \delta a = a(c_L^s)$ and $b(c_L) + \delta b = b(c_L^s)$, c_L^s being different from the fermion (or superfield) mass parameter c_L in this framework. Then the fermion wave functions can still be written $\omega_n^{++/--}(c_L; y)$ while the scalar wave functions $f_n^{++/--}(c_L^s; y)$ are now controlled by an independent mass parameter related to the amount of SUSY breaking.
Note that such a SUSY breaking framework resembles the situation where additional (w.r.t. the pure 5D SUSY Lagrangian) bulk masses e.g. $\delta c_L\sigma'$ would appear for fermions. Indeed, the SUSY bulk masses for fermions $c_L\sigma'$ would be shifted to $c_L^f\sigma' = (c_L+\delta c_L)\sigma'$, a new mass independent from the scalar ones depending on $a(c_L), b(c_L)$ [one would deal here with $\omega_n^{++/--}(c_L^f; y)$ and $f_n^{++/--}(c_L; y)$]. This framework would be quantitatively equivalent to the previous one for final physical masses but would lead to an interesting alternative to usual SUSY breaking frameworks (4D or 5D): here typically both fermions and their scalar superpartners would be initially heavy (mainly due to their large and identical effective Yukawa couplings generated by equal wave functions), i.e. respecting the lower bounds on scalar masses, while the fermions would become lighter (reduced down to their measured masses) because of the effect of their arising SUSY breaking bulk masses [$\delta c_{L/R} > 0$] on wave functions.

Appendix I

4D versus 5D propagators

For a generic bulk field (expressed in terms of $z = \frac{e^{\sigma(y)}}{k}$)

$$\Phi(x^\mu, z) = \sum_n \phi^{(n)}(x^\mu) S_a^{(n)}(z)$$

satisfying the orthonormalization condition

$$\int_R^{R'} dz \left(\frac{R}{z}\right)^3 S_a^{(n)}(z) S_a^{(m)}(z) = \delta_{nm},$$

the 5D action and the corresponding KK decomposed 4D action are given by:

$$\mathcal{S}_5 = -\frac{1}{2}\int d^4x \int_R^{R'} dz \left(\frac{R}{z}\right)^3 \bar{\Phi}(x^\mu, z)\left[\eta^{\mu\nu}\partial_\mu\partial_\nu - \partial_z^2 + \frac{3}{z}\partial_z + \frac{a^2}{z^2}\right]\Phi(x^\mu, z) \tag{I.1}$$

$$\mathcal{S}_4 = -\frac{1}{2}\int d^4x \sum_n \bar{\phi}^{(n)}(x^\mu)\left(\eta^{\mu\nu}\partial_\mu\partial_\nu + m_n^2\right)\phi^{(n)}(x^\mu). \tag{I.2}$$

The equation of motion reads as

$$\left[-\partial_z^2 + \frac{3}{z}\partial_z + \frac{a^2}{z^2}\right] S_a^{(n)}(z) = m_n^2 S_a^{(n)}(z)$$

and the 2-point functions are defined as follows,

$$\text{From } \mathcal{S}_5: \quad \left[p^2 + \partial_z^2 - \frac{3}{z}\partial_z - \frac{a^2}{z^2}\right] G_5^{S_a}(p^2; z, z') = \delta(z - z') \tag{I.3}$$

$$\text{From } \mathcal{S}_4: \quad \left[p^2 - m_n^2\right] G_4^{(n)}(p^2) = 1. \tag{I.4}$$

From above, one can find the relation between the 4D and 5D propagators:

$$G_5^{S_a}(p^2;z,z') = \sum_{n=0}^{\infty} G_4^{(n)}(p^2) S_a^{(n)}(z) S_a^{(n)}(z') = \sum_{n=0}^{\infty} \frac{S_a^{(n)}(z) S_a^{(n)}(z')}{p^2 - m_n^2} \tag{I.5}$$

$$= \frac{S_a^{(0)}(z) S_a^{(0)}(z')}{p^2} + \sum_{n\geq 1} \frac{S_a^{(n)}(z) S_a^{(n)}(z')}{p^2 - m_n^2}. \tag{I.6}$$

Indeed, one can check that:

$$\left[p^2 + \partial_z^2 - \frac{3}{z}\partial_z - \frac{a^2}{z^2}\right] G_5^{S_a}(p^2;z,z') = \left[p^2 + \partial_z^2 - \frac{3}{z}\partial_z - \frac{a^2}{z^2}\right] \sum_n G_4^{(n)}(p^2) S_a^{(n)}(z) S_a^{(n)}(z')$$

$$= \sum_n G_4^{(n)}(p^2) \left[p^2 + \partial_z^2 - \frac{3}{z}\partial_z - \frac{a^2}{z^2}\right] S_a^{(n)}(z) S_a^{(n)}(z') = \sum_n G_4^{(n)}(p^2) \left[p^2 - m_n^2\right] S_a^{(n)}(z) S_a^{(n)}(z')$$

$$= \sum_n S_a^{(n)}(z) S_a^{(n)}(z') = \delta(z - z'). \tag{I.7}$$